A Local Degradation Approach to the Numerical Analysis of Brittle Fracture in Heterogeneous Rocks

A thesis submitted to the University of London

By

Zhi Fang

Petroleum Engineering and Rock Mechanics Research Group

Department of Earth Science and Engineering

Imperial College of Science, Technology and Medicine

In fulfilment of the requirements
for the degree of Doctor of Philosophy of the University of London
and for the Diploma of Imperial College

September 2001

Abstract

Rock is a heterogeneous material, brittle fracture of which in compression is a complicated progressive process caused by isolated microstructural changes, or dissipative processes. This thesis develops a novel numerical methodology for the simulation of these isolated processes, such that the resulting non-linear macroscopic behaviour can be predicted.

The core of the model is elemental degradation. As suggested by laboratory investigations, the microscopic processes involved in rock fracture can be classified into a combination of brittle and ductile processes. The former cause degradation in both local elasticity and strength of a material, with the extent of degradation being determined by the degree of bond breakage in forming crack surfaces or the like, whereas the latter lead only to plastic deformation. Thus, if the deformation of a material is dominated by brittle processes, more degradation occurs than when ductile processes dominate.

The elemental degradation is represented by a parameter degradation index, which is introduced in this research and defined as the ratio of the degradation occurring at a certain confining stress level to the corresponding degradation occurring under uniaxial conditions. In combination with an elasto-plastic constitutive relation, the degradation model yields an elastic-brittle-plastic elemental constitutive behaviour. In the model, failure of an element causes disturbance of the local stress field, which may lead to progressive failure of surrounding elements. A finite difference scheme is used to implement the degradation model.

Brittle fracture of rock specimens in laboratory compression tests has been simulated with the model. The results show that this algorithm, when employing the Weibull distribution function for introduction of heterogeneity and the Hoek-Brown criterion for evaluation of elemental strengths, is capable of reproducing many characteristics associated with brittle fracture in heterogeneous rocks. These include: the development of fracture from the elemental scale to the macroscopic scale; fracture pattern as a function of confining pressure; variation of fracture plane angle with respect to confining pressure; the complete stress-strain curve and corresponding strain energy

dissipation characteristics; dependence of the stress-strain curve on confining pressure; and loading-unloading hysteresis loops.

An engineering application of the degradation model to the analysis of mine pillar behaviour is presented. In terms of isolated fracture processes and the corresponding macroscopic mechanical behaviour, the degradation model produces simulation results that are similar to field observations. This suggests that the degradation model is a powerful approach to the study of macroscopic brittle behaviour encountered in rock mechanics and rock engineering.

This thesis is dedicated to my family

Acknowledgements

The author wishes to express his sincere thanks to the Overseas Research Student Scholarship Scheme (ORS) for a research student scholarship and the Petroleum Engineering and Rock Mechanics Research Group at Imperial College, the Henry Lester Trust and the Great Britain-China Centre for additional financial support in conducting this research.

He would like to thank his supervisor, Dr J. P. Harrison, for precious support to this work, for general advice and guidance throughout the execution of the work, for discussions on the damage and fracture characteristics of rock and rock masses, and for the critical assessment of the draft of the thesis.

He is appreciative to Dr R.W. Zimmerman for the critical review of the first state of the execution of this research, and the arrangement of a bursary for the writing-up stage.

He is grateful to many people in the Petroleum Engineering and Rock Mechanics Research Group for their help during the author's study at Imperial College. These include:

Mr. J. R. Marsden and Mr. J.W. Dennis for their helpful discussions and advice on the laboratory characteristics of rock fracture;

Drs I. W. Yeo, T. R. Reid, and K. Kostakis for advice on the organisation of the transfer report and the use of various software;

Mr. V. Rasouli, Mr. S. D. Lee and Mr. T. Ward, current rock mechanics research students, for technical discussions, friendship and help of many kinds.

In addition, he is thankful to Ms. R. Browning and Mr. J. Stewart, the librarians in the Department of Earth Science and Engineering at Imperial College, for their assistance in reference searching.

Finally, the author wishes to thank his wife, Weichuan, and his daughter, Yuxi, for their constant understanding, patience and assistance, without which this work would not have been completed.

Contents

Abstract..... 2

Acknowledgments.....5

List of figures.....12

List of tables..... 18

Nomenclature..... 19

1 Introduction.....23

1.1 The role of analysis of brittle fracture in heterogeneous rocks.....23

1.2 Current approaches to modelling rock fracture.....24

1.3 Study purpose and approach..... 25

1.4 Structure of the thesis.....26

2 Rock brittle fracture in compression — experimental and field evidence..... 28

2.1 General fracture process and deformation behaviour of rock in compression.....29

2.1.1 Rock fracture in compression..... 29

2.1.2 General deformation behaviour of rock in compression.....31

2.1.3 Fracture process and macroscopic behaviour of rock in compression..... 34

2.2 Microscopic phenomena of fracture formation in rock.....36

2.2.1 Classification of microcracks.....37

2.2.2 Formation of microcracks.....38

2.2.3 Propagation of microcracks..... 41

2.2.4 Coalescence of microcracks.....43

2.3 Effects of microcracking on mechanical behaviour of rock..... 45

2.3.1 Dilatancy.....45

2.3.2 Degradation of stiffness and strength of rock.....45

2.4 Influence of confining pressure on rock failure.....46

2.4.1 Effects on microscopic processes..... 48

2.4.2 Effects on the stress-strain curve..... 49

2.4.3 Effects on formation of fracture.....51

2.5 Rock fracturing processes and associated acoustic emission events.....52

2.5.1 Relation of acoustic emission activities to macroscopic behaviour..... 52
2.5.2 Acoustic emission events and rock properties.....55
2.5.3 Implication of acoustic emission events and formation of faults..... 55
2.6 Fracturing and deformation behaviour of rock in large scale..... 56
2.6.1 Fracture of large scale specimens..... 57
2.6.2 Rock fracture in the field..... 60
2.6.3 Rock fracture in nature..... 63
2.7 Closure..... 65

3 State of the art in the modelling of progressive rock fracture.....67
3.1 Discrete micromechanics models based on fracture mechanics..... 68
3.1.1 Physical models for the extension of microcracks.....68
3.1.2 Micromechanics-based modelling of rock compressive fracture behaviour.....70
3.1.3 Comments on the current micromechanics-based models for rock fracture.....73
3.2 Continuum damage mechanics models.....74
3.2.1 CDM models.....75
3.2.2 Applications of CDM to the analysis of rock fracture.....76
3.2.3 Comments on the current CDM models for rock fracture.....77
3.3 Statistical model.....78
3.3.1 Statistical models.....79
3.3.2 Application of statistical models to rock fracture.....79
3.3.3 Comments on current statistical models for rock fracture.....83
3.4 Closure and ideas for improved model development..... 84

4 Development of a degradation model for brittle fracture of rock.....86
4.1 Background..... 87
4.1.1 Energy balance theory..... 88
4.1.2 Crack extension and corresponding changes in material elastic constants.....89
4.1.3 Independence of energy release and loading configuration.....90
4.1.4 Strength loss of brittle materials undergoing fracturing..... 92
4.2 Degradation and energy dissipation associated with rock compressive failure....92
4.2.1 Degradation associated with microcracking..... 93
4.2.2 Energy dissipation characteristics associated with microcracking..... 94

4.2.3 Degradation index.....95
4.3 A local degradation model for fracture of rock materials in compression.....101
4.3.1 Rock elements.....102
4.3.2 Deformation behaviour of rock elements and the concept of local degradation.....103
4.3.3 Theoretical description of local degradation.....104
4.3.4 Degradation and degradation index of rock elements.....105
4.4 Failure criteria for rock elements.....109
4.4.1 Failure criteria.....109
4.4.2 Representation of degradation associated with failure criteria.....112
4.5 Elemental constitutive relation.....114
4.5.1 Elasto-plastic constitutive relations.....114
4.5.2 Flow rule and the plastic potential function.....114
4.5.3 Determination of λ.....116
4.6 Introduction of heterogeneity.....117
4.6.1 Uniform distribution.....117
4.6.2 Normal distribution.....118
4.6.3 Weibull distribution.....118
4.7 Stress redistribution associated with degradation.....118
4.8 Dissipation of elastic strain energy.....121
4.9 Summary of the degradation model.....122
4.9.1 Model parameters.....123
4.9.2 Model set up.....123
4.9.3 Model analysis.....124
4.10 Closure.....128

5 Implementation of the degradation model.....131

5.1 Selection of an appropriate numerical method.....132
5.1.1 Numerical methods.....132
5.1.2 Selection between FEM and FDM.....133
5.1.3 Explicit and implicit solution methods.....134
5.2 FLAC Code.....134
5.2.1 Basic numerical techniques in FLAC.....135
5.2.2 FLAC embodied constitutive models.....139
5.2.3 Finite difference grid, variables and sign conventions in FLAC.....142

5.2.4 FLAC commands and Fish programming language..... 143
5.2.5 Suitability of FLAC for the implementation of the degradation model..... 147
5.3 FLAC Implementation of the degradation model..... 148
5.3.1 Input and storage of model parameters..... 149
5.3.2 Conversion of strength property parameters..... 151
5.3.3 Introduction of heterogeneity..... 154
5.3.4 Calculation of the minor principal stress..... 157
5.3.5 Calculation and update of the degradation index..... 158
5.3.6 Calculation and update of stiffness degradation..... 158
5.3.7 Calculation and update of strength degradation..... 159
5.3.8 Calculation and update of the bulk and shear moduli..... 159
5.3.9 Calculation and update of other strength parameters..... 159
5.3.10 Calculation of elastic strain energy dissipation..... 163
5.3.11 Representation of fracture of materials..... 164
5.4 Simplified input parameters based on the uniaxial compressive and tensile strengths of rock..... 164
5.5 Summary of the model implementation procedures..... 166
5.6 Closure..... 167

6 Simulation of brittle fracture of rock specimens..... 171

6.1 Numerical model of laboratory tests on rock specimen..... 172
6.1.1 Model set-up..... 172
6.1.2 Loading methods..... 175
6.1.3 Model output..... 175
6.2 Choice of strength distribution and strength criterion for simulation of heterogeneous rock fracture..... 177
6.2.1 Input data..... 178
6.2.2 Investigation of distribution functions..... 179
6.2.3 Investigation of strength criteria..... 183
6.3 Mesh effect..... 185
6.3.1 Mesh effect with the degradation model..... 186
6.3.2 Optimal mesh size..... 187
6.4 Role of degradation parameter n_d..... 188
6.5 Influence of Weibull parameter m_w on simulated rock fracture..... 190

6.6 Simulated fracture process of heterogeneous rocks..... 192
6.6.1 Fracture of a specimen at 0 MPa confining pressure..... 193
6.6.2 Fracture of a specimen at 20 MPa confining pressure..... 194
6.6.3 Fracture of a specimen at 60 MPa confining pressure..... 196
6.7 Remarks..... 198
6.7.1 Microscopic processes..... 199
6.7.2 Final fracture patterns..... 204
6.7.3 Angle of fracture planes..... 205
6.7.4 Macroscopic stress-strain curve..... 206
6.7.5 Energy dissipation characteristics..... 208
6.7.6 Hysteresis loops..... 209
6.8 Closure..... 210

7 Simulation of brittle fracture of mine pillars..... 212
7.1 Definition of the problem..... 213
7.1.1 Conventional pillar design methods..... 213
7.1.2 Performance of pillars *in situ*..... 216
7.1.3 Numerical simulation of progressive fracture of pillars..... 217
7.2 Degradation model for pillars..... 217
7.2.1 Model set-up..... 218
7.2.2 Loading path..... 218
7.2.3 Input data..... 220
7.3 Simulated fracture of pillars..... 220
7.3.1 Slender pillars..... 220
7.3.2 Squat pillars..... 222
7.4 Strength of fracturing pillars..... 225
7.5 Influence of roof and floor contact conditions on pillar fracture..... 226
7.5.1 Friction angle of interfaces..... 227
7.5.2 Roof and floor stiffness..... 227
7.6 Closure..... 231

8 Conclusions and future work..... 233
8.1 Conclusions..... 233
8.1.1 Brittle fracture in heterogeneous rocks: the principal issues..... 233
8.1.2 The new degradation model..... 236
8.1.3 Findings resulting from use of the degradation model..... 238

8.2 Future work.....242

9 References..... 246

Appendix A Description of deformation and motion of material bodies..... 257

A.1 Explanation of terms..... 257

A.2 Lagrangian and Eulerian description..... 258

A.3 Deformation gradient and finite strain tensors.....260

A.4 Infinitesimal deformation theory and infinitesimal strain tensors..... 261

A.5 Equations of motion..... 262

A.6 Gauss divergence theorem..... 263

Appendix B FLAC code for the degradation model for rock specimens..... 264

B.1 Individual modules.....264

B.2 Code variables.....264

B.3 Operation procedure for the FLAC code.....266

B.4 Code listing..... 267

List of figures

2.1 Schematic of failure mechanism of rock specimens under compression.....30

2.2 A failed rock specimen in the laboratory (from Bieniawski, 1967).....30

2.3 Rock failure in uniaxial compression tests.....31

2.4 Marble specimens of equal strength after uniaxial compression, showing a range of failure fracture patterns (from Andreev, 1995).....32

2.5 Rock failure in triaxial compression tests.....33

2.6 Rock material behaviours represented by the stress-strain curve.....33

2.7 Typical stress-strain diagram for compressive test on rock specimens (after Weijermars, 1997).....34

2.8 SEM micrograph of an unstressed Darley Dale sandstone sample (from Wu et al., 2000).....37

2.9 Transgranular cracks at biotite grain boundaries in a stressed Westerly granite specimen (from Tapponnier and Brace, 1976).....39

2.10 Microcracking from quartz-feldspar grain boundary into quartz (from Kranz, 1983).....39

2.11 Schematic diagram of observed microcrack formation phenomena in Tennessee marble (after Olsson and Peng, 1976).....40

2.12 Pore-emanated cracks in a plagioclase grain in a tested Westerly granite sample (from Wong, 1982).....40

2.13 Microcracking from cleavage separation in feldspar in Barre granite (from Kranz, 1979a).....42

2.14 Microcracking leading to, and resulting from, grain crushing in a Darley Dale sandstone sample (from Wu et al., 2000).....42

2.15 Crack arrays formed in a deformed biotite grain in Westerly granite (from Tapponnier and Brace, 1976).....43

2.16 Basic coalescence phenomena of microdefects (after Kranz, 1979b).....44

2.17 Deformation of a rock material under increasing deviatoric stress (from Goodman, 1989).....46

2.18 Degradation of the elastic moduli of a failed rock in the laboratory

(from Hudson and Harrison, 1997)..... 47
2.19 Degradation of the strength of a rock in the laboratory (from Hudson and Harrison, 1997).....47
2.20 Post-peak fracture patterns developed in a diabase (from Wawersik and Brace, 1971).....48
2.21 Complete axial stress-strain curves obtained in triaxial compression tests on Tennessee Marble at various confining pressures (from Brady and Brown, 1992).....50
2.22 Macroscopic brittle failure occurs at larger critical strains as confining pressure increases (from Weijermars, 1997)..... 50
2.23 Deformation behaviours and typical fracture modes of rock in compression.....51
2.24 Stress-strain curve and microcracking frequency-strain for two rocks in uniaxial compression (from Scholz, 1968)..... 53
2.25 Accumulated frequency of microcracking events fitted to the inelastic volumetric strain in the dilatant region for three uniaxial compression tests on Westerly granite (from Scholz, 1968).....54
2.26 Axial stress against axial displacement for Westerly granite at 50 MPa confining pressure (from Lockner et al., 1991).....56
2.27 Sequential plots of locations of acoustic emission (from Lockner et al., 1991)... 56
2.28 Stress and AE event-rate vs time for a Gosford sandstone specimen (from Cox and Meredith, 1993).....57
2.29 Stress and cumulative AE events vs time for a Flechtingen sandstone specimen (from Zang et al., 1996).....57
2.30 Successive failure stages of a 2 foot cube coal specimen tested in the laboratory (from Bieniawski, 1967).....58
2.31 The failure mode of a 1 foot cube coal specimen (from Bieniawski, 1967).....59
2.32 The complete stress-strain curve in uniaxial compression obtained *in situ* for a square coal specimen (from Bieniawski and Van Heerden, 1975).....60
2.33 Tensile splitting fractures in the coal ribside of a longwall mining operation at 600 m depth (from Whittaker et al., 1992).....61
2.34 Failure modes of pillars in underground operations.....62
2.35 Suggested post failure characteristics for different quality rock masses (after Hoek and Brown, 1997).....63
2.36 A natural fractured rock structure (from Pusch, 1995).....64
2.37 Natural loading induced arrays in carbonate rocks of the Swiss Alps

(from Du and Aydin, 1991)..... 64
2.38 Similar fracture patterns on different scales (from Pusch, 1995)..... 64
3.1 Open crack models..... 69
3.2 Sliding crack model..... 69
3.3 Crack growth in Photoelastic plastic (from Brace and Bombolakis, 1963)..... 70
3.4 Crack array configuration and predicted stress-strain curves using the Kemeny and Cook model..... 72
3.5 Stress-strain curves of the Bukit Timah granite predicted by Li et al. (2000)..... 73
3.6 Simulated stress-strain and volumetric strain curves obtained using the Ofoegbu and Curran model (Ofoegbu and Curran, 1992)..... 77
3.7 Simulated stress-strain curves of Westerly granite at different confining pressures obtained using the Costin model (Costin, 1985)..... 78
3.8 Simulated loading-unloading stress-strain curves of Tennessee marble obtained using the Shao and Rudnicki model (Shao and Rudnicki, 2000)..... 78
3.9 Statistical model for local stress distribution within an inhomogeneous body subjected to an applied stress (from Scholz, 1968)..... 80
3.10 Simulated progressive failure of rock and the associated stress-strain curve obtained using the Tang model (from Tang et al., 2000)..... 81
3.11 Simulated progressive failure of rock and the associated stress-strain curve obtained using the Blair and Cook model (from Blair and Cook, 1998)..... 82
4.1 Compliance test piece (after Lawn and Wilshaw, 1975)..... 89
4.2 Illustration of elastic strain energy dissipation induced by a crack extension in constant displacement..... 91
4.3 Energy dissipation during an axial strain increment, $\delta\varepsilon$, of a rock specimen..... 95
4.4 Simplified stress-strain relations of rock under different confining pressures..... 96
4.5 Illustration of the decomposition of strain softening behaviour into a combination of brittle and ductile behaviours..... 97
4.6 Illustration of the definition of the degradation index..... 97
4.7 Variations of the degradation index of two rocks subjected to confining pressures..... 101
4.8 Schematic illustration of microstructural changes in a rock specimen under different confining pressures..... 103
4.9 Schematic illustration of elemental failure induced by microstructural changes within a rock specimen under different confining pressures..... 103
4.10 Simplified stress-strain relations for a rock element under different

confining pressures.....104
4.11 Illustration of the representative degradation in uniaxial compressive strength of rock elements failed in confining conditions..... 106
4.12 The Mohr-Coulomb strength criterion.....110
4.13 Shapes of Weibull distribution function with various values for shape parameter.....119
4.14 Illustration of stress changes induced by (a) elemental degradation and (b) elemental dilation to local vicinity.....120
5.1 Triangular elements in FLAC (after Itasca, 1995a).....136
5.2 Basic explicit calculation cycle in FLAC (after Itasca, 1995a).....139
5.3 Representation of the Hoek-Brown criterion by the linear Mohr-Coulomb surface.....151
5.4 Histogram of uniformly distributed data generated by FLAC.....155
5.5 Histogram of normally distributed data generated by FLAC.....155
5.6 Histogram of data following a Weibull distribution, as generated by FLAC implementation.....156
5.7 Procedures for the implementation of the degradation model.....167
5.8 Degradation module contained in the flow chart presented by Figure 5.7.....169
6.1 Schematic of a cross section from a cylindrical rock specimen.....173
6.2 A plane strain geometry for analysing brittle fracture of rock specimens in the laboratory.....174
6.3 Predicted fracture pattern and corresponding stress-strain curve of a rock specimen subjected to a confining pressure of 60 MPa with the Mohr-Coulomb elemental strength criterion.....184
6.4 Predicted fracture pattern and corresponding stress-strain curve of a rock specimen subjected to a confining pressure of 60 MPa with the Hoek-Brown elemental strength criterion.....184
6.5 Fracture patterns displayed by models with different mesh sizes.....187
6.6 Stress-strain curves corresponding to models with different mesh sizes.....187
6.7 Fracture patterns displayed by models with different parameter n_d.....189
6.8 Stress-strain curves corresponding to models with different parameter n_d.....189
6.9 Illustration of the relation between the degradation index and confining stress.....190
6.10 Fracture patterns displayed by models with different parameter m_w.....191
6.11 Stress-strain curves corresponding to models with different parameter m_w.....191

6.12 Simulated fracture process of a rock specimen under uniaxial compression.....193
6.13 Simulated stress-strain curve and strain energy dissipation characteristics corresponding to the fracture process displayed in Figure 6.12.....194
6.14 Simulated fracture process of a rock specimen subjected to a confining pressure of 20 MPa.....195
6.15 Simulated stress-strain curve and strain energy dissipation characteristics corresponding to the fracture process displayed in Figure 6.14..... 196
6.16 Simulated fracture process of a rock specimen subjected to a confining pressure of 60 MPa.....197
6.17 Simulated stress-strain curve and strain energy dissipation characteristics corresponding to the fracture process displayed in Figure 6.16.....198
6.18 Simulated fracture process of a rock specimen subjected to a confining pressure of 40 MPa.....199
6.19 Simulated stress-strain curve and strain energy dissipation characteristics corresponding to the fracture process displayed in Figure 6.18.....200
6.20 Simulated fracture process of a rock specimen subjected to a confining pressure of 80 MPa.....201
6.21 Simulated stress-strain curve and strain energy dissipation characteristics corresponding to the fracture process displayed in Figure 6.20.....202
6.22 Influence of confining pressure on the initiation of local degradation and on the number of degraded sites at the peak strength.....202
6.23 Isolated fracture process of the rock specimen simulated under 20 MPa confining compression.....203
6.24 Final fracture patterns of real and simulated rock under various confining pressures.....204
6.25 Fracture of sandstone specimens under various confining pressures (from Ramez, 1967).....205
6.26 Fracture of simulated rock specimens under various confining pressures.....206
6.27 Variation of the fracture plane angle of rock specimens as a function of confining pressure.....206
6.28 Stress-strain curves of simulated rock specimens under various confining pressures.....207
6.29 Hysteresis loops produced by the degradation model under uniaxial compression.....209
7.1 Pillar strength vs *w/h* ratio predicted by various empirical formulae.....215

7.2 Pillar stress magnitude and distribution as affected by the width of the pillar as compared with the width of the opening (W_{open}) (After Holland, 1962).....216
7.3 A numerical plane strain model for a single pillar system.....218
7.4 Illustration of loading path for performing numerical analysis of pillar fracture behaviour.....219
7.5 Simulated fracture process of a pillar with a *w/h* ratio of 0.5.....221
7.6 Simulated stress-strain relation for a pillar with a *w/h* ratio of 0.5.....222
7.7 Simulated fracture process of a pillar with a *w/h* ratio of 2.0.....223
7.8 Simulated stress-strain relation for a pillar with a *w/h* ratio of 2.0.....224
7.9 Comparison of pillar strength prediction by the degradation model and the various power or similar formulae in Table 7.1.....225
7.10 Confinement at the centre of the simulated pillar with various *w/h* ratios..... 226
7.11 Simulated fracture patterns of a pillar with a *w/h* ratio of 2.0 and various interface friction angles.....228
7.12 Simulated stress-strain relations for a pillar with a *w/h* ratio of 2.0 and various interface friction angles.....229
7.13 Simulated fracture patterns of a pillar with a *w/h* ratio of unity and various roof and floor stiffnesses.....230
8.1 Hysteresis loops produced by the degradation model with two degradation processes.....234
A.1 Position of typical particle in reference and current configurations (after Mase and Mase, 1999).....258
A.2 Points *P* and *Q* in the reference configuration becomes *p* and *q* in the current configuration (after Mase and Mase, 1999).....260
B.1 Operation procedures for FLAC degradation model code for rock specimens...266

List of tables

2.1 Descriptions of rocks used for experiments (after Scholz, 1968)..... 53

4.1 Estimation of the degradation index for Tennessee marble.....100

4.2 Estimation of the degradation index for Vosges sandstone.....100

4.3 Required parameters for an analysis of brittle fracture of rock with the degradation model.....124

5.1 FLAC grid variables used in the implementation of the degradation model..... 143

5.2 FLAC pre-defined variables used in the implementation of the degradation model.....144

5.3 Basic commands in FLAC..... 145

5.4 Basic statements in Fish language.....147

5.5 Extra variables specified to the degradation model parameters.....150

5.6 Ratio of the uniaxial compressive strength to the tensile strength of rocks (from Pusch, 1995)..... 165

6.1 Composites of rocks from different distribution functions and strength criteria.....178

6.2 Input data for models with different distribution functions.....179

6.3 Fracture patterns displayed by models with different distribution functions and strength criteria.....180

6.4 Stress-strain curves displayed by models with different distribution functions and strength criteria.....181

6.5 Strain energy dissipation characteristics displayed by models with different distribution functions and strength criteria.....182

7.1 Pillar strength formulae (*w* and *h* in metres).....215

7.2 Input data for the simulation of pillar fracture..... 220

B.1 Individual modules in FLAC code of the degradation model for rock specimens.....265

Nomenclature

Latin letters

A	Area
δA	Elemental area
$2a$	Initial crack length
b_i	Force per unit mass
C	Compliance of an elastic system
c	Cohesion
E	Young's modulus
E_{ij}	Lagrangian finite strain tensor
δE	Young's modulus degradation
δE_u	Young's modulus degradation in uniaxial compression
e_{ij}	Eulerian finite strain tensor
F	Force
F_{ij}	Deformation gradient
h	Pillar height
G	Shear Modulus
K	Bulk modulus
k	Slope of the line relating σ_1 and σ_3
k_{pillar}	Strength of a reference specimen in pillar strength formulae
L	Boundary length
m and m_i	Hoek-Brown parameters
n_d	Degradation parameter
n_i	Unit normal pointing out of a surface
P_i	Linear momentum
R	Radius of cylindrical open cracks
r_d	Degradation index
r_{pillar}	Constant in pillar strength formulae
S	Stiffness
δS	Stiffness degradation

δS_u	Stiffness degradation in uniaxial compression
s	Hoek-Brown parameter
T_0	Tensile strength
δt or Δt	Time step or time interval
U	Total energy of a mechanical system
U_a	Potential energy of the applied loading system
U_e	Strain energy of an elastic medium
U_m	Mechanical energy of a mechanical system
U_{rand}	Uniform random number between 0 and 1
U_s	Free energy expended in creating new crack surfaces
δV	Elemental volume
w	Pillar width
x_a and x_b	Minimum and maximum values in the uniform distribution
m_w, x_0 and x_u	Weibull distribution parameters
x_μ and x_σ	Mean and standard deviation in the normal distribution
$\hat{\boldsymbol{e}}_i$ and $\hat{\boldsymbol{I}}_i$	Unit vectors
x, x_i, $\boldsymbol{x}$ or $\boldsymbol{X}$	Rectangular Cartesian coordinates
u, u_i or $\boldsymbol{u}$	Displacement
v_i, $\boldsymbol{v}$, $\dot{\boldsymbol{x}}$ or $\dot{\boldsymbol{X}}$	Velocity
$\boldsymbol{a}$, $\dot{\boldsymbol{v}}$, $\ddot{\boldsymbol{x}}$ or $\ddot{\boldsymbol{X}}$	Acceleration

Greek symbols

α_{pillar} and β_{pillar}	Constants in pillar strength formulae
β	Angle between the normal to a fracture plane and the direction of the major principal stress
γ	Angle between the initial crack plane and the major principal stress direction
δ or Δ	Increment
δ_{ij}	Kronecker delta
ε or ε_{ij}	Strain
θ	Angle between the growing crack plane and the initial crack plane
λ	Parameter in the flow rule
λ^l *and* μ^l	Lamé's constants
ν	Poisson's ratio

ρ	Density
σ or σ_{ij}	Stress or strength
σ_1	Major principal stress
σ_2	Minor principal stress in biaxial stress state and immediate stress in general stress state
σ_3	Minor principal tress in general stress state
σ_c	Uniaxial compressive strength
σ_{con}	Confining stress
σ_f	Critical stress for crack growth
σ_n	Normal stress
$\delta\sigma$	Strength degradation
$\delta\sigma_c$	Degradation in uniaxial compressive strength
$\delta\sigma_{cu}$	Strength degradation in uniaxial compression
τ	Shear stress
φ	Angle of the slope of the line relating σ_1 and σ_3
ϕ	Angle of friction
ψ	Dilation angle
χ	Free surface energy per unit area

Subscripts

d	Degraded value
du	Degraded value in uniaxial compression
duc	Ductility
g	Griffith criterion
h	Hoek-Brown criterion
if	Interface
max	Maximum value
p	Plastic strain
pillar	*Pillar*
u	Uniaxial compression
w	Weibull distribution

Superscripts

e	Elastic strain
l	Lamé's constant

p	Plastic strain

Operators

d	Derivative
∂	Partial derivative

1 Introduction

1.1 The role of analysis of brittle fracture in heterogeneous rocks

Rock is a natural material that is very close to human beings. On one hand, the world that human beings live on is constructed from rock, and on the other hand, rock has been used as a structural material for a far longer period than any other single material (Jaeger, 1979). Many branches of engineering (for example, civil, mining, petroleum, and natural gas engineering) construct and maintain on, or within, rocks structures such as highways, railways, waterways, pipelines, foundations, pillars, tunnels, chambers, shafts, oil reservoir wells, open pit mines, natural and excavated rock slopes, dams, underground storage facilities for oil, gas, water and nuclear waste, and so on (Bieniawski, 1996).

In engineering fields such as those mentioned above, a primary concern with rock is stress-induced brittle fracture. Construction of rock structures, for example, induces perturbed stress fields such that spalling, axial splitting or shear fracturing may be produced within surrounding rock masses, and eventually macroscopic failure of the structures may occur. The lesser outcome of such a type of failure is its influence on the effectiveness and efficiency of the structure, and the increased cost of maintaining the structure. Of more serious concern is that the failure may lead to the termination of the service for which the structure is constructed, and a threat to personal safety. Thus, the prediction of brittle fracture of rock is of prime importance for designing underground excavations, petroleum engineering structures and civil engineering constructions, and for devising methods to prevent such hazards as rockbusts (Bieniawski, 1967).

Brittle fracture is also of interest in the earth sciences. Across a wide range of geological phenomena, extending from the small-scale penetrative deformation associated with hand specimens to the large-scale deformation involved in major tectonic processes, it can be seen that all rocks within the shallow depth of the earth's

crust are fractured, as in faulting, for instance. Effective modelling of the brittle fracture of rock will make a considerable contribution towards our understanding of natural processes within the earth.

1.2 Current approaches to modelling rock fracture

Stress-induced rock fracture can occur in any stress state, whether tension, bending, shearing, or compression. When a rock body is loaded, stress concentrations are induced at the tips, or around the boundaries, of pre-existing flaws contained in the material, such as microcracks, pore spaces, cavities and the like. If the intensified stress acting on a critical flaw exceeds the local strength, microcracks will be initiated from the flaw. In tensile loading, the crack initiation is in the plane perpendicular to the maximum tensile stress direction and each increment of crack growth results in a further increase in stress intensity (Lawn and Wilshaw, 1975; Paterson, 1978; Lockner, 1995). Thus, once crack growth is initiated, even though only one crack is active, the crack extension is unstable until eventual failure occurs. This process and fracture behaviour can be analysed by applying the principles of fracture mechanics (Lawn and Wilshaw, 1975; Paterson, 1978; Costin, 1987).

Rock fracture as a result of compressive stresses, however, is more complicated than that in tension. Detailed studies by many researchers have suggested that at least the following complex processes can be distinguished in compressive failure (Brace, 1963; Brace and Bombolakis, 1963; Hoek and Bieniawski, 1965; Lawn and Wilshaw, 1975; Paterson, 1978; Kranz, 1983; Costin, 1983; 1987; Lockner, 1995). Firstly, for constant boundary conditions in compression, the crack growth, whose direction tends to be parallel to the direction of maximum compressive stress, decreases stress intensity, and further crack extensions require an increase in deviatoric stress to be applied. Secondly, as deviatoric stress increases and rock failure is approached, microcracking changes dramatically from random isolated positions to localised zones, and associated with this are changes in mechanisms for further cracking from tensile to shearing or a combination. Thirdly, fracture under compressive stresses is not caused by the growth of a single or isolated cracks as with tension or shearing, but is a result of the coalescence of many microcracks, in which the crushing, gliding, interlocking and rotation of rock pieces may contribute to the microstructural kinetics. Finally, it is not all the nucleated cracks generated during the loading history, but only those with

favourable configurations, that link with each other to form the eventual fracture or shear bands.

The complexity of the micromechanisms involved in compressive brittle fracture makes modelling the entire fracture process very difficult. Fracture mechanics disciplines have been introduced in order to analyse fracture behaviour in compression and are now capable of dealing with the extension of single or isolated cracks in an elastic continuum (Nemat-Nasser and Horii, 1982; Steif, 1984; Ashby and Hallam, 1986; Sammis and Ashby, 1986; Ingraffea, 1987; Kemeny and Cook, 1987; Li, et al., 2000), but the localisation and coalescence of dense cracks which involve multiple micromechanisms associated with complicated stress patterns are still difficult to formulate.

Damage mechanics is another approach commonly used for the prediction of rock compressive failure (Dragon and Mroz, 1979; Costin, 1985; 1987; Ofoegbu and Curran, 1992; Shao and Rudnicki, 2000). In this approach, the effect of cracking or fracturing on overall structures is taken into consideration, and successes have been seen in reproducing the deformational behaviour of materials. However, as the configuration is mainly based on periodic structures or on uniformly distributed representative elements within the materials, the prediction is only limited to the overall mechanical behaviour rather than the isolated processes of rock undergoing fracture.

Statistical modelling is another technique used in the analysis of brittle failure of rock (Whittaker et al., 1992). This technique uses the concept of sites, or bonds, to represent a material under consideration. These sites or bonds behave in accordance with basic laws or rules, and any mechanistic models about the site or bond behaviour can be incorporated. In addition, heterogeneity of materials can be easily introduced into a statistical model, varying the properties of specific sites or bounds. Thus, with the aid of numerical methods, statistical techniques provide a powerful means to reproduce the fracture process of brittle rock, and successes have been seen in this approach recently (Blair and Cook, 1998; Tang et al., 2000). However, as the principles indicate, when using this technique a more realistic result relies on a more realistic law or rule for site or bond behaviour, and it is this that is sought in this research.

1.3 Study purpose and approach

Rock brittle failure is the eventual result of the progressive process of brittle fracture developed from micro scales. A rational model should be able to predict both the

fracturing process and the associated non-linear mechanical behaviour. This research develops a new approach to handling fracture formation from micro to macro scales in rock brittle failure by means of describing local micromechanisms.

The numerical analysis of brittle fracture requires equations of equilibrium or motion to be formulated on the basis of the deformed microstructural configurations of the material under consideration. Since the micromechanisms involved in compression are complex to handle, the related microstructural configurations are usually unknown in advance of failure and so an alternative approach is required. Failure of rock may be considered to be governed by the local strength or stiffness of the material. Microcracking at one site introduces damage effects to local strength and stiffness, and this redistributes the stress around other sites. In the case of increased loading, microcracking influences damage patterns at these sites. As a result, fracture develops and the material deteriorates. Once cumulative damage reaches such a degree that subsequent damage does not require further increase in external loading, overall failure of the material takes place.

Taking the above into account, a sound mechanistic model is required to couple the damage effect on the strength and stiffness, on a microscopic or elemental scale, with the induced stress redistribution in advancing brittle fracture of rock. This research has developed a new model for analysing brittle fracture of rock by means of this approach.

1.4 Structure of the thesis

This thesis comprises nine chapters, with supporting appendices. Chapter 2 is an extensive review of the literature on the knowledge of rock brittle failure established by laboratory tests, acoustic emission detection and field investigations. The fracture process from micro to macro scales and the resulting mechanical behaviour of rock under compression is presented in detail, and the influence of confining pressure on the development of brittle fracture in rock is highlighted.

In Chapter 3, a literature survey is carried out on the current state of modelling brittle fracture of rock in compression. In this survey, fracture mechanics models, damage mechanics models, and statistical fracture models for predicting fracture of brittle materials are covered and commented. A strategy for developing a new model based on dissipative processes is also given in this chapter.

The development of a new model for simulating the dissipative processes associated with rock brittle fracture is presented in Chapter 4. After a description of the

theoretical basis, the microscopic behaviour of rock undergoing fracture is analysed with the aid of physical evidence. Finally, a new model is developed, in which damage mechanics principles and elasto-plasticity are incorporated with statistical techniques.

Chapter 5 deals with the implementation of the developed model. The finite difference method, with its ability to accommodate large plastic strains and the inclusion of an efficient formulation for multiple non-linear interactions among elements, is used to implement the model.

The results of using the model to simulate rock failure in the laboratory is presented in Chapter 6. Different rocks are emulated to investigate the operation of the model, and as a result the fracture process and the associated mechanical behaviour and dissipative characteristics of heterogeneous rock are explored in detail.

Chapter 7 presents the application of the model to mine pillar fracture behaviour. Pillar failure *in situ* is well documented and has been studied intensively by several numerical methods. Here, pillar fracture behaviour, with respect to isolated fracturing processes, is simulated with the new model. The results compare well with those observed in the field.

Chapter 8 summarises the work in terms of conclusions and recommendations for future work. All the related conclusions drawn from this research are given in this chapter. In addition, based on the discussions and comments on the model results, further research associated with improvements to the model are considered and suggested here.

Finally, all the references that contribute to this research are listed in Chapter 9.

2 Rock brittle fracture in compression — experimental and field evidence

Rock comprises an aggregate of crystals and amorphous particles joined together by varying amounts of cementitious materials (Jaeger and Cook, 1979). The interaction between these crystals, particles and cementitious materials and such voids, pores, slips, cracks, and mini faults as exist gives rise to the various mechanical responses of rocks to applied stresses. Even the same kind of rock, when it is in different shapes or subject to different stress circumstances, will fail in different ways and exhibit different deformation characteristics. Thus, the study of the response of a rock material to an applied disturbance "… involves understanding the material properties and the pre-existing boundary conditions as well as the nature of the disturbance itself" (Hudson, 1989).

Laboratory experiments have been traditionally used as a simple and effective way to investigate the influences of the large number of competing effects on fracture formation of rock materials subjected to a variety of applied stresses, with *in situ* tests being auxiliary. In the past decades, advanced techniques such as optical microscopes, the scanning electron microscope, the transmission electron microscope and acoustic emission detection have been applied to laboratory experiments and *in situ* tests by numerous researchers to monitor fracture creation (Thill, 1972; Hallbauer et al., 1973; Olsson and Peng, 1976; Tapponnier and Brace, 1976; Tullis and Yund, 1977; Kranz, 1979a, b; Wong, 1982; Ashby and Hallam, 1986; Lockner, 1992; Cox and Meredith, 1993; Zang et al., 1996; Baud and Meredith, 1997; Wu et al., 2000). These advanced studies have enhanced our understanding of the progressive nature of fracture.

In this chapter, an extensive literature review of the field is carried out. It surveys the range of published work covering results of laboratory and field tests, in order to establish the current state of the understanding of brittle failure mechanisms in rock. As rock structures normally serve in compressive circumstances, and the failure of brittle rock in compression is typically complicated, the emphasis of the review is placed on the formation of rock fracture under compressive stresses.

2.1 General fracture process and deformation behaviour of rock in compression

Laboratory investigations into failure mechanisms of rocks in compression are normally carried out by uniaxially and triaxially loading circular cylinders of length/diameter ratio 2 to 3 (Paterson, 1978; Jaeger and Cook, 1979; Kovari et al., 1983). Despite the influence of the large number of competing effects on the fracture process, most rocks, at room temperature and in low confinements, exhibit brittle behaviour (see the definition in Subsection 2.1.2) and the influences of the factors on fracture formation of different rocks are similar. Thus, a universal understanding of fracture mechanisms in brittle rocks is possible. On this basis, after a basic introduction of the general behaviour of rock undergoing failure, the fracture process and the associated macroscopic deformation behaviour of rock in compression are described in this section.

2.1.1 Rock fracture in compression

Rock fracture as a result of applied compressive stresses is a progressive process that includes the formation of microcracks at grain scale, and extension and coalescence of microcracks around, or through, grains. When a rock sample is loaded, stress concentrations are induced at the tips (or around the boundaries) of pre-existing flaws, such as microcracks, pore spaces, cavities and the like contained in materials. If the concentrated stress acting on the critical flaw exceeds the local strength, microcracks will be initiated from the flaw that continue to grow with increasing loading, either in the direction parallel to the direction of maximum compressive stress (Brace et al., 1966; Bieniawski, 1967; Bombolakis, 1973; Wong, 1982), or in a plane of high shear stress (Olsson and Peng, 1976; Tullis and Yund, 1977; Kranz, 1979a; Wong, 1982). When the density of microcracks reaches such a degree that the local shear stress components become dominant, the further propagation of microcracks changes direction and coalescence of microcracks occurs. As a result, one or more macroscopic fracture planes may form.

In laboratory tests, the exact formation of fracture planes is dependent on both the inherent properties of the rock in question and the external conditions. The contact conditions between the ends of rock samples and the platens have a noticeable influence on fracture formation (Jaeger and Cook, 1979; Andreev, 1995; Vardoulakis et al., 1998). Due to the frictional effect between the ends of the specimens and the platens,

confining effects are developed within the cone-shaped zones at the two ends of the specimen (Figure 2.1); the stresses between the two cones, however, contain the component of tension. As a result, a rock specimen under compression is susceptible to the formation of a pair of shear faults between these end zones (Wawersik and Fairhurst, 1970; Bieniawski, 1967). Figure 2.2 shows a typical result.

Studies have been carried out on testing rock specimens whilst reducing the interface effect (Andreev, 1995; Vardoulakis et al., 1998). It has been found that under uniaxial compression without end effects most rocks fail by axial splitting in one or more fracture planes (Figure 2.3). This is probably due to the magnitude of the tensile stress component developed within the whole body of the specimen, which is able to exceed the tensile strength more readily than the compressive stress. For some rocks, however, this effect is dependent on their structure. Figure 2.4 shows an example of test results on marble specimens in uniaxial compression under identical test conditions (Andreev, 1995). There are no specific local failure patterns near the ends, which means no frictional effects exist on the interfaces. The sample shown in Figure 2.4 (a) failed by axial splitting; the one shown in Figure 2.4 (b) failed in the form of a fault; Figures 2.4 (c) and (d) show samples that failed in combined patterns with axial splitting prevailing. Although the four samples failed in different patterns, the strength of each sample is similar.

Another external factor that influences the formation of fracture planes is the

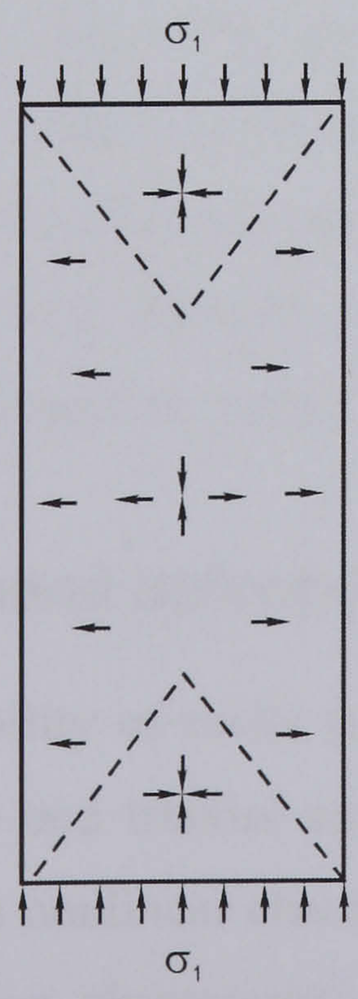
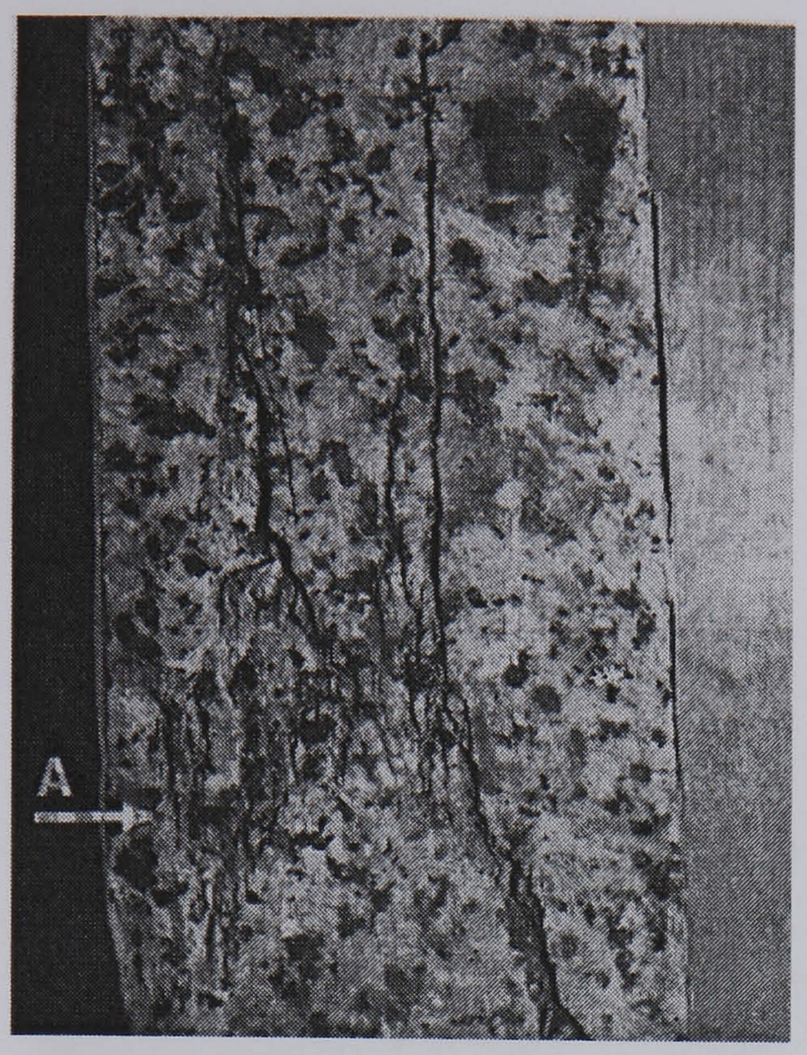


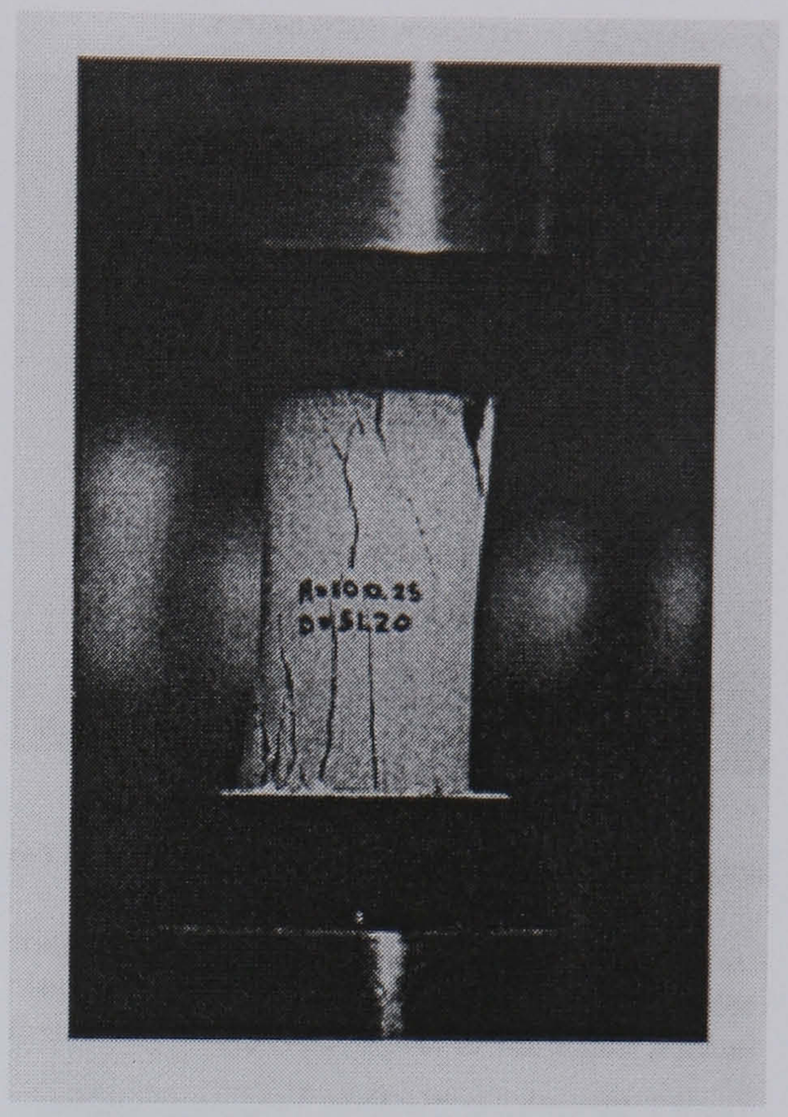
Figure 2.1. Schematic of failure mechanism of rock specimens under compression



Figure 2.2. A failed rock specimen in the laboratory (from Bieniawski, 1967)



(a) Monzonite (from Andreev, 1995)



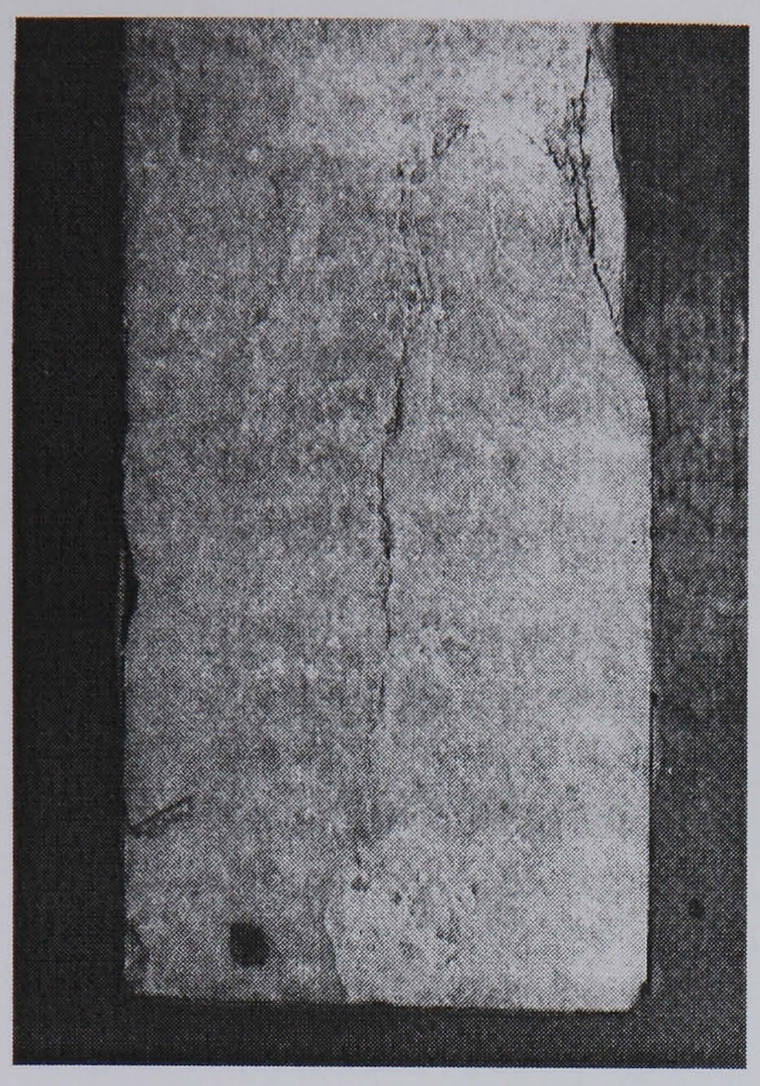
(b) Berea sandstone (from Vardoulakis et al., 1998)

Figure 2.3. Rock failure in uniaxial compression tests

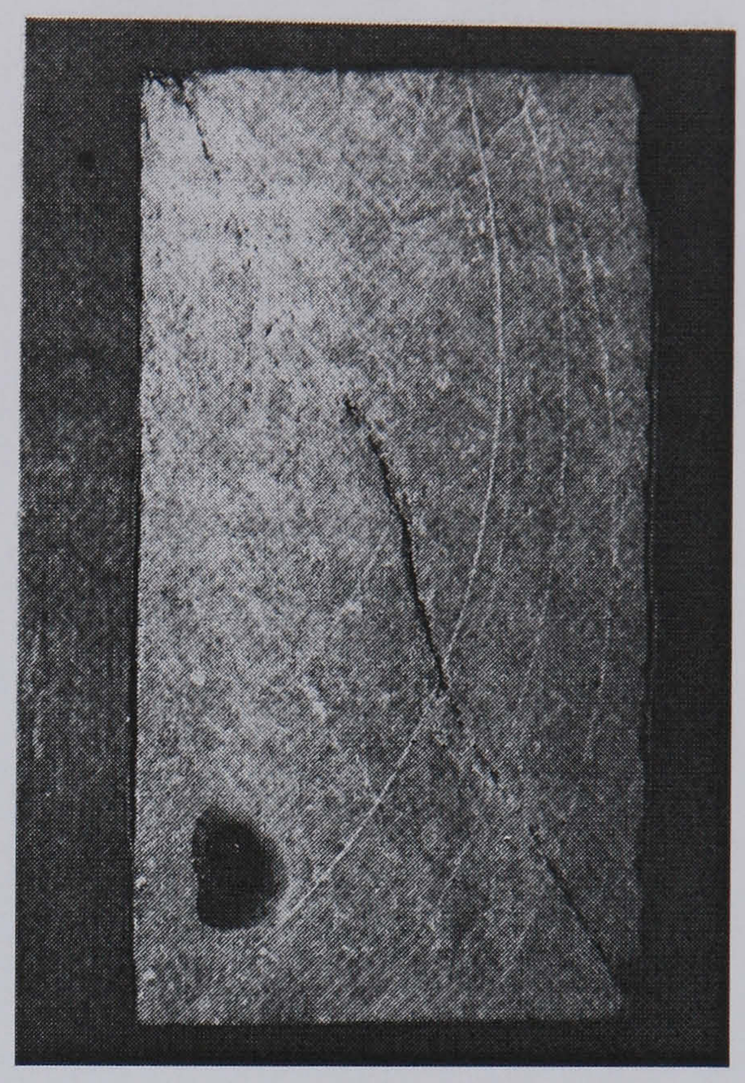
confining pressure. It is often observed that fracture in triaxial tests tends to develop in the form of one or more shear planes, with an angle of less than 45° to the maximum compressive stress (Figure 2.5). The actual angle of the fracture plane is, however, a function of the applied confining pressure: it increases with increasing confinement (Ramez, 1967; Wawersik and Fairhurst, 1970; Bésuelle et al., 2000). That said, when the confining pressure becomes sufficiently large, no fracture plane may be observed: instead, the specimen may fail by plastic flow (Ramez, 1967; Wawersik and Fairhurst, 1970; Thill, 1972; Bésuelle et al., 2000). The influence of the confining pressure on rock behaviour will be further discussed in Section 2.3.

2.1.2 General deformation behaviour of rock in compression

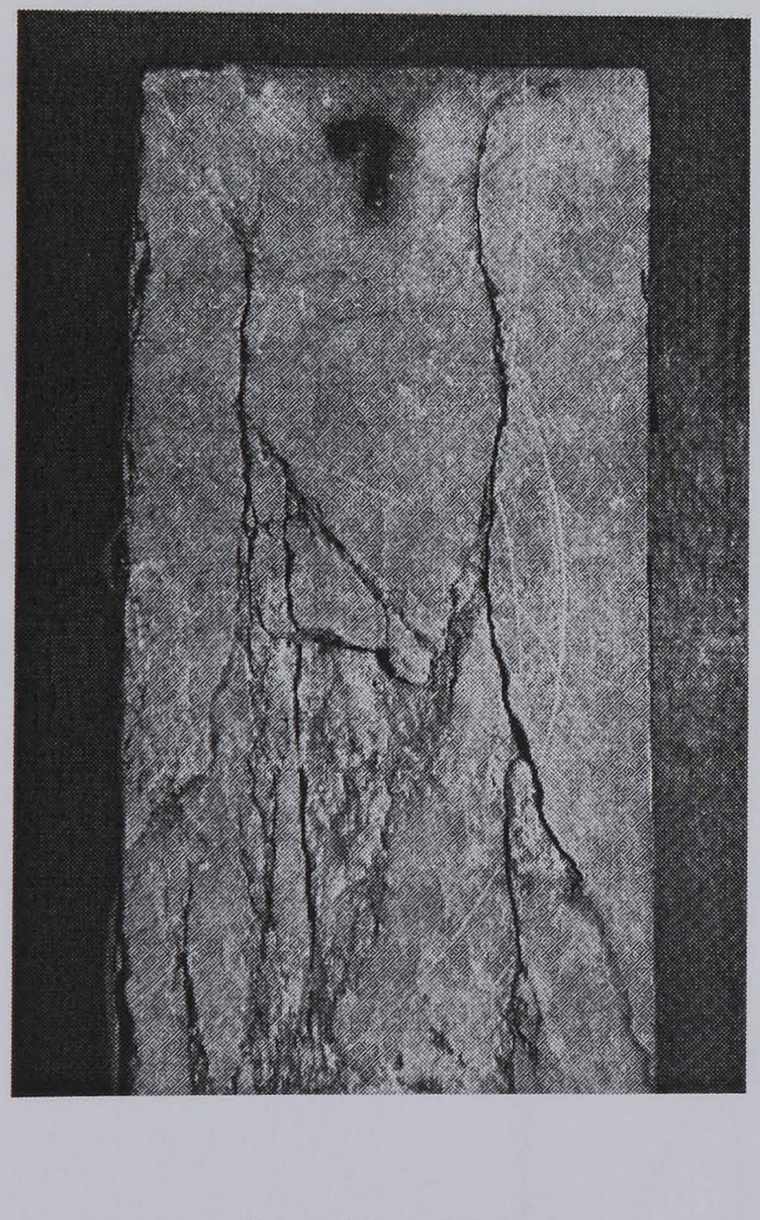
The deformability of rocks is usually expressed using the stress-strain curve obtained from uniaxial and triaxial compression tests in the laboratory. Generally, the overall curve exhibits nonlinear characteristics, with the nonlinearity of the curve being due to the deformation characteristics of the tested materials. There are variations on this theme for the huge variety of rock materials that exist, but in terms of the shape of the curve (Figure 2.6), the behaviour of rock materials can be generally classified into



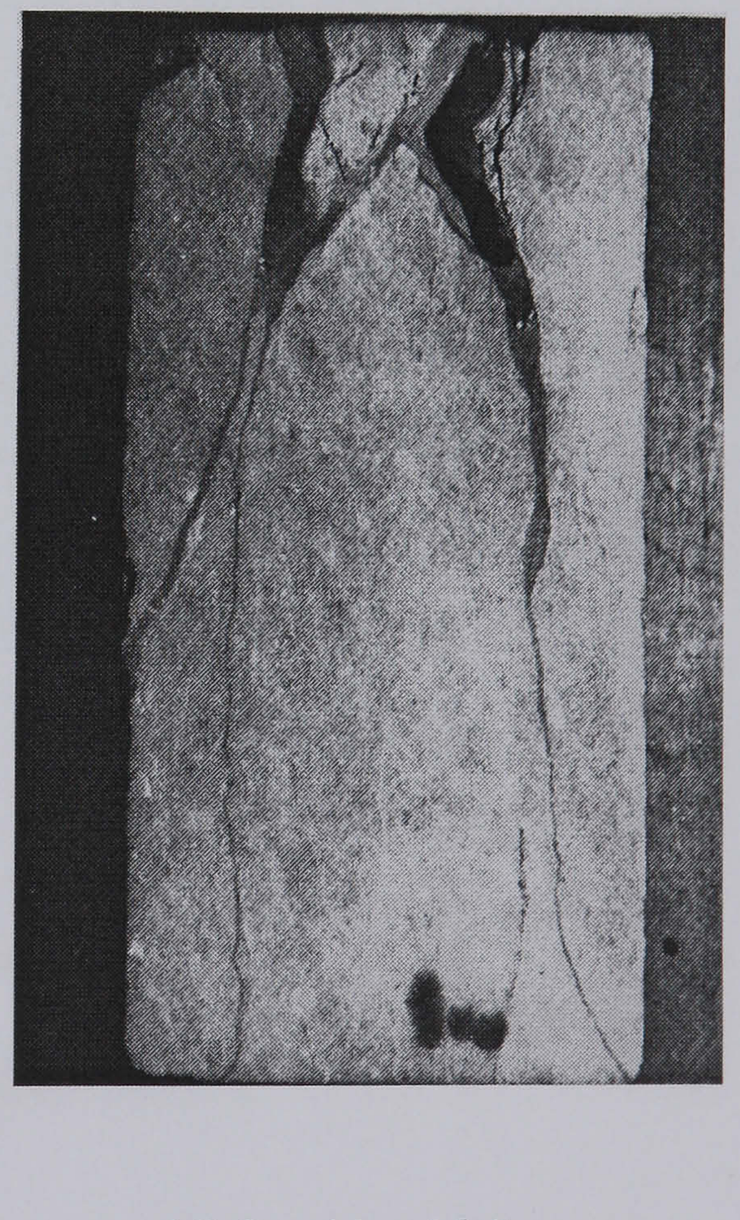
(a) Axial splitting



(b) Faulting

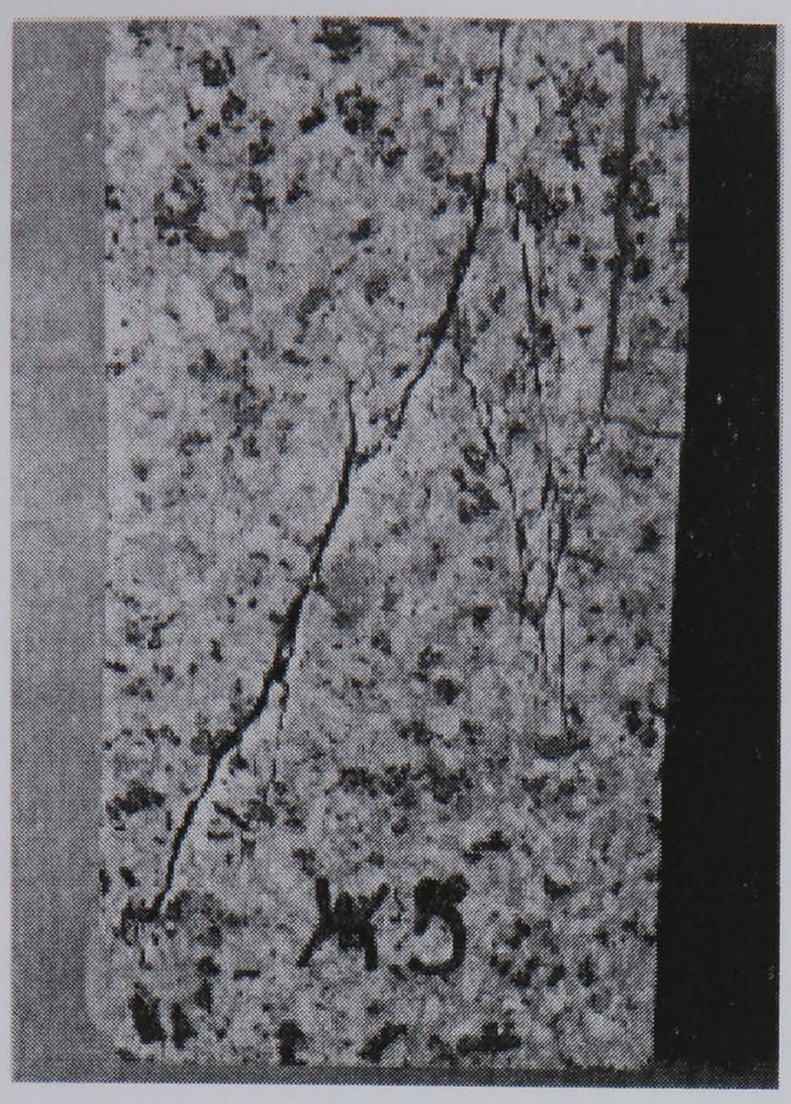


(c) Combined failure

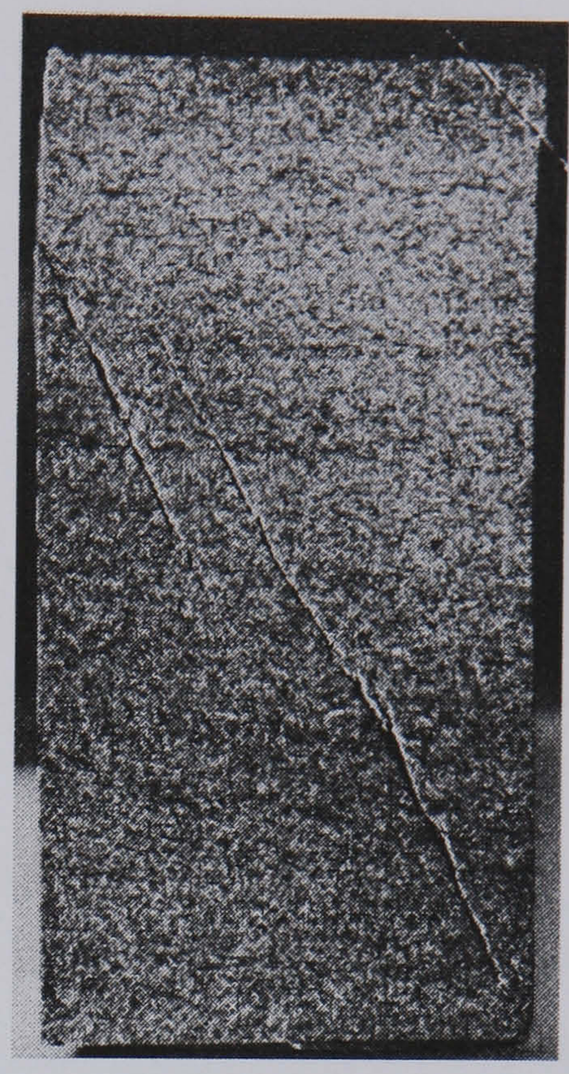


(d) Combined failure

Figure 2.4. Marble specimens of equal strength after uniaxial compression, showing a range of failure fracture patterns (from Andreev, 1995)



(a) Monzonite (from Andreev, 1995)



(b) Limestone (from Vardoulakis and Sulem, 1995)

Figure 2.5. Rock failure in triaxial compression tests

brittle and ductile (Jaeger and Cook, 1979; Brady and Brown, 1992; Hudson and Harrison, 1997).

Brittle behaviour concerns materials whose load carrying capability decreases with increasing deformation after the compressive strength is reached. For materials whose ability to resist load drops suddenly at a given strain level, the behaviour is defined as perfect brittle. On the other hand, a material that loses its load carrying capability progressively with increasing strain after the strength peak is said to behave in a strain-softening manner (Figure 2.6).

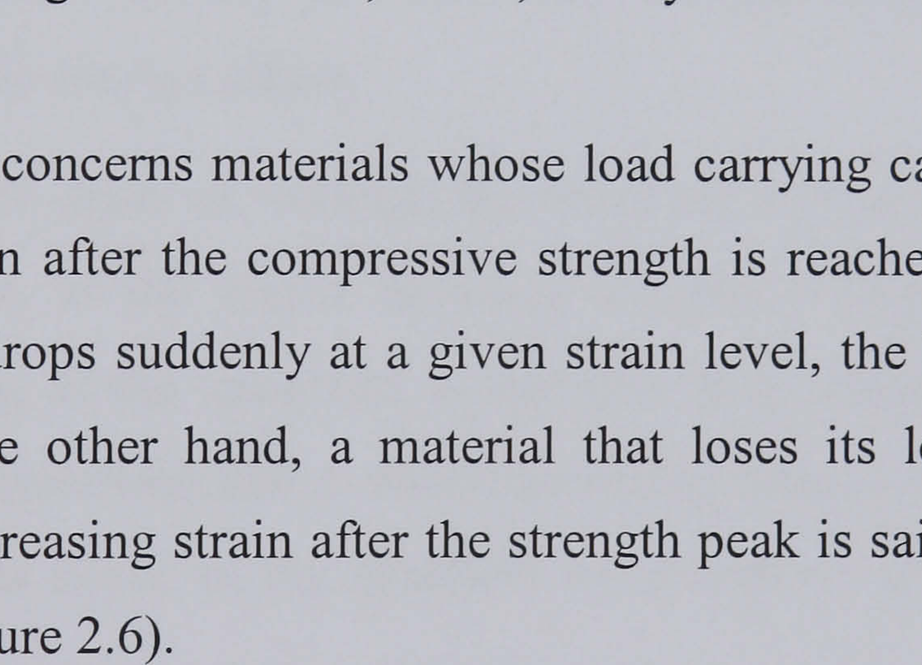


Figure 2.6. Rock material behaviours represented by the stress-strain curve

A ductile material can sustain permanent deformation without losing its load carrying capability. Perfect ductile materials can maintain their load carrying capability under a constant stress level whilst undergoing further permanent deformation. If the load carrying capability increases with increasing permanent strain, the materials are said to be strain-hardening (Figure 2.6).

2.1.3 Fracture process and macroscopic behaviour of rock in compression

In the previous subsection, we have introduced that rock in compression usually exhibits a nonlinear stress-strain relation. The nonlinearity of stress-strain curves is the result of microstructural changes leading to rupture of the material (see Brace et al., 1966; Bieniawski, 1967; Wawersik and Fairhurst, 1970). It is very important to note that the curve corresponds to different characteristics of the fracture process in the material's deformation history, and this is pronounced in brittle failure of rocks. Figure 2.7 shows a general complete stress-strain curve of a rock specimen undergoing uniaxial or low-confined compression. The entire stress-strain curve may be divided into six regions (Weijermars, 1997): OA, AB, BC, CD, DE and EF, and the corresponding fracture processes are described below.

(1) Region OA. At the onset of loading, the stress-strain curves show a slight convex upwards direction, as the elastic modulus and the Poisson's ratio increase with increasing loading. If the specimen is unloaded and reloaded at any point in this region, a slight hysteresis and a non-recoverable strain can be observed, but no irreversible effects occur in the structure or properties of the rock. All of these

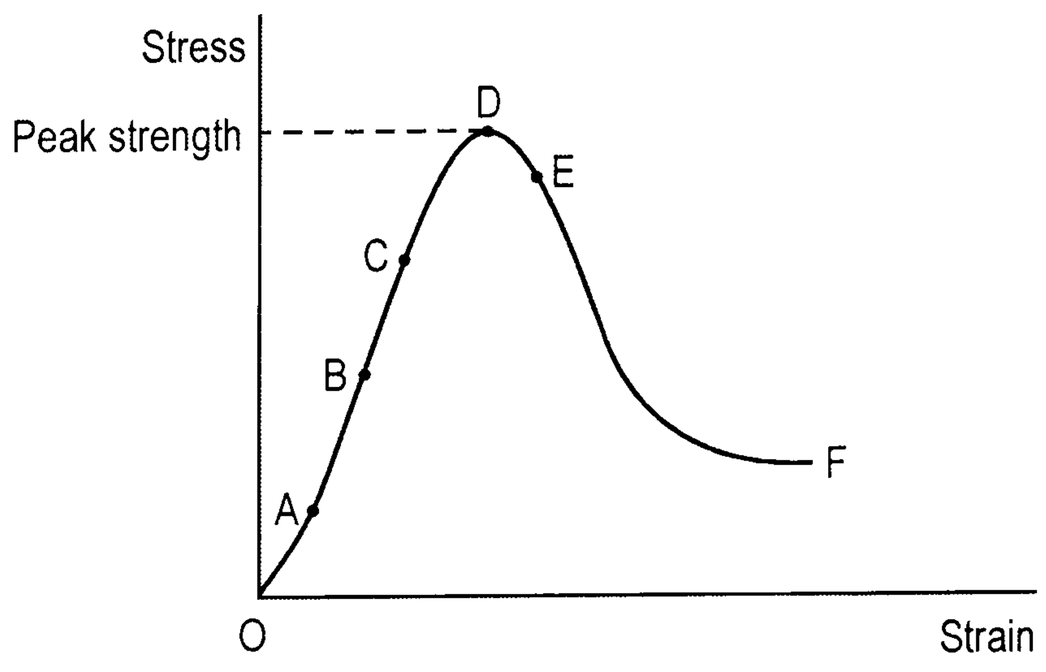


Figure 2.7. Typical stress-strain diagram for compressive test on rock specimens (after Weijermars, 1997)

effects are caused by the closure of pores or open cracks contained in the materials (Bieniawski, 1967; Jaeger and Cook, 1979; Andreev, 1995; Weijermars, 1997).

(2) Region AB. During this stage, no microcracking events take place. The behaviour of the specimen is elastic and all strains are linear with respect to the applied stress. In this region, the elastic modulus and the Poisson's ratio can be related to the axial and lateral strains by Hooke's law (Bieniawski, 1967; Andreev, 1995; Weijermars, 1997).

(3) Region BC. Microcracking begins randomly and crack propagation is stable, since crack growth is a function of the increase in loading (Tapponnier and Brace, 1976; Kranz, 1983; Ashby and Sammis, 1986; Lockner, 1995). As a result of sliding and buckling of rock slivers between cracks, and opening of new cracks, the lateral strain loses its linearity which leads to non-linearity of volumetric strain, and partially elastic volume dilation occurs (Brace et al., 1966; Bieniawski, 1967; Andreev, 1995; Weijermars, 1997). The axial strain, however, remains linear due to microcrack propagation being subaxially oriented to the maximum applied stress (Andreev, 1995). At this stage the Young's modulus remains constant but the Poisson's ratio increases with increasing axial strain (Brace et al., 1966; Bieniawski, 1967; Tapponier and Brace, 1976; Mohlhaus, 1979; Andreev, 1995).

(4) Region CD. The population of microcracks increases dramatically with increasing load, and microcracking tends to be localised near the peak point (Kranz, 1983; Lockner, 1995) and *en echelon* crack arrays may form (Wawersik and Brace, 1971; Tapponnier and Brace, 1976). As cracks grow, the lateral and volumetric strains increase, and the slope (tangent modulus) of the axial stress-strain curve decreases progressively to zero as the stress reaches the peak value; this is characterised as strain-hardening. The Poisson's ratio increases and tends to 0.5 (Andreev, 1995). Irreversible changes occur to the rock in this region, and successive cycles of loading and unloading start to trace out different curves, which are called hysteresis loops (Jaeger and Cook, 1979). This region is usually considered to begin at a stress level of two-thirds of the peak value (Jaeger and Cook, 1979).

(5) Region DE. The microcracking is accelerated to enhance the forking and coalescence of microcracks (Lockner, 1995; Menendez et al., 1996; Weijermars, 1997), and this can be indicated by the dramatic increase of acoustic emission events (Cox and Meredith, 1993; Zang et al., 1996; Baud and Meredith, 1997). As a

result, one or more macroscopic fractures or shear bands form at point E, but the rock remains intact (Lockner, 1995; Menendez et al., 1996; Weijermars, 1997). The stress-strain curve descends, with increasing negative tangent modulus, which is characterised as strain-softening; the secant modulus exhibits significant reduction, associated with the decrease in the load carrying capability of the material. Large permanent strain can be observed on unloading in this region (Jaeger and Cook, 1979).

(6) Region EF. After the formation of macroscopic fractures, rupture occurs by sliding of surfaces against each other, or by splitting. The rock disintegrates into parts and is retained as a whole solely by friction between the pieces (Weijermars, 1997). The stress-strain curve drops to the residual strength, which is characteristic of frictional plasticity.

In the engineering sense, the region OA is unimportant and can be assumed as linear elasticity (Jaeger and Cook 1979), which means that the relationship between the elastic modulus E, the Poisson ratio ν, the stress and strain can be expressed in terms of Hooke's law. Jaeger and Cook (1979) suggest that the region CD can be simplified as linear elasticity as well. This may be the case in engineering terms. However, detailed studies on microcracking phenomena suggest that this region is associated with an unstable cracking process and strain localisation in the deformed solid or structure (see Brace et al., 1966; Bieniawski, 1967; Andreev, 1995), and therefore this region should be analysed appropriately.

2.2 Microscopic phenomena of fracture formation in rock

In the earlier section, we have seen that rock fracture in compression is a progressive process involving the formation, propagation and coalescence of microcracks. Associated with this process is the non-linear macroscopic mechanical behaviour of the structure. In order to understand the nature of the complete rock fracture process, attempts have been made to investigate the microcracking events in the laboratory either by means of direct observation of separated sections or with the aid of the scanning/transmission electron microscopes (Olsson and Peng, 1976; Tapponnier and Brace, 1976; Tullis and Yund, 1977; Kranz, 1979a,b; Wu et al., 2000). As a result the associated phenomena for the nucleation, propagation and coalescence of microcracks

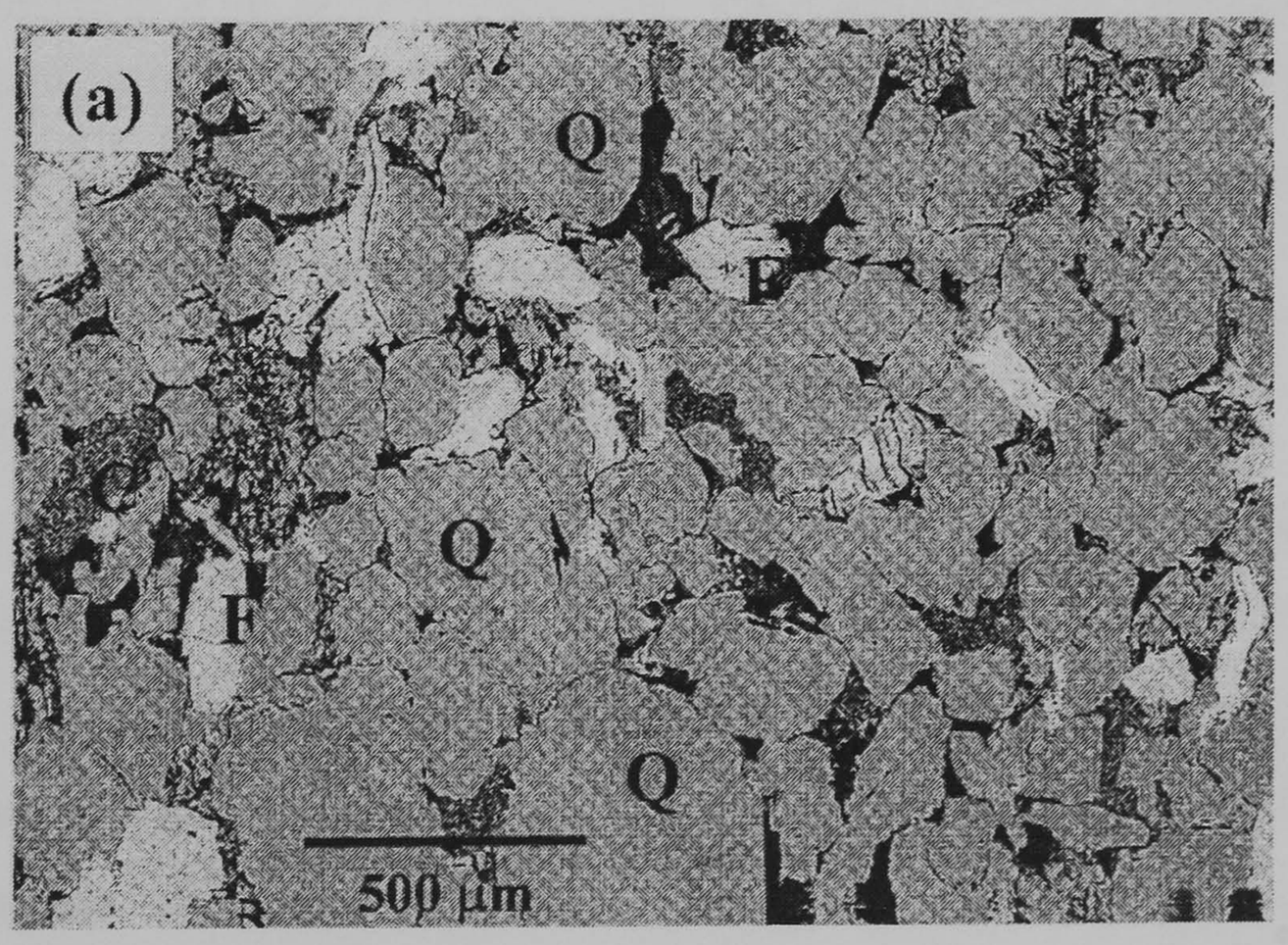
have been identified. A description of these results is given in this section.

2.2.1 Classification of microcracks

"A microcrack is an opening that occurs in rocks and has one or two dimensions smaller than the third" (cited by Kranz, 1983, from Simmons and Richter, 1976). By this definition, microcracks exist abundantly within a rock (Peng and Johnson, 1972; Bombolakis, 1973; Sprunt and Brace, 1974; Kranz, 1983; Wu, et al., 2000). A scanning electron microscope photograph of a Darley Dale sandstone section (Wu, et al., 2000) is presented in Figure 2.8, from which microcracks can be easily identified within, around or among the minerals comprising the rock.

In terms of the nature by which a microcrack exists within a rock, microcracks are subdivided into four groups: grain boundary cracks; intragranular cracks, intergranular cracks and transgranular cracks (Kranz, 1983). Grain boundary cracks are those associated or coincident with the grain boundary. Intragranular cracks are the cracks that exist totally within the grain. The cracks that run from a grain boundary crossing into one or more other grains are termed intergranular cracks. Those extending from grain boundary to grain boundary across a grain are called transgranular cracks.

It is notable to realise that there are plenty of microstructures within a rock that cannot be described as microcracks. These microstructures are the openings whose



(Q-quartz, C-clay and F-feldspar)

Figure 2.8. SEM micrograph of an unstressed Darley Dale sandstone sample (from Wu et al., 2000)

dimensions are of the same order in three directions (dark regions in Figure 2.8, for example). The terms of pore, void and cleavage etc. are representative for these microstructures.

2.2.2 Formation of microcracks

Grain boundaries, preexisting microcracks, pores, voids and other defects contained within a rock are the primary source for microcracking (Wawersik and Fairhurst, 1970; Kranz, 1983). These defects act as stress raisers to induce stress concentration under loading. As a result of the concentrated stress exceeding the local strength, cracks or microstructure collapse are produced. Experimental investigations at a microscopic scale have identified various phenomena of microcrack formation, which are presented below.

Microcracking from grain boundaries

Grain boundaries are particularly susceptible sites for crack formation (Hallbauer et al., 1973; Kranz, 1979a, 1983; Wong, 1982). Under compressive loading, stresses are easily concentrated on the point and line contacts between grains, and local failure may be produced. Tapponnier and Brace (1976) and Kranz (1979a) observed the formation of transgranular cracks from these regions in granite. Figure 2.9 illustrates one of typical results.

When a pair of welded grains, or the like, with different elastic properties are subjected to an externally applied compressive stress, the deformation of the softer grain produces tractions on the boundary of the stiffer one (Kranz, 1983; Andreev, 1995), and extensional cracks may be generated in the stiffer grain (Figure 2.10).

Microcracking at lamella-grain or lamella-lamella boundaries

In a study on marble, Olsson and Peng (1976) identified three types of micro-nucleation associated with twin lamellae (Figure 2.11). In the instance of a packet of twin lamellae intersecting a grain boundary, a crack may form at a high angle to the glide lamella (Figure 2.11(a)), or in the direction parallel to the lamella (Figure 2.11(b)). If two or more glide lamellae intersect each other (Figure 2.11(c)), cracks may be nucleated into single crystals or polycrystals.

Microcracking from the boundary of cavities and existing microcracks

Pores or voids contained within rock normally have irregular geometry. Under

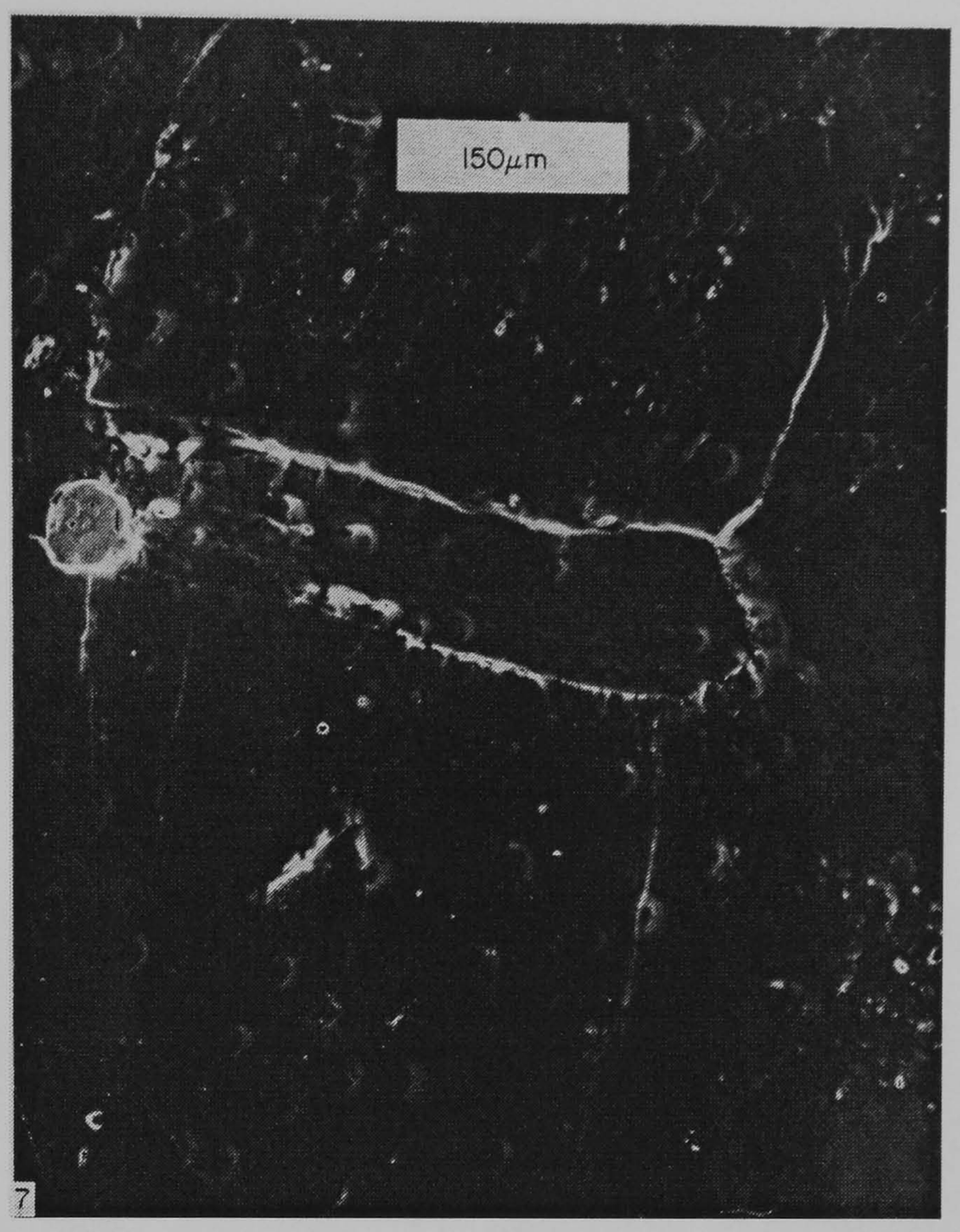


Figure 2.9. Transgranular cracks at biotite grain boundaries in a stressed Westerly granite specimen (from Tapponnier and Brace, 1976)

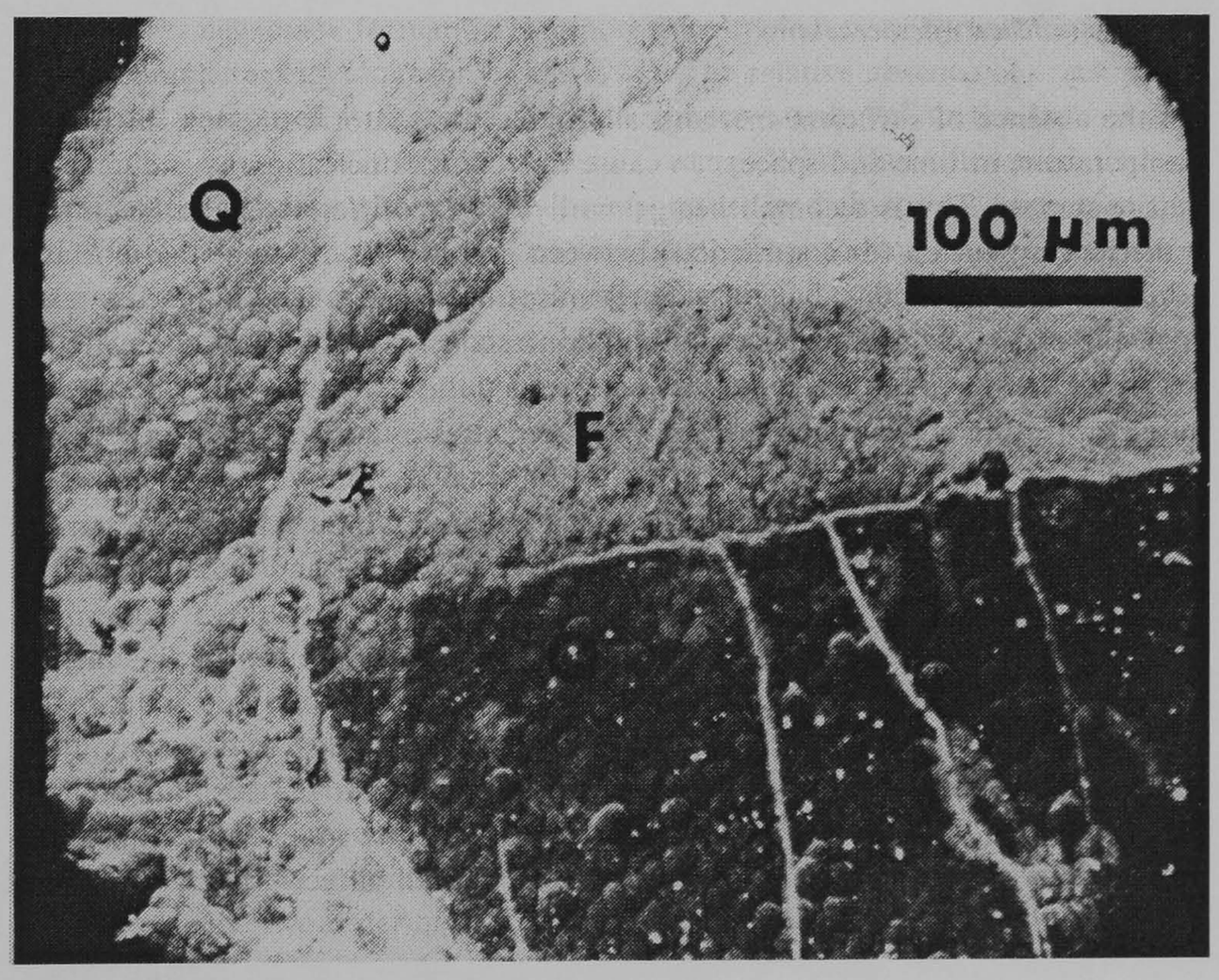
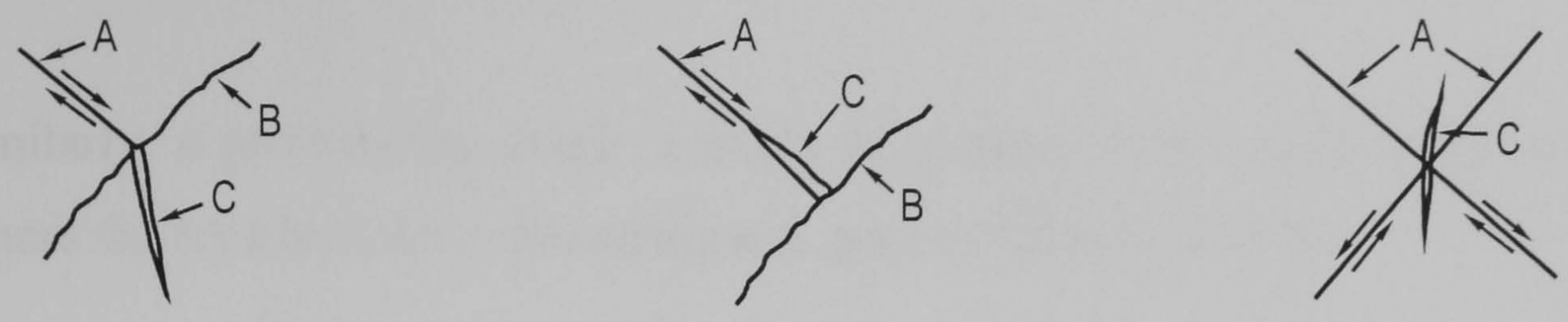


Figure 2.10. Microcracking from quartz-feldspar grain boundary into quartz (from Kranz, 1983)



(A-glide lamella, B-grain boundary and C-crack)

Figure 2.11. Schematic diagram of observed microcrack formation phenomena in Tennessee marble (after Olsson and Peng, 1976)

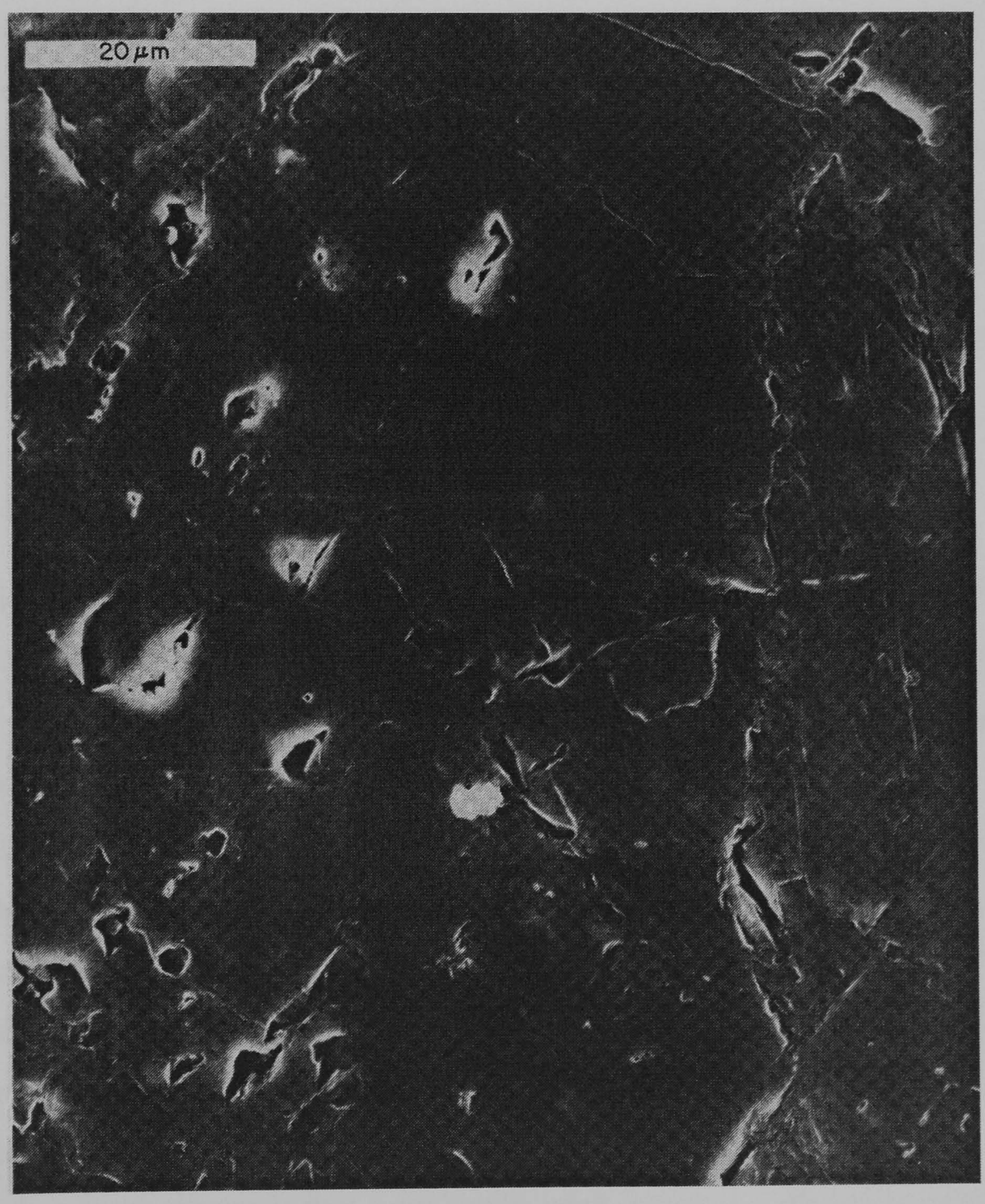


Figure 2.12. Pore-emanated cracks in a plagioclase grain in a tested Westerly granite sample (from Wong, 1982)

compressive loading, stress is concentrated at the acute angled points on the boundary of the microcavities, and one or two cracks may be generated from these points (Figure 2.12).

Similarly, a pre-existing crack is likely to generate new cracks from, or near, its tips, where the tensile stress concentration is greatest (Kranz, 1983).

Microcracking with cleavage separation

Cleavages are the planes that have the lowest bond strength and are contained within grains, such as biotite, microcline and feldspar in granite and calcite in marble (Hallbauer et al., 1973; Olsson and Peng, 1976; Tapponnier and Brace, 1976; Kranz, 1979a; Wu, et al., 2000). Under compression, suitably oriented cleavages easily separate and slide, and additional cracks may form associated with the separation (Figure 2.13).

Multiple cracking from cleavage planes may cause a grain to crush (Hallbauer et al., 1973; Olsson and Peng, 1976; Tapponnier and Brace, 1976; Wu, et al., 2000). Associated with the grain crushing, additional cracks may be induced in the surrounding grains (Olsson and Peng, 1976; Tapponnier and Brace, 1976). Figure 2.14 is a SEM (scanning electron microscope) micrograph indicating grain crushing phenomena in a Westerly granite sample, which was obtained by Wu et al. (2000). Tapponnier and Brace (1976) presented a similar phenomenon.

2.2.3 Propagation of microcracks

The initiation of microcracks decreases the local stress field, so that if the loading configuration remains constant the crack stops and remains stable (Kranz, 1979b; Lockner, 1995). Under increased loading the initiated cracks may grow, along with new microcracks being introduced (Kranz, 1979a).

At the initiation of a microcrack, the growth of nucleated cracks is affected by the heterogeneous nature of brittle materials. Under such influence, a nucleated crack may stop running or change its initial direction when it meets a heterogeneous phase like a hard grain or another defect (Lawn, 1993). In terms of the growing plane, generally there are three phenomena that have been observed in rock associated with the growth of a nucleated crack in compression.

The first phenomenon is that a nucleated crack grows in a direction parallel, or sub-parallel, to the direction of the maximum compressive principal stress (Brace et al., 1966; Bieniawski, 1967; Wawersik and Brace, 1971; Olsson and Peng, 1976). The

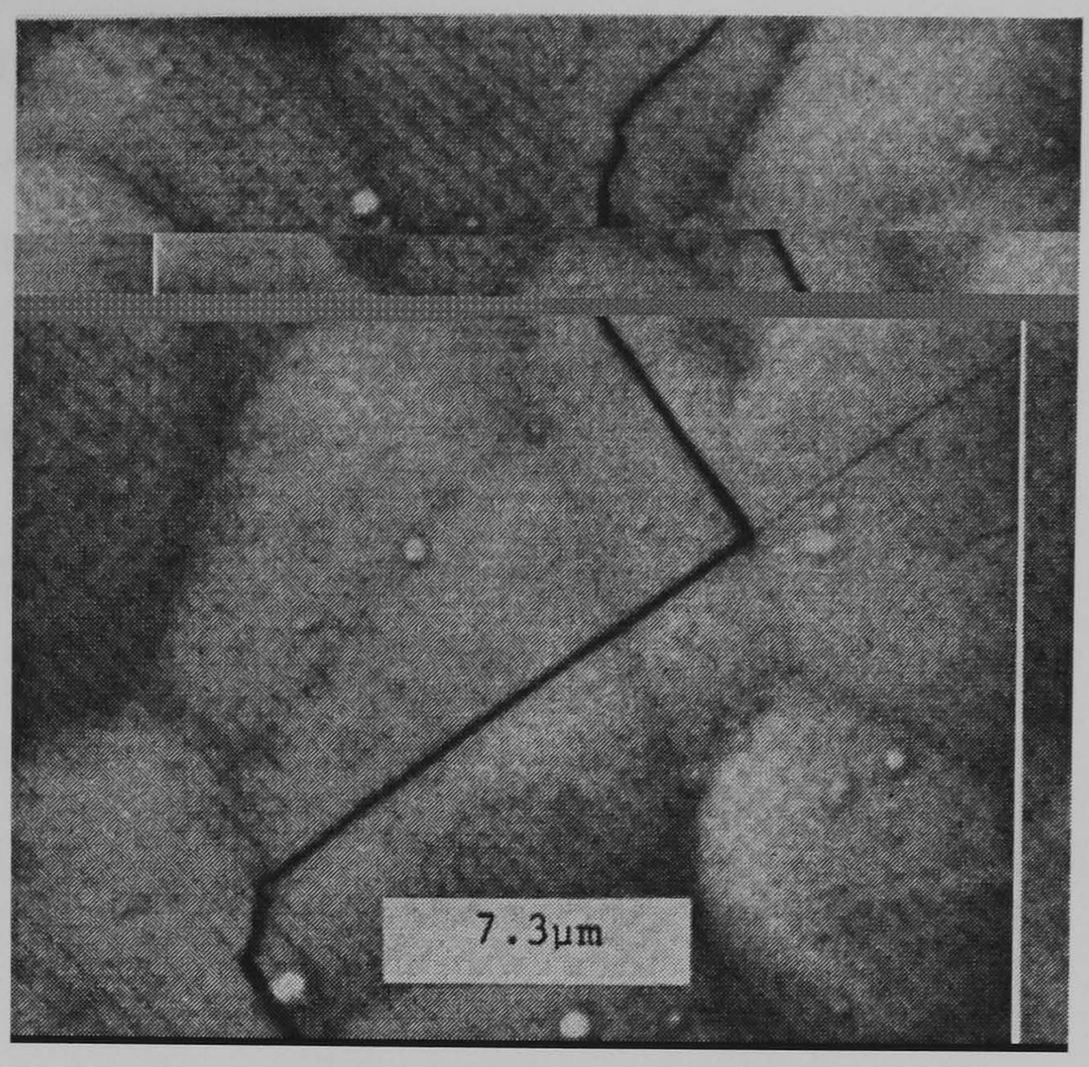


Figure 2.13. Microcracking from cleavage separation in feldspar in Barre granite (from Kranz, 1979a)

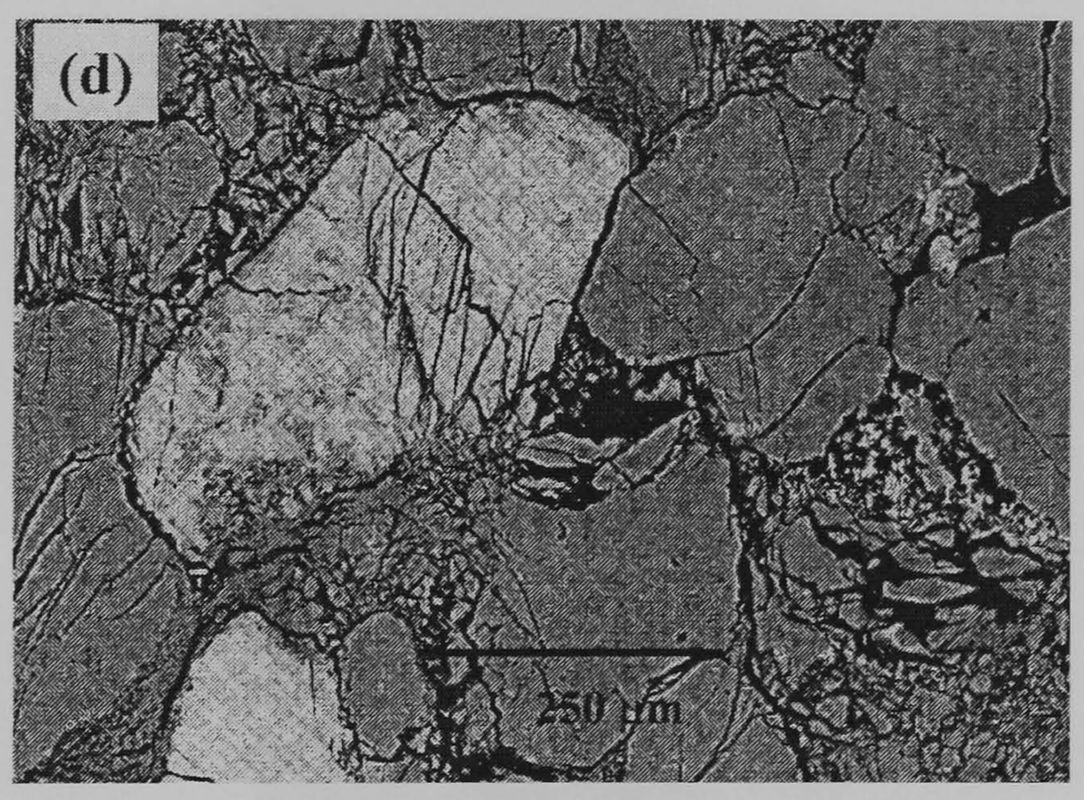


Figure 2.14. Microcracking leading to, and resulting from, grain crushing in a Darley Dale sandstone sample (from Wu et al., 2000)

second observed phenomenon in crack propagation is that the growth of a nucleated crack is in a plane of high shear stress (Olsson and Peng, 1976), inclined to the direction of greatest compression (Wawersik and Brace, 1971; Thill, 1972). The third phenomenon is that a crack tends to propagate in its initial plane (Wawersik and Brace, 1971).

In different stress fields and different rock types, the dominant phenomenon in crack propagation is different (Wawersik and Brace, 1971; Tullis and Yund, 1977).

Under certain circumstances, the propagated microcracks may line up to form one or several crack arrays (Hoek and Bieniawski, 1965; Wawersik and Brace, 1971; Tapponnier and Brace, 1976), which are called *en echelon* arrays (Figure 2.15). These characteristics will be further referred to in Section 2.4.1.

2.2.4 Coalescence of microcracks

Coalescence of microcracks is another complex aspect associated with rock fracture, and attempts have been made to investigate the mechanisms associated with various crack linking phenomena (Kranz, 1979a; Shen, 1993; Wong and Chau, 1997). Most of these have been conducted by predefining crack geometries (Shen, 1993; Wong

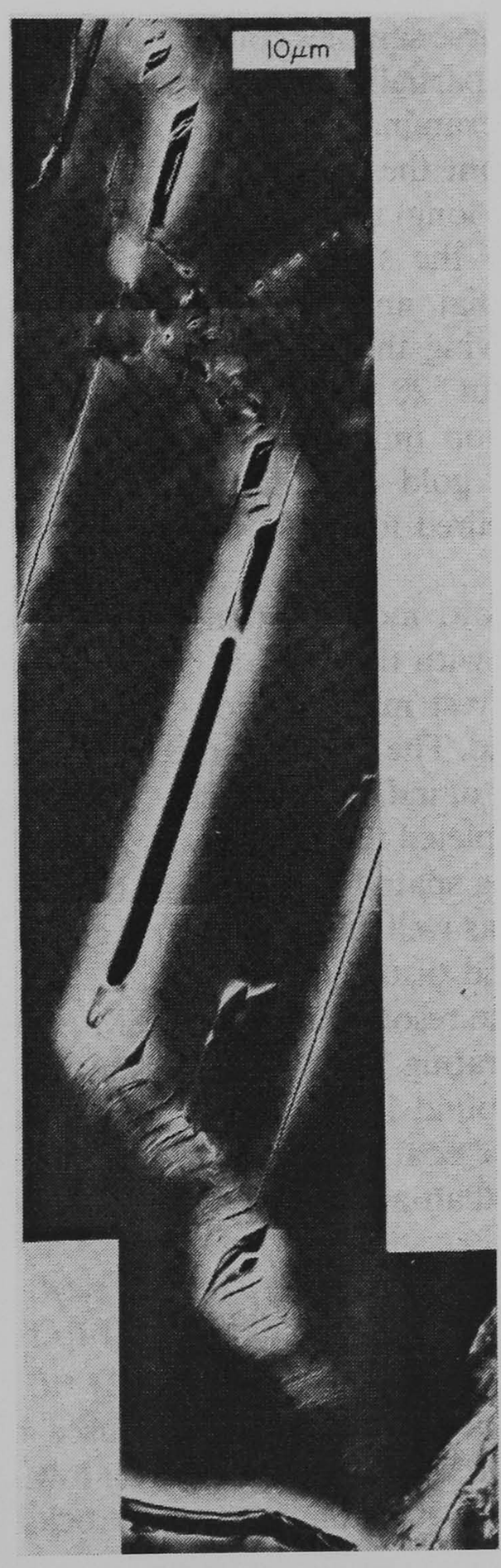


Figure 2.15. Crack arrays formed in a deformed biotite grain in Westerly granite (from Tapponnier and Brace, 1976)

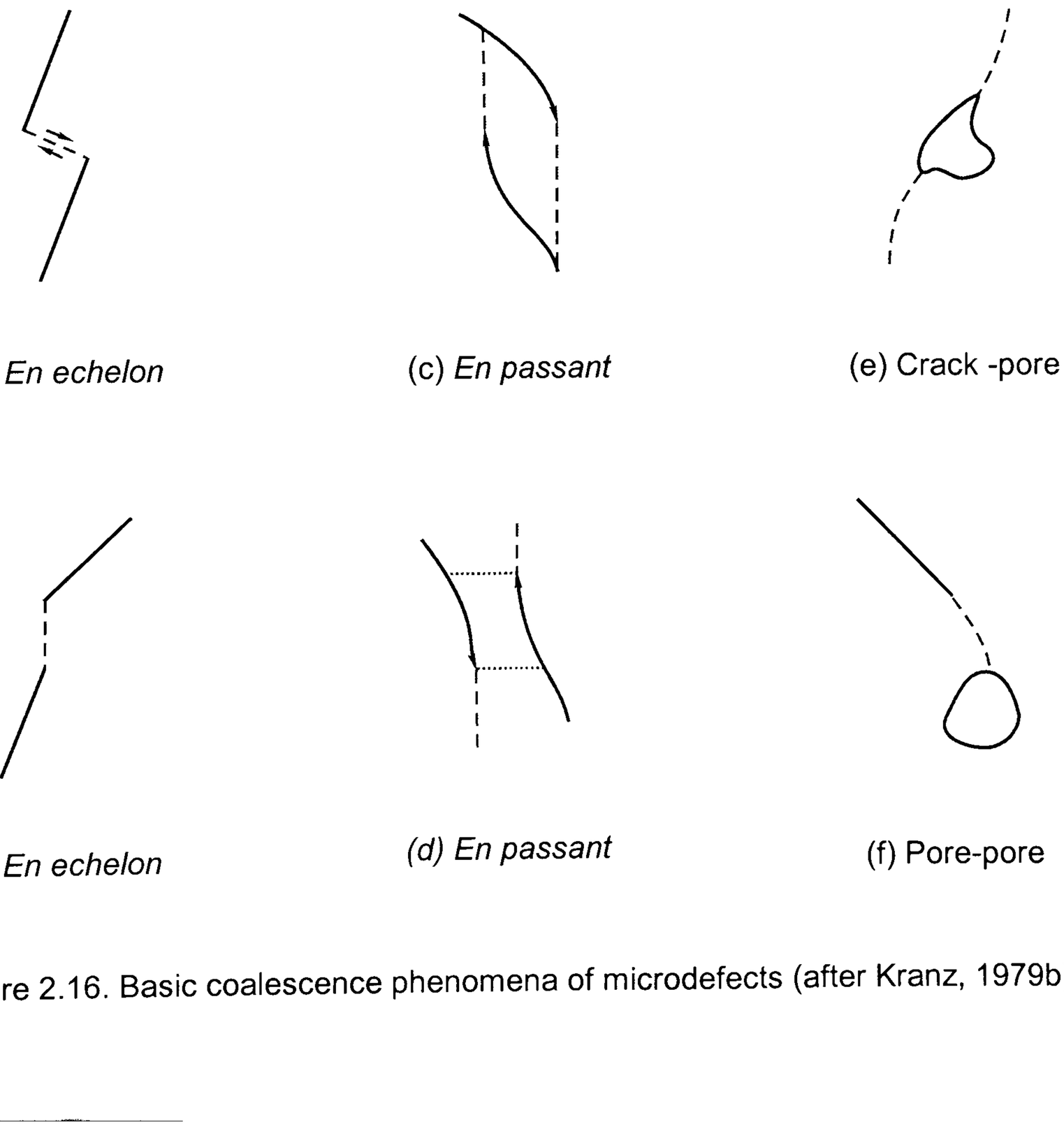
and Chau, 1997). By focusing on the undisturbed rock, the phenomena of crack linkage may be classified as three types: *en echelon*; *en passant*; and crack-pore and pore-pore (Kranz, 1979a).

En echelon *coalescence*

This is operative when a microcrack runs into the field of influence of its neighbours. When both cracks are parallel, or nearly parallel, to each other and lie at a small angle to the direction of maximum compressive principal stress, they link by shearing the bridge between them (Figure 2.16(a)). If one, or both, of the cracks is parallel or sub-parallel to the maximum compressive loading direction, the linkage occurs through tension with a vertical path (Figure 2.16(b)).

En passant *coalescence*

When two microcracks overlap each other, *en passant* interaction between them may occur. In the case of the cracks lying in a direction nearly perpendicular to the maximum compressive loading direction, tensile fractures develop between the ends of the cracks (Figure 2.16(c)), leading to the linkage. When both cracks exist at a small angle to the maximum compressive loading direction, bridge shearing operates (Figure



(a) *En echelon* (c) *En passant* (e) Crack -pore

(b) *En echelon* *(d) En passant* (f) Pore-pore

Figure 2.16. Basic coalescence phenomena of microdefects (after Kranz, 1979b)

2.16(d)).

Crack-pore and pore-pore coalescence

The existence of a pore produces influence on the adjacent cracks or pores. In effect, the influenced crack may change its growth path from its preferred direction and advance towards the pore (Figure 2.16(e)). If the configuration comprises two pores (Figure 2.16(f)), cracks may originate from sharp points on the boundaries of both pores and connect with each other.

2.3 Effects of microcracking on mechanical behaviour of rock

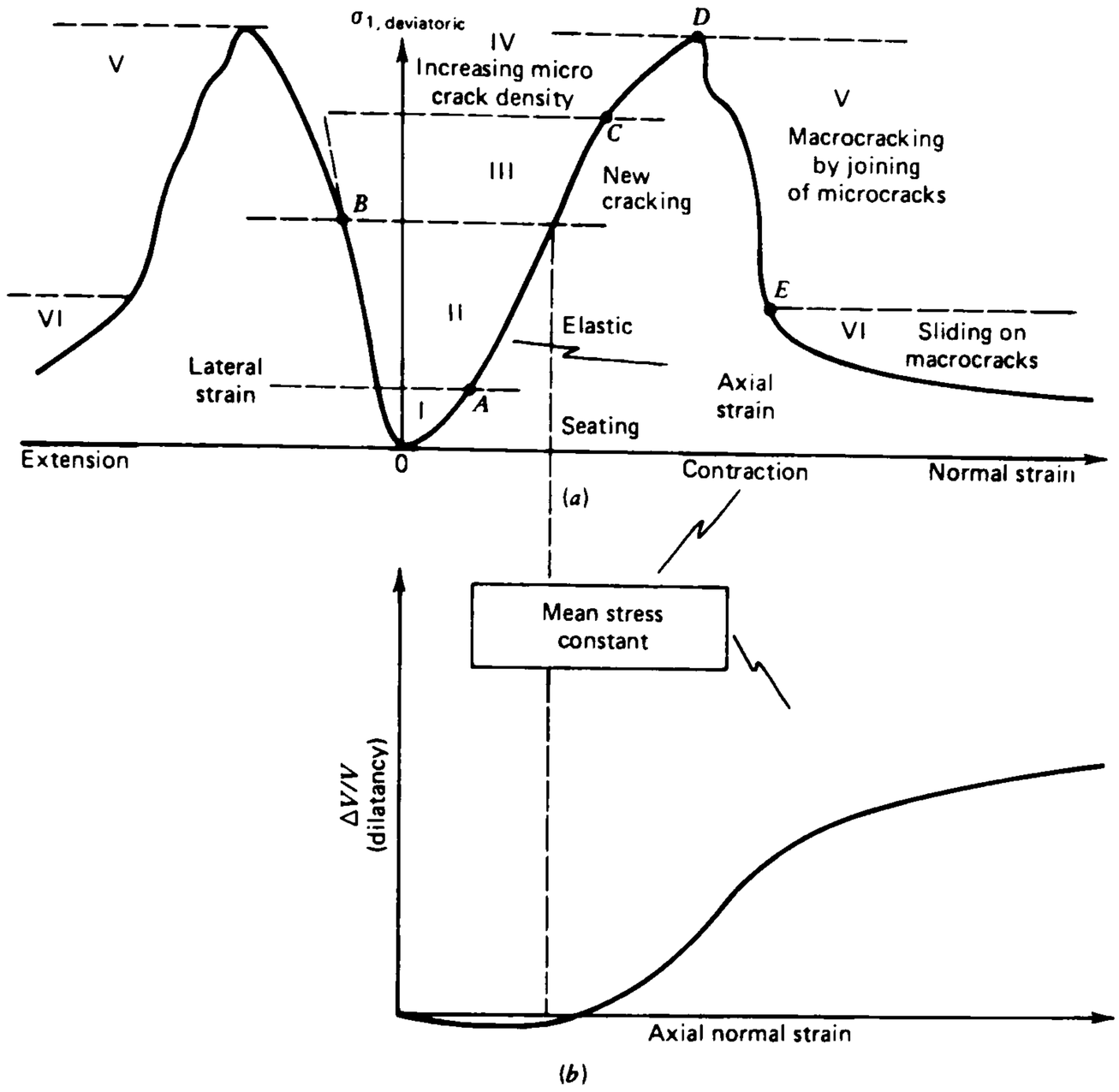
In Section 2.2, it has been seen that microcracking is the primary process preceding the formation of macroscopic fractures in brittle rock undergoing failure. This mechanism gives rise to several distinctive effects in the deformed rock material, which have to be taken into account in studying the complete rock failure mechanism. The most notable are (Costin, 1985): the dilatancy of volumetric strain after the elastic range; the gradual reduction of the elastic moduli with increased loading; and the degradation of material strength associated with the development of eventual faults.

2.3.1 Dilatancy

Brace et al. (1966) and Bieniawski (1967) observed that microcracking leads to volumetric dilation of brittle rock. At the onset of initiation of microcracks during rock deformation, although the axial strain remains linear, the volumetric strain loses its linearity, which denotes that the material dilates (Figure 2.17). At the stage of microcrack coalescence near the peak, the dilatancy accelerates rapidly until the formation of eventual faults, whereupon the curvature of the volumetric strain changes into concave downward (Figure 2.17). This indicates the reduction of the dilatant rate of the fractured rock.

2.3.2 Degradation of stiffness and strength of rock

In compression tests, it is often observed that the elastic moduli of rock specimens are reduced gradually as the microcracking events increase (Wawersik and Fairhurst, 1970; Martin and Chandler, 1994; Hudson and Harrison, 1997).



(a) Axial and lateral normal strain against deviatoric stress;

(b) Volumetric strain against axial strain

Figure 2.17. Deformation of a rock material under increasing deviatoric stress (from Goodman, 1989)

The process of modulus degradation is progressive, as the formation and growth of cracks is irreversible and cumulative. Figure 2.18 illustrates the overall variation in the elastic moduli during the entire failure process, which is established by unloading and reloading the specimen from any point on its complete stress-strain curve, as illustrated in Figure 2.19. With reference to the fracture process (Section 2.1.3), it can be seen from these figures that the reduction in elastic moduli is enhanced by the localisation of cracking and accelerated by the coalescence of the cracks, and has associated with it a rapid decrease in the overall load-carrying capacity of the material. At the residual stage, however, the curve tends to remain constant.

2.4 Influence of confining pressure on rock failure

In previous sections, we have described the various mechanisms of the formation of microcracks and the effects induced by microcracking to the materials. Microcracking, however, is influenced by other factors. Of those, confining pressure is the most

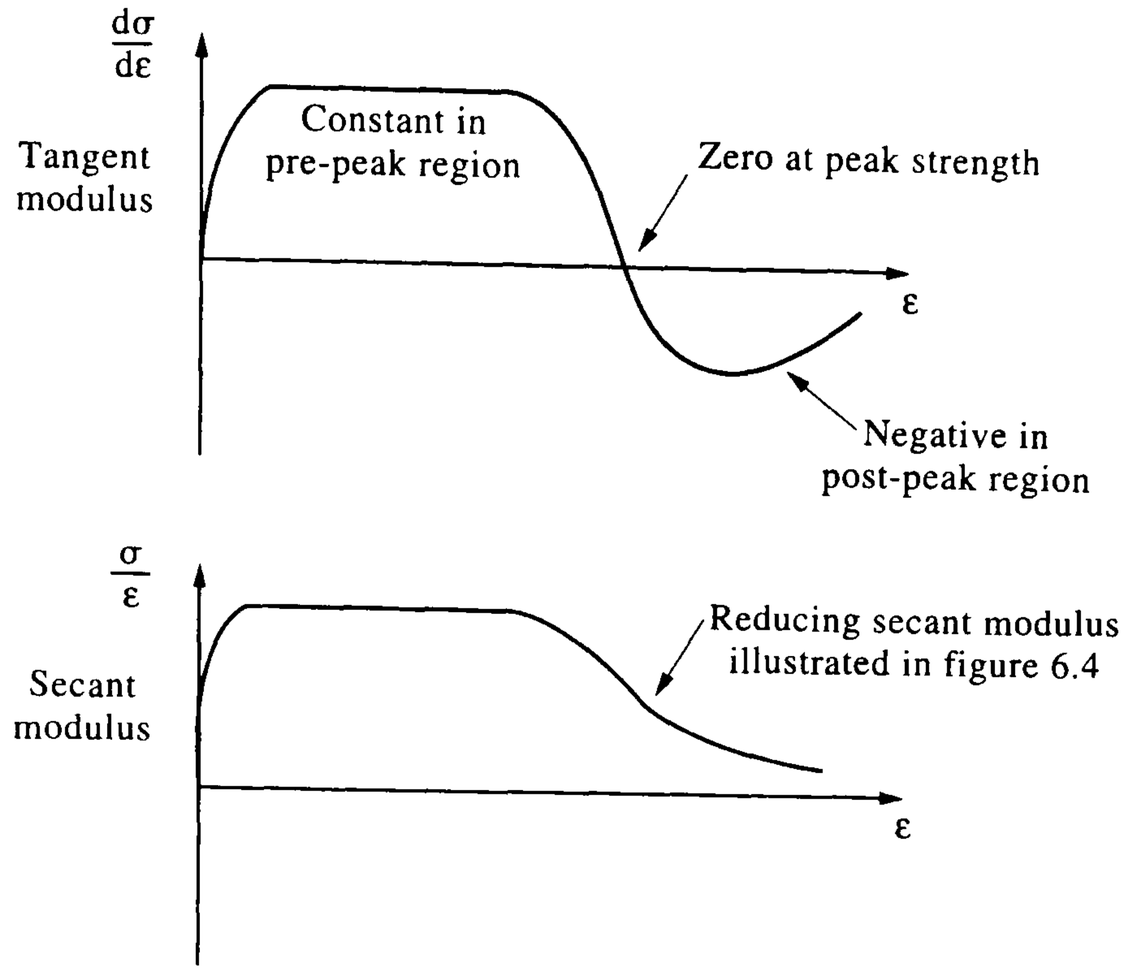


Figure 2.18. Degradation of the elastic moduli of a failed rock in the laboratory (from Hudson and Harrison, 1997)

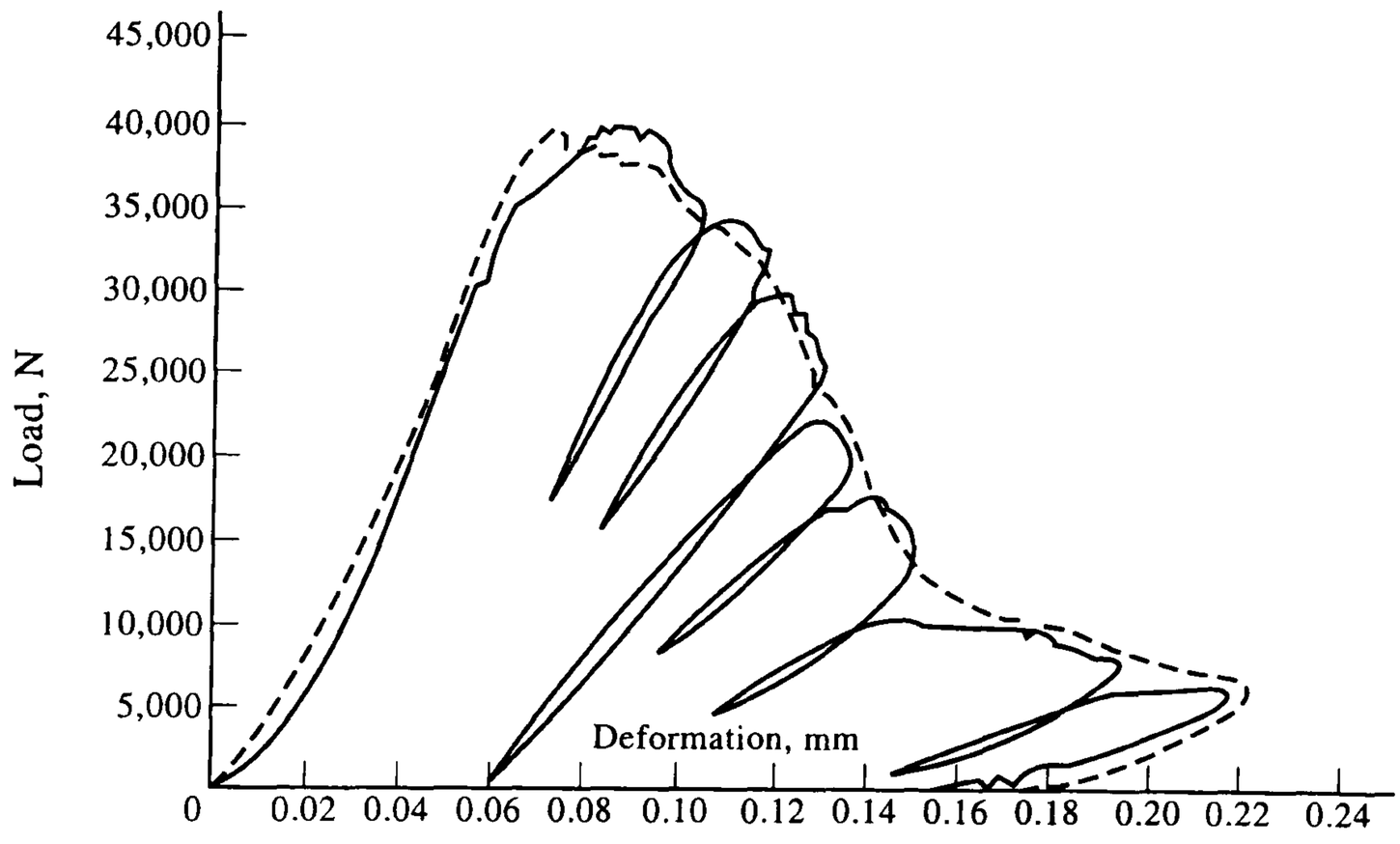


Figure 2.19. Degradation of the strength of a rock in the laboratory (from Hudson and Harrison, 1997)

important.

The presence of a confining pressure, from the point of view of the micromechanisms involved in compressive failure, prohibits the initiation and propagation of microcracks, and provides the frictional resistance between the surfaces of cracks or fractures (Weijermars, 1997). Thus, increasing confining pressure has a significant effect on the fracture formation, strength, and ductility of intact rocks, which are introduced in this section.

2.4.1 Effects on microscopic processes

Effects on formation of microcracks

In uniaxial and low-confined compression, cracks are easy to form. Cleavages within grains and the like (lamellae) are the important source for crack formation (Bombolakis, 1973; Olsson and Peng, 1976; Tullis and Yund, 1977). Higher confining pressures tend to increase the stress levels at which microcrack nucleation starts (Olsson and Peng, 1976; Tullis and Yund, 1977), and this leads to the contribution of some grains, such as quartz in quartzite, and grain boundaries in the formation of microcracks (Hallbauer et al., 1973; Tullis and Yund, 1977).

Effects on propagation of microcracks

In unconfined or low-confined compression tests, crack propagation up to about 90 percent of the peak stress is dominated by axial growth (Brace et al., 1966; Bieniawski, 1967; Wawersik and Fairhurst, 1970; Wawersik and Brace, 1971; Thill, 1972; Hallbauer et al., 1973; Olsson and Peng, 1976). Higher confining stresses, on the other hand, tend to prohibit this phenomenon (Wawersik and Fairhurst, 1970; Wawersik and Brace, 1971; Hallbauer et al., 1973) and some cracks may propagate in a direction

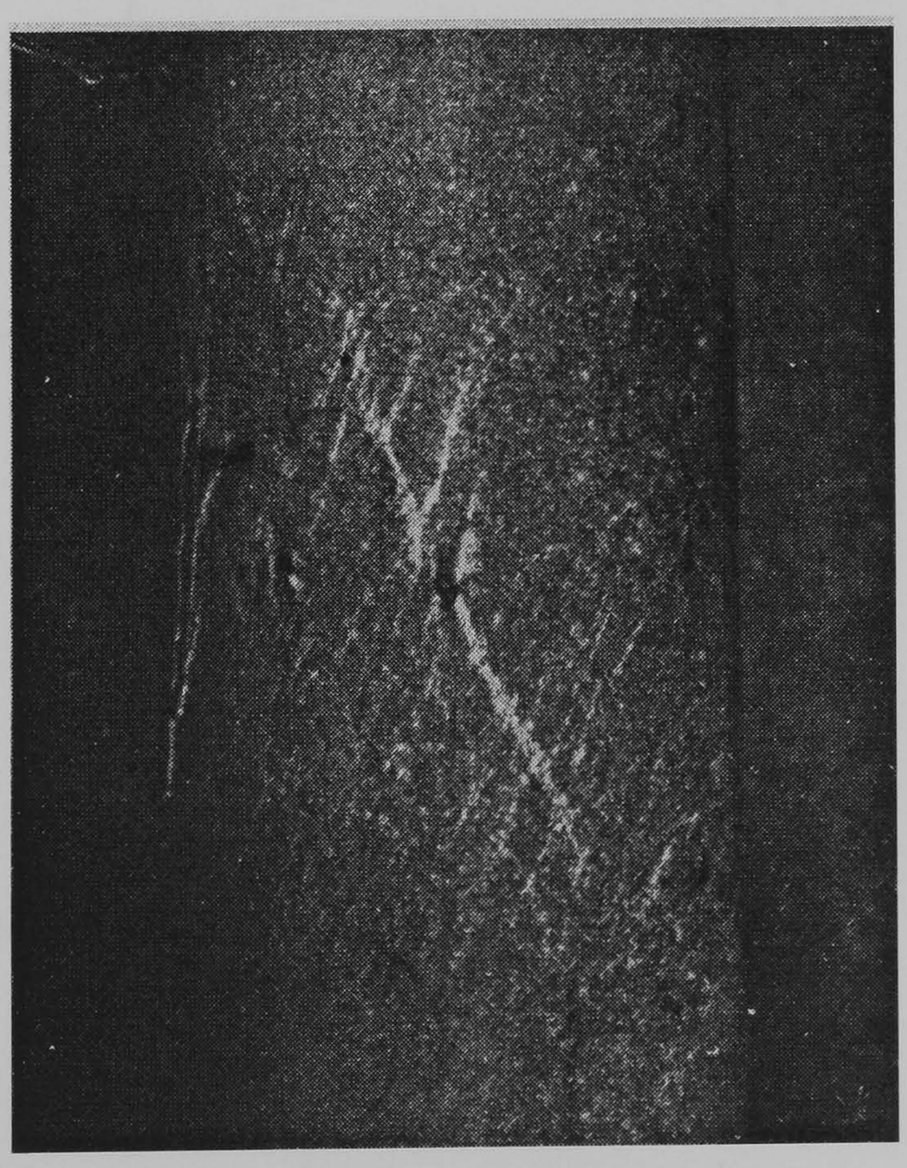


Figure 2.20. Post-peak fracture patterns developed in a diabase (from Wawersik and Brace, 1971)

inclined to the maximum compressive stress direction (Wawersik and Fairhurst, 1970; Wawersik and Brace, 1971). If the confining pressure is extremely high, local cracks tend to propagate in their initial plane manifested by local shear failure and gliding on inclined planes (Figure 2.20) (Wawersik and Brace, 1971; Bésuelle et al. 2000), or by plastic flow and grain crushing (Figure 2.14) (Thill, 1972; Wu et al., 2000).

The length of the propagated cracks seems to be a function of the confining stress (Wawersik and Fairhurst, 1970; Olsson and Peng, 1976). The average crack length in confined compression is less than that in uniaxial compression, and decreases continuously as the confining pressure is raised (Wawersik and Fairhurst, 1970). Olsson and Peng (1976) observed that in uniaxial compression the crack nuclei in marble sometimes propagate for distances of several grain diameters or more; at moderate confining pressures, however, the crack nuclei seldom propagate more than some fraction of a grain diameter.

Effects on density of nucleated microcracks

The density of nucleated cracks is closely related to the level of the confining stress. At zero and very low confining pressure, it is easy for a nucleated crack to grow, lining up with grain boundaries or passing through weaker grains, and fewer cracks are generated during the whole process of final fault formation (Tullis and Yund, 1977).

The nucleated cracks at intermediate confining pressures do not grow as long as at lower confining pressures (Wawersik and Fairhurst, 1970; Olsson and Peng, 1976; and see the previous section). Instead, more cracks are formed within grains or from grain boundaries at a higher stress level (Thill, 1972; Tullis and Yund, 1977). The density of the nucleated cracks prior to the formation of final faults increases as the confining pressure increases.

In their recent study, Wu et al. (2000) arrested this feature in testing Darley Dale sandstones. They observed that during the deformation process the crack density produced at 210 MPa confining pressure was nearly twice that produced at 20 MPa confining pressure. Although these tests were conducted with a 10 MPa pore pressure, the microcracking events observed were primarily dependent on the confining pressure used.

2.4.2 Effects on the stress-strain curve

The kinetics of microscopic events is affected by the boundary conditions (see the

previous section), and this gives rise to different macroscopic mechanical behaviour of tested rock. Figure 2.21 shows the variation of the stress-strain curves obtained in triaxial compression tests on Tennessee marble subject to different confining stress levels (Brady and Brown, 1992). From these and similar data for other rocks, it has been

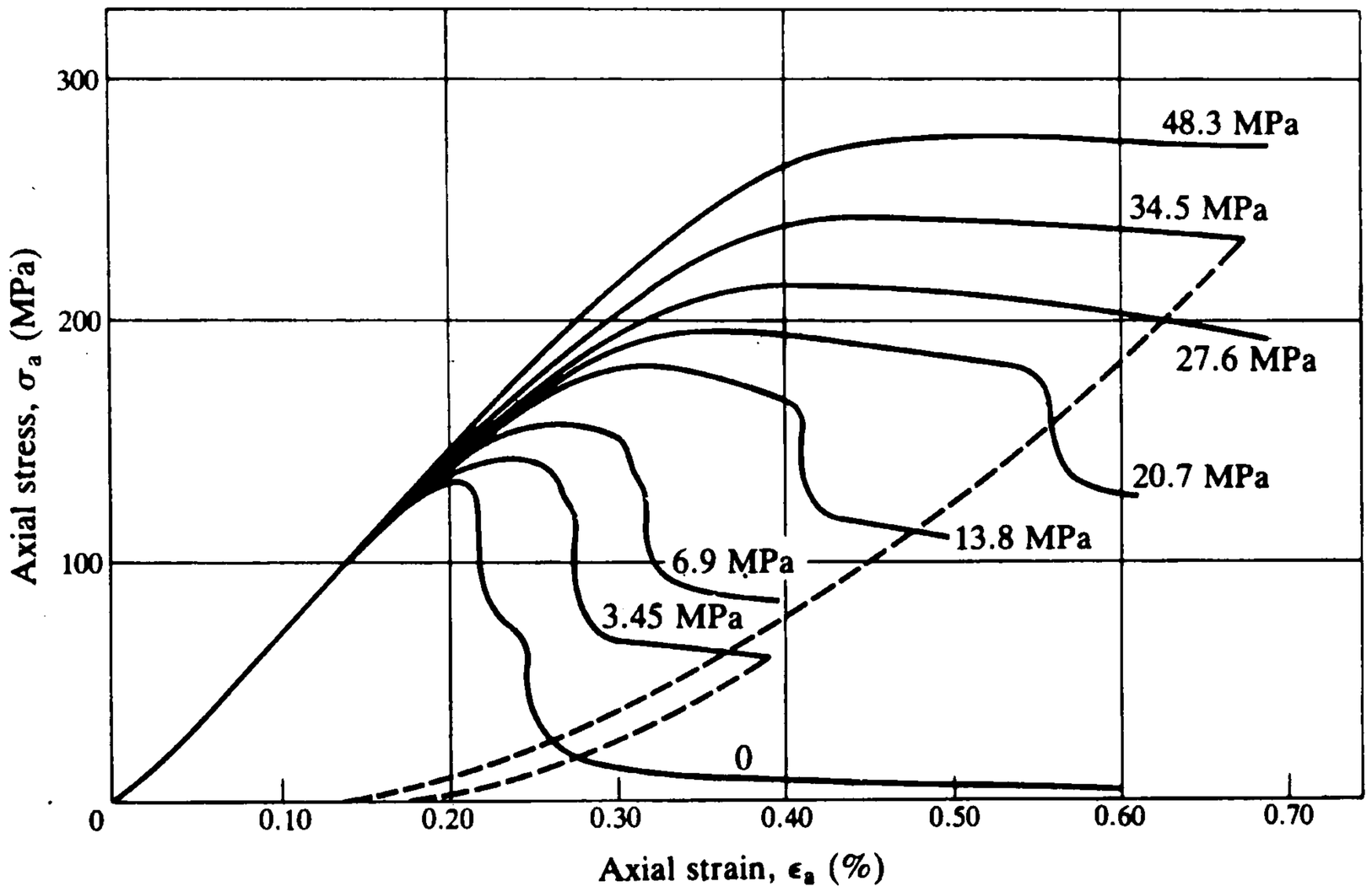


Figure 2.21. Complete axial stress-strain curves obtained in triaxial compression tests on Tennessee Marble at various confining pressures (from Brady and Brown, 1992)

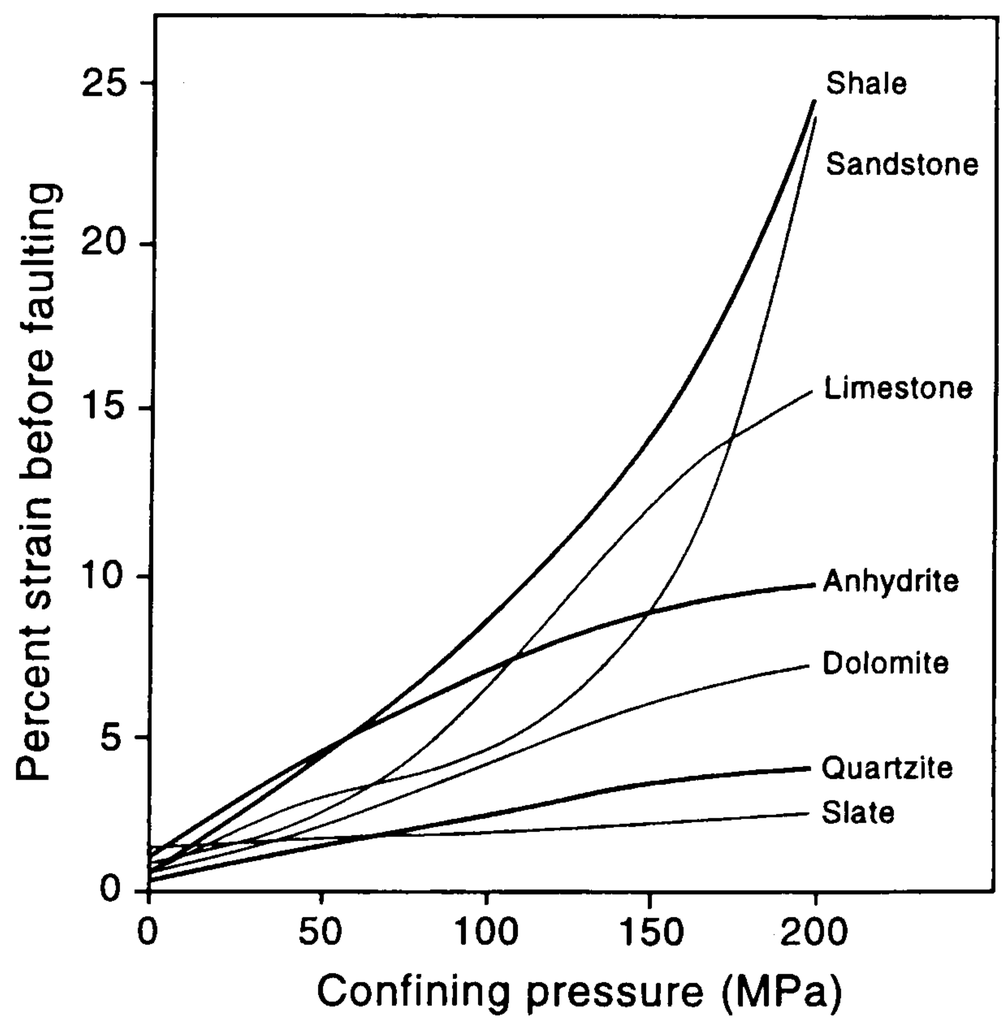


Figure 2.22. Macroscopic brittle failure occurs at larger critical strains as confining pressure increases (from Weijermars, 1997)

concluded (Stagg and Zienkiewicz, 1968; Wawersik and Fairhurst, 1970; Paterson, 1978; Brady and Brown, 1992) that for many rocks with increasing confining pressure:

(a) the peak and ultimate strengths increase;

(b) the extent and degree of strain hardening before the peak stress increases;

(c) the region incorporating the peak stress flattens and widens;

(d) there is a transition from typically brittle to fully ductile behaviour at a certain confining stress level;

(e) the degree of strength loss after failure reduces with increasing confining stress;

(f) the strain reached before macroscopic failure increases. Figure 2.22 shows this characteristic for a number of rocks.

2.4.3 Effects on formation of fracture

The formation of the eventual fracture is another macroscopic feature associated with the distinctive microscopic processes affected by confining stresses (see Wawersik and Fairhurst, 1970; Olsson and Peng, 1976; Tullis and Yund, 1977). Typically, the phenomenon of the final macroscopic fracture has been described as three modes, referring to the stress-strain behaviour of rock subjected to different stress conditions

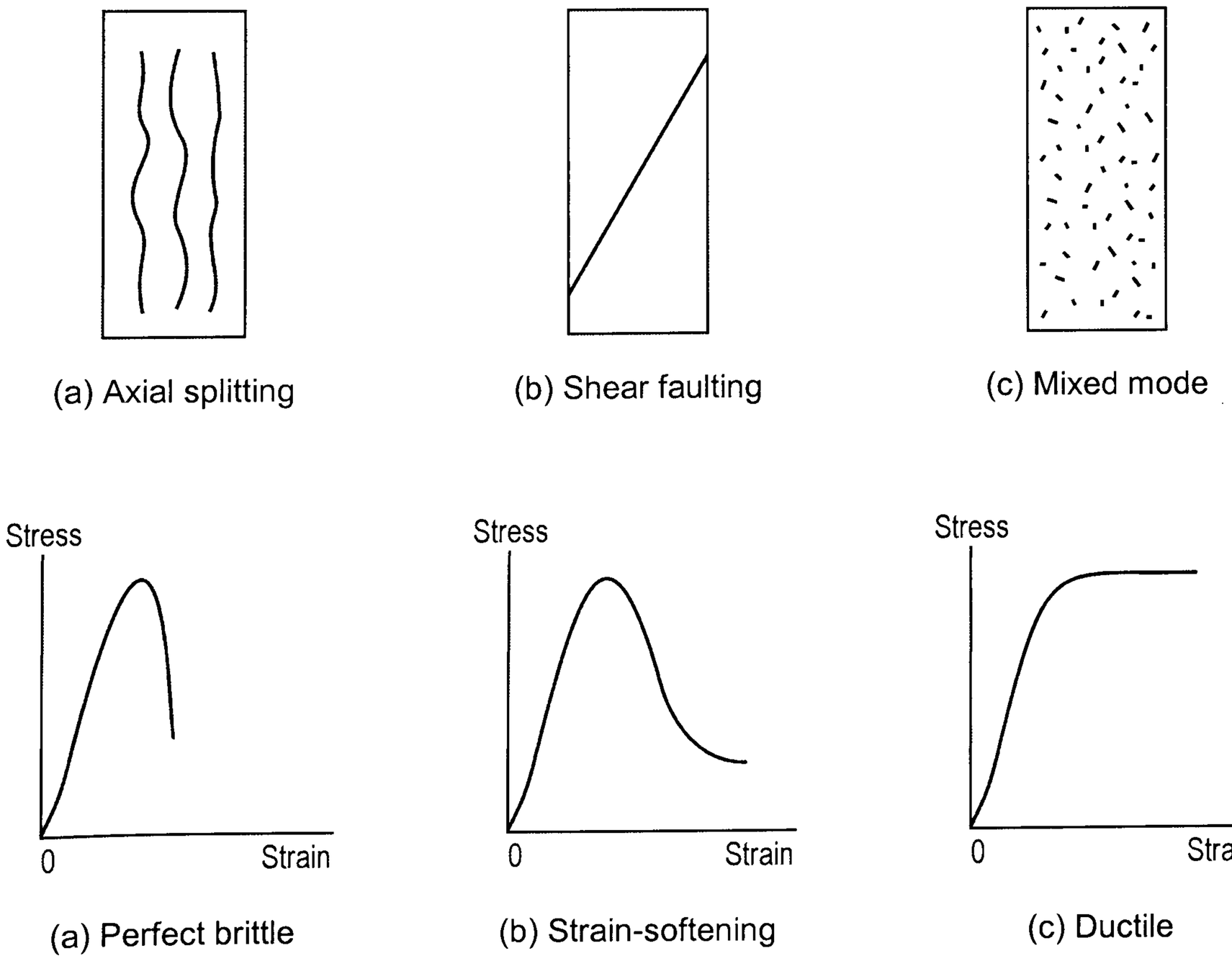


Figure 2.23. Deformation behaviours and typical fracture modes of rock in compression

(Griggs and Handin, 1960; Patterson, 1978; Jaeger and Cook, 1979; Horii and Nemat-Nasser, 1985, 1986; Ashby and Hallam, 1986; Sammis and Ashby, 1986). Figure 2.24 gives the illustration.

In uniaxal compression, cracks can easily align with grain boundaries and weaker grains, and axial splitting with an irregular surface is normally observed (Figure 2.23(a)), relating to brittle behaviour. Shear fracture, with its surface inclined at an angle of less than 45° to the direction of major principal stress, is the typical rupture mode detected under compression with a moderate amount of confining pressure, and the corresponding stress-strain curve shows strain-softening (Figure 2.23(b)). This characteristic is also observed in uniaxial compression on certain rocks such as quartzite (Fairhurst and Cook, 1966), marble and granite (Andreev, 1995). Under increased confining pressures, the fracture mode is replaced by a combination of shear fractures and plastic deformation of individual crystals (Jaeger and Cook, 1979) or by a widened ductile fault (Donath et al., 1971; Paterson, 1978) and the stress-strain curve exhibits fully ductile behaviour (Figure 2.23(c)).

2.5 Rock fracturing processes and associated acoustic emission events

As seen in the previous sections, microcracking is the primary mechanism associated with rock fracture. The formation and propagation of microcracks causes a rapid release of mechanical energy within the material, which is manifested by the radiation of elastic waves accompanied by noise. This physical phenomenon is termed acoustic emission (AE). Obert and Duval (1942) first detected the phenomenon and this feature has been extensively used by other researchers (Scholz, 1968; Lockner et al., 1991; Lockner et al., 1992; Cox and Meredish, 1993; Zang et al., 1996; Wu et al., 2000) as an effective means of observing the microscopic processes that occur during rock deformation. In this section, we describe the usefulness of the AE event detection in describing rock fracture.

2.5.1 Relation of acoustic emission activities to macroscopic behaviour

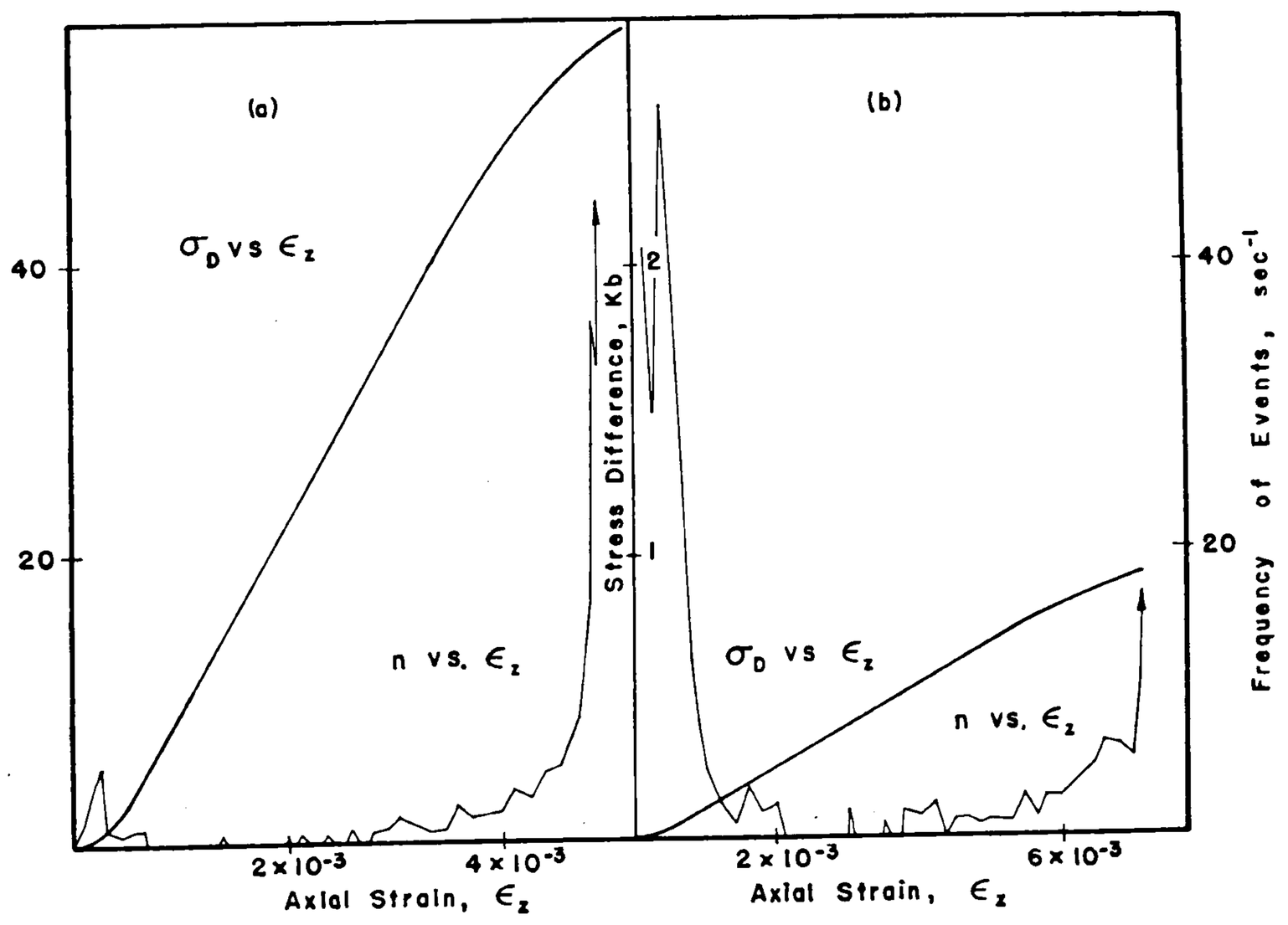
Scholz (1968) studied a series of rocks, and monitored the frequency of cracking events. The rocks being tested were of different density, average grain diameter, porosity (Table

Table 2.1. Description of rocks used for experiments (after Scholz, 1968)

Rock	Density, g/cm^2	Average grain diameter, mm	Total porosity determined by immersion in CCl_4
Westerly granite	2.646	0.75	0.009
Marble	2.688	0.20	0.013
Colorado rhyolite tuff	1.77	0.01	0.41

2.1) and strength. These results confirm that the nonlinearity and dilatancy of deformation behaviour of rock are closely correlated with the frequency of elastic wave radiation.

Figure 2.24 is one of the results obtained by Scholz (1968) on Westerly granite and Colorado rhyolite tuff in uniaxial compression. It can be seen that although the two rocks are very different in their physical properties (Table 2.1) the pattern of microcracking evolution is similar. At a low stress level, a flurry of AE activity occurs and this correlates with the closure of pores and open cracks described in Section 2.1.3; soon, this activity dies down to a very low level, which indicates that little or no



(a) Westerly granite (b) Colorado rhyolite tuff

Figure 2.24. Stress-strain curve and microcracking frequency-strain for two rocks in uniaxial compression (from Scholz, 1968)

microcracking takes place; while the loading stress increases to approximately half the fracture strength, AE events builds up once more with an increasing rate until just before fracture when a very rapid acceleration of activity occurs, which corresponds with random-localised-coalesced characteristic stages of microcracking (see Subsection 2.1.3).

In terms of the stress-strain curve, the evolution of the AE events correlates closely with the non-linearity of the mechanical behaviour of the material. The first occurrence of AE events at low stress level corresponds with the concave-upwards portion of the stress-strain curve (Figure 2.24), but the restart of the build-up of AE event at about half the peak strength is associated with the onset of concave-downwards portion. The development of the curvature in the two regions, however, is different. With increased loading, the curvature of the stress-strain curve in the first region reduces gradually, which indicates that no damage occurs with the AE events; while in the non-linear region of the upper part of the stress-strain curve, the curvature increases with increasing loading, and this indicates the progressive deterioration of the material.

Due to the introduction of new void space produced by microcracking, dilatancy occurs in the region above about half the peak strength (Brace et al., 1966; Bieniawski, 1967). Scholz's results (1968) shown in Figure 2.25 indicate that the accumulated frequency of AE events is proportional to the dilation of the volumetric strain. Figure 2.25 is the plot for three uniaxial compression tests on Westerly granite, in which the

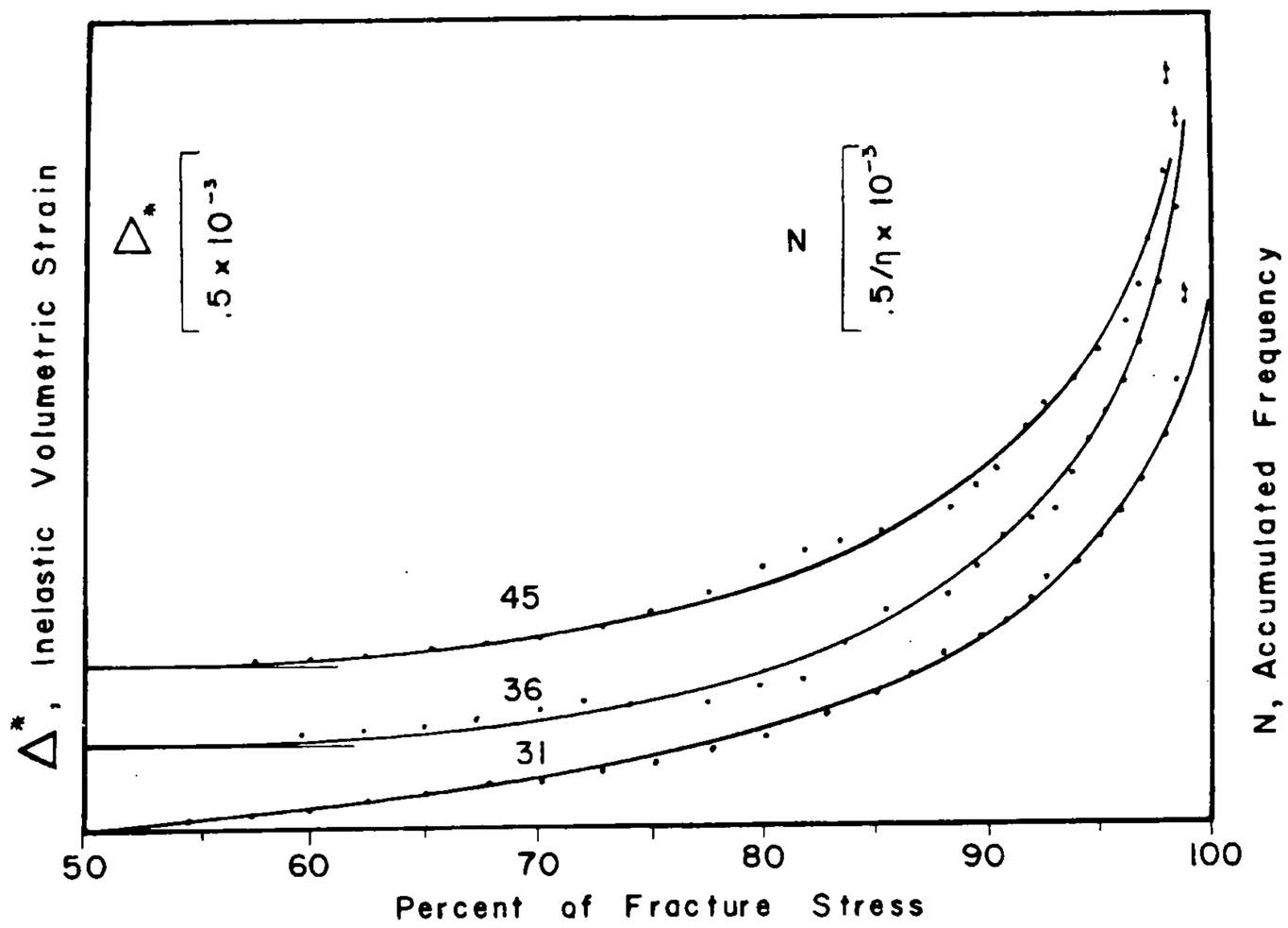


Figure 2.25. Accumulated frequency (data points) of microcracking events fitted to the inelastic volumetric strain (smooth curve) in the dilatant region for three uniaxial compression tests on Westerly granite (from Scholz, 1968)

accumulated frequency of AE events is plotted by data points, and the inelastic volumetric strain is delineated by smooth curves. The inelastic volumetric strain Δ^* is obtained by subtracting an elastic extrapolation from the total measured volumetric strain, and the accumulated frequency of AE events is detected in the dilatant region. These two sets of data are well fitted to each other, except the region above 95% of the peak strength, where AE events rapidly accelerate.

2.5.2 Acoustic emission events and rock properties

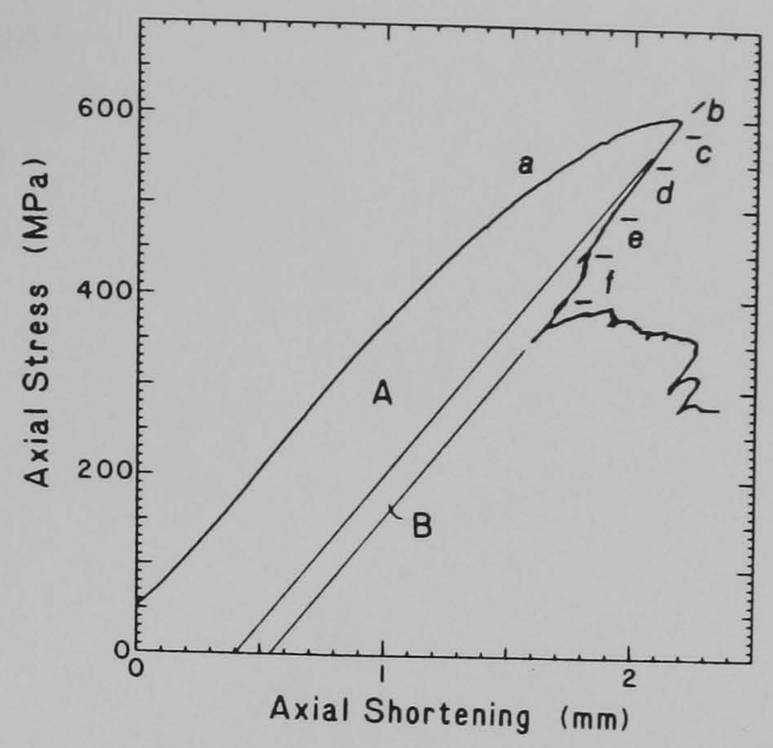
Porosity and strength of rock have a significant influence on producing the AE events. Generally, porosity of rocks correlates with its brittleness and strength. The lower the porosity, the higher brittleness and strength of the rock (Hudson and Harrison, 1997). A rock specimen with higher porosity emits a greater frequency of events at low stress than that with lower porosity (Figure 2.24). At higher stress levels, however, the acceleration rate of the emitted elastic waves is much less than that for rocks with lower porosity (Figure 2.24). Similar features are also seen for marble (Scholz, 1968).

2.5.3 Implication of acoustic emission events and formation of faults

By maintaining a constant acoustic-emission rate, Lockner et al. (1991) successfully captured the hypocentres of acoustic events, which demonstrates the complete development of faults led by microcracking. Figure 2.26 shows the axial stress-axial displacement for the tested Westerly granite at 50 MPa confining pressure. In this plot, the curve is divided into 6 intervals by letters *a-f*, and these letters correspond to the different AE patterns shown in Figure 2.27.

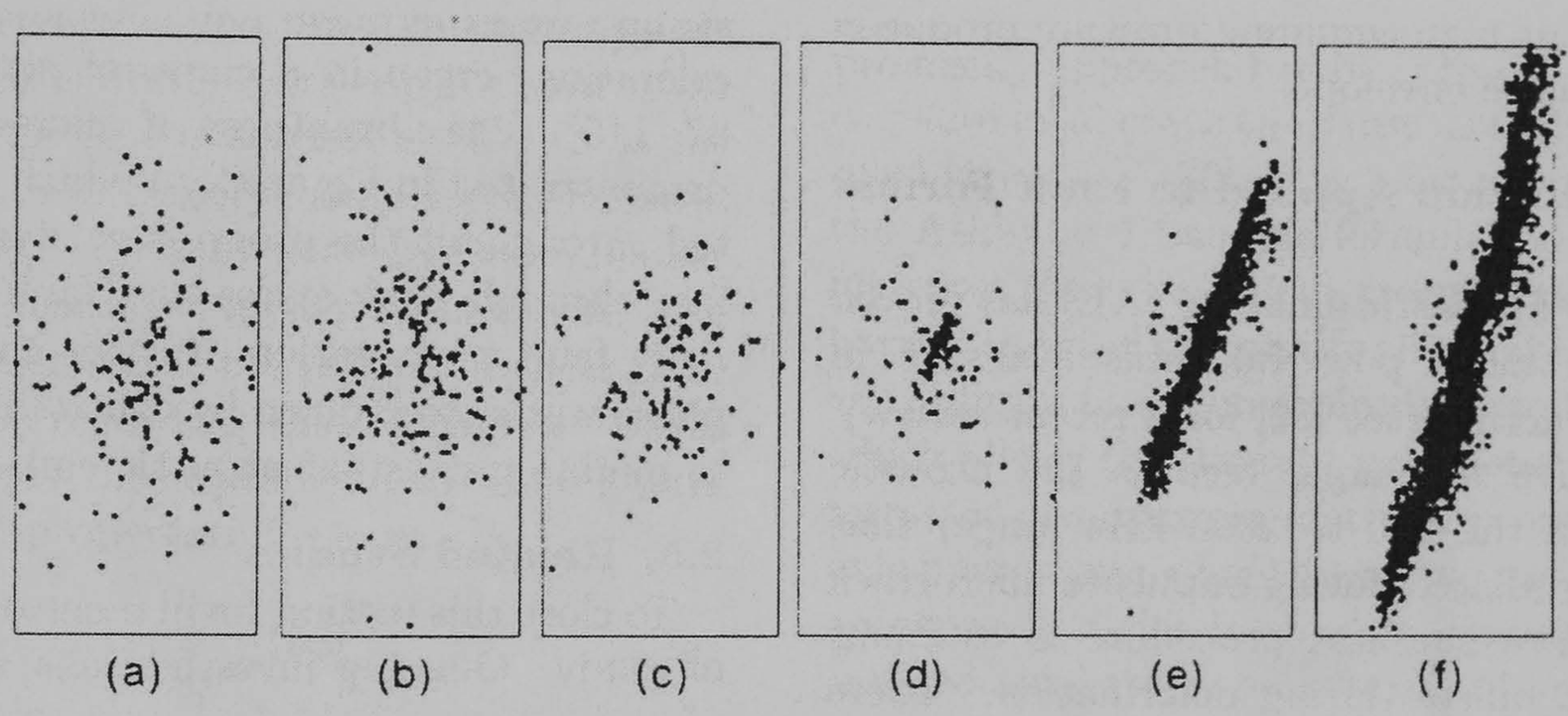
By combining the two figures, it can be seen that, at interval *a*, before the peak, microcracking takes place randomly, which agrees with the results given by other researchers (Scholz 1968, Kranz 1983); at about the peak, interval *b*, the degree of diffuse microcracking reduces, and the occurrence of the events localises at the centre of the sample; at interval *c*, the post peak stage, the localised microcracking events develops along a plane with a certain angle to the axial direction, and this trend remains until the fault fully develops.

Further results by Lockner suggest that the eventual fault in the deformed specimen under compression forms after the peak (Lockner et al., 1991; Lockner, 1995). This is agreed by Menendez et al. (1996) and Weijermars (1997). The complete formation of a



(Letters along curve correspond to plots shown in Figure 2.27)

Figure 2.26. Axial stress against axial displacement for Westerly granite at 50 MPa confining pressure (from Lockner et al., 1991)



(Stress interval for each plot in shown in Figure 2.26)

Figure 2.27. Sequential plots of locations of acoustic emission (from Lockner et al., 1991)

fault produces significant acoustic emission activities, as detected by Cox and Meredith (1993), Zang et al. (1996), and Baud and Meredith (1997). Figures 2.28 and 2.29 show their results, indicating this feature.

2.6 Fracturing and deformation behaviour of rock in large scale

So far, we have obtained a systematic knowledge of brittle fracture process, the corresponding mechanical behaviour and energy dissipation characteristics of custom-sized rock in laboratory compression. How does a large-scale rock specimen in the laboratory or a rock structure in the field fracture or behave? This is described in this

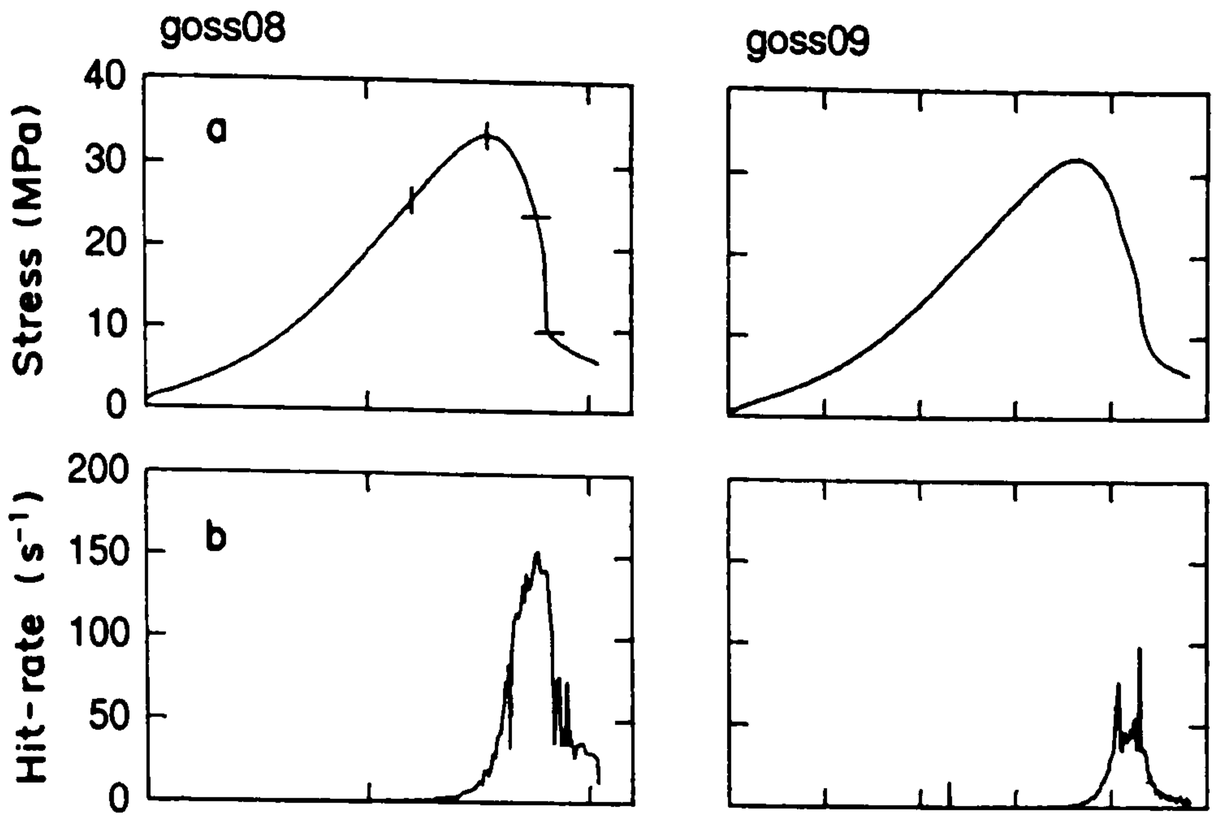


Figure 2.28. Stress (a) and AE event-rate (b) vs time for a Gosford sandstone specimen (from Cox and Meredith, 1993)

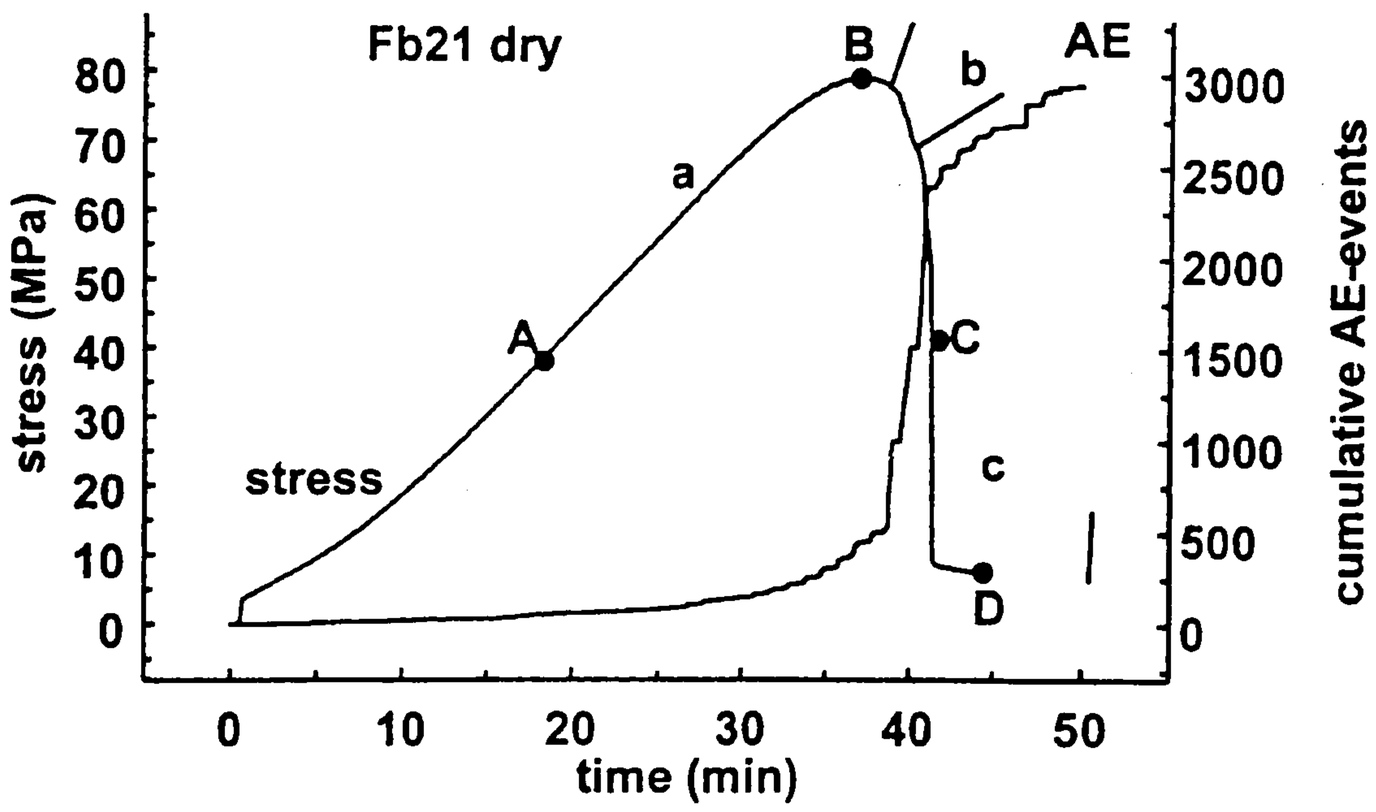


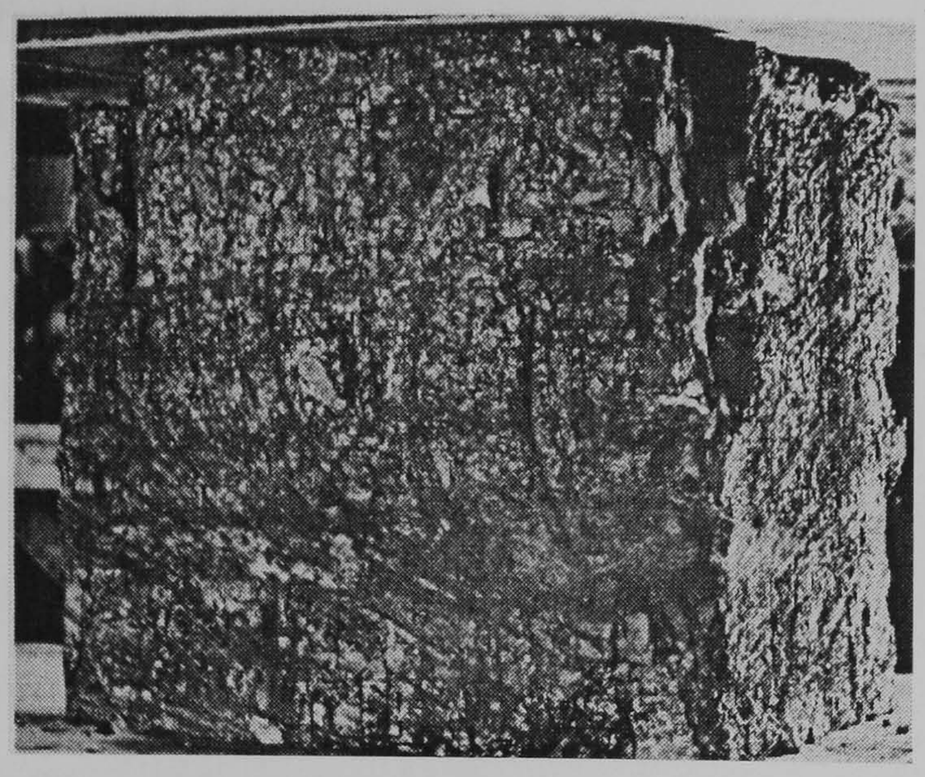
Figure 2.29. Stress and cumulative AE events vs time for a Flechtingen sandstone specimen (from Zang et al., 1996)

section.

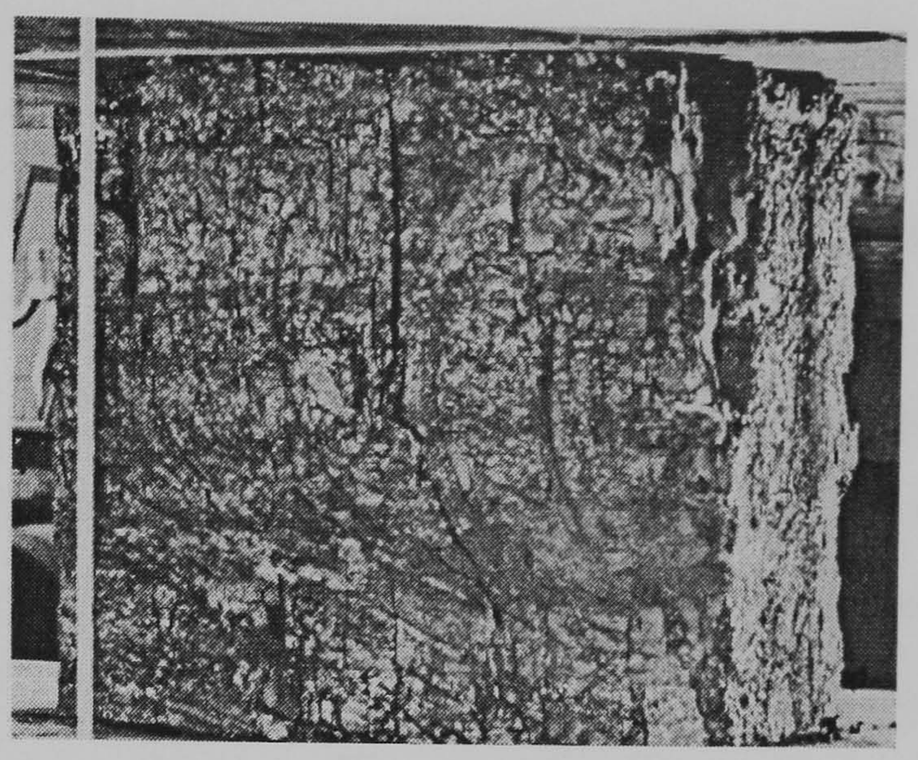
2.6.1 Fracture of large scale specimens

Fracture processes

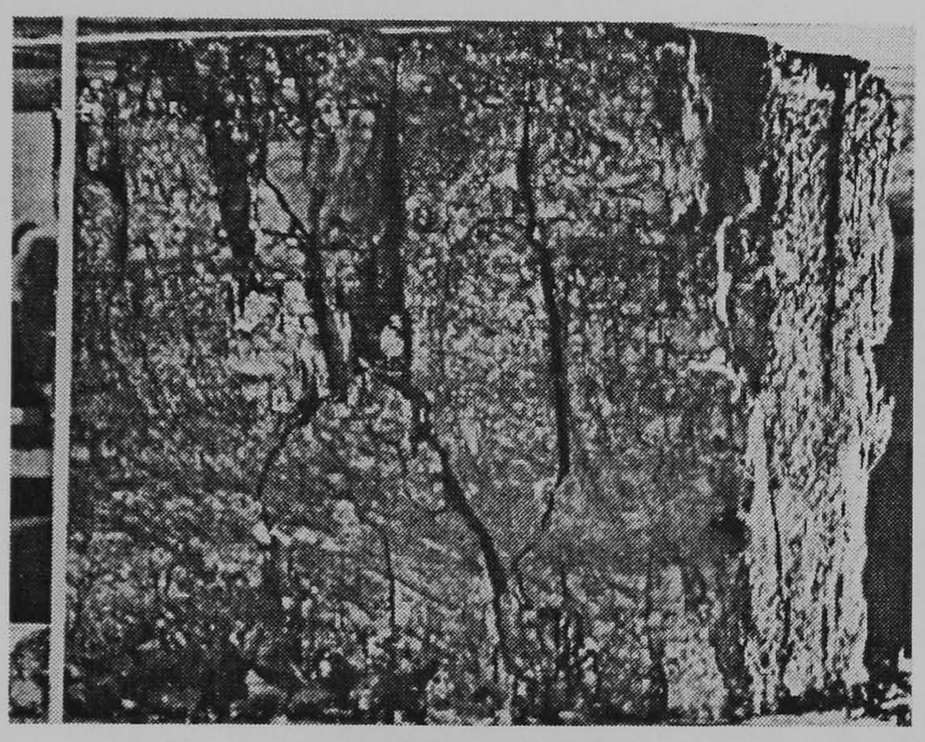
Bieniawski (1967), Wagner (1974), and Bieniawski and Van Heerden (1975) have conducted series of laboratory and *in situ* tests on large cubic coal specimens to investigate deformation behaviour. Figure 2.30 shows the successive fracturing process of 2 foot cube coal specimen leading to collapse. The specimen contains a few visible vertical cracks and cleavages (Figure 2.30(a)), which are the sources of induced fracture



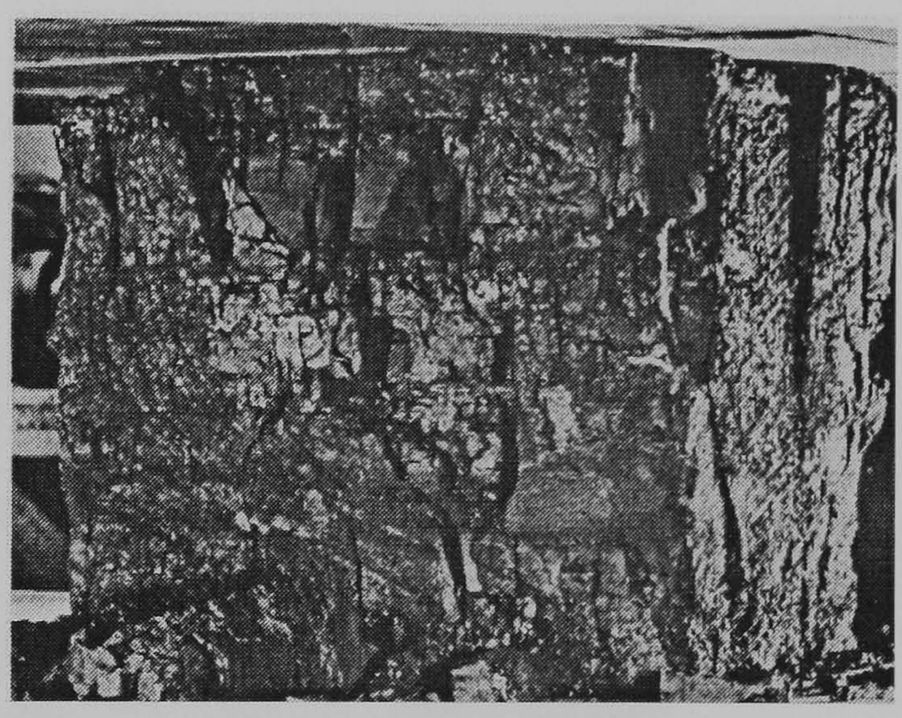
(a)



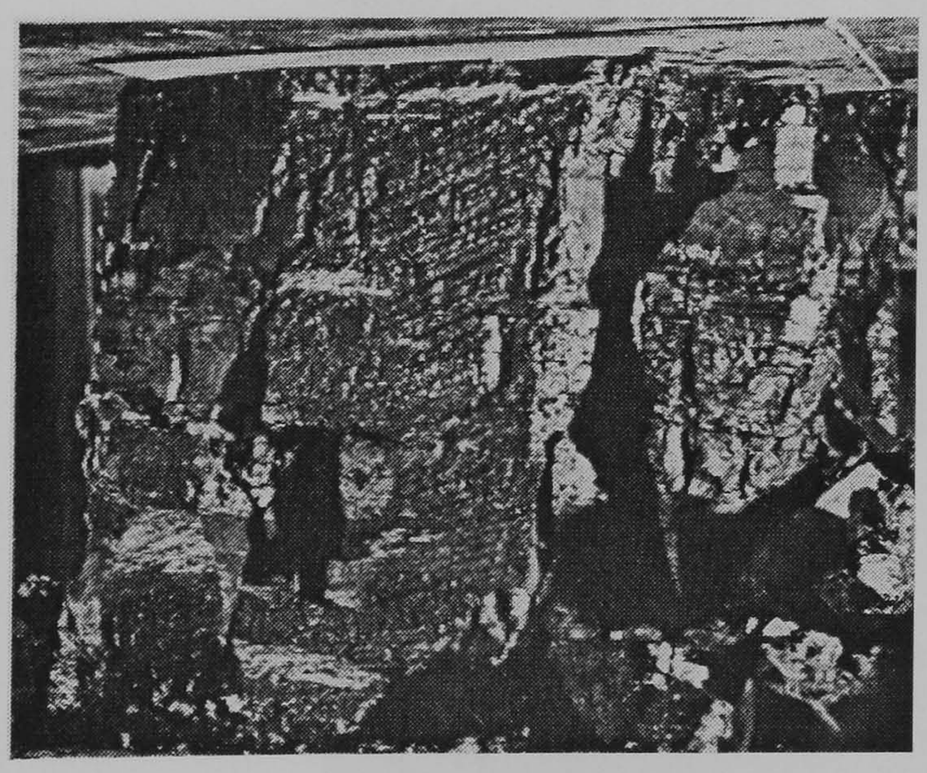
(b)



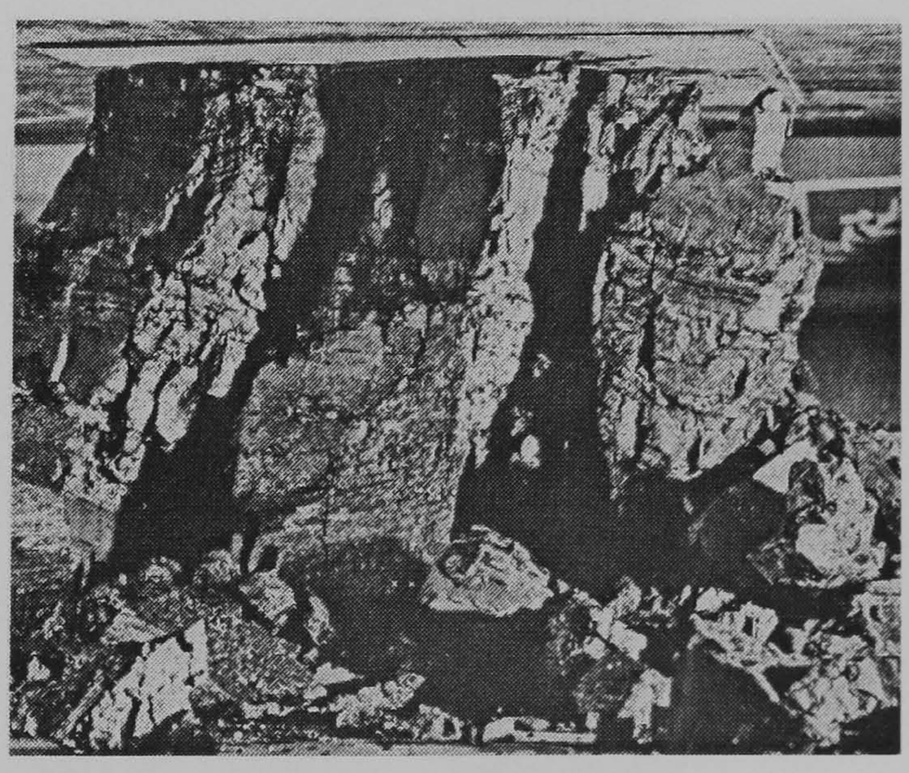
(c)



(d)



(e)



(f)

Figure 2.30. Successive failure stages of a 2 foot cube coal specimen tested in the laboratory (from Bieniawski, 1967)

by vertical loading at fairly low stress level (Figures 2.30(b) and (c)). At this stage, the fractured sample still maintains its capability of sustaining increasing loading. With a further increase in loading, local shear failure develops (Figure 2.30(d)), corresponding to which the specimen loses its load-carrying capability until the residual stage, whereupon the specimen disintegrates into parts (Figures 2.30(e) and (f)).

In the above experiment, it is seen that the large scale pre-existing cracks and cleavages play a dominant role in the formation of fracture. Due to their existence the specimen fails macroscopically due to splitting. In the case of a specimen without such discontinuities, fracture of a specimen starts with splitting and spalling phenomena from near to the faces, migrates into the centre with shearing, and exhibits a final mode of a double pyramid (Bieniawski, 1967; Bieniawski and Van Heerden, 1975). Figure 2.31 shows such a failure of a 1 foot cube coal specimen (Bieniawski, 1967).

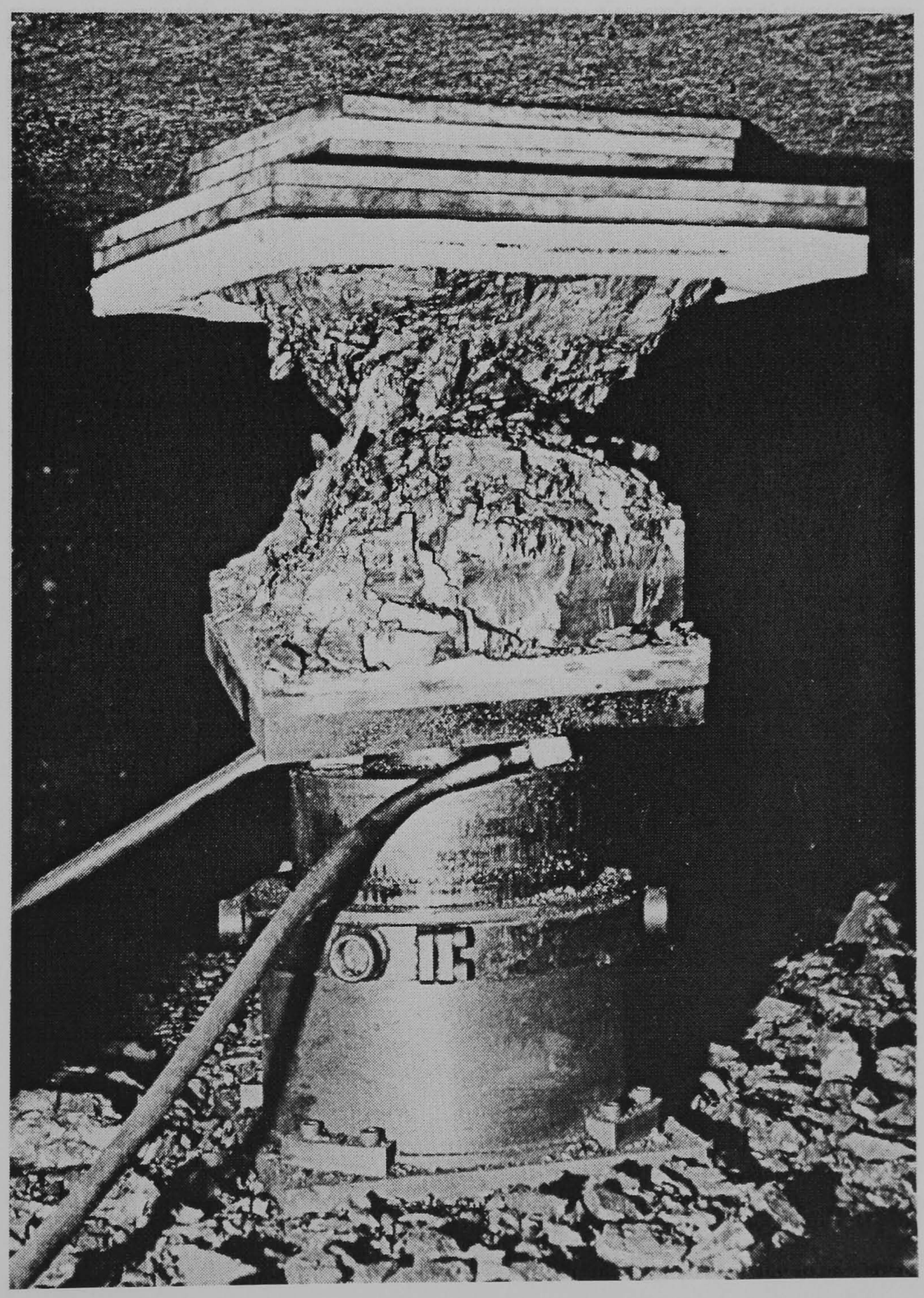


Figure 2.31. The failure mode of a 1 foot cube coal specimen (from Bieniawski, 1967)

Deformation behaviour

Just as a standard-sized rock specimen fails in the laboratory, so the failed large coal specimens in the above test exhibits a non-linear deformation behaviour (Bieniawski, 1967; Wagner, 1974; Bieniawski and Van Heerden, 1975). Figure 2.32 shows a typical complete stress-strain curve obtained by Bieniawski and Van Heerden (1975) during the *in situ* test on a specimen with a width of 1.4 m and width/height ratio of 2.78. Compared with the deformation behaviour exhibited by standard rock samples (Figure 2.6), both curves are very similar in shape, except for the magnitude of the associated deformation properties, *e.g.*, the peak strength, the elastic modulus and the slope of the strain-softening stage, which are different from size to size.

2.6.2 Rock fracture in the field

In the context of failure phenomena observed around underground excavations, the most fundamental problem is splitting and shearing under conditions of compression. As shown in Figure 2.33 (Whittaker et al., 1992), the sidewalls of an excavation often suffer the growth of tensile splitting cracks, and spalling phenomena may be further induced (Vervoort and Jack, 1992). These phenomena are also often observed around openings in hard rock (Hoek et al., 1995).

Failure of pillars encountered in underground operations may be the best example

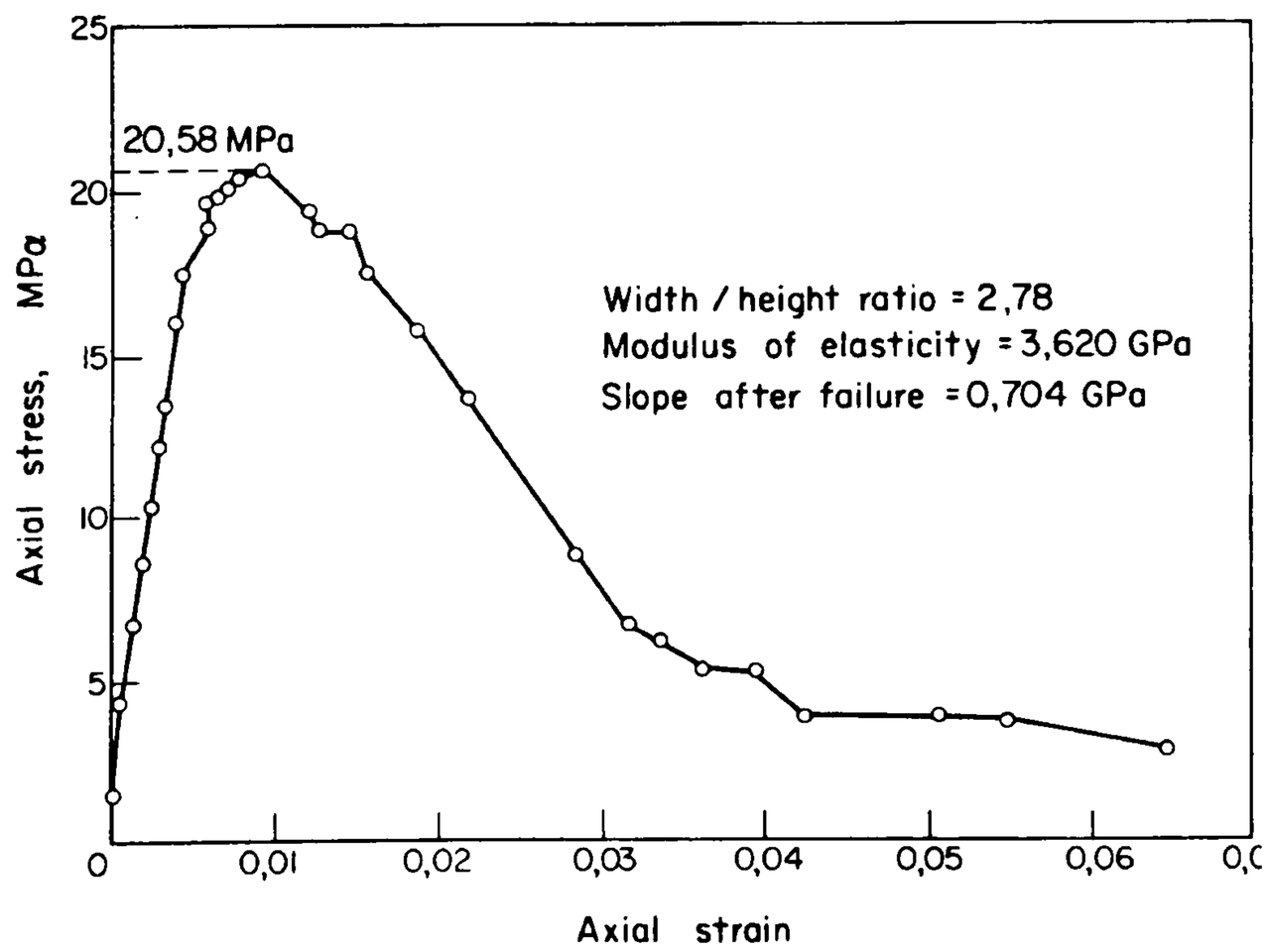


Figure 2.32. The complete stress-strain curve in uniaxial compression obtained *in situ* for a square coal specimen (from Bieniawski and Van Heerden, 1975)

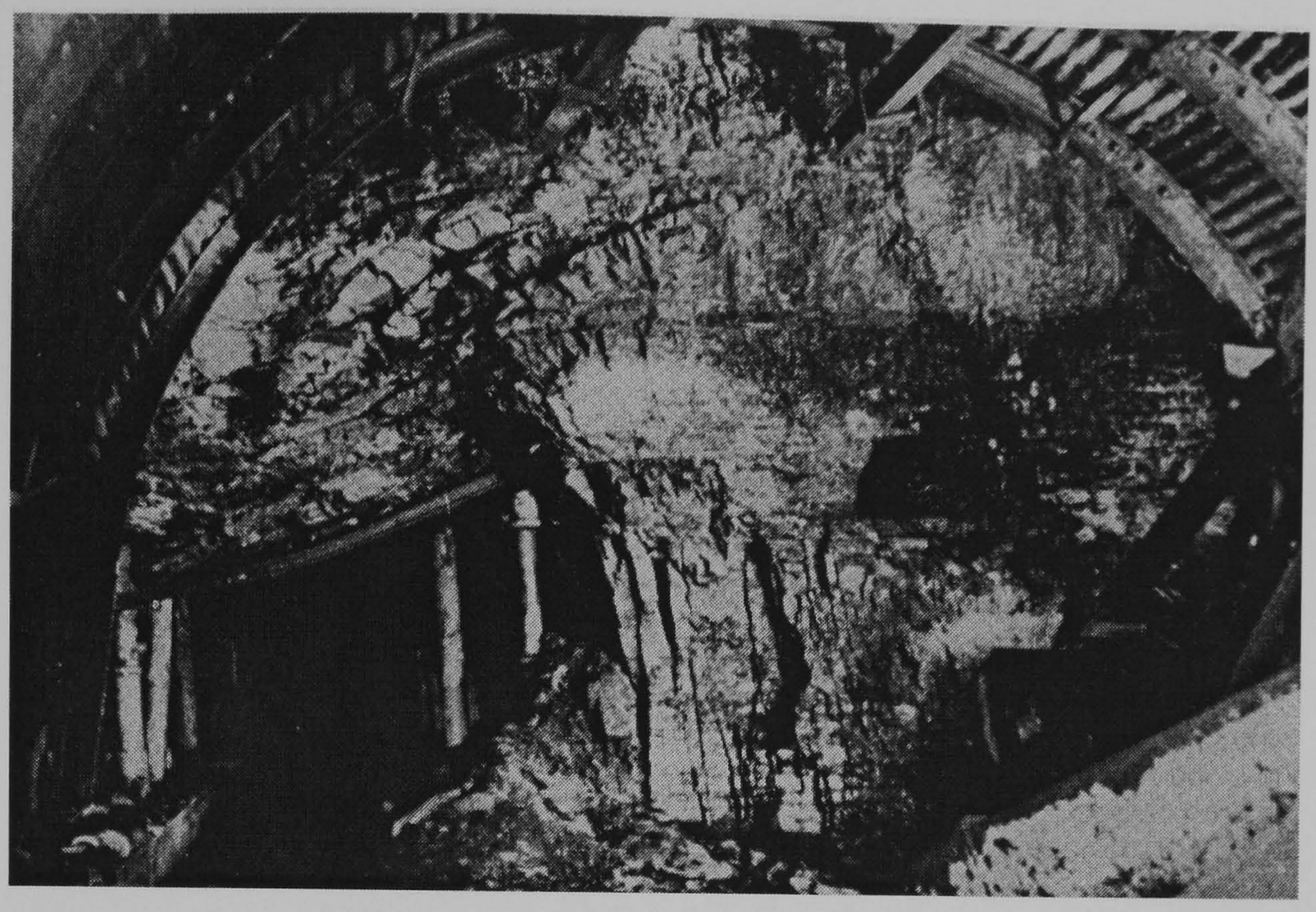


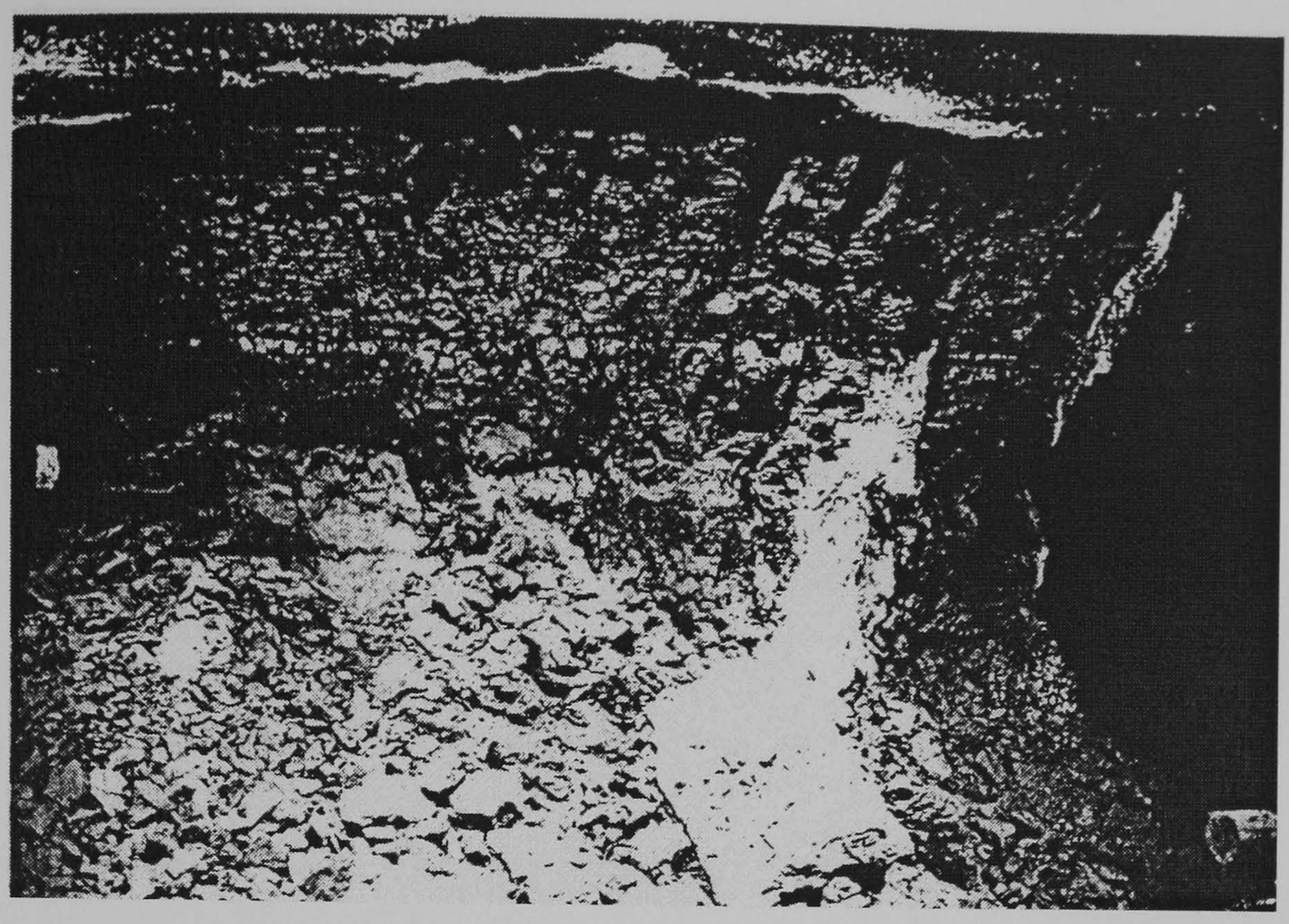
Figure 2.33. Tensile splitting fractures in the coal ribside of a longwall mining operation at 600 m depth (from Whittaker et al., 1992)

that can be used to compare to the failure of specimens in the laboratory. Two such field pillar failures from the literature (Mokgokong and Peng, 1991; Martin and Maybee, 2000) are presented in Figure 2.34. The first of these is a coal pillar, and the second a quartzite pillar. By relating them to the failure of the 1 foot cube coal specimen (Figure 2.31), the evidence in the similarity of failure modes can be easily identified.

Deformation behaviour of rock masses

Large scale rock specimens in experiments (see the previous section) fail in a similar manner to intact rock in the laboratory, and exhibit similar deformation behaviour, with the different quantities in the stress-strain relations being due to the existence of larger scale discontinuities. It is reasonable to postulate that failed rock masses *in situ*, whose failure patterns also resemble those of intact rock in the laboratory, exhibit similar deformation behaviour.

In their comprehensive review, Hoek and Brown (1997) studied the deformational phenomena of *in situ* rock masses around underground openings. They suggest that *in situ* rock masses can typically be grouped into three categories: very good quality hard rock masses; average quality rock masses; and poor quality rock masses. The mechanical characteristics of the three types of rock masses can be classified as: elastic-brittle; strain-softening; and elastic-plastic behaviour, respectively. Figure 2.35 shows



(a) coal pillar (from Mokgokong and Peng, 1991)

(b) quartzite pillar (from Martin and Maybee, 2000)

Figure 2.34. Failure modes of pillars in underground operations

the associated idealised mechanical behaviour.

Elastic-brittle behaviour tends to be encountered with high-modulus rock masses. The spalling that often occurs around highly stressed openings in very good quality hard rock masses is associated with a sudden drop in the rock mass load carrying capability (Hoek, et al., 1995). This suggests that the rock mass behaves in an elastic brittle manner as shown in Figure 2.35(a).

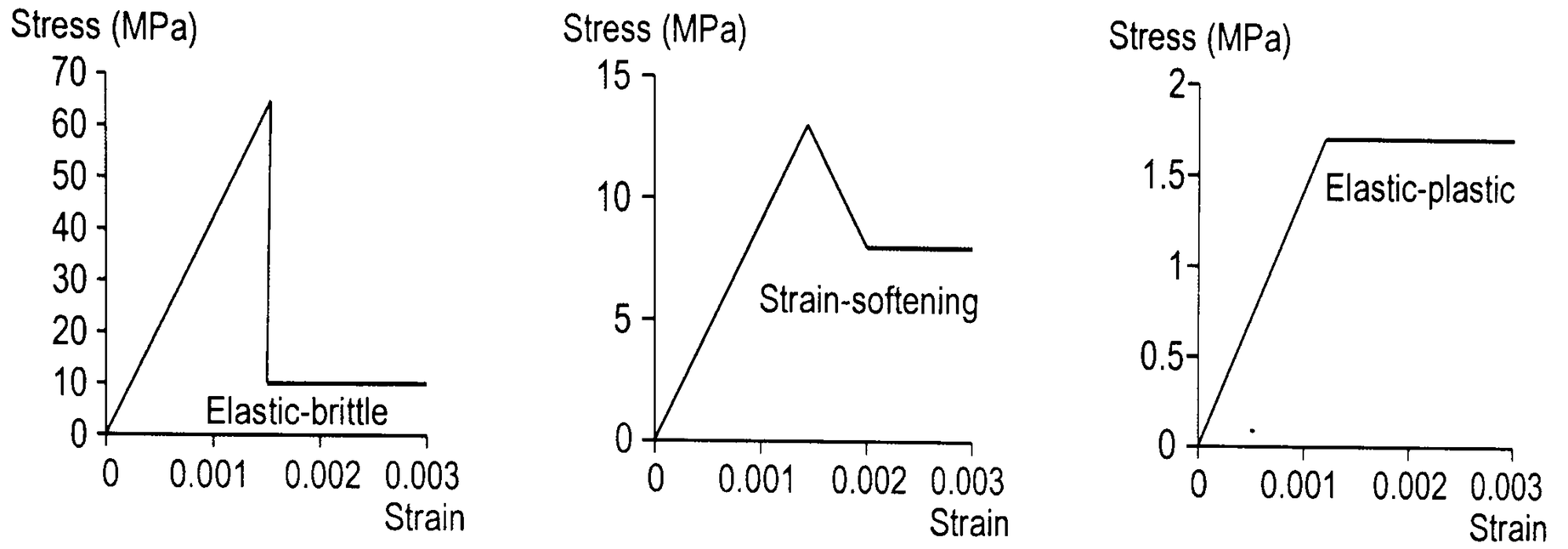


Figure 2.35. Suggested post failure characteristics for different quality rock masses (after Hoek and Brown, 1997)

Strain-softening behaviour is associated with average quality rock masses. Figure 2.35(b) relates to the behaviour of a rock mass of such quality. After the peak point, the strength of the rock mass reduces gradually from the *in situ* to the broken state, and then the strength of the broken rock mass remains at a residual value with no more reduction taking place.

In the case of a poor quality rock mass, the perfect-plastic nature (Figure 2.35(c)) is suggested by the progressive failure of rock masses surrounding tunnels. This means that the rock mass is able to deform at a constant stress level without volume changes with this ongoing failure.

2.6.3 Rock fracture in nature

The stress-induced fracture of brittle rock is phenomenologically consistent across many rock types and rock structures. In nature, we can easily find rock structures that are fractured either by tensile splitting, or by shearing, or by both. Figure 2.36 shows a rock structure in shallow rock that is heavily fractured by splitting and shearing with a spacing of up to several metres. Figure 2.37 shows *en echelon* crack arrays produced by natural loading in carbonate rocks of the Swiss Alps, which are similar with the *en echelon* crack arrays formed within a standard rock specimen in the laboratory (Figure 2.15).

In laboratory scale work and in the field, macroscopic fractures are often accompanied by subcracks (Andreev, 1995; Pusch, 1995; and see Figures 2.3 to 2.5), and this feature of brittle fracture appears to be reproduced on different scales (Pusch, 1995; and see Figures 2.30 and 2.33), including the geological scale (Jaeger and Cook,

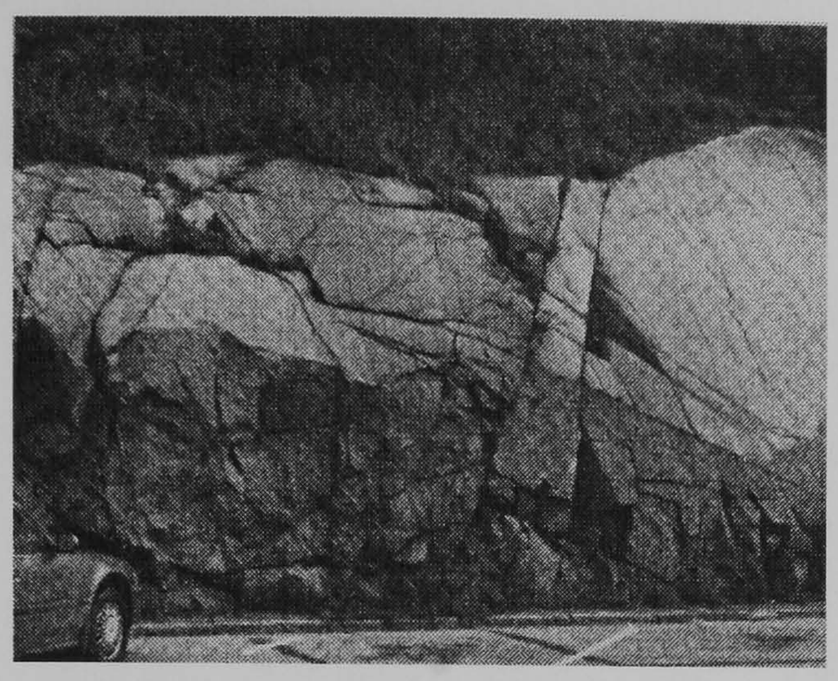


Figure 2.36. A natural fractured rock structure (from Pusch, 1995)

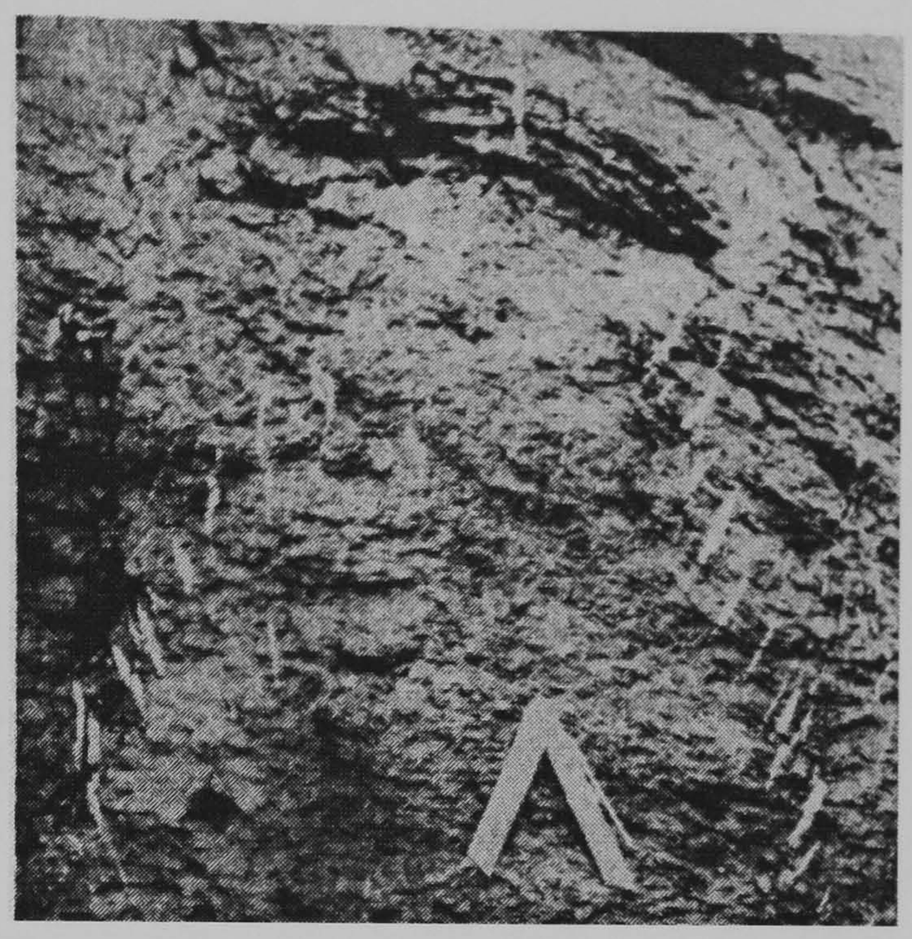
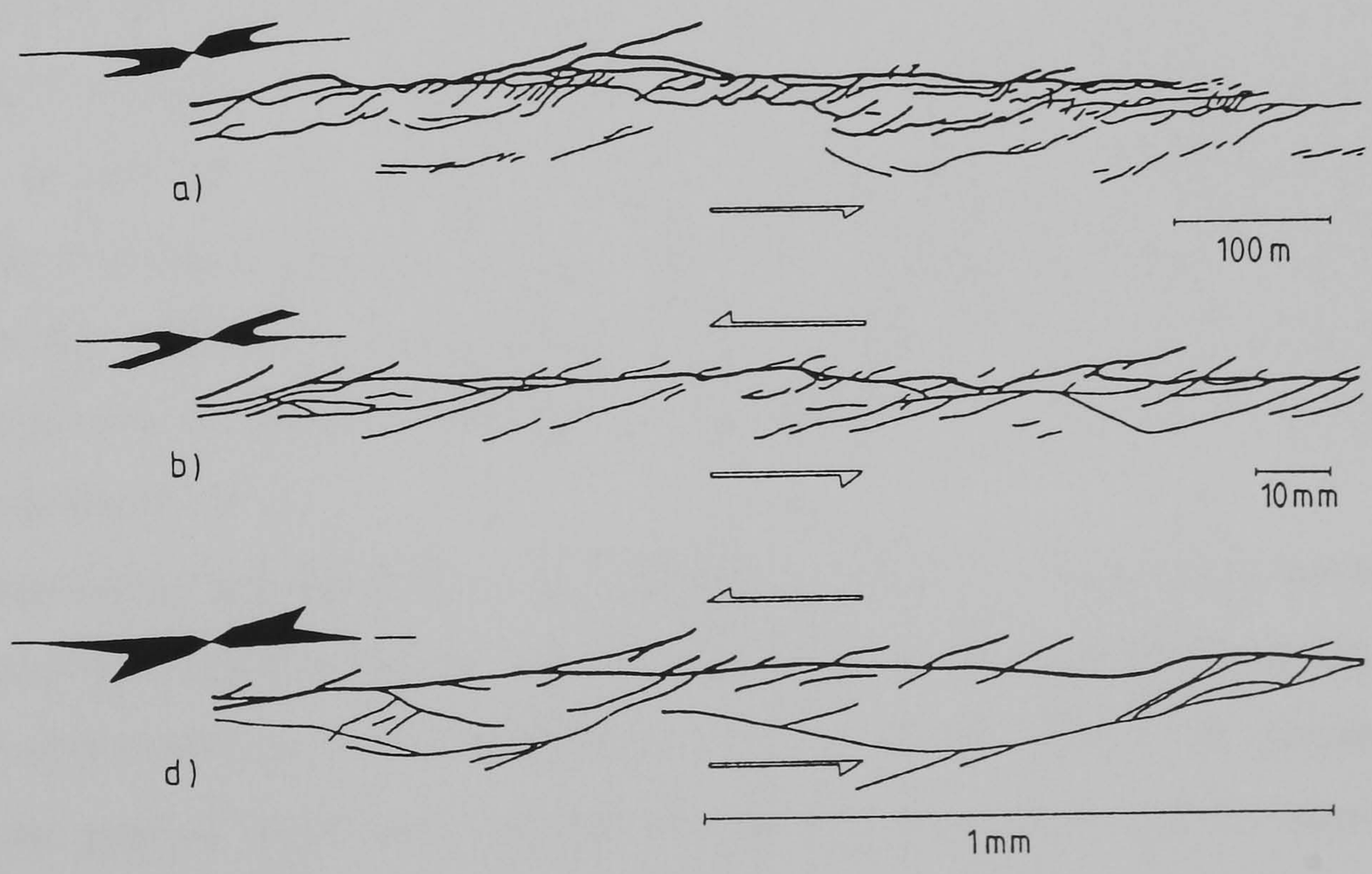


Figure 2.37. Natural loading induced arrays in carbonate rocks of the Swiss Alps (from Du and Aydin, 1991)

1979; and see Figures 2.36 and 2.37). On closer inspection, Figure 2.38 further illustrates a number of fracture patterns developed on different scales in the field and in the laboratory. It can be seen that even though the scale magnitudes of fracture systems are several orders of magnitude different, the physical appearance and the ultimate localisation patterns are at least geometrically similar. Therefore, it would not be



(The upper diagram shows shear-induced surface fractures mapped in eastern Iran, the lower ones are reproduced from laboratory shear tests)

Figure 2.38. Similar fracture patterns on different scales (from Pusch, 1995)

surprising that the behaviour of fracture on one scale can be analysed at another.

2.7 Closure

Rock failure under compression exhibits a variety of complex microscopic processes. These processes include the following:

- At a certain stress level, the initiation of microcracks starts from multiple random sites, such as cleavage, grain boundaries, inclusions, voids, and pre-existing cracks.
- As the load increases, the initiated cracks may grow and new cracks may form from new sites. With load continuously increasing and rock failure being approached, the growth of old cracks and the formation of new cracks tends to localise onto one or several specific planes, and *en echelon* crack arrays may form.
- When the density of the cracks reaches a critical degree the localised cracks or the *en echelon* crack array coalesce to form the eventual fracture plane.
- After the formation of the eventual fracture plane, microcracking events die off dramatically with increased strain.

The microcracking produces significant effects in the material. As a result of these complex microscopic processes, the material exhibits macroscopically a non-linear stress-strain behaviour, characterised by strain hardening and strain-softening stages. It has been established that the strain hardening stage is associated with the initiation, propagation and localisation of microcracking events, and the strain-softening stage is associated with the interaction and coalescence of localised cracks (Hallbauer et al., 1973). In addition, due to the growth of cracks, both strain-hardening and strain softening behaviours exhibit volumetric dilation. Moreover, the strength and stiffness of the material decreases with associated microcracking. Finally, if a loading-unloading-reloading cycle is applied to the tested rock specimen, a hysteresis loop is observed in the stress-strain curve.

Microscopic processes and the resulting macroscopic mechanical behaviour are influenced by confining pressure. Under uniaxial and low-confined compression, the growth of microcracks is in the direction more or less parallel to the direction of the maximum applied stress and eventual macroscopic fracture of rock is manifested by splitting. When confining pressure is moderate, the growth of microcracks may change to the direction inclined to the maximum loading direction, with shear faults a symbol of rock macroscopic failure. If confining pressure is extremely high, sliding between grains and crack surfaces is dominant. As a result of those processes, the corresponding

stress-strain relation displayed by the rock changes from brittle in uniaxial or low-confining compression to quasi-brittle (strain-softening) in moderate confining compression up to ductile in highly confined compression, with increasing strength.

There are many other points that we can draw from the investigations performed in this chapter. These points are not presented here, but are left to Chapter 8 instead in order to avoid duplication. All these points and many figures presented in this chapter will be further referred to in either commenting on the existing modelling methods of rock fracture (Chapter 3), or in developing the new model for rock brittle fracture (Chapter 4), or in interpreting results from the new model (Chapters 6 and 7). Now, we move on to examine the effectiveness of the existing models for brittle fracture of rock.

3 State of the art in the modelling of progressive rock fracture

From the review presented in Chapter 2 of rock fracture in either the laboratory or *in situ*, it is seen that rock fracture in compression is due to complicated microscopic processes. These processes include the formation of microcracks at multiple grain or defect boundaries, and growth and coalescence of microcracks. Associated with these processes are non-linear macroscopic behaviour, volume dilatancy of rock materials. In addition, these microscopic processes and the resulting mechanical behaviour of rock are influenced notably by confining pressure.

The microscopic processes associated with rock fracturing are manifested in the failure of many kinds of brittle materials and structures, such as glasses, concrete, ceramics, and metals. In order to describe the progressive fracture process and the associated macroscopic behaviour, extensive studies have been conducted on different materials and have resulted in a number of failure hypotheses (Griffith, 1921; McClintock and Walsh, 1962; Kachanov, 1958; Weibull, 1939). In the case of brittle fracture of rock materials, three such hypotheses — the discrete fracture mechanics theory, the continuum damage theory, and the statistical theory — appear to be most applicable and have been used or referred to by various workers in the study of fracture of rocks or rock structures.

This chapter will review the representative models developed from these three theories for the modelling of rock fracture, commenting on their capability of capturing the principal features of rock fracture in compression. In order to save space, the theories of discrete fracture mechanics, continuum damage mechanics, and statistical fracture mechanics are not introduced here; interested readers may refer to relevant books (*e.g.*, Atkinson, 1987; Kachanov, 1986; Krajcinovic, 1989; Whittaker et al., 1992).

3.1 Discrete micromechanics models based on fracture mechanics

Fracture mechanics "provides a quantitative treatment, based on stress analysis, which relates fracture strength to the applied load and structure geometry of a component containing defects." (Irwin and de Wit, 1983). In this theory, the defect, which is usually modelled as a crack although it could be a pore or other non-linear defect, is regarded as a stress concentrator and accorded an appropriate importance in controlling brittle fracture. The influence of applied loads on crack extension can be related in terms of certain parameters that characterise the stress and strain intensity near the crack tip (Atkinson, 1987).

Rock material is typically inhomogeneous, containing initial defects such as grain boundaries, cleavages, microcracks and pores (Subsection 2.2.1). Fracture mechanics theory is one of the most popular methods used for the study of fracture behaviour of rock materials under compression. During recent past decades, extensive experiments have been carried out on rock samples with predefined "cracks" (Subsection 3.1.1). These experimental observations have identified the specific mechanisms for the formation and growth of cracks from such a pre-existing defect, and a number of models have been proposed. These models have provided a basis for relating the applied loads to the growth of a discrete crack. This section gives a review of these models.

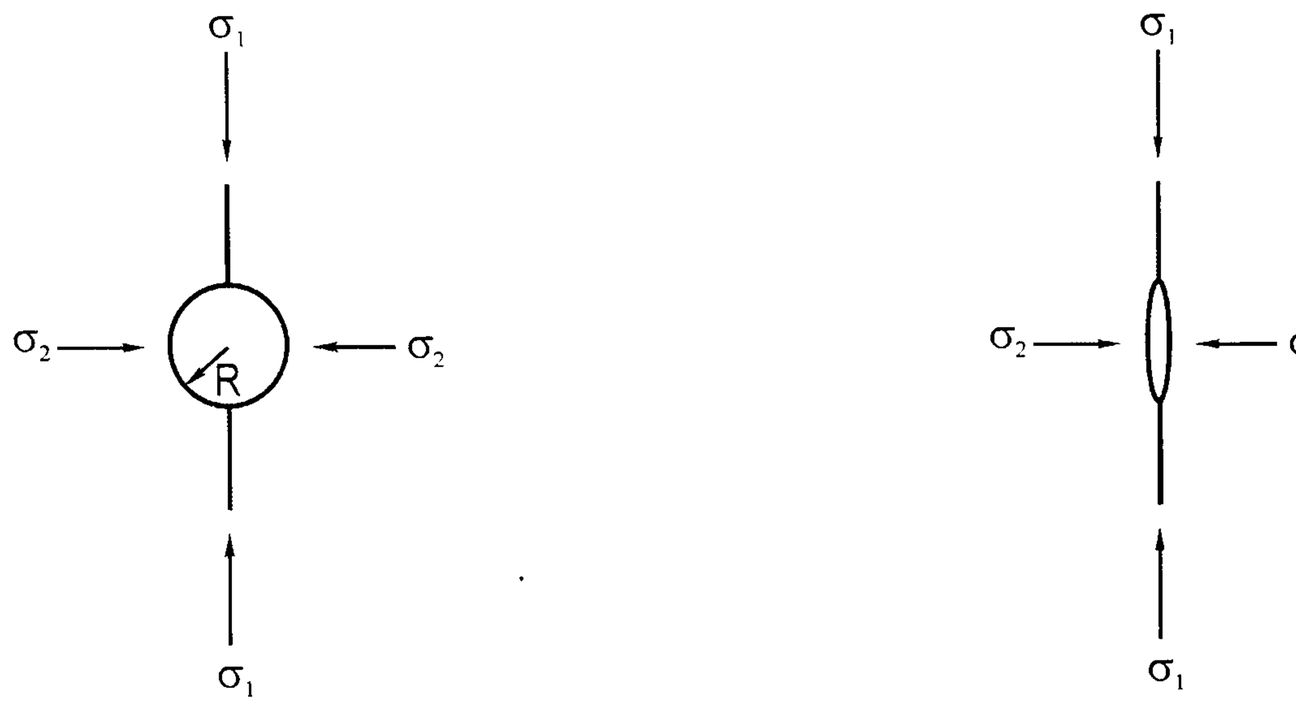
3.1.1 Physical models for the extension of microcracks

Two models are representative in explaining the mechanisms for the formation and extension of cracks. One is the open crack model (Sammis and Ashby, 1986; Zhang et al., 1990; Yuan et al., 1993), and the other the sliding crack model (Brace and Bombolakis, 1963; Brace et al, 1966; Fairhust and Cook, 1966; Horii and Nemat-Nasser, 1985; Ashby and Hallam, 1986).

Figure 3.1 shows the open crack model, which can be in the shape of either a cylindrical pore (Figure 3.1(a)) (Sammis and Ashby, 1986; Zhang et al., 1990), or an elliptical open crack (Figure 3.1(b)) (Yuan et al., 1993). Under external compressive loading, stresses intensify around the pore or the crack tips, and tensile components develop on the boundary of the pore at 90° from the line of action of the smaller applied in-plane stress or near the tips of the elliptical crack. As a result, tensile cracks are induced at the critical point in the direction parallel, or inclined at a small angle, to the

direction of the maximum compressive stress (Figure 3.1).

The sliding crack model, as shown in Figure 3.2, contains an initial crack of length $2a$, oriented at an angle γ with respect to the maximum stress direction, and a pair of curved tensile (or wing) cracks, oriented at an angle θ to the initial crack plane, which represents the growth geometry of the initial crack. As with the open crack model, the sliding crack model regards the initiation and growth of the wing cracks as being due to the intensified tensile stress near the crack tips. The mechanism for inducing the tensile concentration, however, lies mainly in the sliding effect along the surfaces of the initial crack.



(a) Cylindrical (b) Elliptical

Figure 3.1. Open crack models

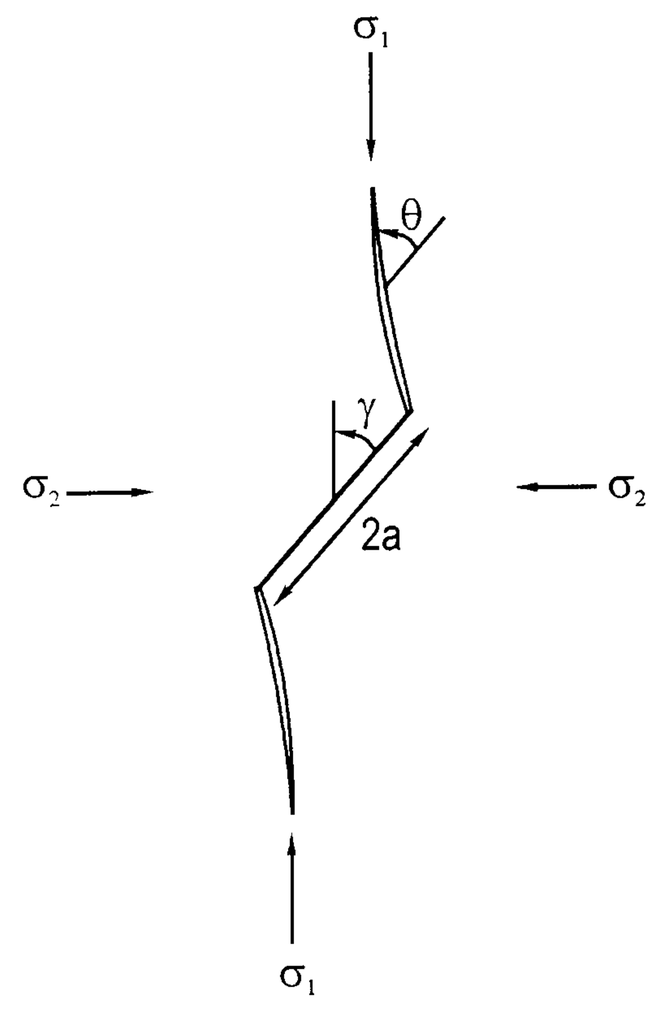


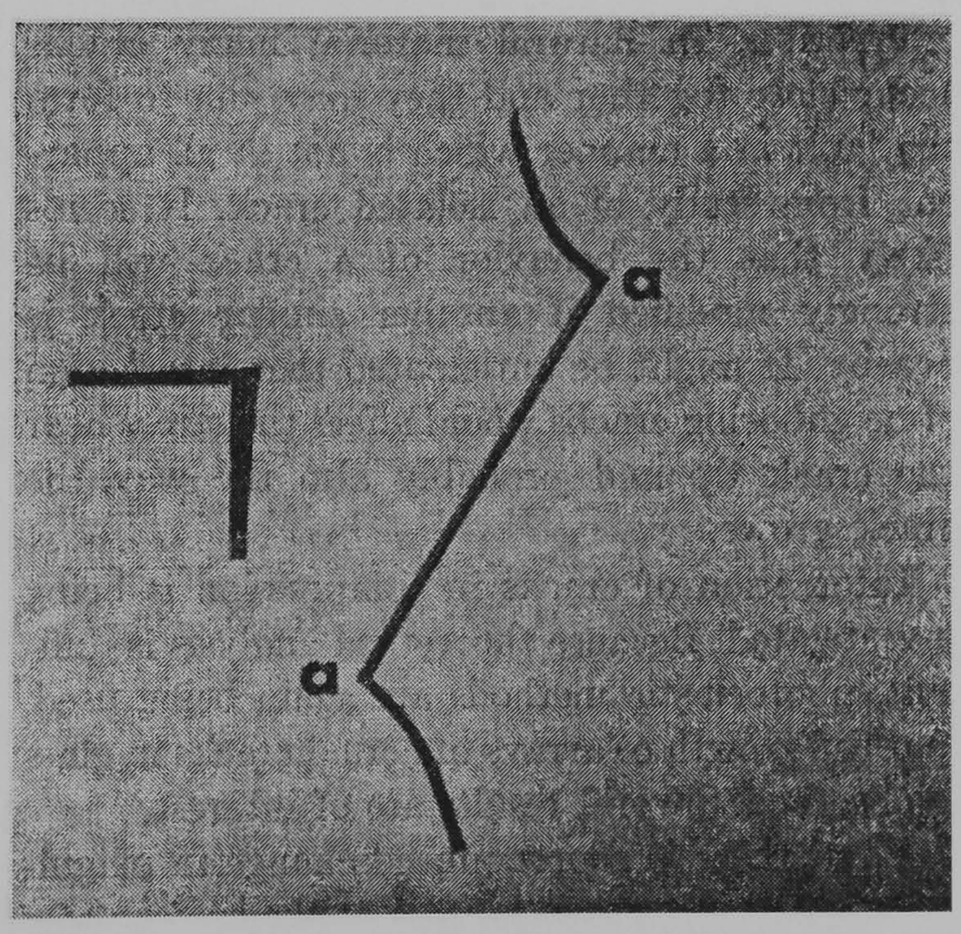
Figure 3.2. Sliding crack model

The sliding crack model was first proposed by Brace and Bombolakis (1963), and is based on experimental observations made during compression of a plate of photoelastic material containing a pre-cut slit inclined to the maximum stress direction. In the experiments, it was observed that the induced crack emanates from a point at the slit tip in a direction out of the slit plane, and develops along a curved path that turns to become parallel to the direction of the maximum stress (Figure 3.3). The same phenomena have also been observed by, amongst others, Hoek and Bieniawski on glass plates (Hoek and Bieniawski, 1965), Nemat-Nasser and Horii (1982), Horii and Nemat-Nasser (1986), and Ashby and Hallam (1986).

3.1.2 Micromechanics-based modelling of rock compressive fracture behaviour

Both the open and sliding crack models have been used to model the compressive fracture behaviour of rock. The concept of a stress intensity factor (SIF) close to the boundary or tips of a specific crack is usually used to relate the growth of a crack to the applied load and the crack geometry. For extensive crack propagation from a cylindrical pore under the condition of $\sigma_1 > 3\sigma_2$, for example, Sammis and Ashby (1986) formulated a SIF expression that shows that the SIF initially increases with crack advance, reaches a maximum, and thereafter decreases with further growth of the crack.

Of the two crack models, the sliding crack model is more representative in



(The maximum stress direction is vertical)

Figure 3.3. Crack growth in Photoelastic plastic (from Brace and Bombolakis, 1963)

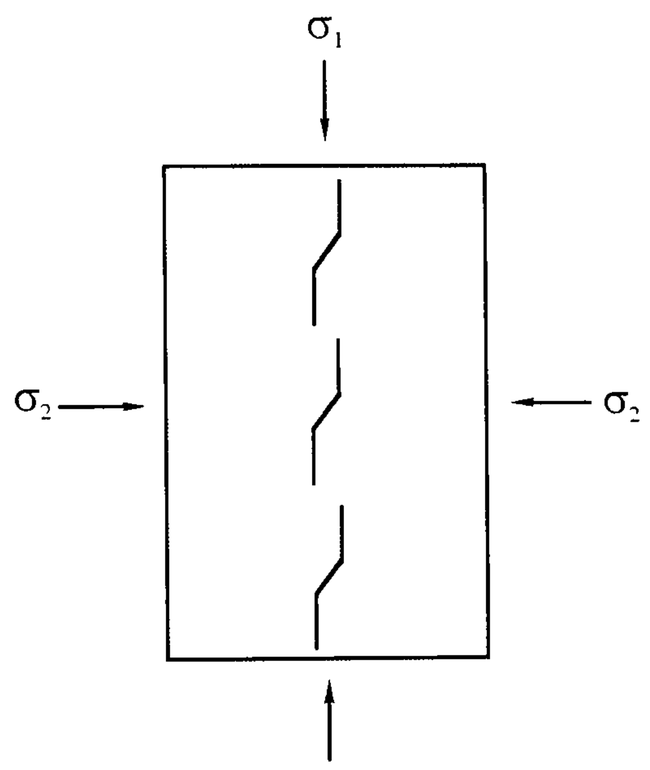
describing fracture behaviour of rock. In this model, the frictional effect that is taken into account in the stress intensity factor for crack extension leads the model widely used by researchers to reproduce the characteristics of the mechanical response of rocks under compressive stresses (Brace et al., 1966; Scholz and Kranz, 1974; Steif, 1984; Horii and Nemat-Nasser, 1986; Ashby and Hallam, 1986; Kemeny and Cook, 1987; Kemeny, 1991; Lehner and Kachanov, 1996; Li et al., 2000). Since the SIF solutions for the crack configurations shown in Figure 3.2 do not exist in analytical form (Kemeny and Cook, 1987), all the SIF models developed for sliding crack growth are based on basic assumptions of simplifying the crack configuration and the crack extension mechanisms.

Horii and Nemat-Nasser (1986) developed a model for the SIF based on the assumption that the entire configuration can be replaced by a single rectilinear crack inclined to the direction of the maximum compressive stress, and that the rectilinear crack is driven by a pair of point forces collinear with the direction of the initial crack. Steif's model (1982) was proposed by assuming that the wing cracks are straight and that the influence of the initial crack on the growth of wing cracks can be represented by a wedging slip displacement. In developing their model, Ashby and Hallam (1986) assumed that wing cracks have a fixed orientation, parallel to the major principal stress, with the normal and shear stresses along the initial crack faces being the driving system for crack extension. Using symmetrically opposite centre forces to drive a crack oriented in the maximum stress direction, Kemeny and Cook (1987) proposed a model of decreasing SIF with increasing crack length. Lehner and Kachanov (1996) reviewed all the models above and proposed that the wing crack extension system can be represented by both the wedge displacement-driven and stress-driven systems, and a SIF model was suggested by equating the wedge displacement and acting stress effects in driving the wing crack growth.

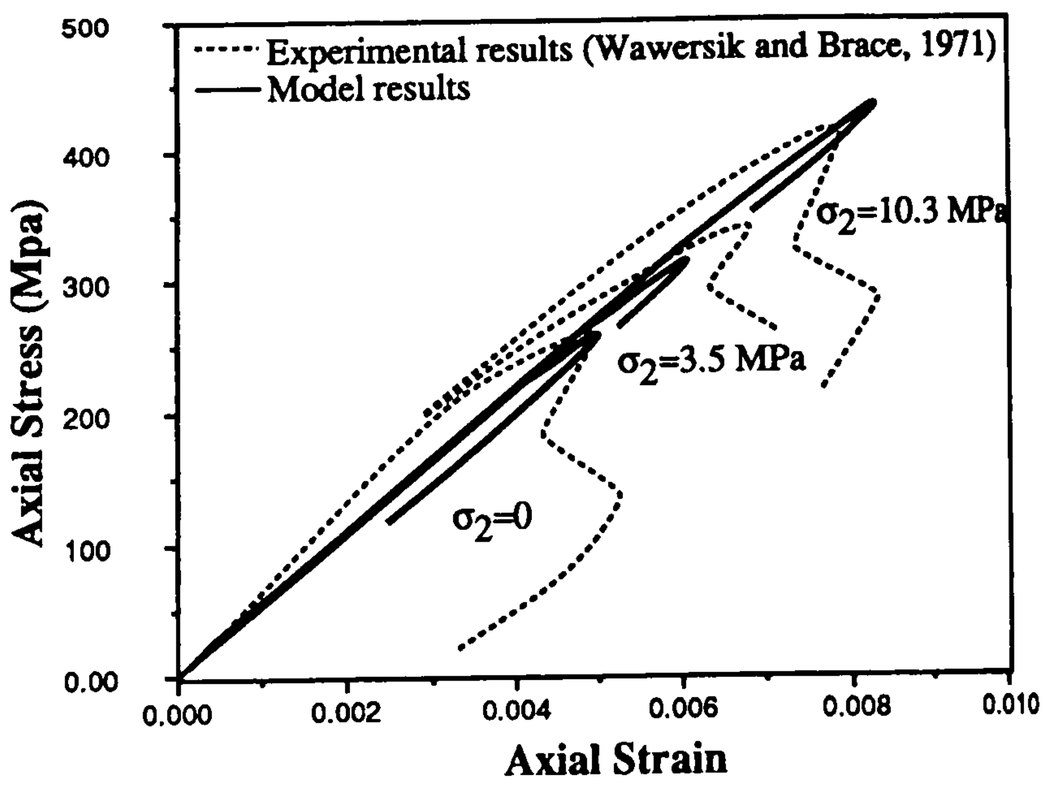
The models above were developed primarily for the extension of wing cracks from isolated sliding cracks. All the models predict similar results corresponding to the growth of wing cracks, in that the growth of isolated wing cracks is stable. This is in accord with laboratory experimental results that the axial extension of microcracks is associated with strain-hardening in the macroscopic mechanical behaviour (see Chapter 2). However, for the stages of approaching the peak and strain-softening of brittle rock materials, in which the localisation and coalescence of cracks come into play, none of these models can be used directly and modifications or additional models have to be incorporated in SIF solutions by introducing either parameters associated with the

distance between cracks (Ashby and Hallam, 1986; Horii and Nemat-Nasser, 1986; Kemeny and Cook, 1987; Kemeny and Tang, 1990; Kemeny, 1991; Lehner and Kachanov, 1996), or the damage effect associated with the density of initial cracks (Ashby and Hallam, 1986; Kemeny and Tang, 1990; Kemeny, 1991).

Figure 3.4(a) shows the collinear array configuration used by Kemeny and Cook (1987), Kemeny and Tang (1990) and Kemeny (1991), and the stress-strain curves at three confining stresses predicted by a modified Kemeny and Cook's model, from the viewpoint of energy equilibrium, are shown in Figure 3.4(b). The figure shows that



(a) Collinear array configuration, cracks are equally spaced with the same geometry (after Kemeny, 1991)



(b) Stress-strain curves for Westerly granite at three confining stresses (From Kemeny, 1991)

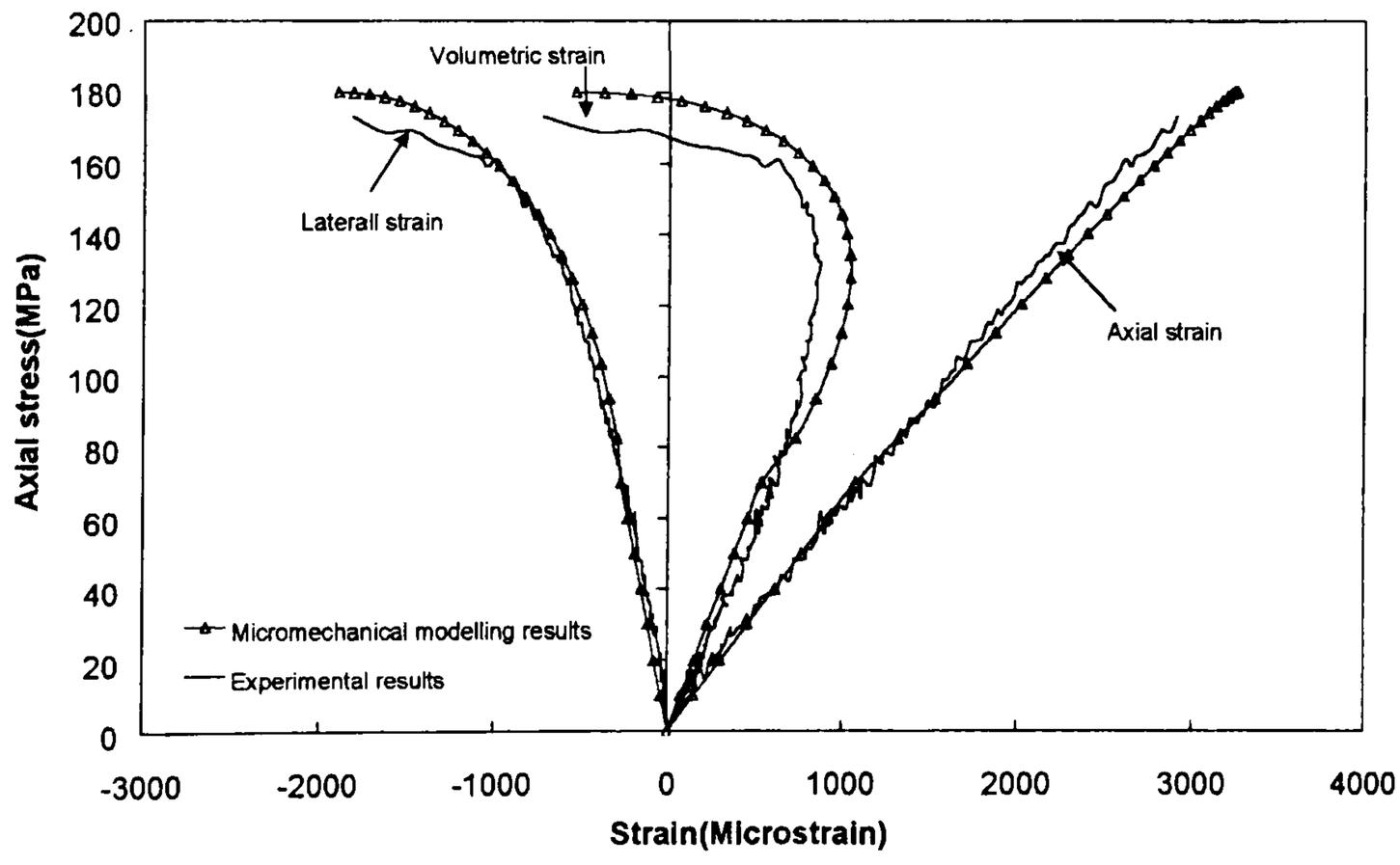
Figure 3.4. Crack array configuration and predicted stress-strain curves using the Kemeny and Cook model

these are comparable to the experimental results on Westerly granite obtained by Wawersik and Brace (1971). A similar approach has been used to obtain more realistic results of axial and lateral strain-stress curves (Figure 3.5), but at the expense of more complicated formulations (Li et al., 2000).

3.1.3 Comments on the current micromechanics-based models for rock fracture

As seen in the previous subsections, SIF solutions in a micromechanics model are based on a well defined crack or defect, and the description of the stress-strain relation near and after the peak relies on the introduction of parameters associated with the spacing or density of cracks. Although these requirements and techniques allow the prediction of axial extension of individual cracks and the non-linear mechanical behaviour of the material (with strain-hardening portion corresponding to the axial extension of cracks and strain softening stage to the interaction of cracks), limitations are encountered in both applying a micromechanics model to practical problems and predicting the localisation and coalescence of microcracks during rock fracture.

The application of micromechanics models requires that the material concerned must have a well defined crack or defect, and that the length, orientation, and spacing between initial cracks, together with the frictional coefficients of the initial crack



(The similar crack array configuration shown in Figure 3.4(a) was assumed in producing these curves)

Figure 3.5. Stress-strain curves of the Bukit Timah granite predicted by Li et al. (2000)

surface, are all known. Since the features of pre-existing cracks within a material are normally undetectable, this method is impractical (Ofoegbu and Curran, 1992; Whittaker et al. 1992).

In addition, because the sliding crack model (Figure 3.2) predicts that a crack grows in the direction of the maximum compressive stress, it can only be used to model strain hardening or rock failure caused by axial splitting fractures (Fairhust and Cook, 1966; Li et al. 2000). Moreover, although the sliding crack model can reproduce many features of rock responses to applied load, its physical expression has never been observed in experiments on natural rock samples.

Finally, the peak strength and the following strain softening characteristics in the stress-strain behaviour displayed by rock in compression are associated with the localisation and coalescence of microcracks (see Sections 2.1 to 2.3). Micromechanics models simply correlate the strain-softening characteristics to the interaction of all existing cracks, avoiding explaining the occurrence of these two phenomena. Hence, micromechanics models cannot predict the localisation and coalescence of microcracks, which play a very important role in leading to eventual rock fracture.

3.2 Continuum damage mechanics models

Given the limitation of fracture mechanics to analyse both complex microscopic processes and their relation to the macroscopic behaviour in the peak and post peak stages of the material, Continuum Damage Mechanics (CDM) has emerged as one of the alternatives to modelling the failure of brittle materials. This is based on damage analysis, which relates the effect of microdefects to the macroscopic material properties through the use of internal state variables (Krajcinovic and Fonseka, 1981; Krajcinovic, 1984; Costin, 1985, 1987).

The mechanical properties and the ultimate strength of engineering materials depend, to a large degree, on the microdefects in their structure. Under the presence of external effects, the microdefects contained in materials may nucleate or grow. These microscopic mechanisms induce a significant effect in the macroscopic elastic constants and strength of the materials, even without failure taking place (Sections 2.1 and 2.3), and this effect may be described by a single or set of internal variables (Krajcinovic and Fonseka, 1981; Krajcinovic, 1984; Costin, 1987).

The concept of averaging the mechanical response corresponding to the changes of internal state of a deformed material was introduced by Kachanov (1958) to study the

effect of void growth on the behaviour of metals undergoing creep. Subsequently, the development of damage mechanics has principally been undertaken in metallurgy in order to give a better understanding of rupture problems in structures, through the definition of a variable that represents the deterioration of the materials before the initiation of a macro-crack (see Krajcinovic, 1984; Lemaitre, 1984). In recent years, this approach has been broadly applied to many fields to describe the deformation and failure of brittle materials under various loading conditions (Lemaitre, 1984). This theory has become very popular, as it provides a relatively effective way to deal with the complex failure process of deformed materials subjected to a variety of stress conditions.

3.2.1 CDM models

A single variable, or a set of variables, is required to describe the changing state of the microstructure of a material being deformed. Although the variables themselves change from case to case, three basic elements are involved in any damage theory. These are: a definition of damage; an evolutionary equation for the damage; and a constitutive equation that relates the strains to the stresses and the damage (Costin, 1987). The definition of damage may or may not consider the physical behaviour of individual microcracks, and the methods for doing so are related to one of two classes of damage models: the phenomenological damage model and the micromechanics-based damage model (Krajcinovic, 1989; Charlez, 1991).

The phenomenological models are those whose foundation is based on purely macroscopic considerations of the material during damage evolution, irrespective of microscopic effects (Charlez, 1991). In this method, the macroscopic quantities of the materials undergoing damage are averaged by relating to the damage variables defined from experiments. The damage evolution law for a given macroscopic stress or strain is derived either from experiments, or from the general framework of thermodynamics (Krajcinovic and Fonseka, 1981; Lemaitre, 1984; Ilankamban and Krajcinovic, 1987). Since the parameters involved in thermodynamic equations are very difficult to be determined (Liao, 1995), the commonly used method for the averaging procedure is to irreversibly reduce the rigidity matrix during the process of irreversible deformation of materials (Lemaitre, 1984; Krajcinovic, 1989; Charlez, 1991).

The micromechanics-based models, in contrast, analyse the damage effect at the microscopic level. The behaviour of microdefects distributed in the material is generally

used to explain the mechanical behaviour of the material, and the technique used in these models is to homogenise a heterogeneous solid induced by the existence and evolution of microdefects into an equivalent continuum that exhibits the macroscopic behaviour of the material (Krajcinovic, 1989; Charlez, 1991). The stress-strain relation of the equivalent continuum is deduced from the average stress-strain relation of the heterogeneous material through the homogenisation techniques, and the evolution law of damage is derived from considering the growth of microdefects.

3.2.2 Applications of CDM to the analysis of rock fracture

Continuum damage mechanics have been broadly applied to modelling the deformation and failure of brittle materials such as concrete and metals, and the ductile plastic, creep and fatigue deformation displayed by those materials under specific conditions can be successfully described (see Lemaitre, 1984). For rock deformation, this approach, by itself or in a combination with other theories, has also been applied by a number of researchers in developing models to account for material deterioration related to the microstructural kinetics of deformation.

In the class of phenomenological CDM, Dragon and Mroz (1979) proposed a strain-softening elasto-plastic constitutive model by relating plastic dilation to damage, in which the structural changes are governed by a softening parameter. Frantziskonis and Desi (1987) proposed a model by decomposing the structure volume into two parts, an elastoplastic continuum part and a damaged part with zero stiffness, and the damage parameter in this model is determined by plastic strain history. Valanis's model (Valanis, 1985) simply reduced the elastic modulus of the material through the use of an exponential function corresponding to the different strain ranges. The same approach was used by Tzou and Chen (1991), but evolution of void density was incorporated. This feature was also used by Sammis and Ashby (1986) and Ashby and Hallam (1986) in studying the effect of interaction of closely spaced defects on the effective elastic modulus of the material. Based on experimental observations, Ofoegbu and Curran (1992) proposed a model that captures both induced volumetric dilation of initially intact rock and subsequent softening by changing the material's elastic stiffness, shear strength and dilation ratio.

In the class of micromechanics-based CDM, the model developed by Costin (1985) is exemplary. In this model, the damage parameter was defined by those cracks that are under either propagation or interaction, and an equivalent macroscopic damage criterion was able to relate to the microcracking processes. This model was further modified by

Shao and Rudnicki (2000) by taking into account the density and orientation of microcracks.

All these damage models exhibit a certain success in modelling the features of the macroscopic mechanical behaviour of fractured rock, when compared to experimental results. Figure 3.6 is the axial stress-axial strain and volumetric strain-axial strain curves given by Ofoegbu and Curran's model (Ofoegbu and Curran, 1992). Figure 3.7 shows the simulated stress-strain curves of Westerly granite (Costin, 1985), and these are comparable with the results presented in Figure 3.4(b). Figure 3.8 presents the deviatoric stress-axial strain and the deviatoric stress-radial strain curves obtained by Shao and Rudnicki's modified Costin model (Shao and Rudnicki, 2000).

3.2.3 Comments on the current CDM models for rock fracture

Continuum damage models take into account the effects of crack evolution on the macroscopic behaviour of a material undergoing microstructural changes. the phenomenological damage models average these effects over the entire material without considering microscopic events at all. This means the phenomenological damage models are only able to describe the quantitative macroscopic behaviour of the material, but not localisation and coalescence of microscopic events.

On the other hand, although the micromechanics-based damage models consider the evolution of crack density or the growth of a single crack, the effect is

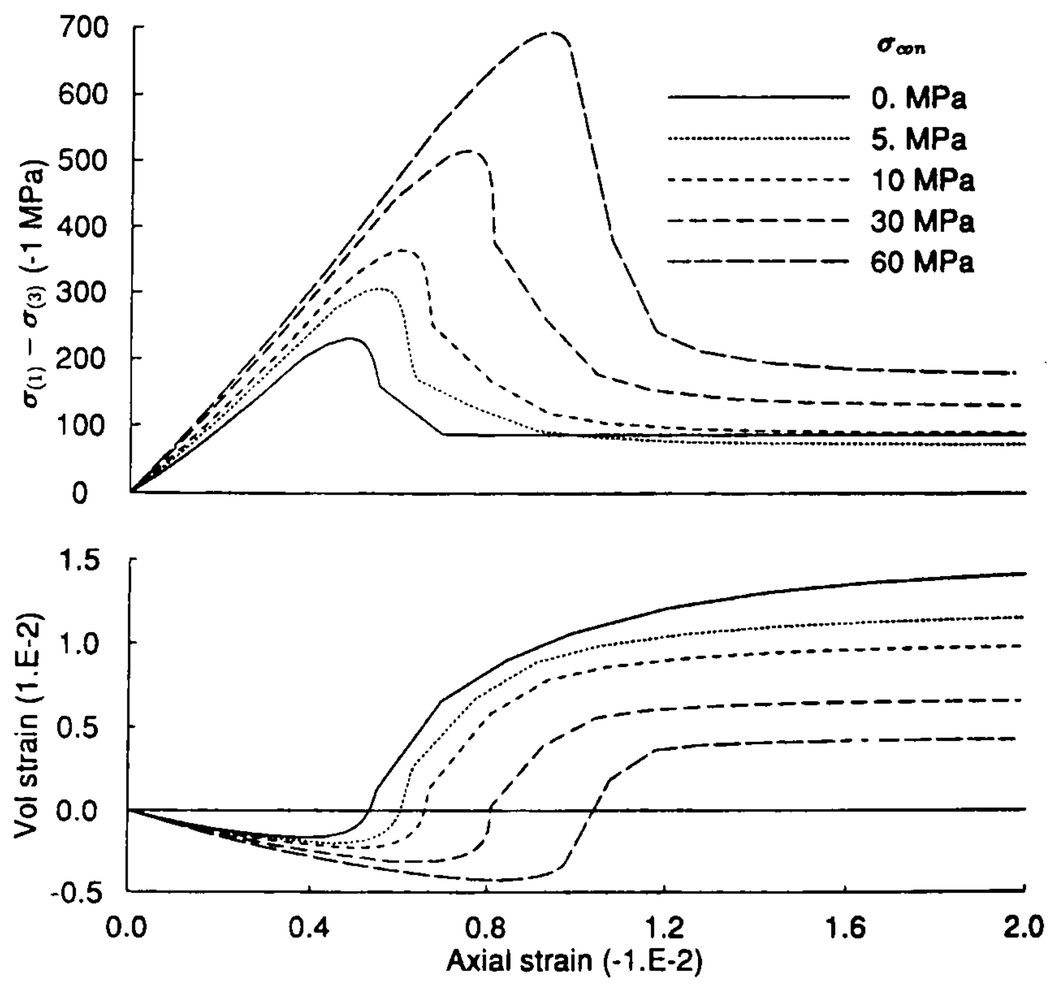


Figure 3.6. Simulated stress-strain and volumetric strain curves obtained using the Ofoegbu and Curran model (Ofoegbu and Curran, 1992)

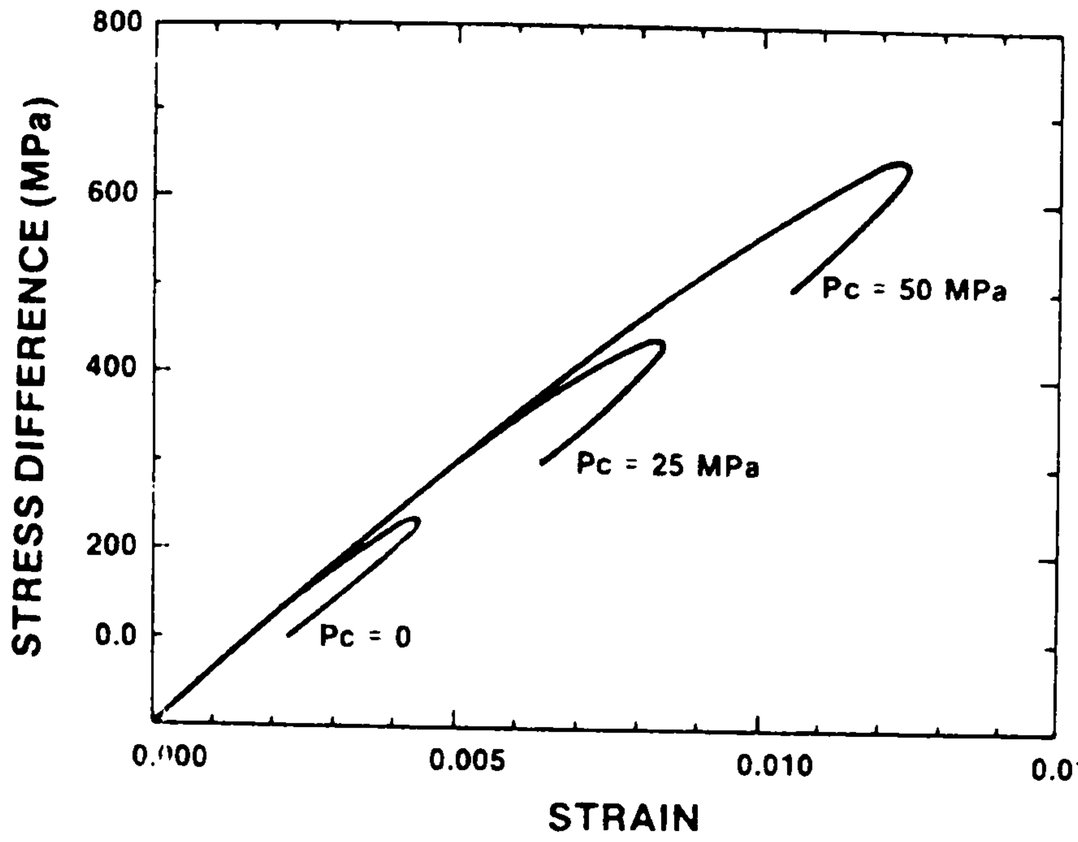


Figure 3.7. Simulated stress-strain curves of Westerly granite at different confining pressures obtained using the Costin model (Costin, 1985)

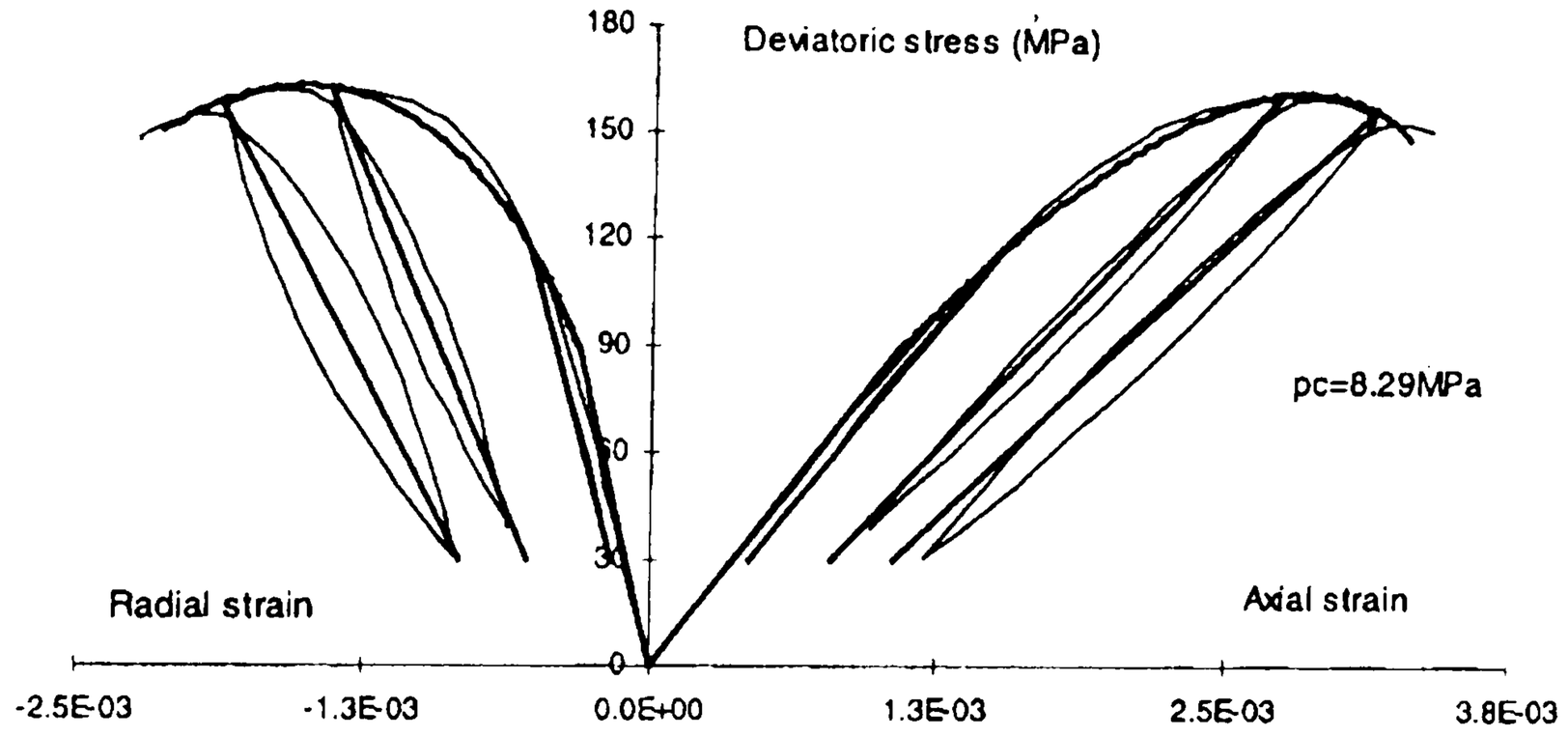


Figure 3.8. Simulated loading-unloading stress-strain curves of Tennessee marble obtained using the Shao and Rudnicki model (Shao and Rudnicki, 2000)

conventionally averaged over a periodic structure or uniformly distributed representative volume elements. These models can provide the overall stress-strain relation, which reflects the effects of the growth of, and interaction among, microdefects, but are still unable to reproduce the localisation and coalescence of microcracks in rock fracture, because of a more or less uniform or periodic distribution of microdefects being assumed.

3.3 Statistical model

Statistical theory is another method that can be used to analyse the fracture process of a

heterogeneous material. The fundamentals of the statistical theory lie in the fact that a real material inherently contains a large number of defects that are related to microstructural features of the material, such as elemental strength or elastic constants. These defects are assumed to be statistically distributed within the material. The existence of the defects produces a stress concentration under external loading, and local failure takes place when the concentrated stress exceeds the local strength. Thus, fracture of the material as a whole is determined by the local strength of its elements. If elemental physical features of a material are known, an ideal system can be constructed using the statistical technique. This allows this type of theory to examine the effects of heterogeneity at an elemental scale on the macroscopic properties of the material.

3.3.1 Statistical models

In terms of the failure criterion applied to structural failure, there are two types of statistical models (Whittaker et al., 1992). The first is the global failure model, which assumes that the failure of the overall structure is determined by the failure of many defects or cracks, subjected to the probability of the number of failed cracks or defects.

The other statistical model is the local failure model, which considers that the failure of the overall structure is produced by the failure of a single crack or defect. Both laboratory experiments and field observations have shown that the failure of rock in compression is caused by multiple microcracking events (see Chapter 2). Clearly, on this basis the local failure model is not appropriate for describing rock failure in compression.

3.3.2 Application of statistical models to rock fracture

Scholz was one of the first to describe the failure of rock from a statistical viewpoint (Kranz, 1983). Based on analysing the radiated elastic waves associated with rock fracture (Scholz, 1968; and see Section 2.5), Scholz proposed that due to the nature of heterogeneity the local stresses within a stressed rock will fluctuate significantly from the applied value. Scholz divided the stressed rock medium into small volumetric regions each of which have a specific strength (Figure 3.9(a)), and assumed that the stresses on each region are randomly different but constant over an individual partition. The local stress state can then be described by a distribution function $f(\sigma;\overline{\sigma})$ that changes as the mean (applied) stress changes (Figure 3.9(b)). When the local strength is exceeded by the local stress, the region fails, and a crack propagates which may be



(a) Partition representation of an inhomogeneous body

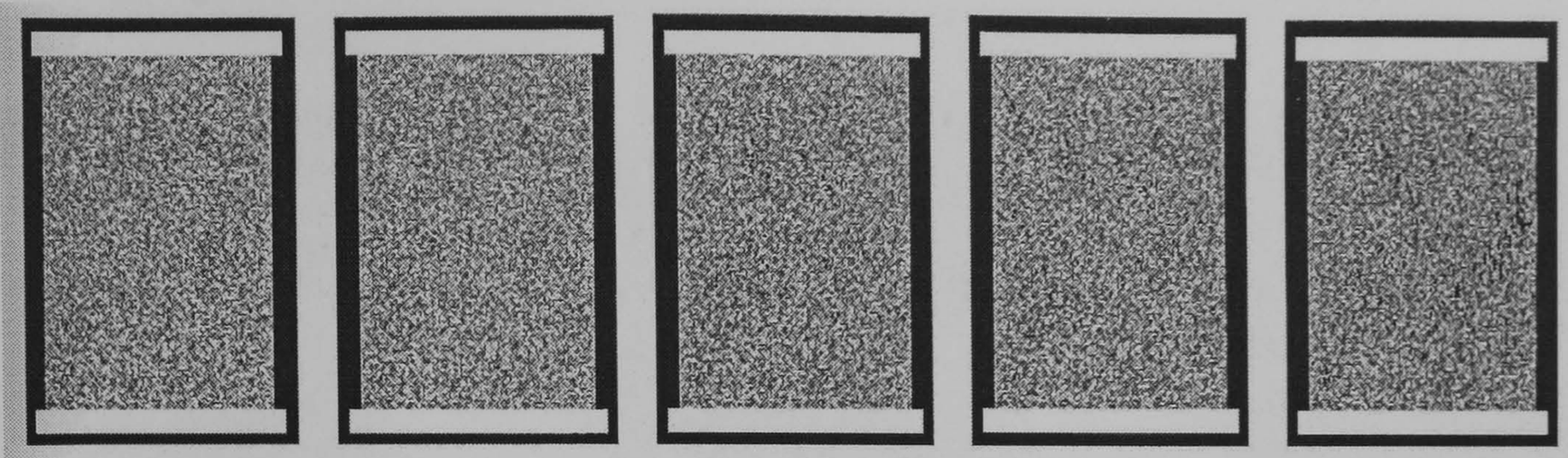
(b) Stress probability function and the local strength distribution

Figure 3.9. Statistical model for local stress (σ) distribution within an inhomogeneous body subjected to an applied stress ($\overline{\sigma}$) (from Scholz, 1968)

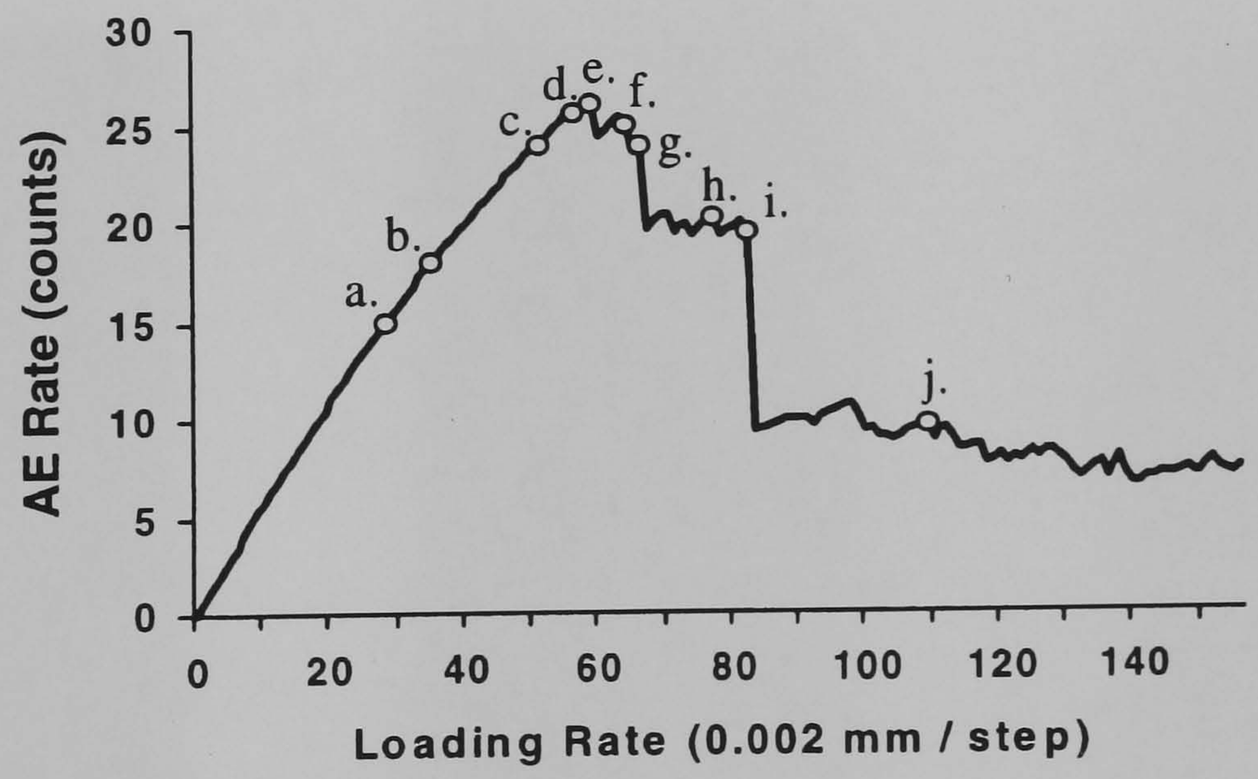
arrested if it enters a region of higher strength or lower stress. As the applied stress increases, the region with the next highest stress concentration will fail, and so on. Consequently, the local stress distribution function moves to the left (Figure 3.9(b)), so that the probability of failed regions increases, until some sort of instability produces fracture of the entire body.

Recently, two works that relate to Scholz's notion of using statistical techniques to model rock fracture have been seen. One such model is that developed by Tang et al. (2000). In this model, the microstructural heterogeneity of the rock material is represented by various elemental strength and elastic modulus, and is described by the Weibull distribution function (Weibull, 1951). Elasto-brittle behaviour with zero residual strength is assigned to each element, and elemental failure is governed by a compressive strength failure criterion. Since the stress-strain calculation was introduced into the model so that it could be incorporated into numerical analysis, both the fracturing process and the associated macroscopic stress-strain behaviour can be modelled. One example of the model's output for laboratory scale rock samples is shown in Figure 3.10.

Another interesting statistical model for rock fracture is a lattice type model developed by Blair and Cook (1998). This model decomposes the stress field in a cracked rock into one of an elastic continuum and one of a cracked elastic body. Similarly, the strength heterogeneity of the model is introduced by assigning different tensile strength values to different sites, but the stress heterogeneity within the material is simulated by introducing a perturbation to the continuum stress field. When the



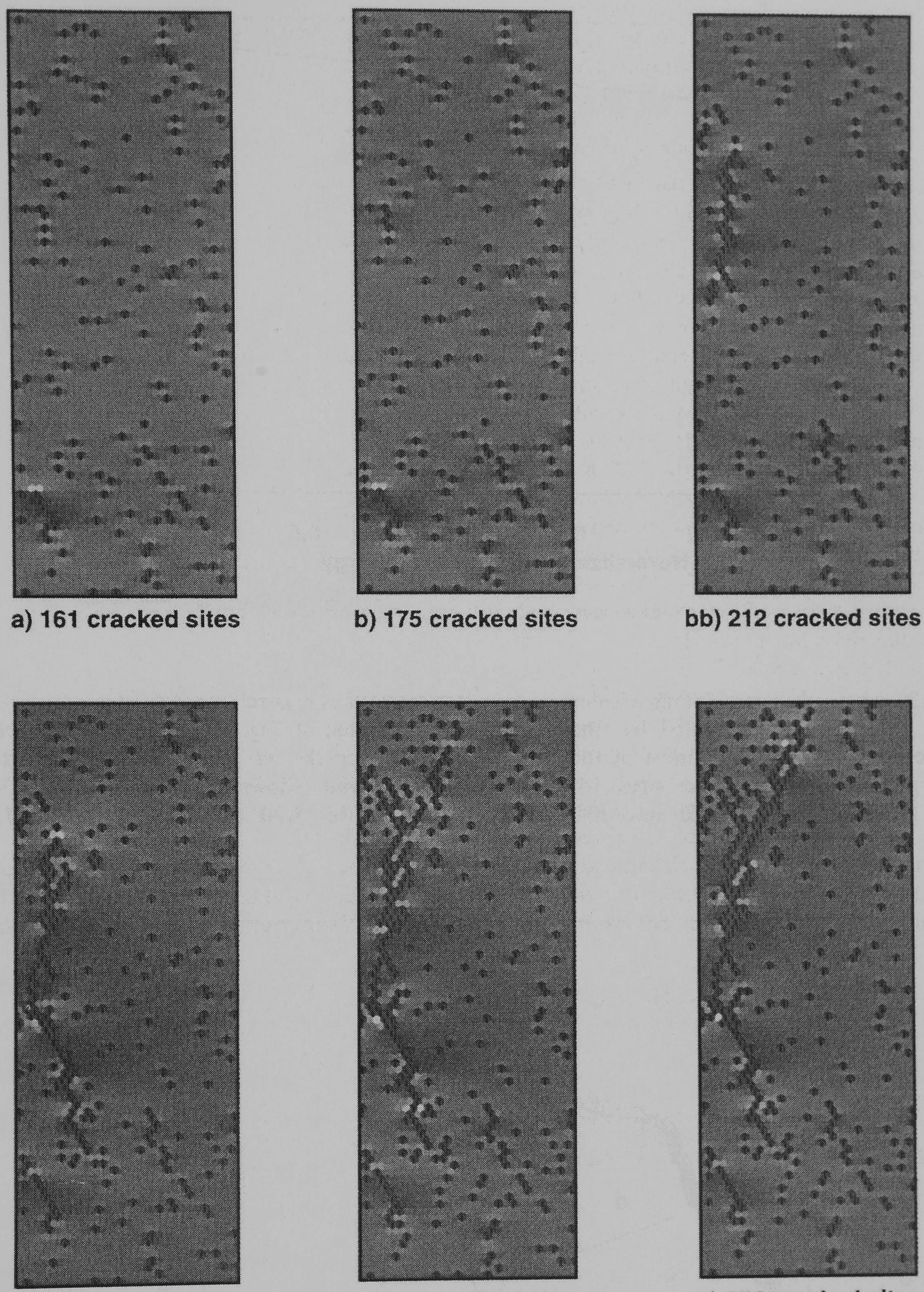
(a) Progressive failure process



(b) The associated stress-strain curve, corresponding to Figure (a) above

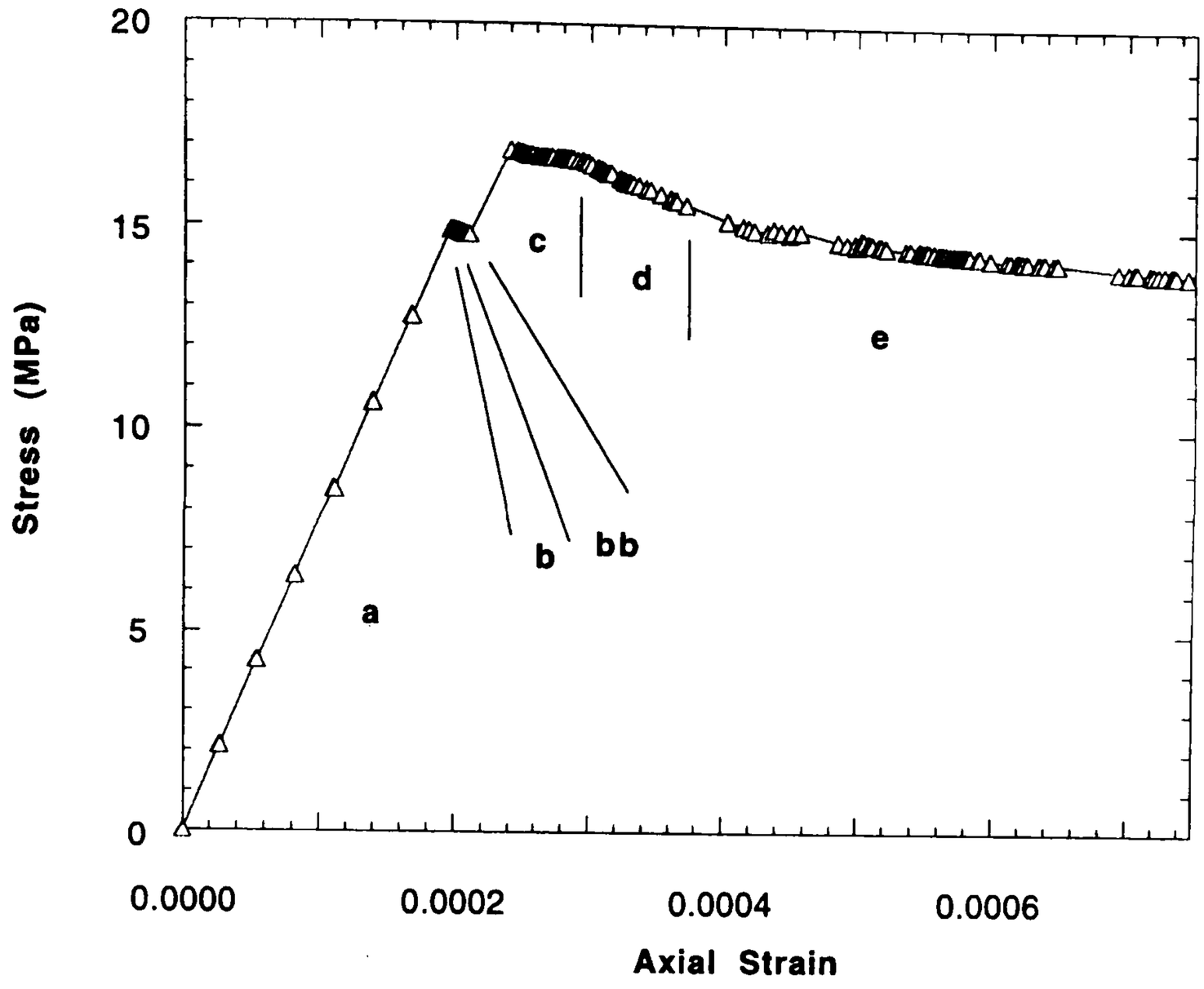
Figure 3.10. Simulated progressive failure of rock and the associated stress-strain curve obtained using the Tang model (from Tang et al., 2000)

perturbed tensile stress exceeds the local tensile strength, the site breaks and the energy thus dissipated contributes to a decrease in stress. Thus, although the model uses a linear system, it produces non-linear behaviour, along with an explicit prediction of the cracking process. Figure 3.11 shows a simulated microcracking process and the associated macroscopic stress-strain curve.



(a) Progressive failure process

Figure 3.11. Simulated progressive failure of rock and the associated stress-strain curve obtained using the Blair and Cook model (from Blair and Cook, 1998)



(b) The associated stress-strain curve, corresponding to Figure (a) in the previous page

Figure 3.11 (continued)

3.3.3 Comments on current statistical models for rock fracture

Apparently, statistical models enjoy a number of advantages for studying fracture in heterogeneous materials such as rock. One of these is that local heterogeneity can be incorporated very easily (Blair and Cook, 1998), and this allows the statistical model to investigate irreversible processes at the microscopic scale, provided that the mechanism for the process can be identified and incorporated. This feature is worth considering for the study of fracture of heterogeneous materials.

Another advantage statistical models enjoy is that the fracture law can be simple. In many cases definitions of only local fracture strengths and elastic properties of the elements suffices (van Mier et al., 1995). Oversimplification, however, may produce limitations to the model application or to the output results. For example, the tensile strength criterion used in the Blair-Cook model may only be applicable to those cases or stages where a local splitting mechanism prevails. For the phenomena of shear fracturing or shear bands (which often occur under confined compression), the model may require an additional fracture criterion. The oversimplified elemental constitutive

behaviour, as another example, makes many features of macroscopic stress-strain relations unobtainable, including the dependence of the strength drop after the peak on the confining pressure and hysteresis losses. To capture these features, the definition of local fracture strengths and other properties such as physical and mechanical properties of the elements may need to be incorporated into the model.

3.4 Closure and ideas for improved model development

With the aim of describing the dissipative processes and their relation to the macroscopic behaviour of a brittle rock in compression, a number of approaches have been developed. These include the micromechanics crack model, the damage mechanics model, and the statistical model.

The advantage of the micromechanics crack model lies in that it can describe fracture behaviour explicitly, and the most widespread method used in this field is the sliding crack model. This model can relate overall material behaviour to the growth of a single crack, or to the interaction of equal-spaced cracks, by making specific assumptions, and many features of rock response to applied loads can be produced.

The limitations of this model, however, exist in applying the model to a wider range of rock fracture in compression. Firstly, since it mainly relies on a well-defined crack or crack system, which is difficult to measure in a natural rock, the model is somewhat impractical. Secondly, the sliding crack model predicts axial extension of a pre-existing crack, and so the shearing phenomenon of rock fracture in triaxial tests cannot be analysed by this model directly. Finally, the microscopic dissipative processes associated with rock fracturing are manifested by multiple random formation, localisation, and coalescence of microcracks, and current micromechanics models cannot explain why and how those processes evolve.

Features of multiple cracks contained within a material can be considered in damage mechanics models by using a technique to average the effect of crack evolution on the material behaviour. Unlike the micromechanics model, this approach can be used to produce results for a variety of failure phenomena, from brittle through to ductile and creep behaviours.

The shortcoming of this method, however, is the averaging effect throughout either the entire material or uniformly distributed representative volume elements, even when the material undergoes fracturing. This leads to the approach being limited to predicting the macroscopic behaviour of a material, rather than predicting localised cracking

events and the formation of eventual fracture.

Statistical models enjoy the advantage that features acting as stress concentrations and modifiers, which promote the formation and development of cracks, can be easily incorporated. This allows the method to model a heterogeneous material more easily than the approaches discussed above.

One drawback of this method is the need to determine an appropriate distribution function for the heterogeneity. This can, however, be overcome by using the model as a reverse modeller, whereby the heterogeneity features affecting the model's behaviour can be pre-assigned, and the model result compared with physical phenomena. This provides us with the possibility to understand micro mechanisms that are uncertain or unknown at present. This method could be expected to produce more realistic results, from physical microscopic processes to the associated macroscopic material behaviour.

This work seeks to develop a more realistic model to describe the multiple dissipative processes associated with rock fracture under compression. Taking the advantages of various current methods, the development of the model will be based on the statistical approach, incorporating the damage effect at the elemental level. Since analytical solutions for multiple dissipative phenomena are unavailable, the model developed will need to be based on a numerical approach. The development of the model is described in the following chapter.

4 Development of a degradation model for brittle fracture of rock

The experimental and field studies reviewed in Chapter 2 show that rock fracture is both a complicated and a progressive process, involving the destruction of bonds, the extension and coalescence of microcracks, and sliding between individual grains and crack surfaces. As a result of these microscopic activities, the macroscopic responses of rock generally exhibit a non-linear mechanical behaviour. Chapter 3 showed that these responses, corresponding to irreversible microscale (mesoscale in the case of rock engineering structures) processes, may be modelled using either discrete fracture mechanics, continuum damage mechanics, or statistical fracture mechanics approaches. The macroscopic responses can be related to either the development of a single fracture, or the evolution of microscopic processes, or the dissipative dynamics of multiple cracking events at the microscopic scale.

As chapter 3 shows, micromechanics fracture models have been successfully used for relating non-linear macroscopic behaviour of a material to the growth of a single crack. However, rock fracture is manifested by complex phenomena ranging from multiple cracking to eventual fault formation, all of unknown geometry, which renders this approach impractical due to the requirement of keeping track of the spatially distributed dissipative processes (Ofoegbu and Curran, 1992).

Damage mechanics models exhibit a potentially wider range of application to modelling material behaviour, and in combination with the micromechanics fracture method offers an alternative that should be capable of capturing more features of macroscopic material behaviour. However, in these models, the effect of microscopic processes on macroscopic behaviour is normally averaged rather than isolated, meaning that multiple microscopic phenomena involved in rock failure, such as the formation of *en echelon* crack arrays and coalescence of such cracks, cannot be reproduced.

Heterogeneity is the main cause of microcracking. The existence of heterogeneity results in non-uniform stress and strain distributions within a stressed material, and local failure enhances the non-uniformity. Statistical methods provide a means to capture this

characteristic. Using this approach, the dissipative processes that occur along grain boundaries or within grains can be analysed. Furthermore, this method can be used as a means of predicting macroscopic behaviour, by studying isolated microscopic processes, pre-specifying simple rules (including criteria for crack formation or local failure), and including a constitutive behaviour related to the cracked sites. This is different from other approaches, in which the macroscopic responses are obtained by averaging cracking effects uniformly over the entire volume of the material.

A model for analysing rock fracture behaviour associated with isolated microscopic processes will be developed in this chapter. It was mentioned in Chapter 2 that microcracking causes degradation and dilatation effects on rock materials subjected to compressive stresses. The model developed here takes into account the degradation and dilatation effects of microcracking at local sites, which are associated with energy release from the local stored elastic strain energy, and incorporates a statistical technique, plasticity theory and damage mechanics principles to describe these phenomena and the associated effects. Along this line, it should be emphasized that the simplicity of a proposed model is almost as important an issue to consider as the model itself. A literature survey easily reveals models that are mathematically very elegant, but pose overwhelming computational difficulties. It is thus believed that a model, although rigorous in theory, should also be suitable for use in computation and should lend itself well to efficient implementation in computer codes (Yazdani and Schreyer, 1990). In addition, simplicity will allow the model to be applicable to the analysis of rock subjected to a wide range of external disturbances. This chapter gives the theoretical basis for, and the features of, such a model.

4.1 Background

The formation and extension of a crack in a solid body takes energy from the system and results in distinctive changes to the material properties. In this Section, we will describe this phenomenon theoretically. We first introduce the energy balance theory proposed by Griffith (1921), followed by a description of material degradation caused by crack extension. We also show that energy dissipation is loading path independent. All of these theoretical descriptions form the basis for the model development in the following sections.

It should be noted that in the following equations compressive stresses or forces and contractile strains take the positive sign and tensile stresses or forces and extensile

strains take the negative sign. The sign for displacements are in accord with the stresses that cause the displacements.

4.1.1 Energy balance theory

Griffith (1921) proposed that the failure of a brittle solid is caused by the propagation of pre-existing cracks in the solid, and that the creation of a new crack surface requires energy, proportional to the area of the new surface, to overcome cohesive forces of molecular attraction across the new surface. Using this point of view, the total energy of a cracked plate U can in general be expressed as (Lawn and Wilshaw, 1975; Lawn, 1993)

$$U = U_m + U_s , \tag{4-1}$$

where U_m is the mechanical energy of the plate and U_s is the free energy expended in creating the new crack surfaces. The mechanical energy in turn can be expressed as (Lawn and Wilshaw, 1975; Lawn, 1993)

$$U_m = U_e + U_a , \tag{4-2}$$

where U_e is the strain energy stored in the elastic medium; and U_a is the potential energy of the applied loading system, being negative associated with any displacements of the loading point.

For a crack within an elastic solid body deformed by specified surface forces, to extend the crack by a small increment, say, *da*, the equilibrium requirement is (Lawn and Wilshaw, 1975; Lawn, 1993)

$$\frac{dU}{da} = 0 , \tag{4-3}$$

and by making use of Equations 4-1 and 4-2 we have

$$dU_e + dU_a + dU_s = 0 . \tag{4-4}$$

The extension of a crack requires $dU_s > 0$. This energy, as indicated by Equation 4-4, is balanced by either a decrease in the strain energy, or an increase in the work done by the external force, or by a combination of the two (Whittaker et al., 1992).

Equation 4-4 is called the energy balance theory, or the law of energy conservation. It is the building block for all brittle fracture theory (Lawn, 1993). In this work, the theory forms the basis for the model developed in the following sections (Sections 4.1.3, 4.2 and 4.3).

4.1.2 Crack extension and corresponding changes in material elastic constants

It is known that the extension of a crack in an elastic body causes a reduction in the stiffness of the body. This section describes this aspect, in terms of Hooke's law.

Considering an elemental crack system such as that shown in Figure 4.1, the system is assumed to be linearly elastic and contains a slit of length $2a$, the walls of which are traction-free. A tensile force F is applied to the upper end of the system, and the lower end is fixed. If the slit is constrained at its tips so as to prevent crack extension, and in such a way that the constraint does no work, the system will behave as an elastic spring in accordance with Hooke's law (Lawn and Wilshaw, 1975; Lawn, 1993). Thus we have

$$u = CF\,, \tag{4-5}$$

where u is the elongation and C is the elastic compliance of the system.

If whilst maintaining the load configuration on the system, we remove the end constraints on the slit, and allow the slit to extend by an amount da at both ends, the system extends by an amount du, and the force increases by an amount dF. By differentiating Equation 4-5, we obtain (Lawn and Wilshaw, 1975; Lawn, 1993)

$$du = CdF + dCF\,, \tag{4-6}$$

which on rearranging yields

$$dC = \frac{du - CdF}{F}. \tag{4-7}$$

It has been stated above that, for a crack extension of da, we have $dF \geq 0$. Thus,

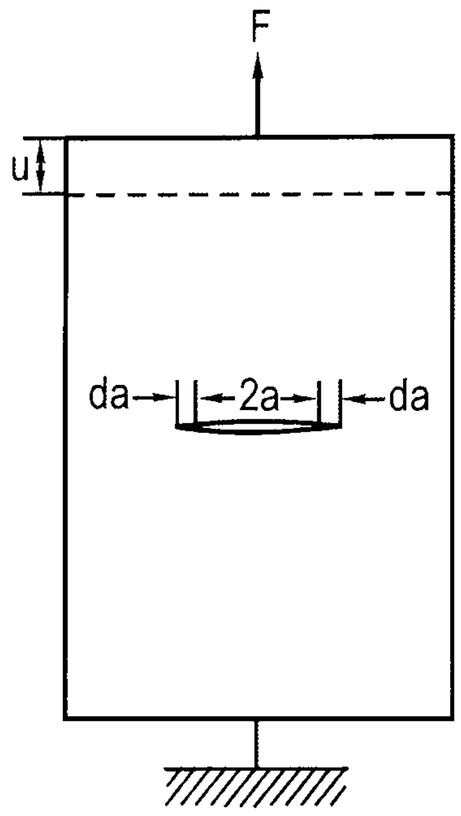


Figure 4.1. Compliance test piece (after Lawn and Wilshaw, 1975)

Equation 4-7 shows that for $du \leq 0$ we have $dC \geq 0$ always. This indicates that the extension of the slit causes an increase in the elastic compliance, or a decrease in the stiffness, which is the theoretical evidence supporting laboratory observations that the elastic modulus of a material degrades associated with the development of microscopic cracking processes (Figure 2.19).

4.1.3 Independence of energy release and loading configuration

According to Griffith's energy balance theory (Subsection 4.1.1), the creation of new crack surfaces in an elastic body expends energy from either the stored strain energy or the external work. In this section, we will further demonstrate that the amount of released energy due to crack extension is independent of the loading configuration. These demonstrations are given according to Lawn (1993) with a few variations.

As shown in Figure 4.1, for the elongation u produced by force F in accord with Equation 4-5, the strain energy in the system is equivalent to the work done by the elastic loading, *i.e.*

$$U_e = \int_0^u F(u)du = \frac{1}{2}Fu\,. \tag{4-8}$$

Substituting Equation 4-5 in Equation 4-8 the elastic strain energy can also be expressed as

$$U_e = \frac{1}{2}Fu = \frac{1}{2}F^2C = \frac{1}{2}\frac{u^2}{C}\,. \tag{4-9}$$

When the crack extends, the mechanical energy term of the system decreases (Subsection 4.1.1). Now, we examine the energy decrement by considering two extreme loading configurations: (a) constant displacement and (b) constant load.

For case (a), as shown in Figure 4.2, there are no changes in the displacement of the loading system with crack propagation, and the work done by the applied load is

$$dU_a = 0\,, \tag{4-10}$$

and the corresponding change in the elastic strain energy, from Equation 4-9, is

$$dU_e = -\frac{1}{2}\left(\frac{u^2}{C^2}\right)dC = -\frac{1}{2}F^2dC\,. \tag{4-11}$$

Thus, the total mechanical energy change (area OAB in Figure 4.2), from Equation 4-2, is

$$dU_m = dU_a + dU_e = 0 + \left(-\frac{1}{2}F^2 dC\right) = -\frac{1}{2}F^2 dC\,. \tag{4-12}$$

For case (b), the applied force remains constant as the crack extends, and the work done by the applied load is

$$dU_a = -Fdu = -F^2 dC\,, \tag{4-13}$$

and the corresponding change in the elastic strain energy is, from Equations 4-5 and 4-9,

$$dU_e = \frac{1}{2}F^2 dC\,. \tag{4-14}$$

Thus, the total mechanical energy change (dU_m) is

$$dU_m = dU_a + dU_e = -F^2 dC + \frac{1}{2}F^2 dC = -\frac{1}{2}F^2 dC\,. \tag{4-15}$$

The results in Equations 4-12 and 4-15 are identical, which indicates that the mechanical energy released during incremental crack extension is independent of the loading configuration. The independence of strain energy release due to crack extension with respect to the loading configuration will be referred to in development of the model (Subsection 4.3.3).

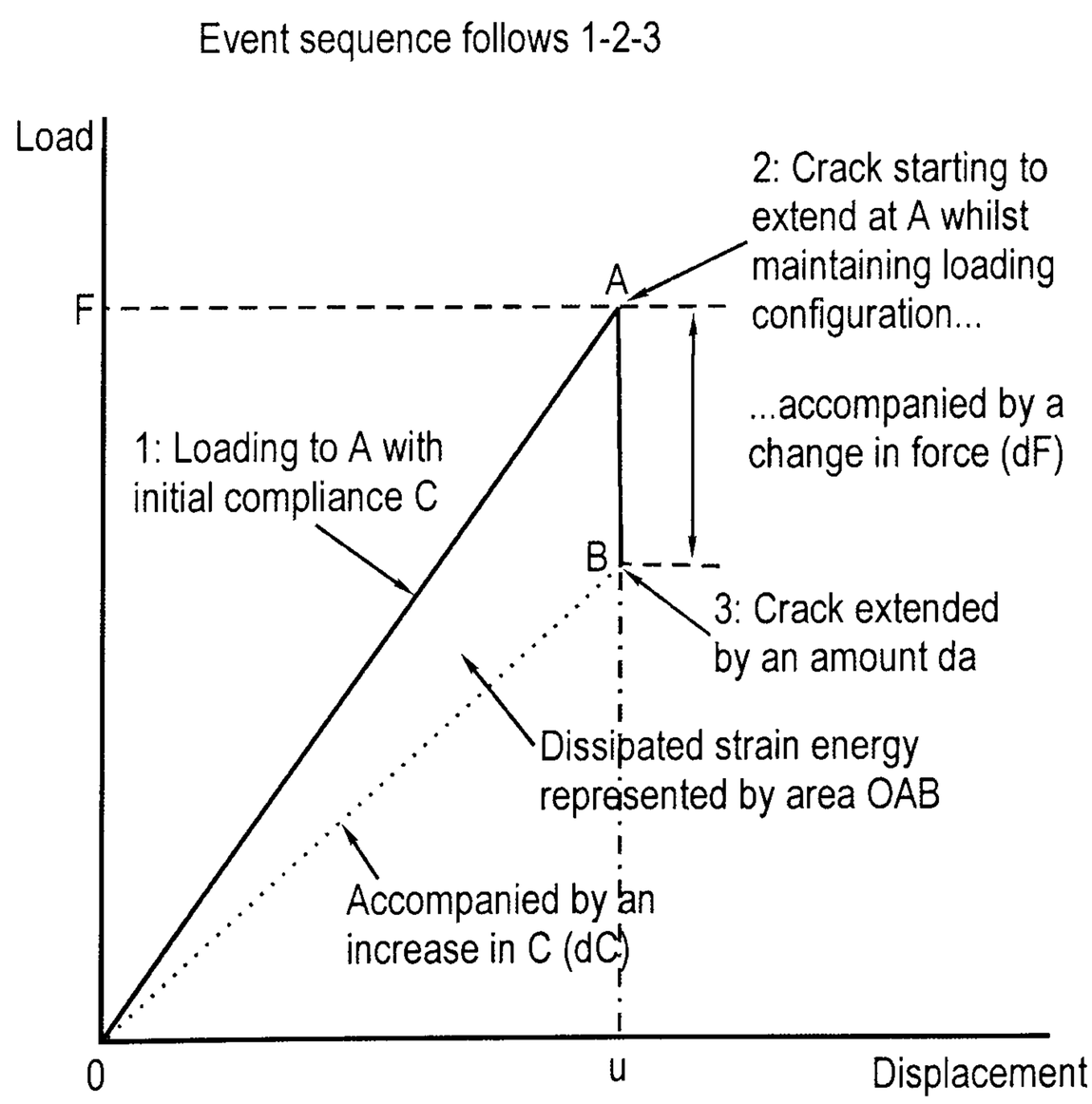


Figure 4.2. Illustration of elastic strain energy dissipation induced by a crack extension in constant displacement

4.1.4 Strength loss of brittle materials undergoing fracturing

If the system shown in Figure 4.1 is reloaded with the same loading configuration, but without constraining the ends of the slit, we assume that the slit will grow if the applied tensile force reaches a critical value (see Griffith, 1921). Based on Griffith's energy concept, this critical value is given in terms of the stress σ_f (Lawn, 1993; Whittaker et al., 1992; Andreev, 1995), which is given by

$$\sigma_f = \sqrt{\frac{2E'\chi}{\pi a}}, \tag{4-16}$$

where $E' = E$ for plane stress and $E' = E/(1-\nu^2)$ for plane strain, E is Young's Modulus, ν is Poisson's ratio, and χ is the free surface energy per unit area, being constant for a given material.

Equation 4-16 has the crack length in the denominator, and demonstrates that, after each increment of the crack length, the stress required for further crack propagation is less than that applied to the previous crack geometry. This indicates that crack extension reduces the capability of the material for sustaining tensile loads. When the fracture fully develops, the material loses its integrity and cannot sustain any tensile loads. In terms of the load-displacement curve, the material's behaviour is elastic-brittle.

4.2 Degradation and energy dissipation associated with rock compressive failure

The previous sections presented theoretically that the extension of a crack within an elastic solid body requires a decrease in either the strain energy, an increase in the external work, or both. It is also demonstrated that the extension of a crack results in a reduction in both material stiffness and strength. All of these descriptions are theoretical evidence for the degradation and energy dissipation phenomena displayed during rock failure induced by stress.

However, as presented in Chapter 2, under compressive loading, rock fracture develops in a different manner from that in a tensile field. For example, the extension of a crack does not cause a reduction in macroscopic material compressive strength, but requires an extra loading for a further extension, resulting in other cracks to spread (stages BC and CD in Figure 2.7). In addition, the final fracture forms by linking up of extended local cracks rather than the propagation of a single crack across a specimen

(stage DE in Figure 2.7). Furthermore, rock fracture in compression is a process involving plastic flow rather than pure elastic deformation (Figure 2.19). Due to these discrepancies and complexities, the energy dissipation and strength degradation features are different from those presented in the section above. For instance, in perfectly plastic deformation processes, the elastic strain energy does not change although the loading system contributes work. On the other hand, in quasi-brittle and brittle deformation processes, the elastic strain energy reduces although the external work increases. In this section, the energy dissipation and strength degradation characteristics associated with rock fracture in compression are analysed from a microscopic point of view, with the aid of those concepts introduced in the earlier sections. Based on this analysis, a degradation index is developed to describe degradation features displayed by rock under different compressive circumstances.

4.2.1 Degradation associated with microcracking

As presented in Chapter 2, rock fracture in compression develops in a manner dependent on the loading conditions. In unconfined or low-confined conditions, rock fails by splitting, and its mechanical behaviour is elastic-brittle. Under moderate confinements, rock fails by shearing along eventual fracture planes with quasi-brittle deformation behaviour. In the case of a sufficiently high confining stress, rock exhibits plastic flow that produces ductile deformation behaviour (see Subsection 2.4.3 and Figures 2.21 and 2.23).

With respect to the stress-strain curves of rock displayed under different confining pressures (Figures 2.7 and 2.21), if we examine processes at the microscopic level (reviewed in Sections 2.2 and 2.4), it may be summed up that the nonlinearities in rock compressive behaviour are attributed to two distinct microstructural changes associated with two deformation behaviours (Ofoegbu and Curran, 1992): one is the development of microcracks and microvoids, associated with brittle deformation behaviour; the other is sliding between particles and crack surfaces (plastic flow), associated with ductile deformation behaviour. We shall define the former as microcracking, consistent with the definition given by other researchers (Section 2.2), and the latter as microsliding. Microcracking destroys interparticle bonds, and hence decreases the load-bearing capacity and elastic stiffness (Yazdani and Schreyer, 1990; Ofoegbu and Curran, 1992; also see Subsections 4.1.2 and 4.1.4). On the other hand, microsliding (plastic flow) breaks few interparticle bonds, and as a result this process produces no, or little, effect

on the elastic stiffness (Yazdani and Schreyer, 1990; Ofoegbu and Curran, 1992) and on the load-bearing capability.

These two non-linear microstructural deformation changes can occur under all loading conditions, and certain circumstances may favour one more than the other. Under low confinements, for example, most observed microstructural changes before the strain associated with the peak stress are elongations of microcracks (see Subsection 2.4.1), and the coalescence of these elongated cracks produces a more brittle stress-strain relation. However, with increasing confining stress, sliding between individual particles and crack surfaces becomes prevalent (Subsection 2.4.1), and the final failure patterns correspond to a more ductile stress-strain curve. In general, the various degrees of the strain-softening behaviour of rock are produced by a combination of both mechanisms (Ofoegbu and Curran, 1992; also see Figure 2.21).

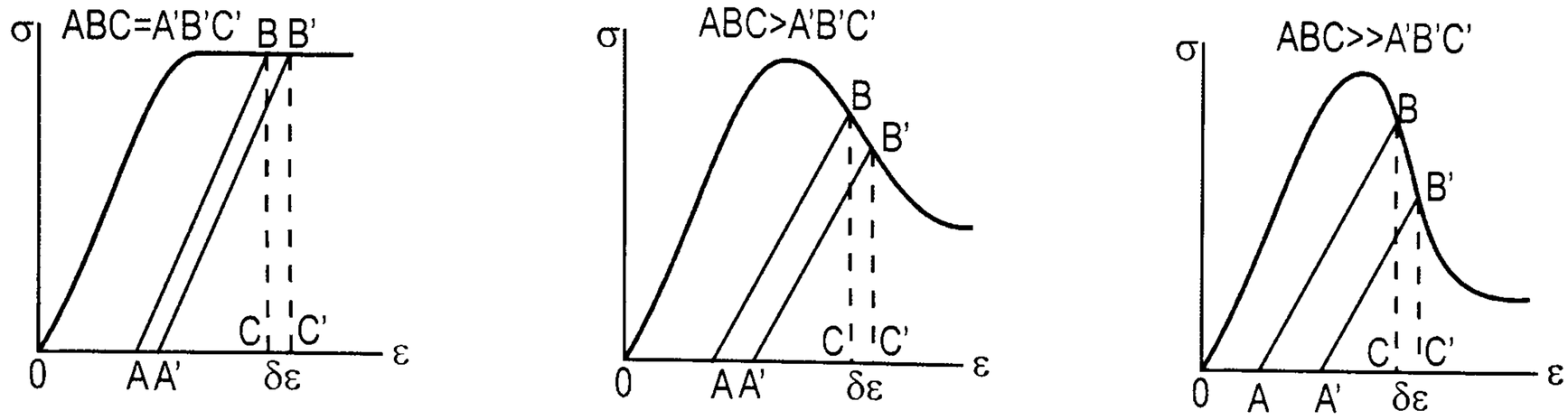
It has been demonstrated (Section 4.1) that microstructural changes dissipate energy from either the internal strain energy or the external work. We now move on to investigate this feature in the context of rock fracture in compression.

4.2.2 Energy dissipation characteristics associated with microcracking

Following the description of the relation between material macroscopic behaviour and microscopic processes given in the previous section, here we continue to examine the relation between energy dissipation and microscopic activities. It is readily seen that these two different microstructural changes result in different degrees of energy dissipation.

To describe the features of energy dissipation associated with rock failure in compression, it is useful to recall the three typical rock deformation behaviours (Figures 2.23 (c), (b) and (a)). These three deformation behaviours are redrawn and presented here as Figure 4.3. Note that energy features associated with lateral expansion are omitted in order to simplify the description.

Referring to Figure 4.3(a), we note that perfectly plastic deformation only produces further plastic strain, with the stiffness and volumetric elastic strains remaining constant. These features indicate that the sliding processes associated with perfectly plastic deformation do not dissipate energy from the stored elastic strain energy, but from the work done by the loading system. The external work is entirely dissipated within the specimen through friction (Gerogiannopoulos and Brown, 1978), and no



(a) Perfectly plastic, Area *ABC* = Area *A'B'C'* means no elastic strain energy change

(b) Strain softening, Area *ABC* > Area *A'B'C'* means elastic strain energy reduces

(b) Brittle, Area *ABC* – Area *A'B'C'* is larger than that in (b), indicating more elastic strain energy is dissipated

(Area *ABC* and Area *A'B'C'* represent the elastic strain energy within the specimen before and after $\delta\varepsilon$)

Figure 4.3. Energy dissipation during an axial strain increment, $\delta\varepsilon$, of a rock specimen

fracture surfaces associated with the deformation are formed.

On the other hand, in quasi-brittle and brittle deformations, associated with the macroscopic behaviour shown in Figures 4.3(b) and 4.3(c), processes other than purely frictional ones take place (Gerogiannopoulos and Brown, 1978) and the stored elastic strain energy contributes to the non-frictional microstructural changes. The unloading-reloading stress-strain curve after the peak for the brittle or quasi-brittle failure of rock exhibits a gradual reduction in both stiffness and strength, corresponding to a reduction in the elastic strain energy (Figures 2.18, 4.3(b) and 4.3(c)). This indicates that at least part of the energy required for forming fracture surfaces comes from the stored elastic strain energy (with respect to Equation 4-4). For a specific strain increment, the more brittle the stress-strain curve is, the more elastic strain energy the deformation dissipates, and the more degradation the material suffers. This is illustrated by comparing the area representing the dissipated elastic strain energy between the Figure 4.3(b) and Figure 4.3(c). This feature may be described mathematically, which is considered in the next section.

4.2.3 Degradation index

In the previous sections, it has been shown that different confining conditions induce different combinations of the two microstructural changes, *i.e.* microcracking and microsliding, and different combinations of the two microstructural changes result in different degrees of macroscopic material degradation. In this section, we describe this

characteristic mathematically.

Referring to Figures 2.19 and 2.21, we draw a series of representative deformation behaviours exhibited by a rock in compression with different confining pressures. These are shown in Figure 4.4. In drawing these representative curves, the strain hardening portion has been replaced by a linear elastic relation, as suggested by Jaeger and Cook (1979). These curves possess the following features:

- different amount between the peak and residual strength, which decreases with confining pressure increase;
- different slope in the descending portion, which decreases with confining pressure increase; and
- different secant stiffness (secant Young's modulus) at the residual level, which increases up to the initial with confining pressure increase.

Furthermore, as analysed in Subsections 4.1.3, 4.2.1 and 4.2.2 and indicated by Figure 4.2, we decompose any elastic-strain softening behaviour into two parts as shown in Figure 4.5: one is the elastic-brittle behaviour produced by microcracking; and the other is the elastic-ductile behaviour produced by microsliding. The brittle behaviour does not produce plastic strain but results in a reduction in material stiffness and strength, and the ductile behaviour only produces plastic strain but no effect on the

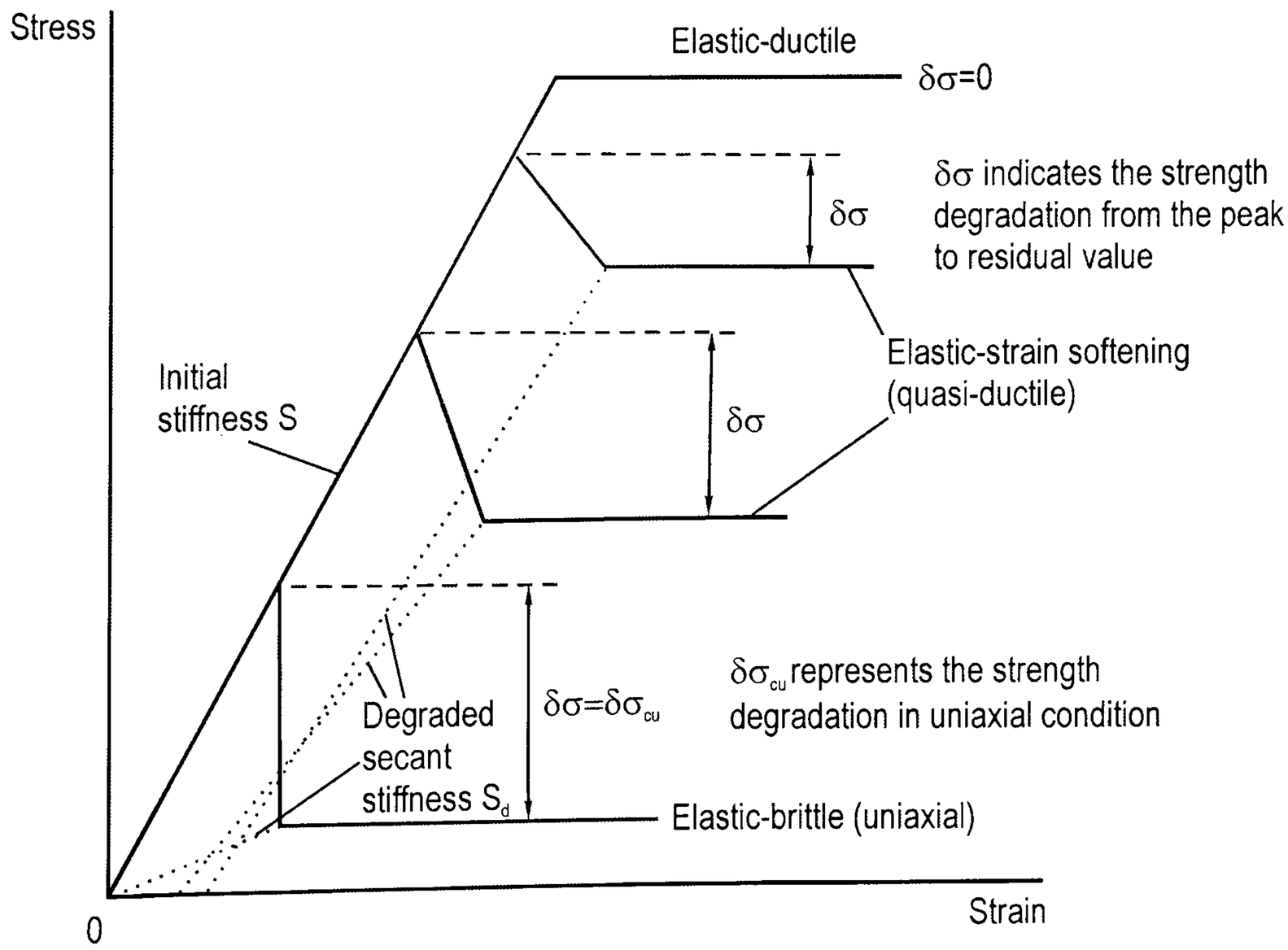


Figure 4.4. Simplified stress-strain relations of rock under different confining pressures

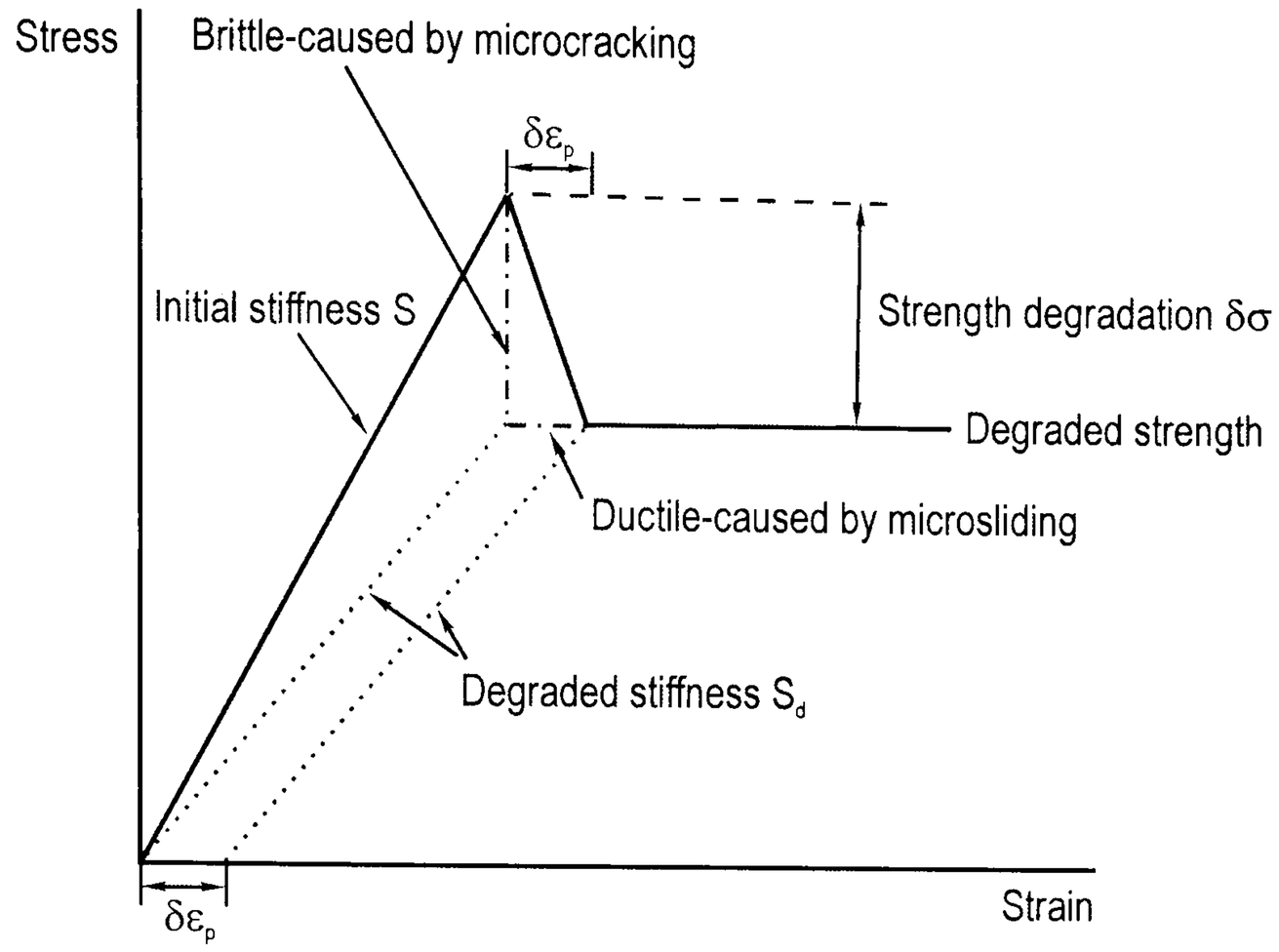


Figure 4.5. Illustration of the decomposition of strain softening behaviour into a combination of brittle and ductile behaviour

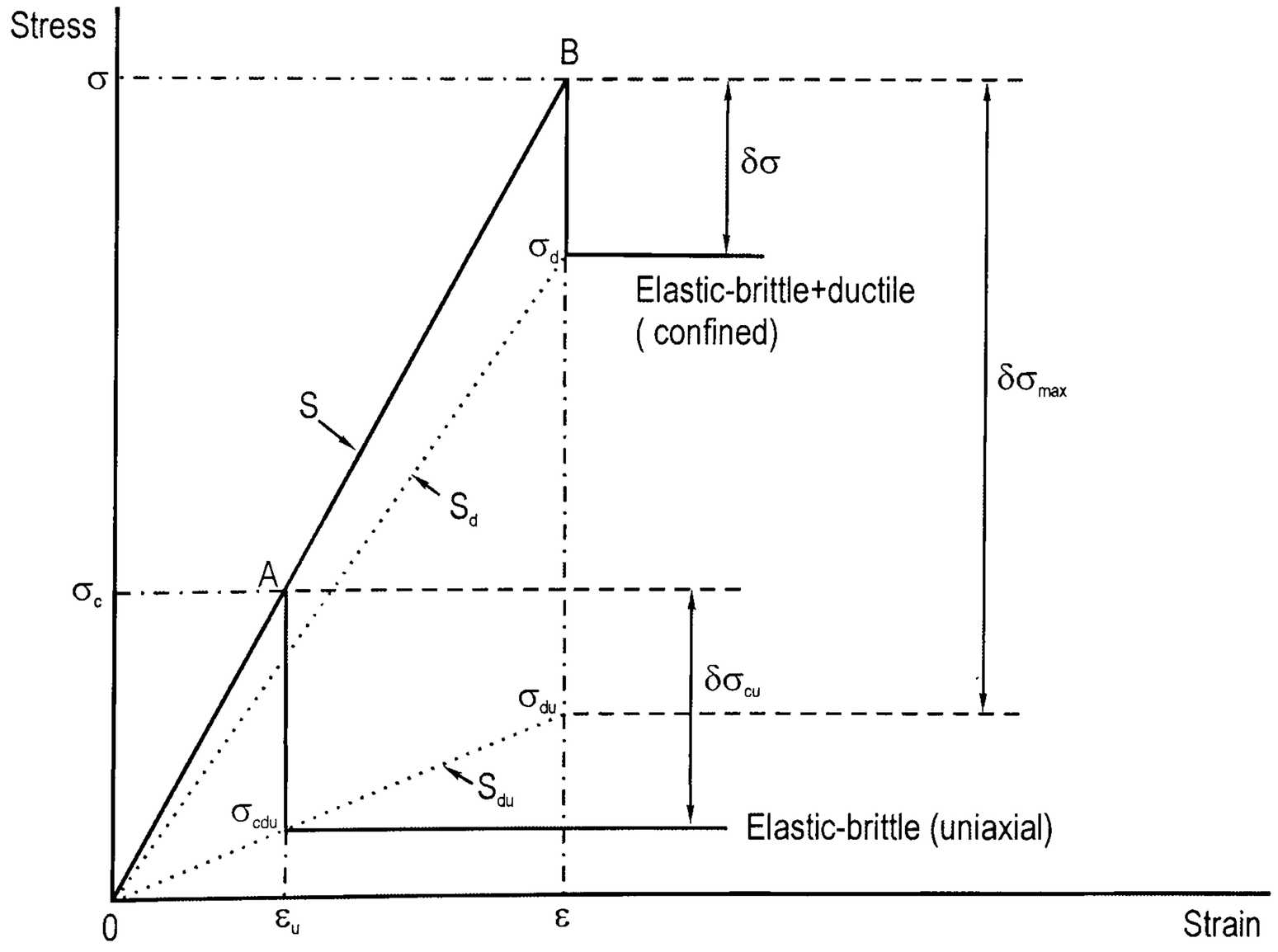


Figure 4.6. Illustration of the definition of the degradation index

stiffness and strength.

Now, we define an index r_d for the degradation that a material suffers after its failure, ranging from 0 (no degradation) to 1 (complete degradation). Laboratory experimental results indicate that rock that fails under uniaxial conditions suffers

maximum degradation (Figure 2.21). We redraw two behaviours exhibited by rock in compression in Figure 4.6: one is the behaviour with the maximum degradation that rock displays in uniaxial compression; the other is the one with less degradation displayed by the rock under any moderate confining compression. For such a behaviour, we may find a ratio of the degradation at a certain confining stress level relative to the maximum degradation value corresponding to unaxial degraded stiffness, which we define as the degradation index, r_d, *i.e.*

$$r_d = \frac{\delta p}{\delta_{max} p}, \tag{4-17}$$

where δp is the degradation in any parameter associated with a certain confining condition ($\delta\sigma$ in Figure 4.6, for example), and $\delta_{max}p$ is the maximum degradation at the strain level corresponding to the uniaxial degraded stiffness ($\delta\sigma_{max}$ in Figure 4.6, for instant). As ductile behaviour with $\delta p = 0$ has a degradation index of 0, and brittle behaviour in unconfined conditions has an index value of 1 (since $\delta p = \delta_{max}p$), any deformation behaviour between the two extremes has a value between 0 and 1 for its degradation index.

For example, with respect to the strength degradation shown in Figure 4.6, Equation 4-17 can be written as

$$r_{\sigma d} = \frac{\sigma - \sigma_d}{\sigma - \sigma_{du}} = \frac{\delta\sigma}{\delta\sigma_{max}}, \tag{4-18}$$

where $r_{\sigma d}$ is the degradation index for strength; σ and σ_d are the peak and degraded strength associated with a certain confining stress, respectively; σ_{du} is the degraded strength at this strain level corresponding to the uniaxial degraded stiffness; $\delta\sigma$ is the strength degradation associated with this strain level, which decreases as confining pressure increases (Figure 4.6); and $\delta\sigma_{max}$ is the maximum strength degradation at this strain level corresponding to uniaxial degraded stiffness, which increases as confining pressure increases (Figure 4.6).

Similarly, for the stiffness degradation index $r_{sd,}$ the expression is written as (see Figure 4.6)

$$r_{sd} = \frac{S - S_d}{S - S_{du}} = \frac{\delta S}{\delta S_{max}}, \tag{4-19}$$

where S is the initial stiffness, S_d is the degraded stiffness under a certain confining stress, and S_{du} is the degraded stiffness associated with uniaxial conditions (Figure 4.6).

Equation 4-18 contains the parameter σ_{du}, which is inconvenient to measure or calculate in a practical application. We now derive an expression for $r_{\sigma d}$ in terms of parameters that are easy to measure in the laboratory.

From the geometry presented in Figure 4.6, we find two relations of the form

$$\frac{OA}{OB} = \frac{\delta\sigma_{cu}}{\delta\sigma_{max}}, \tag{4-20}$$

and

$$\frac{OA}{OB} = \frac{\sigma_c}{\sigma}. \tag{4-21}$$

In Equations 4-20 and 4-21, $\delta\sigma_{cu}$ and σ_c are the strength degradation and the peak strength at uniaxial conditions, respectively; σ is the peak strength at a certain confining stress; and points A and B refer to σ_c and σ, respectively (Figure 4.6).

By equating the right side of the above two equations and rearranging, the following relation is obtained

$$\delta\sigma_{max} = \frac{\delta\sigma_{cu}\sigma}{\sigma_c}. \tag{4-22}$$

Substituting Equation 4-22 into Equation 4-18, we find

$$r_{\sigma d} = \frac{\sigma_c \delta\sigma}{\sigma\delta\sigma_{cu}}. \tag{4-23}$$

In this relation, all the four parameters, σ_c, $\delta\sigma$, σ and $\delta\sigma_{cu}$, are conveniently measurable in laboratory experiments. For example, using Equation 4-23, the degradation indices for Tennessee marble and Vosges sandstone at different confining pressures are computed and tabulated in Tables 4.1 and 4.2, respectively. The source data for Tennessee marble were obtained by estimating the peak and residual strengths of each behaviour corresponding to the associated confining stress shown in Figure 2.21, and the data for Vosges sandstone were provided by Dr Bésuelle (also see Bésuelle et al., 2000). Figure 4.7 shows graphically the variations of the indices of the two rocks subjected to confining pressures.

Now, we derive an expression for r_{sd}. According to Hooke's law and from Figure 4.6, the following relations can be obtained

$$S = \frac{\sigma}{\varepsilon}, \tag{4-24}$$

Table 4.1. Estimation of the degradation index for Tennessee marble*

Item	Value (MPa except $r_{\sigma d}$)							
Confining pressure σ_{con}	0	3.45	6.9	13.8	20.7	27.6	34.5	48.3
Peak strength σ	130**	145	160	180	195	215	245	275
Residual strength σ_d	10	60	80	110	130	180	230	270
Strength degradation $\delta\sigma$	120***	85	80	70	65	35	15	5
$r_{\sigma d}$	1.0	0.6351	0.5417	0.4213	0.3611	0.1764	0.0663	0.0197

Table 4.2. Estimation of the degradation index for Vosges sandstone****

Item	Value (MPa except $r_{\sigma d}$)						
Confining pressure σ_{con}	0.5	10	20	30	40	50	60
Peak strength σ	33.5**	83	114	134	149	167	174
Residual strength σ_d	0	49	94	116	135	154	165
Strength degradation $\delta\sigma$	33.5***	34	20	18	14	13	9
$r_{\sigma d}$	0.9853	0.4096	0.1754	0.1343	0.0940	0.0778	0.0517

* The source data were from Figure 2.21.

** σ_c

*** $\delta\sigma_{cu}$

**** The source data were from Dr Bésuelle (also see Bésuelle et al., 2000).

$$S_{du} = \frac{\sigma_{du}}{\varepsilon}, \tag{4-25}$$

and

$$S_d = \frac{\sigma_d}{\varepsilon}. \tag{4-26}$$

In the above three equations, ε is the strain corresponding to σ, the peak strength at

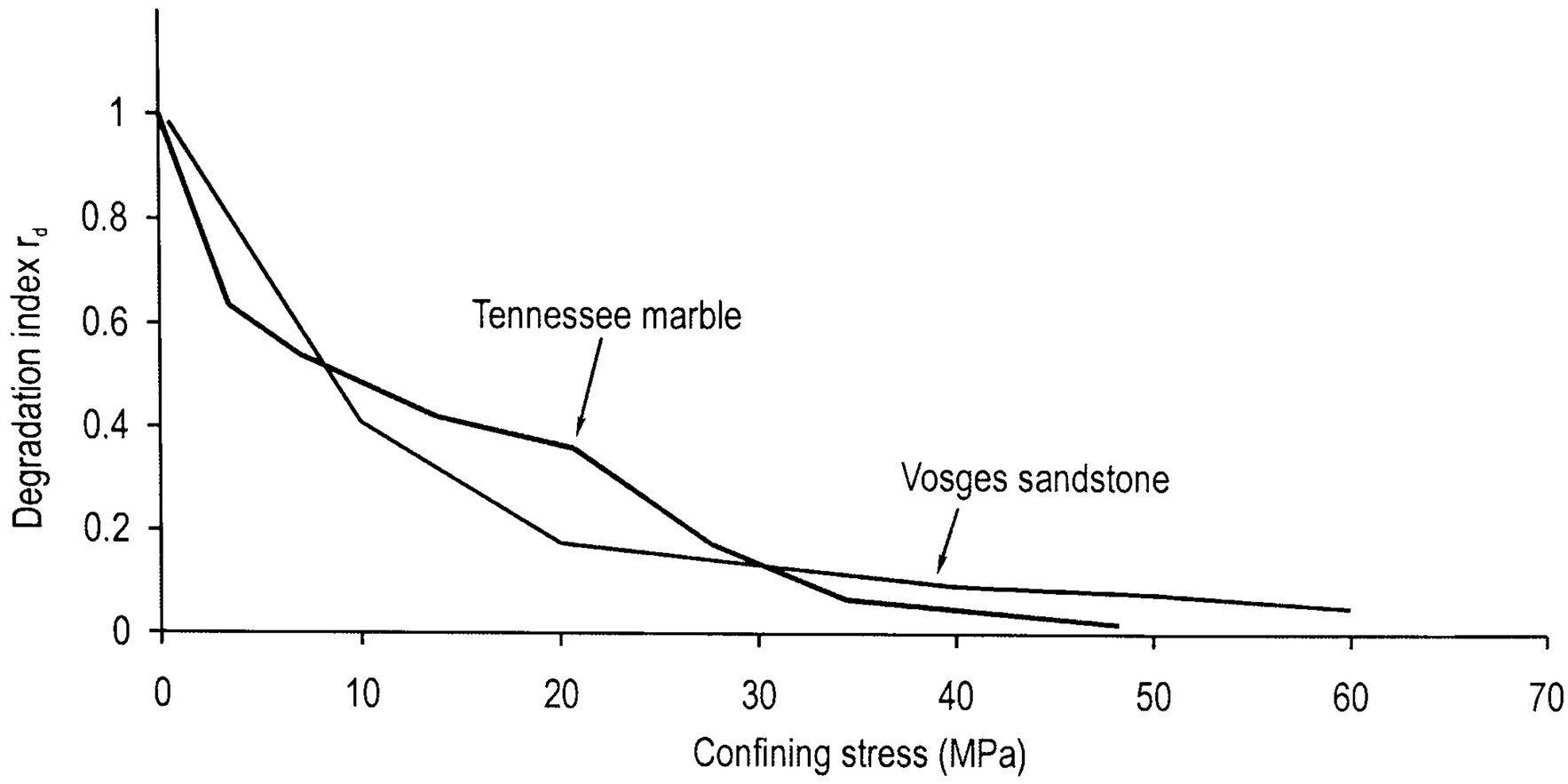


Figure 4.7. Variations of the degradation index of two rocks subjected to confining stresses

a particular confining stress.

Substituting Equations 4-24 to 4-26 into Equation 4-19, we finally have the following expression for r_{sd}

$$r_{sd} = \frac{S - S_d}{S - S_{du}} = \frac{\varepsilon - \varepsilon}{\frac{\sigma}{\varepsilon} - \frac{\sigma_{du}}{\varepsilon}} = \frac{\sigma - \sigma_d}{\sigma - \sigma_{du}} = r_{\sigma d} \,. \tag{4-27}$$

Equation 4-27 indicates that $r_{\sigma d}$ and r_{sd} are identical. Thus, r_d can be used for the degradation index of a material in either strength ($r_{\sigma d}$) or stiffness (r_{sd}).

The degradation index, r_d, defined here will be used later for evaluating local failure induced by microcracking (Subsection 4.3.4).

4.3 A local degradation model for fracture of rock materials in compression

The literature review presented in Chapter 2 shows that rock fracture in compression is preceded by either the formation, extension, and coalescence of microcracks, or by sliding between individual particles and crack surfaces, or by their combination. The theoretical analysis presented above shows that different combinations of the two microstructural mechanisms dissipate different amounts of stored elastic strain energy, and the dissipation of the stored elastic strain energy corresponds to a reduction in both the local stiffness and strength of the material.

The microstructural failure phenomena manifested in rock fracture are complex, and so rather than study these phenomena themselves we will consider the effect of these microstructural changes on elastic stiffness and strength of a given element of rock. This effect can be described in two ways (Ofoegbu and Curran, 1991). One is to account for the forces on, and deformations of, each individual element and add these vectorially to those of the uncracked rock material. The other approach is to describe the effect in a given element of rock in terms of a continuously varying field function. Since the aim of this work is to isolate dissipative processes, which are those fields that behave differently from the others, the second approach is used in this work. We now go on to derive the relations appropriate to this approach.

4.3.1 Rock elements

If we examine intact rock at the microscopic level (say, a rock element of the size of a few grain diameters), the rock element may contain a void, a crack, grain boundaries, or the like. In this respect, the rock element is just like an intact rock specimen.

When rock is deformed under compression, microcracks may form at the grain scale, or extend to a length that crosses a number of grains, at strains less than that associated with the macroscopic peak strength (Subsection 2.4.1). Microscopic inspection undertaken in the laboratory (Subsection 2.4.1) reveals that, as shown in Figure 4.8, under low confining stresses, the formation and extension of microcracks are in a direction parallel to that of the major principal stress (Figure 4.8(a)); under moderate confining stresses, microcracks develops in a plane inclined to this direction (Figure 4.8(b)); and under high confining stresses, the formation and growth of microcracks are inhibited and instead sliding may occur between grain boundaries or crack surfaces (Figure 4.8(b)).

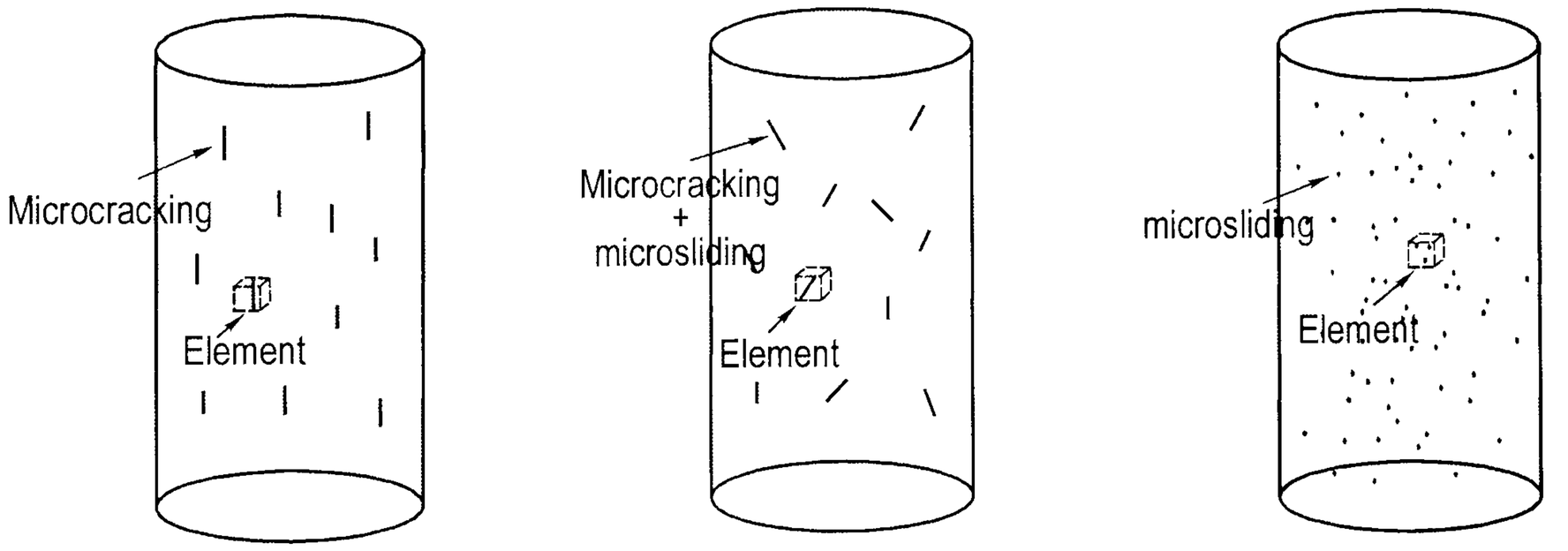
Within a stressed rock specimen, an element suffering such microstructural changes as mentioned above (the element is indicated in Figure 4.8) may experience one of the three processes shown in Figure 4.9, even though the rock specimen has not failed. These processes are: splitting under low confining pressures (Figure 4.9(a)); shearing along a fracture plane under moderate confining pressures (Figure 4.9(b)); and plastic flow under high confining pressures (Figure 4.9(c)). Comparing the elemental failure behaviours shown in Figure 4.9 with those macroscopic fracture phenomena displayed by a rock specimen under different confining conditions, which are shown in Figure 2.23, it can be argued that fracture of a rock element within a compressively stressed

rock specimen is analogous to fracture of the rock specimen itself.

Based on this observation, the deformation behaviour of a rock element is derived in the next section.

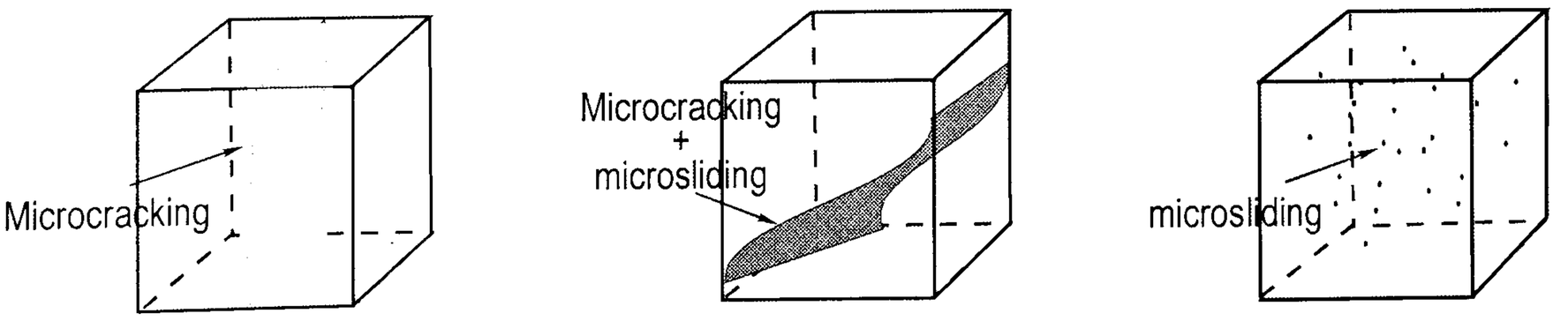
4.3.2 Deformation behaviour of rock elements and the concept of local degradation

In the previous section, it was concluded that, by comparing laboratory microscopic occurrences with macroscopic fracture phenomena displayed by a rock under various confining conditions, a rock element within a rock specimen can be considered as analogous to the rock specimen itself. Thus, it may be reasonable to assume that the deformation behaviour of a rock element is similar to that displayed by the rock specimen (Figure 2.23), *i.e.* an element suffering a microscopic dissipative process may exhibit one of the three typical deformation behaviours: strain hardening-brittle, strain hardening-strain softening, and strain hardening-perfectly plastic.



(a) Low confining (b) Moderate confining (c) High confining

Figure 4.8. Schematic illustration of microstructural changes in a rock specimen under different confining pressures



(a) Low confining (b) Moderate confining (c) High confining

Figure 4.9. Schematic illustration of elemental failure induced by microstructural changes within a rock specimen under different confining pressures

If the size of the element undergoing a non-linear deformation process is very small with respect to the overall structure under consideration, the influence of the strain hardening portion on the behaviour of the whole structure may be negligible (Jaeger and Cook (1979) suggest that this portion can be simplified to linear elasticity), and thus our interest can be taken to lie in how the behaviour of the element after failure produces disturbances in the stress and strain fields of its neighbours. Thus, the behaviour of the element undergoing failure may be simplified as shown in Figure 4.10, *i.e.* elastic-brittle, elastic-strain softening (brittle+ductile), and elastic-ductile (plastic) behaviours, depending on the particular confining pressure.

This derivation implies that local failure caused by microcracking results in local degradation to strength, stiffness or both in circumstances of low to moderate confining pressures. If an element displays plastic flow under higher confining pressures, no local degradation occurs. In the next section, these concepts will be examined theoretically from the point of view of strain energy dissipation.

4.3.3 Theoretical description of local degradation

Consider an element with potential failure produced by microstructural changes in a material under continuous loading. At any instant, the stress state at a point in the material is σ_{ij} with corresponding strain state ε_{ij}, where i and j take value 1 to 3. Prior to failure, the element is assumed to be isotropic and to behave elastically in accordance with Hooke's law. We rewrite Hooke's law in terms of stress σ_{ij}, strain ε_{ij}, and elastic material stiffness S_{ijkm}:

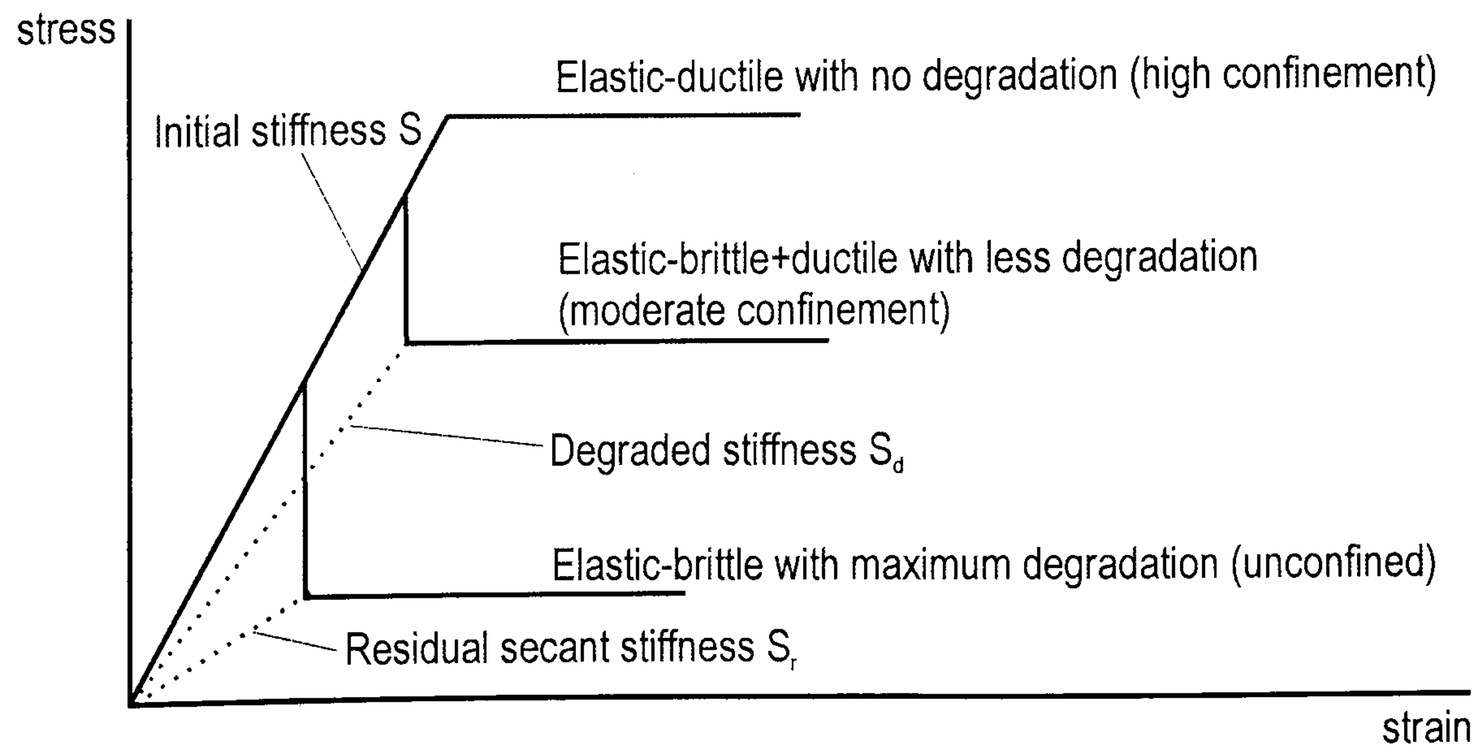


Figure 4.10. Simplified stress-strain relations for a rock element under different confining pressures

$$\sigma_{ij} = S_{ijkm}\varepsilon_{km}. \tag{4-28}$$

The elastic strain energy stored in the element is given by

$$U_e = \frac{1}{2}\sigma_{ij}\varepsilon_{ij} = \frac{1}{2}S_{ijkm}\varepsilon_{ij}\varepsilon_{km}. \tag{4-29}$$

We have seen how the formation of fracture surfaces causes an amount of the stored elastic strain energy within the element to be dissipated, and corresponding to this dissipation is a decrease in material stiffness and strength. Since energy release is independent of the loading configuration (see Section 4.1.3), the decrement of material stiffness and strength can be analysed based on the constant strain configuration. Thus, by differentiating Equation 4-29 with respect to material stiffness, and rearranging, the degradation in stiffness, dS_{ijkm}, corresponding to the amount of released strain energy, dU_e, is expressed as

$$dS_{ijkm} = \frac{2dU_e}{\varepsilon_{ij}\varepsilon_{km}}. \tag{4-30}$$

Similarly, the reduction in the elemental strength, $d\sigma_{ij}$, corresponding to the released strain energy is given by

$$d\sigma_{ij} = \frac{2dU_e}{\varepsilon_{ij}}. \tag{4-31}$$

In the case of crack extension expending part of the elastic strain energy, an elastic solid degrades its stiffness and strength. This is theoretically shown by Equations 4-30 and 4-31, from the point of view of strain energy dissipation.

4.3.4 Degradation and degradation index of rock elements

Equations 4-30 and 4-31 derived in the previous section indicate how, with a knowledge of the dissipated amount of elastic strain energy, the computation of the degradation in material stiffness and strength is straightforward. However, the literature reveals that determination of the strain energy released from a body undergoing cracking remains a difficult issue (see the approaches used in the recent work of Li et al. (2000) and of Shao and Rudnicki (2000)), and so an alternative appropriate for the estimation of elemental degradation is required.

Material degradation is attributed to microcracking that results in brittle behaviour (discussed in Section 4.2.1). Figure 4.11 shows two behaviours that a rock element within a stressed rock body may display: one is the elastic-brittle behaviour exhibited by

an element in uniaxial conditions; the other is elastic-brittle+ductile behaviour exhibited by the element under a certain confining stress. Comparing this figure with Figure 4.6, our interest now is that, provided that we know the degradation of the element that fails in uniaxial condition (particularly $\delta\sigma_{cu}$ in Figures 4.6 and 4.11, for example), we require to be able to determine how much would be the degradation if the element fails under some other confining stress ($\delta\sigma$ in Figure 4.11). Furthermore, since rock compressive failure is often analysed in terms of the uniaxial compressive strength (see Section 4.4), how the degradation ($\delta\sigma$) is represented by the degradation undertaken by the uniaxial compressive strength ($\delta\sigma_c$ in Figure 4.11) is of particular interest. Thus, we need to find a relation between the uniaxial compressive strength degradations in uniaxial and any other confining conditions, *i.e.*

$$\delta\sigma_c = f\left(\delta\sigma_{cu}, \sigma_{con}\right), \tag{4-32}$$

where σ_{con} is confining pressure.

In Subsections 2.3.2 and 2.4.2, we have seen that the amount of degradation in either material stiffness or strength can be measured from laboratory experiments on rock specimens. The analysis given in Subsection 4.2.3 has related the degradation undertaken by a rock under a certain confining stress condition by a degradation index.

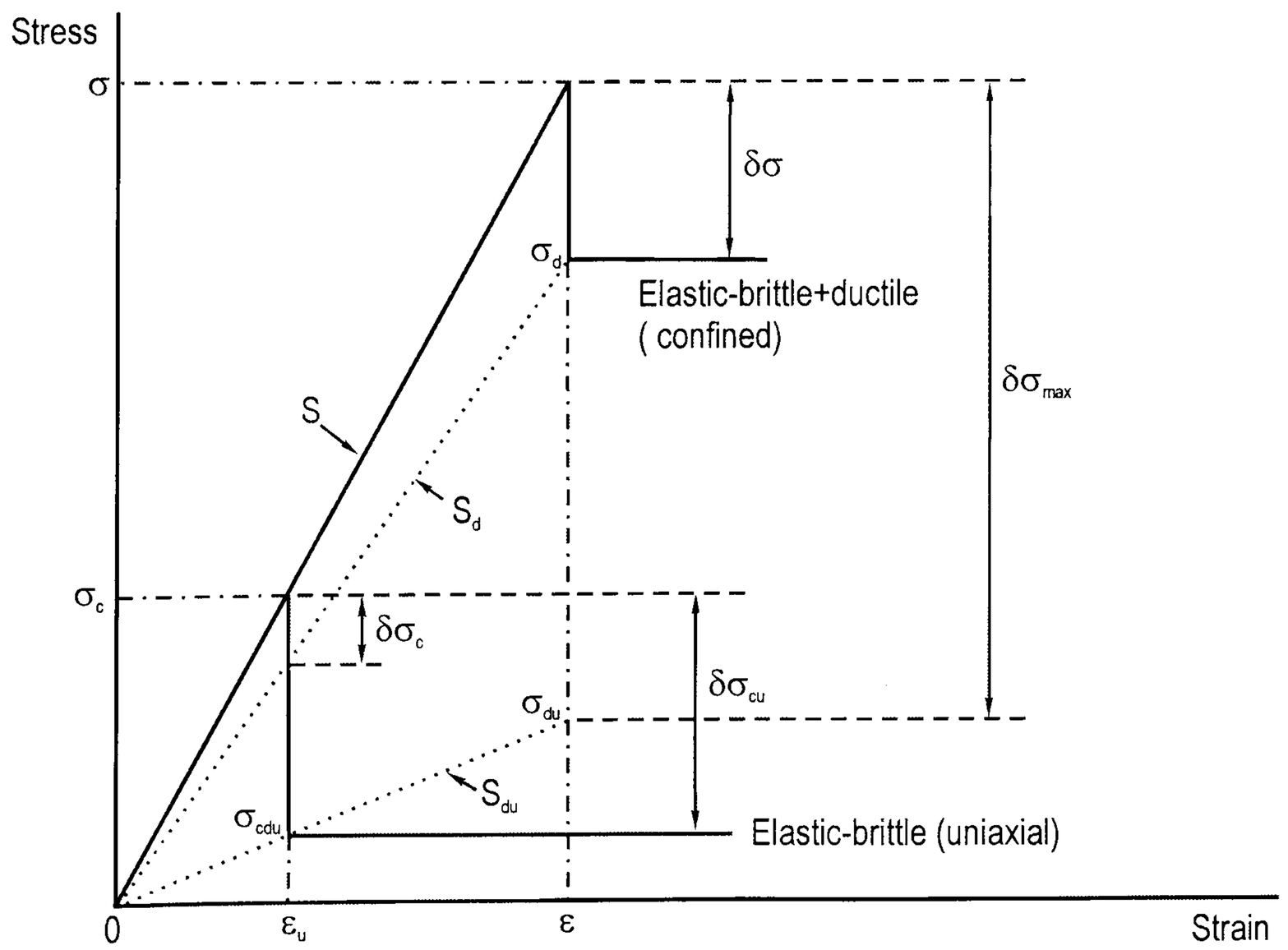


Figure 4.11. Illustration of the representative degradation in uniaxial compressive strength of rock elements failed in confining conditions

A rock element within a stressed rock specimen behaves in a similar way to the rock specimen itself (Subsection 4.3.1), and thus, we may use the degradation index to describe elemental degradation through the values measured during laboratory experiments on customary specimens.

From the geometry indicated in Figure 4.11, we find that

$$\frac{\delta\sigma_c}{\delta\sigma_{cu}} = \frac{\delta\sigma}{\delta\sigma_{max}}. \tag{4-33}$$

The right side of the above equation is the degradation index, r_d, which is defined in Subsection 4.2.3. Thus, we find

$$\delta\sigma_c = r_d \delta\sigma_{cu}. \tag{4-34}$$

In Subsection 4.2.3, it has been also demonstrated that the degradation index for material stiffness is equal to the strength degradation index. Thus, for a degradation in material stiffness under a certain confining stress level, δS, the following relation holds

$$\delta S = r_d \delta S_u, \tag{4-35}$$

where δS_u is the material stiffness degradation in uniaxial conditions.

From Equations 4-34 and 4-35 we see that an estimation of r_d values corresponding to different deformation behaviours is required. Since the material degradation is significantly influenced by confining pressure (Section 2.4.2), and it is this influence that is our current interest in this investigation, a relation between r_d and the confining pressure may be proposed. By definition (Subsection 4.2.3), this relation requires that the values of r_d must lie between 0 and 1 inclusive, representing behaviours from brittle in a non-confining condition, quasi-brittle in a moderate confining condition, to ductile in a high confining condition. With reference to Figure 4.7, two expressions may be proposed for the relationship between r_d and confining stress. They are either a power form of

$$r_d = \left(1 - \frac{\sigma_3}{\sigma_{duc}}\right)^{n_d} \tag{4-36a}$$

or a negative exponential form of

$$r_d = \exp(-n_d \sigma_3). \tag{4-36b}$$

In these two relations, σ_3 is the minor principal stress imposed on the element and must be not less than zero (taking zero when $\sigma_3<0$) under the convention of compressive stresses being positive; the parameter n_d describes either the linearity

(Equation 4-36a) or the curvature (Equation 4-36b) of the relations. In order to meet the requirements discussed in the earlier paragraph, σ_3 in the first relation (Equation 4-36a) is additionally required to be no larger than σ_{duc} (taking σ_{duc} when $\sigma_3 > \sigma_{duc}$), where σ_{duc} is the lowest confining stress level at which the element displays perfect plastic (ductile) behaviour. Since the parameter σ_{duc} is often unavailable, we choose Equation 4-36b as the expression for the degradation index of rock elements.

In order to use either degradation index expressions (Equation 4-36), the parameter n_d is required to be accessible from laboratory experiments on customary rock specimens. In the case of Equation 4-36b, by linear regression on the data listed in Table 4.1, the value of n_d for Tennessee marble is obtained as 0.075; using the same technique on the data listed in Table 4.2, the n_d value for Vosges sandstone is about 0.055. This indicates that the degradation index is a property of rock materials, and that different rocks may have different value for n_d. Thus, laboratory experiments are required to determine this parameter for a practical application. In Section 6.6, the sensitivity of rock fracture to n_d will be investigated.

Finally, by combining Equation 4-36 with Equations 4-34 and 4-35, the full expression for the degradation of material stiffness and strength is given as

$$\begin{aligned} r_d &= \exp(-n_d \sigma_3) \\ \delta S &= r_d \delta S_u \qquad \text{with } \sigma_3 = 0 \text{ for } \sigma_3 < 0, \\ \delta\sigma_c &= r_d \delta\sigma_{cu} \end{aligned} \tag{4-37}$$

with the degraded stiffness, S_d, and uniaxial compressive strength, σ_{cd}, given by (with respect to Figure 4.11)

$$\begin{aligned} S_d &= S - \delta S \\ \sigma_{cd} &= \sigma_c - \delta\sigma_c \end{aligned}. \tag{4-38}$$

It is seen from Equation 4-37 that in order to determine the degradation that an element displays after failure under a certain stress state, at least the other two parameters, *i.e.* δS_u and $\delta\sigma_{cu}$, have to be known. According to experimental results (Chapter 2), this is physically meaningful for rock specimens at the scale of laboratory testing. Since an rock element is analogous to a rock specimen and since no techniques appear to be available for testing micro scale samples in the laboratory, it is required that these two parameters can be determined through laboratory tests on rock samples of customary size as well. For this purpose, a scaling parameter may be required to relate the magnitudes between the two scales. However, as this study is aimed at describing the brittle fracture process and the associated macroscopic behaviour of heterogeneous

rocks in general, estimated values according to general experimental data will be used for these parameters.

4.4 Failure criteria for rock elements

A failure criterion is required for determining failure of an element. This requirement is dealt with in this section.

As presented earlier (Section 2.4), the formation and extension of individual microcracks in rocks under compression are associated with either tensile splitting determined by local tensile stresses or sliding between individual particles and crack surfaces which is controlled by the presence of local shear stresses (Yazdani and Schreyer, 1990). Moreover, it is evident that a shearing mechanism exists when microcracks coalesce (Robet, 2000; Meglis et al., 1995; Shen, 1993). Thus, in order to model the microscopic processes associated with rock fracturing in compression, both tensile and shearing mechanisms have to be incorporated into the model.

However, due to the lack of techniques for testing a rock element of microscopic scale in the laboratory, there are no specific failure criteria for a rock element. Again, if we follow the argument developed in Subsection 4.3.1 that a rock element within a rock specimen can be considered as analogous to a rock specimen itself, the failure criteria developed based on testing rock specimens may be used for rock elements. We first introduce a number of failure criteria that are commonly used in rock mechanics, and then the representation of degradation associated with these failure criteria is addressed.

4.4.1 Failure criteria

Tensile failure

For a material under tensile loading, when the tensile stress acting on the material reaches a critical value, tensile failure occurs. The tensile failure criterion for a material element is simply written as

$$\sigma_3 = -T_0, \tag{4-39}$$

where σ_3 is the minor principal stress developed over an element, and T_0 is the tensile strength of the element.

Shear failure

The shear failure criterion is normally defined in principal stress space, σ_1, σ_2 and σ_3

($\sigma_1 > \sigma_2 > \sigma_3$), and has the form

$$f(\sigma_1, \sigma_2, \sigma_3) = 0. \tag{4-40}$$

For shear failure of rock, a number of criteria have been developed (see Sheorey, 1997). Among these criteria, the linear Mohr-Coulomb criterion is much referred to and used in practice (Jaeger and Cook, 1979; Lockner, 1995; Sheorey, 1997; Zhao, 2000) because of its simple form and general fit to brittle materials. This criterion suggests the shear strength of a material is controlled by two material parameters, the cohesion c and the angle of internal friction ϕ, and that the material fails when the shear stress, τ, that is developed on a specific plane (plane *a-b* in Figure 4.12(a), for example) reaches a critical value. The criterion is written as

$$\tau = c + \sigma_n \tan\phi, \tag{4-41}$$

where σ_n is the normal stress acting on a plane (plane *a-b* in Figure 4.12(a)).

By applying the stress transformation equations, one can obtain

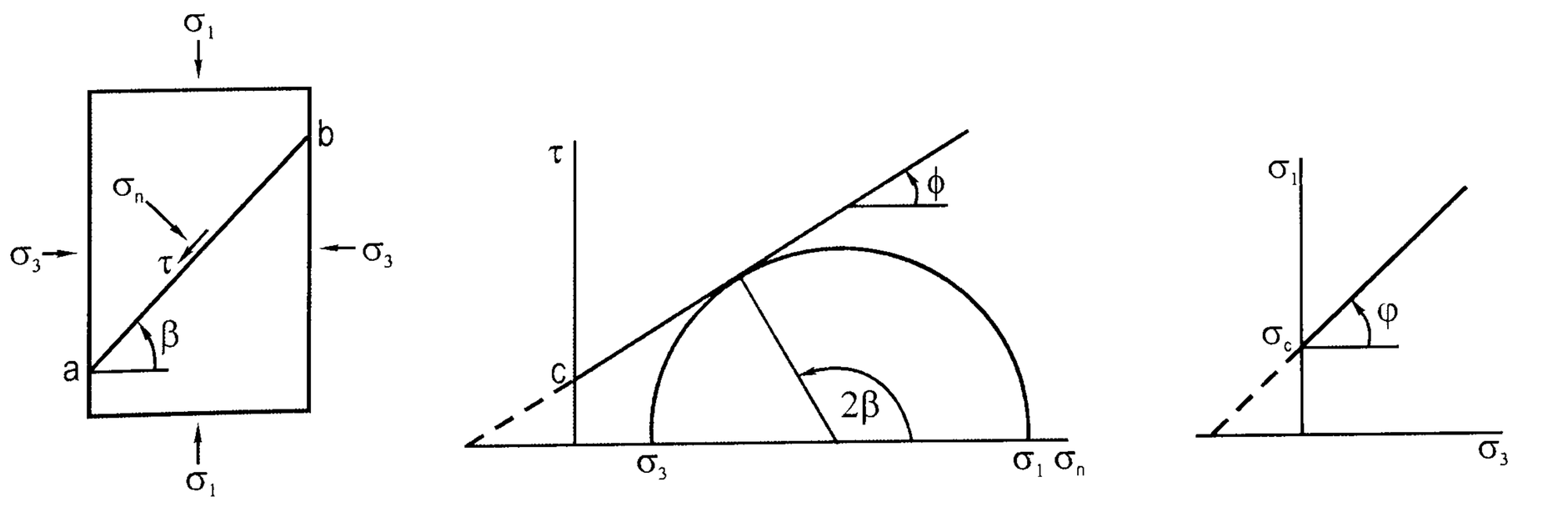
$$\sigma_n = \frac{1}{2}(\sigma_1 + \sigma_3) + \frac{1}{2}(\sigma_1 - \sigma_3)\cos 2\beta \tag{4-42}$$

and

$$\tau = \frac{1}{2}(\sigma_1 - \sigma_3)\sin 2\beta, \tag{4-43}$$

where σ_1 and σ_3 are the major and minor principal stresses respectively, and β the angle between the normal to the plane and the direction of the major principal stress (Figure 4.12(a)).

From Figure 4.12(b), we find



(a) Shear failure on plane *a-b*

(b) Strength envelope of shear and normal stresses

(c) Strength envelope of principal stresses

Figure 4.12. The Mohr-Coulomb strength criterion

$$\beta = \frac{\pi}{4} + \frac{\phi}{2} \tag{4-44}$$

and making use of Equations 4-42 to 4-44, Equation 4-41 can be written as

$$\sigma_1 = \frac{2c\cos\phi + \sigma_3(1+\sin\phi)}{1-\sin\phi}, \tag{4-45}$$

from which we find that the uniaxial compressive strength, σ_c, and uniaxial tensile strength, T_0, are given in terms of c and ϕ as

$$\sigma_c = \frac{2c\cos\phi}{1-\sin\phi}, \tag{4-46}$$

and

$$T_0 = \frac{2c\cos\phi}{1+\sin\phi}. \tag{4-47}$$

In practical rock mechanics use, the uniaxial tensile strength often has a cut-off value, in accordance with the tensile failure criterion, Equation 4-39, or is taken as zero (Zhao, 2000).

The principal stress form of the Mohr-Coulomb criterion can simply be written as

$$\sigma_1 = \sigma_c + k\sigma_3, \tag{4-48}$$

where k is the slope of the line relating σ_1 and σ_3 and is given by

$$k = \tan\varphi = \frac{1+\sin\phi}{1-\sin\phi}, \tag{4-49}$$

where φ is the angle of the slope of the line relating σ_1 and σ_3 (Figure 4.12(c)). In terms of k, Equation 4-46 can be rewritten as

$$\sigma_c = 2c\sqrt{k}. \tag{4-50}$$

Equations 4-48 to 4-50 will be referred to in implementing the degradation model in Chapter 5.

Although the Mohr-Coulomb criterion predicts a linear strength envelope, laboratory results of triaxial tests on rocks often show a curved strength envelope (Hoek and Brown, 1980). Various researchers have therefore proposed non-linear criteria, based on laboratory investigations (see Sheorey, 1997). The most representative and commonly used one is the Hoek-Brown criterion (Sheorey, 1997; Hoek and Brown, 1997; Bieniawski, 1996). This criterion has the form

$$\sigma_1 = \sigma_3 + \sqrt{m\sigma_c\sigma_3 + s\sigma_c^2}\ , \tag{4-51}$$

where m and s are the so-called Hoek-Brown constants for the rock material. s takes the value 1 for any intact rock, and less than unity for disturbed rock (Hoek and Brown, 1997). The values for m are different from rock to rock, with a range between about 1.4 and 40.7 (Sheorey, 1997). The Hoek-Brown criterion also provides a relation between the tensile and compressive strengths, of

$$T_0 = \frac{\sigma_c}{2}\left(\sqrt{m^2 + 4s} - m\right). \tag{4-52}$$

It is important to realise that both the Mohr-Coulomb and the Hoek-Brown criteria are empirical. The only theoretical criterion used in the analysis of fracture of brittle materials is that following on from Griffith's theory. By considering the importance of flaws in controlling the strength of brittle materials, Griffith derived a criterion based on the energy balance concept (Griffith, 1921), which is expressed as

$$\begin{aligned} (\sigma_1 - \sigma_3)^2 &= 8\,\mathrm{T}_0(\sigma_1 + \sigma_3) && \text{for } \sigma_1 + 3\sigma_3 > 0 \\ \sigma_3 &= -\mathrm{T}_0 && \text{for } \sigma_1 + 3\sigma_3 < 0 \end{aligned}\ , \tag{4-53}$$

where T_0 is the uniaxial tensile strength of the material.

When σ_3=0, the first equation in Equation 4-53 gives, for the relation between the uniaxial compressive strength σ_c and the uniaxial tensile strength T_0, the expression

$$\sigma_c = 8T_0\,. \tag{4-54}$$

These three criteria — Mohr-Coulomb, Hoek-Brown and Griffith — will be examined later for incorporation in the degradation model (Chapters 5, 6 and 7).

4.4.2 Representation of degradation associated with failure criteria

Tensile failure

As indicated by Equation 4-16, when tensile failure occurs in an element, the tensile strength of the element is degraded to zero.

Shear failure

When an element fails, as determined by one of the criteria given by Equations 4-48, 4-51 and 4-53, the uniaxial compressive strength of the element is degraded by an amount of $\delta\sigma_c$, as determined by Equation 4-37. The degraded uniaxial compressive

strength of the element, σ_{cd}, is given by the second equation in Equation 4-38, *i.e.*

$$\sigma_{cd} = \sigma_c - \delta\sigma_c . \tag{4-38}$$

For the failure determined by the Mohr-Coulomb criterion, Equation 4-48, the value of σ_{cd} can be represented by directly substituted into the criterion. The Hoek-Brown failure criterion (Equation 4-51) contains two parameters m and s, which represent strength features of rock materials subjected to various disturbed conditions (Hoek and Brown, 1997). In order to describe strength degradation, $\delta\sigma_c$, upon material failure determined by the Hoek-Brown criterion, the values for the two parameters change accordingly, with respect to σ_{cd}. One method of determining this change is through the use of the Geological Strength Index (GSI). GSI is a parameter to describe the degree of the disturbance to a material with the value from 100 for an undisturbed material descending to 10 for a very loose material (Hoek and Brown, 1997). In terms of GSI, expressions for the parameters m and s are given as (Hoek and Brown, 1997)

$$s = \exp\left(\frac{\mathrm{GSI} - 100}{9}\right) \tag{4-55}$$

and

$$m = m_i \exp\left(\frac{\mathrm{GSI} - 100}{28}\right), \tag{4-56}$$

where m_i is the initial value of the Hoek-Brown parameter m for the undisturbed material.

Using s_d and m_d for the Hoek-Brown parameters s and m, corresponding to the uniaxial compressive strength degradation, σ_{cd}, defined by Equation 4-38, the parameter s_d can be derived by substituting $\sigma_3 = 0$ and replacing σ_1 with σ_{cd} in the Hoek-Brown strength criterion (Equation 4-51), which gives

$$s_d = \left(\frac{\sigma_{cd}}{\sigma_c}\right)^2 . \tag{4-57}$$

Combining Equations 4-55 to 4-57 then gives

$$m_d = m_i \exp\left(\frac{9\ln s_d}{28}\right). \tag{4-58}$$

For the Griffith failure criterion (Equation 4-53), the uniaxial compressive strength degradation is represented by the parameter T_0, whose degraded value T_{0d} is given by

replacing σ_c with σ_{cd} in Equation 4-54, which gives

$$T_{0d} = \frac{\sigma_{cd}}{8}. \tag{4-59}$$

These procedures will be implemented in the numerical analysis of rock fracture presented in Chapters 5, 6 and 7.

4.5 Elemental constitutive relation

In section 4.2, it was suggested that a rock element in compression behaves in a similar way to a rock specimen under the same circumstances. This section deals with the constitutive relations for rock elements, and these relations will be used in the numerical analysis of rock fracture in the following chapters (Chapters 5, 6 and 7).

4.5.1 Elasto-plastic constitutive relations

In the flow theory of elastic-plastic solids, the strain increment tensor in the plastic range is usually decomposed into elastic components $d\varepsilon_{ij}^{e}$ and plastic components $d\varepsilon_{ij}^{p}$. By this theory, the total strain increment $d\varepsilon_{ij}$ is expressed as (Vermeer and De Borst, 1984)

$$d\varepsilon_{ij} = d\varepsilon_{ij}^{e} + d\varepsilon_{ij}^{p}. \tag{4-60}$$

The stress increment $d\sigma_{ij}$ is described by Hooke's law as

$$d\sigma_{ij} = S_{ijkm} d\varepsilon_{km}^{e}, \tag{4-61}$$

where S_{ijkm} is the current stiffness of the material.

Making use of Equation 4-60, Equation 4-61 becomes

$$d\sigma_{ij} = S_{ijkm}\left(d\varepsilon_{km} - d\varepsilon_{km}^{p}\right), \tag{4-62}$$

From which it can be seen that an expression for $d\varepsilon_{ij}^{p}$ is required. This is considered in the next section.

4.5.2 Flow rule and the plastic potential function

The increment of plastic strain is defined by the flow rule, which provides a relationship between the orientation of the plastic strain rates and the orientation of the stress. The

flow rule can be expressed as (Vermeer and De Borst, 1984)

$$d\varepsilon_{ij}^{p} = \lambda \frac{\partial g}{\partial \sigma_{ij}} \quad , \tag{4-63}$$

where λ is a positive parameter whose magnitude is dependent on the stress history and the properties of the material (determination of λ is considered in Subsection 4.6.3), and g is the plastic potential function, which is required to provide the magnitude and direction of the plastic deformation increments. As a means of defining a failure criterion, the plastic potential function is also defined in stress space, where it has the form

$$g(\sigma_1, \sigma_2, \sigma_3) = 0 \, . \tag{4-64}$$

Since different materials have different characteristics of plastic deformation, the flow rule described by such a plastic potential function can have the form of either an associated or a non-associated flow rule. If the plastic potential function has the same form as the yield function, the flow rule is called an associated flow rule; otherwise, it is a non-associated flow rule.

For geomaterials, dilatancy is a notable phenomenon associated with shearing processes. It is found that to describe dilatancy phenomena, a non-associated flow rule is appropriate, and the corresponding plastic potential function usually has the form (Vermeer and De Borst, 1984)

$$g = \sigma_1 - \sigma_3 k_\psi + \text{constant} \, , \tag{4-65}$$

where

$$k_\psi = \frac{1 + \sin\psi}{1 - \sin\psi} \, , \tag{4-66}$$

and ψ is the dilation angle. Equations 4-65 and 4-66 closely resembles the Mohr-Coulomb failure criterion (Equation 4-48, together with Equation 4-49), the only difference being that the angle of internal friction ϕ is replaced by the dilation angle ψ.

Since dilatancy is associated only with shearing of materials (see Vermeer and De Borst, 1984), for tensile failure in order to dissipate tensile stresses across the failed element a plastic potential function that has the same form as the failure criterion has to be used (see Pande et al., 1990), *i.e.*

$$g = \sigma_3 \, . \tag{4-67}$$

Differentiating the plastic functions given by Equations 4-65 and 4-67 with respect to stresses leads to the relevant flow rules (as indicated by Equation 4-63).

4.5.3 Determination of λ

A very clear explanation of the determination of λ is given by Vermeer and De Borst (1984). We follow that treatment here, with a few variations to the nomenclature.

Substituting Equation 4-63 into 4-62, leads to

$$d\sigma_{ij} = S_{ijkm} d\varepsilon_{km} - \lambda A_{ij}, \tag{4-68}$$

where

$$A_{ij} = S_{ijkm} \frac{\partial g}{\partial \sigma_{km}}. \tag{4-69}$$

Upon failure, the incremental stress state must remain on the failure surface in order to maintain plastic flow. This condition gives, for the failure criteria introduced in the form of Equation 4-40, the relation

$$df = \frac{\partial f}{\partial \sigma_{ij}}^{\mathrm{T}} d\sigma_{ij} = 0. \tag{4-70}$$

Substitution of Equation 4-68 into 4-70 leads to

$$\lambda = \frac{B_{ij}^{T}}{\alpha} d\varepsilon_{ij}, \tag{4-71}$$

where

$$B_{ij}^{T} = \frac{\partial f}{\partial \sigma_{km}}^{T} S_{kmij} \tag{4-72}$$

and

$$\alpha = \frac{\partial f}{\partial \sigma_{ij}}^{T} A_{ij}. \tag{4-73}$$

Finally, the expression for the stress-strain relation is obtained by substituting Equation 4-71 into 4-68 to give

$$d\sigma_{ij} = \left(S_{ijkm} - \frac{1}{\alpha} A_{ij} B_{km}^{T} \right) d\varepsilon_{km}. \tag{4-74}$$

In general, this equation requires numerical procedures to obtain the resulting

stresses for a given strain history, since it is impossible for the equation to be integrated analytically (Vermeer and De Borst, 1984).

4.6 Introduction of heterogeneity

Rock materials consist of crystals, grains, cementitious materials, and voids, pores, and cracks (Jaeger and Cook 1979). Such microstructures may display very different size, shape or elastic constants. The presence of these microstructures produces the heterogeneity in individual particle strength, and local differential strain and stress (Scholz, 1968). As a result, multiple failures continuously occur from site to site during a complete rock failure process, as evidenced by detailed laboratory observations (as discussed in Chapter 2).

As early as the 19th century, it was noticed that the tensile strength of a material is not constant, but varies significantly from test to test (Bazant and Chen, 1997). Later studies on this subject showed that the variation of material tensile strength can be described statistically (Weibull, 1939), and so too can the compressive strength, shear strength and any rock property that is associated with fracture (Hudson and Fairhurst, 1969).

Many theories have been developed to account for the statistical aspects involved in rock failure (Whittaker et al., 1992). However, rock failure is a complex process, so that it is difficult for any simple theory to be flexible enough to cope with all possibilities (Hudson and Fairhurst, 1969). It may be also argued that different types of rock have different statistical features, which require different functions for their description. In a general study on rock fracture, a number of distribution functions should be investigated for determining heterogeneity of elemental properties. Thus, the uniform, normal and Weibull distribution function — all of these have been seen in the literature (see Scholz, 1968; Hudson and Fairhurst, 1969; Blair and Cook, 1998; Tang et al., 2000) — are considered further here.

4.6.1 Uniform distribution

The uniform distribution function has the form

$$\Pr(x) = 1 - \frac{x_b - x}{x_b - x_a} \qquad \text{for } x_a < x < x_b, \tag{4-75}$$

where x_a and x_b are the minimum and maximum values of x, respectively.

4.6.2 Normal distribution

The normal distribution function is written as

$$\Pr(x) = \frac{1}{\sqrt{2\pi}x_\sigma} \exp\left(-\frac{(x - x_\mu)^2}{2x_\sigma^2} \right) \quad \text{for } -\infty < x < +\infty, \tag{4-76}$$

where x_μ is the mean, and x_σ the standard deviation. The normal distribution has a finite probability associated with negative values, and this feature may be inappropriate for describing heterogeneity in rocks (Hudson and Fairhurst, 1969), because the values for certain properties must be always positive, *e.g.* the internal friction angle.

4.6.3 Weibull distribution

Finally, the expression for the Weibull distribution is given by (Weibull, 1939, 1951)

$$\Pr(x) = 1 - \exp\left[-\left(\frac{x - x_u}{x_0} \right)^{m_w} \right] \quad \text{for } x_u \le x < \infty, \tag{4-77}$$

where m_w is the shape parameter describing the scatter of x, x_0 is a scale parameter, and x_u the location parameter, specifying the lower bound value of x. Equation 4-77 is called the three-parameter Weibull distribution function. When $x_u = 0$, Equation 4-77 becomes a two-parameter form as

$$\Pr(x) = 1 - \exp\left[-\left(\frac{x}{x_0} \right)^{m_w} \right] \quad \text{for } x \ge 0. \tag{4-78}$$

Since it contains the variable shape parameter m_w, the Weibull distribution function is very general (Hudson and Fairhurst, 1969). For example, with m_w = 1 the Weibull distribution function (Equation 4-77) becomes the exponential distribution function. As m_w increases, a distribution similar to the normal distribution is obtained. Figure 4.13 shows a number of distributions given by Equation 4-78, with m_w varying from 1 to 5.

The distribution functions above will be used in heterogeneity consideration in the implementation and application of the degradation model (Chapters 5, 6 and 7).

4.7 Stress redistribution associated with degradation

In the degradation model, when an element fails either its elastic modulus or strength degrades. Associated with the degradation is a reduction in the stress sustained by the

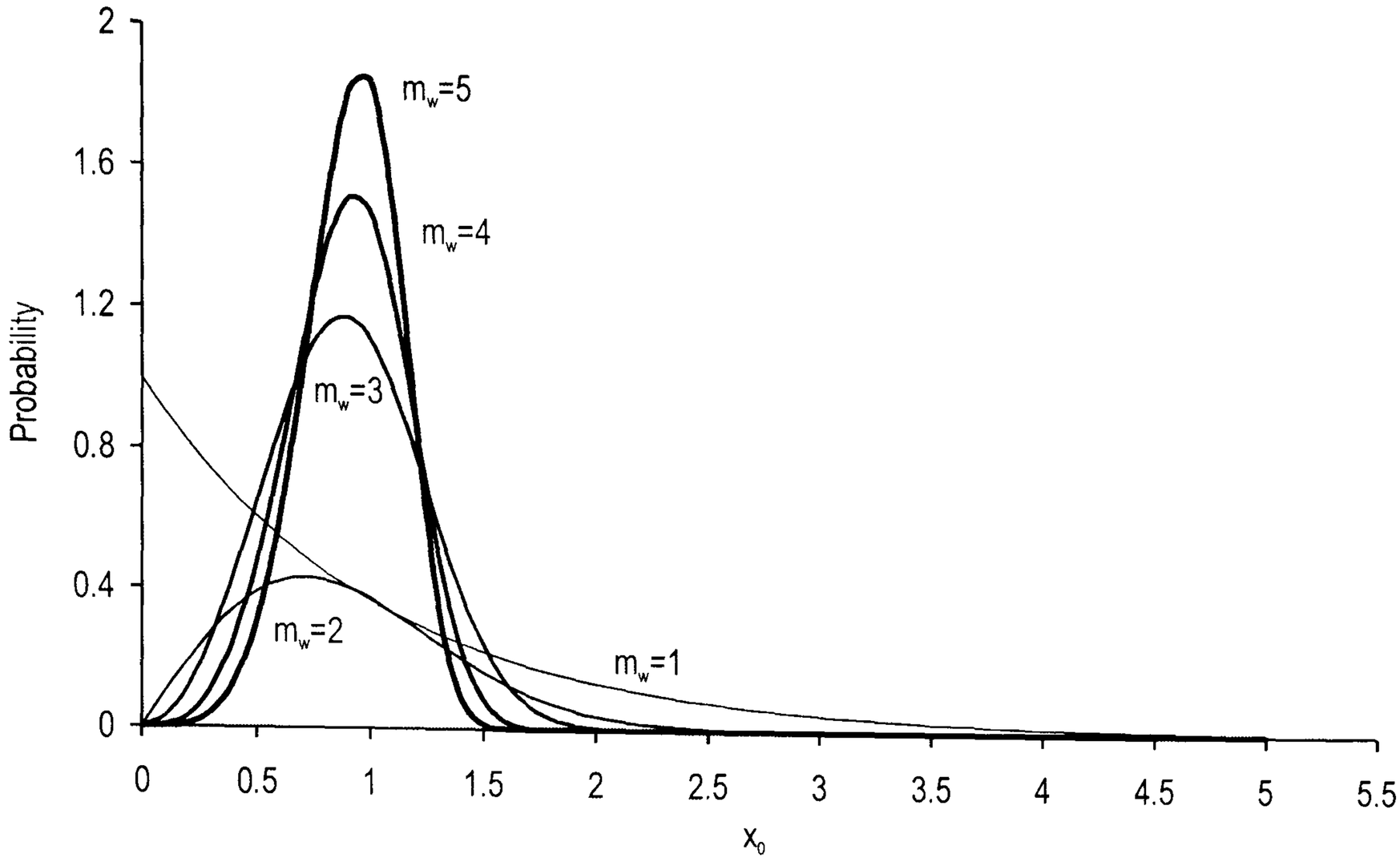


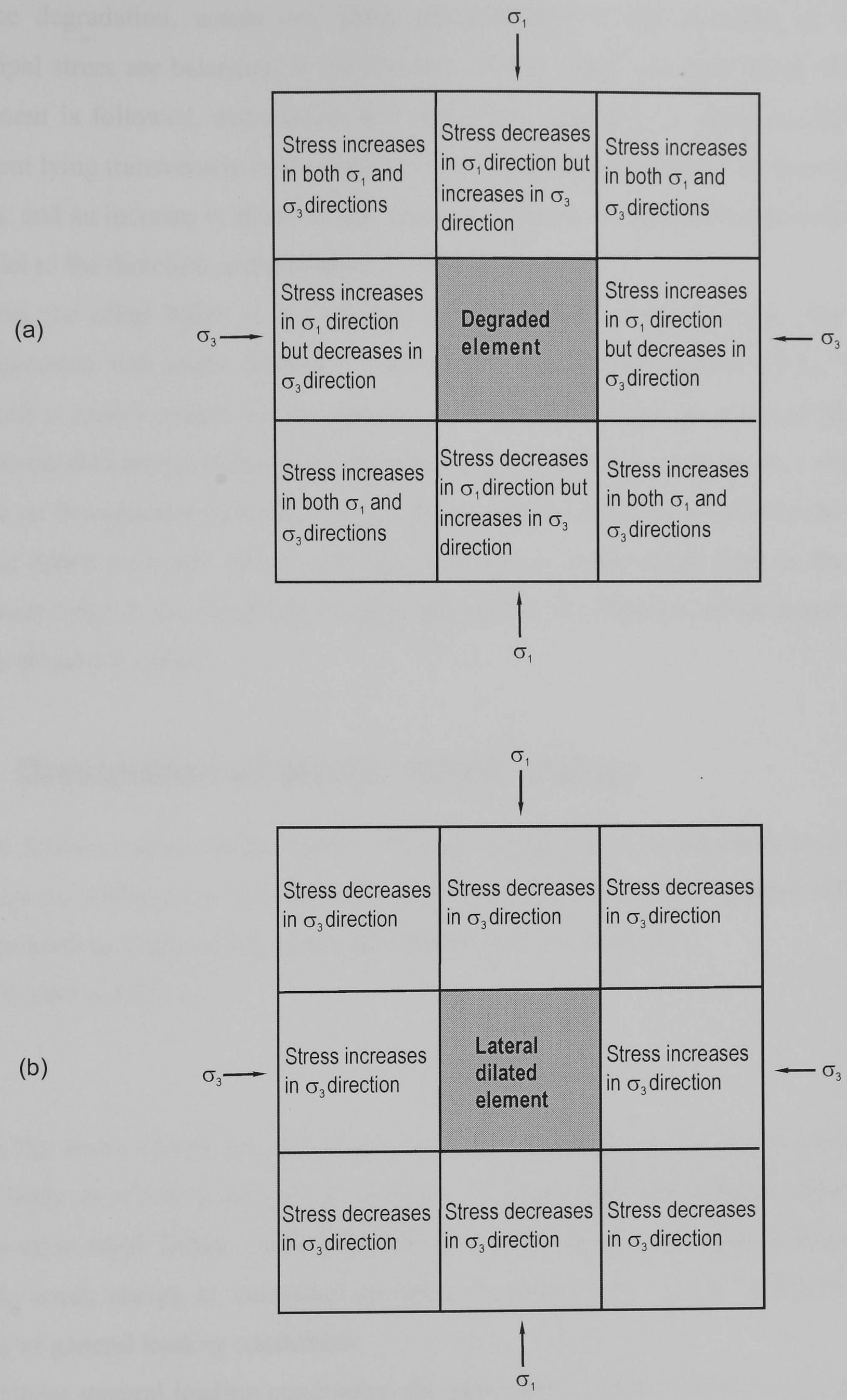
Figure 4.13. Shapes of Weibull distribution function with various values for shape parameter

degraded element, and as a result, the stress and strain field within its vicinity is redistributed.

In general, in a heterogeneous rock body, the stress redistribution caused by elemental degradation is so complex that numerical procedures are require to obtain the resulting stress distributions. This is undertaken in Chapter 5, but it is instructive to consider the process of stress redistribution from a mechanistic point of view.

Figure 4.14 shows a representative structure comprising a degraded element, at the centre of the structure, and its eight adjacent elements. With respect to the degraded element, we denote the vertical direction as the direction of the major principal stress acting on the element prior to its failure, and the horizontal direction the direction of the corresponding minor principal stress (Figure 4.14).

At the instant of failure of the element, the major principal stress shed by the element is $\delta\sigma$ (see Figure 4.11). In the major principal stress direction (vertical in Figure 4.14(a)), the shed stress will be shared by the adjacent elements lying transversely in the direction parallel to the direction of the minor principal stress; and the adjacent elements in the transverse direction parallel to the direction of the major principal stress undergo a reduction in their sustained stress. To compensate this reduction, the stress on the adjacent elements in diagonal directions, with respect to the direction of the major and minor principal stresses, increases too, and so on, so that the stress changes, produced



(σ_1 and σ_3 represent the major and minor principal stress with respect to the degraded element prior to failure)

Figure 4.14. Illustration of stress changes induced by (a) elemental degradation and (b) elemental dilation to local vicinity

by the degradation, across any plane perpendicular to the direction of the major principal stress are balanced. In the direction of the minor principal stress, if the same argument is followed, degradation will result in a reduction in stress on the adjacent element lying transversely in the direction parallel to the direction of the minor principal stress, and an increase in stress on the adjacent elements lying in the transverse direction parallel to the direction of the major principal stress.

On the other hand, in the direction of the minor principal stress, the shearing displacement will cause dilation to the failed element (Subsection 4.5.2). This may produce a reverse result, *i.e.* an increase in stress on the adjacent element lying in the transverse direction parallel to the direction of the minor principal stress, a reduction in stress on the adjacent elements lying in the transverse direction parallel to the direction of the major principal stress, even may produce a tensile stress field to the adjacent elements lying in the transverse direction parallel to the direction of the major principal stress (Figure 4.14(b)).

4.8 Dissipation of elastic strain energy

Local fracture causes the dissipation of strain energy, which corresponds to a reduction in material stiffness (see Section 4.1). With reference to specific degraded stiffness, the corresponding elastic strain energy dissipation may be calculated.

Equation 4-29, *i.e.*

$$U_e = \frac{1}{2}\sigma_{ij}\varepsilon_{ij}, \tag{4-29}$$

gives the strain energy per unit volume of a linearly elastic body. For a heterogeneous rock body as is considered in this research, the stress fields are different from place to place once local failure takes place (Section 4.7). Hence, in order to calculated the elastic strain energy of individual elements, Equation 4-29 requires to be rewritten in terms of general loading conditions.

Under general loading conditions, the stress-strain relation of an isotropic medium may be expressed as (Mase and Mase, 1999)

$$\sigma_{ij} = \lambda^l \delta_{ij}\varepsilon_{kk} + 2\mu^l \varepsilon_{ij}, \tag{4-79}$$

where δ_{ij} is Kronecker delta, and λ^l and μ^l are Lamé's constants, defined as

$$\lambda^l = \frac{\nu E}{(1+\nu)(1-2\nu)} \tag{4-80}$$

and

$$\mu^l = \frac{E}{2(1+\nu)}. \tag{4-81}$$

where E is Young's modulus and ν is Poisson's ratio.

Substituting Equation 4-79, with Equations 4-80 and 4-81, into Equation 4-29, the expression for the elastic strain energy per unit volume under general loading conditions is obtained in terms of strains

$$U_e = \frac{1}{2}\lambda^l \delta_{ij}\varepsilon_{kk}\varepsilon_{ij} + \mu^l \varepsilon_{ij}\varepsilon_{ij}. \tag{4-82}$$

It should be noted that since the introduction of Lamé's constants in the above expressions stiffness degradation of a fractured element can be interpreted by degradation in Young's modulus. Thus, referring to Equations 4-80 and 4-81, it is seen that corresponding to the degraded Young's modulus E_d from the previous value E_0 of a fractured element, the dissipated strain energy from the element, δU_{ed}, would be

$$\delta U_{ed} = \frac{\delta E}{E_0} U_{e0} \delta V, \tag{4-83}$$

where: $\delta E = E_0 - E_d$; U_{e0} is the strain energy per unit volume, corresponding to E_0, of the element; and δV is the volume of the element (becoming the area δA in plane strain conditions).

The dissipation of the elastic strain energy associated with elemental fracture is one of the model outputs used to relate to acoustic emission in analysing brittle fracture of rock in Chapter 6.

4.9 Summary of the degradation model

In this chapter a degradation model has been developed to analyse the fracture process in heterogeneous rock. However, as this model has been dealt with aspect by aspect in the previous sections, it is necessary to sum up the contents of the model. This is treated in this section.

The main concepts of the degradation model are catalogued into three groups. The first group concerns the model parameters required to undertake a physical analysis on

rock, and parameters specific to the degradation model. The second group refers to the methods used to set up a representative physical objective model for rock, including the distribution functions for representing material heterogeneity. The third group concerns model analyses, in which all the equations necessary to perform an analysis are covered. Features related to numerical analysis are not included here, but will be considered in the next chapter.

It should be noted that in this section the equation sequencing is kept identical with the previous sections, for the sake of convenience.

4.9.1 Model parameters

As indicated in the formulations contained in the previous sections, the data required for an application of the degradation model to the analysis of rock fracture behaviour are those representing the material physical and mechanical properties and those designating the external (*i.e.* boundary) conditions. These data consist also of four subgroups. One subgroup includes the parameters for the calculation of deformation (stress-strain relation) (see Section 4.5); another subgroup is associated with property heterogeneity (Section 4.6); and the other two subgroups contain those parameters indicating elemental failure and degradation (see Sections 4.4 and 4.3). In the subgroups indicating property heterogeneity and elemental failure, different distribution functions or failure criteria require different input parameters. Table 4.3 lists the parameters required for performing an analysis with the degradation model.

4.9.2 Model set-up

The previous section has introduced the parameters required to undertake an analysis of rock fracture with the degradation model. Following the specification of these parameters, data need to be assigned to each element. This can be easily done for the parameters with a constant value, but for data that vary, a distribution function is required. As discussed in Section 4.6, three distribution functions can be considered in this respect, *i.e.* uniform, normal, and Weibull distributions, as listed below.

Uniform distribution

$$\Pr(x) = 1 - \frac{x_b - x}{x_b - x_a} \qquad \text{for } x_a < x < x_b, \tag{4-75}$$

where x_a and x_b are the minimum and maximum values of x, respectively.

Table 4.3. Required parameters for an analysis of brittle fracture of rock with the degradation model

Group		Parameters
Deformation		Young's modulus E, Poisson's ratio ν, and dilation angle ψ
Property distribution function	Uniform	Lower and upper bound values x_a and x_b
	Normal	Mean x_μ and standard deviation x_σ
	Weibull	Shape parameter m_w, scale parameter x_0, and location parameter x_u
Strength criterion	Mohr-Coulomb	Internal friction angle ϕ, cohesive strength c, and tensile strength T_0
	Hoek-Brown	Hoek-Brown parameters m_i and uniaxial compressive strength σ_c of intact rock
	Griffith	Tensile strength T_0
Degradation		Uniaxial degradation in strength, $\delta\sigma_{cu}$, and in stiffness, δS_u, and parameter n_d

Normal distribution

$$\Pr(x) = \frac{1}{\sqrt{2\pi}x_\sigma}\exp\left(-\frac{(x-x_\mu)^2}{2x_\sigma^2}\right) \quad \text{for } -\infty < x < +\infty, \tag{4-76}$$

where x_μ is the mean and x_σ the standard deviation.

Weibull distribution

$$\Pr(x) = 1 - \exp\left[-\left(\frac{x-x_u}{x_0}\right)^{m_w}\right] \quad \text{for } x_u \le x < \infty, \tag{4-77}$$

where m_w is the shape parameter describing the scatter of x, x_0 is a scale parameter, and x_u the location parameter, specifying the lower bound value of x.

4.9.3 Model analysis

After the set-up of a model, a formal analysis can be performed. The analysis contains

three parts. One is calculation of the stress-strain relation for an element, another is determination of elemental failure through use of a failure criterion, and the last is the specification of degradation following elemental failure. One stress-strain relation (Section 4.5) and one degradation rule (Section 4.3) are used in the degradation model, and three failure criteria — the Mohr-Coulomb, Hoek-Brown, and Griffith failure criteria — are incorporated (Section 4.4). The various equations are listed below.

Stress-strain relation

$$d\sigma_{ij} = \left(S_{ijkm} - \frac{1}{\alpha} A_{ij} B_{km}^{T} \right) d\varepsilon_{km}, \tag{4-74}$$

where

$$\alpha = \frac{\partial f^{T}}{\partial \sigma_{ij}} A_{ij}, \tag{4-73}$$

$$A_{ij} = S_{ijkm} \frac{\partial g}{\partial \sigma_{km}}, \tag{4-69}$$

$$B_{ij}^{T} = \frac{\partial f^{T}}{\partial \sigma_{km}} S_{kmij}, \tag{4-72}$$

with

$$g = \sigma_1 - \sigma_3 k_\psi + \text{constant} \qquad \text{(for shear failure)}, \tag{4-65}$$

$$g = \sigma_3 \qquad \text{(for tensile failure)}, \tag{4-67}$$

and

$$k_\psi = \frac{1 + \sin\psi}{1 - \sin\psi}, \tag{4-66}$$

where S_{ijkm} is the current stiffness of the material, f represents a failure criterion in the form of $f(\sigma_1, \sigma_2, \sigma_3) = 0$, and ψ is the dilation angle.

Strength criteria

The Mohr-Coulomb criterion is given by

$$\sigma_1 = \sigma_c + k\sigma_3 \qquad \text{for } \sigma_3 > -T_0, \tag{4-48}$$

and

$$\sigma_3 = -T_0 \qquad \text{otherwise,} \tag{4-39}$$

with

$$\sigma_c = 2c\sqrt{k}\,, \tag{4-50}$$

and

$$k = \tan\varphi = \frac{1+\sin\phi}{1-\sin\phi}, \tag{4-49}$$

where: σ_c is the elemental uniaxial compressive strength; k is the slope, and φ is the angle of the slope, of the line relating σ_1 and σ_3; T_0 is the uniaxial tensile strength of the element; c is the cohesion; and ϕ is the angle of internal friction.

The Hoek-Brown criterion is given by

$$\sigma_1 = \sigma_3 + \sqrt{m\sigma_c\sigma_3 + s\sigma_c^2}\,, \tag{4-51}$$

and

$$\sigma_3 = -T_0 = \frac{\sigma_c}{2}\left(m - \sqrt{m^2+4s}\right), \tag{4-52}$$

where m and s are the Hoek-Brown constants for the rock material, and T_0 is the uniaxial tensile strength of the element.

The Griffith criterion is given by

$$\begin{aligned} (\sigma_1-\sigma_3)^2 &= 8\,T_0(\sigma_1+\sigma_3) && \text{for } \sigma_1+3\sigma_3>0 \\ \sigma_3 &= -T_0 && \text{for } \sigma_1+3\sigma_3<0 \end{aligned}\,. \tag{4-53}$$

Degradation rule

The degraded stiffness, S_d, and strength, σ_{cd}, are given by

$$\begin{aligned} S_d &= S-\delta S \\ \sigma_{cd} &= \sigma_c - \delta\sigma_c \end{aligned}\,, \tag{4-38}$$

where S and σ_c is the initial stiffness and uniaxial compressive strength of elements, and δS and $\delta\sigma_c$ are the stiffness and strength degradation displayed by an element in any confined compression and are given by

$$\begin{aligned} \delta S &= r_d\,\delta S_u \\ \delta\sigma_c &= r_d\,\delta\sigma_{cu} \end{aligned}\,, \tag{4-37}$$

where δS_u and $\delta\sigma_{cu}$ are the stiffness and strength degradation displayed by an element under uniaxial compression, respectively, and r_d is the degradation index and is expressed as

$$r_d = \exp(-n_d \sigma_3) \qquad \text{with } \sigma_3 = 0 \text{ for } \sigma_3 < 0, \tag{4-37}$$

where n_d is a degradation parameter and is determined by experiments.

Strength degradation with the Mohr-Coulomb criterion is operated by directly replacing σ_c in Equation 4-48 with σ_{cd}. Strength degradation operation with the Hoek-Brown criterion is given by

$$m_d = m_i \exp\left(\frac{9 \ln s_d}{28}\right), \tag{4-58}$$

and

$$s_d = \left(\frac{\sigma_{cd}}{\sigma_c}\right)^2, \tag{4-57}$$

where m_d and s_d are the Hoek-Brown parameter m and s, representing the degree of degradation, and m_i is the initial value of the Hoek-Brown parameter m for the undisturbed material.

Strength degradation operation with the Griffith criterion is given by

$$T_{0d} = \frac{\sigma_{cd}}{8}, \tag{4-59}$$

where T_{0d} is the degraded tensile strength of the degraded element.

Elastic strain energy dissipation

Elemental elastic strain energy dissipation associated with degradation is given by

$$\delta U_{ed} = \frac{\delta E}{E_0} U_{e0} \delta V, \tag{4-83}$$

with

$$U_{e0} = \frac{1}{2}\lambda^l \delta_{ij} \varepsilon_{kk} \varepsilon_{ij} + \mu^l \varepsilon_{ij} \varepsilon_{ij}, \tag{4-82}$$

$$\lambda^l = \frac{\nu E_0}{(1+\nu)(1-2\nu)}, \tag{4-80}$$

and

$$\mu^l = \frac{E_0}{2(1+\nu)}. \tag{4-81}$$

where E_0 is the Young's modulus prior to degradation, δE is the degradation in Young's modulus, δA is the elemental area, and ν is Poisson's ratio.

4.10 Closure

This chapter has shown that the creation of new crack surfaces within an elastic solid expends energy from either the elastic strain energy, the external work, or both. It is further shown that, corresponding to the strain energy dissipation, the creation of new crack surfaces causes a reduction in both the elastic modulus and strength of the material.

As presented in Chapter 2, rock fracture in compression primarily exhibits two distinctive microstructural changes. One is the development of microcracks and microvoids, which is associated with creation of new crack surfaces and is defined as microcracking; the other is sliding between particles and crack surfaces, which is associated with frictional processes and is defined as microsliding (Section 4.2.1). In the light of the theoretical basis (Section 4.1) and observed laboratory phenomena (Section 2.2; and also see Section 4.2), we have deduced the following three points:

(1) With rock fracture in compression, microcracking causes dissipation of elastic strain energy, resulting in a reduction in both elastic modulus and strength, and produces brittle behaviour. Contrary to this, microsliding only expends external work, causes little or no reduction in either elastic modulus or strength, and produces ductile behaviour.

(2) The various stress-strain curves exhibited by rock under compression at different confining pressures are a combination of the two microstructural changes. The lower the confining pressure, the more the microcracking, the more elastic strain energy is dissipated, and the more brittle is the material behaviour. It is proposed that this phenomenon be described by a parameter degradation index, the derivation of which was given in Subsection 4.2.3.

(3) As the two microstructural changes are similar to the macrostructural changes that a rock specimen presents in the laboratory, it is proposed that a rock element suffering one of the two microstructural changes within a stressed rock body can be regarded as a small-scale rock specimen. On this basis, it is assumed that rock elements behave in a similar way to rock specimens in the laboratory, *i.e.* elastic-brittle, elastic-

strain softening and elastic-ductile, depending on the magnitude of the applied minor principal stress.

Based on these deductions, in this chapter a degradation model has been developed to describe brittle fracture in heterogeneous rocks. This model takes into account the degradation effect, at a local scale, induced by microcracking. This mircocracking is determined by a failure criterion. When an element fails, either the elastic modulus, strength or both degrade to represent the introduction of dissipative processes, and the degradation of the failed element produces further disturbances to the local stress and strain fields, and so on.

Under different circumstances, an element exhibits different degradation. The degree of elemental degradation corresponds to the energy dissipated from the local elastic strain energy, and is controlled by the degradation index of the element. The degradation index may be influenced by a number of factors, with confining pressure being the most important.

The degradation occurs when an element fails, and failure criteria are needed to specify elemental failure. Although no such criteria have been developed based on the testing of rock elements at a microscopic scale, the analogy between rock elements and rock specimens allows us to adopt the failure criteria developed for rock specimens, which include the Mohr-Coulomb, Hoek-Brown and Griffith failure criteria.

To represent heterogeneity, a statistical technique is required in this model to introduce an elemental property distribution. No evidence has been found for any specific statistical distribution function appropriate for rock elemental strength, and so three common distribution functions have been incorporated into this model, *i.e.* uniform, normal and Weibull distributions. Of these distribution functions, the most appropriate one will be clarified in Chapter 6, by matching model results with laboratory data.

An elasto-plastic relation is used for elemental behaviour. This relation indicates that plastic flow of materials takes place at a degraded strength level, which is appropriate for the model concept. Moreover, in this relation, the volumetric dilation is incorporated through a non-associated flow rule, which enhances the disturbances to the local stress and strain fields.

This model is expected to reproduce all the features of rock fracture in compression, including isolated microscopic dissipative processes, the associated macroscopic stress-strain relation, acoustic emission (energy dissipation) features, and the hysteresis loops. These will be examined in Chapters 6 and 7.

The rules used in this model are very basic and very simple. This leads to the easy implementation of the model into a computer code. Almost all the numerical methods and computer codes written for stress and strain analysis in geomaterials could be considered in this respect, and selection of the most appropriate code will be discussed in Chapter 5.

Since the key feature of this model is the dependent degradation of elemental elastic modulus and strength, this model is termed:

"Local Stiffness and Strength Degradation Model for Brittle Fracture in Heterogeneous Rocks".

5 Implementation of the degradation model

Chapter 2 showed that rock fracture in compression involves two types of microstructural changes, namely, microcracking and microsliding (these terms are defined in Section 4.2.1). Microcracking relates to the formation or extension of new cracks and results in brittle behaviour, while microsliding refers to frictional processes between particles or crack surfaces, and produces ductile behaviour. In the previous chapter it was shown that the creation of new crack surfaces expends energy from either the elastic strain energy, the external work, or both, and results in degradation in both the elastic modulus and strength of the material. On this basis, rock fracture under various compression circumstances has been analysed, and the conclusion drawn that degradation exhibited in rock compressive fracture is associated with the dissipation of elastic strain energy within the rock body. The more degradation a material suffers, the more the elastic strain energy is dissipated, and the more brittle the material behaviour is.

Section 4.3 showed how it is possible to regard the behaviour of a rock element within a stressed rock body as being similar to the behaviour of a rock specimen in the laboratory. Applying the concept of degradation described above to a rock element suffering microcracking within a stressed rock body, a degradation model has been developed in this study that tracks the fracturing process of brittle rock under compression (Chapter 4). This model takes into account the local degradation effect induced by microcracking to describe the isolated dissipative processes, and the degradation of materials is estimated by a parameter degradation index, which is associated with the dissipative processes and defined as being dependent on the minor principal stress (Subsection 4.3.4).

The model has a simple form. This simplicity makes it feasible to implement the model in a computer code, and this chapter deals with such implementation. Thus, following a discussion of suitable numerical methods or computer codes, the implementation of the model in the explicit finite difference code FLAC is described.

5.1 Selection of an appropriate numerical method

5.1.1 Numerical methods

Two different approaches are popular for the numerical modelling of rock behaviour (see Pande et al., 1990; Pietruszczak and Mroz, 1981; Cundall and Strack, 1979; Fairhurst and Pei, 1990; Zhu and Wang, 1993; Kuijpers, 1995; Potyondy et al., 1996; Kavamoto and Aydan, 1999; Cundall, 2001). One is the continuum approach, which includes the Finite Element Method (FEM), and the Finite Difference Method (FDM) (see Pietruszczak and Mroz, 1981; Fairhurst and Pei, 1990; Zhu and Wang, 1993; Itasca, 1995a). This approach treats rock materials as a continuum, and elements of a finite size are used to discretise the continuum under consideration. A set of equilibrium equations are written for each element, including constraints at the boundaries, and the unknowns of the system are then obtained by solving these equations. Rigid motion of the body is usually not included in the formulation, and the discontinuities or cracks in real materials (either pre-existing or in the course of formation) are described by specially formulated elements (see Pietruszczak and Mroz, 1981) whose properties approximately reflect the influence of discontinuities on the deformation and strength of rock masses (Fairhurst and Pei, 1990).

The other approach to modelling rock behaviour is to consider the material as a discontinuum, and this includes the Distinct Element Method (DEM) and Discontinuous Deformation Analysis (DDA) (see Cundall and Strack, 1979; Fairhurst and Pei, 1990; Itasca, 1995b; Lin et al., 1996; Potyondy et al., 1996; Kavamoto and Aydan, 1999; Cundall, 2001). The principle of this approach is to treat the object material as an assemblage of discrete polygons or particles, which may be assumed to be either rigid or deformable, and which interact with each other via contact forces at their boundaries. The contact forces change with the motion and deformation of the individual bodies or particles according to specific constitutive models. Finite translational and rotational displacements of discrete bodies are permitted, and the contacts between discrete bodies can be identified and updated automatically during the course of calculation.

As the principles indicate, the two approaches exhibit distinctive features in representing the existence of discontinuities or the formation of fracture in brittle materials. The continuum approach uses a continuous material with equivalent deformation and strength properties to represent components undergoing structural changes and disturbances. This approach is suitable for modelling materials whose deformation is more or less continuous. In the DEM, the existence of discontinuities and

the formation of fracture can be explicitly described by the separation between, or the slip along, the contacts between individual bodies. This method would be advantageous in modelling the deformation behaviour of a structure controlled by displacements along the discontinuities it contains (Souley and Homand, 1995), or the rebounding phenomena associated with these contacts (Potyondy et al., 1996; Cundall, 2001).

The degradation model can be implemented by either of the two approaches, as long as the degradation effect is formulated in an appropriate form and the resulting complex boundaries can be handled. This model described here has been developed using a continuum approach (Chapter 4), in which the local failure is represented by an equivalent continuum rather than tracking the geometry of individual cracks. Thus, the continuum approach is considered in this work. Further selection between the FEM and FDM continuum approaches is addressed in the next section.

5.1.2 Selection between FEM and FDM

In terms of the solution of sets of differential equations containing initial values and boundary values, the finite element method and finite difference method are both suitable for numerically analysing the behaviour of an intact rock or rock structure that deforms macroscopically continuously. Both methods produce a set of algebraic equations to replace the governing difference equations for the problem.

In the finite element method, these equations are derived from element stiffness matrices, and solved using implicit (see the next section) matrix-oriented solution schemes (see Pietruszczak and Mroz, 1981; Fairhurst and Pei, 1990). When the number of finite elements is sufficiently large and the field variables are many, the complexity in programming and computational time becomes substantial. In addition, the FEM is limited to relatively small displacements of the deformed body (Fairhurst and Pei, 1990), which may not be appropriate if large displacements and strains need to be followed.

The finite difference method is an explicit method (see the next section) and is more advantageous in these respects mentioned in the earlier paragraph. In finite difference methods, every derivative in the set of governing equations is replaced directly by an algebraic expression written in terms of the field variables at discrete points in space. It is relatively efficient to regenerate the finite difference equations in this way at each step, and a suitable time step algorithm in calculation should be able to accommodate the large displacements and rotations required by geomaterials (Souley

and Homand, 1996). Moreover, finite difference equations can be derived for elements of any shape and any element can have any property value (Itasca, 1995a). These features thus favour this technique in analysing complex problems associated with heterogeneous materials, compared to a finite element formulation. For these reasons the explicit finite difference approach has been chosen in this work.

5.1.3 Explicit and implicit solution methods

Two methods exist for a finite difference solution, *i.e.* explicit or implicit. If one unknown value is expressed directly in terms of known values, the numerical method is called explicit. The procedure for this method is to calculate the unknown values of particular parameters from the known boundary and initial values, and then compute more unknown values in terms of the first, and so on until all unknown values have been determined. On the other hand, the implicit solution refers to a method by which the calculation of an unknown value is in terms of other unknown values. The procedure for solving a problem this way is to solve a set of simultaneous equations for the unknown variables.

The explicit method uses equations that are solved recursively, with each recursion separated from its predecessor and successor by a small time step. The method is computationally simple, but it requires very small values for the time step in order to obtain a stable solution. The implicit method offers an unconditionally stable solution regardless of timestep, but a large amount of computational error may be introduced per timestep (Itasca, 1995a). In addition, since large matrices representing the simultaneous equations are required in an implicit method to solve for the unknown values, a robust iteration scheme is necessary for complex constitutive models, and this may lead to problems in slow convergence. Referring to the complexity of constitutive models associated with rock fracturing, it can therefore be concluded that the explicit method is the more suitable of the two.

A survey of commercially available codes shows that Fast Lagrangian Analysis of Continua (FLAC), produced by Itasca Consulting Group, is an explicit finite difference program for analysing engineering mechanics. We now go on to describe the numerical features of this code in the context of its possible use for hosting the degradation model.

5.2 FLAC Code

The degradation model, developed using a continuum approach in Chapter 4, requires a

description of large strains or displacements associated with complex constitutive behaviour of individual elements. In the preceding section we have discussed that, for implementing the degradation model, the explicit finite difference numerical technique is appropriate. Among the many existing computer codes, the program FLAC, which is an acronym for Fast Lagrangian Analysis of Continua, is an explicit finite difference program developed by Itasca Consulting Group for the analysis of continua (Itasca, 1995a). This code contains unique features that may be suitable for the implementation of the degradation model. In this section, a basic introduction to this code is outlined, and the implementation of the degradation model in this code is dealt with in the next section. There is no attempt to describe this code in detail and readers who are interested in the techniques used in this code may refer to the FLAC manual (*e.g.* Itasca, 1995a).

5.2.1 Basic numerical techniques in FLAC

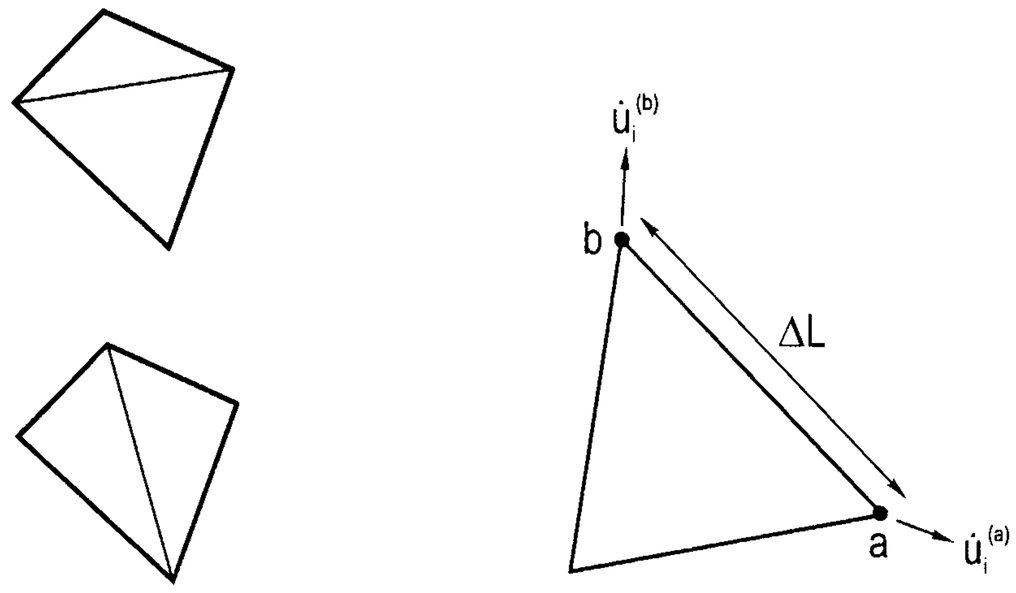
A numerical code, whose purpose is the computation of engineering mechanics, has to cope with a number of essential numerical problems. These are: (i) representation of the object's geometry; (ii) the constitutive relations of the materials; (iii) the numerical scheme for describing the deformation of materials; (iv) the algorithm to integrate the equilibrium equation (the equation of motion). The numerical features used in FLAC for these are presented in this section, except for (ii), which is dealt with in the introduction of FLAC embodied constitutive models in Subsection 5.2.2.

Representation of solid bodies

In FLAC, the solid body is discretised into a mesh that defines quadrilateral elements that are further subdivided into two overlaid sets of triangular elements (Figure 5.1(a)). Each element behaves according to a prescribed stress-strain relation in response to the applied forces or boundary restraints, and a grid can deform and move corresponding to changes in stresses or forces. Consequently, the material represented by these elements can deform, yield, or flow.

Finite difference scheme

The finite difference scheme used in FLAC to represent the displacements and strains of the internal elements is the one proposed by Wilkins (1964), in which the Gauss's divergence theorem (Equation A-28 in Appendix A) is applied to define a difference scheme suitable for internal finite difference elements. The principle of this method is



(a) Overlaid quadrilateral elements used in FLAC

(b) Typical triangular element with velocity vectors

(c) Nodal force vector

Figure 5.1. Triangular elements in FLAC (after Itasca, 1995a)

given below, in order that the implementation of the degradation model discussed in Section 5.3 may be clearly understood.

For a function, f, and its gradient defined on an area A of boundary L, Gauss's divergence theorem (see Appendix A and Equation A-28) may be written in the form

$$\int_L n_i f dL = \int_A \frac{\partial f}{\partial x_i} dA\,, \tag{5-1}$$

where n_i is the unit normal directed out of the surface, A. We know that the average of the gradient of a function f over the area A may be defined as

$$\left\langle \frac{\partial f}{\partial x_i} \right\rangle = \frac{1}{A} \int_A \frac{\partial f}{\partial x_i} dA \tag{5-2}$$

where the angle brackets $\langle \cdot \rangle$ are read as 'average'. Thus, by substitution of Equation 5-1, we find that

$$\left\langle \frac{\partial f}{\partial x_i} \right\rangle = \frac{1}{A} \int_L n_i f dL \tag{5-3}$$

and for a triangular sub-element, Equation 5-3 can be written as

$$\left\langle \frac{\partial f}{\partial x_i} \right\rangle = \frac{1}{A} \sum_L \langle f \rangle n_i \Delta L\,, \tag{5-4}$$

where ΔL is the length of a side of the triangle and the summation extends over the three sides of the triangle. Here, $\langle f \rangle$ is the mean value of all forces over each side.

Equation 5-4 allows the velocity gradients for the triangle shown in Figure 5.1(b) to be computed as

$$\frac{\partial \dot{u}_i}{\partial x_j} \cong \frac{1}{2A}\sum_L \left(\dot{u}_i^{(a)} + \dot{u}_i^{(b)}\right) n_j \Delta L, \tag{5-5}$$

where a and b are two consecutive nodes on the triangle boundary (Figure 5.1(b)). From this, the strain rate of the triangular element can be obtained (see Equation A-23) as

$$\dot{\varepsilon}_{ij} = \frac{1}{2}\left[\frac{\partial \dot{u}_i}{\partial x_j} + \frac{\partial \dot{u}_j}{\partial x_i}\right]. \tag{5-6}$$

The stress changes of the triangular element, corresponding to the strain rate, are then derived from the constitutive relation specific to the element. Once the stresses σ_{ij} have been calculated, the nodal forces of an element can then be obtained by

$$F_i = \frac{1}{2}\sigma_{ij}\sum_{k=1}^{2}\left(n_j^k L^k\right), \tag{5-7}$$

where n_j^k is the outward unit normal to L^k. Then the forces from the two sets of pairs of triangles within each quadrilateral element are averaged to give the nodal force of the quadrilateral.

When one node is shared by a number of quadrilaterals, the total forces from all surrounding quadrilaterals are summed to form the net nodal force vector, $\sum F_i$. If $\sum F_i$ is non-zero, the node will be accelerated according to the finite difference form of Newton's second law of motion,

$$\frac{d\dot{u}_i}{dt} = \frac{\sum F_i}{m_n}, \tag{5-8}$$

where m_n is the mass lumped at this node.

Using a central difference time stepping scheme for the left-hand side, for the time interval t-$\Delta t/2$ to t+$\Delta t/2$, we find

$$\left(\frac{d\dot{u}_i}{dt}\right)^{(t)} = \left(\frac{\dot{u}^{(t+\Delta t/2)} - \dot{u}^{(t-\Delta t/2)}}{\Delta t}\right), \tag{5-9}$$

where the superscripts denote the time at which the corresponding variable is evaluated.

Rearranging Equations 5-8 and 5-9, the following expression is obtained

$$\dot{u}_i^{(t+\Delta t/2)} = \dot{u}_i^{(t-\Delta t/2)} + \sum F_i^{(t)} \frac{\Delta t}{m_n}. \tag{5-10}$$

Thus the velocity at time step $t+\Delta t/2$ is completely determined in terms of known quantities at time step t and $t-\Delta t/2$.

The displacements u_i at time step $t+\Delta t$ may now be expressed in terms of previously calculated displacements as

$$u_i^{(t+\Delta t)} = u_i^{(t)} + \dot{u}_i^{(t+\Delta t/2)} \Delta t\,. \tag{5-11}$$

The incremental displacements are added to the coordinates so that the grid moves and deforms with the material it represents. This is termed a Langrangian formulation in FLAC (see Appendix A for defination).

Boundary conditions

In FLAC, either stress or displacement may be applied at the boundary of a solid body. At a displacement boundary, displacements are specified in terms of prescribed velocities at given gridpoints. At a stress boundary, the derivation of the appropriate forces is through

$$F_i^b = \sigma_{ij}^b n_j \Delta L\,, \tag{5-12}$$

where n_i is the unit outward normal vector of the boundary segment, and ΔL is the length of the boundary segment over which the stress σ_{ij}^b acts. The force F_i contributes to the force sum for the appropriate gridpoint ($\sum F_i$ in Equation 5-10).

Mechanical damping

To solve static problems, the equations of motion (Equation 5-10) must be damped to provide static or quasi-static solutions. The damping used in FLAC is proportional to the unbalanced force, and so the equation of motion (Equation 5-10) is replaced by

$$\dot{u}_i^{(t+\Delta t/2)} = \dot{u}_i^{(t-\Delta t/2)} + \left\{\sum F_i^{(t)} - \zeta \left|\sum F_i^{(t)}\right| \mathrm{sgn}\left(\dot{u}_i^{(t-\Delta t/2)}\right)\right\} \frac{\Delta t}{m_{nf}}, \tag{5-13}$$

where ζ is a dimensionless constant (0.8 in FLAC), and m_{nf} is a fictitious nodal mass (see Itasca, 1995a).

Calculation cycle for the numerical analysis in FLAC

As illustrated above, the explicit method is adopted in FLAC to solve Newton's second

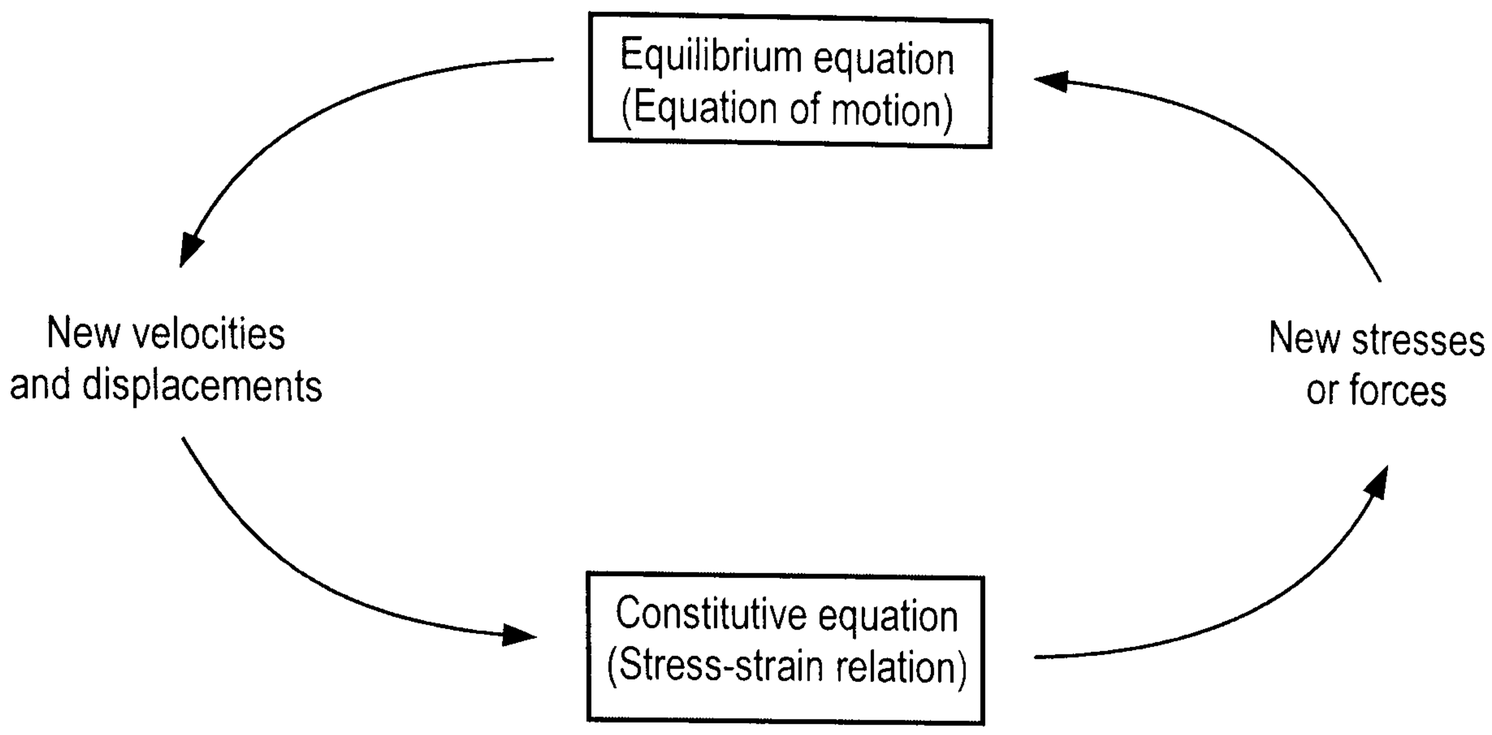


Figure 5.2. Basic explicit calculation cycle in FLAC (after Itasca, 1995a)

law with a constitutive relation to find a static solution to a problem. Figure 5.2 illustrates the general calculation sequence operated by FLAC. New velocities corresponding to stresses or forces are first derived by invoking the equation of motion with damping. Then, new displacements are calculated from velocities using a small strain Lagrangian formulation (see Appendix A), which represents the movement and deformation of the material. Strain rates are also derived from velocities, and from these new stresses are derived according to the constitutive relation. Corresponding to the stress changes are new velocities, and the calculation repeats.

During the calculation, one time step is taken for every cycle around the loop. The time step is selected to be so small that stresses changed in one element could not physically propagate as a stress wave to its neighbours in one cycle. Thus, each step in the calculation cycle updates its grid variables, *e.g.* stress, strain rate and displacement, from known values.

From the numerical techniques described above, we see how FLAC, with a constitutive relation, is able to handle the complex constitutive behaviours that may be exhibited by a material. Now we move on to present the constitutive relations embedded in FLAC.

5.2.2 FLAC embodied constitutive models

Associated with the numerical techniques described in Section 5.2.1, FLAC embodies a number of constitutive models, which include the null model (representing a hole or an excavation), two elastic models (the isotropic and the transversely isotropic elastic models), six plasticity models (Drucker-Prager, Mohr-Coulomb, strain

softening/hardening, modified Cam-Clay, double yield, and ubiquitous joint models), and one interface model that represents sliding of separating planes (Itasca, 1995a). No attempt is made here to introduce all of these models, but only those that are used for the implementation of the degradation model (see the next section and Chapters 6 and 7) are outlined. These models are the isotropic elastic model, the Mohr-Coulomb model, and the interface model, and are introduced in terms of the specific features displayed by each model and the properties that each model requires.

Isotropic elastic model

The model behaviour is interpreted by Hooke's law. The mechanical responses produced by this model are linear, path dependent and reversible associated with unloading (Itasca, 1995a). The properties required for using this model are density, bulk modulus and shear modulus.

In most cases of studying material mechanical responses, the available parameters are the Young's modulus, E, and the Poisson's ratio, ν. The bulk modulus, K, and shear modulus, G, can be obtained from these two parameters through the following relations

$$K = \frac{E}{3(1-2\nu)}, \tag{5-14}$$

and

$$G = \frac{E}{2(1+\nu)}. \tag{5-15}$$

The isotropic elastic model can be used to model materials whose mechanical behaviour is either linear or non-linear elastic. The latter require that the elastic modulus is a function of some parameter, such as confining stress (Itasca, 1995a). The isotropic elastic model will be used for representing the platen in the model of rock testing system (Section 6.1).

The Mohr-Coulomb model

The Mohr-Coulomb failure criterion with tension cut-off (Equations 4-48 and 4-39) and the classic elasto-plastic stress-strain relation (Equation 4-74) along with the plastic flow rules (Equations 4-63, 4-65 and 4-67) are incorporated into this model. This model gives a linear stress-strain relation before the material fails, and a perfectly plastic flow upon failure.

For the use of the Mohr-Coulomb model, the user has to provide the following

properties: density, bulk modulus, shear modulus, friction angle, cohesion, dilation angle and tensile strength.

This model can be used for an analysis of shear failure of materials whose strength property is determinable by the Mohr-Coulomb failure criterion, *e.g.* soils and rocks (Vermeer and De Borst, 1984). The Mohr-Coulomb model embodied in FLAC will be used for the implementation of the degradation model developed in Chapter 4, by modifying the representative property parameters as described in Section 5.3.

The interface model

An interface is a plane within or between materials on which sliding or separation may occur. FLAC provides three interface models: glued interfaces, on which no slip or opening is allowed; Coulomb shear-strength interfaces, on which slip is controlled by the Coulomb shear-strength criterion (see below); and tension bonded interfaces, on which breakage occurs when the tensile stress across the interfaces exceeds the tensile bond strength.

The Coulomb shear-strength interface permits a wider range of suitability for a slipping plane due to the strength criterion used, which is implemented as

$$F_{sif} = c_{if} L_{if} + F_{nif} \tan \phi_{if} , \tag{5-16}$$

where F_{sif} and F_{nif} are the shear and normal stresses acting on the interface, c_{if} is cohesion along the interface, L_{if} is the effective contact length, and ϕ_{if} is the friction angle of the interface surfaces. Other properties required by the Coulomb-strength interface include the tensile strength, normal stiffness and shear stiffness. Values for the cohesion, friction angle and tensile strength are readily obtained from either laboratory tests or experience. However, in the absence of laboratory test results for the normal and shear stiffnesses, it is suggested that they are set to be 10 times the equivalent stiffness of the stiffest neighbouring zone (see Itasca, 1995a; also see Appendix B).

The Coulomb-strength interface model will be adopted to represent the interfaces between the rock specimen and platens in investigation of fracture of rock specimens, including interface effects on material failure (Chapter 7).

So far, we have seen the basic numerical techniques (Subsection 5.2.1) and the constitutive relations (Subsection 5.2.2) used in FLAC. For a clearer understanding of the implementation procedures of the degradation model, there are also a few issues related to FLAC that require to be introduced. These are given in the following subsections.

5.2.3 Finite difference grid, variables and sign conventions in FLAC

The finite difference grid

FLAC discretises the body under investigation into a mesh, represented by the finite difference grid, with the grid specified by the number of zones i in the horizontal (x) direction, and the number of zones j in the vertical (y) direction. A zone and gridpoint in the grid are uniquely identified by a pair of i, j indices, and the pairs of indices are numbered from the left-bottom corner of the grid with (1,1), extending to the right-top corner. There is one number more in specifying the gridpoints than in specifying zones in both horizontal and vertical directions (see Itasca, 1995a).

When performing a calculation, FLAC creates a number of grid variables relating to either an individual gridpoint or a zone (see Itasca, 1995a). These variables cover parameters such as the stresses, velocities, displacements, strains, coordinates, forces, pressures, and material properties (subjected to the embodied constitutive models), and can be referred to in an analysis by specifying the row and column numbers in parentheses immediately following the variable name. It is pointless to list all the grid variables here, since readers can refer to a FLAC manual (*e.g.* Itasca, 1995a). However, a list of the most often used grid variables is useful to help assimilate the implementation procedures of the degradation model in FLAC (Section 5.3). These variables are tabulated in Table 5.1.

The finite difference grid identifies the storage location of all state variables in an objective model (Itasca, 1995a). Gridpoints are the locations at which all vector quantities, such as forces, velocities and displacements are stored; while the zone centroid locations are used to store all scalar and tensor quantities, *e.g.* stresses, pressure and material properties. The quantities represented by the extra variables (*ex_n*(*i*,*j*) in Table 5.1) can be associated with either gridpoints or zone centroids (Itasca, 1995a).

FLAC also contains many other pre-defined variables for performing a general analysis. Table 5.2 presents those variables used in the FLAC implementation of the degradation model (see Section 5.3).

Sign conventions

FLAC uses different sign conventions from those utilised in this work. In FLAC, tensile stresses, extensile strains and pressures acting towards the surface of a body in a normal direction are positive. Displacements and velocities are defined by the coordinate directions.

Table 5.1. FLAC grid variables used in the implementation of the degradation model

Variable	Description
`bulk_mod`	bulk modulus
`cohesion`	cohesive strength
`density`	zone density
`dilation`	dilation angle
`ex_n`	extra variables, *n* is an integer specified by "config extra = *n*" command (see Subsection 5.2.4 and Appendix B)
`friction`	friction angle
`model`	constitutive model states with: 1-null model, 2-elastic model, 3-Mohr-Coulomb model
`shear_mod`	shear modulus
`state`	plastic state: 0-elastic, 1-currently at yield in shear, 2-yield in the past, 3-currently at yield in tension
`sxx`	*xx*-stress
`sxy`	*xy*-stress
`syy`	*yy*-stress
`szz`	*zz*-stress
`tension`	uniaxial tensile strength
`x`	*x*-coordinate
`xdisp`	*x*-displacement
`xvel`	*x*-velocity
`y`	*y*-coordinate
`ydisp`	*y*-displacement
`yvel`	*y*-velocity

5.2.4 FLAC commands and Fish programming language

FLAC is a command-driven code, which means that command lines must be entered as input in order for FLAC to operate (Itasca, 1995a). Each command consists of a primary

Table 5.2. FLAC pre-defined variables used in the implementation of the degradation model

Variable	Description
`degrad`	$\pi/180$ (for conversion from degrees to radians)
`igp`	total number of gridpoints in the *i*-direction
`izones`	total number of zones in the *i*-direction
`jgp`	total number of gridpoints in the *j*-direction
`jzones`	total number of zones in the *j*-direction
`pi`	π
`urand`	random number (0.0 to 1.0) drawn from uniform distribution

command word followed by one or more keywords and values, as in the following format:

```
com(mand)   key(word)   value... ;
```

In this format, the brackets indicate that omission of letters in a long command word is permitted; the ellipsis indicates that an arbitrary number of such parameters may be given; and the semicolon is an interpreter for FLAC to terminate the command line so that comments can be appended to a line by the user to aid understanding of the code.

FLAC contains over 40 main commands and nearly 400 command modifiers (Itasca, 1995a). There is no need here to present all the commands, but those required to set up a complete objective model are given in Table 5.3, along with a short description. For those commands not listed in Table 5.3, but appear in the FLAC code of the degradation model that is given in Appendix B, a brief description of the commands is given in the source code.

It may be also useful to demonstrate how to use FLAC commands. The following is an example that builds a small model, and consists of a few commands covering the functions of configuring extra variables, generating the grid, specifying the model state, assigning properties, applying pressure boundaries, executing timesteps, displaying variables and saving files.

```
;specify 5 extra variables for storing data beyond FLAC
;pre-specified variables
Config extra 5
;create a grid with 5 zones in x-direction and 10 zones in
```

Table 5.3. Basic commands in FLAC

Function	Command	Interpretation
extra variable creation	`config`	specify extra variables for storing data
grid generation	`grid` `gen`	create a grid shape a grid
material/model properties	`model` `property`	specify a constitutive model assign material properties

boundary/initial conditions	`apply`
	`fix`
	`initial`
		specify boundary conditions
		remain value unchangeable
		define initial values

initial equilibrium	`step`	step to an equilibrium state

perform alterations	`model`
	`property`
	`apply`
		change model properties
		change material properties
		change boundary conditions

save/restore problem state	`save` `restore`	save a stage file restore a saved file
data output	`plot` `print`	produce output to screen or hardcopy produce output to screen or files

```
;y-direction
grid 5 10
;shape the grid within x-coordinates of 1-2 m and y-
;coordinates of 1-3 m.
gen 1,1 1,3 2,3 2,1
;specify the Mohr-Coulomb constitutive relation
model mohr
;assign bulk and shear moduli to the material
prop bul 15e9 she 10e9
;apply pressure boundary condition on all gridpoints with
;i=1
apply pressure 10e5 i=1
;fix x-velocities of the gridpoints with i=6
fix x i=6
;execute 100 timesteps
```

```
step 100
;display y-direction displacement contours on screen
plot ydisp
;display x-direction stresses on screen
print sxx
;save file as demo1.sav
save demo1.sav
;return to keyboard control
    ret
```

Fish language

FLAC embodies a programming language FLACish, which is shortened Fish, to allow users to extend the range of problems to which FLAC can be applied (see Itasca, 1995a). With Fish, users can access FLAC variables to examine the state of the model, and can define new variables and new functions to perform a specific analysis. What is more important, Fish users can write a program to incorporate their own specific constitutive relations for the problem under investigation. In short, Fish provides an efficient tool for FLAC users to write programs that allow investigation of a wide range of problems.

A Fish program can be simply embedded in a normal FLAC data file. Fish programs entered via a FLAC data file are translated into a list of instructions stored in FLAC's memory space, and are executed whenever a Fish function is invoked (Itasca, 1995a). In this way the function defined in a Fish program is executed by FLAC.

The contents of Fish are so huge that it is impossible to outline all aspects in a clear short way, and readers should refer to the FLAC manual to explore its power. Here we only introduce a number of basic Fish statements, which are used in the Fish code of the degradation model in Appendix B. These statements and their brief descriptions are listed in Table 5.4. For those statements that are not presented in Table 5.4 but appear in the Fish code of the degradation model, an explanation is given in the source code (see Appendix B).

The simple example given below, which inputs friction angle to all zones within a model, demonstrates how to use Fish statements in programming.

```
;define a function for setting model properties
def data_setup
  ;loop over all columns
```

Table 5.4. Basic statements in Fish language

Statement	Description
`define` *function-name* … `end`	Characterise a complete Fish function named as *function-name*

`if` *expr1 test expr2* `then`
…
`else`
…
`end_if`
	Control statement. *expr1 test expr2* is a mathematical expression for a condition. If the expression is satisfied, the function before the word "`else`" is executed. Otherwise, the function after "`else`" is executed.

`loop` *var (expr1, expr2)* … `end_loop`	Recursion statement, which allows an evaluation for a variable, *var*, to be carried out from *expr1* `to` *expr2*.

```
loop i (1,izones)
  ;loop over all rows
  loop j (1,jzones)
    ;set test condition for friction angle
    if friction(i,j) < 45 then ;
      ;set lower friction angle
      friction(i,j)=40
    else
      ;set upper friction angle
      friction(i,j)=50
    end_if
  end_loop
end_loop
end
```

5.2.5 Suitability of FLAC for the implementation of the degradation model

As noted above, FLAC uses an explicit, Lagrangian and time-marching finite difference numerical scheme to solve Newton's second law to compute the deformation of continua. Under this scheme, FLAC embodies a number of constitutive models. These

models permit the simulation of highly non-linear, irreversible responses representative of geological, or similar, materials and hence enable FLAC to offer a wide range of capabilities to solve complex problems in mechanics, such as failure localisation, subsequent material weakening and large strain problems that are encountered in both rock mechanics and rock engineering (see Kuijpers, 1995). In addition, FLAC contains a built-in programming language FISH (see Itasca, 1995a), with which users can write a function to implement their own constitutive models. These capabilities mean that FLAC is a suitable code for implementation of the degradation model. In the next section, we will describe the implementation procedures of the degradation model in FLAC.

5.3 FLAC Implementation of the degradation model

In Section 5.1, it was discussed that the degradation model developed in Chapter 4 requires the explicit finite difference numerical technique to describe large strains or displacements associated with complex constitutive behaviour of individual elements. In Section 5.2 we have those code elements of FLAC whose features favour the implementation of the degradation model.

FLAC provides several basic constitutive models for use in analysing the mechanical behaviour of geomaterials. For the responses of rock materials under external disturbances, the Mohr-Coulomb model is generally suitable. Since the same constitutive relation is incorporated in the degradation model (see Sections 4.4.1 and 5.2.2), the FLAC intrinsic Mohr-Coulomb model is utilised to implement the degradation model. This section deals with the implementation procedures of the degradation model in this code.

Before the start of this section in detail, we need to look through the components of the degradation model. In Section 4.8, we have summarised all aspects of the degradation model and the equations used. With respect to these aspects and equations, we may describe the implementation of the degradation mode in FLAC component by component, which contains:

(a) the input and storage of model parameters;

(b) the conversion of strength property parameters;

(c) the introduction of heterogeneity;

(d) the calculation and update of the degradation index;

(e) the calculation and update of the degraded Young's modulus;

(f) the calculation and update of the degraded uniaxial compressive strength;

(g) the calculation and update of the degraded bulk and shear moduli;

(h) the calculation and update of the degraded cohesion and friction angle;

(i) the calculation of the dissipated elastic strain energy associated with degradation; and

(j) the representation of fracture of materials.

The calculations listed above are associated with the specific features exhibited by the degradation model. For a general analysis of a problem, some other calculations may be required, such as calculations of the axial stress and strain of a rock specimen under compression. Since they are not specific to the degradation model, such implementations are not included in this section, but accompany the problem analysis (*e.g.* Section 6.1).

5.3.1 Input and storage of model parameters

Input of model parameters

In Subsection 4.9.1, we have discussed the parameters required for performing an analysis of rock fracture, which include those representing material physical and mechanical properties (Table 4.3) and those designating external (boundary) conditions.

The Mohr-Coulomb criterion is one of the criteria that are adopted in the degradation model, and so the data required for a problem that uses this criterion can be inputted directly from a series of standard FLAC commands into the FLAC intrinsic Mohr-Coulomb model. These data may vary in terms of their distribution function (Subsections 4.6 and 5.3.3), which is written in Fish programming language (Subsection 5.2.4; and also see Itasca, 1995a) to represent heterogeneity of materials. During the course of simulation, any change to these properties is computed by a specific function (Subsection 4.9.3), and assigned to the element undergoing such a change. This enables the degradation model to be incorporated (see Chapters 6 and 7, and Appendix B).

For the problem models described by the Hoek-Brown and Griffith criteria, an expression in the form of the Mohr-Coulomb criterion may be obtained by deriving equivalent parameters (see Subsection 5.3.2). By inputting the equivalent parameters, the two criteria can be incorporated into the Mohr-Coulomb program in FLAC. For the details, see Subsection 5.3.2, Chapter 6, and Appendix B.

Boundary conditions can be applied to a problem model in terms of either stresses or displacements through the associated commands in FLAC (Itasca, 1995a; and also

see Subsection 5.2.1, Chapter 6 and Appendix B in this thesis). These values can also be inputted in such a way that they vary from point to point along the model boundaries in accordance with a specific boundary condition. Further details of this approach (which is not required in this work) may be found in Itasca (1995a).

Storage of model parameters

When performing an analysis, it is necessary to store all the data associated with the parameters required (Table 4.3 lists most of these parameters). FLAC has a number of pre-specified grid variables for the common parameters (see Table 5.1), and for those not specified in FLAC, a number of extra variables (see Table 5.1 and the example for demonstrating the use of FLAC commands) may be created for their storage. Table 5.5 shows the allocation of the extra grid variables to those parameters not intrinsic to FLAC. These parameters are presented either in Table 4.3 or in the subsections below, as appropriate.

Table 5.5. Extra variables specified to the degradation model parameters

Extra Variable	Parameter
`ex_1`	degradation index r_d
`ex_2`	initial Young's modulus E
`ex_3`	Young's modulus degradation in uniaxial conditions δE_u
`ex_4`	degraded Young's modulus E_d
`ex_5`	initial uniaxial compressive strength σ_c
`ex_6`	initial cohesive strength c_0
`ex_7`	initial tensile strength T_0
`ex_8`	strength degradation in uniaxial conditions $\delta\sigma_{cu}$
`ex_9`	m_i (Hoek-Brown parameter m for intact rock)
`ex_10`	m_d (degraded Hoek-Brown parameter m)
`ex_11`	s_d (degraded Hoek-Brown parameter s)
`ex_12`	T_{0d} (degraded uniaxial tensile strength in the Griffith criterion)
`ex_13`	elastic strain energy dissipation in an interval of certain timesteps
`ex_14`	active shear failure during an interval of certain timesteps
`ex_15`	active tension failure during an interval of certain timesteps

5.3.2 Conversion of strength property parameters

In the degradation model, three different strength criteria, *i.e.* the Mohr-Coulomb, the Hoek-Brown and the Griffith criteria, were proposed to evaluate an element failure (Subsection 4.4.1). In Subsection 4.9.1, we have shown that the material strength parameters required for performing an analysis of rock fracture are different from criterion to criterion (see Table 4.3). For a problem that uses the degradation model associated with the Mohr-Coulomb criterion, the data for the strength parameters can be inputted directly from a series of standard commands into the FLAC intrinsic Mohr-Coulomb model to perform an analysis. However, in order to implement a degradation model incorporated with either the Hoek-Brown or the Griffith criterion, an expression in the form of the Mohr-Coulomb criterion must be obtained by deriving equivalent parameters, *i.e.* the equivalent cohesive strength and friction angle. This is given in this subsection.

Conversion of the Hoek-Brown strength property parameters

Suppose that on a Hoek-Brown failure envelope, the material fails at a stress state corresponding to a minor principal stress value σ_3 (Figure 5.3). By differentiating Equation 4-51, the equivalent parameter k in Equation 4-48 can be obtained as (Sheorey, 1997)

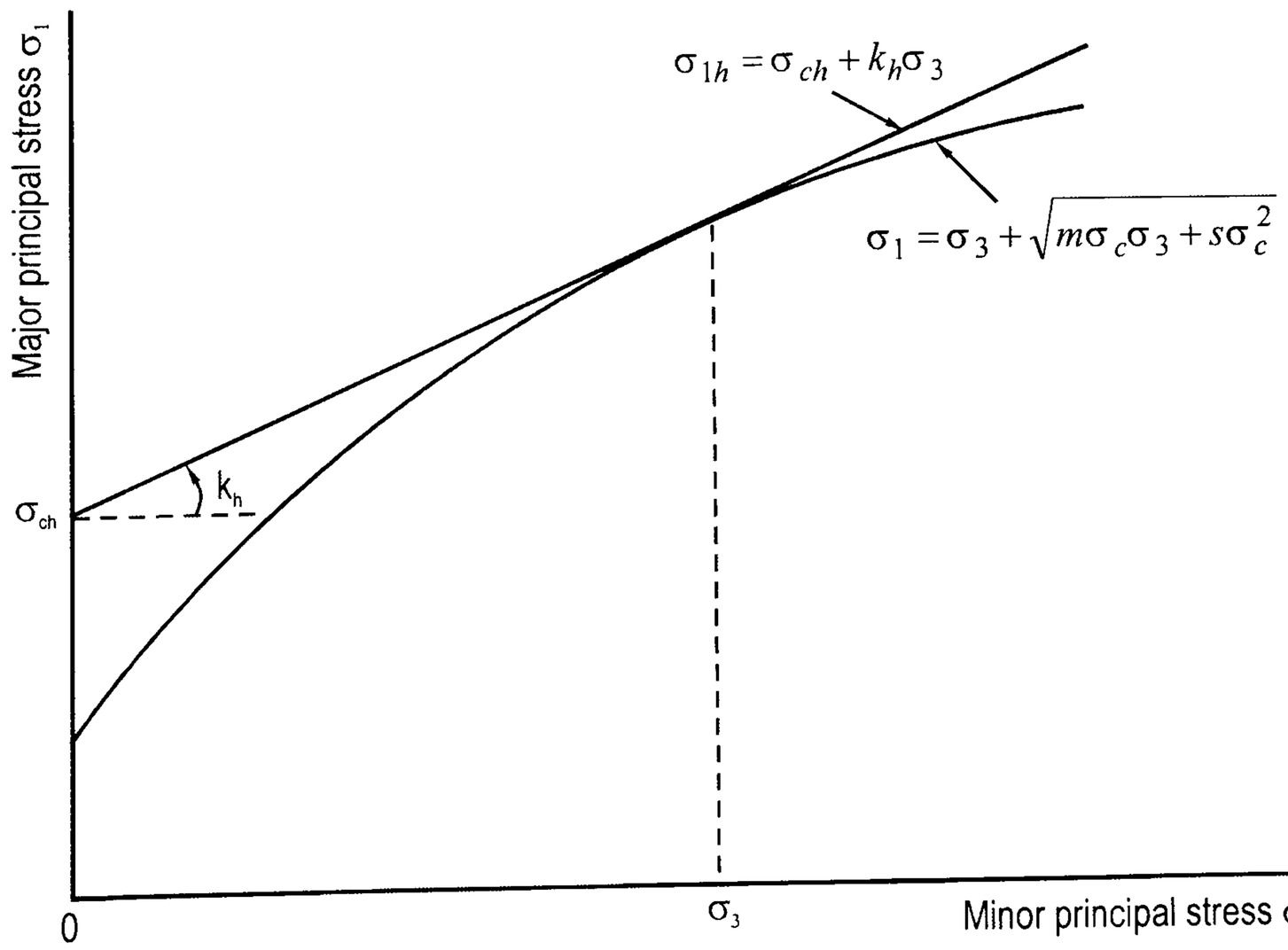


Figure 5.3. Representation of the Hoek-Brown criterion by the linear Mohr-Coulomb surface

$$k_h = \frac{d\sigma_1}{d\sigma_3} = 1 + \frac{m}{2\sqrt{m\frac{\sigma_3}{\sigma_c} + s}}. \tag{5-17}$$

The equivalent uniaxial compressive strength of the material σ_{ch} is given by equating Equation 4-48, with the substitution of Equation 5-17, to Equation 4-51. It reads as

$$\sigma_{ch} = \frac{m\sigma_3 + 2s\sigma_c}{2\sqrt{m\frac{\sigma_3}{\sigma_c} + s}}. \tag{5-18}$$

The cohesive strength c_h has the form (with respect to Equation 4-50)

$$c_h = \frac{\sigma_{ch}}{2\sqrt{k_h}}, \tag{5-19}$$

and by rearranging Equation 4-49, the equivalent friction angle ϕ_h is written as

$$\phi_h = 2\,\mathrm{atan}\sqrt{k_h} - \frac{\pi}{2}. \tag{5-20}$$

These four equations will be referred in describing strength degradation in Subsection 5.3.9.

The implemented form of Equations 5-17 to 5-20 is as follows:

```
;restore the initial uniaxial compressive strength
s_c=ex_5(i,j)
;restore HB parameter m for degraded rock
m_h=ex_10(i,j)
;restore HB parameter s for degraded rock
s_h=ex_11(i,j)
;parameter for converting angle from radians to degrees
dm_degrad=1.0/degrad
temp1=(m_h*s3/s_c+s_h)^(-0.5) ;Eq. 5-18 component
k_h=1.0+0.5*m_h*temp1 ;Eq. 5-17
s_ch=(0.5*m_h*s3+s_h*s_c)*temp1 ;Eq. 5-18
temp2=sqrt(k_h) ;component of Eq. 5-19
cohesion(i,j)=0.5*s_ch/temp2 ;Eq. 5-19
friction(i,j)=2*atan(temp2)*dm_degrad-90 ;Eq. 5-20
```

These expressions above are embodied in the Fish code of the FLAC implementation of the degradation model (Appendix B).

Conversion of the Griffith strength property parameters

As with the Hoek-Brown criterion, equivalent values for the parameter k and the uniaxial compressive strength σ_c can be derived for the implementation of the Griffith criterion. These two representative parameters k_g and σ_{cg} have the form

$$k_g = 1 + 2\sqrt{\frac{T_0}{\sigma_3 + T_0}} \tag{5-21}$$

and

$$\sigma_{cg} = 4T_0 + (2\sigma_3 + 4T_0)\sqrt{\frac{T_0}{\sigma_3 + T_0}}. \tag{5-22}$$

It is noted that Equations 5-21 and 5-22 are only valid under the condition

$$\sigma_3 + T_0 > 0. \tag{5-23}$$

The cohesive strength c_g has the same form as Equation 5-19, namely

$$c_g = \frac{\sigma_{cg}}{2\sqrt{k_g}}, \tag{5-24}$$

and the equivalent friction angle ϕ_g is written as (with the same form with Equation 5-20)

$$\phi_g = 2\,\mathrm{atan}\sqrt{k_g} - \frac{\pi}{2}. \tag{5-25}$$

The above equations will be referred in describing strength degradation in Subsection 5.3.9.

The implemented form of Equations 5-21 to 5-25 are

```
;restore the degraded uniaxial tensile strength
T_0=ex_12(i,j)
temp1=sqrt(T_0/(s3+T_0)) ;component of Eq. 5-22
k_g=1.0+2.0*temp1 ;Eq. 5-21
s_cg=4.0*T_0+(2.0*s3+4.0*T_0)*temp1 ;Eq. 5-22
temp2=sqrt(k_g) ;component of Eq. 5-24
cohesion(i,j)=0.5*s_cg/temp2 ;Eq. 5-24
friction(i,j)=2*atan(temp2)*dm_degrad-90 ;Eq. 5-20
```

These expressions above are embodied in the Fish code of the FLAC implementation of the degradation model (Appendix B).

5.3.3 Introduction of heterogeneity

Heterogeneity is the difference in some property (*e.g.* elasticity, tensile strength, uniaxial compressive strength, and the like) from point to point within a material. In a numerical analysis, heterogeneity is represented by a statistical distribution function associated with a specific material physical property. Many statistical distribution functions have been proposed by other researchers, and for rock behaviour analysis, statistical distribution functions commonly employed include the uniform, normal, and Weibull distributions (see Section 4.4).

With FLAC, material properties can be specified as a function of grid position within a model, and this allows the influence of heterogeneity in a material to be studied. Any type of statistical property distribution may be introduced, and the most appropriate way to apply an initial profile of a property to a grid is via a Fish function. This section describes the FLAC implementation of the uniform, normal and Weibull distribution functions.

Uniform random distribution

FLAC contains an intrinsic function to draw a random number U_{rand} from a uniform distribution between 0.0 and 1.0 (see Table 5.2). This feature allows a FISH function to be easily developed that introduces heterogeneity of any material property distributed uniformly with respect to a specific range. A uniform random number R_u can be obtained with a value between a lower bound value, x_a, and an upper bound value, x_b, through use of the function

$$R_u = x_a(1-U_{rand}) + x_b U_{rand}\,. \tag{5-26}$$

The implemented form of Equation 5-26 is

```
;obtain a random uniform number between 0 and 1
urand1=urand
R_u=x_a*(1.0-urand1)+x_b*urand1 ;Eq. 5-26
```

Specifying x_a = 0 and x_b = 200, Figure 5.4 shows a histogram of 2160 values generated by a FLAC implementation of Equation 5-26. It should be noted that the number of the generated data need not be limited to 2160, but this replicates a mesh size of 30×72, which is the mesh size most used in performing numerical tests on fracture of rock specimens in Chapter 6.

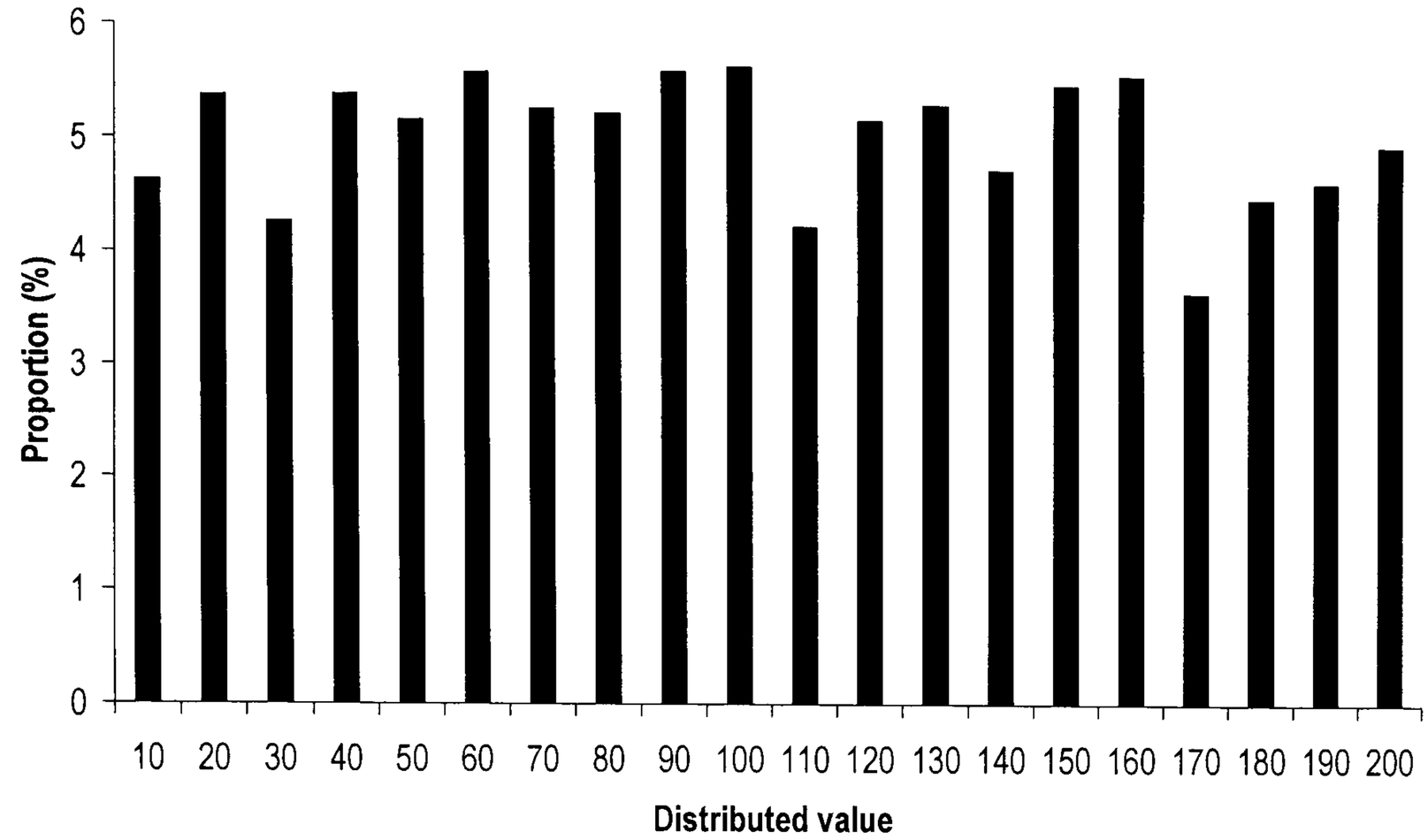


Figure 5.4. Histogram of uniformly distributed data generated by FLAC

Normal distribution

The generation of normally distributed property values is also intrinsic to FLAC. In order to generate a sequence of normally distributed values, the user is required to specify a standard deviation and the mean of the required distribution. Figure 5.5 shows the distribution of 2160 values generated by FLAC using a mean value of 100 and a standard deviation of 20.

A drawback with the normal distribution is that, when the standard deviation is

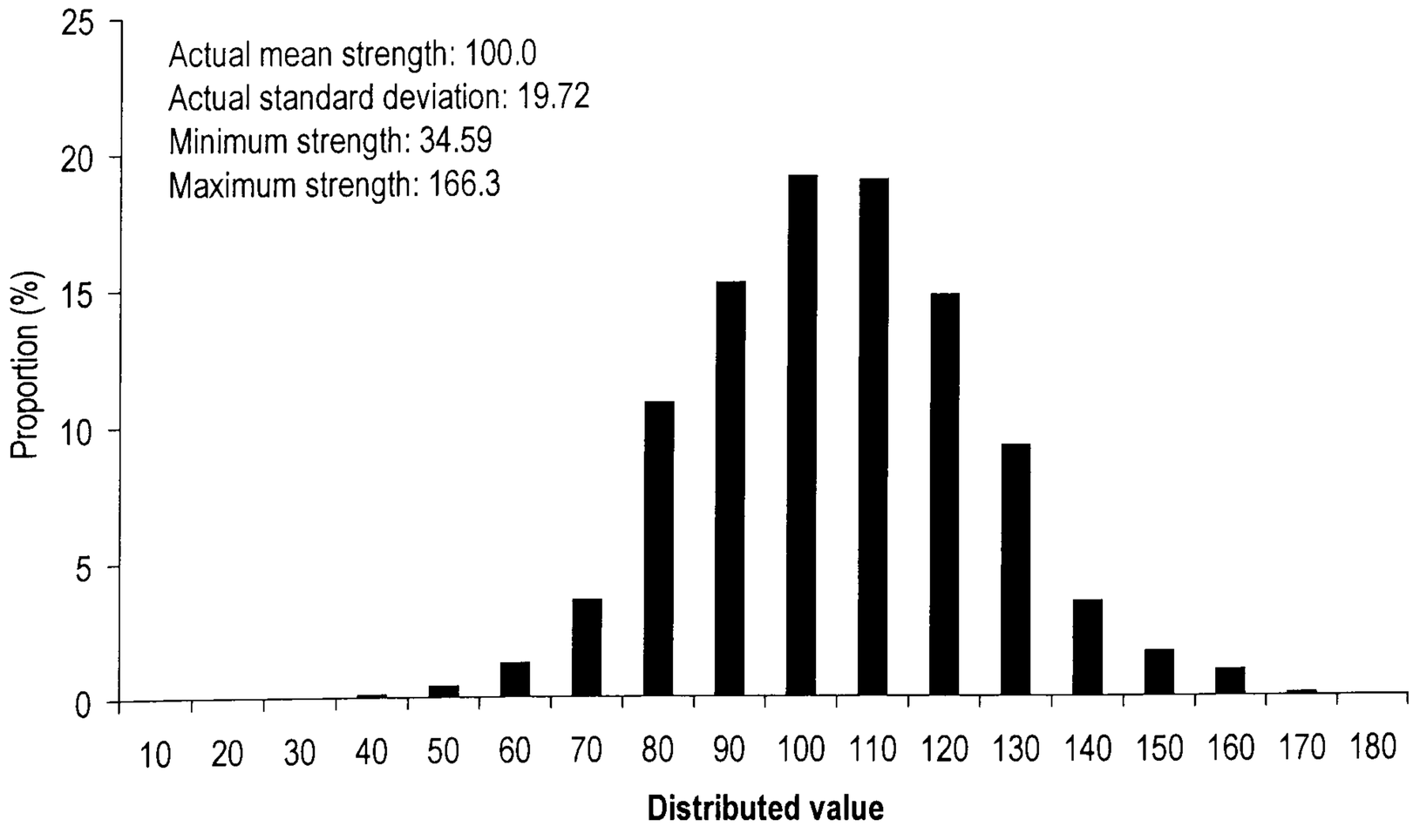


Figure 5.5. Histogram of normally distributed data generated by FLAC

large, negative values may be generated (Hudson and Fairhurst, 1969; Itasca, 1995a). Therefore, when adopting this technique, care should be taken to avoid the assignment of negative numbers to a material property that must always have positive values.

Weibull distribution

Random numbers having a Weibull distribution with a specified Weibull modulus m_w, scale parameter x_0 and location parameter x_u can be generated from U_{rand}, a random number uniformly distributed between 0.0 and 1.0. If R_w is a random number with a Weibull distribution, then by developing further the method proposed by Ghosh (1998) for Equation 4-77, it can be computed using

$$R_w = x_0\left[-\ln\left(1-U_{rand}\right)\right]^{\frac{1}{m_w}} + x_u . \tag{5-27}$$

The implemented form of Equation 5-27 is

```
R_w=x_0*(-ln(1.0-urand))^(1.0/m_w)+x_u ;Eq. 5-27
```

Figure 5.6 shows an example of a data distribution generated by FLAC through implementation of Equation 5-27. The values used in this Weibull distribution for three parameters x_0, x_u and m_w are 100, 0.0 and 2.0, respectively.

It should be noted that, since different properties may be input into a model using those distribution functions, the parameter names in the implemented form of Equations 5-26 and 5-27 are changed in the source code, in accordance with the associated

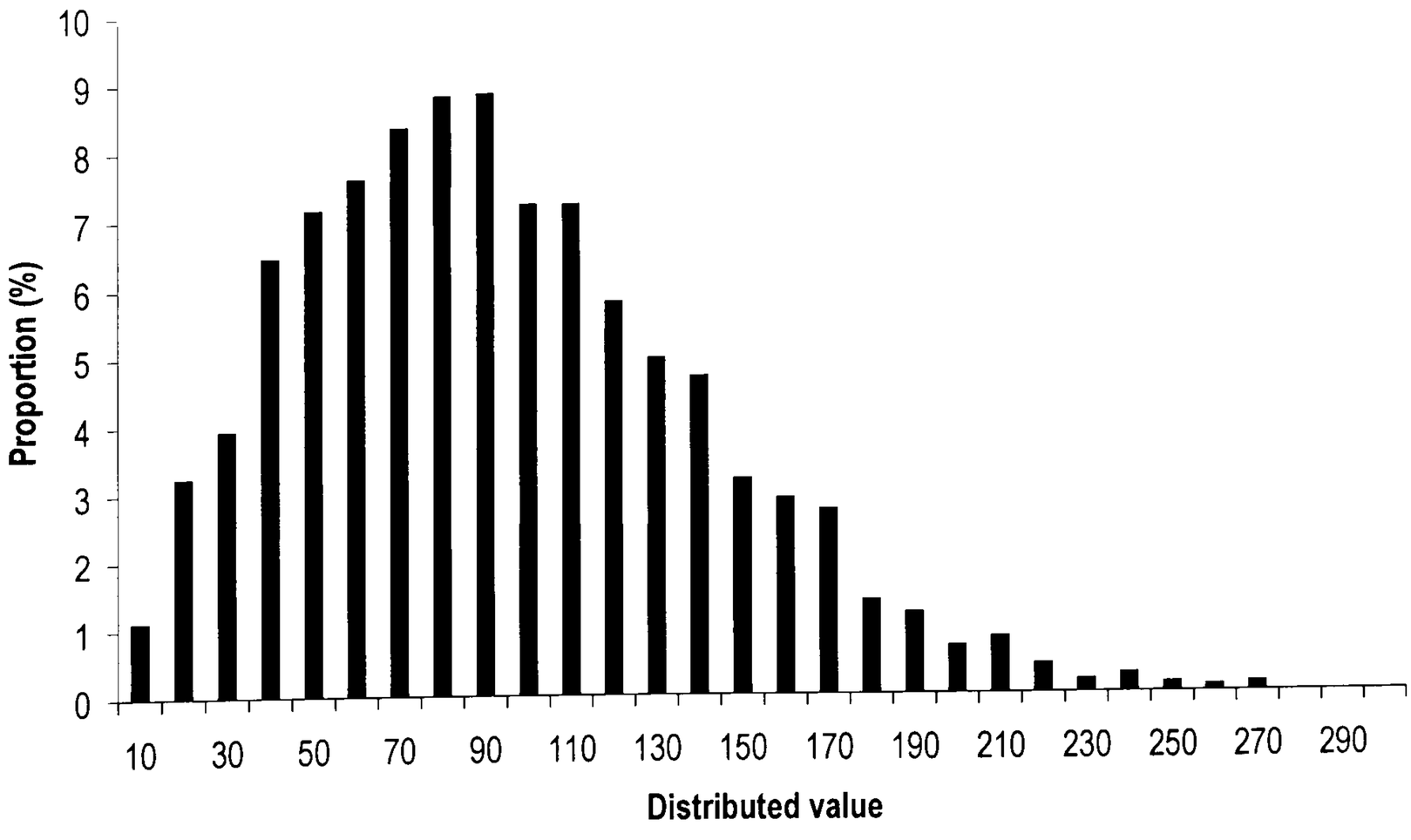


Figure 5.6. Histogram of data following a Weibull distribution, as generated by FLAC implementation

property names (Appendix B).

5.3.4 Calculation of the minor principal stress

In Subsection 5.3.2 we have seen that operation of the degradation model requires the value of the minor principal stress, and we will also see this requirement in the forthcoming subsection. In this subsection, we deal with the implementation of the minor principal stress calculation.

Under the convention of $\sigma_1 > \sigma_3$, the minor principal stress is computed with the following equation (Jaeger and Cook, 1979)

$$\sigma_3 = \frac{1}{2}\left(\sigma_{xx} + \sigma_{yy}\right) - \sqrt{{\sigma_{xy}}^2 + \frac{\left(\sigma_{xx} - \sigma_{yy}\right)^2}{4}}, \qquad (5\text{-}28)$$

where σ_{xx}, σ_{yy}, and σ_{xy} are the x-x coordinate, y-y coordinate and shear stresses, respectively.

FLAC computes the horizontal, vertical and shear stresses for each zone and stores stress components in zone centroids as variables `sxx(i,j)`, `syy(i,j)`, `szz(i,j)`, and `sxy(i,j)`, respectively (see Subsection 5.2.3). Also, FLAC uses the convention that the tensile stresses are positive (see Subsection 5.2.3) and denotes $\sigma_1 < \sigma_3$ (see Itasca, 1995a). Making use of these variables with the sign convention used here, Equation 5-28 is implemented as

```
;change from tension positive to compression positive
dmsxx=-sxx(i,j)
dmsyy=-syy(i,j)
dmsxy=-sxy(i,j)
dmszz=-szz(i,j)
;implement Eq. 5-28
temp1=0.5*(dmsxx+dmsyy)
temp2=sqrt(dmsxy^2+0.25*(dmsxx-dmsyy)^2)
s3=temp1-temp2
```

In addition, in plane strain conditions FLAC recognizes the out of plane stress (`szz`) as one of the principal stresses. Thus the minor principal stress is further evaluated by

```
s3=min(temp1-temp2, dmszz) ;
```

where `min( )` is a FLAC intrinsic function which returns minimum of the two values.

The value of σ_3 may be modified for use in special cases. For example, in the calculation of the degradation index, one of the modifications to the value of σ_3 is that σ_3 =0 when σ_3 is computed to be less than zero (see Equation 4-37; and also see the next subsection).

5.3.5 Calculation and update of the degradation index

If an element undergoes degradation, the degradation index r_d is computed by the first equation in Equation 4-37. The implemented form is

```
s3=max(s3*1e-6,0) ;s3 is in MPa and no less than zero
r_d=exp(-n_d*s3) ;degradation index
```

The extra variable *ex_1(i,j)* is reserved for the storage of the degradation index. When the current value of the degradation index is larger than the pre-stored value, degradation proceeds. When all the calculations are completed, the current value is updated to *ex_1(i,j)*. The following is the implemented procedure:

```
if r_d>ex_1(i,j) then
  … ;command lines for proceeding degradation
  ;update the storage of the degradation index
  ex_1(i,j)=r_d
end_if
```

The degradation calculations are given in the following subsections.

5.3.6 Calculation and update of stiffness degradation

Once an element undergoes degradation, the elemental stiffness degrades. Using the current value of r_d (see Subsection 5.3.5), the degradation can be calculated using the second equation in Equation 4-37, and the degraded stiffness is then given by the first equation in Equation 4-38. Both the initial stiffness S and the stiffness degradation in uniaxial condition δS_u of an element are pre-defined parameters, and are stored in *ex_2(i,j)* and *ex_3(i,j)*, respectively (see Table 5.5). By changing S to E for a distinction from the implemented form of strength symbol σ (see the next subsection), the implemented forms for the calculations of stiffness degradation are written as

```
d_E=r_d*ex_3(i,j) ;Eq. 4-37
E_d=ex_2(i,j)-d_E ;Eq. 4-38
```

The extra variable *ex_4(i,j)* is used to store the value of E_d. After the calculation

of elastic strain energy dissipation, which is subjected to the pre-stored value of E_d (see Subsection 5.3.10), the current value of E_d is updated to `ex_4(i,j)` by

```
ex_4(i,j)=E_d ;update stiffness degradation
```

for use in successive degradation calculations.

5.3.7 Calculation and update of strength degradation

In a similar fashion to that shown above, the degradation in the uniaxial compressive strength and the degraded uniaxial compressive strength of an element undergoing degradation is computed by the implemented forms of the third equation in Equation 4-37 and the second equation in Equation 4-38, respectively, *i.e.*

```
d_sc=r_d*ex_8(i,j) ;Eq. 4-37
s_cd=ex_5(i,j)-d_sc ;Eq. 4-38
```

where `ex_5(i,j)` and `ex_8(i,j)` are the extra variables for storing the initial uniaxial compressive strength σ_c and the degradation of the uniaxial compressive strength in uniaxial conditions $\delta\sigma_c$ displayed by a rock element, respectively.

5.3.8 Calculation and update of the bulk and shear moduli

The Mohr-Coulomb model embodied in FLAC uses the bulk and shear moduli rather than Young's modulus in relating the stress and strain of materials (Section 5.2; and also see Itasca, 1995a). Equations 5-14 and 5-15 allow us to compute these two properties in terms of Young's modulus and Poisson's ratio. The implemented forms for the degraded values of the two parameters, corresponding to the degraded Young's modulus E_d, are as follows, respectively,

```
bulk_mod(i,j)=E_d/(3*(1-2*dm_rpr)) ;Eq. 5-14
shear_mod(i,j)=0.5*E_d/(1+dm_rpr) ;Eq. 5-15
```

It is seen from above that the current values for the two parameters are updated directly, without the need for extra variables.

5.3.9 Calculation and update of other strength parameters

In the Mohr-Coulomb strength criterion, the material compressive strength is represented by two parameters, *i.e.* the cohesive strength c and the angle of friction ϕ (Equations 4-48 to 4-50). With respect to brittle fracture, a process that destroys the

interparticle bonds (see Subsection 4.2.1) and loosens the material, this definition is physically meaningful, *i.e.* brittle fracture causes a reduction in both the cohesive strength and the internal friction angle of a material. In order to describe the degradation in the uniaxial compressive strength, the corresponding degradation in the two parameters must be obtained. This section deals with this respect in terms of the different strength criteria, *i.e.* the Mohr-Coulomb, Hoek-Brown and Griffith criteria.

Degradation with the Mohr-Coulomb criterion

Suppose that the uniaxial compressive strength of a fractured material has reduced to σ_{cd}, determined by Equation 4-38 or its implemented form as given in Subsection 5.3.7. Corresponding to σ_{cd}, the apparent cohesive strength c_d is given by (see Equation 4-50)

$$c_d = \frac{\sigma_{cd}}{2\sqrt{k_d}}, \tag{5-29}$$

where k_d is the coefficient of friction for the degraded material, which is defined by (see Equation 4-49)

$$k_d = \frac{1+\sin\phi_d}{1-\sin\phi_d}, \tag{5-30}$$

where ϕ_d is the degraded internal friction angle of the fractured material. However, a difficulty arises in the use of this technique in that it is difficult to make an initial estimate of either ϕ_d or c_d, even if σ_{cd} is given. To deal with this problem, two approaches may be considered. One approach is to reduce the cohesive strength of the material alone, with the internal friction angle remaining constant. The other approach is to estimate the cohesive strength of the material by primarily giving an arbitrary value to the degraded internal friction angle. This degraded friction angle may be in the range covering intact rock to very loose rock material, with corresponding values of 60°-15° (see Vermeer and De Borst, 1984; Lockner, 1995; Pusch, 1995; Hoek and Brown, 1997). To avoid the selection of an arbitrary degradation in friction angle, here we use a degradation of cohesion, computed from the degraded uniaxial compressive strength. Thus, using Equation 4-50 to substitute for $2\sqrt{k}$ in Equation 5-29, we find

$$c_d = \frac{c\sigma_{cd}}{\sigma_c}. \tag{5-31}$$

The same ratio of degradation is performed to the tensile strength as

$$T_{0d} = \frac{T_0 \sigma_{cd}}{\sigma_c}. \tag{5-32}$$

The implemented form of Equations 5-31 and 5-32 is

```
cohesion(i,j)=ex_6(i,j)*s_cd/s_c ;Eq. 5-31
tension(i,j)=ex_7(i,j)*s_cd/s_c ;Eq. 5-32
```

where `s_cd` is the parameter calculated in Subsection 5.3.7; `ex_5(i,j)`, `ex_6(i,j)` and `ex_7(i,j)` are the extra variables for storing the initial uniaxial compressive strength σ_c, cohesion c and tensile strength T_0 of a rock element, respectively.

Degradation with the Hoek-Brown criterion

With the Hoek-Brown criterion, the degraded uniaxial compressive strength is represented by the degraded Hoek-Brown parameters m_d and s_d (Equations 4-57 and 4-58). Replacing m and s in Equations 5-17 and 5-18 with m_d and s_d, respectively, the equivalent degraded values for parameter k_{hd} and the uniaxial compressive strength σ_{chd} can be obtained. The same procedure, replacing σ_{ch} and/or k_h in Equations 5-19 and 5-20 with σ_{chd} and k_{hd} as appropriate, the equivalent degraded cohesion c_{hd} and the equivalent friction angle ϕ_{hd} can be computed, respectively.

The variations of both the cohesive strength and the internal friction angle of a degraded material are coupled through GSI, which relates the Hoek-Brown parameters m and s to the degradation state of rock materials (see Equations 4-55 to 4-58). This feature overcomes the shortcoming of the linear Mohr-Coulomb criterion in describing material strength degradation (including the degraded uniaxial tensile strength, see Equation 4-52) as described in the previous subsection.

Degradation with the Hoek-Brown criterion is finally implemented as

```
;restore the initial uniaxial compressive strength
s_c=ex_5(i,j)
;restore the Hoek-Brown parameter m for intact rock element
m_i=ex_9(i,j)
s_d=(s_cd/s_c)^2 ;Eq. 4-57
m_d=m_i*exp((9*ln(s_d))/28.0) ;Eq. 4-58
temp1=1.0/(m_d*s3/s_c+s_d)^(0.5) ;component calculation
k_hd=1.0+0.5*m_d*temp1 ;Eq. 5-17
s_chd=(0.5*m_d*s3+s_d*s_c)*temp1 ;Eq. 5-18
```

```
temp2=sqrt(k_hd) ;component of Eq. 5-19
cohesion(i,j)=0.5*s_chd/temp2 ;Eq. 5-19
friction(i,j)=2*atan(temp2)*dm_degrad-90 ;Eq. 5-20
tension(i,j)=0.5*s_c*(sqrt(m_d^2+4*s_d)-m_d) ;Eq. 4-52
```

where `ex_5(i,j)` is the extra variable for the storage of the initial uniaxial compressive strength σ_c, and `ex_9(i,j)` is the variable for the storage of m_i, the Hoek-Brown parameter m for intact rock (see Table 5.5).

The extra variables of `ex_10(i,j)` and `ex_11(i,j)` are reserved for storing the values of m_d and s_d. The updates of the current values of the two parameters are simply implemented as

```
ex_11(i,j)=m_d ;update m_d
ex_12(i,j)=s_d ;update s_d
```

The updated values are used for the next timestep.

Degradation with the Griffith criterion

Corresponding to the degraded uniaxial compressive strength σ_{cd}, the implementation of the degradation described by the Griffith criterion in the FLAC Mohr-Coulomb model takes similar procedures to those for the Hoek-Brown criterion. First, the degraded value for the tensile strength T_{0d} is obtained from Equation 4-59. Then, the value of T_{0d} is used to replace T_0 in Equations 5-21 and 5-22 to obtain the equivalent Mohr-Coulomb parameters k_{gd} and σ_{cgd}, and the degraded cohesive strength c_{gd} and the equivalent friction angle ϕ_{gd} are computed by replacing σ_{cg} and k_g in Equations 5-24 and 5-25 with σ_{cgd} and k_{gd}, respectively. These are implemented as

```
T_0d=s_cd*0.125 ;Eq. 4-59
temp1=sqrt(T_0d/(s3+T_0d)) ;component calculation
k_gd=1.0+2.0*temp1 ;Eq. 5-21
s_cgd=4.0*T_0d+(2.0*s3+4.0*T_0d)*temp1 ;Eq. 5-22
temp2=sqrt(k_gd) ;component of Eq. 5-24
cohesion(i,j)=0.5*s_cgd/temp2 ;Eq. 5-24
friction(i,j)=2*atan(temp2)*dm_degrad-90 ;Eq. 5-25
tension(i,j)=T_0d ;equivalent degraded T0
```

The extra variables of `ex_12(i,j)` is used to store the value of T_{0d}, and the update of the current value of T_{0d} is implemented as

```
ex_12(i,j)=T_0d ;update T_0d
```

The updated values are used for the next timestep.

5.3.10 Calculation of elastic strain energy dissipation

The dissipated elastic strain energy is computed by Equations 4-80 to 4-83 (Section 4.8). In order to use those equations, strain components in a plane strain state are calculated first as follows (Mase and Mase, 1999):

$$\varepsilon_{xx} = \frac{1+\nu}{E}\left[\sigma_{xx} - \nu\left(\sigma_{xx} + \sigma_{yy}\right)\right], \tag{5-33}$$

$$\varepsilon_{yy} = \frac{1+\nu}{E}\left[\sigma_{yy} - \nu\left(\sigma_{xx} + \sigma_{yy}\right)\right], \tag{5-34}$$

and

$$\varepsilon_{xy} = \frac{1+\nu}{E}\sigma_{xy}, \tag{5-35}$$

where ν is Poisson's ratio and E is Young's modulus.

Using these, the calculations of elastic strain energy dissipation are implemented as

```
;change from tension positive to compression positive
dmsxx=-sxx(i,j)
dmsyy=-syy(i,j)
dmsxy=-sxy(i,j)
;restore the previous Young's modulus of the material
E_0=ex_4(i,j)
temp1=dm_rpr*E_0/((1.0+ dm_rpr)*(1.0-2.0* dm_rpr)) ;Eq. 4-80
temp2=0.5*E_0/(1.0+ dm_rpr) ;Eq. 4-81
temp3=(1.0+dm_rpr)/E_0 ;coefficient calculation
temp4= dm_rpr*(dmsxx+dmsyy) ;component calculation
temp5=temp3*(dmsxx-temp4) ;Eq. 5-33
temp6=temp3*(dmsyy-temp4) ;Eq. 5-34
temp7=temp3*dmsxy ;Eq. 5-35
temp8=temp5+temp6 ;summation of strain components
;Eq. 4-82
u_e0=0.5*temp1*temp8^2+temp2*(temp5^2+temp6^2+0.5*temp7^2)
d_ued=(1.0-E_d/E_0)*u_e0*delt_A ;Eq. 4-83
```

The extra variable *ex_13(i,j)* is allocated to store and update the dissipated elastic strain energy (Table 5.5). The value stored in *ex_13(i,j)* is the strain energy

dissipation rate, *i.e.* the strain energy dissipated with respect to an interval of timesteps, and its initial value needs to be zero before an evaluation. For further details in this respect, see Appendix B.

5.3.11 Representation of fracture of materials

As presented in Chapter 4, the degradation model has been developed to describe the brittle fracture process of heterogeneous rocks, and in particular to examine the development of degradation displayed by rock materials during the course of a simulation. With respect to the acoustic emission technique used in detecting rock local failure, as presented in Subsection 2.5.4, two ways may be considered in representing rock fracture by the development of degradation: one is to display the accumulated degradation events; the other is to display degradation events occurred at each loading stage.

The extra variable `ex_1(i,j)` is used to indicate the cumulative degradation that has occurred to an element during the whole course of a simulation. To indicate the degradation events at a particular stage, we specify two other extra variables `ex_14(i,j)` and `ex_15(i,j)`. The variable `ex_14(i,j)` is used to represent the stage degradation induced by shear failure and the variable `ex_15(i,j)` is used to indicate the stage degradation events induced by tensile failure. For further details, see the FLAC code of the degradation model given in Appendix B.

5.4 Simplified input parameters based on the uniaxial compressive and tensile strengths of rock

The previous section has shown how the degradation model with different failure criteria is implemented in the FLAC embodied Mohr-Coulomb model. For this purpose, a conversion between the criterion parameters is required, in order that the material properties represented by other criterion parameters can be transformed in to equivalent Mohr-Coulomb parameters.

In order to use the Mohr-Coulomb criterion, the three strength parameters of cohesion, friction angle and tensile strength are required. However, in rock mechanics and rock engineering, the uniaxial compressive strength is often used in combination with the cohesion and the friction angle. In addition, the uniaxial tensile strength often uses a cut off value which does not relate to any other strength property parameters (see

Subsection 4.4.1). This introduces a problem in applying this theory to the analysis of heterogeneous rocks, in which either only the uniaxial compressive strength or the uniaxial tensile strength is available, or the relation between the uniaxial tensile strength and other properties is required.

An approach to determine the relation between these parameters is sought in this section. First, the ratio of the uniaxial compressive strength to the tensile strength is clarified, followed by the determination of the relation between the ratio and other parameters, in which the Hoek-Brown parameter *m* plays a vital role.

Relation between uniaxial compressive and tensile strength

Although the Griffith's theory predicts that the uniaxial compressive strength equals 8 times the uniaxial tensile strength (Equation 4-54), a variation in the ratio of the uniaxial compressive and tensile strength has been encountered in laboratory experiments. A survey given by Pusch (1995), presented in Table 5.6, indicates that a ratio of 10-13 is exhibited by many rocks. In terms of an individual type of rock, the ratio may cover a wider range up to 3-104 (McClintock and Walsh, 1962).

The laboratory data referred to above suggest that the ratio of the uniaxial compressive and the tensile strength may follow a statistical distribution function, with a wide range and a mean value (10-13, for example). Referring to the common distribution functions (see Section 4.4), we propose that the same function as is used for other property distributions will be used to determine the ratio of the uniaxial

Table 5.6. Ratio of the uniaxial compressive strength to the tensile strength of rocks (from Pusch, 1995)

Rock type	σ_c/T_0
Granite	10~12
Gneiss	10~20
Diabase	11~13
Quartzite	9~16
Marble	12~14
Shale	>=10
Sandstone	12~14
Limestone	8~15

compressive strength to the tensile strength in this study (see Chapters 6, 7 and Appendix B).

Relation between Hoek-Brown and Mohr-Coulomb parameters

Parameters in the Mohr-Coulomb failure criterion, *i.e.* the cohesive strength and the internal friction angle, can be related with each other by the Hoek-Brown parameter *m*. Denoting $\sigma_3 = 0$ and $s = 1$ in Equations 5-17 and 5-18, the parameters k_h and σ_{ch} for an intact rock in the uniaxial case are expressed as

$$k_h = 1 + \frac{m}{2} \tag{5-36}$$

and

$$\sigma_{ch} = \sigma_c . \tag{5-37}$$

Substituting these results into Equations 5-19 and 5-20, it is seen that the determination of both the cohesive strength and the internal friction angle for an intact rock rely on the value of parameter *m*.

Rearranging Equation 4-52 and specifying *s* as unity, an expression for *m* of an intact rock can be obtained. It reads as

$$m = \frac{\sigma_c}{T_0} - \frac{T_0}{\sigma_c} . \tag{5-38}$$

Equation 5-38 shows that once the ratio of the uniaxial compressive strength to the tensile strength of an intact rock is settled, the determination of the value for parameter *m* is straightforward, and hence so are the values for the cohesive strength and the internal friction angle (Equations 5-19, 5-20, 5-24, 5-25, 5-36 and 5-37). This approach is utilised to determine values for these parameters in the model application (see Chapters 6 and 7).

5.5 Summary of the model implementation procedures

The earlier sections have presented the major procedures in the FLAC implementation of the degradation model proposed in Chapter 4. For a complete simulation of a problem using the degradation model in FLAC, another two components have to be included. One is the generation of a grid, which defines the geometry of the problem, and the other is the equilibrium state corresponding to the initial boundary conditions, prior to application of any loading. These two steps can be easily handled with the

associated FLAC commands (see Subsection 5.2.4).

In this summary, we present a comprehensive flow chart for the FLAC implementation of the degradation model, including the two components mentioned in the previous paragraph. This flow chart is shown in Figure 5.7.

As illustrated by the flow chart in Figure 5.7, after the geometry of the problem under investigation has been defined, the heterogeneity in two material strength property parameters, *i.e.* the uniaxial compressive strength and uniaxial tensile strength, are determined with a distribution function. Then, other strength property parameters are specified based on the ratio between the uniaxial compressive strength and the uniaxial tensile strength, along with uniform material properties and the specification of the initial boundary conditions. This procedure is followed by bringing the model to equilibrium under the initial boundary conditions.

At this stage, a perturbation that produces strain increments may be applied, and an elastic solution of stress is computed by application of a constitutive relation to the total strain increment. Then, the principal stresses and corresponding principal directions are calculated and ordered, and if these stresses violate the elemental failure criterion, the element fails and both degradations in strength and stiffness or plastic flow may occur to the element. The degradation in effect causes stress and strain changes to the element's surroundings, and this is involved in the new cycle of calculation, together with further stress disturbances.

5.6 Closure

Numerical implementation of the degradation model proposed in Chapter 4 has been presented in this chapter. Although the degradation concept could be incorporated into the discrete element method, the continuum approach has been considered in implementing this model, since the model has been developed using the concept of continuum mechanics.

The degradation model requires large strains or displacements to be followed. In this respect, the explicit finite difference method, as exemplified by the commercial code FLAC, is more advantageous than the finite element method. FLAC uses an explicit time marching scheme to describe material deformation, and provides capabilities to solve complex problems in rock mechanics and rock engineering. It also contains a built-in programming language Fish, which permits users to write a function to implement their own constitutive models. Thus, FLAC has been adopted for the

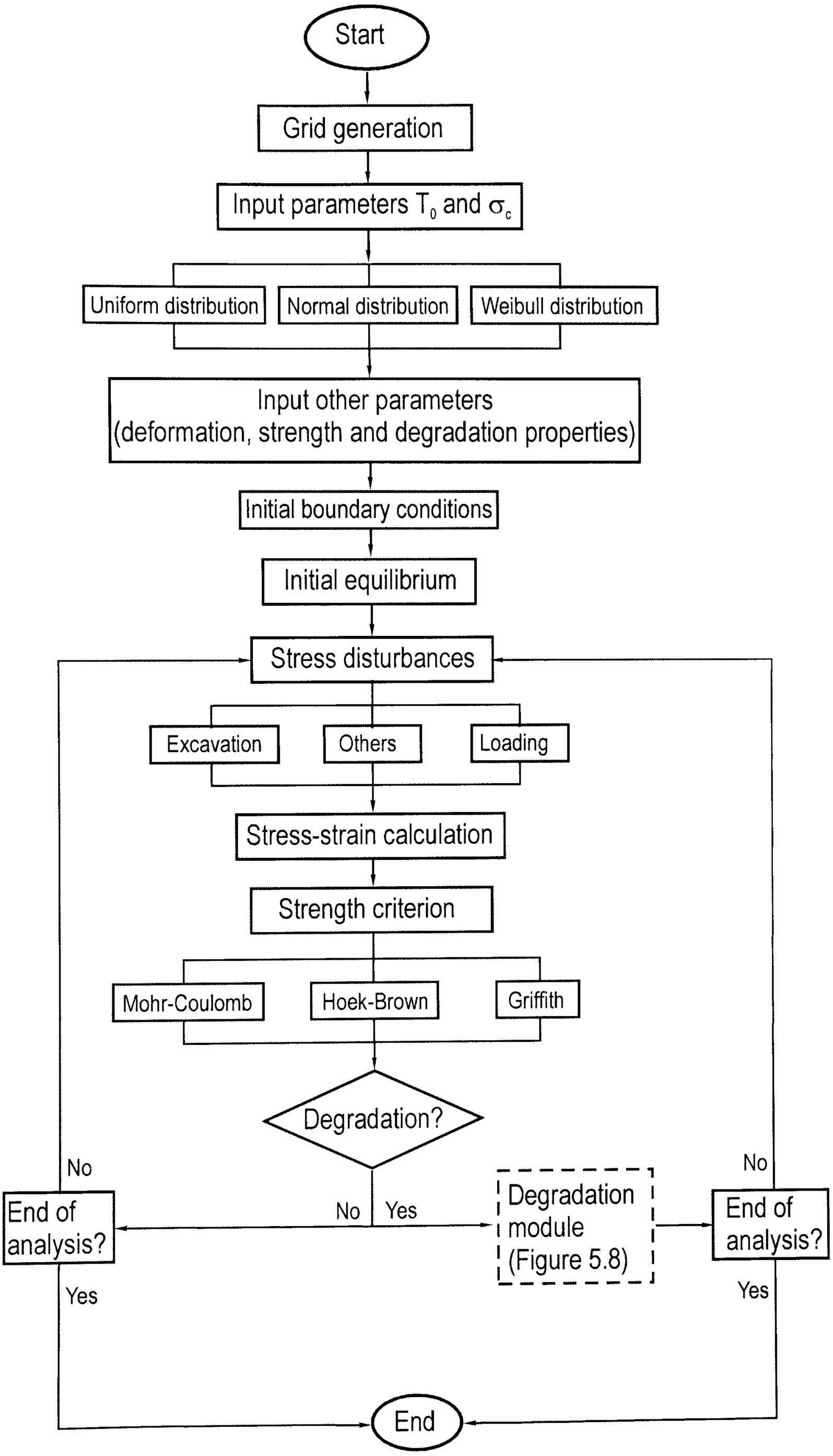


Figure 5.7. Procedures for the implementation of the degradation model

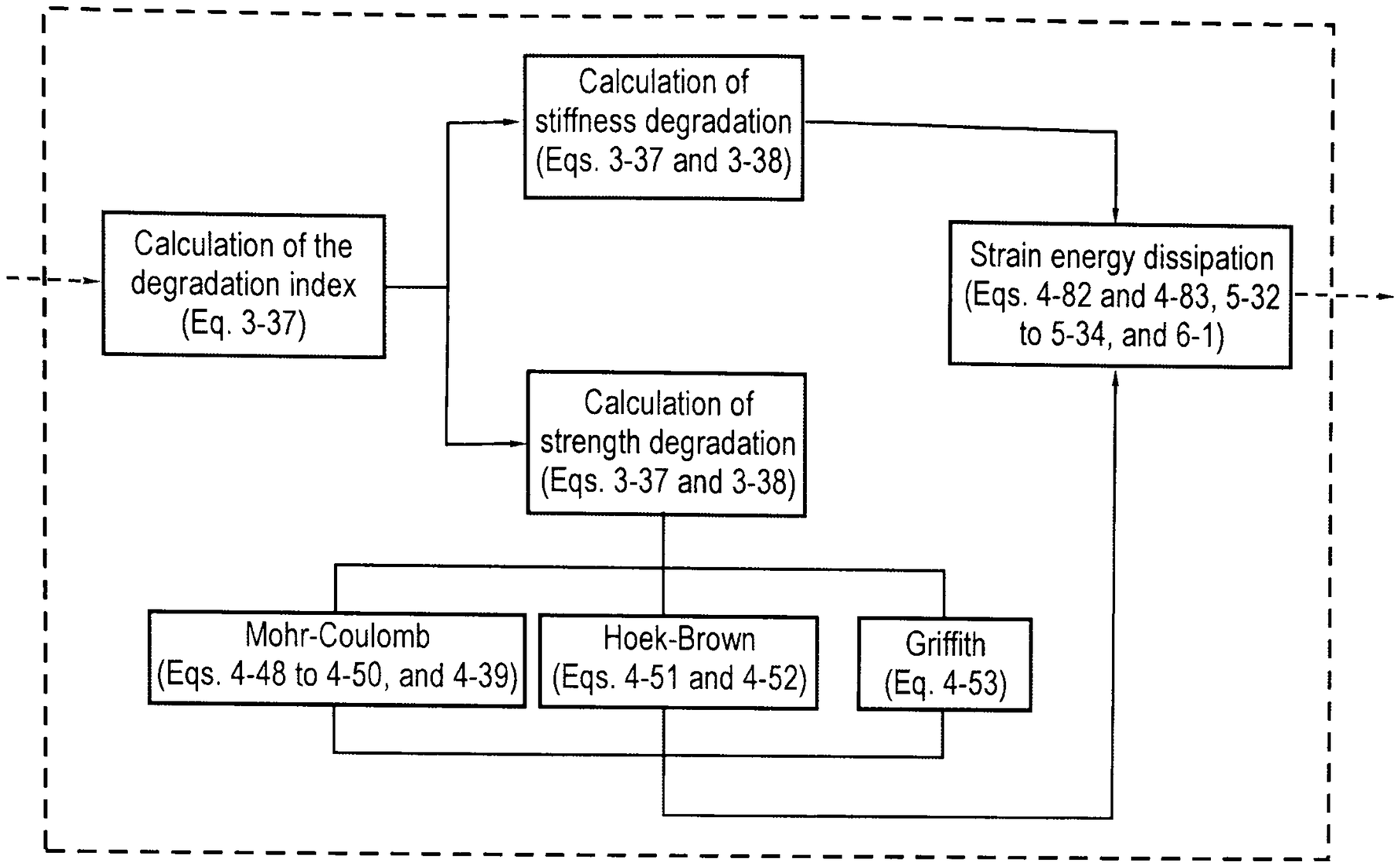


Figure 5.8. Degradation module contained in the flow chart presented by Figure 5.7

implementation of the degradation model.

FLAC embodies the Mohr-Coulomb failure criterion, which is incorporated into the elasto-plasticity constitutive relation for the behaviour of geomaterials. The program also allows degradation to be described either by reducing material cohesive strength, or the internal friction angle, or both. For a problem defined by either the Hoek-Brown or Griffith failure criterion, equivalent values for the two Mohr-Coulomb parameters are derived, in order that these criteria can be replaced by a locally equivalent Mohr-Coulomb failure surface. The Hoek-Brown parameters allow material degradation to be introduced by reducing both the cohesive strength and the internal friction angle in a coupled way. By specifying the ratio of the uniaxial compressive strength to the tensile strength of a material, the two Hoek-Brown parameters relate all the parameters representing the material failure surface in a problem model.

In the degradation model, material heterogeneity can be introduced by one of the three distribution functions, namely, the uniform, normal and Weibull distribution functions. In this respect, an intrinsic function contained in FLAC, which draws a random number from a uniform distribution between 0.0 and 1.0, can be utilised for the uniform distribution in material property. Another intrinsic function in FLAC allows the data that follow a normal distribution to be generated, by specifying a mean and a standard deviation. For the property distribution following a Weibull distribution, a transformation function is introduced, that takes as input a random uniformly distributed

number.

In the following two chapters, the FLAC implementation of the degradation model is used to simulate brittle fracture of rock specimens in the laboratory and of a rock engineering structure. It is shown that the degradation model is able to represent the complex fracturing behaviour, associated with dissipative processes, of heterogeneous rocks.

6 Simulation of brittle fracture of rock specimens

In Chapter 2, it was shown that rock fracture starts with the formation of microcracks either within grains or around the boundaries of grains and defects such as pores, lamellae, cleavages or cracks, and that the formation and extension of these microcracks produce degradation effects in materials. In Chapter 4, the degradation effects associated with the complex microstructural changes are theoretically described, and a local degradation model for the description of rock fracture developed together with a definition of a degradation index. In the numerical implementation of the model discussed in Chapter 5, it was seen that an explicit numerical method is required to deal with the corresponding complex elemental constitutive behaviour, and a commercially available code, FLAC, is therefore used to implement the degradation model.

In order to validate the model, the FLAC implementation is used to simulate fracture of heterogeneous rock samples in the laboratory. This subject is chosen because laboratory uniaxial and triaxial tests are widely used in the rock mechanics community to characterise rock behaviour (ISRM, 1978; Kovari et al., 1983; Andreev, 1995), and moreover, as presented in Chapter 2, numerous efforts have been made to the detailed study of this subject and a great deal of information is available for use in inputting model data and comparing model results, including tracing the dissipative processes by locating acoustic emissions during compression tests.

This chapter outlines the results of numerical simulations carried using the FLAC implementation of the degradation model. After introducing the set-up of the numerical model to simulate laboratory tests on rock specimens, a series of numerical tests replicating rock specimens subject to various confining stresses have been performed. We use these results to first identify the most appropriate elemental strength distribution function and elemental strength criterion. Then, the results of an investigation into mesh effect on model results is given and this is followed by an analysis of both the influence of the degradation parameter n_d (in Equation 4-37) and heterogeneity on rock fracture. Finally, based on these investigations, the fracture process and the associated

mechanical behaviour of a rock specimen subjected to different confining conditions are fully explored.

6.1 Numerical model of laboratory tests on rock specimen

6.1.1 Model set-up

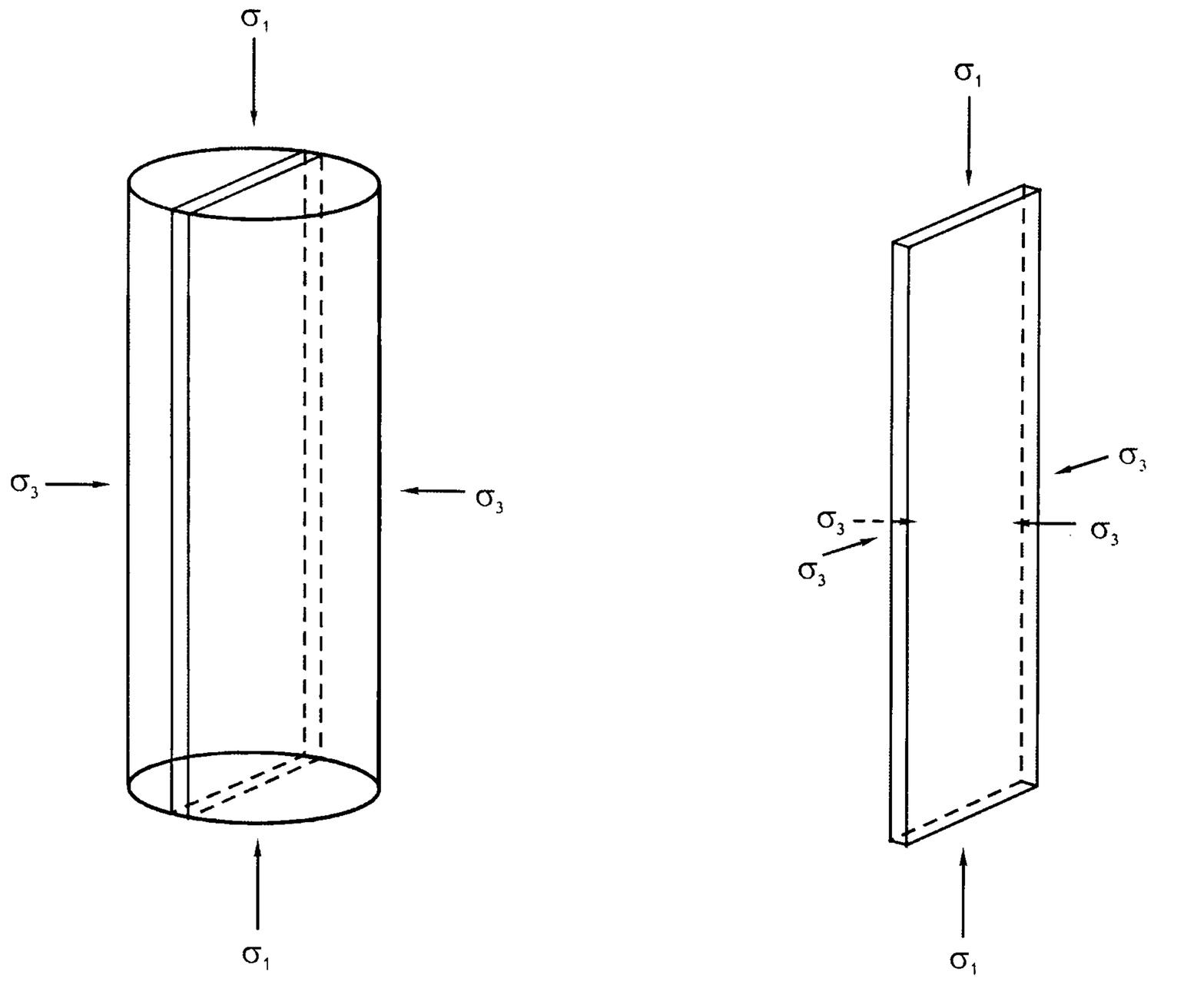
Laboratory experimental system

Laboratory experiments on rock fracture in compression are normally carried out by uniaxially or triaxially loading circular cylindrical specimens (ISRM, 1978; Kovari et al., 1983; Jaeger and Cook, 1979; Paterson, 1978). Although a laboratory experimental system for a triaxial test can be very complicated (*e.g.* Bésuelle et al., 2000; Thill, 1972; Ayling et al., 1995), with respect to numerical modelling, the interest lies in the core of the system, which consists mainly of a rock specimen and a pair of steel or aluminium platens. When performing a test, a rock specimen with a length to diameter ratio of between 2 and 3 (Paterson, 1978; Jaeger and Cook, 1979; Kovari et al., 1983; Andreev, 1995) is inserted between the two platens and a loading frame used to load the top platen so that compressive load is transmitted to the rock specimen. In the cases of triaxial testing, an extra loading device is used to provide confining pressures against the rock specimen under tested (see Kovari et al., 1983).

Plane strain analysis

In a number of engineering applications, specific body geometry and loading patterns lead to a reduced two-dimensional form of the equations of plane elasticity (Mase and Mase, 1999), and plane elasticity can considerably simplify an analysis of three dimensional engineering problems without significant errors. Many three-dimensional rock engineering problems can be idealised as two-dimensional plane strain problems by analysing a cross section, such as a tunnel, as long as the cross section deforms in its own plane but cannot move normally towards another cross-section (see Sheorey, 1997).

With respect to a rock specimen in the triaxial test, we may consider a section crossing the transverse axis of the specimen (Figure 6.1(a)). Under increased compressive loading with constant radial confining pressure (which includes uniaxial compression), the vertical stress across the cross section increases, and prior to fracture



(a) Specimen and cross section

(b) Deforming cross section

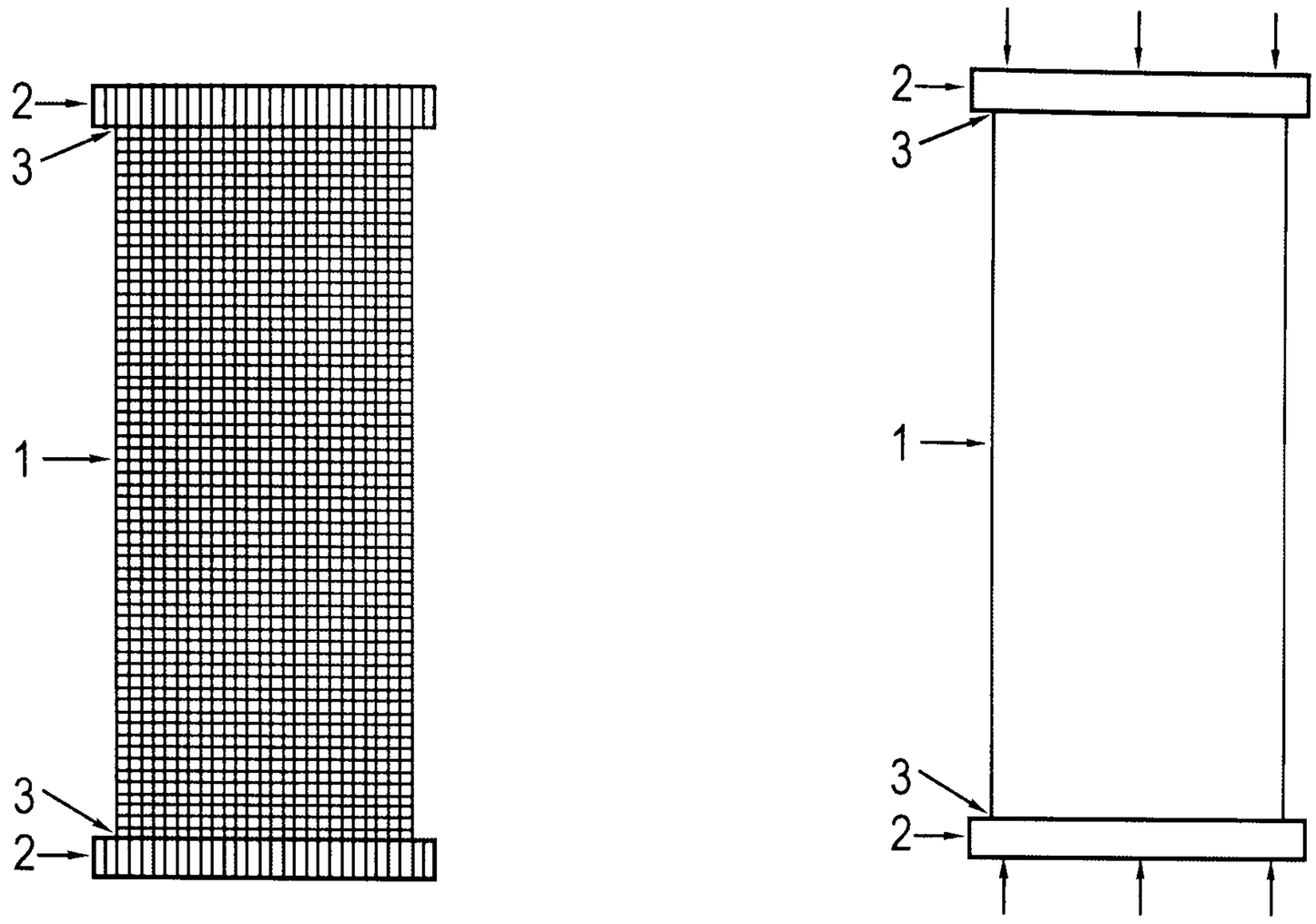
Figure 6.1. Schematic of a cross section from a cylindrical rock specimen

of the specimen the stresses in the other two directions remain constant. This loading configuration assures the induced deformation of the cross section is in its own plane (Figure 6.1(b)).

When a fracture plane develops within the specimen, deformation geometry becomes complicated. However, in most cases, the deformation of the fractured rock specimen is manifested by displacement along, or separation from, the fracture plane, which is in a direction normal to the fracture plane. If we consider this extreme case for a cross section, whose normal is perpendicular to the normal of the fracture plane, it is suggested that the development of fracture within a specimen may still be analysed by plane strain elasticity. Although a plane strain analysis of fracture of a rock specimen is therefore used here, application of the degradation model to a three dimensional analysis is suggested for the future work.

Numerical experimental model for rock specimens

The plane strain geometry shown in Figure 6.2 is used for the numerical model of laboratory test systems on rock specimens. It comprises a rock sample, a pair of platens and the interfaces between the rock specimen and the platens. Both the rock body and



(a) Finite difference grid

(b) Performing loading

(1-rock body, 2-platens, 3-interfaces)

Figure 6.2. A plane strain geometry for analysing brittle fracture of rock specimens in the laboratory

the platens are discretised into a mesh of elements (Figure 6.2(a)). The platens deform elastically and are not allowed to break or fracture during the tests. Hence, the platens are regarded as homogeneous and are represented by the FLAC isotropic elastic model (Subsection 5.2.2), with all platen elements having identical elastic properties, *i.e.* bulk modulus, shear modulus, Poisson's ratio and density.

The rock specimen, on the other hand, is the objective of the investigation, and failure takes place within it due to the heterogeneity of its properties. The rock specimen is regarded as heterogeneous and is represented by the FLAC Mohr-Coulomb model, with each element having individual strength properties. For simplicity, the other features of the elements representing the deformation of a rock specimen (which include bulk modulus, shear modulus, Poisson's ratio and dilation angle) are identical prior to local failure occurring. During the simulation, the bulk and shear moduli of an element may degrade once the strength criterion is violated, but the other parameters, such as Poisson's ratio and dilation angle, remain constant throughout the entire course of a simulation.

The interfaces between the platen and the ends of a rock specimen are represented by the interface model embodied in FLAC (see Subsection 5.2.2).

6.1.2 Loading methods

Representative uniaxial loading

In all numerical experiments representing uniaxial tests on rock specimens, axial loading is performed with axial incremental displacements being applied in a sequence of steps to the surface of the both platens. This is given by specifying a displacement velocity to both the top grid points of the upper platen and the bottom grid points of the bottom platen (Figure 6.2(b); and also see Itasca, 1995a).

Representative triaxial loading

To simplify, in performing a numerical experiment representative of a triaxial test on a rock specimen, a stress boundary (see Itasca, 1995a) is used first on the two sides of the rock specimen and on the outer surfaces of both platens to achieve a hydrostatic stress state at a level of a specific confining pressure (with reference to Figure 6.2), followed by the platen incremental displacement axial loading method for the deviatoric axial stresses (see above description and the FLAC code of the degradation model in Appendix B).

Following the set-up of the model as described above, we are able to perform a series of numerical experiments on rock specimens. As seen in Chapter 4, the degradation model comprises a number of components, which can have various forms (Sections 4.9 and 5.5). The appropriateness of these forms in modelling the problem needs to be identified, and identification of the optimal elemental strength distribution and strength criterion is given in Section 6.2.

6.1.3 Model output

The degradation model aims at reproducing the isolated fracture process and the associated macroscopic mechanical behaviour. Thus, three outputs are used in the model results. These are failure pattern, the axial stress-strain curve and the strain energy dissipation characteristics associated with fracture processes.

Failure patterns

The numerical presentation of the fracture patterns exhibited by rock materials under compression is a principal objective for the degradation model (Chapter 4), and this is represented by failed elements. When the stress state of an element violates the elemental strength criterion, the element fails and is marked to distinguish it from

unfailed elements. As loading increases, the number of failed elements increases, and the failed elements may connect to form elongated sites corresponding to fractures. A plot of these failed elements indicates the development of failure patterns predicted by the degradation model.

Two types of failure patterns are given in the simulation results. One is the cumulative failure pattern, which is a plot of all the failed elements during the previous deformation history; the other is the active failure pattern, which indicates those elements undergoing degradation within an instant of a few timesteps (50 timesteps was used in producing the model results shown in this work). The former is used for most model results in this chapter, and the latter is only used to produce the results in which the stage development of fracture patterns are required to be isolated (Sections 6.6 and 6.7).

Relation between axial stresses and strains

In laboratory experiments on rock specimens, the axial stress is calculated by dividing the applied load by the initial cross sectional area of the rock specimen. However, in the numerical simulation, a small timestep is used so that within one calculation cycle the information within one element cannot be transmitted to another (see Subsection 5.2.1), and this results in a difference in the stress distribution within the meshed rock body from layer to layer at a given time instant. Thus, the axial stress is calculated by averaging the axial stresses over all elements contained in the model (see FLAC code of the degradation model in Appendix B). More simply, the axial strain is able to be given by averaging the relative displacement between the top and bottom grid points of the rock specimen with respect to its initial length (see Appendix B).

The stress-strain curve can be produced by relating the computed axial stress and strain. It should be noted that, unless it is specified otherwise, the axial stress in all the simulated stress-strain curves presented in this chapter is the axial deviatoric stress.

Dissipation of strain energy

The dissipated strain energy, δU_{ed}, of a linearly elastic element subjected to general loading conditions is given by Equation 4-83, with substitution of Equations 4-80 to 4-82, and the implementation of these are given in Subsection 5.3.10. With continuous loading, dissipative processes may occur at multiple sites within a body. The dissipation rate, ΔU_{ed}, of strain energy of the entire specimen with respect to a specific time period δt is

$$\Delta U_{ed} = \sum_{1}^{n} \sum_{0}^{\delta t} \delta U_{ed} \ , \tag{6-1}$$

where n is the total number of elements. Equation 6-1 is used in the model output to account for the strain energy dissipation associated with material degradation (see Appendix B and model results in the following Sections).

6.2 Choice of strength distribution and strength criterion for simulation of heterogeneous rock fracture

Of those components contained in the degradation model (Sections 4.9 and 5.5), two deal with the heterogeneity distribution and failure criterion associated with material elemental strength properties. Since no physical evidence has been discovered for an appropriate function for element strength properties at a microscopic level, three well-known distribution functions have been included into the model for determining the heterogeneous elemental strength (Section 4.6), and three existing strength criteria for evaluating elemental failure (Section 4.4).

It is the Author's general belief that a numerical model for rock fractures should be capable of reproducing the most important physical and mechanical fracture features displayed by rock materials subject to various compressive stress conditions. These features, with reference to the laboratory and field investigations on rock fracture (Chapter 2), include the development of fracture from elemental scale to macroscopic scale (Section 2.1), the corresponding non-linear stress-strain curve (Subsections 2.1.3 and 2.4.2) and the corresponding acoustic emission characteristics (Section 2.5). By comparing the numerical results (Section 6.1.3) with laboratory test results of rock fracture, the most appropriate functions for describing elemental heterogeneity and strength of rock materials are investigated in this section.

With respect to the distribution functions used in describing elemental strength heterogeneity of rock materials (Sections 4.6 and 4.4), the numerical investigations are performed in three groups, namely, uniform distribution (UD), normal distribution (ND), and Weibull distribution (WD). In each group, three strength criteria are examined, *i.e.* the Mohr-Coulomb (MC), Hoek-Brown (HB), and Griffith (G) criteria, which results in nine simulated composites of rocks (see Table 6.1). In order to identify the most appropriate strength distribution function, each numerical experiment uses a

Table 6.1. Composites of rocks from different distribution functions and strength criteria

Identity	Mohr-Coulomb	Hoek-Brown	Griffith
Uniform distribution	UD + MC	UD + HB	UD + G
Normal distribution	ND + MC	ND + HB	ND + G
Weibull distribution	WD + MC	WD + HB	MD + G

confining pressure of 20 MPa, since according to the published data on rock fracture in the laboratory (see Ramez, 1967; Trill, 1972; Wu, 1991; Bésuelle et at., 2000) fracture phenomena can be distinguished well at this confining stress level for rocks whose uniaxial compressive strength is no less than this confining stress. After identifying the most appropriate strength distribution function, the most appropriate strength criterion is examined. This order is adopted, as further information is required and multiple confining pressures covering a larger range are required to be investigated.

The numerical tests on these two subjects provide a basis for further numerical investigations associated with other components of the degradation model. These are considered in the forthcoming sections (Sections 6.3 to 6.5).

6.2.1 Input data

In the numerical experiments performed on the three groups of models in this subsection, the elemental deformation properties used are identical. The input data of the elemental strength properties, however, are different and follow the specific distribution function. These input data are given in Table 6.2.

Table 6.2. Input data for models with different distribution functions

Identity		UD	ND	WD
Average density		2300 kg/m^3		
Deformation property		Platen: elastic modulus 30 GPa, Poisson's ratio 0.25 Rock specimen: initial elastic modulus 30 GPa, Poisson's ratio 0.25, dilation angle 4°		
Strength property	σ_c	x_a 270 MPa, x_b 70 MPa	Mean 150 MPa, deviation 30 MPa	x_0 200 MPa, x_u 70 MPa, m_w 2.5
	σ_c/T_0	x_a 3, x_b 30	Mean 15, deviation 3	x_0 10, x_u 30, m_w 2.5
Degradation property		$\delta\sigma_{cu}$ 90% the initial uniaxial compressive strength, δE_u 90% the initial elastic modulus, n_d 0.05		
Mesh size		30 zones in horizontal direction and 72 zones in vertical direction for rock with a length/diameter ratio of 2.4		

6.2.2 Investigation of distribution functions

The outputs of the numerical experiments on the nine composite models are given in Tables 6.3 to 6.5. Table 6.3 shows the final fracture patterns displayed by the nine models; Table 6.4 shows the corresponding stress-strain curves; and Table 6.5 shows the corresponding elastic strain energy dissipation with respect to an interval of 50 timesteps. To start with, we first inspect the fracture patterns displayed by the individual composites. Laboratory data on rock specimen fracture suggest that, at this confining stress level, a rock specimen often fails by a single (Paterson, 1978) or several macroscopic shear fracture planes crossing the middle portion of the entire specimen (see Figure 2.5). Although all three groups of the models reproduce shear fracture planes (Table 6.3), the fractures predicted by the normally distributed group develop close to the specimen ends, and grow towards the interfaces between the platens and the specimen (the second row in Table 6.3), rather than growing towards the centre of the specimen. Thus, we can conclude that the normal distribution is inappropriate for describing the heterogeneity of elemental strengths within rocks.

With respect to the uniform and Weibull distribution functions, we are not able to distinguish between them on the basis of fracture planes, since they both predict fracture

Table 6.3. Fracture patterns displayed by models with different distribution functions and strength criteria

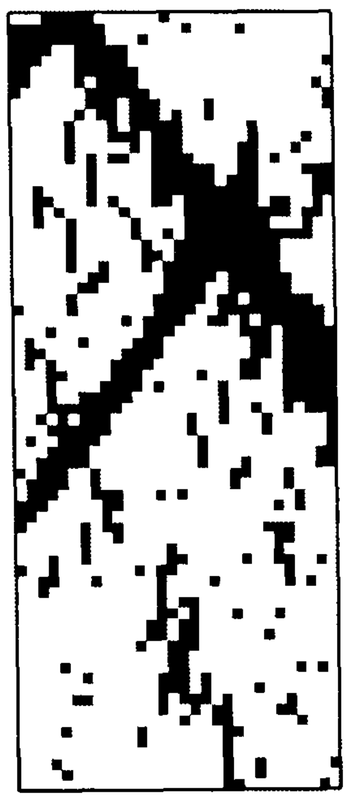
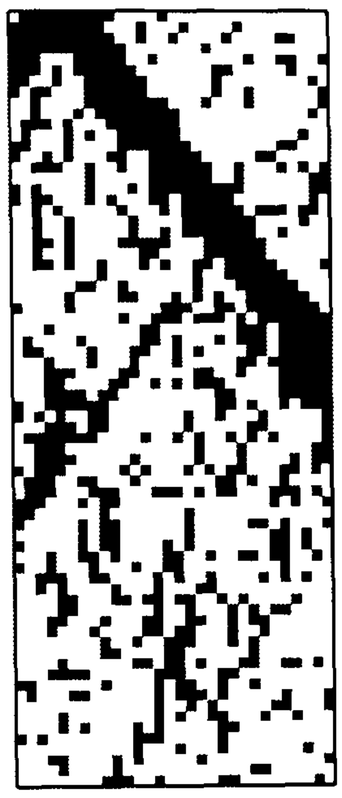
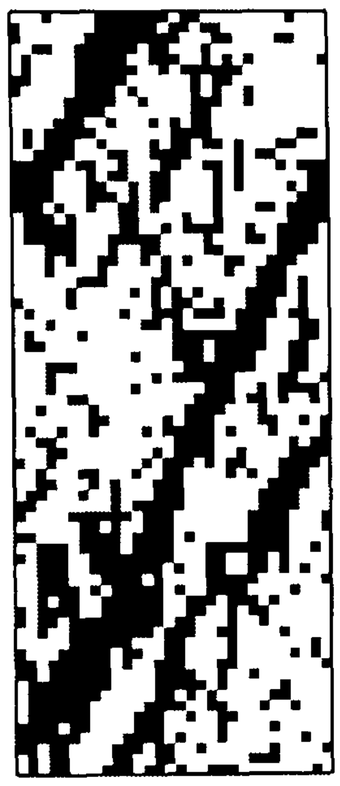
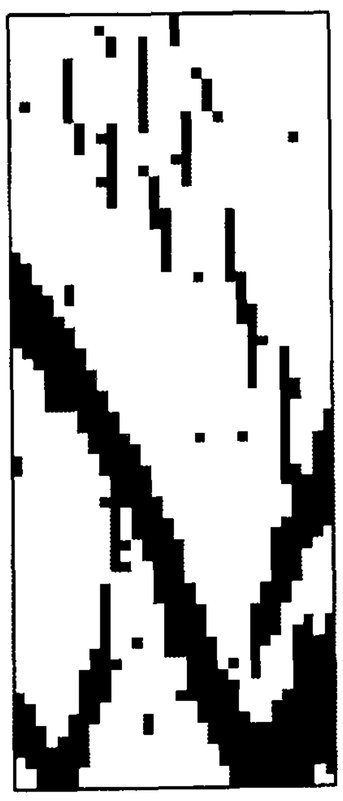
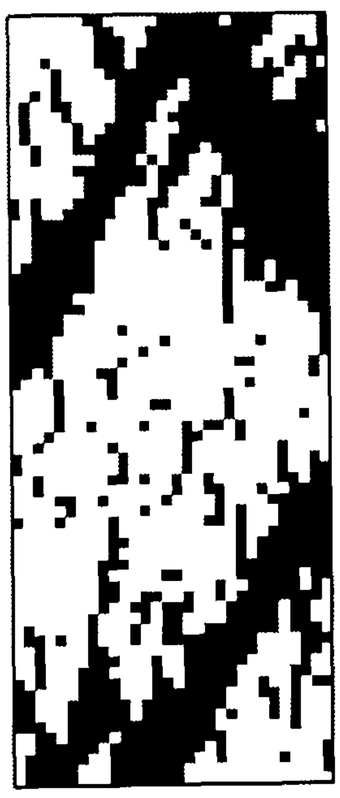
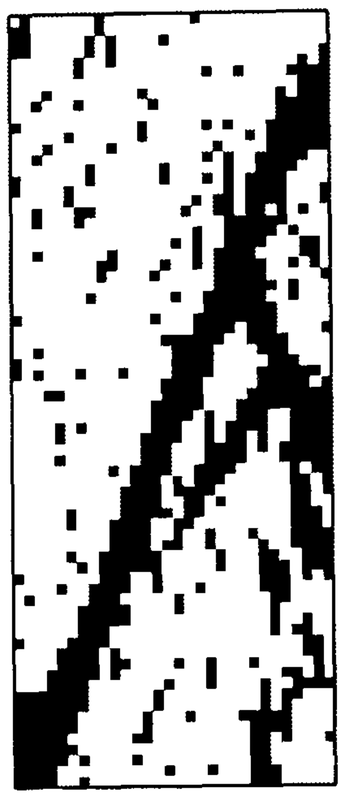
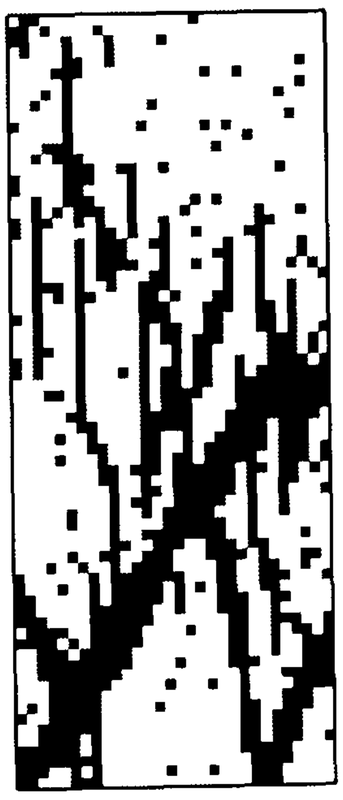
Identity	MC	HB	G
UD			
ND			
WD			

Table 6.4. Stress-strain curves displayed by models with different distribution functions and strength criteria (the vertical axis is axial differential stress in MPa and the horizontal axis is millistrain)

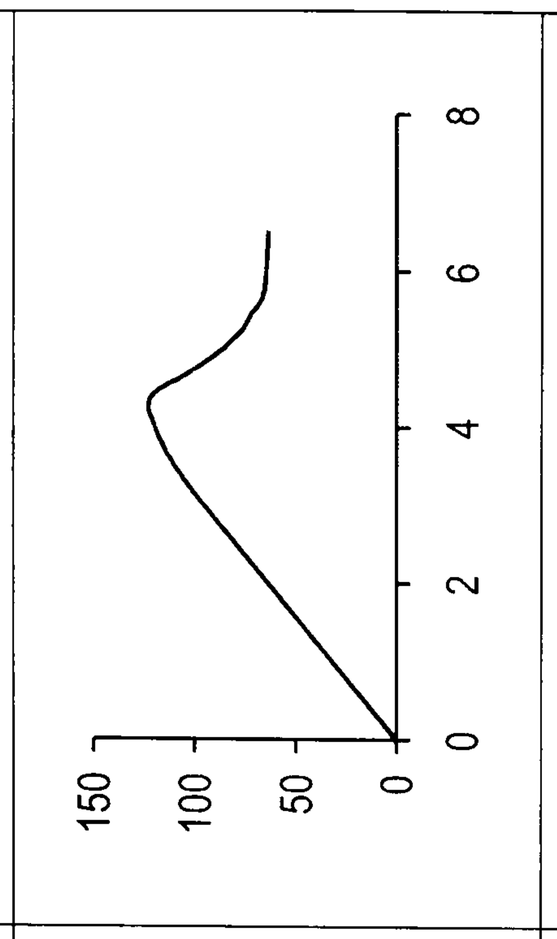
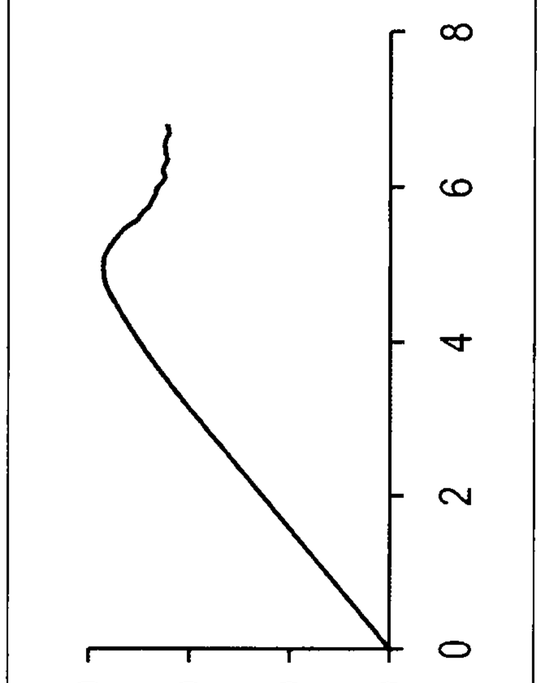
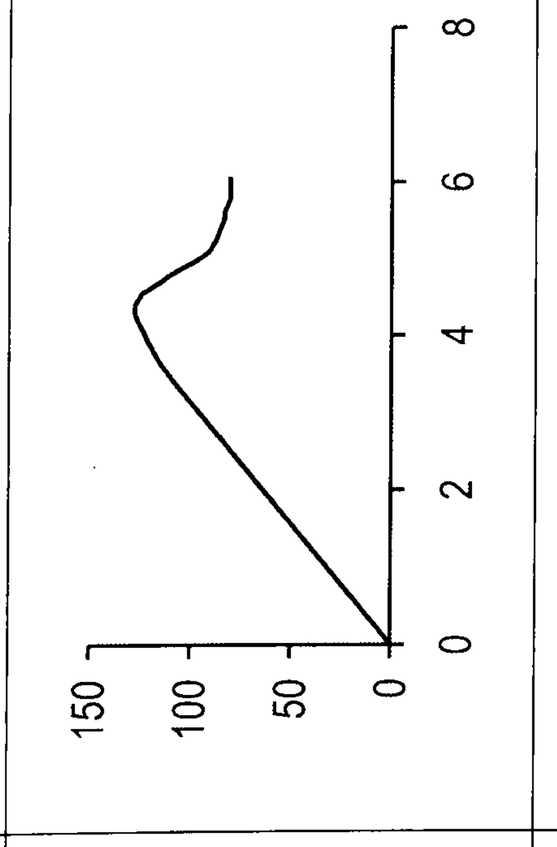
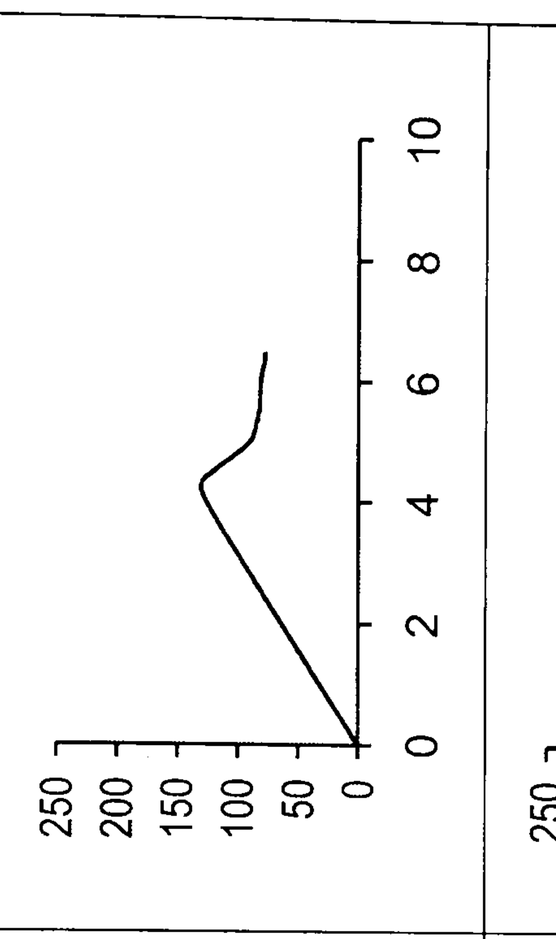
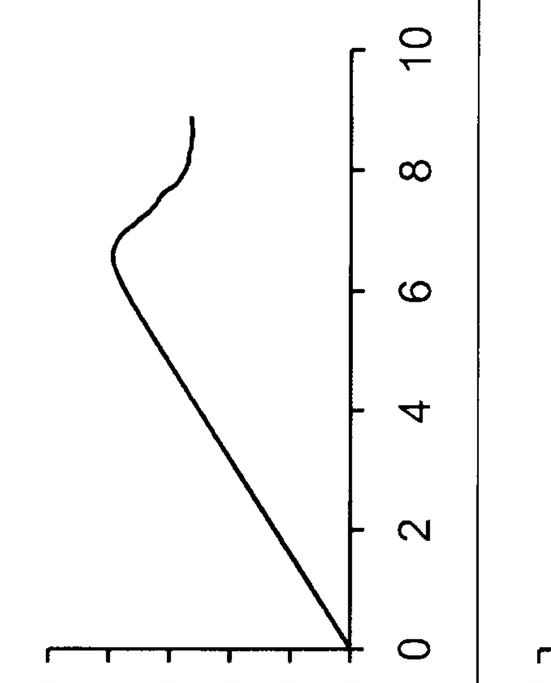
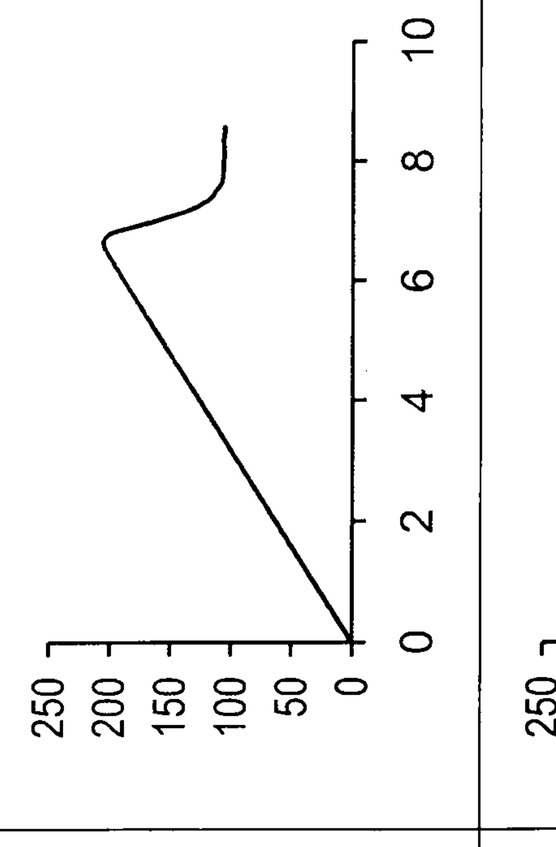
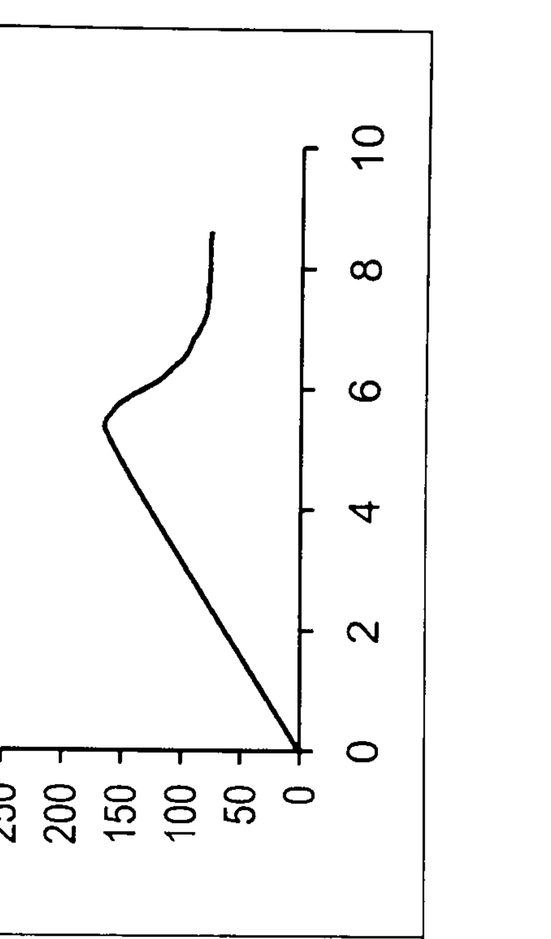
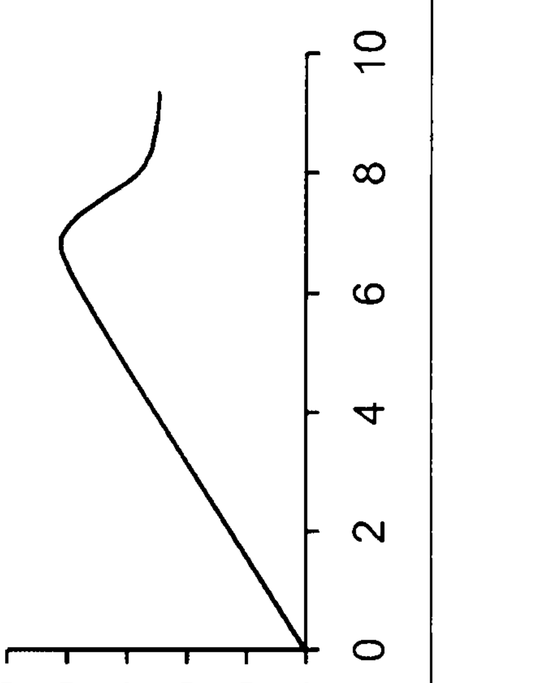
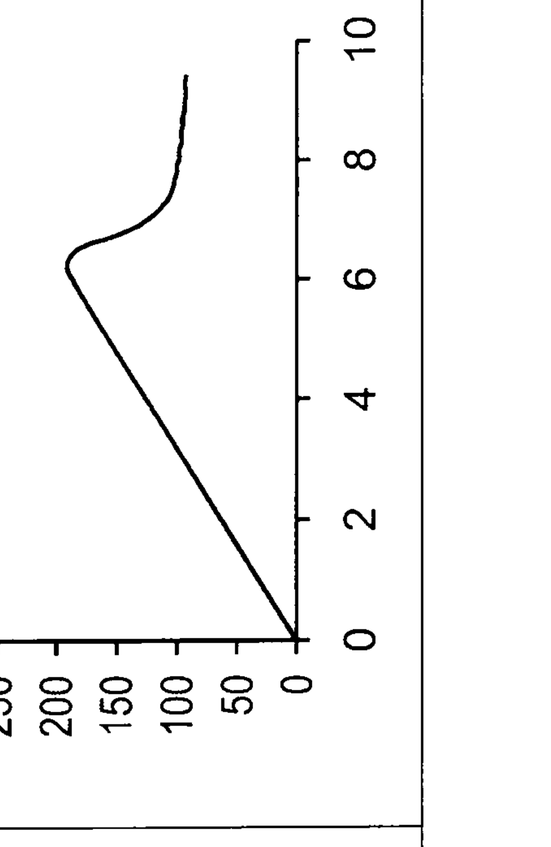
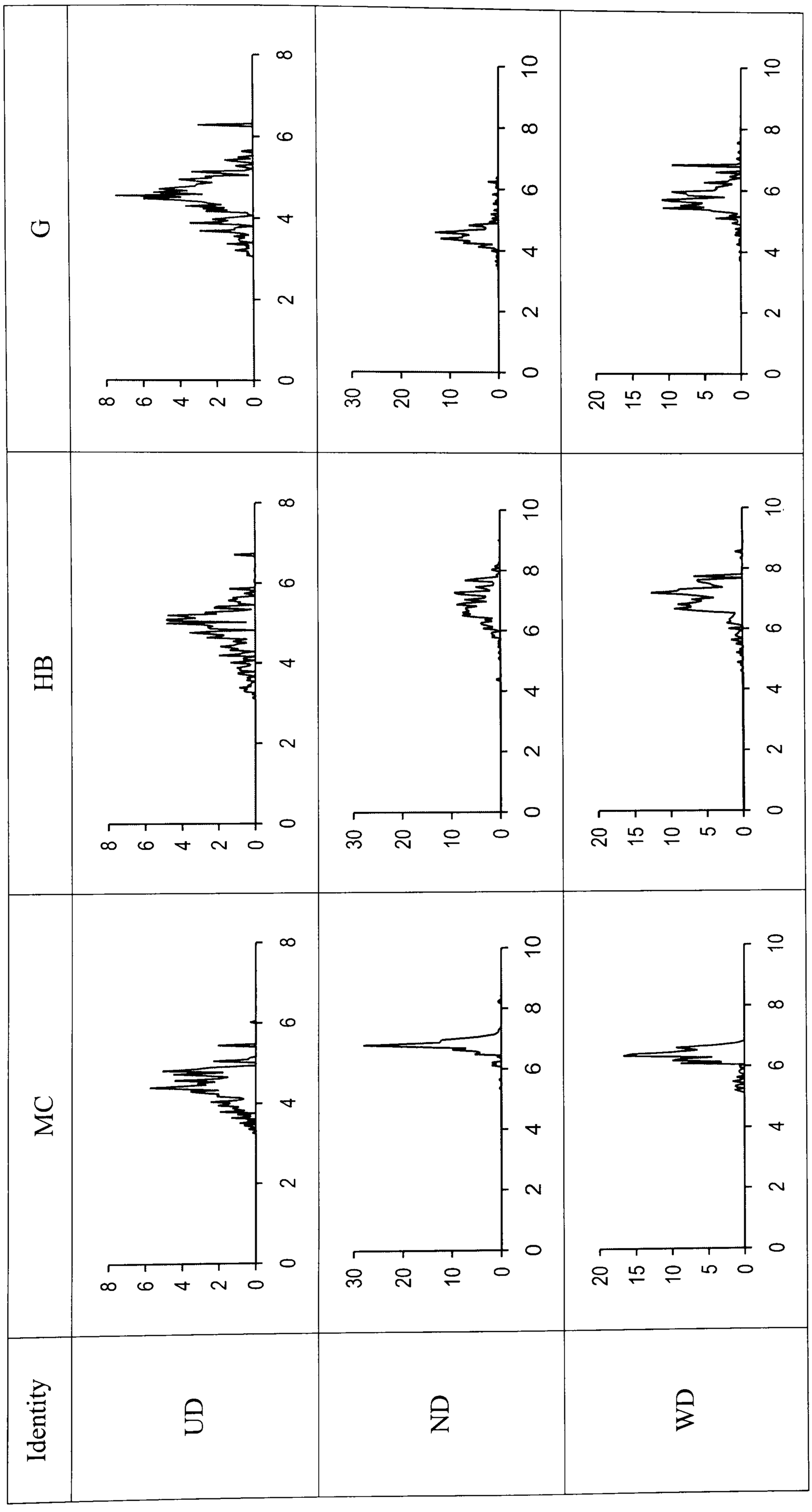
Identity	G	HB	MC
UD			
ND			
WD			

Table 6.5. Strain energy dissipation characteristics displayed by models with different distribution functions and strength criteria (the vertical axis is strain energy dissipation in Nm and the horizontal axis is millistrain)



planes consistent with observed phenomena in the laboratory (the first and the third row in Table 6.3). We therefore focus on the strain energy dissipation characteristics (Table 6.5). The dissipation of mechanical energy is correlated to acoustic emission events that are detectable in experiments (see Scholz, 1968; and also see Section 2.5), and it is laboratory evidence that the rate of acoustic emission events increases gradually until the cracks extend, whereupon it increases rapidly as the cracks link with each other to form macroscopic fracture planes (see Figures 2.24, 2.28 and 2.29). This is agreed by the predicted energy dissipation given by the Weibull distribution (the third row in Table 6.5), but not by the uniform distribution (the first row in Table 6.5). Therefore, we may say that among the three groups, only the Weibull distribution reproduces fracture features in agreement with laboratory data.

6.2.3 Investigation of strength criteria

The previous subsection demonstrated that the Weibull distribution function is the most appropriate for describing the heterogeneity of rock elemental strengths. With the aid of this distribution function, we further examine the preferable strength criterion — from the Mohr-Coulomb, Hoek-Brown and Griffith criteria — for rock elements.

As indicated by the third row in Tables 6.3 to 6.5 (*i.e.* the Weibull distribution), at a confining stress level of 20 MPa the three criteria give numerical results that are in agreement with laboratory data, in terms of the fracture plane (the third row in Table 6.3), the stress-strain curve (the third row in Table 6.4), and the energy dissipation characteristics (the third row in Table 6.5). Apart from the eventual fracture plane, however, the Griffith criterion predicts many additional subfractures (the final figure in the third row in Table 6.3), which are unlikely to develop in a rock specimen at a confining stress of 20 MPa. Moreover, the Griffith criterion predicts lower peak strength than do both the Mohr-Coulomb and Hoek-Brown criteria (see the third row in Table 6.4). This discrepancy lies in the fact that the Griffith criterion is for crack initiation rather than failure of a material, and the stress level at which a crack initiates within a rock body in compression is much lower than the stress that causes material collapse (Bieniawski, 1967; Paterson, 1978; Andreev, 1995; and also see Subsection 2.1.3). As the degradation we describe here is associated with elemental peak strength, we may conclude that the Griffith criterion is inappropriate to describe elemental degradation within rock materials.

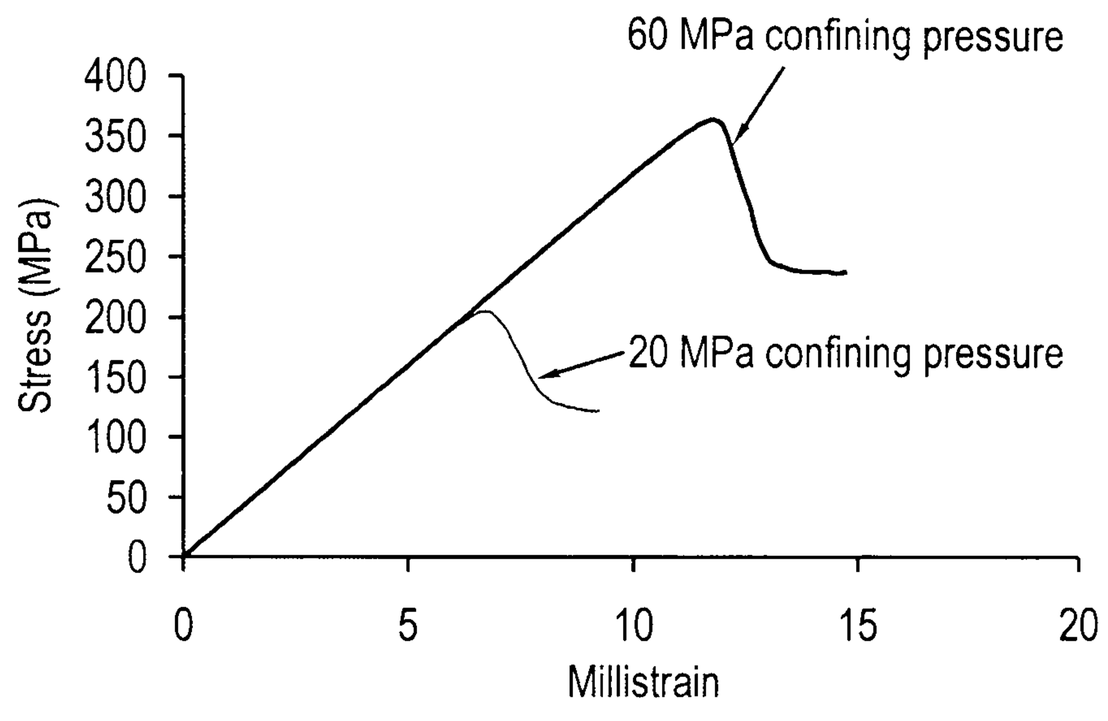
As for the Mohr-Coulomb and Hoek-Brown criteria, we can see that the

Mohr-Coulomb criterion predicts fewer failed sites prior to the formation of the eventual fracture plane than does the Hoek-Brown criterion (see the first and second figures in the third row of Table 6.3), resulting in a more brittle stress-strain behaviour (see the first and second figures in the third row in Table 6.4). To further identify this phenomenon, an additional numerical test is performed with a confining pressure of 60 MPa, at which the model behaviour is expected to be more ductile.

Figure 6.3 shows the resulting fracture pattern and stress-strain curve given by the



Fracture pattern

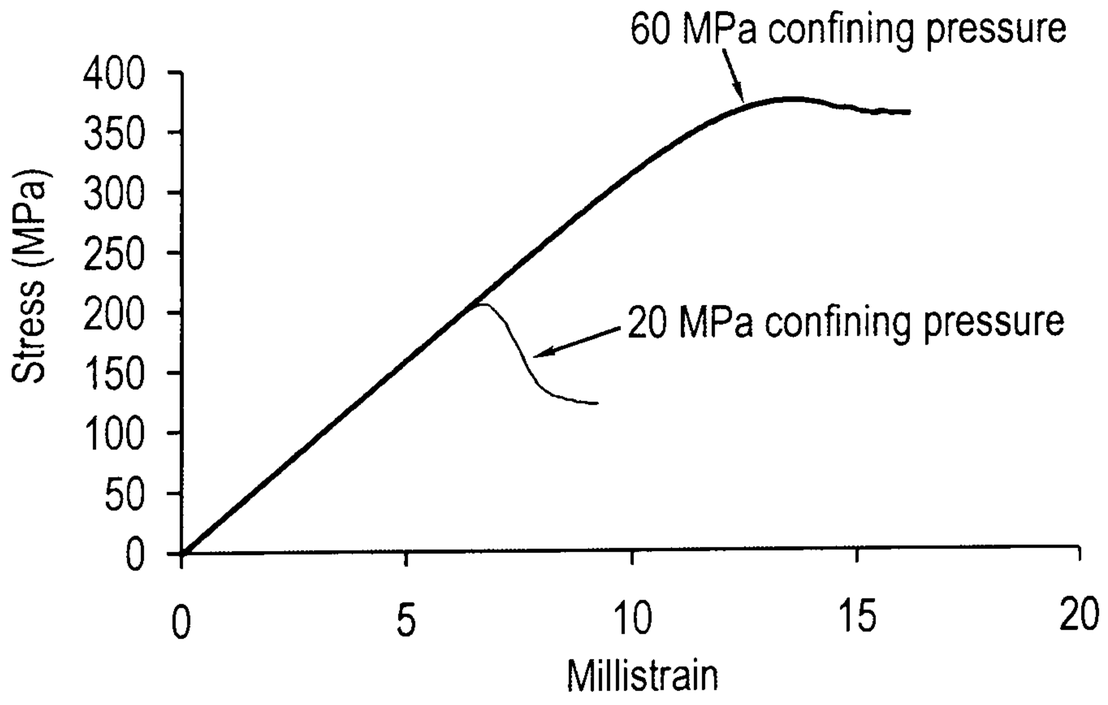


Stress-strain curve

Figure 6.3. Predicted fracture pattern and corresponding stress-strain curve of a rock specimen subjected to a confining pressure of 60 MPa with the Mohr-Coulomb elemental strength criterion



Fracture pattern



Stress-strain curve

Figure 6.4. Predicted fracture pattern and corresponding stress-strain curve of a rock specimen subjected to a confining pressure of 60 MPa with the Hoek-Brown elemental strength criterion

Mohr-Coulomb criterion at this higher confining pressure. Compared with the simulation results presented in Tables 6.3 and 6.4 (the first figure in the third row in the two tables), it is seen that the Mohr-Coulomb criterion gives an unlikely prediction at this highly confined stress condition. The fracture plane is sharper, and the model mechanical behaviour is more brittle, than those displayed under 20 MPa confining pressure.

Contrary to the Mohr-Coulomb criterion, the Hoek-Brown criterion predicts results (Figure 6.4) that are consistent with laboratory observations: the fracture plane is less sharp and the stress-strain curve is more ductile than those predicted under 20 MPa confining pressure (the second figure in the third row in Tables 6.3 and 6.4). Based on these investigations, we may say that the Hoek-Brown criterion is the most appropriate for evaluating elemental peak strengths.

Thus, we have demonstrated that the Weibull distribution function and the Hoek-Brown failure criterion are the most appropriate for describing rock elemental strength features, and these two functions will be exclusively used in the successive numerical simulations. However, in order to fully explore the model, other aspects associated either with the degradation model or with numerical analyses require to be investigated. These include the mesh effect that is associated with numerical analyses of engineering mechanics, the role of the degradation parameter n_d in Equation 4-37 in rock fracture, and the influence of heterogeneity on rock fracture. These form the subjects of the next three sections.

6.3 Mesh effect

The preceding section demonstrates that the fracture process and the corresponding mechanical behaviour can be predicted by the degradation model, when the Weibull distribution function for heterogeneity and the Hoek-Brown criterion for elemental failure are incorporated. The behaviour of a numerical model for an object, however, is usually influenced by the grid size. It is usual that the more number of elements or zones are used to model the problem, the better approximation to the solution is calculated. This is called the mesh effect (see Pande et al., 1990).

The mesh effect may produce significant computation errors in the analysis of practical problems, and in order to diminish the effect, more zones are used in meshing (Pande et al., 1990). However, increasing the number of zones incurs penalties in both computation complexity and computation time (see Pande et al., 1990). To balance

these side effects, an optimal mesh size should be found for a problem under investigation.

To examine the mesh effect associated with the degradation model, we consider two points. One is to investigate the mesh effect associated with producing model results; the other is to identify the optimal mesh size with respect to the problem geometry. For these purposes, the rock specimen used in Section 6.2 is remeshed by 10×24, 20×48, 40×96 and 50×120 zones (each with a height/width ratio of 2.4). With respect to the mesh used in the example in Section 6.2, which is 30×72, the former two are regarded as coarse meshes and the latter two as fine meshes. Using the same distribution function and associated parameters we examine the mesh effect by comparing the results produced by these remeshed models in terms of the fracture pattern and stress-strain curve.

6.3.1 Mesh effect with the degradation model

The numerical rock specimen model defined by the Weibull distribution function and the Hoek-Brown criterion in the previous section is simulated repeatedly by mesh sizes of 10×24, 20×48, 40×96 and 50×120 zones in addition to the mesh of 30×72 used previously. Figure 6.5 is the fracture pattern displayed by the five models. The corresponding stress-strain curves are shown in Figure 6.6.

These figures indicate that the model results are influenced by the mesh size. Generally, the coarser the mesh, the coarser the results (Figure 6.5). In terms of the fracture pattern, the coarser meshes produce fewer failed sites before the formation of the macroscopic fracture plane than do the finer meshes, while more fracture planes develop with the finer meshes than do with the coarser meshes. Correspondingly, the stress-strain curve given by the meshes becomes more brittle as the meshes become coarser (Figure 6.6).

With respect to the peak strength displayed by those models, it is general that the coarser models give lower peak strength values than do the finer models (Figure 6.6). An exclusive case is the model of 10×24, which predicts a higher peak strength value than others. This discrepancy lies in the minimum elemental strength distributed within the mesh. The elemental strength distributed within a finer mesh covers a wider range, in which a lower value may be included, than that in a coarse mesh. For example, the minimum strength value in the model of 10×24 is 96.48 MPa, but is less than 85.49 MPa in the other four models.

6.3.2 Optimal mesh size

As presented above, mesh sizes have an influence on the results produced by the degradation model, and in this subsection we deal with the issue of selecting the optimal mesh size for the analysis of a problem.

Examining again the results presented in Figures 6.5 and 6.6, it can be seen that a mesh smaller than 20×48 zones produces poor results in both the fracture patterns and the stress-strain curves, when compared with laboratory results. On the other hand,

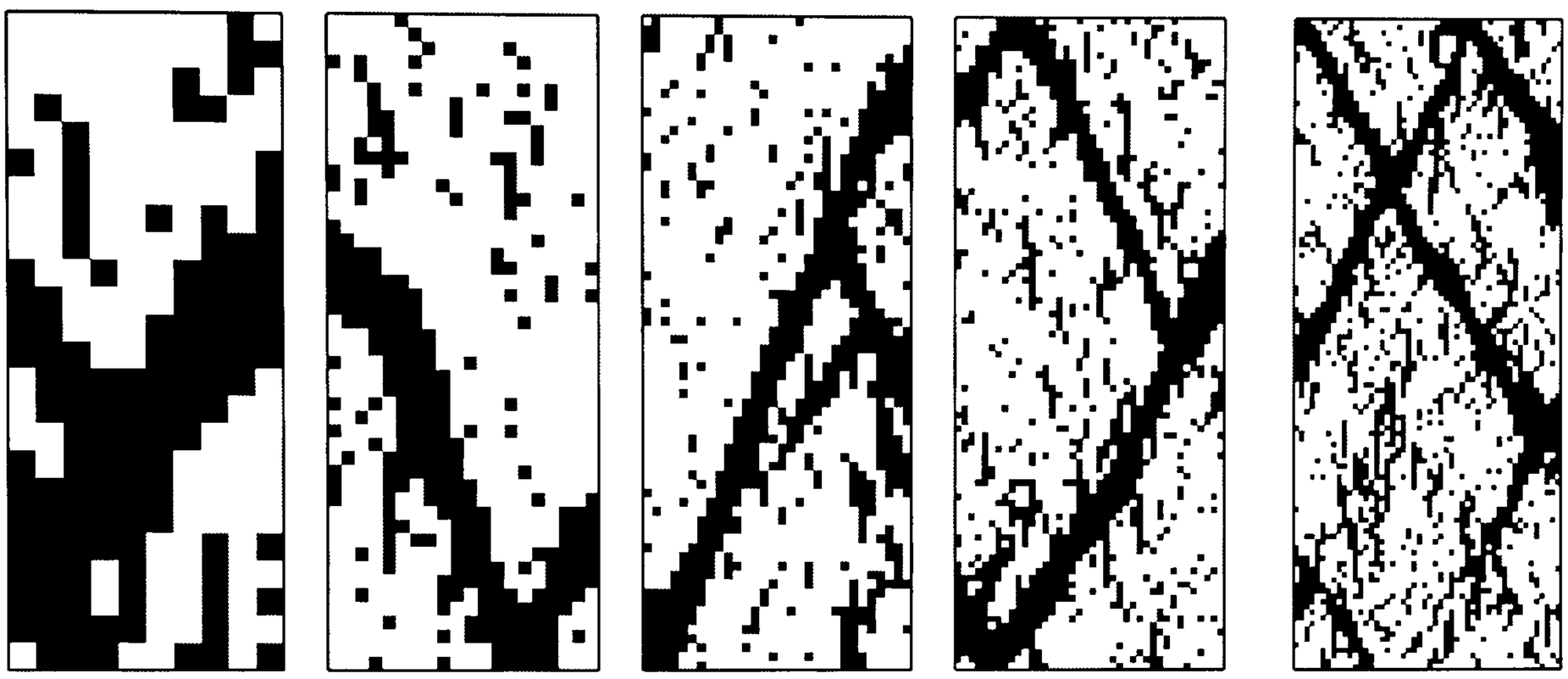


Figure 6.5. Fracture patterns displayed by models with different mesh sizes

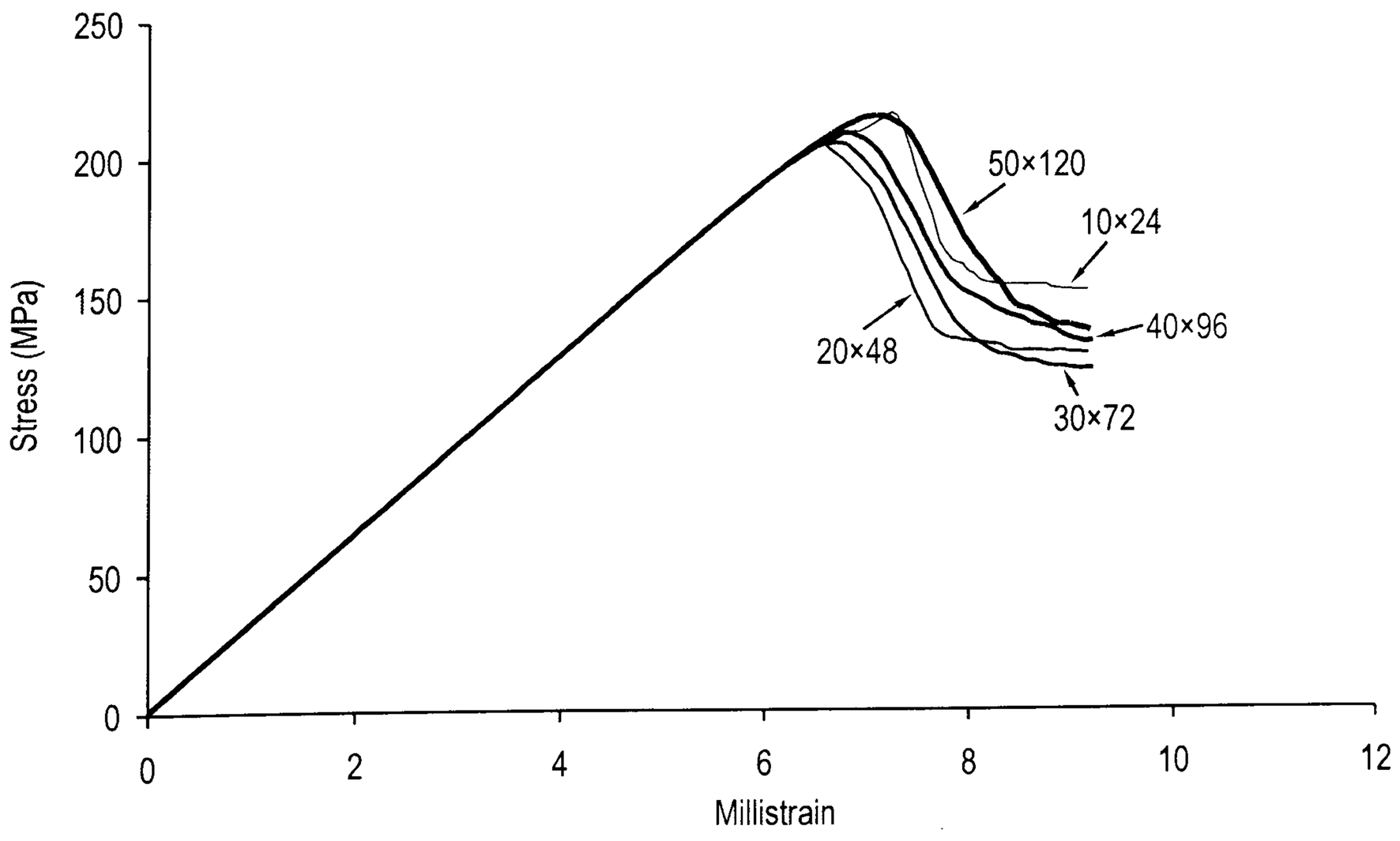


Figure 6.6. Stress-strain curves corresponding to models with different mesh sizes

although each of the finer meshes whose size is greater than 40×96 more smoothly captures the stress-strain curve, more fracture planes develop within the stressed rock specimen. It seems that only the mesh with a size of around 30×72 gives results that are in a good agreement with laboratory results in these three aspects. This may imply that the mesh size is associated with the length scale at which microcracks develop, and it is suggested that laboratory investigations are undertaken in future work to relate the mesh size to the length scale. Here, it is assumed that, with respect to the geometry of a rock specimen, the optimal mesh size is 20-40 zones transversely, and as a result most simulations performed in this chapter use a mesh size of 30×72 zones.

6.4 Role of degradation parameter n_d

In developing the degradation model in Chapter 4, we defined a degradation index to describe the local effects associated with dissipative processes (Subsection 4.3.4). The expression of the degradation index for rock elements contains the parameter n_d (Equation 4-37), whose value determines the value of the degradation index r_d. As the definition of the degradation index implies, values of n_d may be different from rock to rock. In this section, we investigate the influence of n_d on the model behaviour.

In Subsection 4.3.4, we showed that the value of n_d for Tennessee marble is 0.075 and for Vosges sandstone is 0.055 or so. As suggested by these, five values, *i.e.* 0.01, 0.03, 0.05, 0.07 and 0.10, are assigned to n_d and the model results examined in terms of the fracture pattern and the stress-strain curve. Figure 6.7 shows the fracture patterns predicted by the five different n_d-value models, and the stress-strain curves are presented in Figure 6.8.

With respect to the fracture patterns shown in Figure 6.7, we can see that the main fracture plane is not significantly influenced by n_d values. However, different n_d values result in differences in the development of microscopic processes. For example, the length of crack extension prior to coalescence increases as n_d decreases, and more diffused failed sites occur within a stressed rock body as n_d increases. As a result of these microscopic processes, discrepancies are displayed in the stress-strain relations produced by these models. With n_d increasing, both the peak strength and the residual strength of the model increase (Figure 6.8).

Figure 6.9 is the plot of the relation between the degradation index r_d and parameter n_d, against confining pressure. This shows that the degradation parameter n_d controls how fast the value of r_d approaches zero, corresponding to perfectly plastic behaviour,

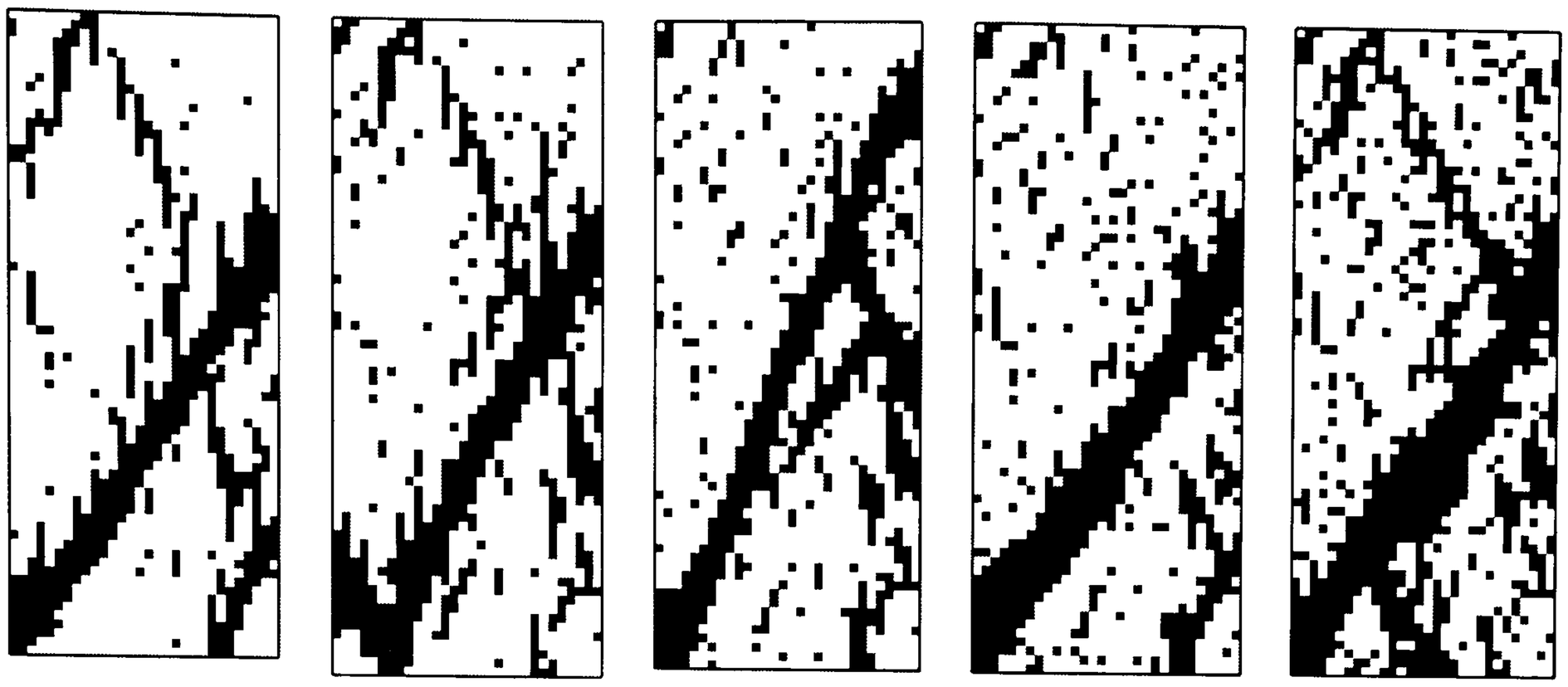


Figure 6.7. Fracture patterns displayed by models with different parameter n_d

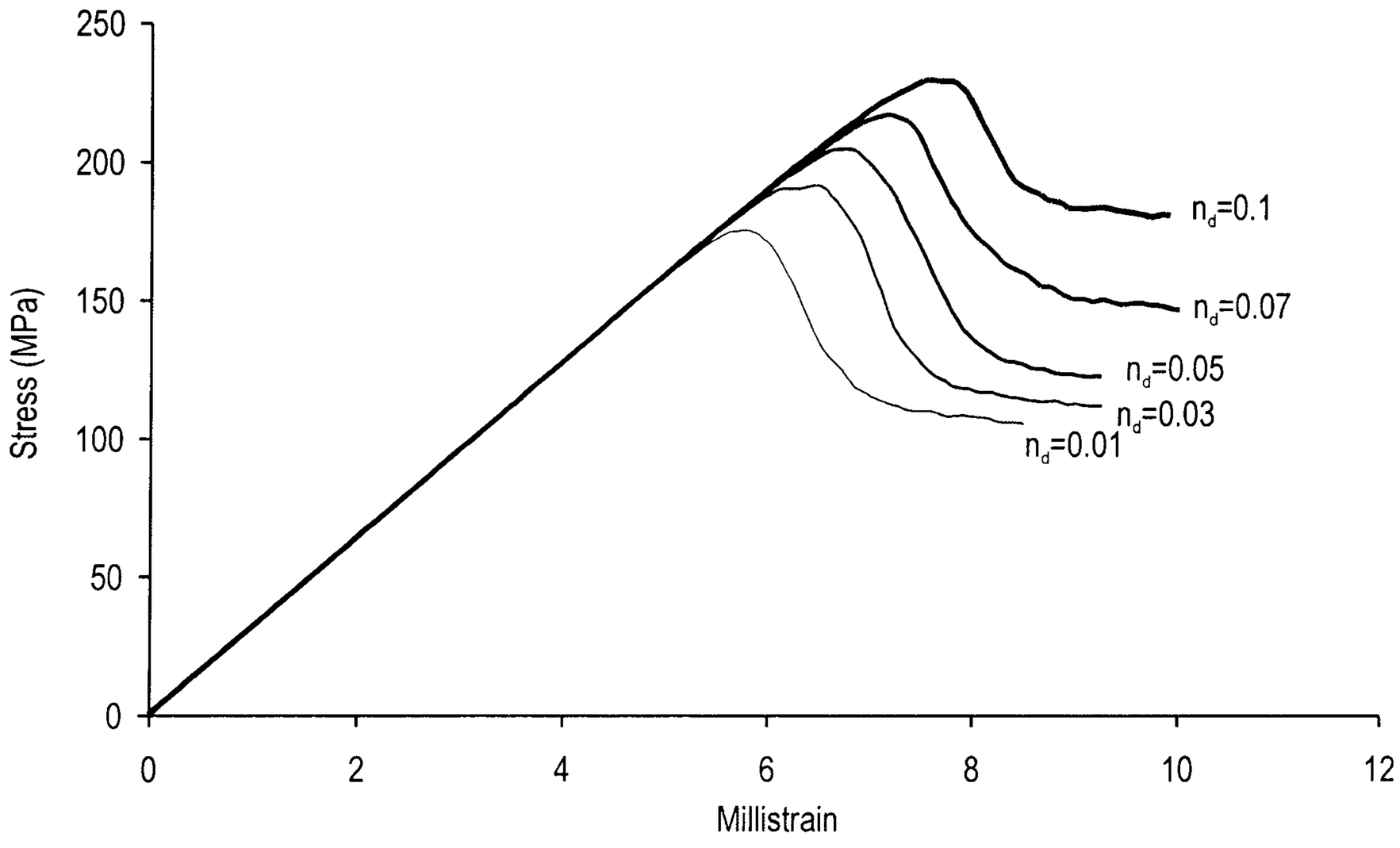


Figure 6.8. Stress-strain curves corresponding to models with different parameter n_d

with respect to confining pressure. For a specific confining pressure, the smaller n_d is, the larger r_d is, and the more degradation occurs to the material. When n_d increases, r_d approaches zero very rapidly and the material degrades little with increasing confining pressure (Figure 6.9).

These results suggest that, for an application of the degradation model to a specific problem the value for n_d should be determined through laboratory investigations. Here, as this is a general study of fracture process of rocks, the value of 0.05 is used for n_d.

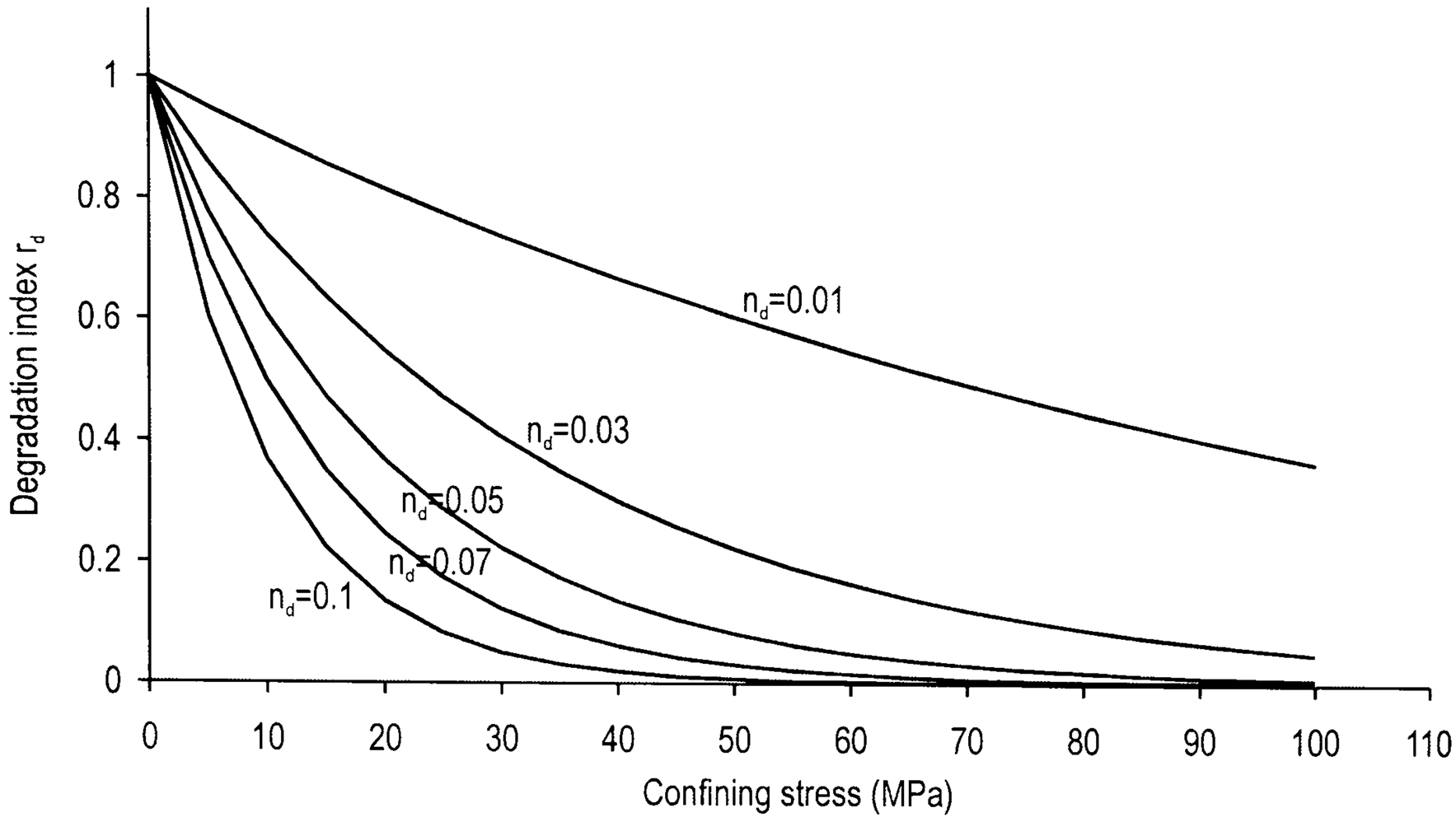


Figure 6.9. Illustration of the relation between the degradation index and confining stress

6.5 Influence of Weibull parameter m_w on simulated rock fracture

The previous sections have shown that the fracture process and associated macroscopic behaviour of heterogeneous rocks can be realistically reproduced by the degradation model. In this section we consider the influence of heterogeneity on rock fracture.

In the degradation model, the heterogeneity in material strength is represented by the Weibull distribution (Sections 4.6 and 6.2), in which the shape parameter m_w (Equation 4-77) plays a significant role. Simulations are therefore performed using the model with various values for this parameter, in order to investigate the independent influence of this parameter on rock fracture.

When the Weibull distribution function was introduced in Section 4.6, we presented the distribution shapes given by this function with various values for the shape parameter (Figure 4.13). The values for the shape parameter range from 1 to 5, which covers shapes ranging from the exponential distribution function (when m_w=1) to an approximation to the normal distribution (when m_w=5). These values are used to investigate the influence of parameter m_w on rock fracture, respectively, with other input data remaining the same as specified in Section 6.2. Figure 6.10 shows the fracture patterns produced by the five models.

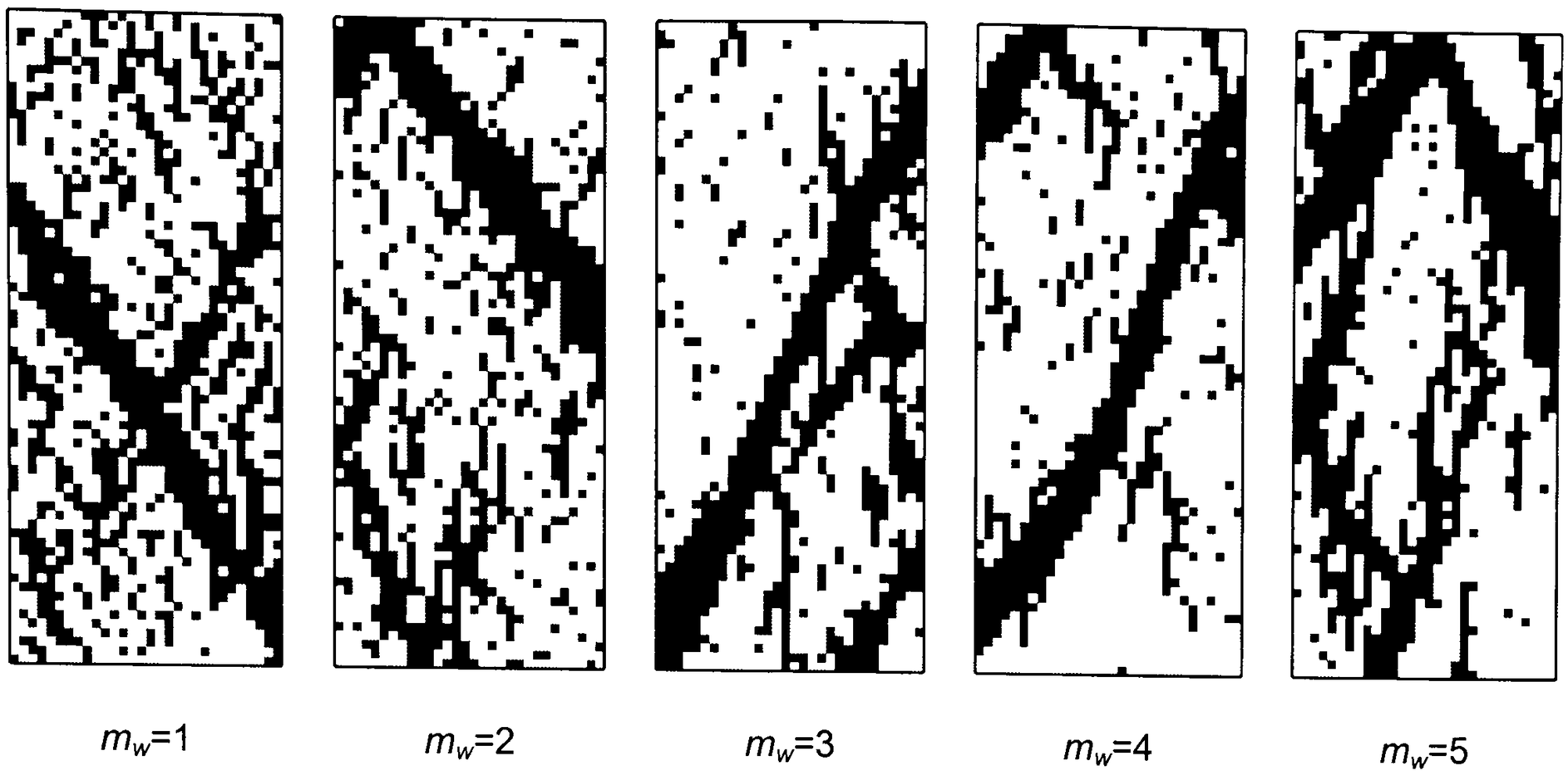


Figure 6.10. Fracture patterns displayed by models with different parameter m_w

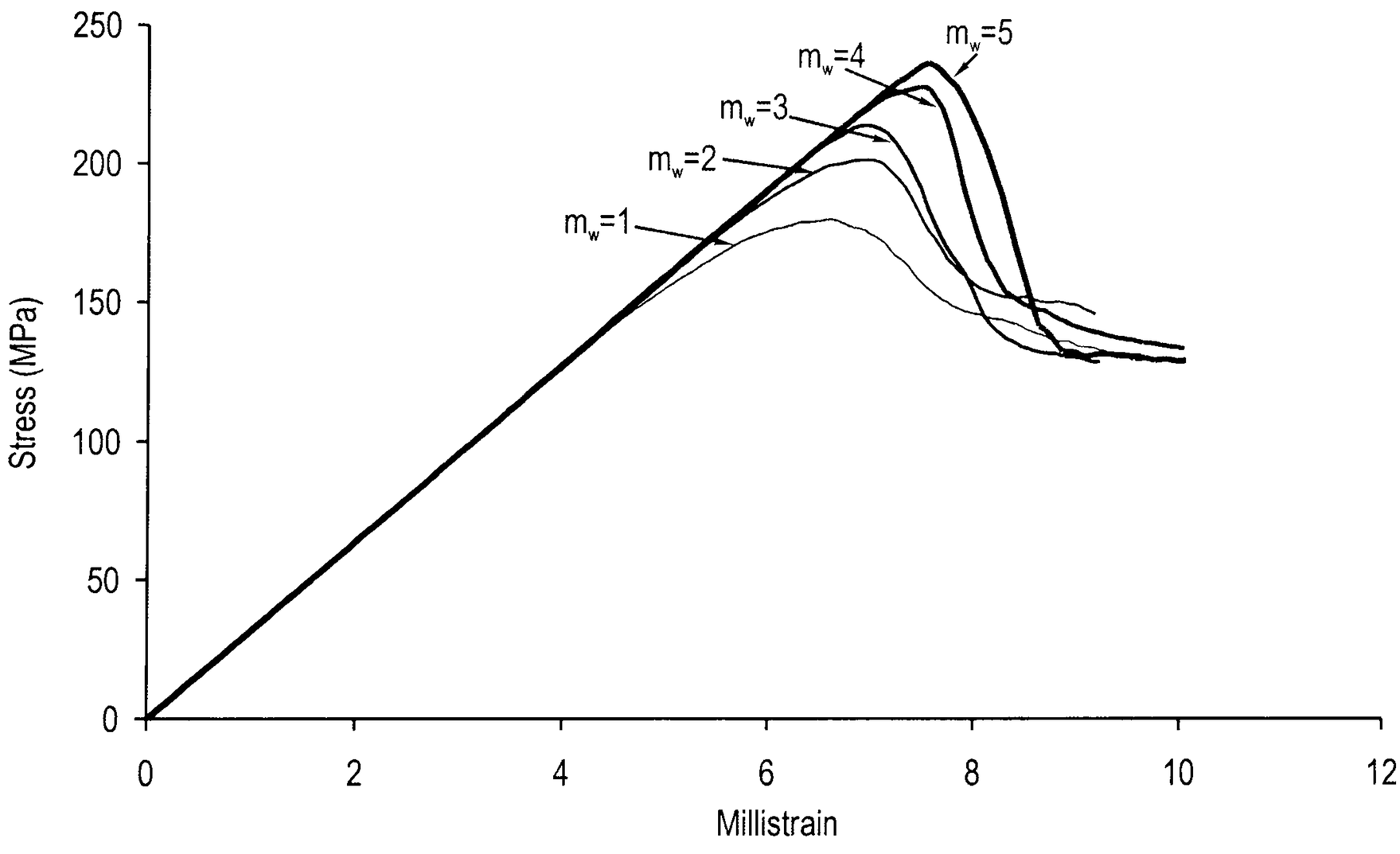


Figure 6.11. Stress-strain curves corresponding to models with different parameter m_w

From Figure 6.10, it is seen that the microscopic processes and the formation of the eventual fracture plane are determined by the distribution shape of elemental strengths. Thus, the number of diffused failed sites increases when m_w reduces, and as m_w increases, the angle of the eventual fracture plane tends to become sharp. Comparing the fracture patterns in Figure 6.10 with those displayed in Table 6.3, we find that the fracture patterns with m_w=1 and 2 are similar to those associated with the uniform distribution function (the second figure in the first row in Table 6.3), and that the

fracture pattern with m_w=5 is similar to that associated with the normal distribution (the second figure in the second row in Table 6.3). These results suggest that values of 2 to 4 for m_w are more appropriate for most rocks.

The corresponding stress-strain curves are shown in Figure 6.11. By relating each curve in Figure 6.11 to the corresponding fracture pattern in Figure 6.10, we can see that rock fracture patterns are related to brittleness in mechanical behaviour. Thus, the lower m_w is, the greater the number of failed sites, and the more ductile the model behaviour; the higher m_w is, the sharper the eventual fracture plane, and the more brittle the stress-strain curve. This suggests that hard (*i.e.* brittle) rock has a higher m_w value than soft (*i.e.* ductile) rock.

So far, we have investigated all the aspects of the influence of the components contained in the degradation model in describing brittle fracture of heterogeneous rocks. Now we can move on to fully explore the degradation model when applying it to the simulation of the fracture process of rock under various confining pressures. This is presented in the next section.

6.6 Simulated fracture process of heterogeneous rocks

In the previous section, we have identified that the Weibull distribution function is the most appropriate function to describe the heterogeneity of rock elemental strengths. It is further highlighted that the Hoek-Brown criterion gives the better predictions of rock elemental failure subject to various confining stresses. With respect to mesh effect, it is identified that 20-40 zones along the minimum dimension of a rock sample is optimal. In addition, we have investigated the influence of both the degradation parameter n_d and heterogeneity on rock failure, and found that both the n_d value and heterogeneity are correlated to the peak strength, failure pattern and stress-strain curve of a model, and n_d=0.05 and m_w=2 to 4 can be used for a general analysis of rock fracture.

Using the results from the investigations mentioned above, the fracture of heterogeneous rocks are fully explored in this section. This includes the complete fracture process from elemental scale to macroscopic scale, the associated stress-strain curve and the strain energy dissipation characteristics of a rock specimen subject to confining pressures of 0 MPa, 20 MPa and 60 MPa. It is shown in this section that the simulation results reproduced by the degradation model are close to the laboratory data presented in Chapter 2.

It should be noted that these results in this section refer to a simulated rock

specimen with an identical set of properties to those described for the Weibull distribution model in Section 6.2 (Table 6.2).

6.6.1 Fracture of a specimen at 0 MPa confining pressure

To begin, the fracture behaviour of a simulated rock specimen under uniaxial compression is investigated. Figure 6.12 shows the resulting simulated fracture process, and the corresponding stress-strain curve and strain energy dissipation characteristics

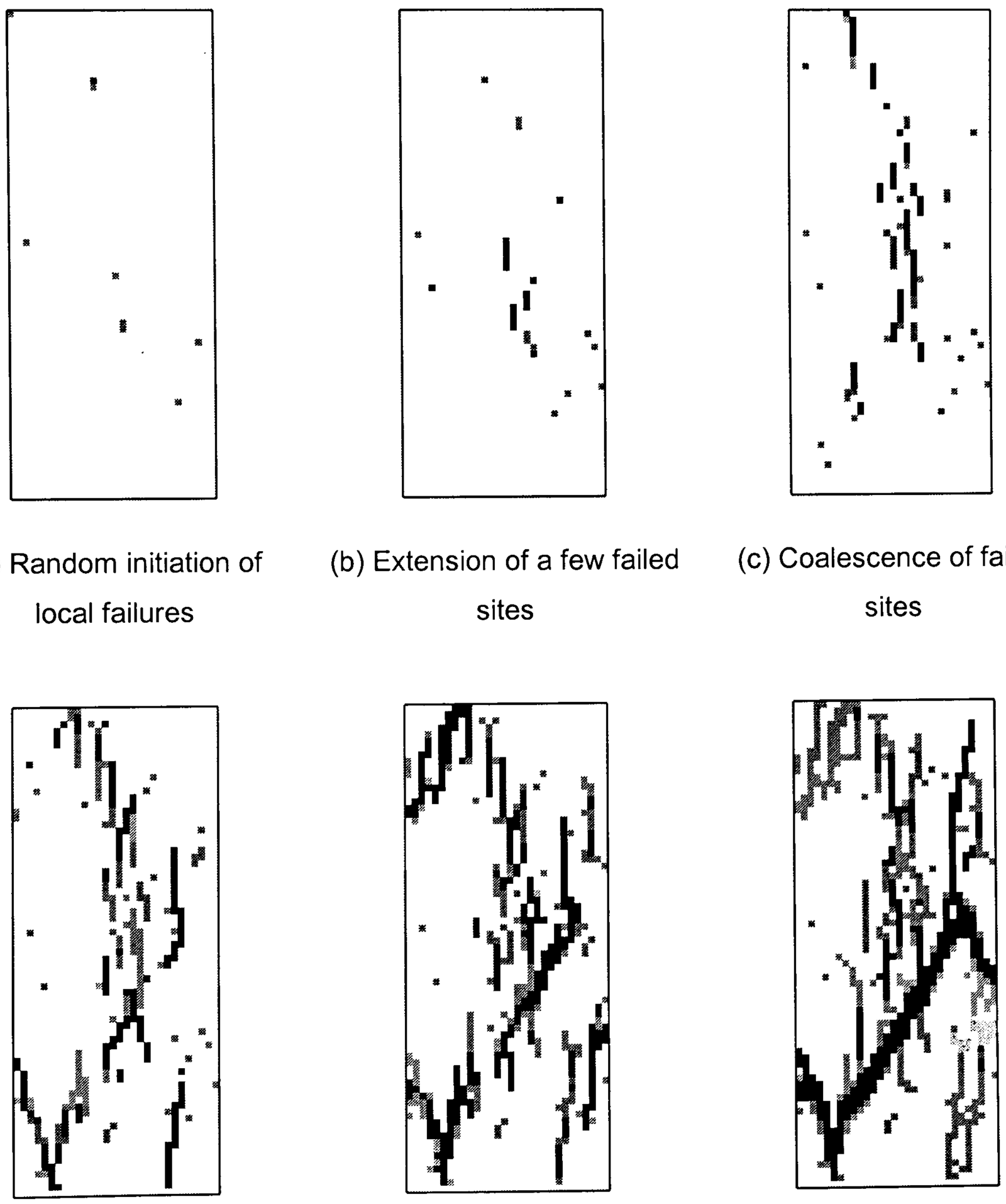


Figure 6.12. Simulated fracture process of a rock specimen under uniaxial compression

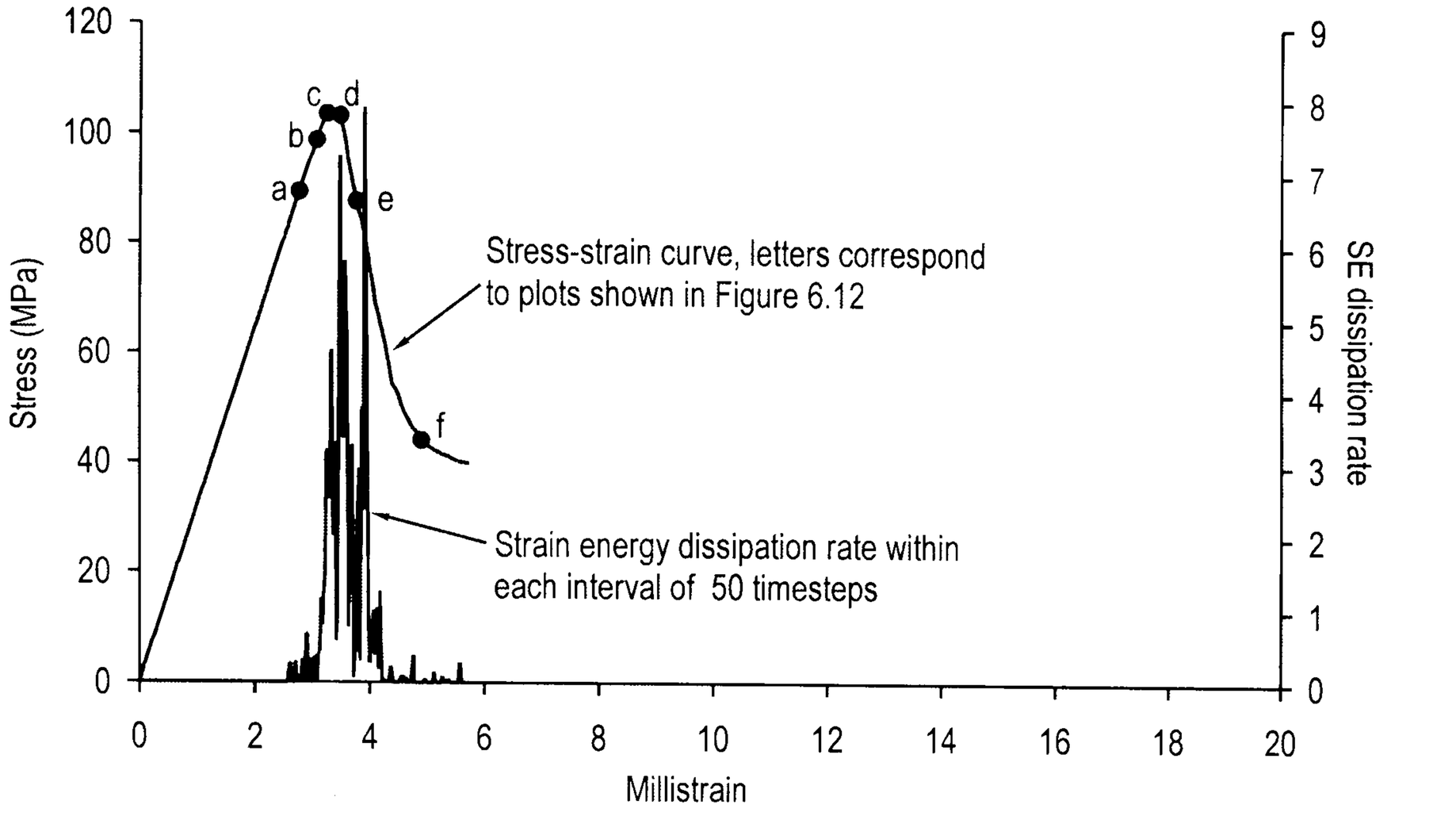


Figure 6.13. Simulated stress-strain curve and strain energy dissipation characteristics corresponding to the fracture process displayed in Figure 6.12

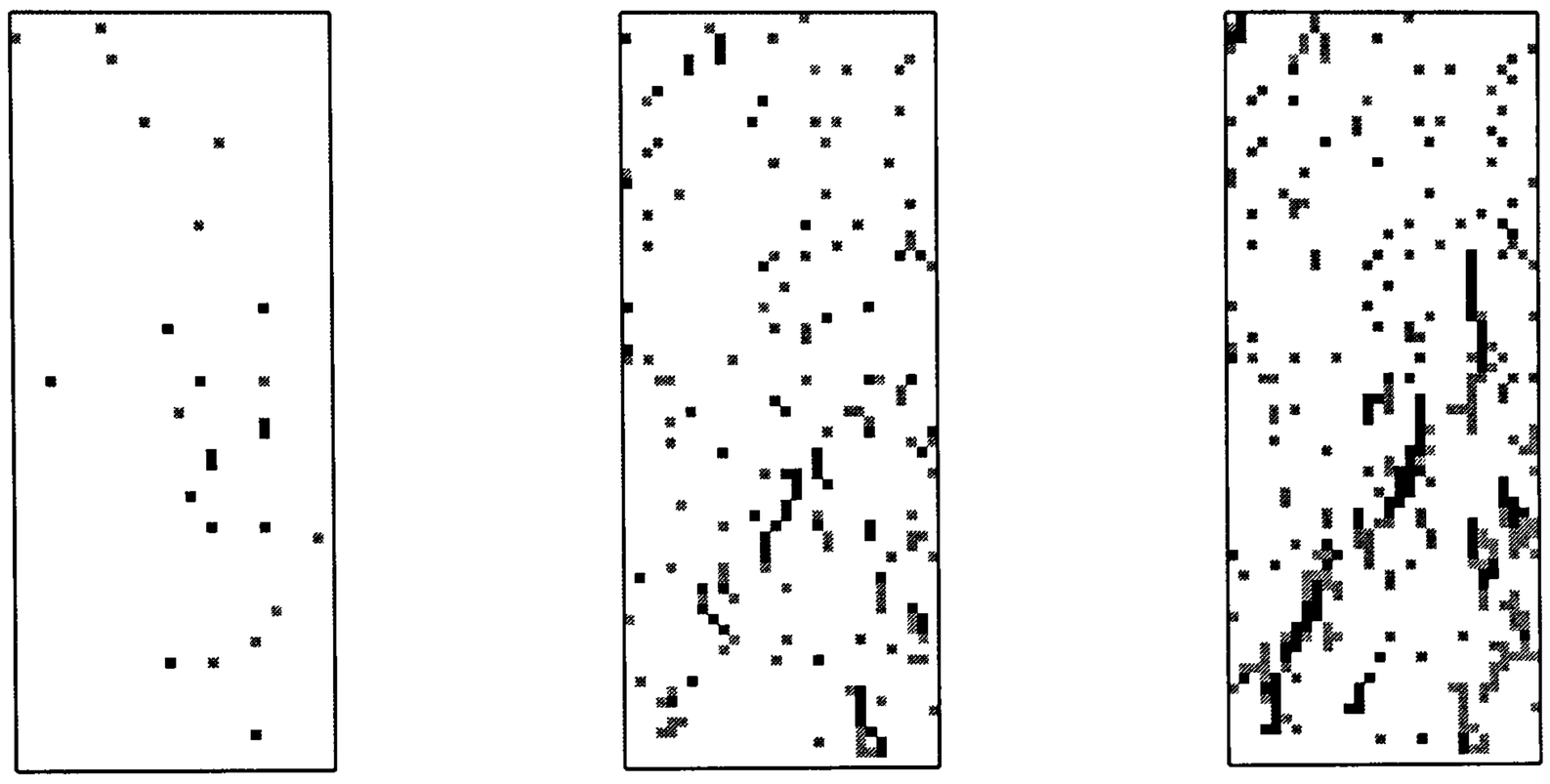
are shown in Figure 6.13.

As indicated in Figure 6.12, at a strain level of 2.5‰ (corresponding to an axial stress of 88.9 MPa, point *a* in Figure 6.13), local failures are initiated at a few sites (Figure 6.12(a)). With a very little increase in axial strain, along with new sites failing, some of the previously failed sites extend in the direction parallel to the major principal stress (Figure 6.12(b)), resulting in the stress-strain curve deviating from linearity (point *b* in Figure 6.13). This process continues up to the peak (point *c* in Figure 6.13), when linkage starts to take place between elongated failed sites (Figure 6.12(c)). Further increases in axial strain lead to a further increase in the elongation and coalescence of the failed sites (Figure 6.12(d)), corresponding to a rapid dissipation of strain energy (corresponding to point *d* in Figure 6.13), and the stress-strain curve descends (point *d* in Figure 6.13), followed by a rapid development in the formation of a macroscopic fracture plane (Figure 6.12(e)). Finally, the eventual failure of the specimen is symbolised by disintegration of the specimen into pieces by a combination of axial splitting and local shearing (Figure 6.12(f)), with the energy dissipation reducing down to zero (corresponding to point *f* in Figure 6.13).

6.6.2 Fracture of a specimen at 20 MPa confining pressure

At a confining pressure of 20 MPa, the rock specimen fails more progressively than

does the unconfined rock specimen. Figure 6.14 shows the simulated fracture process of the specimen with the corresponding stress-strain curve and the energy dissipation characteristics illustrated in Figures 6.15. Compared with Figure 6.12, after initiation of local failure at various sparse sites at a strain level of 4.5‰ (see the energy dissipation rate characteristics in Figure 6.15), the failed sites do not tend to extend until more failed sites are induced (comparing Figures 6.14(a) and (b)). When the diffused failed



(The grey zones indicate previous failed sites and the dark zones represent sites currently undergoing failure)

Figure 6.14. Simulated fracture process of a rock specimen subjected to a confining pressure of 20 MPa

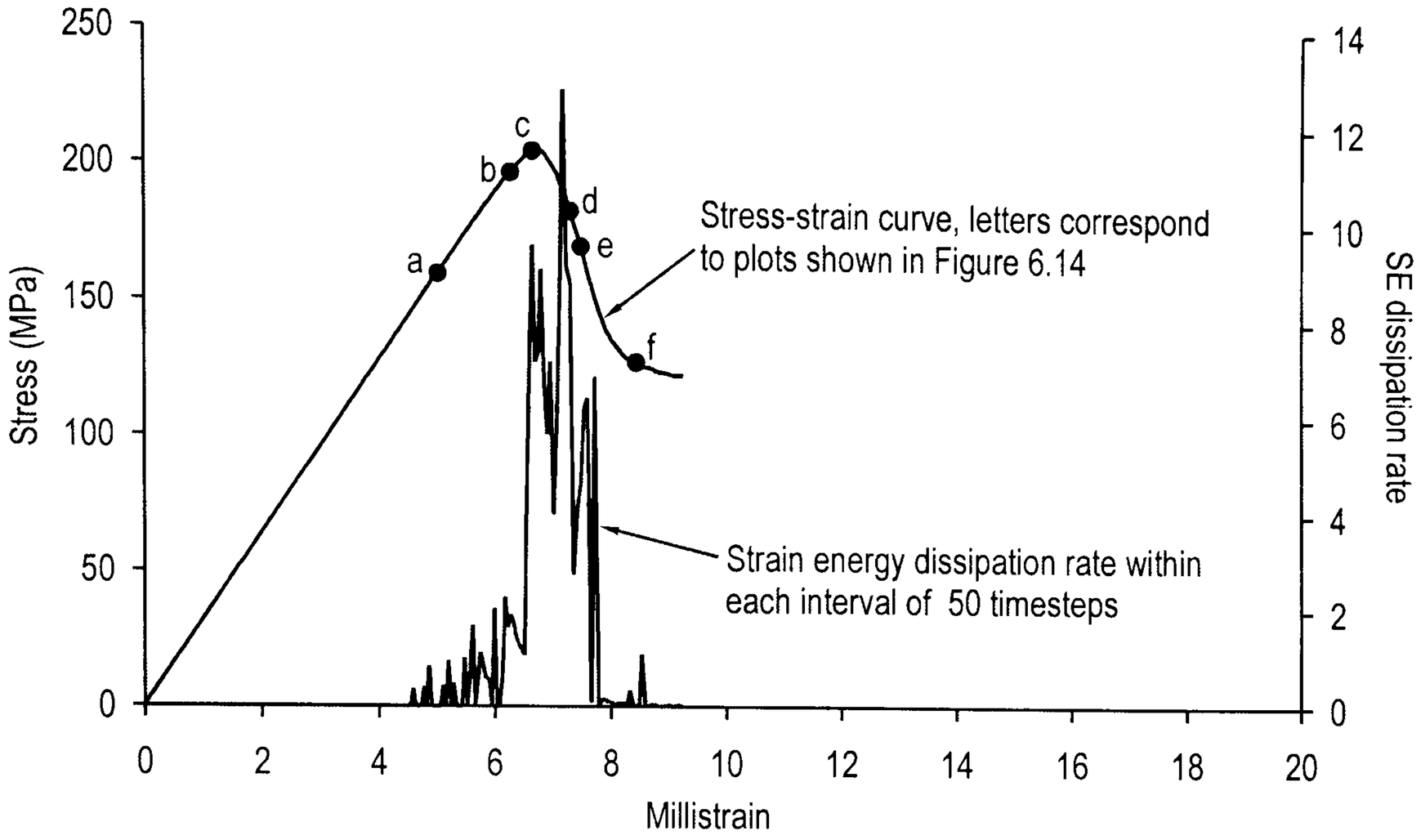


Figure 6.15. Simulated stress-strain curve and strain energy dissipation characteristics corresponding to the fracture process displayed in Figure 6.14

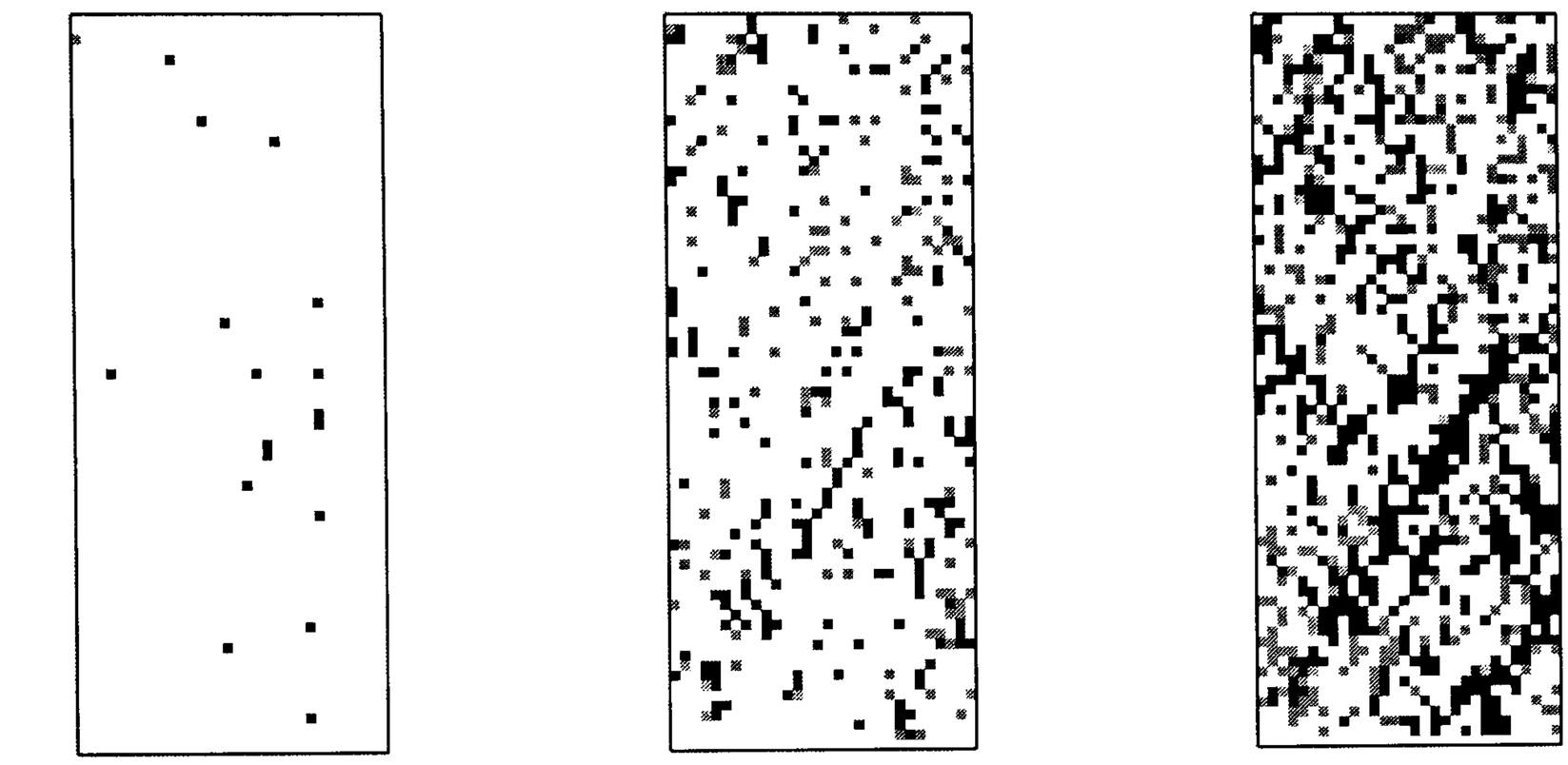
sites become dense, extensile cracks are propagated from a number of the failed sites, and *en echelon* arrays of cracks develop (Figure 6.14(b)), and correspondingly the stress-strain curve diverts from linearity. A further increment in axial strain causes these cracks to tend to link with each other (Figure 6.14(c)), corresponding to the peak strength of the specimen (point *c* in Figure 6.15). Subsequent increase in strain enhances the linkage between failed sites to form a macroscopic shear fracture plane (Figure 6.14(d)), and the stress-strain curve descends rapidly together with the energy dissipation rate reaching a maximum (around point *d* in Figure 6.15). The shear fracture plane continues to grow (Figure 6.14(e), corresponding to point *e* in Figure 6.15). Finally, at point *f* in Figure 6.15, the formation of the macroscopic shear fracture plane is complete (Figure 6.14(f)), with the energy dissipation dying off (corresponding to point *f* in Figure 6.15) and the specimen failing completely by a single shear fracture plane (Figure 6.14(f)).

6.6.3 Fracture of a specimen at 60 MPa confining pressure

Figures 6.16 and 6.17 show the fracture process, the corresponding stress strain curve and the dissipated strain energy when the rock specimen is subjected to a confining pressure of 60 MPa.

From Figure 6.16(a), we can see that elemental failure is initiated at a strain level of 5.8‰ (see the first appearance of strain energy dissipation in Figure 6.17). When the

axial stress increases to 317 MPa (10.34‰ strain, point *b* in Figure 6.17), the failed sites become dense and a few sites extend short distances to form arrays of cracks (Figure 6.16(b)), with the corresponding stress-strain curve starting to divert from linearity (point *b* in Figure 6.17). Figure 6.16(c) shows the failed sites beginning to coalesce and form local shear bands. Subsequently, a macroscopic shear band forms (Figure 6.16(d), corresponding to the specimen's peak strength (point *d* in Figure 6.17). Note that the peak energy dissipation rate occurs prior to the peak strength (see the strain energy



(a) Random initiation of local failures

(b) Formation of *en echelon* crack arrays

(c) Coalescence of arrayed cracks

(d) Formation of macroscopic fractures

(e) Completion of macroscopic fractures

(The grey zones indicate previous failed sites and the dark zones represent sites currently undergoing failure)

Figure 6.16. Simulated fracture process of a rock specimen subjected to a confining pressure of 60 MPa

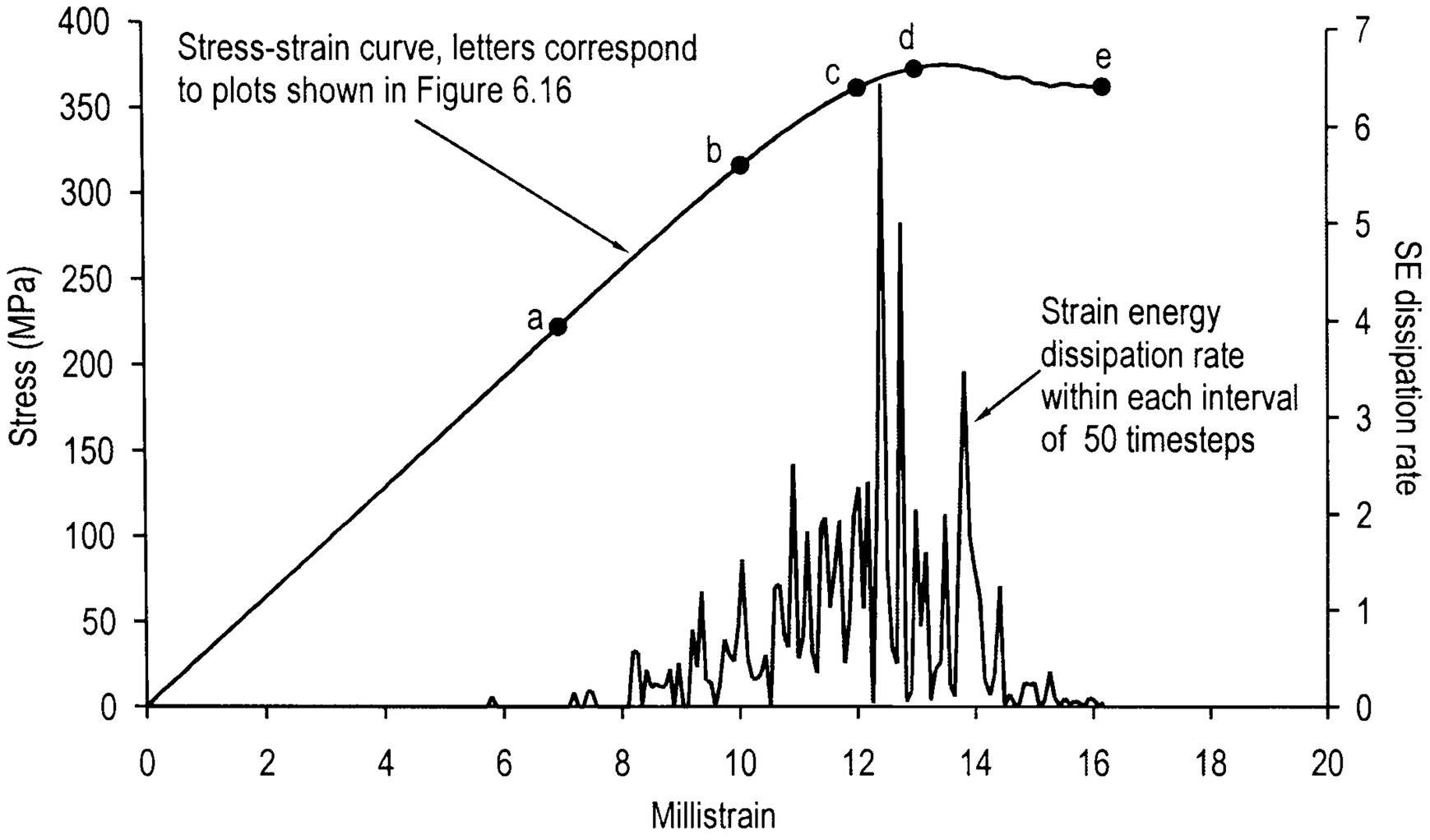


Figure 6.17. Simulated stress-strain curve and strain energy dissipation characteristics corresponding to the fracture process displayed in Figure 6.16

dissipation rate prior to point *d* in Figure 6.17). Further increments in axial strain tends to widen the shear bands (Figure 6.16(e)), the strain energy dissipation tends to diminish (corresponding to point *e* in Figure 6.17), and the material behaves in a ductile fashion due to the localised deformation within the widened shear band (Figure 6.17).

6.7 Remarks

In the previous section, the complete fracture process, from elemental scale to macroscopic scale, of rock specimens under compression and subjected to various confining pressures are simulated using the degradation model. In this section, we validate the degradation model by comparison of the simulation results with respect to laboratory data, in terms of the microscopic process, formation of fracture planes, fracture plane angle, stress-strain curve, and strain energy dissipation characteristics.

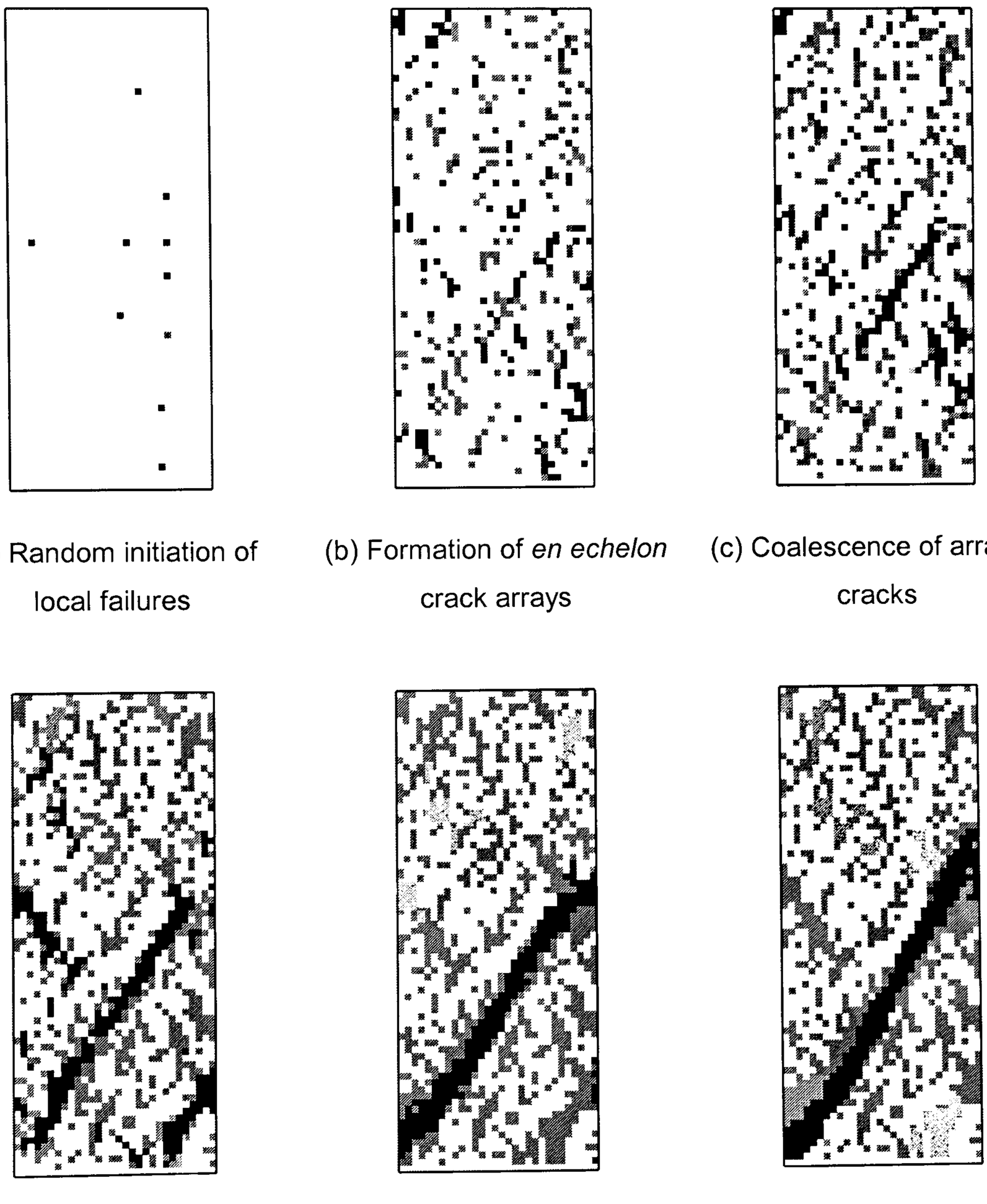
In order to describe the features of the degradation model over a wider range of confining pressures, two additional simulations at confining pressures of 40 MPa and 80 MPa are performed. Figures 6.18 and 6.19 show the fracture patterns and the associated stress-strain curve and energy dissipation rate displayed by the model at a confining pressure of 40 MPa. Figures 6.20 and 6.21 give the corresponding results at a confining pressure of 80 MPa. The full suite of results (*i.e.* confining pressures of 0, 20, 40, 60

and 80 MPa) is referred to in the subsection below.

6.7.1 Microscopic processes

Isolated microscopic processes

Laboratory results have established that rock fracture is preceded by isolated microscopic processes (Sections 2.1 and 2.2). It is observed that microscopic processes



(a) Random initiation of local failures

(b) Formation of *en echelon* crack arrays

(c) Coalescence of arrayed cracks

(d) Formation of macroscopic fractures

(e) Further development of macroscopic fractures

(f) Completion of macroscopic fractures

(The grey zones indicate previous failed sites and the dark zones represent sites currently undergoing failure)

Figure 6.18. Simulated fracture process of a rock specimen subjected to a confining pressure of 40 MPa

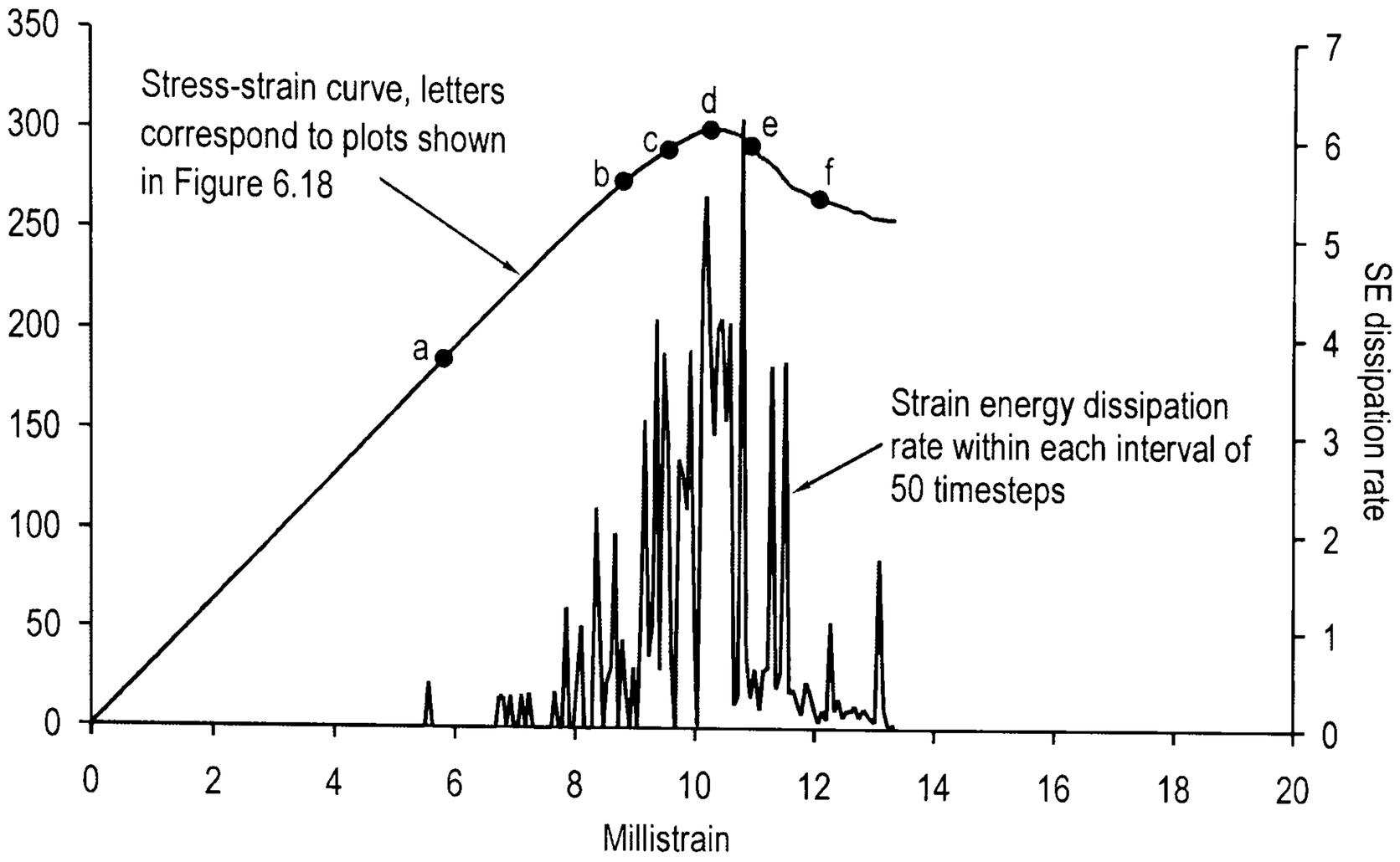
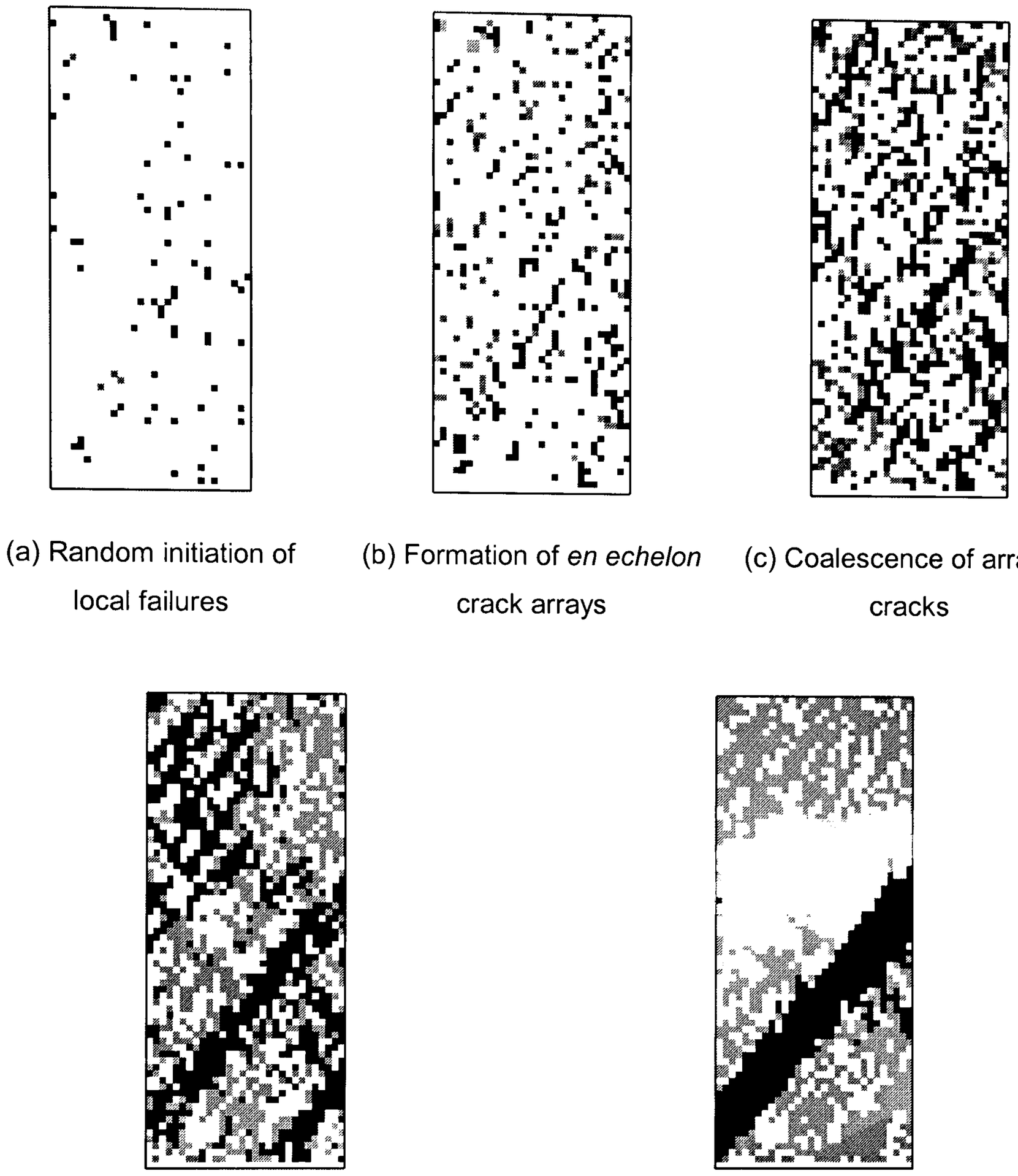


Figure 6.19. Simulated stress-strain curve and strain energy dissipation characteristics corresponding to the fracture process displayed in Figure 6.18

start from random initiation and develop with extension of microcracks into the formation and coalescence of arrayed cracks. It is also observed that the degree of crack extension is influenced by the presence of the confining pressure (Section 2.4).

The degradation model is capable of predicting these microscopic processes. Local failures are initiated at a strain level well before the peak (Figures 6.12(a), 6.14(a), 6.16(a), 6.18(a) and 6.20(a)). With increased loading, along with new failure sites occurring, some of failed sites extend in the direction of the major principal stress and cause crack arrays to form (Figures 6.12(b), 6.14(b), 6.16(b), 6.18(b) and 6.20(b)). Further loading causes coalescence of arrayed cracks (Figures 6.12(c), 6.14(c), 6.16(c), 6.18(c) and 6.20(c)) and development of macroscopic fracture planes.

In addition, the degradation model predicts the influence of confining pressure on the microscopic processes. As the confining pressure increases, the axial strain level at which local degradation is initiated increases (comparing the first occurrence of the strain energy dissipation rate in Figures 6.13, 6.15, 6.17, 6.19 and 6.21), the number of degraded sites at the peak strength point increases (comparing the marked sites in Figures 6.12(c), 6.14(c), 6.16(d), 6.18(d) and 6.20(d)), and the extension of failed sites is suppressed by the confining pressure (comparing Figures 6.12(b) and (c) with Figures 6.14(b) and (c), 6.16(b) and (c)). Figure 6.22 shows the first two trends.



(a) Random initiation of local failures

(b) Formation of *en echelon* crack arrays

(c) Coalescence of arrayed cracks

(d) Formation of macroscopic fractures

(e) Completion of macroscopic fractures

(The grey zones indicate previous failed sites and the dark zones represent sites currently undergoing failure)

Figure 6.20. Simulated fracture process of a rock specimen subjected to a confining pressure of 80 MPa

Formation of fracture plane

The formation of fracture planes from coalescence of arrayed cracks has been described by many researchers through laboratory observations (Peng and Johnson, 1972; Hallbauer, et al., 1973), and Lockner et al. (1991) detected the forming of a shear fracture plane by locating the acoustic emission events (Figure 2.27 in Chapter 2). It is interesting to describe this process using stage degradation events. The dark sites in

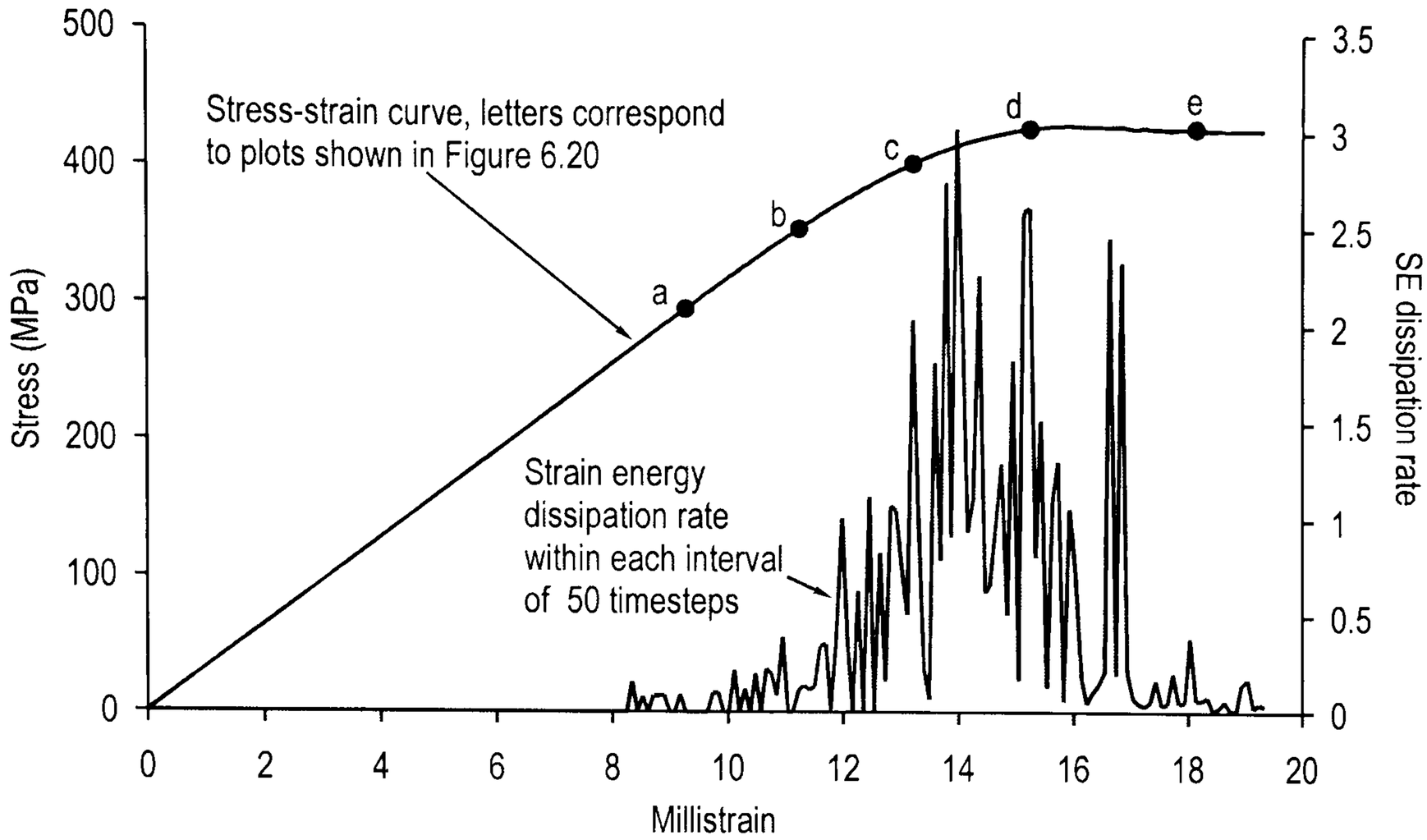


Figure 6.21. Simulated stress-strain curve and strain energy dissipation characteristics corresponding to the fracture process displayed in Figure 6.20

Figures 6.12, 6.14, 6.16, 6.18 and 6.20 represent these sites that have undergone degradation within the latest 50 timesteps during the simulation. These degradation events in Figure 6.14 are summarised in Figure 6.23, and comparing these to the map of acoustic emission events shown in Figure 2.27, the formation process of fracture planes is clearly demonstrated by the degradation model, *i.e.* random initiation of local failures

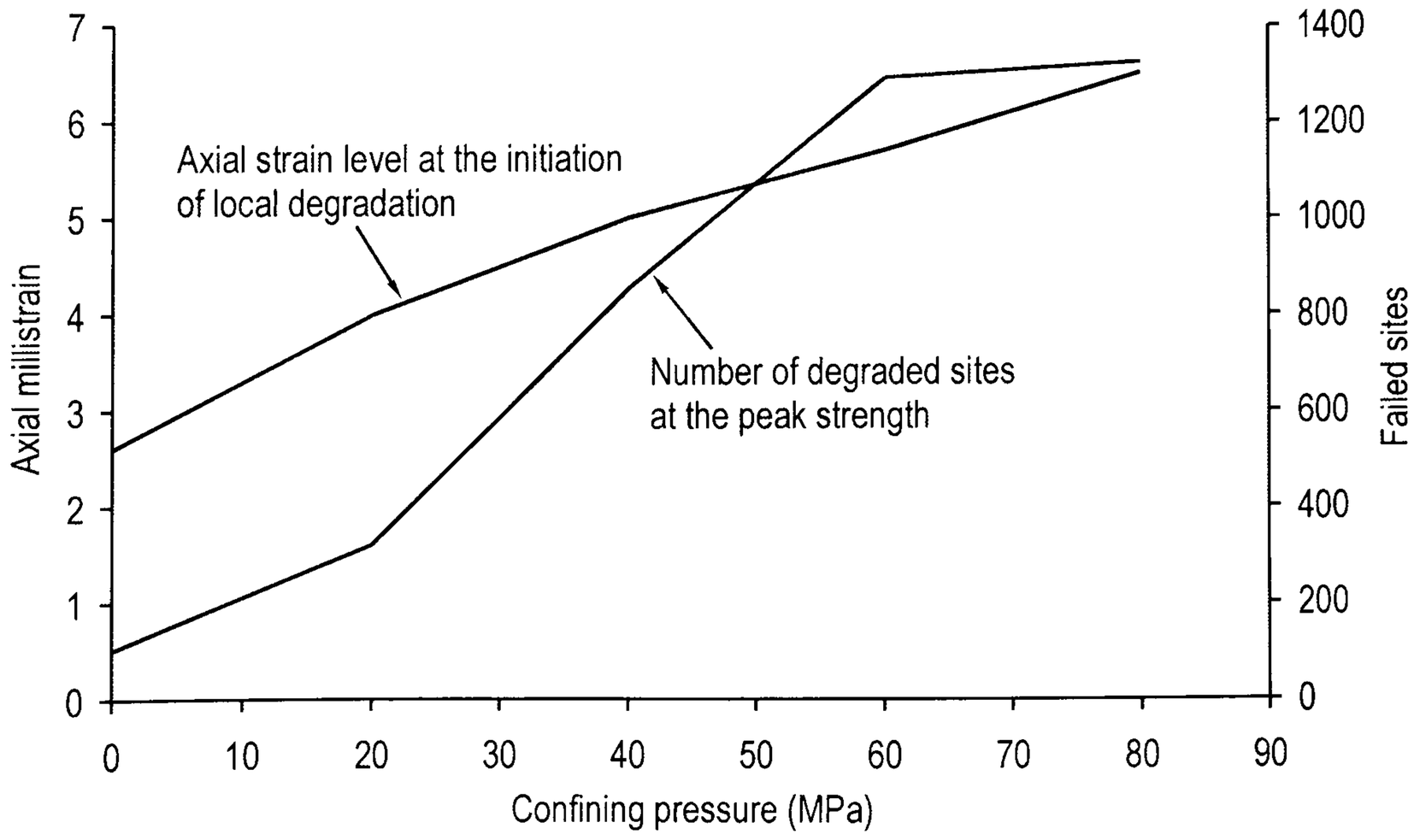
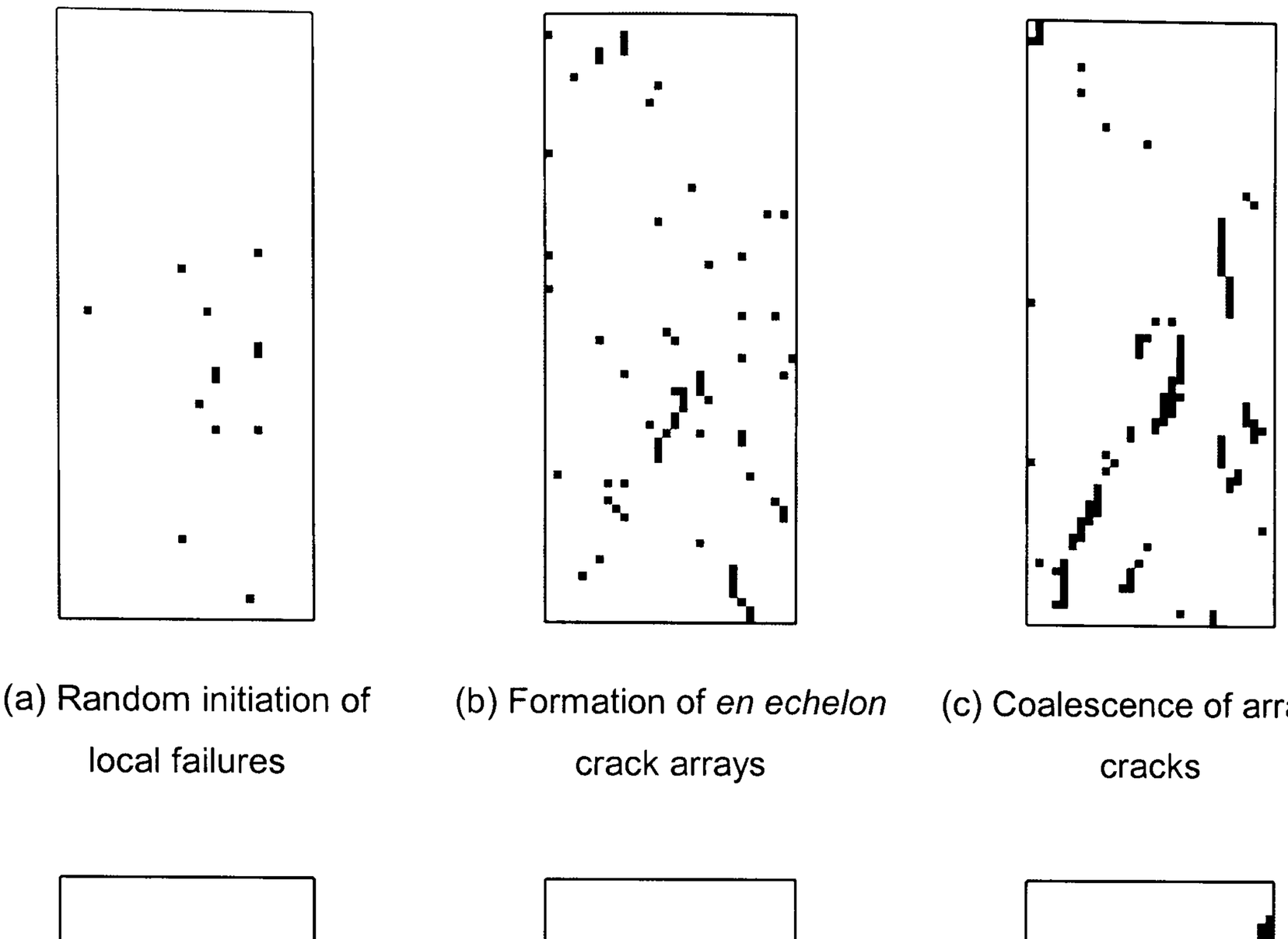


Figure 6.22. Influence of confining pressure on the initiation of local degradation and on the number of degraded sites at the peak strength



(a) Random initiation of local failures

(b) Formation of *en echelon* crack arrays

(c) Coalescence of arrayed cracks

(d) Formation of macroscopic fractures

(e) Further development of macroscopic fractures

(f) Completion of macroscopic fractures

(Stage letters corresponds to the points in Figure 6.15)

Figure 6.23. Isolated fracture process of the rock specimen simulated under 20 MPa confining compression

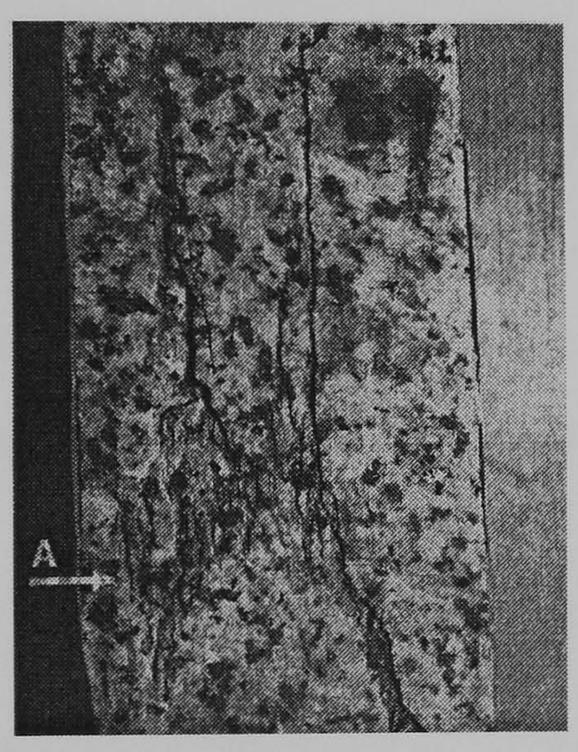
(Figure 6.23(a)), extension (Figure 6.23(b)) and coalescence (Figure 6.23(c)) of the failed sites, and formation of the shear fracture plane (Figures 6.23(d), (e) and (f)).

6.7.2 Final fracture patterns

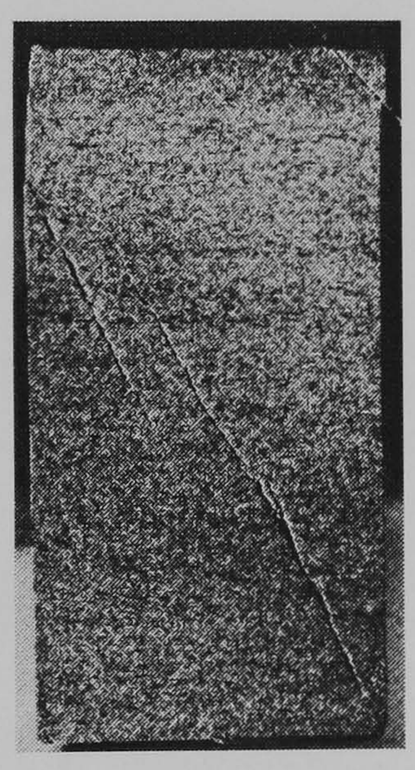
Laboratory investigations have concluded that the coalescence of cracked or weakened sites leads to the formation of eventual fracture planes or shear bands within a rock specimen under compression (Subsection 2.1.3). In uniaxial compression, the collapse

of a rock specimen is often manifested by extensile fracture (see Figures 2.3 and 2.4; also see Paterson, 1978; Andreev, 1995). At low confining pressures, the eventual failure of a specimen is mainly characterised by a single or several shear fracture planes (see Figure 2.5; also see Ramez, 1967; Donath, 1971; Paterson, 1978; Jaeger and Cook, 1979; Andreev, 1995; Bésuelle et al., 2000). At higher confining pressures, the appearance of intense deformation is exhibited by a ductile fault (Donath, 1971), which is a sharply defined shear fracture that has broadened into a shear zone (Paterson, 1978).

The degradation model captures these features. Figure 6.24 represents a few final failure patterns displayed both by a real rock in the laboratory and by a simulated rock with the degradation model, subjected to different confining pressures. These figures are shown in pairs and by comparing each pair of figures, it is easy to see how similar the



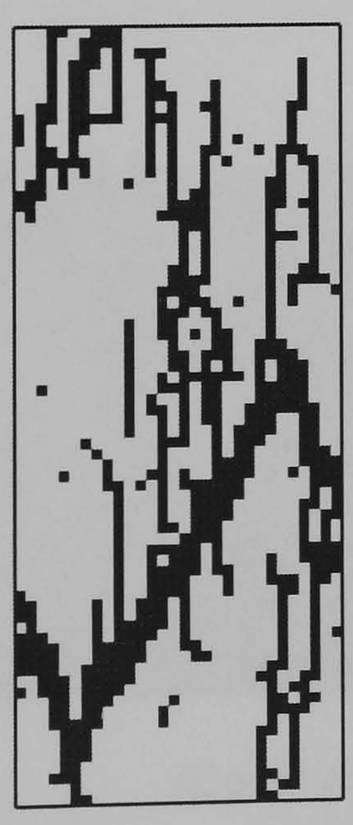
Unconfined (Andreev, 1995)



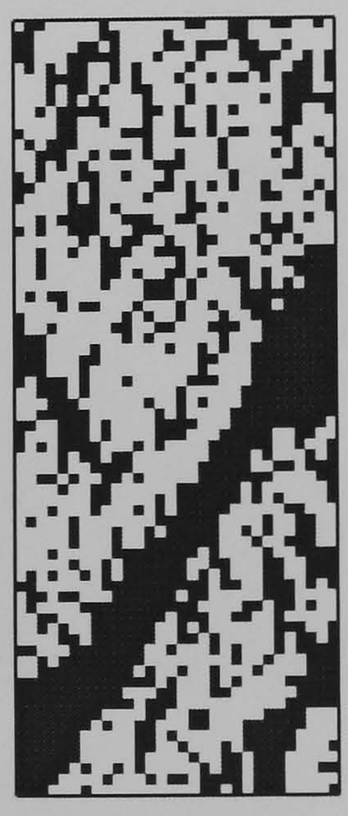
Moderately confined (Vardoulakis et al., 1995)



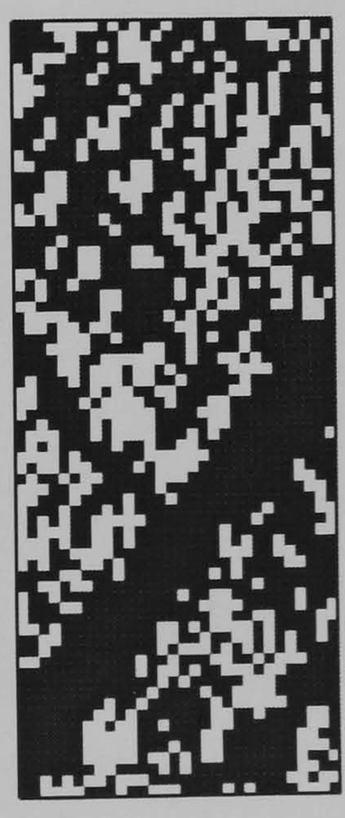
80 MPa confining pressure (Donath et al., 1971)



Unconfined



40 MPa confining pressure



80 MPa confining pressure

Figure 6.24. Final fracture patterns of real and simulated rock under various confining pressures

simulation results are to laboratory results.

6.7.3 Angle of fracture planes

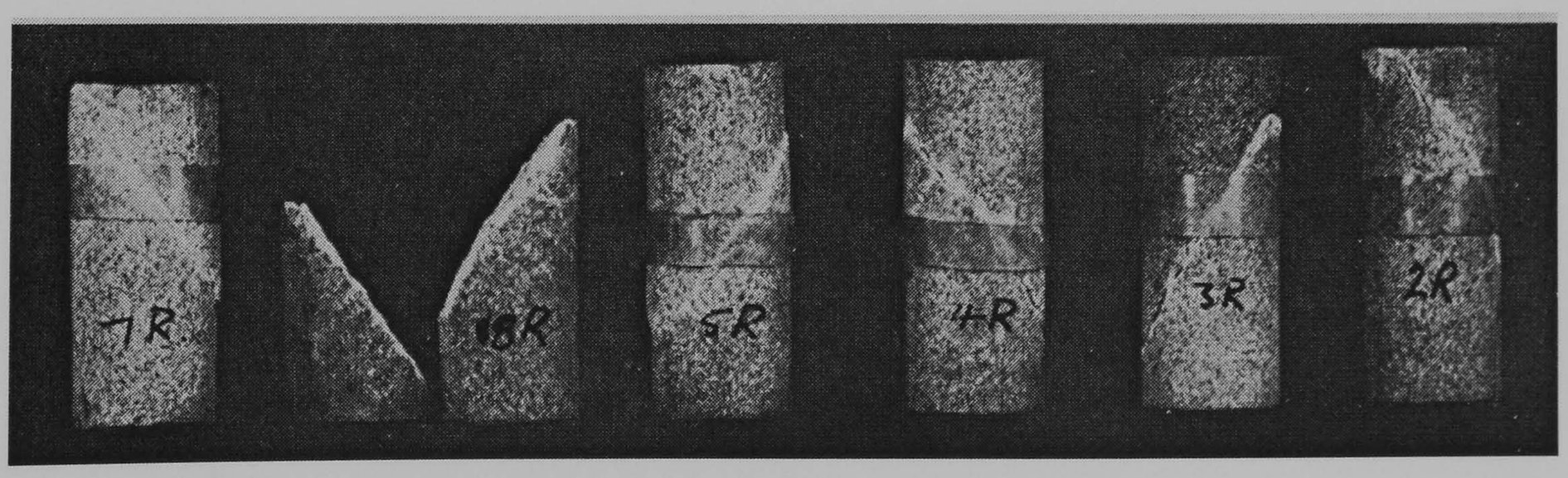
In general, the shear fractures developed during triaxial compression tend to occur at a fairly well-defined angle, usually between 20° and 30° to the direction of the major principal stress (Paterson, 1978), although the specific fracture angle often increases with increasing confining pressure (Ramez, 1967; Wawersik and Fairhurst, 1970; Paterson, 1978; Bésuelle et al., 2000). Figure 6.25 shows a set of fractured sandstone specimens tested by Ramez (1967), which indicates the slight changes in fracture angles subjected to variations in confining pressure.

Figure 6.26 shows the eventual fracture planes of the simulated rock under confining pressures of 20 MPa, 40 MPa, 60 MPa and 80 MPa, respectively. A sharp shear fracture plane with a small angle forms at a confining pressure of 20 MPa (Figure 6.26(a)), and a notable increase in the angle is seen at a confining pressure of 40 MPa (Figure 6.26(b)). When the confining pressure increases to 60 and 80 MPa, the angle of the shear plane of the specimen increases a little further (Figures 6.26(c) and (d)). Figure 6.27 shows the variation of the fracture plane angle against confining pressure.

6.7.4 Macroscopic stress-strain curve

General relation between the curve and the microscopic processes

As reviewed in Sections 2.1.3 and 2.4.2, the macroscopic stress-strain behaviour displayed by a rock in compression is generally non-linear, and the non-linearity of the curve is closely related to microscopic processes. The hardening range corresponds to

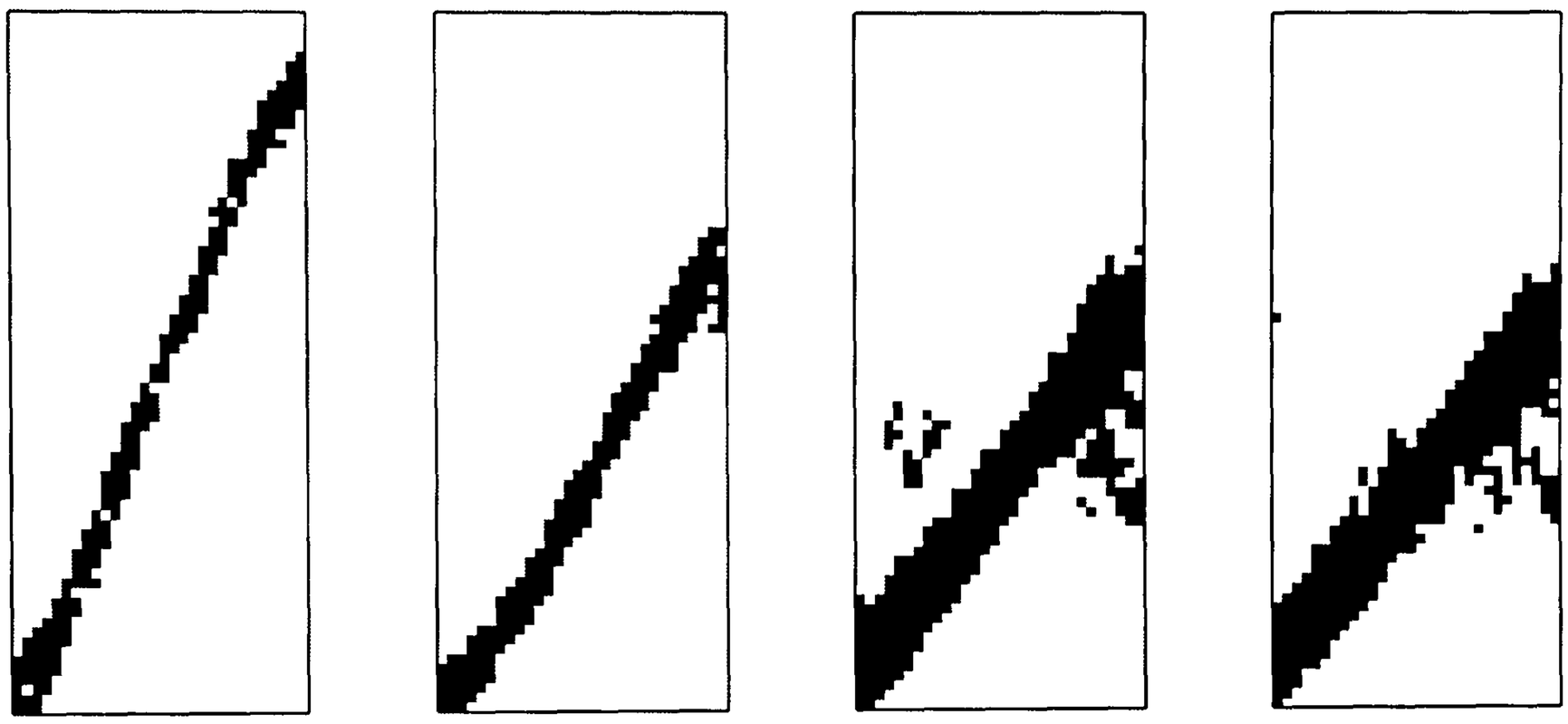


(Confining pressure: 17 MPa for 2R; 24 MPa for 3R; 52 MPa for 4R; 69MPa for 5R; 93 MPa for 7R; 103 MPa for 8R)

Figure 6.25. Fracture of sandstone specimens under various confining pressures (from Ramez, 1967)

the formation of arrayed cracks; while the peak and the downward plunge of the stress-strain curve are preceded by coalescence of the arrayed cracks. The flattened residual portion of the curve is associated with friction between the fractured pieces (Figure 2.7).

The degradation model is able to reproduce these characteristics. Under uniaxial and low confining pressures, the diversion of the stress-strain curve from linearity is associated with extension of cracks and the peak strength corresponds to the coalescence of extended cracks (relating the stage between points *b* and *c* in Figures 6.13 and 6.15 to Figures 6.12(a) and (b), and 6.14(a) and (b), respectively). When the



(a) 20 MPa (b) 40 MPa (c) 60 MPa (d) 80 MPa

Figure 6.26. Fracture of simulated rock specimens under various confining pressures

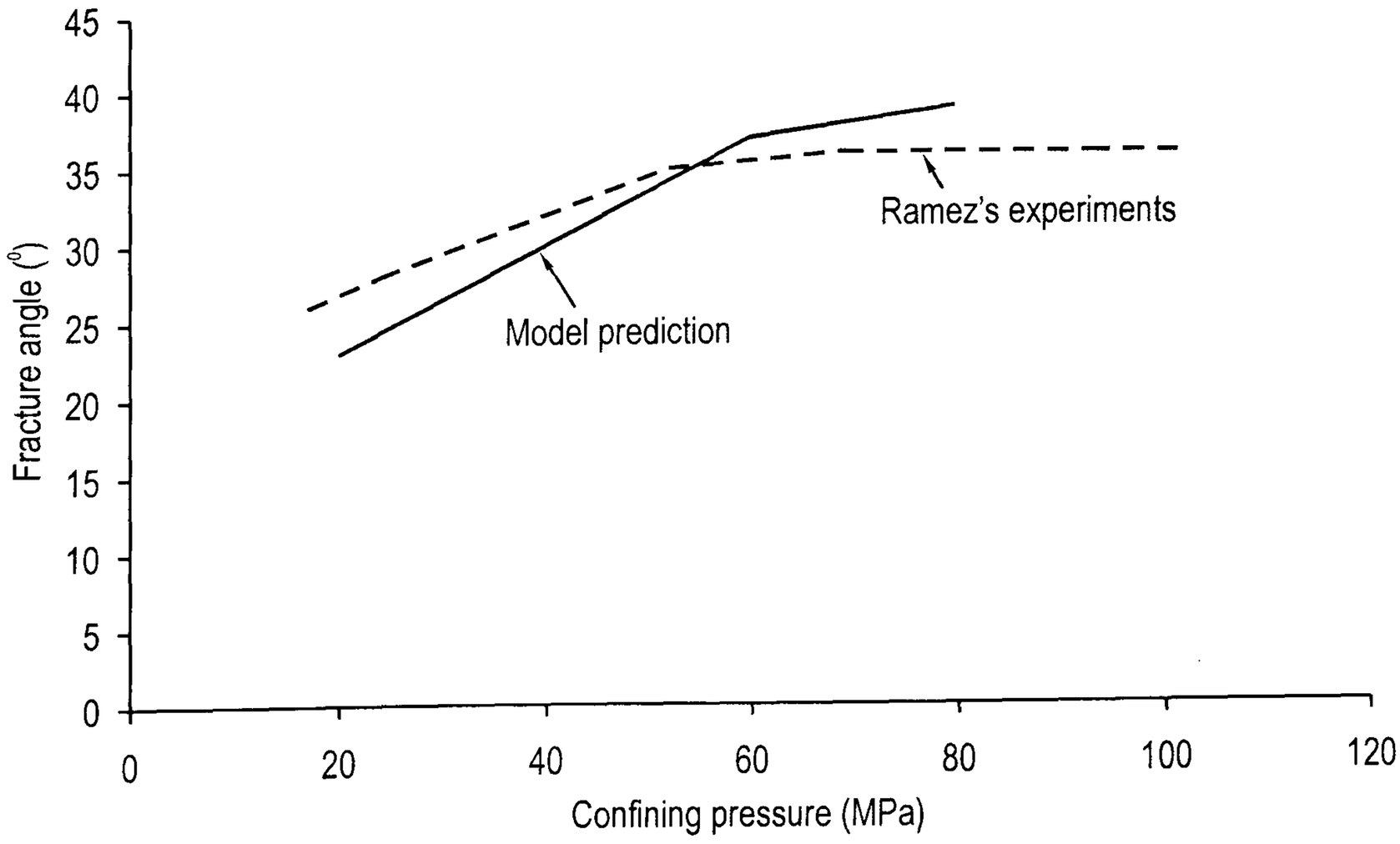


Figure 6.27. Variation of the fracture plane angle of rock specimens as a function of confining pressure

confining pressure increases, however, these two processes tends to develop at a earlier axial strain stage, and the coalescence of the extended cracks occurring prior to the peak (relating point *c* in Figures 6.17, 6.19 and 6.21 to Figures 6.16(c), 6.18(c) and 6.20(c), respectively). Consequently, the formation of the macroscopic fracture plane symbolises the peak strength (relating point *d* in Figures 6.17, 6.19 and 6.21 to Figures 6.16(d), 6.18(d) and 6.20(d), respectively). This is an interesting prediction given by the degradation model and no literature has been found on laboratory investigations in this respect.

Relation between the stress-strain curve and confining pressure

Laboratory results further indicate that the non-linearity of the stress-strain curve is influenced by confining pressure (Section 2.4.2). As confining stress increases, the hardening range widens and the strength drop in the softening range decreases, with the material becoming perfectly plastic when the confining pressure is sufficiently large (Figure 2.21).

Figure 6.28 brings together the stress-strain curves displayed by the model at all the applied confining pressures, *i.e.* 0, 20, 40, 60 and 80 MPa. Under uniaxial compression, the microscopic processes develop very quickly so that the specimen collapses within a very small strain range and the behaviour of the material is brittle (see the curve of 0 MPa in Figure 6.28). As confining pressure increases, the strain hardening range

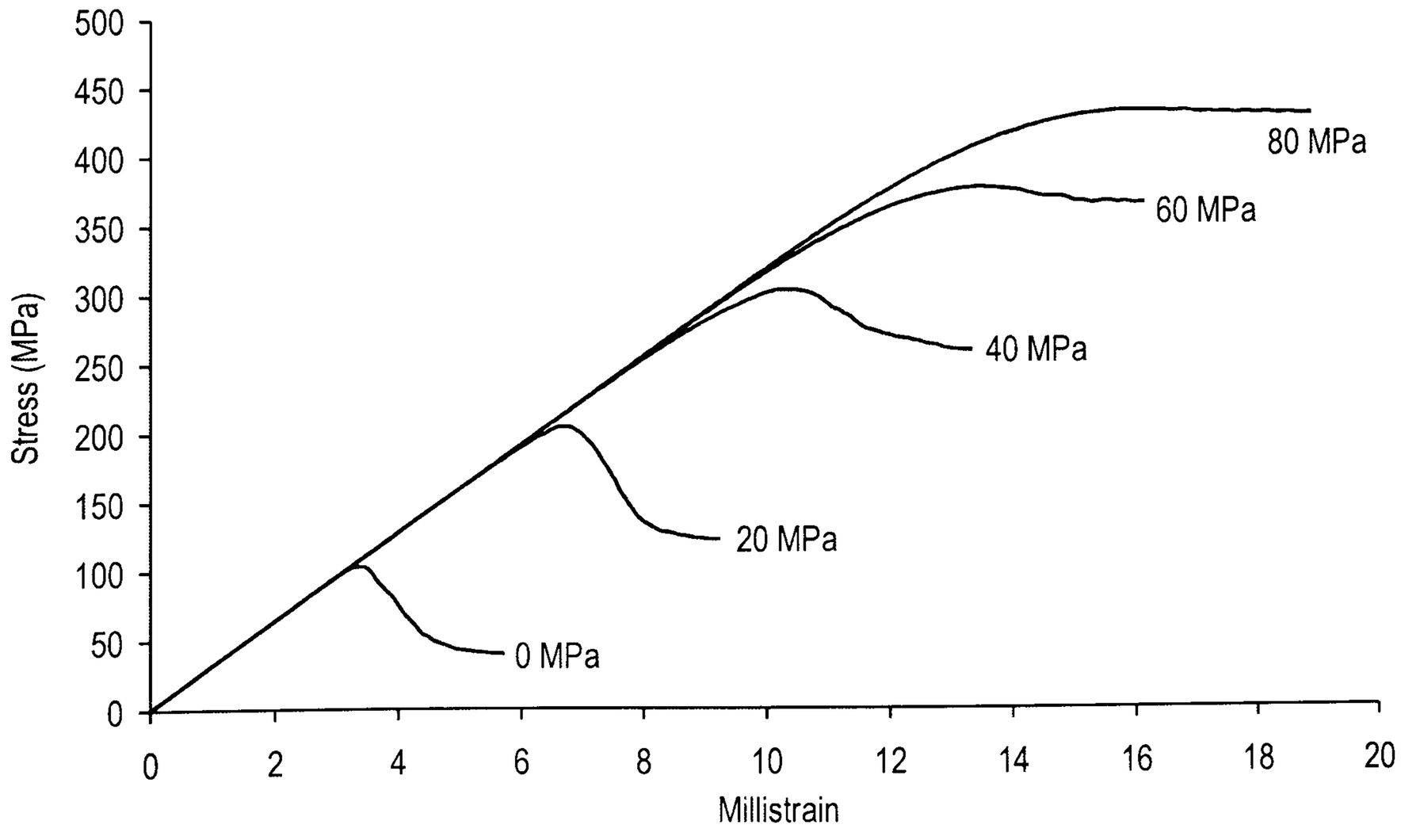


Figure 6.28. Stress-strain curves of simulated rock specimens under various confining pressures

increases and both the strength loss after the peak and the brittleness of the curve reduce (see the curves of 20, 40 and 60 MPa in Figure 6.28). When the confining pressure increases up to 80 MPa, the material behaviour becomes perfectly plastic (see the curve of 80 MPa in Figure 6.28). These curves show that the degradation model is capable of reproducing the whole range of the stress-strain curve, from brittle to perfectly plastic, displayed by rock subjected to various confining pressures.

6.7.5 Energy dissipation characteristics

Acoustic emission (AE) can be used to detect the microscopic processes associated with rock fracture (Section 2.5). AE events are not notable until the occurrence of nonlinearity in the stress-strain curve and the rate at which the AE events appear changes with the development of fracture. The AE events increase gradually with extension of the cracks, and increase rapidly as the cracks link with each other (Figure 2.24). When the final fracture planes form, the rate maximises, which is in the post-peak region of the stress-strain curve (Figures 2.28 and 2.29).

The strain energy dissipation associated with elemental failure predicted by the degradation model mimics these features of AE events. Local failures occur well before the peak, and increase gradually as failed sites extend (relating points *a* and *b* in Figures 6.13, 6.15, 6.17, 6.19 and 6.21 to Figures 6.12(a) and (b), 6.14(a) and (b), 6.16(a) and (b), 6.18(a) and (b) and 6.20(a) and (b), respectively). Failure sites increase rapidly with the coalescence of the failed sites (relating points *b* and *c* in Figures 6.13, 6.15, 6.17, 6.19 and 6.21 to Figures 6.12(b) and (c), 6.14(b) and (c), 6.16(b) and (c), 6.18(b) and (c) and 6.20(b) and (c), respectively). When the eventual fracture plane forms, the energy dissipation rate maximises (relating points *d* in Figures 6.13, 6.15, 6.17, 6.19 and 6.21 to Figures 6.12(d), 6.14(d), 6.16(d), 6.18(d) and 6.20(d), respectively). Finally, the energy dissipation events diminish as the rock specimen approaches its residual state (relating point *f* in Figures 6.13, 6.15 and 6.17 and point *e* in Figures 6.19 and 6.21 to Figures 6.12(f), 6.14(f), 6.16(f), 6.18(e) and 6.20(e), respectively).

Laboratory results suggest that the maximum rate of AE events appears in the post-peak range (Section 2.5). This is predicted by the degradation model at uniaxial and low confining pressures (points *d* in Figures 6.13 and 6.15). However, the degradation model predicts that the point of maximum energy dissipation changes with confining pressure. Thus, as the confining pressure increases, this point moves towards the strength peak (points *d* in Figures 6.19) and occurs well before the strength peak when

the confining pressure is sufficiently high (points *d* in Figures 6.17 and 6.21). This is again a prediction given by the degradation model for which no reports have been found from laboratory observations in this respect.

6.7.6 Hysteresis loops

During loading-unloading-reloading cycles on rock specimens, it is often observed that the stress-strain curves demonstrate hysteresis (Figure 2.19).

As the degradation model replicates a displacement controlled test, by moving the platens apart unloading can be modelled. As a result, hysteresis is traced by the degradation model that simulates uniaxial compression. Figure 6.29 is the plot of the stress-strain curve, together with the one obtained by continuous loading under unconfined conditions (Figure 6.13). Comparing this figure with Figure 2.19, it is clearly seen that the hysteresis loops produced by the degradation model are close to those produced in the laboratory. This indicates that the degradation model provides an efficient means to relate energy loss to microscopic processes.

6.8 Closure

The degradation model developed in Chapter 4 for fracture of heterogeneous rocks has

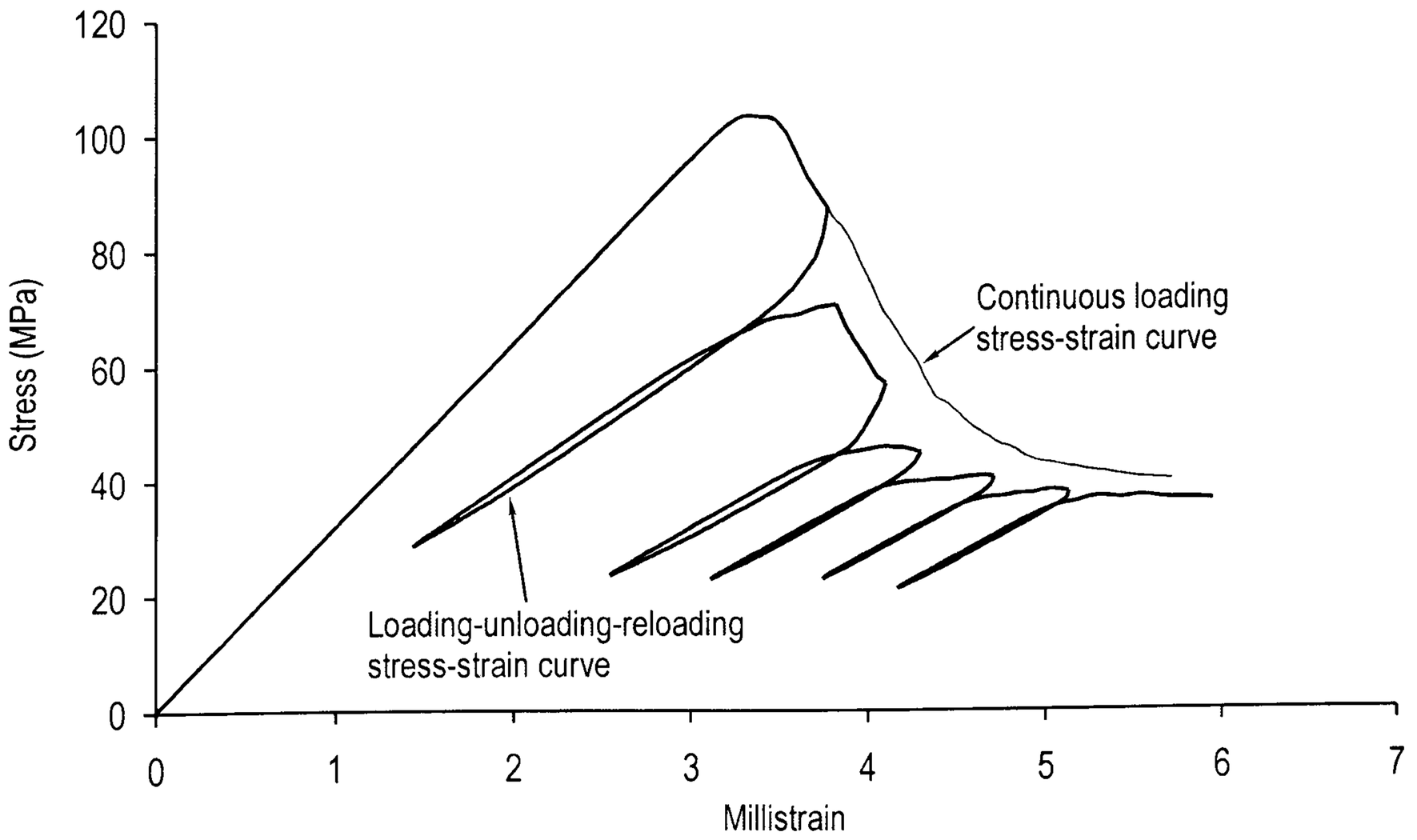


Figure 6.29. Hysteresis loops produced by the degradation model under uniaxial compression

been used to simulate the fracture of rock specimens in the laboratory. The model as a whole is first refined, since it contains a number of components in which various forms can be used to deal with specific problems. It is shown that the Weibull distribution function and the Hoek-Brown criterion are appropriate in describing elemental strength features of rock materials.

Using the Weibull distribution function and the Hoek-Brown failure criterion, a series of investigations have been performed into the influence of a number of parameters on rock fracture. In particular, rock fracture under various confining stresses has been explored. The investigation into the influence of the degradation parameter n_d on rock fracture indicates that this parameter controls the degree of degradation relative to confining pressure, and that as n_d increases, the elemental degradation decreases. As a result, the number of failed sited prior to the formation of macroscopic fracture plane increases, and both the peak strength and the residual strength of the model increase.

The investigation into the influence of the Weibull parameter m_w on rock fracture indicates that the shape of elemental strength distribution influences the formation of the final fracture plane. When m_w increases, the number of diffused failed sites and the angle of the eventual fracture plane tends to decrease and the brittleness of the resulting stress-strain curve increases. Further discussion on this topic suggests that values in the range between 2 and 4 are appropriate for m_w in representing elemental strength distribution of rock materials.

The numerical results on rock specimens subjected to various confining pressures indicate that the degradation model can closely predict the fracture process and the associated macroscopic behaviour displayed by rock under compression, including the development of fracture from elemental scale to macroscopic scale, the associated stress-strain curve, and the strain energy dissipation characteristics. Under uniaxial compression, local failure development is mainly manifested by the extension of failed sites in the direction of the major principal stress, and the final failure of the rock specimen is induced by a combination of axial splitting and shearing. With confining pressure present, the extension of the failed sites is suppressed, the eventual failure of the rock specimen is induced by shear fracture plane, the angle of the shear fracture plane changes, and the stress-strain behaviour becomes more ductile. When the confining pressure is sufficiently large, the specimen fails by deformation of a widened shear fault, and the corresponding stress-strain relation becomes perfectly plastic.

In addition, the degradation model predicts two phenomena for which no literature has been found from laboratory investigations. With respect to the strength peak, the

point at which the macroscopic fracture plane forms appears to vary. Under uniaxial and low confining pressure, the formation of the macroscopic fracture plane is in the post-peak stage. However, it moves towards the peak point as confining pressure increases, and at sufficient high values of confining pressure, the formation of the macroscopic fracture plane may occur prior to the peak. Consequently, the appearance of the maximum energy dissipation rate (corresponding to AE events) moves from the post peak region to the pre-peak region as confining pressure increases.

To sum up, the degradation model represents a powerful approach to the simulation of brittle fracture processes in heterogeneous rocks. In the next chapter, we shall apply the degradation model to the fracture behaviour of mine pillars, which is a common occurrence of rock failure in the field.

7 Simulation of brittle fracture of mine pillars

In the previous chapter, the degradation model has been validated through the simulation of brittle fracture of rock specimens in the laboratory. The investigations indicate that the Weibull distribution and the Hoek-Brown criterion are the most appropriate for representing elemental failure of rock materials. Also, the model can reproduce the complete fracture process of rock specimens under compression, including isolated dissipative events, the formation of fracture planes from the elemental to macroscopic scale, the variation of fracture plane angles, and the associated non-linear stress-strain curves and the energy dissipation characteristics.

As an engineering application, the local degradation model is used here to simulate the progressive fracture of mine pillars. Pillar fracture is a common occurrence of rock fracture in underground operations, and has incurred a great deal of investigation into pillar failure mechanisms and mechanical behaviour (Salamon and Munro, 1967; Mokgokong and Peng, 1991; Ozbay et al., 1995; Madden et al., 1998; Lunder and Pakalnis, 1997). In recent years, attempts to numerically study pillar behaviour in terms of progressive development of fracture have been carried out (Kaiser and Tang, 1998; Martin and Maybee, 2000). However, to date it has proved impossible to reproduce the fracture process in agreement with observed field phenomena (Figure 2.34). In this chapter, we will demonstrate how the degradation model can be applied to the simulation of fracture processes in mine pillars such that the associated mechanical behaviour and dissipative characteristics of pillars can be predicted.

Following the definition of the investigation into the problem associated with pillars, the numerical model for simulating pillar fracture behaviour is described. Then, the fracture process and the associated behavioural features of pillars with different width to height (w/h) ratios are explored. These are found to compare well with field observations. Finally, the influence of contact conditions and the stiffness of the roof and floor on pillar fracture behaviour are demonstrated.

7.1 Definition of the problem

Pillars are *in situ* rock structures between two or more underground openings, and have been utilised by all underground mining methods as major structural elements, either temporary or permanent, to maintain the integrity of underground excavations like rooms or entries for safe extraction of ore. Since pillars generally consist of mineral ore, minimising pillar sizes has historically been pursued in pillar design in order to maximise the extraction ratio. This pursuit, however, often leads to the collapse, (which is a gradual fracturing process), of slender or squat pillars *in situ* (see Figure 2.34). Thus, an understanding of the fracture process of such pillars plays a vital role in designing stable pillars in underground operations.

In this section, after introducing the conventional pillar design procedure in which the determination of pillar strength is a key element, the popularly used formulae in determining pillar strength are presented. Since this design procedure leads to a variation in pillar geometry, subjected to the mining depth and the safety factor (see Subsection 7.1.1), the performance of pillars *in situ* is also reviewed. Those elements will be referred to when considering the simulation results in Sections 7.3 and 7.4.

7.1.1 Conventional pillar design methods

Pillar design is of primary importance for the safe and economic extraction of ore. Early designs of pillar dimensions and road widths were based on experience obtained through trial and error (Madden et al., 1998). It was not until an intensive investigation into the strength of coal pillars following the Coalbrook Colliery disaster of 1960, in which the collapse of 900 pillars resulted in the loss of 437 lives (Salamon, 1999), Salamon and Munro (1967) proposed a pillar design procedure for underground mining operations.

In this pillar design procedure, a probabilistic notion of safety factor is used. The safety factor, which is required to be greater than unity, is defined as the ratio of pillar strength to the load sustained by the pillar. It is written as (Salamon and Munro, 1967; Salamon, 1967, 1999)

$$\text{Safety Factor} = \frac{\text{Pillar Strength}}{\text{Load}}. \tag{7-1}$$

In this equation, load is calculated using the Tributary Area Theory in which it is assumed that each pillar carries the weight of the overburden immediately above it (Salamon and Munro, 1967). The Tributary Area Theory is operationally convenient, as

it leads to fixed pillar load determination for any given seam material and depth. The determination of pillar strength, however, depends on pillar geometry, the contact conditions, and the strength of the material comprising the pillar. Extensive research based on either experimental investigations (Obert and Duvall, 1967; Bieniawski, 1968; Bieniawski and Van Heerden, 1975) or back-calculation (Salamon and Munro, 1967; Hedley and Grant, 1972) has led to a number of pillar strength formulae. These formulae are simply expressed in terms of the ratio of pillar width and height (*w/h*), and are usually in either a power form of

$$\sigma_{pillar} = k_{pillar} \frac{w^{\alpha_{pillar}}}{h^{\beta_{pillar}}} \tag{7-2}$$

or a linear form of

$$\sigma_{pillar} = k_{pillar}\left[r_{pillar} + \left(1 - r_{pillar}\right)\frac{w}{h} \right], \tag{7-3}$$

where σ_{pillar} is the pillar strength; α_{pillar}, β_{pillar} and r_{pillar} (r_{pillar} <1) are dimensionless constants; and k_{pillar} is the strength of a reference specimen.

The difference between individual formulae that have the same form as either Equation 7-2 or Equation 7-3 lies in the values taken for those parameters (α_{pillar}, β_{pillar} and r_{pillar}). In the earlier application of the power formula (Equation 7-2) to pillar design, for example, Salomon and Munro (1967) studied 98 stable and 27 collapsed coal pillar cases from South African mines, and suggested that 0.46, 0.66 and 7.176 MPa for α_{pillar}, β_{pillar} and k_{pillar}, respectively, were appropriate in the design of coal pillars for South African bord-and-pillar workings. In an attempt to apply Equation 7-2 to other hard rock pillar designs, however, the values for α_{pillar} and β_{pillar} have been replaced by 0.5, 0.75 and 133 MPa (Hedley and Grant, 1972; Hedley et al., 1984), respectively. Table 7.1 lists a number of pillar strength formulae for specific rock pillars. Figure 7.1 shows the predicted pillar strength from these various formulae using a pillar height of 3 m, with the pillar strengths normalised to the laboratory uniaxial compressive strength. As Figure 7.1 shows, different equations or parameter values result in different strength profiles. Generally, the linear formulae predict lower pillar strength than do the power formulae, particularly with increasing *w/h* ratio. However, Equation 7-8, which is based on 178 pillar performance observations (Lunder and Pakalnis, 1997), predicts very similar pillar strength to Equation 7-4. This may imply that the power or similar form of formulae may present the best-fit profile of pillar strengths.

Table 7.1. Pillar strength formulae (*w* and *h* in metres)

Pillar strength formula (MPa)	Rock type and σ_c (MPa)	Reference	Sequence
$\sigma_{pillar} = 133\frac{w^{0.5}}{h^{0.75}}$	Quartites (230)	Hedley and Grant, 1972	(7-4)
$\sigma_{pillar} = 65\frac{w^{0.46}}{h^{0.66}}$	Metasediments (94)	Von Kimmelmann et al., 1984	(7-5)
$\sigma_{pillar} = 35.4\left[0.778 + 0.222\frac{w}{h}\right]$	Limestone (100)	Krauland and Soder, 1987	(7-6)
$\sigma_{pillar} = 74\left[0.778 + 0.222\frac{w}{h}\right]$	Limestone and Skarn (240)	Sjoberg, 1992	(7-7)
$\sigma_{pillar} = 0.44\sigma_c\left[0.68 + 0.52k_{lp}\right]$	Hard rocks	Lunder and Pakalnis, 1997	(7-8)*

* $k_{lp} = \tan\left[\cos^{-1}\left(\frac{1-c_{lp}}{1+c_{lp}}\right)\right]$, where $c_{lp} = 0.46\left[\log\left(\frac{w}{h}+0.75\right)\right]^{\frac{1.4}{(w/h)}}$

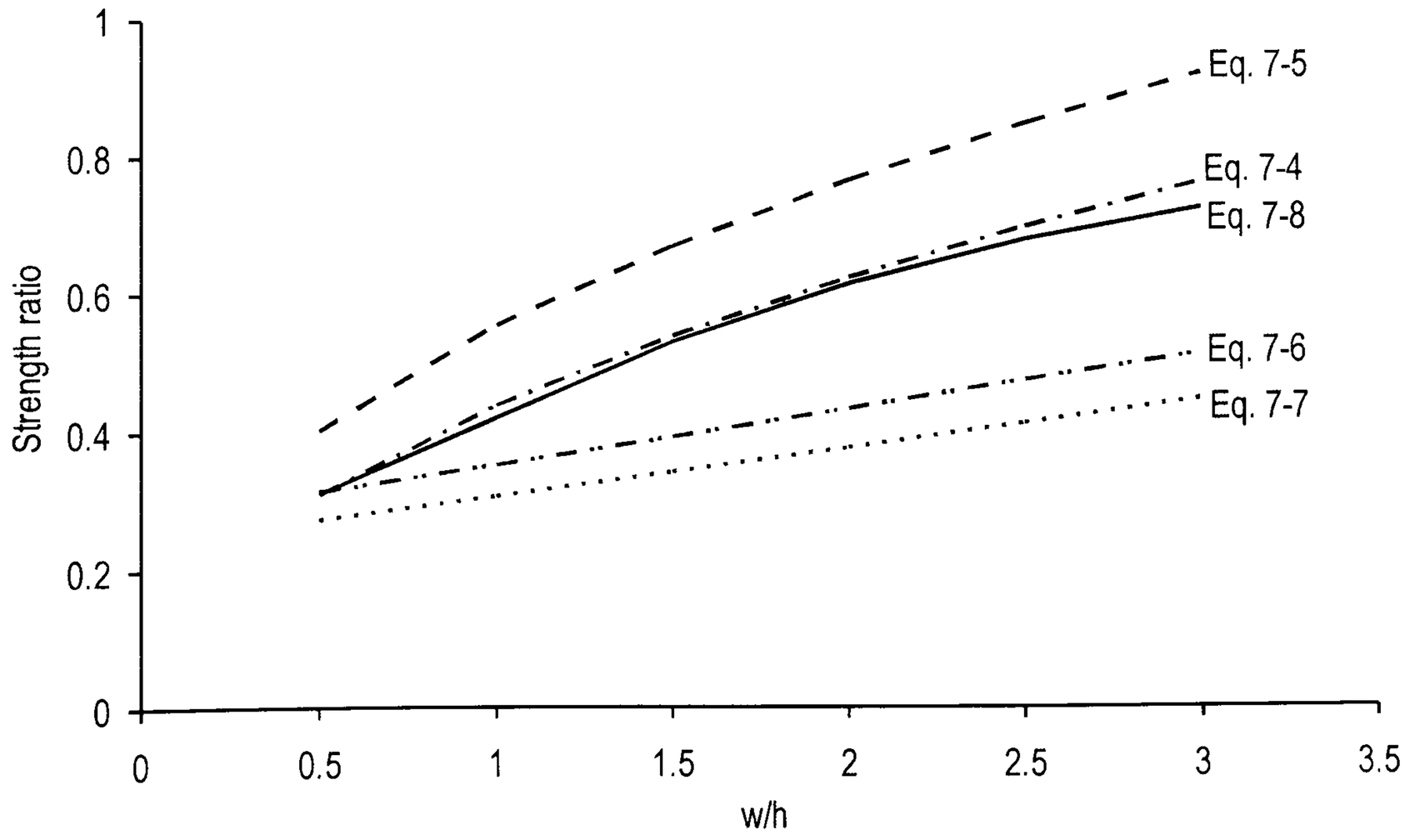
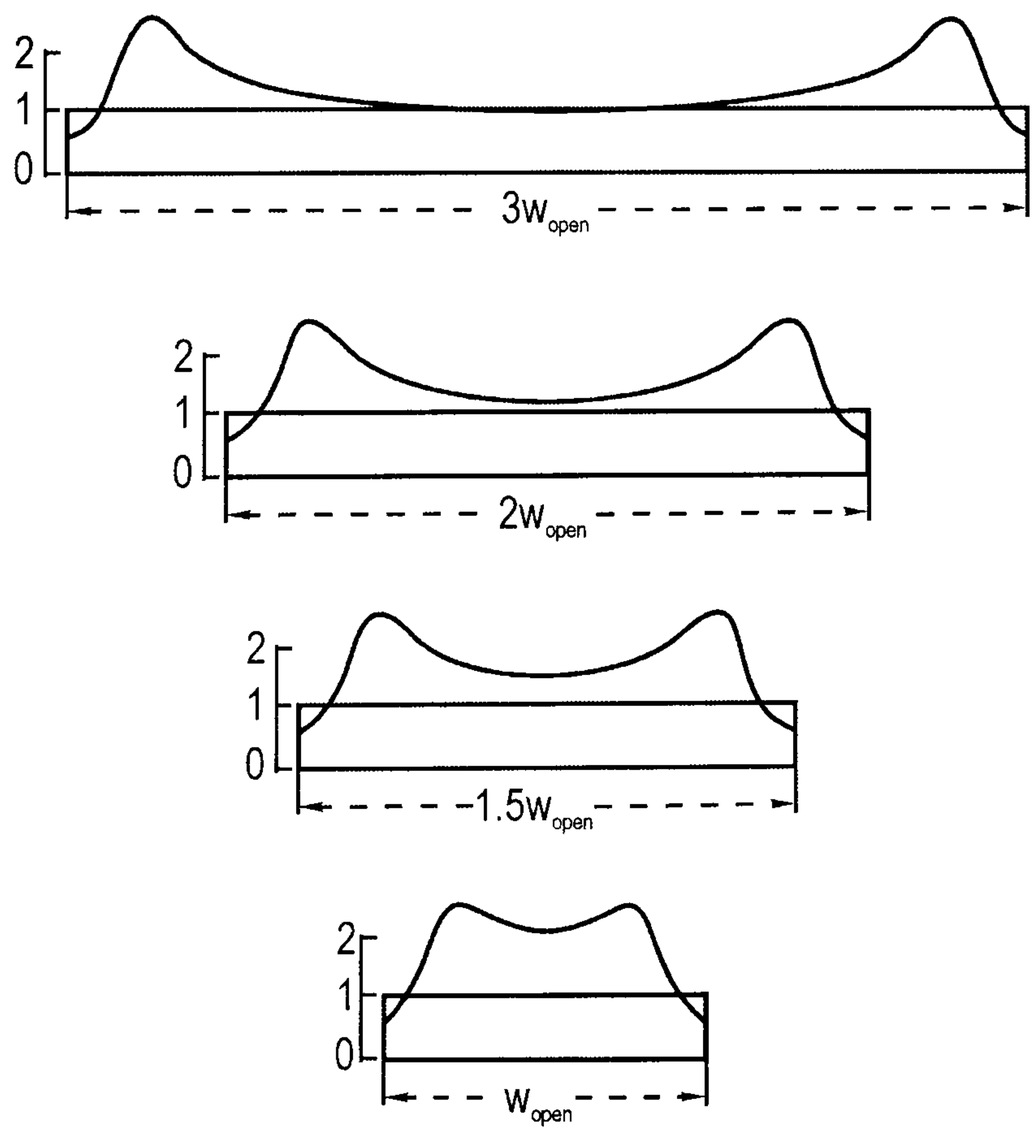


Figure 7.1. Pillar strength vs *w/h* ratio predicted by various empirical formulae

7.1.2 Performance of pillars *in situ*

Underground excavations induce stress redistribution around openings, and pillars suffer stress concentrations that may be a few times the undisturbed stresses (Holland, 1962; Salamon, 1999). Figure 7.2 shows the profiles of the redistributed stresses on pillars of different width compared with the width of the opening. This figure indicates that a considerably higher stress than the average lies near the edge of every pillar, and that the magnitude of the maximum stress tends to stay constant with any further increase in pillar width (Holland, 1962).

The pillar design procedure introduced in the earlier section leads to a variation in pillar geometry, represented by the *w/h* ratio, subjected to the depth of the mining site and the strength of the representative material comprising the pillar. Under the effect of stress concentrations, pillars with low *w/h* ratios are prone to collapse, even with a safety factor much greater than unity. It is indicated by Salamon (1999) that most collapsed coal pillars had a *w/h* ratio less than 3.7. For hard rock, the maximum *w/h* ratio of the collapsed pillars tended to reduce to 2.5 (Ozbay et al., 1995; also see Martin and Maybee, 2000). The calculated safety factor of those collapsed pillars was found to be up to 5.6 (Madden et al., 1998).



(The scale besides each figure represents stress magnitude with unity indicating the *in situ* stress)

Figure 7.2. Pillar stress magnitude and distribution as affected by the width of the pillar as compared with the width of the opening (W_{open}) (After Holland, 1962)

The collapse of pillars is manifested by progressive fracturing. Observations in the field indicate that after the excavation of a pillar, slabbing or spalling occurs first at the pillar sides and migrates progressively into the centre of the pillar. As a result, the hourglass shape is a typical failure mode of a slender pillar (Figure 2.34(b)). For squat pillars, spalling migrating towards the pillar centre is replaced by gradual formation of shear fractures (Figure 2.34(a)). Associated with the progressive fracturing process, a pillar with a low *w/h* ratio deteriorates gradually and may finally lose its load carrying capability.

7.1.3 Numerical simulation of progressive fracture of pillars

The pillar strength formulae introduced in Subsection 7.1.1 are based on the concept of average pillar strength and load, where it is assumed that the local strength and the load are distributed uniformly across the entire pillar. However, as indicated in earlier subsections, the material strength and pillar stresses are both not uniform: they are affected by the opening geometry and influenced by the fracturing processes of the pillar. This causes difficulties in application of simple formulae to define the strength of a pillar, particularly very squat pillars, and an alternative is to compute pillar strength numerically from sound mechanistic models (Salamon, 1999).

Obviously, an understanding of pillar progressive failure behaviour in a complete mining environment is important for the design of pillars, and a number of attempts have been made to numerically analyse pillar behaviour in the context of progressive failure (Kaiser and Tang, 1998; Martin and Maybee, 2000). By assuming elastic-brittle material behaviour, Kaiser and Tang (1998) modelled the shear failure of slender pillars. Using the same constitutive material behaviour and referring pillar failure to the yield of all elements across the pillar, Martin and Maybee (2000) simulated the strengths of pillars with various *w/h* ratios up to 2.5. Regardless of the unrealistic pillar failure modes produced by, or considered in, the approaches, these efforts highlight the requirement for a robust model in analysing progressive fracture processes of pillars.

Here, with respect to Figure 2.34, an attempt to simulate the complex fracturing process of pillars is pursued with the degradation model, and this is presented in the following sections.

7.2 Degradation model for pillars

A general pillar system *in situ* may be represented by a single pillar, together with the

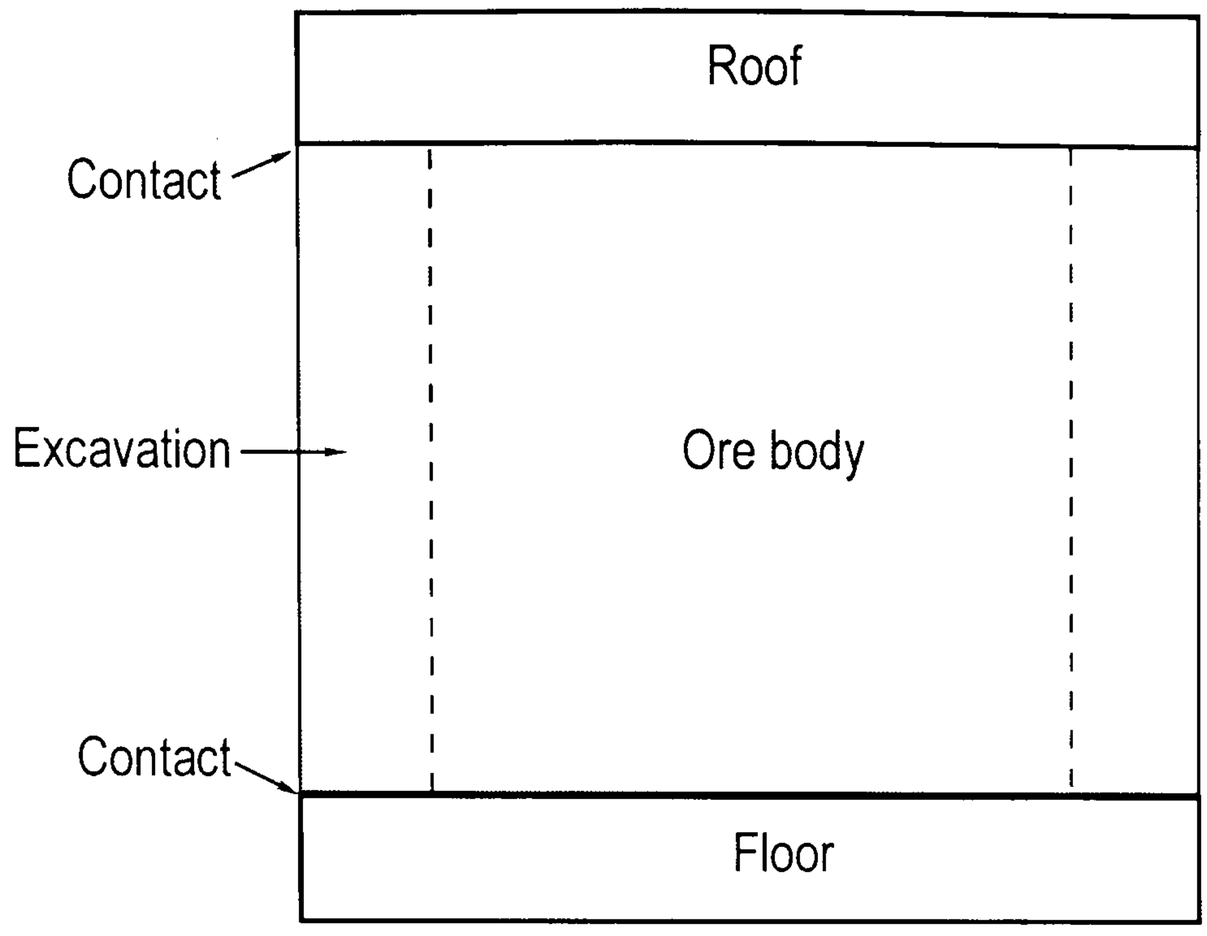


Figure 7.3. A numerical plane strain model for a single pillar system

roof and floor (with reference to Figure 2.34). The physical and mechanical properties of these three components are usually different (see Mokgokong and Peng, 1991; Madden et al., 1998). In addition, the contact conditions between a pillar and its surrounding rocks may influence fracture of the pillar. To simulate fracture behaviour of a pillar, these features have to be accounted for in a numerical model. This section deals with the set-up of the numerical model for pillars, along with the input data for performing numerical analyses of the fracture process of pillars.

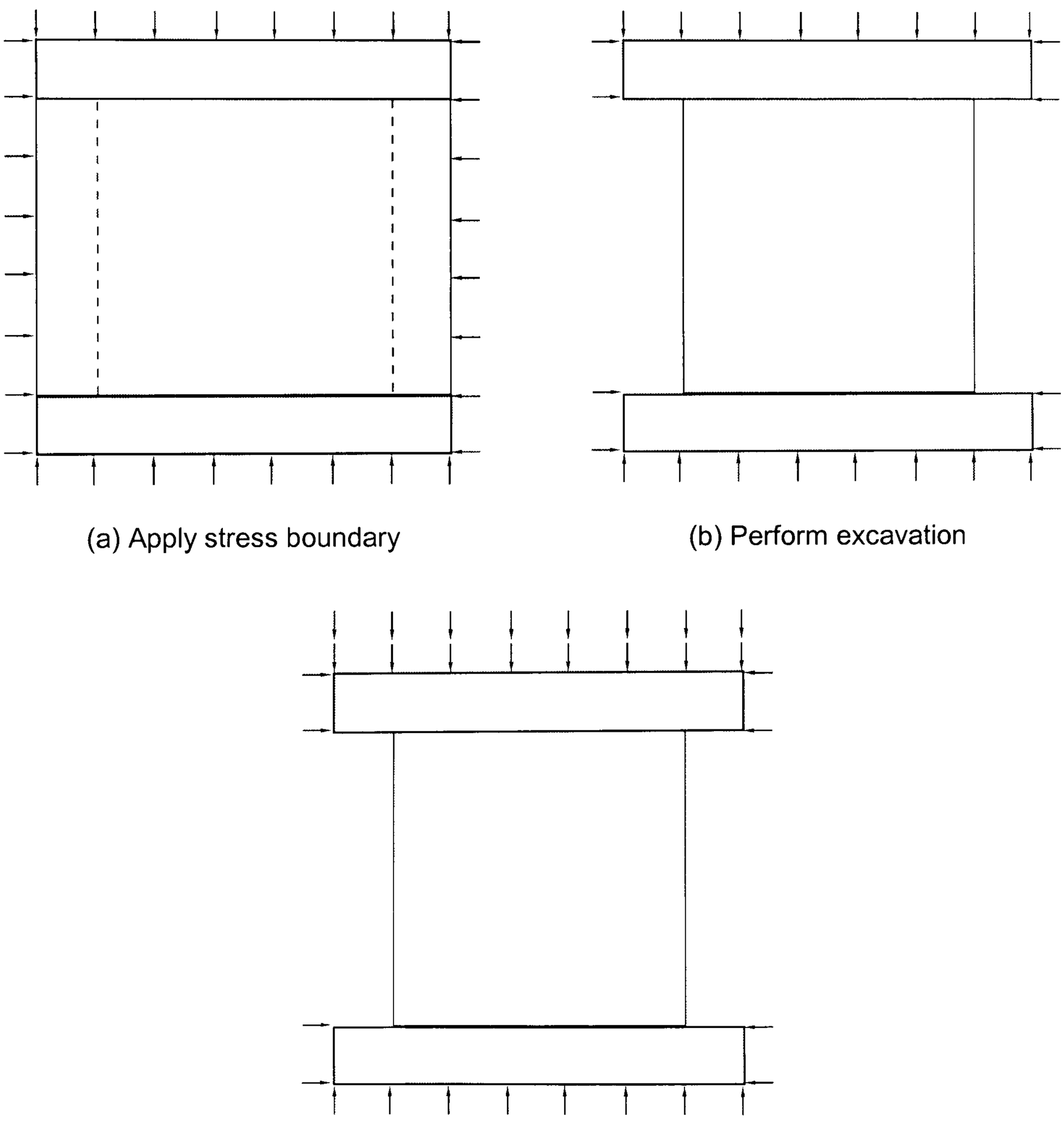
7.2.1 Model set-up

The plane strain model shown in Figure 7.3 is used to simulate pillar fracture behaviour. Before any excavation is performed, the model primarily consists of the ore body, roof, floor and contacts between the ore body and roof/floor. The ore body is represented by the Mohr-Coulomb model in FLAC, with each element having different strength properties. Since our attempt is to simulate the progressive fracture behaviour of pillars, the roof and floor may be simply represented by the FLAC isotropic elastic model. The contacts between the ore and its roof and floor are represented by the FLAC intrinsic interface model and the associated properties can be designated by the frictional angle and cohesion to the interfaces (see Subsection 5.2.2).

7.2.2 Loading path

Pillars are constructed *in situ*, where prior to pillar construction the pre-existing stress

state has been established. Moreover, as mentioned in Subsection 7.1.2, excavations around a pillar induce stress concentrations on the pillar. Considering these features, the following procedure is used to apply pillar load (referring to Subsection 6.1.2). Firstly, a stress boundary equivalent to the pre-existing stress conditions is applied to the overall model to establish the representative *in situ* stresses (Figure 7.4(a)); secondly, the openings are excavated and the stress boundary removed from both sides of the ore body (Figure 7.4(b)) to form the representative pillar system; thirdly, loading from the roof is performed using the controlled constant displacement method (Figure 7.4(c)). In order to simulate the complete fracture process of a pillar, loading is continued passed the peak and up to the residual strength of each simulated pillar.



(a) Apply stress boundary

(b) Perform excavation

(c) Perform further loading

Figure 7.4. Illustration of loading path for performing numerical analysis of pillar fracture behaviour

7.2.3 Input data

Four models with different geometries, *i.e. w/h* ratios of 0.5, 1, 2, and 3, are used to simulate pillar fracture behaviour. The input data for each model are tabulated in Table 7.2. The parameters for all four models are the same in each simulation, except for the individual pillar geometry. The parameters for the roof, floor and interfaces are kept the same in the general study of pillar fracture behaviour in Section 7.3, but will be adjusted in order to simulate their independent influence on pillar fracture in Sections 7.4 and 7.5. Those variations are given in the associated sections.

7.3 Simulated fracture of pillars

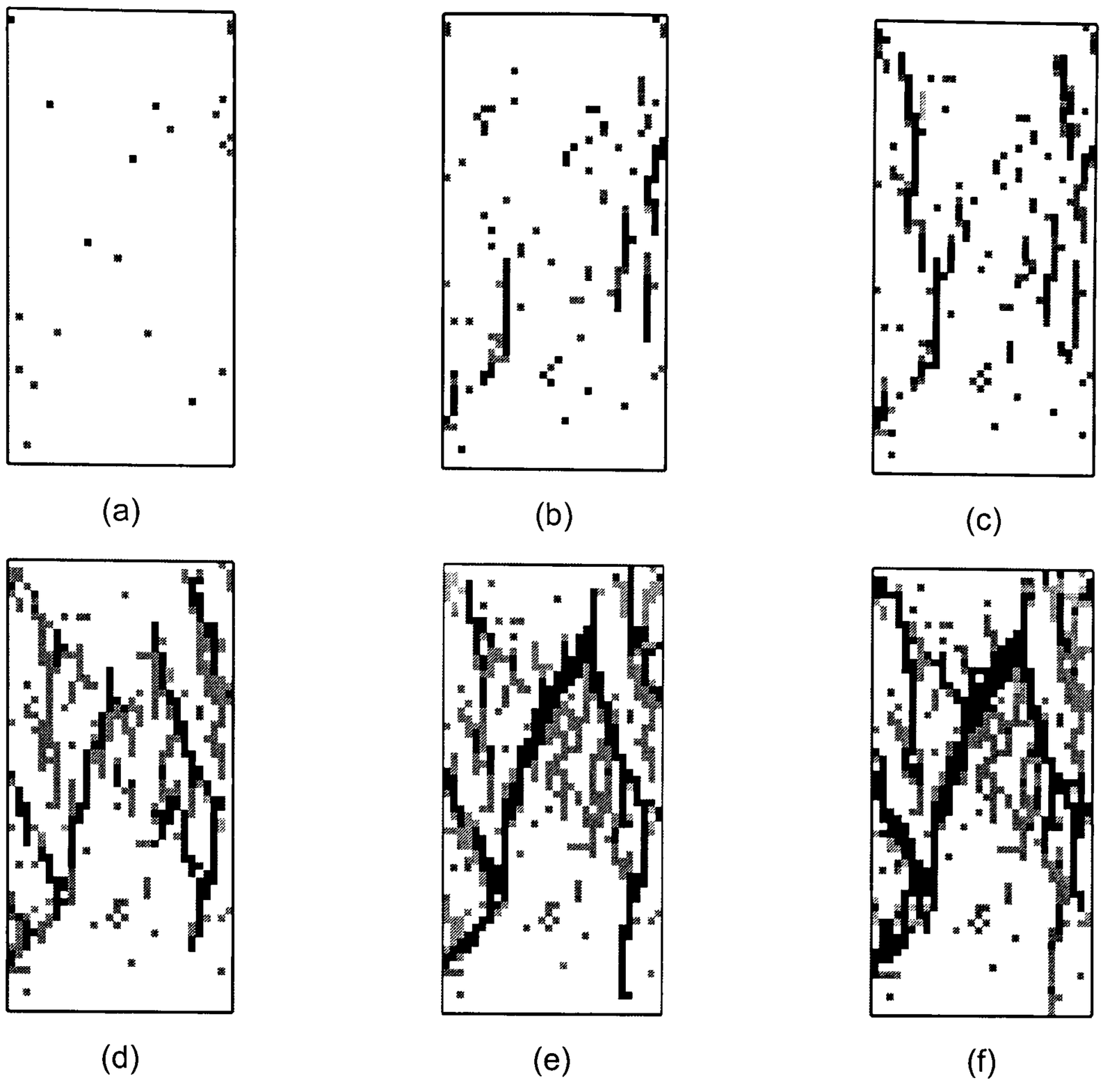
Using the model described above, the fracture behaviour of pillars with *w/h* ratios of 0.5 and 2 (Table 7.2) are simulated and presented in this section.

7.3.1 Slender pillars

Figure 7.5 is the fracture process of the pillar with a *w/h* ratio of 0.5, and the

Table 7.2. Input data for the simulation of pillar fracture

Identity	Model 1	Model 2	Model 3	Model 4
w/h ratio	0.5	1.0	2.0	3.0
Mining depth	500 m			
Pillar height	3 m			
Average density	2800 kg/m^3			
Deformation property	Roof and floor: elastic modulus 40 GPa, Poisson's ratio 0.25 Pillar: initial elastic modulus 40 GPa, Poisson's ratio 0.25, dilation angle 4°			
Strength property	Pillar σ_c: x_0 200 MPa, x_u 20 MPa, m_w 2.5 Pillar σ_c/T_0 ratio: x_0 10, x_u 30, m_w 2.5 Interface: friction angle 10°, cohesion 5 MPa			
Pillar degradation property	$\Delta\sigma_{cu}$ 90% the initial uniaxial compressive strength, ΔE_u 90% the initial elastic modulus, n_d 0.05			
Mesh size	20 grids/m			



(The grey zones indicate previous failed sites and the
dark zones represent sites currently undergoing failure)

Figure 7.5. Simulated fracture process of a pillar with a *w/h* ratio of 0.5

corresponding stress-strain curve is shown in Figure 7.6. After random initiation of local failure at a low strain level (Figure 7.5(a), corresponding to point *a* in Figure 7.6), a few failed sites extend in the loading direction (Figure 7.5(b)); further loading causes more failed sites to grow, and slabbing or spalling results (Figure 7.5(c)) when the pillar approaches its peak load-carrying capability (point *c* in Figure 7.6). Subsequent loading produces arrays of cracks, and these arrayed cracks coalesce to form shear bands (Figure 7.5(d)), resulting in a loss of strength (the stage between points *c* and *d* in Figure 7.6). In consequence of further development of the shear bands, the pillar disintegrates into parts (Figure 7.5(e)) and further deformation takes place at residual strength (Figure 7.5(f), corresponding to point *f* in Figure 7.6). The pillar is seen to behave in a brittle fashion.

Comparing Figure 2.34(b) with the fracture process simulated above, it is found that the hourglass shape of the deteriorated pillar (Figure 2.34(b)) forms around point *d*

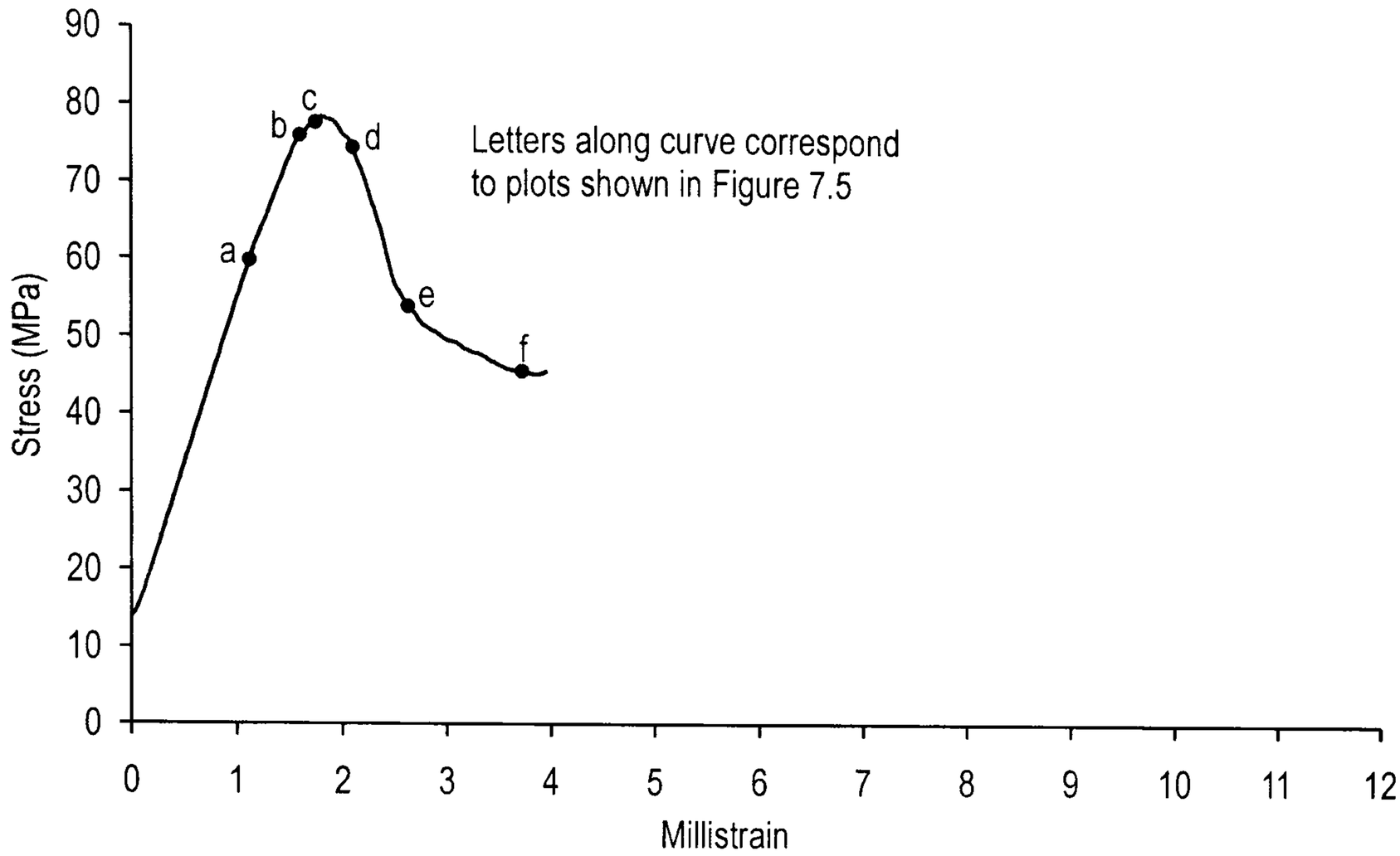


Figure 7.6. Simulated stress-strain relation for a pillar with a *w/h* ratio of 0.5

in Figure 7.6, the immediate post peak stage. This indicates that the pillar in Figure 2.34(b) has lost its stability.

7.3.2 Squat pillars

Figures 7.7 and 7.8 show simulated fracture process and the corresponding stress-strain curve of a pillar with *w/h* of 2.0. After the random initiation of local failures (Figure 7.7(a)), slabbing or spalling is induced by the growth and coalescence of the failed sites (Figure 7.7(b)). When shear fracture forms, however, a different process is presented from that with the slender pillar. The shear fracture tends to start from one of the pillar ends (Figure 7.7(c)) and grows toward the other end at an angle inclined into the pillar centre (Figure 7.7(d)). Subsequent loading causes additional such shear fractures further into the core of the pillar (Figure 7.7(d)). When shear fractures developing from both sides of the pillar meet at the pillar core, the pillar reaches its peak strength (Figure 7.7(e), corresponding to point *e* in Figure 7.8). Further development of shear fractures is associated with strain softening of the pillar (Figure 7.7(f), corresponding to point *f* in Figure 7.8). The pillar is seen to behave in a more ductile fashion.

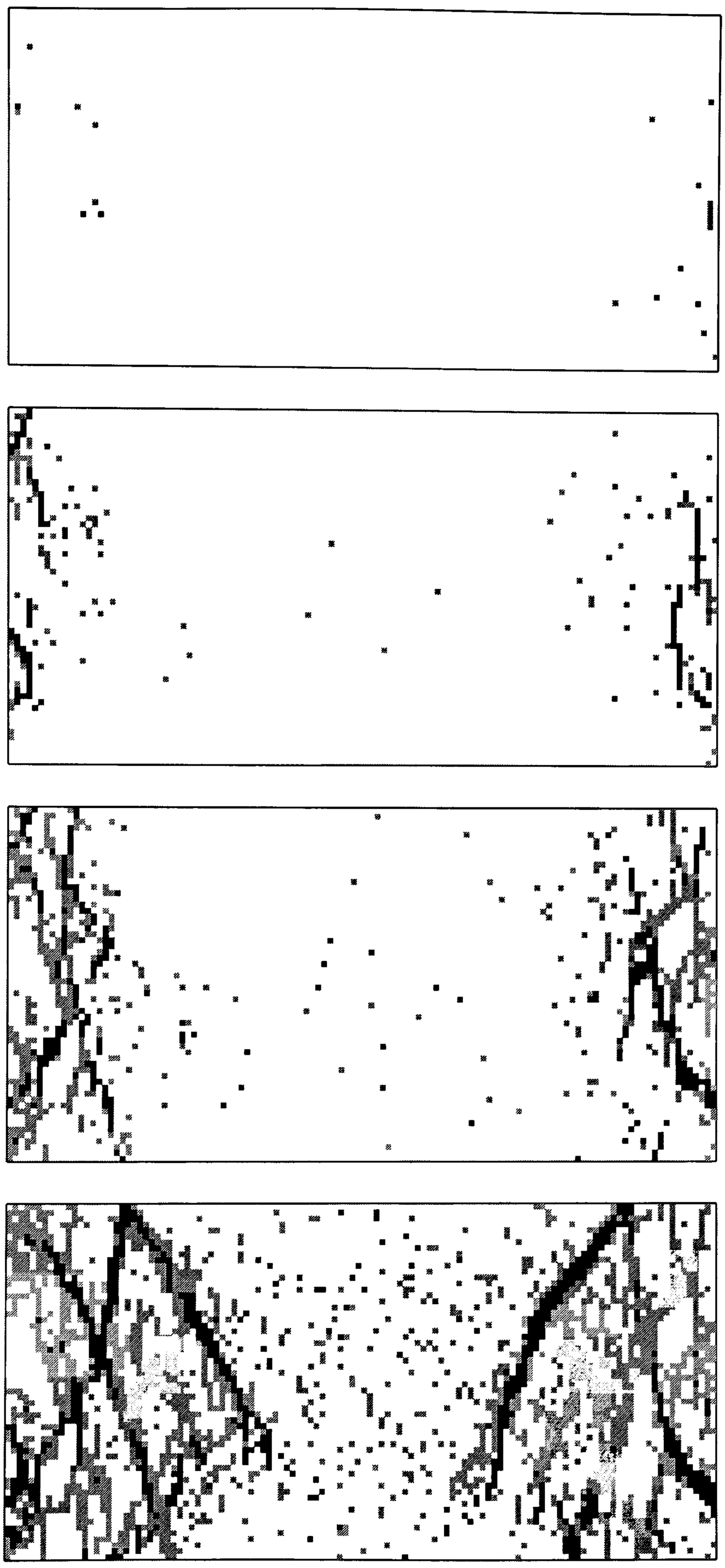
Comparing Figure 2.34(a) with the fracture process presented in Figure 7.7, it is readily seen that the pillar state shown in Figure 2.34(a) resembles stage *e* in Figure 7.7. The corresponding stress-strain curve (point *e* in Figure 7.8) indicates that the pillar

(a)

(b)

(c)

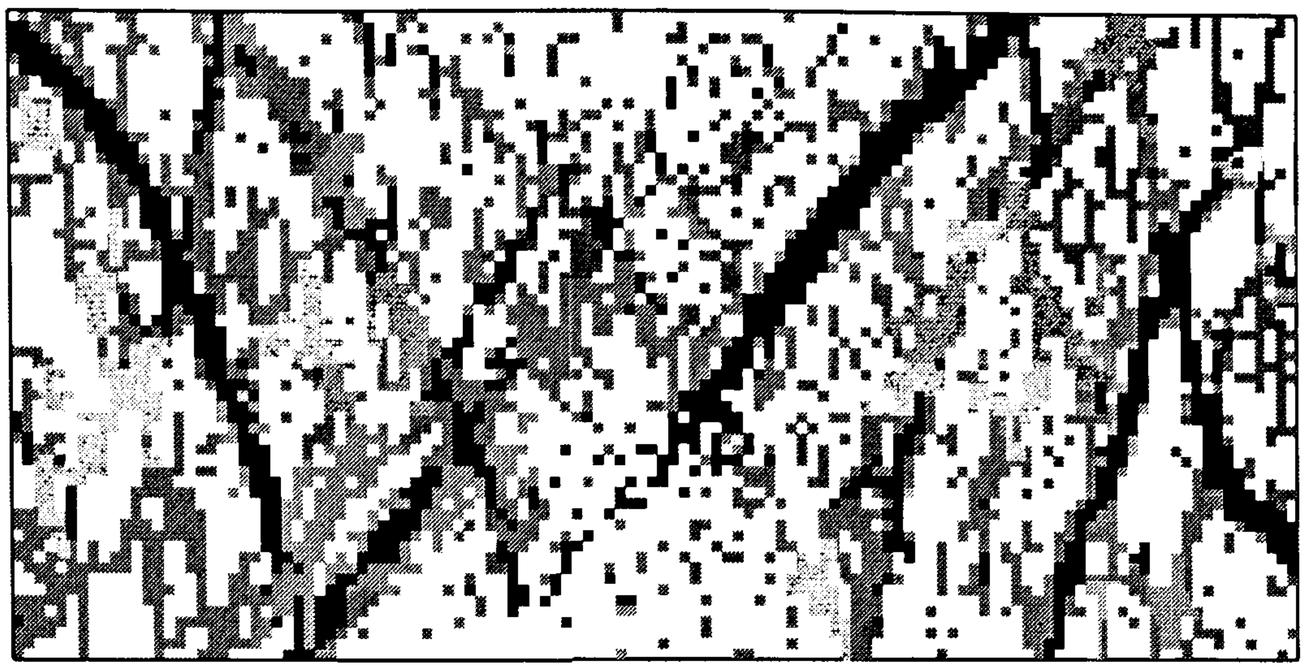
(d)



(The grey zones indicate previous failed sites and the
dark zones represent sites currently undergoing failure)

Figure 7.7. Simulated fracture process of a pillar with a *w/h* ratio of 2.0

(e)



(f)



Figure 7.7 (continued)

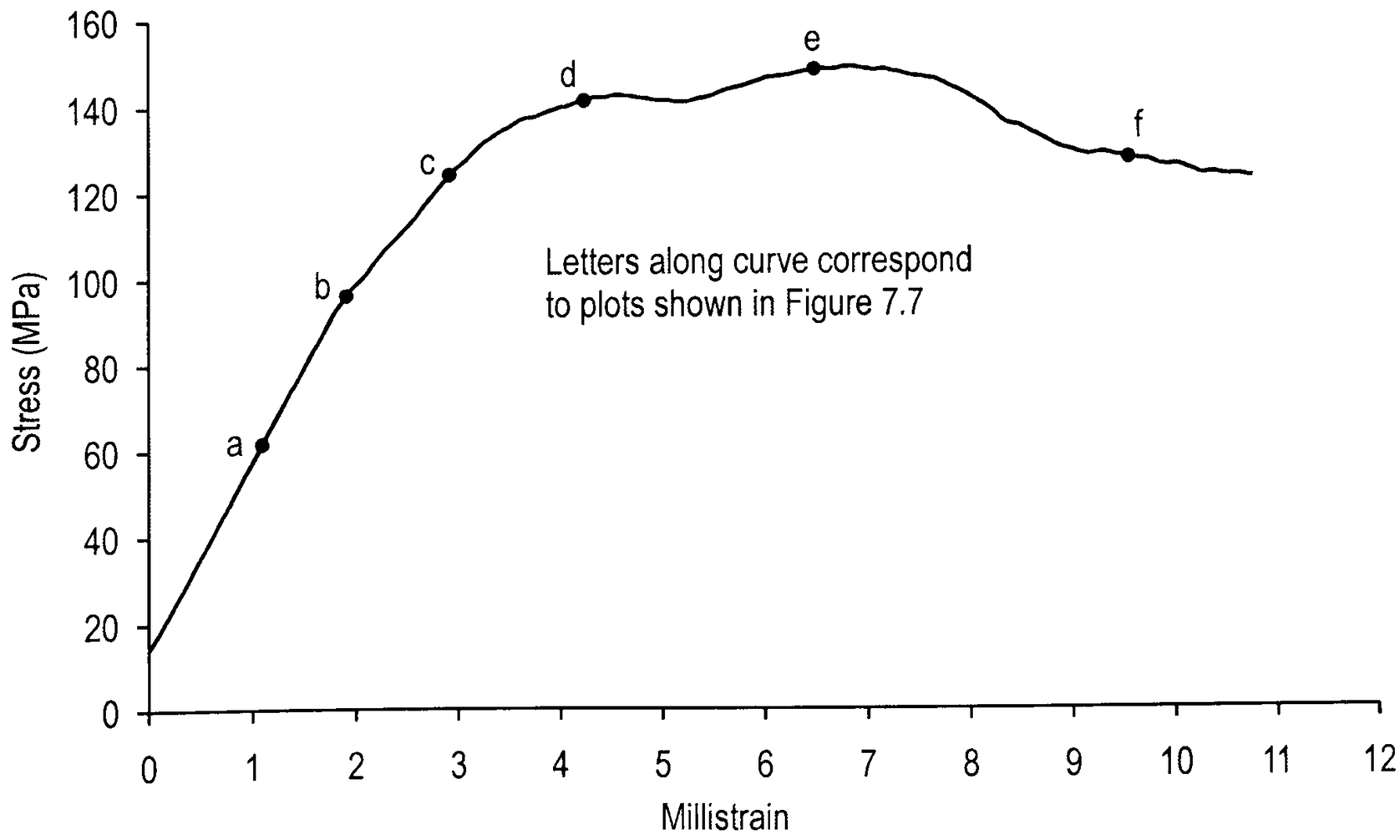


Figure 7.8. Simulated stress-strain relation for a pillar with a *w/h* ratio of 2.0

shown in Figure 2.34(a), although heavily fractured, still maintains its load-carrying capability.

In ending this section, it may be concluded from both the simulation results and field observations that the fracture process of a pillar with a low *w/h* ratio includes the initiation of local failure, extension of failed sites, coalescence of extended sites, slabbing/spalling of pillar ribsides, and formation of shear bands. The degradation model shows how pillar behaviour changes with variation of *w/h*.

7.4 Strength of fracturing pillars

In the above section, the fracture processes of pillars with *w/h* ratios of 0.5 and 2.0 have been examined using the degradation model. In this section, we consider the peak strength displayed by pillars undergoing fracturing, and for this purpose, two other pillars with *w/h* ratios of 1.0 and 3.0 have been simulated. In order to compare the simulation results with predictions from the pillar strength formulae listed in Table 7.1, the simulated pillar strengths given by the various *w/h* ratios are normalised and plotted in Figure 7.9, together with the pillar strengths predicted by a number of the pillar strength formulae from Table 7.1.

As shown in Figure 7.9, for *w/h* ratios in the range of 0.5 to 2.0, the results from the degradation model are in good agreement with the strength lines predicted by the pillar

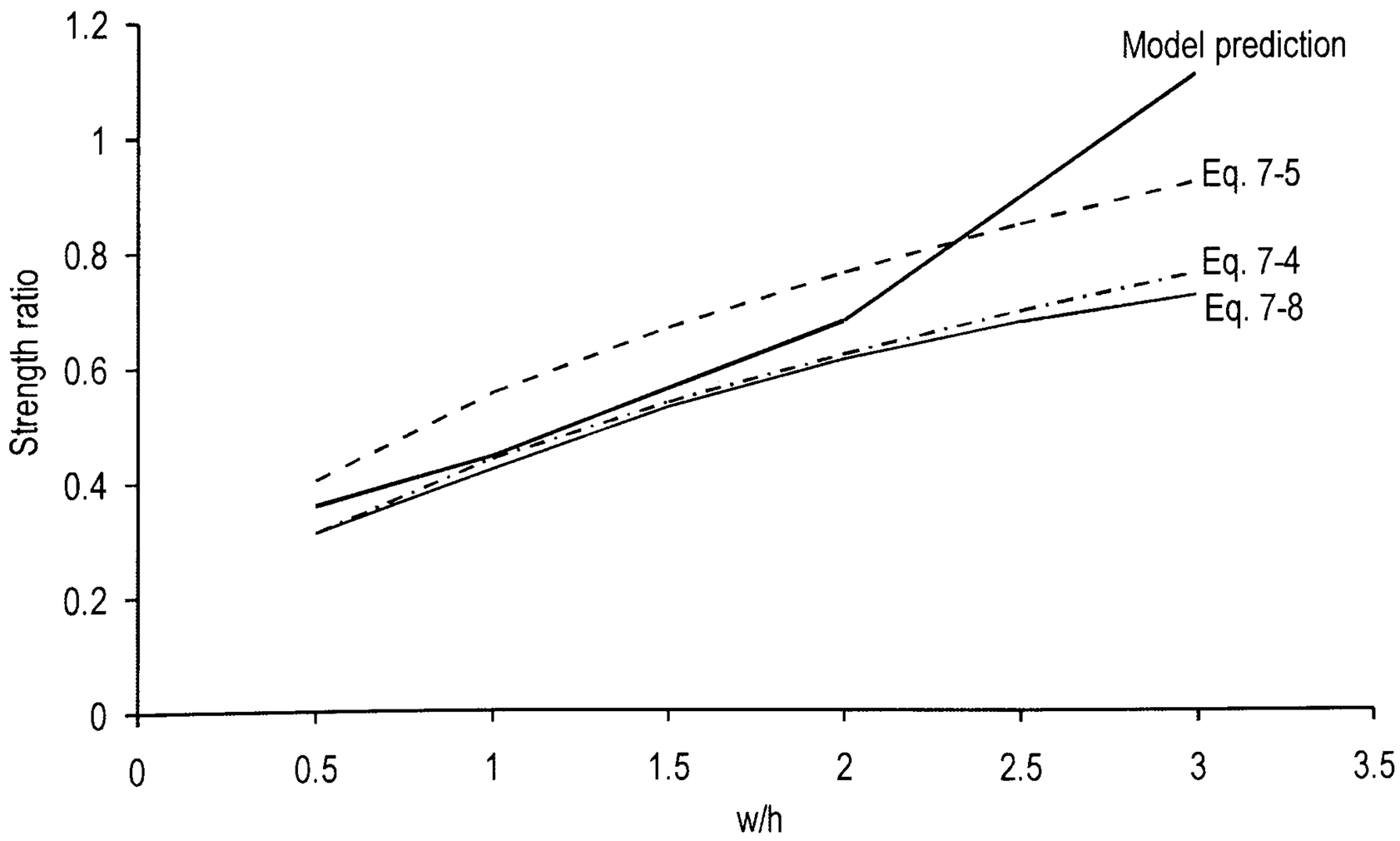


Figure 7.9. Comparison of pillar strengths prediction by the degradation model and by the various power or similar formulae in Table 7.1

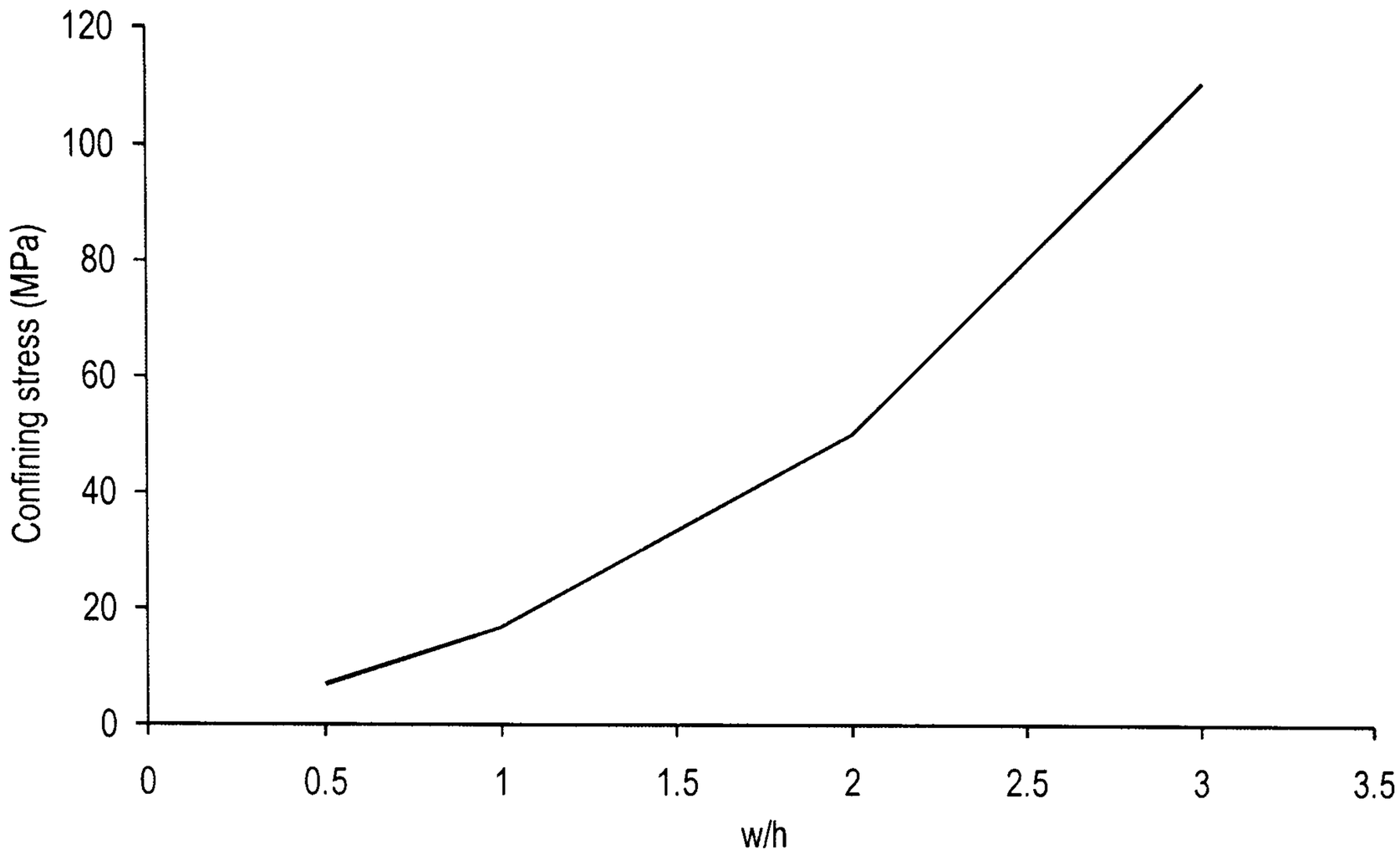


Figure 7.10. Confinement at the centre of the simulated pillar with various *w/h* ratios

strength formulae. However, for pillars with *w/h* ratios of more than 2.0, the degradation model predicts higher pillar strength. This phenomenon is attributed to the effect of confinement at the core of pillars in the simulated models, and the evidence for this is given by a plot of average confining stress along the pillar centre line when each pillar is at its peak strength, as shown in Figure 7.10. This indicates that the confining pressure at the centre of a pillar increases significantly with increasing *w/h* ratios, particularly when the *w/h* ratio is greater than 2.0.

Interestingly, in a review of coal pillar strength determination, Salamon (1999) commented that empirical pillar strength formulae may underestimate the strength of coal pillars if the *w/h* ratio is larger than 4. The maximum *w/h* ratio of collapsed hard rock pillars observed in the field is 2.5, and so the question is, do the same formulae underestimate the strength of pillars with a *w/h* ratio greater than 2.5? A further investigation is clearly required in this respect.

7.5 Influence of roof and floor contact conditions on pillar fracture

In the previous sections, the degradation model has shown that fracture of a pillar is influenced by its *w/h* ratio. The strength of a pillar may also be influenced by other factors (see Madden et al., 1998) that are not explicitly included in pillar design

formulae (Equations 7-2 and 7-3). Principal among those factors may be the contact conditions between the pillar and the roof and floor, and the elastic properties of the roof and floor. The influence of these two factors on pillar fracture is investigated using the degradation model in this section.

7.5.1 Friction angle of interfaces

With reference to Model 3, the pillar system with a *w/h* ratio of 2.0, in Table 7.2, the influence of interface friction on pillar fracture is investigated by assigning friction angles of 0°, 5°, 15°, and 20° to the interfaces (see Equation 5-16), respectively, with other parameters remaining the same as in Table 7.2. Figure 7.11 is the fracture patterns displayed by those models, including the one simulated in Section 7.3.

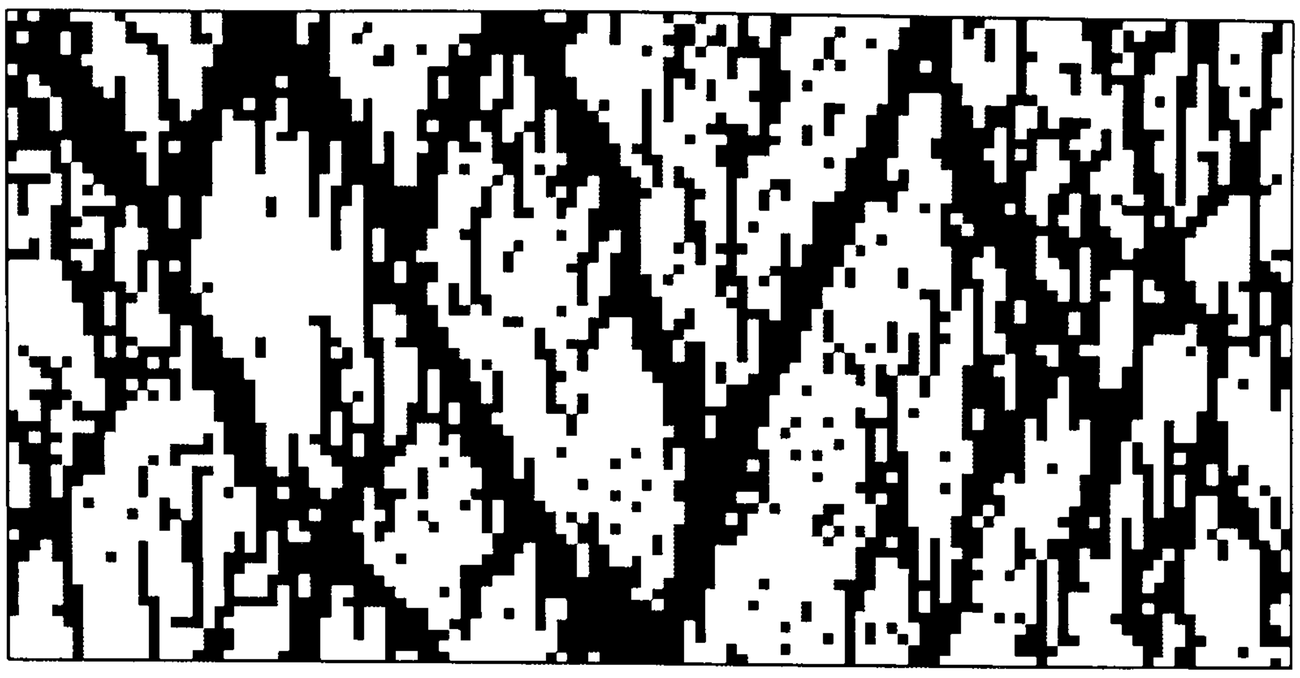
It is seen from Figure 7.11 that the fracture pattern of a pillar is significantly influenced by interface friction. With zero friction, shear fracture planes tend to start from the top interface, where the loading is performed, and develop gradually down to the bottom of the pillar with a constant plunge angle towards the centre of the pillar (Figure 7.11(a)). With an increase in interface friction angle, the fracture planes tend to curve (Figures 7.11(b) and (c)), and the interval between individual fracture planes reduces (Figure 7.11(c)). If the interface friction angle increases further, the curvature of the shear fracture plane increases and more failed sites between fracture planes are induced (Figures 7.11(d) and (e)). This is due to the interface friction angle producing a non-uniform confining effect within the pillar (referring to Figure 2.1), with the effect that the failure pattern of the pillar is influenced.

Corresponding to the fracture processes described above, pillars with different interface friction angles exhibit very different strength properties. Figure 7.12 is the stress-strain curves displayed by these pillars. As shown in Figure 7.12, the peak strength increases significantly and the post-peak behaviour becomes more ductile as the friction angle increases. This implies that a pillar with the same geometry and material properties may behave differently when subjected to different interface friction properties.

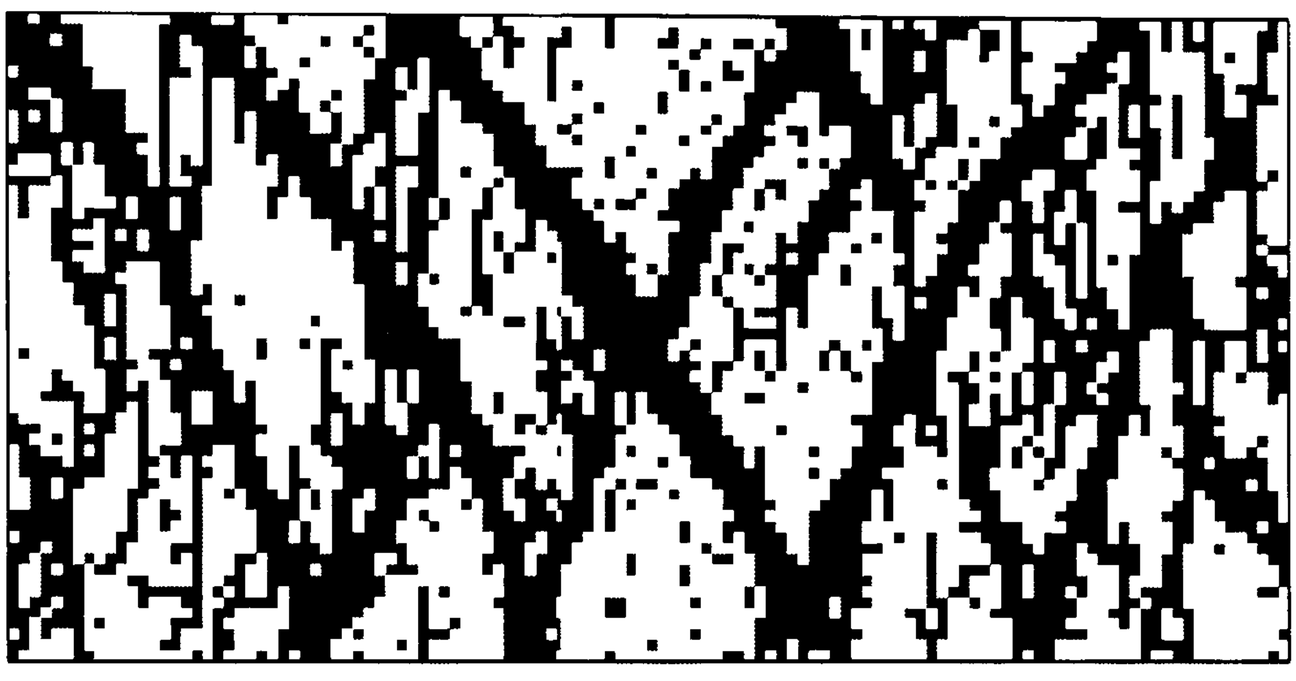
7.5.2 Roof and floor stiffness

The influence of roof and floor stiffness on pillar fracture is examined by reducing by 50% the elastic modulus of the roof and floor of Model 2 in table 7.2, whilst keeping the other parameters unchanged.

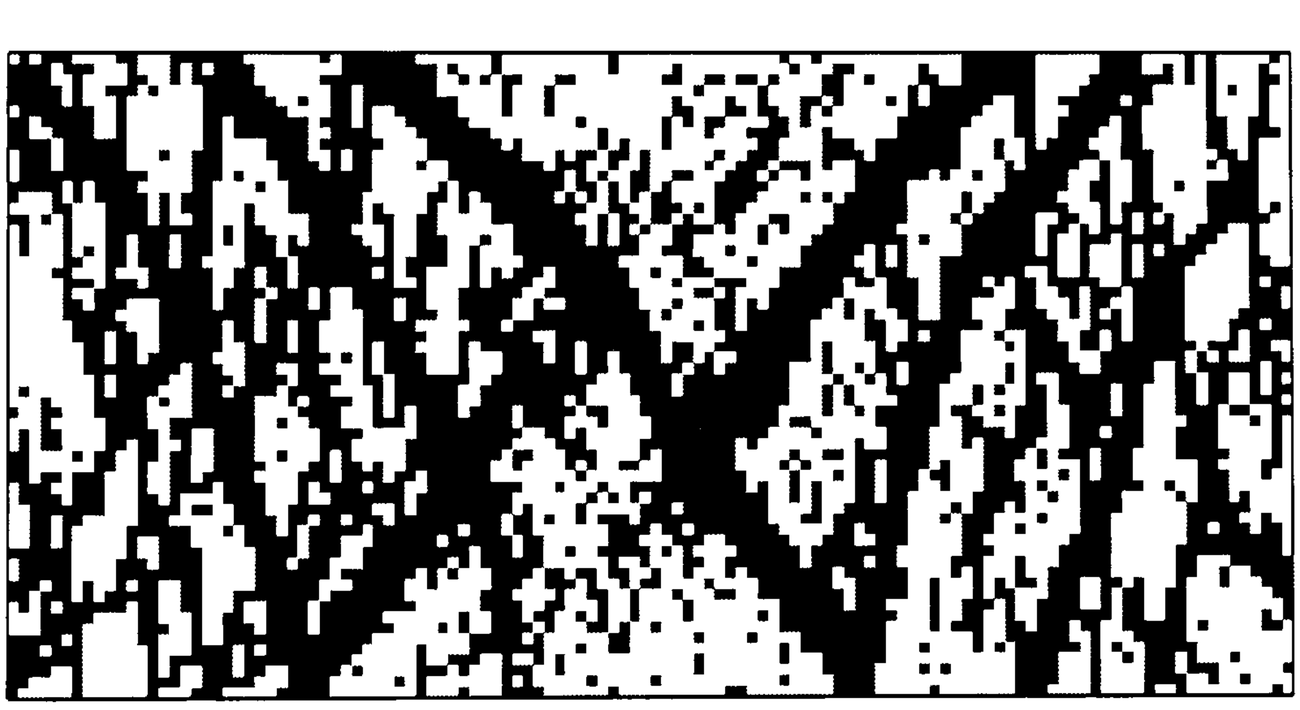
(a) 0°



(b) 5°



(c) 10°



(d) 15°

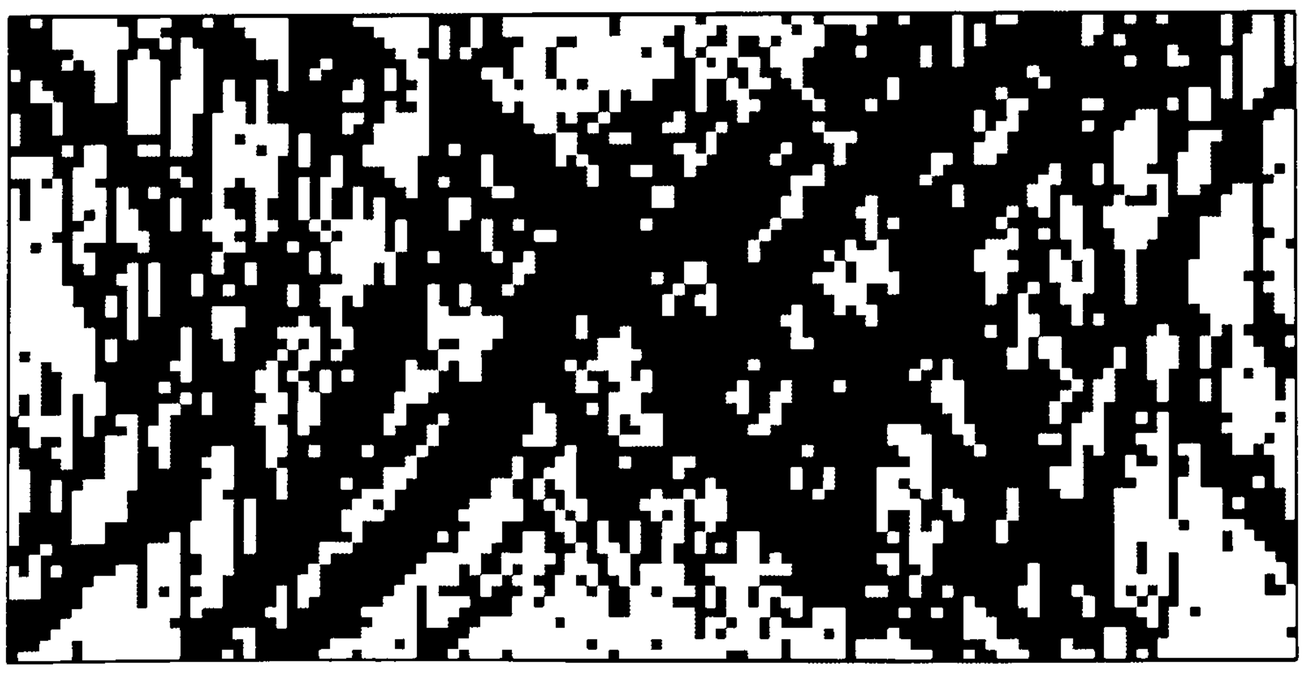


Figure 7.11. Simulated fracture patterns of a pillar with a *w/h* ratio of 2.0 and various interface friction angles

(e) 20°

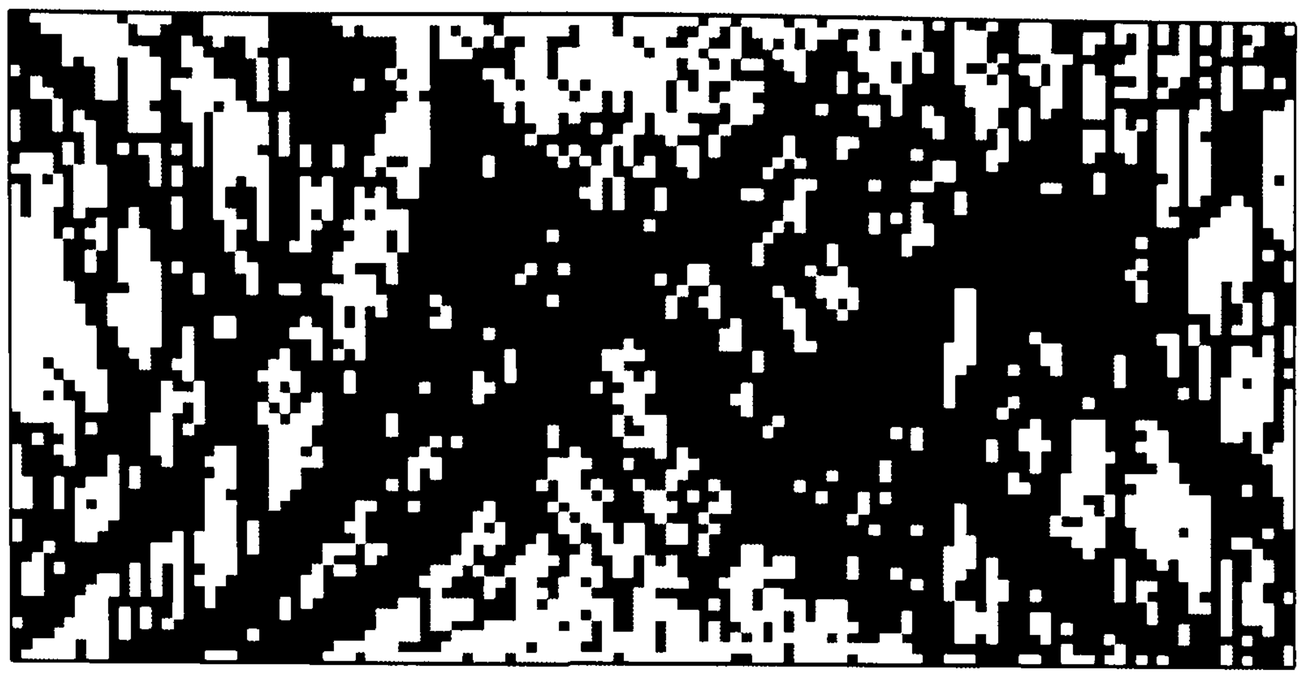


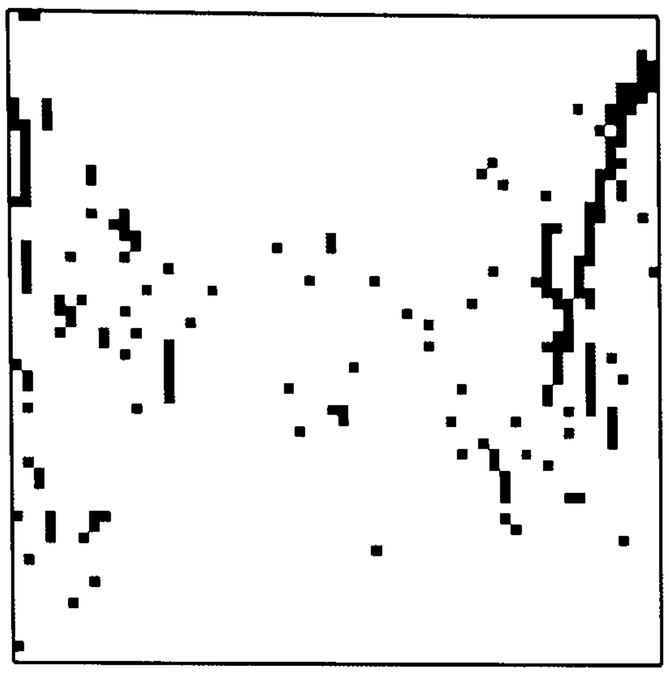
Figure 7.11 (continued)



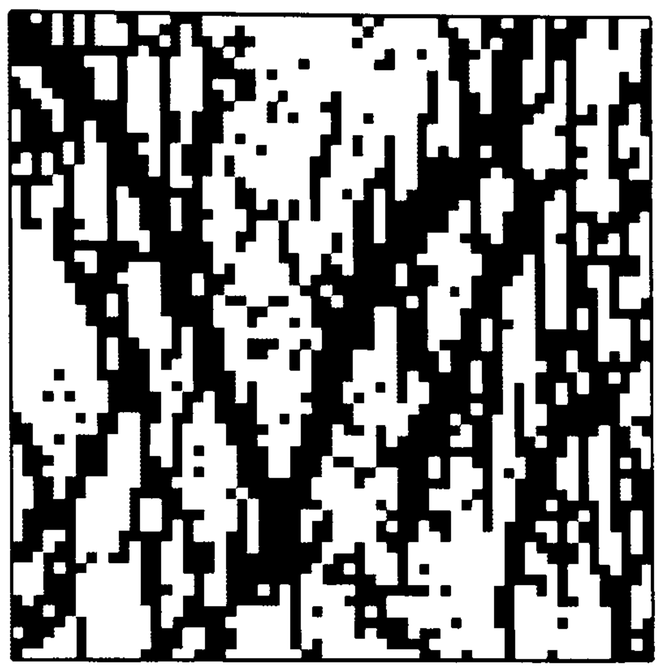
Figure 7.12. Simulated stress-strain relations for a pillar with a *w/h* ratio of 2.0 and various interface friction angles

Figure 7.13 shows the fracture patterns exhibited by the pillars. As demonstrated in Section 7.3, spalling of the ribsides (Figure 7.13(a)) and shear fracturing within the core of the pillar (Figure 7.13(b)) is a typical deterioration mode for the pillar with a stiff roof and floor.

In the case of a soft roof or floor, the mismatch between lateral extensions of the roof or floor and pillar produce tensile stresses within the ends of the pillar. As a result, fracture formation close to the ends of the pillar accompanies fracture development from the ribsides (Figures 7.13(c) and (e)). Subsequent loading induces additional such fractures, and the final failure pattern of the pillar is characterised by disintegration of

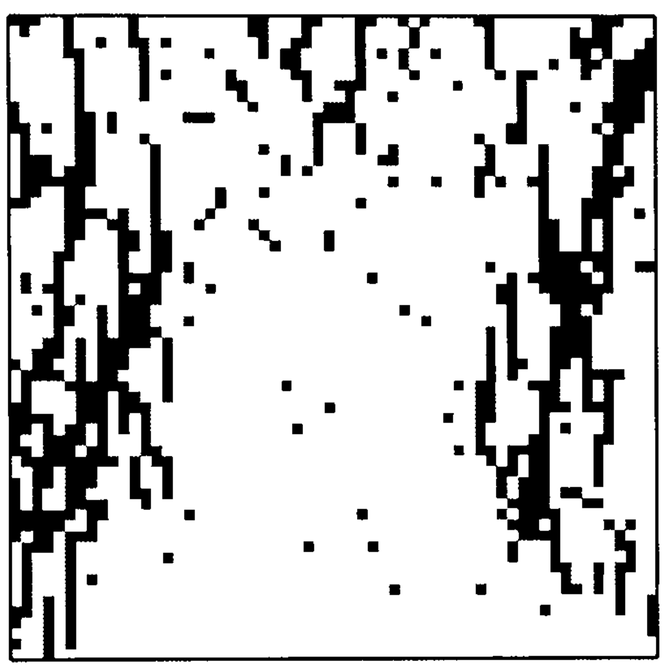


(a) Initial failure pattern

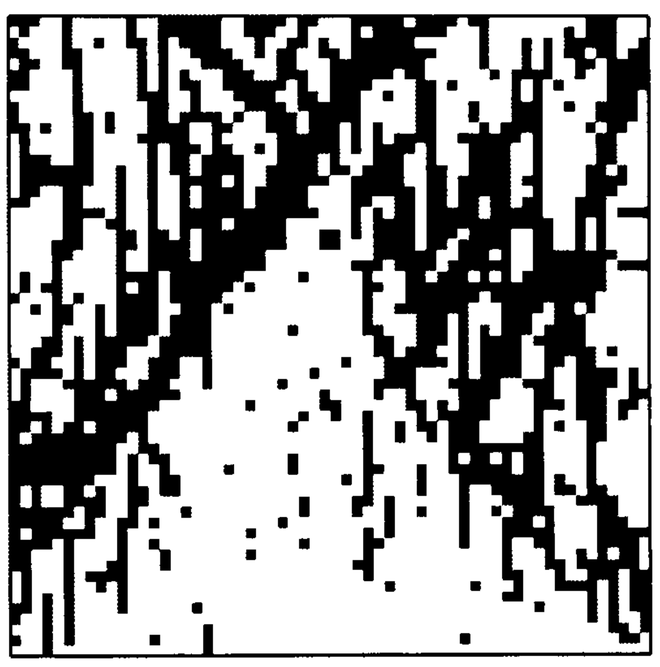


(b) Final failure pattern

Stiffer roof and floor

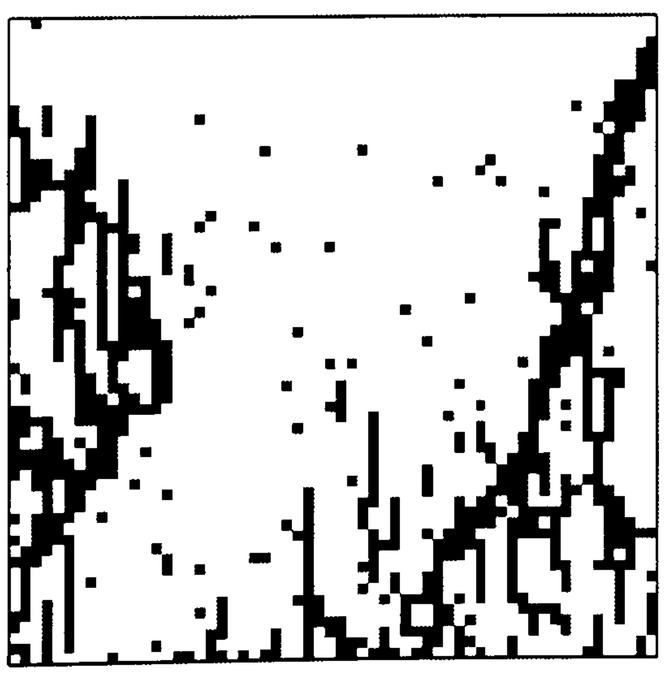


(c) Initial failure pattern

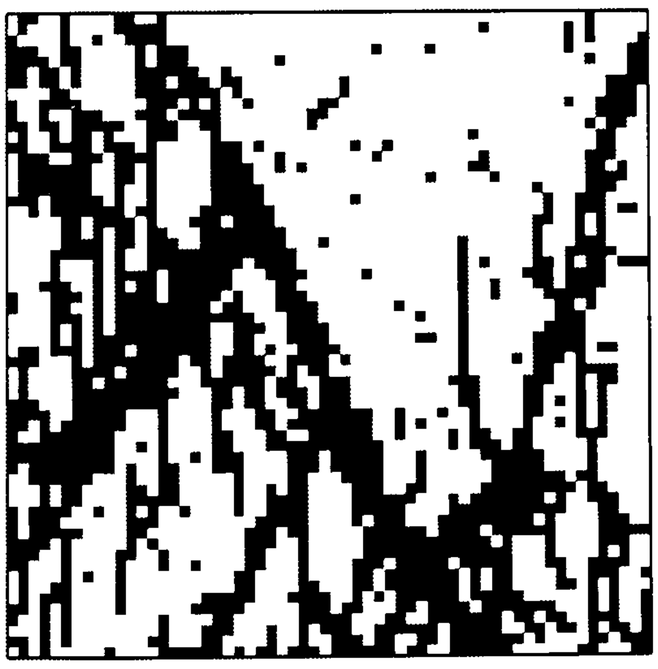


(d) Final failure pattern

Softer roof/stiffer floor



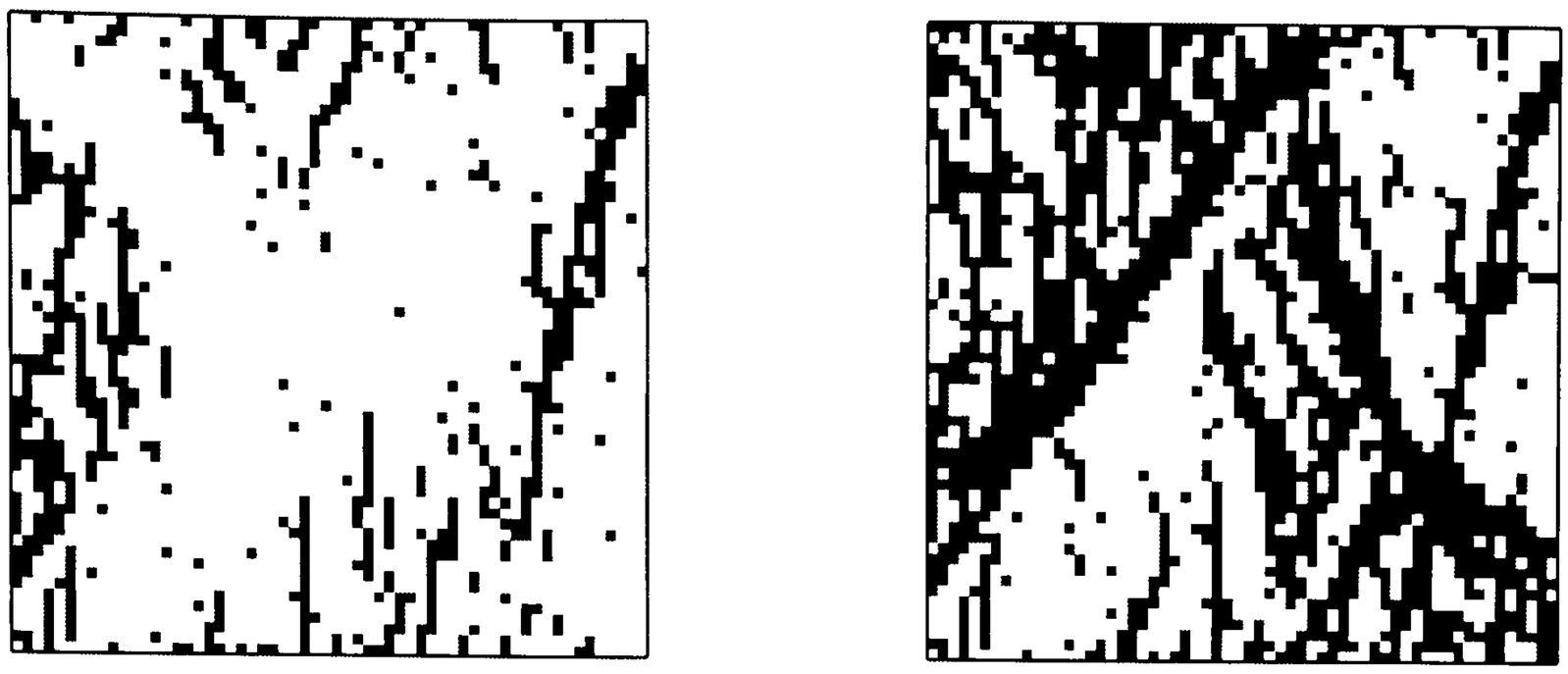
(e) Initial failure pattern



(f) Final failure pattern

Stiffer roof/softer floor

Figure 7.13. Simulated fracture patterns of a pillar with a *w/h* ratio of unity and various roof and floor stiffnesses



(g) Initial failure pattern (h) Final failure pattern

Softer roof and floor

Figure 7.13 (continued)

the pillar in a region adjacent to the soft roof or floor of the pillar (Figures 7.13(d) and (f)).

With this knowledge of the fracture pattern that develops in a pillar with a soft roof or floor, we may expect the failure of a pillar with both a soft roof and floor to be characterised by fracture from both the top and bottom of the pillar. This is indeed the case, as show in Figures 7.13(g) and (h).

The peak strength displayed by these models is dependent on the rigidity of the roof or/and floor. The peak strength exhibited by the pillar with stiffer roof and floor is 98 MPa, but this reduces to 92 MPa when a soft roof is present and 85 MPa in the case of soft floor. If both the floor and roof are softer than the pillar, a further loss in strength is encountered by the pillar, only reaching 80 MPa at the peak. This shows how pillar strength is reduced through the presence of either a soft roof or floor.

7.6 Closure

The fracture process of pillars has been simulated with the degradation model in this chapter, and the simulated fracture process is shown to compare well with field observations.

From both the simulation results and the field observations, two typical modes of pillar fracture may be classified. One is a fracture mode in which spalling from the ribsides is dominant, and this type of fracture is associated with very slender pillars of, say, *w/h* ratio under unity. The other failure mode is progressive development of shear

fractures, which is encountered with most other pillars. As a whole, however, the fracture process of a pillar may be interpreted as the initiation of random local failures, extension of the failed sites, coalescence of the extended sites, slabbing or spalling of the ribsides, and development of shear fractures.

The development of fracture in a pillar is influenced by its contact conditions with the roof and floor. With frictionless interfaces, fractures develop within a pillar at a constant inclined angle and a constant separation. With the presence of an interface friction angle, the development of fractures is along a curved plane and the distance between individual fracture planes decreases towards the centre of the pillar. The curvature of the fracture planes increases as the interface friction angle increases. This is because the interface friction produces a non-uniform confining stress within the pillar, which in turn is enhanced as the interface friction angle increases.

A soft roof and/or floor is another factor that influences pillar fracture. With the presence of soft roof and/or floor, additional tensile fractures develop from within the end of the pillar adjacent to the soft roof or floor. These fractures accelerate the deterioration of the pillar, and the pillar exhibits lower strength than with a stiffer roof and floor.

The degradation model predicts that pillar strength increases with increase in its *w/h* ratio. Within the range of between 0.5 and 2.0 in *w/h* ratio, the prediction of pillar strength from the degradation model is in good agreement with the predictions given by the so-called best-fit empirical pillar strength formulae. For a pillar with a *w/h* ratio beyond 2.0, the degradation model overestimates strength, and further research on this topic is suggested for the future.

8 Conclusions and future work

This work contributes to an understanding of brittle fracture occurring in heterogeneous rocks by means of a novel numerical approach to simulate the complete physical processes from the microscopic/mesoscopic scale to the macroscopic scale. The intensive investigations carried out in this work yield or refer to a number of conclusions. In addition, the necessarily limited scope of this study means that a number of tasks cannot be pursued in here, and should be considered in the future. Both the conclusions and future work are presented in this chapter.

8.1 Conclusions

The conclusions drawn from the study are reorganised in terms of subjects and listed below, in the sequence of their appearance.

8.1.1 Brittle fracture in heterogeneous rocks: the principal issues

Rock fracture and microscopic processes

Rock is one of the geomaterials that exhibit heterogeneity in their local physical and mechanical properties. Extensive laboratory and field investigations conducted on rock materials or rock structures by others researchers, in terms of compressive stress fields, have concluded the following (Chapter 2).

(a) Brittle fracture of rock is preceded by microstructural changes, or microscopic processes, manifested by cavity collapses, formation of cracks from the tip or boundary of flaws, extension and coalescence of cracks, and sliding between individual grains and crack surfaces.

(b) The extension of microcracks is influenced by confining pressure. Under uniaxial and low-confined compression, microcracks grow mainly in the direction of maximum principal stress, and the extension length reduces as confining pressure

increases. When confining pressure is sufficient, the growth of microcracks changes to a direction inclined to the maximum principal stress direction. If confining pressure is extremely high, sliding between grains and crack surfaces prevails.

(c) It is the coalescence of cracks that leads to eventual rock collapse, characterised by the formation of a single or several macroscopic fracture planes. In uniaxial compression, axial splitting is often induced. Under triaxial compression, however, shear fracture at an angle inclined to the maximum principal stress direction is the common mode of rock failure. At high confining pressures, a ductile shear fault may form, or the entire material body undergoes plastic flow. These indicate that coalescence only occurs to those cracks that in a favourable direction to such eventual fracture planes or faults.

(d) Corresponding to the microscopic processes, rock as a whole behaves in a varying manner. Associated with the appearance of microscopic processes, volume dilation occurs, and the lateral strain of rock loses its linearity. As these events increase, the axial stress-strain curve diverts but further axial strain requires extra loading. When microcracks localise and tend to coalesce, the rock exhibits its maximum load-carrying capability. The subsequent coalescence of microcracks leads to a gradual reduction in load carrying capability with additional strain, until the residual strength is reached when the formation of eventual fracture planes is complete. Associated with the complete microscopic processes, the secant modulus of the material degrades.

(e) As confining pressure influences microscopic processes, the mechanical behaviour of rock is highly dependent on confining pressure. In uniaxial compression, rock exhibits brittle behaviour. With increasing confining pressure, the reduction in elastic constants decreases, the peak strength of the rock increases, the strength loss after the peak decreases, and the mechanical behaviour of rock is characterised as strain softening. When rock displays plastic flow under high confinement, no strength loss and elastic constant reduction occur, and the corresponding mechanical behaviour becomes perfectly plastic.

These conclusions above indicate that brittle fracture in heterogeneous rocks involves complicated microscopic processes. These points form the physical basis for both developing and examining the validity of a method to describe fracture processes and the resulting macroscopic mechanical behaviour of materials.

Applicability of existing methods for describing fracture processes

With considering the complexity of microscopic processes associated with brittle fracture in heterogeneous rocks, a survey conducted in this research on the principles of existing methods has concluded the following (Chapter 3).

(a) Fracture mechanics theory, in which the mechanical behaviour of a fracturing material is related to the growth of a single isolated crack, cannot reproduce brittle fracture of heterogeneous rock under compression.

(b) Damage mechanics theory, that describes the overall behaviour of an object undergoing microstructural changes, does not describe isolated fracture processes of rock explicitly.

(c) Statistical techniques that deal with materials at individual sites or bonds are an alternative to take into account the role of heterogeneity of materials in fracture process.

Therefore, a sound mechanistic model that incorporates a failure theory at individual sites or bonds would be able to provide a means to examine fracture processes and the resulting mechanical behaviour of brittle rock from a micro to macro scale. To develop such a model for reproducing the observed physical phenomena in rock fracture from the microscopic to the macroscopic scale is the subject of this research.

Theoretical derivation of microscopic behaviour of rock

Based on the theoretical description of the creation of cracks and the corresponding results, analyses carried out in this research on the physical features of rock fracture have concluded the following (Chapter 4).

(a) The main mechanisms in rock fracture in compression can be classified into two types: breaking of particle bonds (microcracking) and sliding between the surfaces of particles or cracks (microsliding). The breakage of particle bonds causes a release in elastic strain energy and a reduction in strength and stiffness, whereas the sliding dissipates energy from the external loading through plastic deformation.

(b) At the microscopic level, a rock element undergoing these two mechanisms exhibits both elastic and plastic deformation. This is analogous to the fracture phenomena displayed by a rock specimen in the laboratory. Hence, it can be assumed that a rock element suffering these two mechanisms behaves in a similar way to the rock specimen itself in the laboratory, *i.e.* brittle if no confinement is present, strain-

softening if confinement is low to moderate with the softening degree decreasing as confining pressure increases, perfectly plastic if confinement is sufficient.

It appears that a rock element displays different combinations of the two microscopic mechanisms depending on the confining stress, and that the variations in the combination of the two microscopic mechanisms corresponds to variations in material degradation. This forms a key principle in the new model in describing brittle fracture of heterogeneous rocks from the microscopic to the macroscopic scale.

8.1.2 The new degradation model

The proposed degradation index of rock

Based on experimental results from rock specimens in the laboratory, the concept of degradation index has been developed in this research to describe the degradation that rock displays subjected to various confining pressures. The following explains the concept of the degradation index (Chapter 4).

(a) Degradation displayed by collapsing rock reduces with increasing confining pressure. This reduction may be described by the degradation index. The degradation index is defined in this research as the ratio of the degradation occurring at a certain confining stress level to the degradation corresponding to the uniaxial degraded stiffness (Figure 4.6).

(b) Four parameters are required to calculate the degradation index. They are the uniaxial compressive strength, the strength loss in uniaxial compression, the peak strength and strength loss under a specific confining pressure (Equation 4-23). These four parameters are experimentally determinable.

(c) It is likely that the relation between the degradation index of a rock and the variation of confining pressure is non-linear (Figure 4.7).

The degradation index is further referred to in associating rock elemental degradation behaviour in the new model.

Modelling of brittle fracture of rock

Brittle fracture can be regarded as the processes of: creation of cracks; variation of local properties; disturbance of local stress fields; extension of local failures; and formation of fracture planes. The physical occurrence of these processes and the resulting macroscopic mechanical behaviour are influenced by a number of factors, with

confining pressure considered as the most important in this work. This research has developed a model to capture the microscopic processes and the corresponding macroscopic mechanical behaviour of rock materials. This model contains four components. These are as follows (Chapter 4).

(a) Elemental degradation. The degradation of local elements is represented by the degradation index. The degradation index for rock elements can be expressed as being dependent on the minor principal stress, and may be derived from experimental data on customary specimens by means of linear regression. The negative exponential form with confining stress contained in the exponent may be the simplest and most convenient expression of the degradation index for rock elements (Equation 4-37).

(b) Elemental strength criterion. Rock fracture is manifested by progressive development of local failures. In order to trace this process, a strength criterion is required to evaluate local failures. Among the commonly used strength criteria, the Hoek-Brown criterion is in general more appropriate to describe the peak strength of rock elements subjected to various confining pressures.

(c) Elemental strength distribution. In terms of local strengths, rock is one of the highly heterogeneous brittle materials. A statistical function is required to describe heterogeneity of local strengths within rock. In this respect, the Weibull distribution function is appropriate.

(d) Constitutive behaviour. The elasto-plastic constitutive relation is appropriate for the deformation behaviour of rock elements. Due to the occurrence of strength degradation upon elemental collapse, plastic flow is maintained at the degraded strength level. Hence, this constitutive relation produces elastic-brittle-plastic elemental deformation behaviour.

There are no analytic forms available for this model, and hence a numerical procedure is sought to implement the degradation model.

Numerical implementation of the degradation model

The discussion of the model requirements, the principles of numerical techniques and the capability of computation facilities have concluded the following (Chapter 5).

(a) Explicit Finite difference method. As both heterogeneity and local degradation are to be included, the explicit finite difference method is most able to accommodate the

analysis required by the degradation model.

(b) FLAC code. The degradation model requires an incorporation of large strains. Fast Lagrangian Analysis of Continua (FLAC), which is a commercial code and is written using the explicit finite difference method, is appropriate for implementation of the degradation model.

8.1.3 Findings resulting from use of the degradation model

Fracture of rock specimens in the laboratory

The degradation model has been applied to simulate brittle fracture of rock specimens in the laboratory. The simulation results indicate that the degradation model can produce many characteristics of brittle fracture in heterogeneous rocks. These include the following (Chapter 6).

(a) The degradation model can reproduce the development of fracture from the elemental scale to the macroscopic scale subjected to variations of confining pressure. Local failures are initiated at a strain level well before the peak. With increased loading, along with new failure sites occurring, some of failed sites extend either in, or inclined to, the maximum principal stress direction. As a result, crack arrays may form. Further loading induces the coalescence of arrayed cracks, and a macroscopic fracture plane starts to form. As confining pressure increases, the strain level at which local failures are initiated increases, the number of failed sites before the formation of the eventual fracture plane increases, and the extension of failed sites is suppressed by the confining pressure. These predictions are unique to this model.

(b) The degradation model can reproduce the formation of arrayed cracks, and this is unique to this model. In uniaxial compression, the crack array forms mainly in the direction of the applied stress. With increasing confining stress, the array develops in a direction inclined to the maximum principal stress. The crack length developed under different confining pressures seems to contribute to the formation of eventual rock fracture.

(c) The degradation model can reproduce all the features of the dependence of stress-strain curves on confining pressure. These features include the following (Figures 2.21 and 6.28): as confining stress increases, the peak and residual strengths increase; the extent and degree of strain hardening before the peak stress increases;

the region incorporating the peak stress flattens and widens; a transition from typically brittle to fully ductile behaviour occurs at a certain confining stress level; the degree of strength loss after failure reduces; and the strain reached before macroscopic failure increases. These realistic predictions are unique to this model.

(d) The degradation model produces fracture patterns that are dependent on confining pressure (Figure 6.24). Under uniaxial compression, local failure development is mainly manifested by the extension of the failed sites in the direction of maximum principal stress, and the final failure of the rock specimen is induced by combination of axial splitting and shearing. With confining pressure present, the extension of the failed sites is suppressed, and the eventual failure of the rock specimen is due to the development of a shear fracture plane. When confining pressure is sufficiently large, the specimen fails by deforming across a widened shear fault. These predictions are unique to this model.

(e) The degradation model can reproduce the variations of fracture plane angle due to confining pressure. Under uniaxial compression, axial splitting dominates rock fracture. With the presence of a low confining pressure, a sharp shear fracture plane at a small angle to the major principal stress direction forms crossing the specimen. As the confining pressure increases, the angle of the fracture plane increases. This prediction is unique to this model.

(f) The degradation model can reproduce the energy dissipation features associated with acoustic emission. The strain energy dissipates at a gradually increasing rate as local failure occurs, and when failed sites coalesce the dissipation rate increases rapidly. When the eventual fracture plane forms the dissipation rate increases explosively. The final point in this prediction is unique to this model.

(g) The model results suggest that, with reference to the strength peak, the point at which the formation of macroscopic fracture planes completes varies. Under uniaxial and low confining pressure, the formation of the macroscopic fracture plane is in the post-peak stage. However, it moves towards the peak point as confining pressure increases. In the case of confining pressure being adequate, the formation of the macroscopic fracture plane may occur prior to the peak. Consequently, the appearance of the maximum energy dissipation rate (corresponding to the AE events) moves from the post peak regime to the region prior to the peak, as confining pressure increases. There appears to be no literature to support this

prediction.

(h) The degradation model can produce unloading and reloading hysteresis loops (Figure 6.29). This prediction is unique to this model.

Influence of model parameters

The model behaviour is influenced by both the degradation index and heterogeneity. Investigations have been carried out on these two topics and have led to the following conclusions (Chapter 6):

(a) The degradation parameter n_d, which determines the degradation index r_d, influences rock fracture. As n_d increases, the elemental degradation decreases. As a result, the number of failed sites prior to the formation of a macroscopic fracture plane increases, and both the peak strength and the residual strength predicted by the model increase.

(b) The shape parameter m_w in Weibull distribution function influences the formation of the fracture plane. When m_w increases, the heterogeneity reduces and hence the number of diffused failed sites and the angle of the eventual fracture plane tends to decrease. As a result, the peak strength and the brittleness of the resulting stress-strain curve increases. In addition, values between 2 and 4 seem appropriate for m_w in representing elemental strength distribution of rock materials.

Fracture of pillars

The degradation model is capable of reproducing the features associated with brittle fracture in heterogeneous rocks, and an application of the degradation model has been to analyse mine pillar behaviour. The results show the following (Chapter 7).

(a) The degradation model produces simulation results of the pillar fracture process that are in close agreement with field observations.

(b) The simulation results indicate that two pillar failure modes can be distinguished, *i.e.* ribside spalling and interior shear fracturing. The former is encountered by slender pillars, and the latter is exhibited by squat pillars. However, as a whole, the fracture process of a pillar can be interpreted as the initiation of random local failures, extension of the failed sites, coalescence of the extended sites, slabbing/spalling of ribsides, and development of shear fractures.

(c) The fracture pattern with a pillar is influenced by its roof and floor. With frictionless

interfaces, sets of fractures develop within a pillar at a constant inclined angle and a constant spacing. With the presence of an interface friction angle, the development of fractures is along a curved plane and the distance between individual fracture planes decreases towards the pillar centre. The curvature of the fracture planes increases as the interface friction angle increases.

(d) The development of fracture within a pillar is also influenced by the elasticity of the roof and floor. With the presence of a soft (*i.e.* very elastic) roof or/and floor, additional tensile fractures develop from within the end of the pillar adjacent to the soft roof/floor. These fractures accelerate the deterioration of the pillar, and the pillar exhibits lower strength than do its counterparts with a stiffer roof and floor.

(e) The degradation model predicts that pillar strength increases with increasing *w/h* ratio. With *w/h* ratio between 0.5 and 2.0, the prediction of strength from the degradation model is in good agreement with the predictions given by best-fit empirical pillar strength formulae. However, for a pillar with a *w/h* ratio greater than 2.0, the degradation model overestimates strength. This is because the confining effect within the pillar, which increases rapidly as the *w/h* ratio increases.

Other conclusions

There are other conclusions that cannot be grouped into the previous subjects, and these are listed below.

(a) Brittle fracture in heterogeneous rocks can be simulated by means of continuum approaches, provided the effects caused by microstructural changes are included.

(b) The commercial code FLAC, which has been developed to model ductile behaviour of rock materials, can be used to incorporate specific models that analyse brittle fracture in heterogeneous rocks.

(c) The linear Mohr-Coulomb failure criterion cannot be used to predict rock behaviour under highly confined compressions.

(d) The Normal distribution function is not appropriate for describing the heterogeneity of rock.

In short, all of these conclusions show that the degradation model is a sound mechanistic model for simulation of brittle fracture in heterogeneous rocks, and a wide range of application is expected for it.

8.2 Future work

The degradation model successfully reproduces many features associated with brittle fracture in heterogeneous rocks. However, with respect to four specific components, *i.e.* local degradation, the elemental constitutive relation, the elemental strength criterion, and heterogeneity distribution, the degradation model was proposed in its simplest form. In the light of knowledge of current understanding of general, rather than specific problems, limitations or shortcomings may be encountered in an application of the current degradation model to a practical problem. For an application of the degradation model to a specific problem, these four components may need to be modified to address different fundamental assumptions about the material's physical and mechanical properties. In addition, some other specific aspects associated with rock behaviour, such as the scale effect and anisotropy, are beyond the scope of this work and therefore have not been investigated. The following are suggestions for either further development or modification of the degradation model in considering these specific features.

(a) Degradation rule. In this research (Subsection 4.3.4), the degradation index is proposed to describe the post-peak behaviour displayed by brittle rock. The degradation index is expressed as either a power or a negative exponential function (Equations 4-36a and 4-36b), and the negative exponential function is used in this research. This may be different from rock to rock, and adequate data are required for validation. Therefore, further investigation into the expression of the degradation indices of rocks is suggested. The data required are (Equation 4-23) the peak and residual strengths that rock displays under various confining pressures, ranging from zero to the stress level at which the rock behaves perfectly plastic. It is likely that an investigation using a range of rock types is sufficient in this respect. Moreover, such an investigation also provides a database for the degradation index, the associated parameters (n_d in Equation 4-37, for example), the strength criterion (see the next point) and the degradation properties (estimated values are used in this work), which would be advisable for a practical application of the degradation model to a problem.

(b) Elemental strength criterion. In the current degradation model, the Hoek-Brown criterion is used to evaluate failure of rock elements. For most rocks or rock masses, the Hoek-Brown criterion gives a good prediction of strengths as a function of confining pressure. However, for some rocks, *e.g.* the soft rocks used by Wu (1991)

and Bésuelle et al. (2000), the Hoek-Brown criterion is inadequate in describing the strength features in the upper range of confining pressure, and an application of the degradation model to these cases may need some other form of the strength criterion. This may also be one of the reasons for the over estimation of the strength of mine pillars with *w/h* ratios greater than 2.0 (Section 7.4). Therefore, an investigation into strength criteria for a wider range of rocks is suggested, such that the results may be included in the degradation model for a more accurate simulation of brittle fracture in heterogeneous rocks.

(c) Constitutive relation. In this research, local degradation occurs at the instant local material failure occurs (elastic-brittle-plastic behaviour). This may produce limitations in the model results. One of the limitations that can be seen is in the production of hysteresis loops (Figure 6.29). In producing this phenomenon, degradation is not allowed during unloading and subsequent reloading over strains that correspond to the unloading cycle, otherwise too much degradation would occur during the unloading and reloading process (Figure 8.1). A modification is suggested in controlling the degradation process associated with the unloading-reloading cycles, perhaps in terms of time or a strain component, and this should be included in the expression of the degradation rule (Equation 4-37). Further research is suggested in this respect.

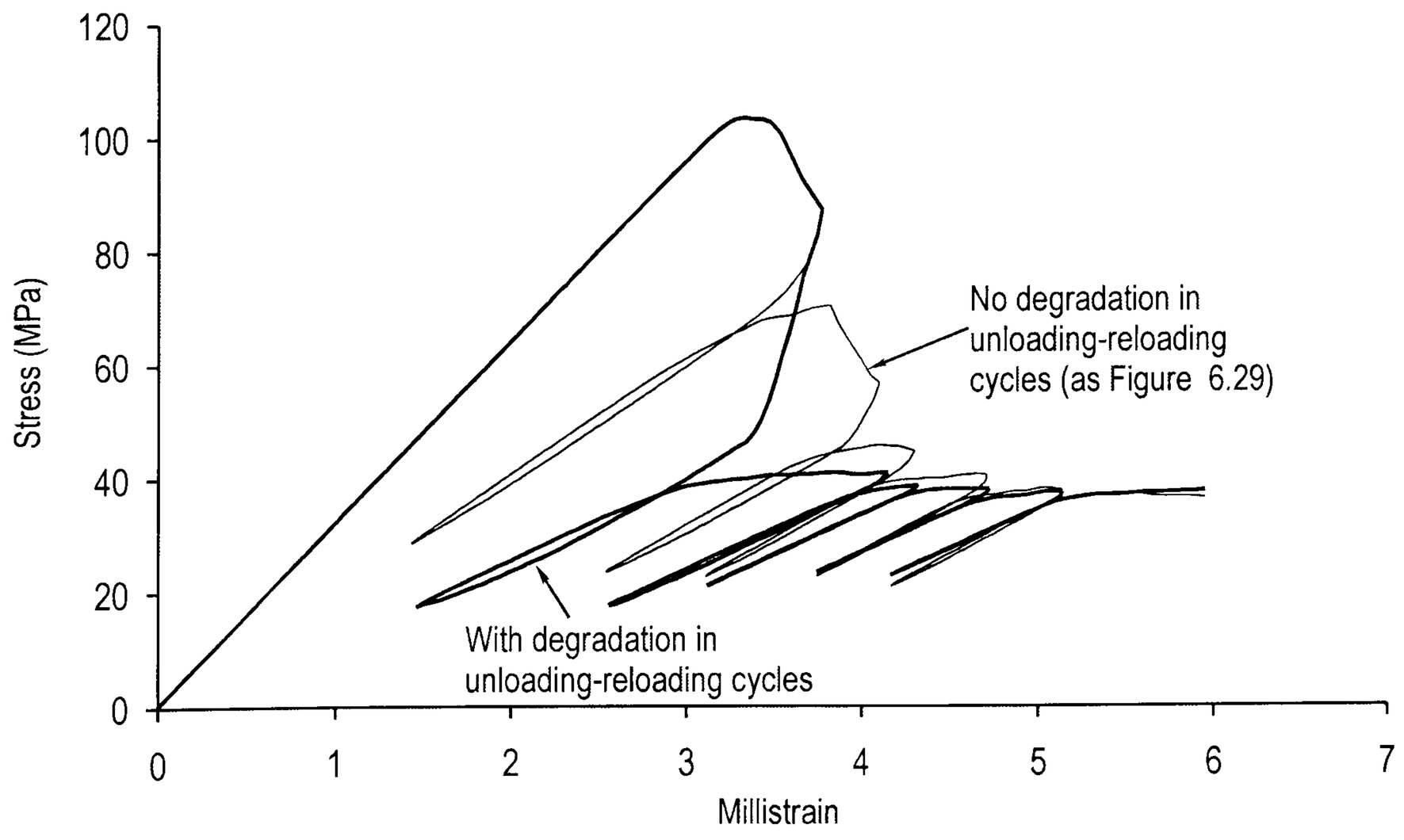


Figure 8.1. Hysteresis loops produced by the degradation model with two degradation processes

(d) Incorporation of other factors that influence degradation. In the current degradation rule, only the influence of confining pressure is considered. However, degradation may be influenced by other parameters, such as water content, temperature and time. These parameters may require to be included in describing the degradation behaviour of rock materials, and hence further research is suggested.

(e) Scale effect and mesh size. The scale effect is a common phenomenon in rock mechanics and rock engineering. In the degradation model, this effect is not addressed explicitly but implied by assigning strength properties of a problem model. In Section 6.3, it was seen that the model results are influenced by mesh sizes. It is likely that the mesh size could correlate to the scale effect. Further investigation is required for the incorporation of the scale effect in the degradation model by taking into account the mesh effect.

(f) Anisotropy. So far in this research, it has been assumed that the mechanical response of rock material is isotropic. However, rocks consist of an assemblage of minerals or particles with microstructures that contain a fabric of some sort (Jaeger and Cook, 1979). Because of some preferred orientation in the fabric, microstructure, or individual grains, or the presence of bedding or cleavage planes, the elastic properties and strength of many rocks, such as sedimentary rocks and metamorphic rocks, is anisotropic (Jaeger and Cook, 1979; Brady and Brown, 1992). To simulate brittle fracture of these rocks, the anisotropy may be considered in the behaviour of rock elements. Further research is suggested in this respect.

(g) Laboratory investigations into the formation of fracture planes within rock specimens. The degradation model predicted a phenomenon that the point at which the eventual fracture plane forms moves from the post-peak stage towards the peak point and into the pre-peak stage as confining pressure increases (Subsection 6.7.4), associated with the corresponding maximum strain energy dissipation rate (Subsection 6.7.5). Since no literature from laboratory observations has been found in this particular respect, a laboratory investigation is suggested for the future work to examine this prediction.

(h) Suitability of the Mohr-Coulomb strength criterion. One of the strength criteria incorporated in the degradation model is the Mohr-Coulomb strength criterion. This criterion gave a good prediction of brittle fracture and the corresponding macroscopic mechanical behaviour of rock over a low range of confining pressure

(the left column in Table 6.3). However, in the upper range of confining pressure, an unlikely prediction was encountered with this criterion in that the fracture plane becomes sharper associated with more brittle behaviour (Figure 6.3). The reasons for this phenomenon remain open, and hence, further investigation is suggested.

(i) Pillar strength. Literature on pillar strength suggests that pillar design remains a difficult task in underground operations, and an alternative is the numerical computation of the complex behaviour of failing rock from sound mechanistic models (Salamon, 1999). The simulation results of pillar behaviour from the degradation model in Chapter 7 suggest that the complex pillar behaviour in a complete mining condition can be simulated, provided a number of parameters such as the properties of the roof and floor, and the interfaces between the pillar and the roof and floor, could be determined. Further research, together with laboratory investigations, is suggested in this respect.

9 References

Andreev, G.E. 1995. Brittle Failure of Rock Materials: Test Results and Constitutive Models. Balkema, Rotterdam, 446p.

Ashby, M.F. and Hallam, S.D. 1986. The failure of brittle solids containing small cracks under compressive stress states. Acta Metall. 34:497-510.

Atkinson, B.K. 1987. Introduction to fracture mechanics and its geophysical applications. Fracture Mechanics of Rock, Atkinson, B.K. (ed.), Academic Press, London, 1-26.

Ayling, M.R., Meredith, P.G. and Murrell, S.A.F. 1995. Microcracking during triaxial deformation of porous rocks monitored by changes in rock physical properties. Tectonophys. 245:205-221.

Baud, P. and Meredith, P.G. 1997. Damage accumulation during triaxial creep of Darley Dale sandstone from pore volumometry and acoustic emission. Int. J. Rock Mech. Min. Sci. & Geomech. Abstr. 34(3-4): Paper No. 024.

Bazant, Z.P. and Chen, E.P. 1997. Scaling of structural failure. Appl. Mech. Rev. 50:593-627.

Bésuelle, P., Desrues, J. and Raynaud, S. 2000. Experimental characterisation of the localisation phenomenon inside a Vosges sandstone in a triaxial cell. Int. J. Rock Mech. Min. Sci. 37:1223-1237.

Bieniawski, Z.T. 1967. Mechanism of Brittle Fracture of Rock. PhD thesis, University of Pretoria, 226p.

Bieniawski, Z.T. 1968. *In situ* strength and deformation characteristics of coal. Eng. Geol. 2:325-340.

Bieniawski, Z.T. 1976. Rock mass classification in rock engineering. Exploration for Rock Engineering, Bieniawski, Z.T. (ed.), Balkema, Rotterdam, 1:97-106.

Bieniawski, Z.T. 1996. Milestones in Rock Engineering – the Bieniawski Jubilee Collection. Balkema, Rotterdam, 438p.

Bieniawski, Z.T. and Van Heerden, W.L. 1975. The significance of *in situ* tests on large rock specimens. Int. J. Rock Mech. Min. Sci. & Geomech. Abstr. 12:101-113.

Blair, S.C. and Cook, N.G.W. 1998. Analysis of compressive fracture in rock using statistical techniques: part I. a non-linear rule-based model. Int. J. Rock Mech. Min. Sci. 35(7):837-848.

Bombolakis, E.G. 1973. Study of the brittle fracture process under uniaxial compression. Tectonophys. 18:231-248.

Brace, W.F. and Bombolakis, E.G. 1963. A note on brittle crack growth in compression. J. Geophys. Res. 68(12):3709-3713.

Brace, W.F., Paulding, B.W. and Scholz. C. 1966. Dilatancy in the fracture of crystalline rocks. J. Geophys. Res. 71(16): 3939-3953.

Brady, B.H.G. and Brown, E.T. 1992. Rock Mechanics for Underground Mining, 2nd edition. Chapman & Hall, 571p.

Charlez, PH. A. 1997. Rock Mechanics, Vol. 2: Theoretical Fundamentals. Editions Technip, Paris.

Costin, L.S. 1985. Damage mechanics in the post-failure regime. Mech. Mater. 4:149-160.

Costin, L.S. 1987. Time-dependent deformation and failure. Fracture Mechanics of Rock, Atkinson, B.K. (ed.), Academic Press, London, 167-215.

Cox, S.J.D. and Meredith, P.G. 1993. Microcrack formation and material softening in rock measured by monitoring acoustic emissions. Int. J. Rock Mech. Min. Sci. & Geomech. Abstr. 30(1): 11-24.

Cundall, P.A. 2001. A discontinuous future for numerical modelling in geomechanics? Geotech. Eng. 149(1):41-47.

Cundall, P.A. and Strack, O.D.L. 1979. A discrete numerical model for granular assemblies. Geotechniq. 29(1):47-65.

Donath, F.A., Faill, R.T. and Tobin, D.G. 1971. Deformational model fields in experimentally deformed rock. Geol. Soc. Amer. Bull. 82:1441-1462.

Dragon, A. and Mroz, Z. 1979. A continuum model for plastic-brittle behaviour of rock and concrete. Int. J. Engng. Sci. 17:121-137.

Du, Y. and Aydin, A. 1991. Interaction of multiple cracks and formation of echelon

crack arrays. Int. J. Num. Anal. Meth. Geomech. 15:205-218.

Fairhurst, C. and Cook, N.G.W. 1966. The phenomenon of rock splitting parallel to a free surface under compressive stress. Proc. 1st Congr. ISRM, Lisbon, 1:687-692.

Fairhurst, C. and Pei, J. 1990. A comparison between the distinct element method and the finite element method for analysis of the stability of an excavation in jointed rock. Tunn. Undergr. Sp. Tech. 5(1/2):111-117.

Feng, Z. 1996. Continuum Mechanics and Its Numerical Modelling (in Chinese). Wuhan University, 276p.

Frantziskonis, G. and Desai, C.S. 1987. Constitutive model with strain softening. Int. J. Solids Struct. 23(6):733-750.

Gerogiannopoulos, N.G. and Brown, E.T. 1978. The critical state concept applied to rock. Int. J. Rock Mech. Min. Sci. & Geomech. Abstr. 15:1-10.

Ghosh, A. 1999. A Fortran program for fitting Weibull distribution and generating samples. Comput. & Geosci. 25:729-738.

Goodman, R.E. 1989. Introduction to Rock Mechanics, 2nd edition. John Wiley & Sons, 562p.

Griffith, A.A. 1921. The phenomena of rupture and flow in solids. Phil. Trans. Roy. Soc. Lond. A211: 163-198.

Griffith, A.A. 1924. The theory of rupture. Proc. 1st Int. Congr. Appl. Mech., Biezeno, C.B. and Burfers, J. M. (eds.), Waltman, London, 55-63.

Griggs, D. and Handin, J. 1960. Observations on fracture and a hypothesis on earthquakes. Rock Deformation, Griggs, D. and Handin, J. (eds.), Geol. Soc. Amer., 347-364.

Hallbauer, D.K., Wanger, H. and Cook, N.G.W. 1973. Some observations concerning the microscopic and mechanical behaviour of quartzite specimens in stiff, triaxial compression tests. Int. J. Rock Mech. Min. Sci. 10:713-726.

Hedley, D.G.F. and Grant, F. 1972. Stope-and-pillar design for the Elliot Lake Uranium Mines. Bull. Can. Inst. Min. Metall. 65:37-44.

Hedley, D.G.F., Roxburgh, J.W. and Muppalaneni, S.N. 1984. A case history of rock bursts at Elliot Lake. Proc. 2nd Int. Conf. Stab. Undergr. Min., Szwilski, A.B. and Brawner, C.O. (eds.), Soc. Min. Eng., AIME, New York, 210-234.

Hoek, E and Bieniawski, Z.T. 1965. Brittle fracture propagation in rock compression. Int. J. Fract. Mech. 1:137-155.

Hoek, E. and Brown, E.T. 1980. Underground Excavations in Rock. Inst. Min. Metall., Stephen Austin and Sons, London, 527p.

Hoek, E. and Brown, E.T. 1997. Practical estimates of rock mass strength. Int. J. Rock Mech. Min. Sci. & Geomech. Abstr. 34(8):1165-1186.

Hoek, E., Kaiser, P.K. and Bawden, W.F. 1995. Support of Underground Excavations in Hard Rock. Balkema, Rotterdam, 215p.

Holland, C.T. 1962. Design of pillars for overburden supports – part II. Min. Congr. J. 48(4):66-71.

Horii, H. and Nemat-Nasser, S. 1985. Compression-induced microcrack growth in brittle solids: axial splitting and shear failure. J. Geophys. Res. 90:3105-3125.

Horii, H. and Nemat-Nasser, S. 1986. Brittle failure in compression: splitting, faulting and brittle-ductile transition. Phil. Trans. Roy. Soc. Lond. A319:337-374.

Hudson, J. A. 1989. Rock Mechanics Principles in Engineering Practice. CIRIA, Butterworths, 72p.

Hudson, J.A. and Fairhurst, C. 1969. Tensile strength, Weibull's theory and a general statistical approach to rock failure. Structure, Solid Mechanics and Engineering Design, Te'eni, M. (ed.), Univ. Southampton, 901-914.

Hudson, J.A. and Harrison, J.P. 1997. Engineering Rock Mechanics: an Introduction to the Principles. Pergamon, 444p.

Ilankamban, R. and Krajcinovic, D.1987. A constitutive theory for progressively deteriorating brittle solids. Int. J. Solids Struct. 23(11):1521-1534.

Ingraffea, A.R. 1987. Theory of crack initiation and propagation in rock. Fracture Mechanics of Rock, Atkinson, B.K. (ed.), Academic Press, London, 71-110.

Irwin, G.R. and de Wit, R. 1983. A summary of fracture mechanics concepts. J. Test. and Eval. 11(1):56-65.

ISRM, 1978. Suggested methods for determining the uniaxial compressive strength and deformability of rock materials. Int. J. Rock. Mech. Min. Sci. & Geomech. Abstr. 16:137-140.

Itasca 1995a. Fast Lagrangian Analysis of Continua, Version 3.3, Minnesota.

Itasca 1995b. Partical Flow Code in 2 Dimensions, Version 1.1, Minnesota.

Jaeger, J.C. and Cook, N.G.W. 1979. Fundamentals of Rock Mechanics, 3rd edition. Chapman and Hall, London, 593p.

Kachanov, L.M. 1958. The time to fracture under creep conditions (English translation). Izv. Akad. Nauk SSSR, Otdel. Tekh. Nauk, 8:26-31.

Kachanov, L.M. 1986. Introduction to Continuum Damage Mechanics, Martinus Nijhoff Publishers, Dordrecht, 135p.

Kaiser, P.K. and Tang, C.A. 1998. Numerical simulation of damage accumulation and seismic energy release during brittle rock failure — part II: rib pillar collapse. Int. J. Rock Mech. Min. Sci. 35(2):123-134.

Kavamoto, T. and Aydan, O. 1999. A review of numerical analysis of tunnels in discontinuous rock masses. Int. J. Num. Anal. Meth. Geomech. 23:1377-1391.

Kemeny, J.M. 1991. A model for non-linear rock deformation under compression due to sub-critical crack growth. Int. J. Rock. Mech. Min. Sci. & Geomech. Abstr. 28(6): 459-467.

Kemeny, J.M. and Cook, N.G.W. 1987. Crack models for the failure of rock under compression. Proc. 2nd Int. Conf. Cons. Laws for Eng. Mater. 2:879-887.

Kemeny, J.M. and Tang, F.F. 1990. A numerical damage model for rock based on microcrack growth, interaction, and coalescence. Am. Soc. Mech. Eng., Appl. Mech. Div., AMD, 109:103-116.

Kovari, K., Tisa, A., Einstein, H.H. and Franklin, J.A. 1983. Suggested methods for determining the strength of rock materials in triaxial compression: revised version. Int. J. Rock Mech. Min. Sci. & Geomech. Abstr. 20:283-290.

Krajcinovic, D. and Fonseka, G.U. 1981. The continuous damage theory of brittle materials — part 1: general theory. J. Appl. Mech., Trans. ASME, 48: 809-815.

Krajcinovic, 1984. Continuum damage mechanics. Appl. Mech. Rev. 37(1):1-6.

Krajcinovic, 1989. Damage Mechanics. Mech. Mater. 8:117-197.

Kranz, R.L.1979a. Crack growth and development during creep of Barre granite. Int. J. Rock Mech. Min. Sci. & Geomech. Abstr. 16:23-35.

Kranz, R.L. 1979b. Crack-crack and crack-pore interaction in stressed granite. Int. J. Rock Mech. Min. Sci. & Geomech. Abstr. 16:37-47.

Kranz, R.L. 1983. Microcracks in rocks: a review. Tectonophys. 100:449-480.

Krauland, N. and Soder, P.E. 1987. Determining pillar strength from pillar failure observations. Eng. Min. J. 8:34-40.

Kuijpers, J.S. 1995. Numerical simulation of failure processes in brittle rock. Fractured and Jointed Rock Masses, Myer, Cook, Goodman and Tsang (eds), Balkema, Rotterdam, 687-694.

Lamaitre, L. 1984. How to use damage mechanics. Nucl. Eng. Des. 80:233-245.

Lawn, B.R. 1993. Fracture of Brittle Solids, 2nd edition. Cambridge Univ. Press.

Lawn, B.R. and Wilshaw, T.R. 1975. Fracture of Brittle Solids. Cambridge Univ. Press, 204p.

Lehner, F. and Kachanov, M. 1996. On modelling of "winged" cracks forming under compression. Int. J. Fract. 77:R69-R75.

Li, H.B., Zhao, J. and Li, T.J. 2000. Micromechanical modelling of the mechanical properties of a granite under dynamic uniaxial compressive loads. Int. J. Rock Mech. Min. Sci. 37:923-935.

Liao, J.S. 1995. An elastoplastic-damage model for rock like materials. Mechanics of Jointed and Faulted Rock, Rossmanith, H.P. (ed.), Balkema, Rotterdam, 247-252.

Lin, C.T., Amadei, B., Jung, J. and Dwyer, J. 1996. Extensions of discontinuous deformation analysis for jointed rock masses. Int. J Rock Mech. Min. Sci. & Geomec. Abstr. 33(7):671-694.

Lockner, D.A., Byerlee, J.D., Kuksenko, V. Ponomarev, A. and Sidorin, A. 1991. Quasi-static fault growth and shear fracture energy in granite. Nature, 350(7):39-42.

Lockner, D.A., Moore, D.E. and Reches, Z. 1992. Microcrack interaction leading to shear fracture. Proc. 33rd US Symp. Rock Mech., Tillerson, J.R. and Wawersik, W.R. (eds.), Balkema, Rotterdam, 807-816.

Lockner, D.A. 1995. Rock failure. Rock Physics and Phase Relations: a Handbook of Physical Constants, Ahrens, T.J. (ed.), AGU, Washington, 127-147.

Lunder, P.J. and Pakalnis, R.C. 1997. Determination of the strength of hard-rock mine pillars. CIM Bull. 90(1013):51-55.

Madden, B.J., Canbulat, I. and York, G. 1998. Current South African coal pillar research. J. S. Afr. Inst. Min. Metall. 98(1):7-10.

Martin, C.D. and Chandler, N.A. 1994. The progressive fracture of Lac du Bonnet granite. Int. J. Rock Mech. Min. Sci. & Geomech. Abstr. 31:643-659.

Martin, C.D. and Maybee, W.G. 2000. The strength of hard rock pillars. Int. J. Rock Mech. Min. Sci. 37:1239-1246.

Mase, G.T. and Mase, G.E. 1999. Continuum Mechanics for Engineers, 2nd edition. CRC Press, 377p.

McClintock, F.A. and Walsh, J.B. 1962. Friction on Griffith cracks in rocks under pressure. Proc. 4th US Nat. Congr. Appl. Mech. 1015-1021.

Meglis, I.L., Chow, T.M., Young, R.P. 1995. Progressive microcrack development in test on Lac du Bonnet: I. emission source location and velocity measurements. Int. J. Rock Mech. Min. Sci. & Geomech. Abstr. 32(8):741-750.

Menendez, B., Zhu, W., Wong, T.F. 1996. Micromechanics of brittle faulting and cataclastic flow in Berea sandstone. J. Struct. Geol. 18:1-16.

Mohlhaus, H.B. 1979. On the structure of stress-strain rate relations for time independent deformations in crystalline rocks. Proc. 4th Congr. ISRM, Montreux, 2:447-453.

Mokgokong, P.S. and Peng, S.S. 1991. Investigation of pillar failure in the Emaswati Coal Mine, Swaziland. Min. Sci. and Tech. 12:113-125.

Moss, W.C. and Gupta, Y.M. 1982. A constitutive model describing dilatancy and cracking in brittle rocks. J. Geophys. Res. 87(B4):2985-2998.

Nemat-Nasser, S. and Horii, H. 1982. Compression-induced nonplanar crack extension with application to splitting, exfoliation, and rockburst. J. Geophys. Res. 87(B8):6805-6821.

Obert, L. and Duvall, W. 1942. Use of subaudible noise for prediction of rockbursts. U.S. Bureau of Mines Rept. Invest. 3634:13.

Obert, L. and Duvall, W. 1967. Rock Mechanics and the Design of Structure in Rock. John Wiley & Sons, 650p.

Ofoegbu, G.I. and Curran, J.H. 1991. Yielding and damage of intact rock. Can. Geotech. J. 28:503-516.

Ofoegbu, G.I. and Curran, J.H. 1992. Deformability of intact rock. Int. J. Rock Mech. Min. Sci. & Geomech. Abstr. 29(1):35-48.

Olsson, W.A. and Peng, S.S. 1976. Microcrack nucleation in Marble. Int. J. Rock Mech. Min. Sci. & Geomech. Abstr. 13:53-59.

Ozbay, M.U., Ryder, J.A. and Jager, A.J. 1994. The design of pillar systems as practised in shallow hard-rock tabular mines in South Africa. J. S. Afr. Inst. Min. Metall. 95(1):7-18.

Pande, G.N., Beer, G. and Williams, J.R. 1990. Numerical Methods in Rock Mechanics. John Willey & Sons, 327p.

Paterson, M.S. 1978. Experimental Rock Deformation: the Brittle Field. Springer Verlag, Berlin, 254p.

Peng, S. and Johnson, A.M. 1972. Crack growth and faulting in cylindrical specimens of Chelmsford granite. Int. J. Rock Mech. Min. Sci. 9:37-86.

Pietruszczak, S. and Mroz, Z. 1981. Finite element analysis of deformation of strain-softening materials. Int. J. Num. Meth. Engng. 17:327-334.

Potyondy, D.O., Cundall, P.A. and Lee, C.A. 1996. Modelling rock using bonded assemblies of circular particles. Proc. 2nd N. Amer. Rock Mech. Symp., Montreal, Canada.

Pusch, R. 1995. Rock Mechanics on a Geological Base. Elsevier, Amsterdam, 498p.

Ramez, M.R.H. 1967. Fractures and the strength of a sandstone under triaxial compression. Int. J. Rock Mech. Min. Sci. 4:257-268.

Robet, A. 2000. Initiation of secondary cracks in compression. Eng. Fract. Mech. 66(2):187-219.

Salamon, M.D.G. 1967. A method of designing bord and pillar workings. J. S. Afr. Inst. Min. Metall. 68:68-78.

Salamon, M.D.G. and Munro, A.M. 1967. A study of the strength of coal pillars. J. S. Afr. Inst. Min. Metall. 68:55-67.

Salamon, M.D.G. 1999. Strength of coal pillars from back-calculation. Rock Mechanics for Industry: Proc. 37th U.S. Rock Mech. Symp., Amadei, B., Kranz, R.L., Scott, G.A. and Smeallie, P.H. (eds.), Vail, Colorado, 29-36.

Sammis, C.G. and Ashby, M.F. 1986. The failure of brittle porous solids under compressive stress states. Acta Metall. 34:511-526.

Scholz, C.H. 1968. Microfracturing and the inelastic deformation of rock in

compression. J. Geophys. Res. 73(4): 1417-1432.

Shao, J.F. and Rudnicki, J.W. 2000. A microcrack-based continuous damage model for brittle geomaterials. Mech. Mater. 32:607-619.

Shen, B. 1993. Mechanics of Fractures and Intervening Bridges in Hard Rocks. PhD thesis, Royal Institute of Technology, Stockholm, Sweden.

Sheorey, P.R. 1997. Empirical Rock Failure Criteria. Balkema, Rotterdam, 176p.

Simmons, G. and Ritcher, D. 1976. Microcracks in rock. The Physics and Chemistry of Minerals and Rocks, Strens, R.G.J. (ed.), Willey, New York, 105-137.

Sjoberg, J. 1992. Failure modes and pillar behaviour in the Zinkgruvan mine. Proc. 33rd U.S. Rock Mech. Symp., Tillerson, J.A. and Wawersic, W.R. (eds.), Rotterdam, Balkema, 491-500.

Souley, M. and Homand, F. 1996. Stability of jointed rock masses evaluated by UDEC with an extended Saeb-Amadei constitutive law. Int. J Rock Mech. Min. Sci. & Geomec. Abstr. 33(3):233-244.

Sprunt, E.S. and Brace, W.F. 1974. Direct observation of microcavities in Crystalline rocks. Int. J. Rock Mech. Min. Sci. & Geomech. Abstr. 11:139-150.

Stagg, K.G. and Zienkiewicz, O.C. 1968. Rock Mechanics in Engineering Practice. John Wiley & Sons, 442p.

Steif, P.S. 1984. Crack extension under compressive loading. Eng. Fract. Mech. 20(3):463-473.

Tang, C., Liu, H, Lee, P.K.K., Tsui, Y. and Tham, L.G. 2000. Numerical studies of the influence of microstructure on rock failure in uniaxial compression — part I: effect of heterogeneity. Int. J. Rock Mech. Min. Sci. 37:555-569.

Tapponier, P. and Brace, W.F. 1976. Development of stress-induced microcracks in Westerly granite. Int. J. Rock Mech. Min. Sci. & Geomech. Abstr. 13:103-112.

Thill, R.E. 1972. Acoustic methods for monitoring failure in rock. New Horizons in Rock Mechanics: Proc. 14th Symp. Rock Mech., Hardy, H.R. and Stefanko, R. (eds.), Penn. State Univ., ASCE, New York, 649-687.

Tullis, J. and Yund, R.A. 1977. Experimental deformation of dry Westerly granite. J. Geophys. Res. 82(36):5705-5718.

Tzou, D.Y. and Chen, E.P. 1991. Mesocrack damage induced by a macrocrack in heterogeneous materials. Eng. Fract. Mech. 39(2):347-358.

Valanis, K.C. 1985. On the uniqueness of solution of the initial value problem in softening materials. J. Appl. Mech. 52:649-653.

Van Mier, J.G.M., Schlangen, E. and Vervuurt, A. 1995. Lattice type fracture models for concrete. Continuum Models for Materials with Microstructure. Muhlhaus, H.B. (ed.), John Wiley & Sons, 482p.

Vardoulakis, I., Labuz, J., Papamichos, E. and Tronvoll, J. 1998. Continuum fracture mechanics of uniaxial compression on brittle materials. Int. J. Solids Struct. 35(31-32):4313-4335.

Vardoulakis, I. and Sulem, J. 1995. Bifurcation Analysis in Geomechanics. Blackie Academic & Professional, Chapman & Hall, 462p.

Vermeer, P.A. and De Borst, R. 1984. Non-associated plasticity for soils, concrete and rock. Heron, 29(3):5-64.

Vervoort, A. and Jack, B. 1992. Analysis of sidewall fracturing and spalling during coal-pillar extraction. J. S. Afr. Inst. Min. Metall. 92(1):3-11.

Von Kimmelmann, M.R., Hyde, B. and Madgwick, R.J. 1984. The use of computer applications at BCL Limited in planning pillar extraction and design of mining layouts. Design and Performance of Underground Excavations, Brown, E.T. and Hudson, J.A. (eds.), BGS, London, 53-63.

Wagner, H. 1974. Determination of the complete load-deformation characteristics of coal pillars. Advances in Rock Mechanics: Proc. 3rd ISRM Congr., IIB, Dener, Colorado, 1076-1081.

Wawersik, W.R. and Brace, W.F. 1971. Post-failure behaviour of granite and diabase. Rock Mech. 3:61-85.

Wawersik, W.R. and Fairhurst, C. 1970. A study of brittle rock fracture in laboratory compression experiments. Int. J. Rock Mech. Min. Sci. & Geomech. Abstr. 7:561-575.

Weibull, W. 1939. A statistical theory of the strength of materials. Ing. Vetenskaps Akad. Handl. 151:5-44.

Weibull, W. 1951. A statistical distribution function of wide applicability. J. Appl.

Mech.18:293-297.

Weijermars, R. 1997. Principles of Rock Mechanics. Alboran Science Publishing, 359p.

Whittaker, B.N., Singh, R.N. and Sun, G. 1992. Rock Fracture Mechanics. Elsevier, 570p.

Wong. R.H.C. and Chau, K.T. 1997. Crack coalescence in a rock-like material containing two cracks. Int. J. Rock Mech. Min. Sci. 35:147-164.

Wong, T.F. 1982. Micromechanics of faulting in Westerly granite. Int. J. Rock Mech. Min. Sci. & Geomech. Abstr. 19:49-64.

Wu, B. 1991. Investigations into the Mechanical Behaviour of Soft Rocks. PhD thesis, Imperial College of Science, Technology and Medicine, University of London. 485p.

Wu, X.Y., Baud, P. and Wong, T.F. 2000. Micromechanics of compressive failure and spatial of anisotropic damage in Darley Dale sandstone. Int. J. Rock Mech. Min. Sci. 37:143-160.

Yazdani, S. and Schreyer, H.L. 1990. Combined plasticity and damage mechanics model for plain concrete. J. Eng. Mech. 116:1435-1450.

Yuan, Y.G., Lajtai, E.Z. and Ayari, M.L. 1993. Fracture nucleation from a compression-parallel, finite-width elliptical flaw. Int. J. Rock Mech. Min. Sci. & Geomech. Abstr. 30(7):873-876.

Zang, A., Wagner, C.F. and Dresen, G. 1996. Acoustic emission, microstructure, and damage model of dry and wet sandstone stressed to failure. J. Geophys. Res. 101(B8):17507-17521.

Zhang, J.X., Wong, T.F. and Davis, D.M. 1990. Micromechanics of pressure-induced grain crushing in porous rocks. J. Geophys. Res. 95:341-351.

Zhao, J. 2000. Applicability of Mohr-Coulomb and Hoek-Brown strength criteria to the dynamic strength of brittle rock. Int. J. Rock Mech. Min. Sci. 37:1115-1121.

Zhu, W. and Wang, P. 1993. Finite-element analysis of jointed rock masses and engineering application. Int. J Rock Mech. Min. Sci. & Geomech. Abstr. 30(5):537-544.

Appendix A Description of deformation and motion of material bodies

The degradation model has been developed using a continuum approach (Chapter 4), and a commercial code for analysis of continua (FLAC) has been chosen for its implementation (Chapter 5). On these bases, an introduction to the basic principles of continuum mechanics theory may be useful for a full understanding of the implementation procedure of the degradation model. This Appendix outlines the essentials of the theory in describing the deformation and motion of material bodies. These essentials include the associated terms and fundamental laws, such as the Lagrangian description and the equation of motion, and are presented in a form similar to that given by Mase and Mase (1999) and Feng (1996).

A.1 Explanation of terms

A material body occupies a region of physical space, and according to Mase and Mase (1999), it may be assumed "that the substance of such a body is distributed uniformly throughout, and completely fills the space it occupies". Thus, field quantities may be ascribed to each and every point of the region of space that the body occupies and the deformation and motion of the material body may be described. This section explains the terms used in describing the deformation and motion of a material body.

With respect to a material body as a set of elements or particles, the specification of the position of all the particles with respect to a fixed origin at some instant of time is said to define the *configuration* of the body at that instant. A change in configuration is referred to a *displacement* of the body. A *deformation* is a change in size, or shape, or both of the body. *Motion* of the body is a continuous time sequence of displacements that carries the set of particles into various configurations in a stationary space.

Certain configurations of the body have special meaning. The configuration the body occupied at time $t = 0$ is called *the initial configuration*, and the one the body occupies at the current time is called *the current configuration*. A *reference configuration* is a configuration from which all displacements are reckoned, and the

initial configuration is often chosen as the reference configuration.

A.2 Lagrangian and Eulerian description

Consider a material body with a volume V and a boundary surface A, and assume that the body undergoes a displacement with a change in size or/and shape. As illustrated in Figure A.1, let vector $\boldsymbol{X}$ ($X1$, $X2$, $X3$) denote the position P of a particle X in the body in the reference configuration at time $t = 0$. At a later time, the point moves to another position p. Then the mapping of the current configuration of the particle can be described in terms of the position vector $\boldsymbol{X}$ and time t, with respect to the reference configuration, as

$$\boldsymbol{x} = \boldsymbol{x}(\boldsymbol{X}, t), \tag{A-1}$$

where

$$\boldsymbol{X} = X_i \hat{\boldsymbol{I}}_i, \tag{A-2}$$

where the components X_i are called the material coordinates, and $\hat{\boldsymbol{I}}_i$ are the unit vectors along coordinate axes. The description given by Equation A-1 is called the material description or the Lagrangian description.

On the other hand, the current configuration of the body can also be described in terms of the usual Cartesian coordinates $\boldsymbol{x}$ (spatial coordinates) as

$$\boldsymbol{X} = \boldsymbol{X}(\boldsymbol{x}, t), \tag{A-3}$$

where

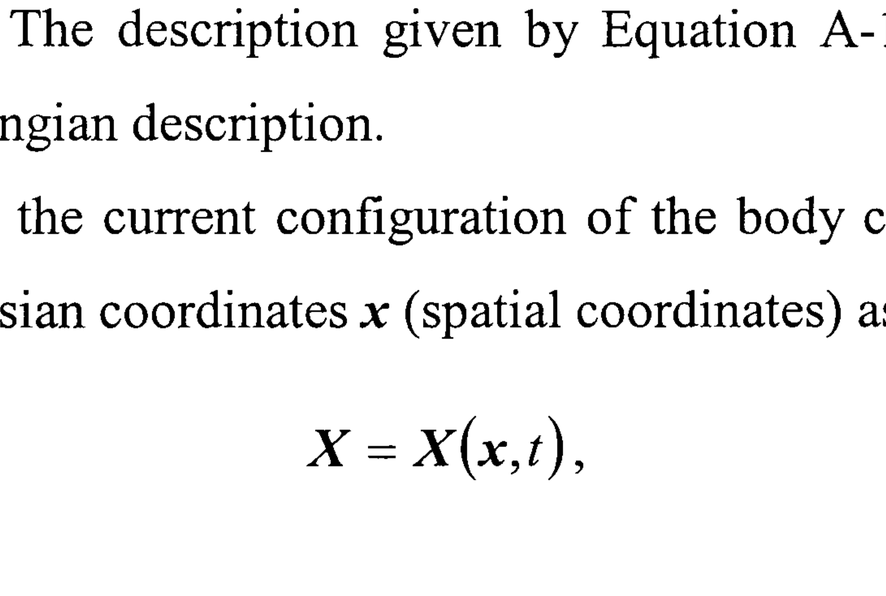


Figure A.1. Position of typical particle in reference and current configurations (after Mase and Mase, 1999)

$$\boldsymbol{x} = x_i \hat{\boldsymbol{e}}_i \,, \tag{A-4}$$

where $\hat{\boldsymbol{e}}_i$ are the unit vectors.

The description given by Equation A-3 is called the spatial or Eulerian description.

Comparing these two descriptions above, it is noted that the Lagrangian description interprets what is happening to the individual particles during the motion, whereas the Eulerian description describes the events taking place at specific points in space (Mase and Mase, 1999).

In the description of material deformation and motion, the velocity v_i of a point is defined as

$$\boldsymbol{v} = \dot{\boldsymbol{x}} = \frac{\partial \boldsymbol{x}(\boldsymbol{X}, t)}{\partial t}, \tag{A-5}$$

in the Lagrangian context, and

$$\boldsymbol{v} = \dot{\boldsymbol{X}} = \frac{\partial \boldsymbol{X}(\boldsymbol{x}, t)}{\partial t}, \tag{A-6}$$

in the Eulerian context. Similarly, the acceleration a_i of a point is defined as

$$\boldsymbol{a} = \dot{\boldsymbol{v}} = \ddot{\boldsymbol{x}} = \frac{\partial \boldsymbol{x}^2(\boldsymbol{X}, t)}{\partial t^2}, \tag{A-7}$$

in the Lagrangian context, and

$$\boldsymbol{a} = \dot{\boldsymbol{v}} = \ddot{\boldsymbol{X}} = \frac{\partial \boldsymbol{X}^2(\boldsymbol{x}, t)}{\partial t^2}, \tag{A-8}$$

in the Eulerian context. Finally, the displacement of the particle X is given as

$$\boldsymbol{u} = \boldsymbol{x} - \boldsymbol{X} = \boldsymbol{x}(\boldsymbol{X}, t) - \boldsymbol{X} \,, \tag{A-9}$$

in the Lagrangian context, and

$$\boldsymbol{u} = \boldsymbol{x} - \boldsymbol{X} = \boldsymbol{x} - \boldsymbol{X}(\boldsymbol{x}, t), \tag{A-10}$$

in the Eulerian context. The differentiation of Equation A-9, with respect to time t, yields

$$\frac{d\boldsymbol{u}}{dt} = \frac{d(\boldsymbol{x} - \boldsymbol{X})}{dt} = \frac{d\boldsymbol{x}}{dt} = \boldsymbol{v} \,, \tag{A-11}$$

to give an alternative definition for velocity.

A.3 Deformation gradient and finite strain tensors

The differentiation of Equation A-1 with respect to X_j gives the deformation gradient of the body, F_{ij}, which has the form

$$F_{ij} = \frac{\partial x_i}{\partial X_j} . \tag{A-12}$$

Furthermore, as shown in Figure A.2, consider two neighbouring particles of the body situated at the points P and Q in the undeformed configuration, and moved to the points p and q, respectively, in the deformed configuration. The magnitude squared of the distance between the points P and Q is

$$(dX)^2 = d\boldsymbol{X} \cdot d\boldsymbol{X} = dX_i dX_j = \delta_{ij} dX_i dX_j . \tag{A-13}$$

The magnitude squared of the distance between the points p and q is expressed as

$$(dx)^2 = d\boldsymbol{x} \cdot d\boldsymbol{x} = dx_i dx_j = \delta_{ij} dx_i dx_j . \tag{A-14}$$

Since

$$dx_i = \frac{\partial x_i}{\partial X_j} dX_j , \tag{A-15}$$

we find that

$$(dx)^2 = \frac{\partial x_k \partial x_k}{\partial X_i \partial X_j} dX_i dX_j . \tag{A-16}$$

Therefore, the difference between Equations A-13 and A-14 is expressed as

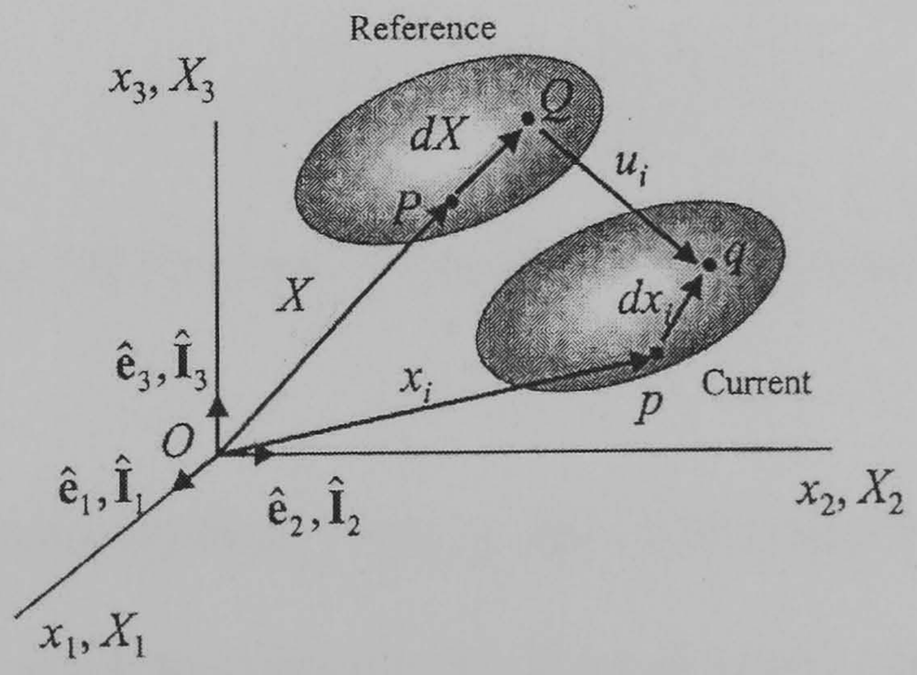


Figure A.2. Points *P* and *Q* in the reference configuration becomes *p* and *q* in the current configuration (after Mase and Mase, 1999)

$$(dx)^2 - (dX)^2 = \left(\frac{\partial x_k \partial x_k}{\partial X_i \partial X_j} - \delta_{ij} \right) dX_i dX_j = 2E_{ij} dX_i dX_j, \qquad \text{(A-17)}$$

where

$$E_{ij} = \frac{1}{2}\left(\frac{\partial x_k \partial x_k}{\partial X_i \partial X_j} - \delta_{ij} \right) \qquad \text{(A-18)}$$

is called the Lagrangian finite strain tensor.

The difference $(dx)^2 - (dX)^2$ can also be developed in terms of the Eulerian variables in a similar way as

$$(dx)^2 - (dX)^2 = \left(\delta_{ij} - \frac{\partial X_k \partial X_k}{\partial x_i \partial x_j} \right) dx_i dx_j = 2e_{ij} dx_i dx_j, \qquad \text{(A-19)}$$

where

$$e_{ij} = \frac{1}{2}\left(\delta_{ij} - \frac{\partial X_k \partial X_k}{\partial x_i \partial x_j} \right) \qquad \text{(A-20)}$$

is called the Eulerian finite strain tensor.

By making use of Equations A-9 and A-10, the expressions for the two tensors in terms of the displacement gradients are as

$$E_{ij} = \frac{1}{2}\left(\frac{\partial u_i}{\partial X_j} + \frac{\partial u_j}{\partial X_i} + \frac{\partial u_k \partial u_k}{\partial X_i \partial X_j} \right), \qquad \text{(A-21)}$$

and

$$e_{ij} = \frac{1}{2}\left(\frac{\partial u_i}{\partial x_j} + \frac{\partial u_j}{\partial x_i} - \frac{\partial u_k \partial u_k}{\partial x_i \partial x_j} \right). \qquad \text{(A-22)}$$

These two equations will be used to derive the infinitesimal deformation theory in the next section.

A.4 Infinitesimal deformation theory and infinitesimal strain tensors

If the numerical values of all the components of the displacement and the displacement gradient tensors are very small, the products of these quantities may be neglected. Thus, the Lagrangian and Eulerian finite strain tensors (Equations A-21 and A-22) may be

expressed in a reduced form as

$$E_{ij} = \frac{1}{2}\left(\frac{\partial u_i}{\partial X_j} + \frac{\partial u_j}{\partial X_i}\right) \tag{A-23}$$

and

$$e_{ij} = \frac{1}{2}\left(\frac{\partial u_i}{\partial x_j} + \frac{\partial u_j}{\partial x_i}\right), \tag{A-24}$$

which are called the infinitesimal Lagrangian and Eulerian strain tensors, respectively. In this case, since the difference between $\frac{\partial u_i}{\partial x_j}$ and $\frac{\partial u_i}{\partial X_j}$ can be ignored, we find that

$$E_{ij} \approx e_{ij}\,. \tag{A-25}$$

Therefore, to the first order of approximation for the case of small displacement gradients, the two descriptions can be regarded as equal.

A.5 Equations of motion

Consider a material continuum body having a current volume V and bounding surface A and density ρ. The body is subjected to surface traction $t_i^{(\hat{n})} = \sigma_{ji} n_j$ (where σ_{ij} is the stress tensor, and n_j is the outward normal to the surface) and disturbed body forces ρb_i (b_i is the force per unit mass), and is in motion under the velocity field $v_i = du_i / dt$. The linear momentum of the body is defined as

$$P_i(t) = \int_V \rho v_i dV\,. \tag{A-26}$$

According to the Newton's second law, the rate of change with respect to time of linear momentum is equal to the resultant force acting on the body. The principle of linear momentum gives (Mase and Mase, 1999)

$$\sigma_{ji,j} + \rho b_i = \rho \dot{v}\,, \tag{A-27}$$

where the comma indicates the partial differentiation with respect to the space variables.

Equation A-27 is called the equation of motion, which is an essential for describing the deformation of material bodies.

A.6 Gauss divergence theorem

For a finite region of a continuum material body subjected to a tensile field $T_{ij\ldots k}$, the Gauss divergence theorem provides a relationship between the surface integral having $T_{ij\ldots k}$ as integrand to the volume integral for which a coordinate derivative of $T_{ij\ldots k}$ is the integrand. This theorem has the form

$$\int_A T_{ij\ldots k} n_q \, dA = \int_V T_{ij\ldots k,q} \, dV \,, \tag{A-28}$$

where V is the volume, A is the bounding surface, and n_i is the outward normal to this bounding surface with $dA_i = n_i dA$.

Appendix B: FLAC codes for the degradation model for rock specimens

The FLAC implementation (Chapter 5) of the degradation model developed in this work (Chapter 4) has been used to simulate fracture of rock specimens in the laboratory (Chapter 6) and various programs have been written for performing these numerical tests. In order for readers to understand the complete numerical test procedure, these programs are presented here. We first interpret the function of each module and various variables contained, followed by explanation of the code format. After the listing of the source code, the data used in performing the series of numerical tests in Chapter 6 are finally given in Section B.4, as an example of how to operate the FLAC code for an analysis of brittle fracture of rock specimens.

It should be noted that apart from the source code that is given in Sections B.4, the individual module names are denoted by bold font in the following presentation. These module names can be readily distinguished from the section titles in the similar font type.

B.1 Individual modules

In Chapter 5, we presented a flow chart for the implementation of the degradation model (Figure 5.7). For performing a numerical test, individual modules have been defined and written following the sequence shown by this flow chart. Table B.1 lists these modules and their functions, in accordance with the components shown in the flow chart (Figure 5.7).

B.2 Code variables

The code introduced here includes two types of variables: those that are used by more than one module, which we call 'global variables'; and those that are only used in a single procedure, which we call 'local variables'. To distinguish these from each other, the global variables have the prefix '`dm_`' and local variables have either a form similar

Table B.1. Individual modules in FLAC code of the degradation model for rock specimens

Module	Function	Subroutine and function
Grid_generation	Generate grid representing geometry for platen, rock specimen and interface	
sc_T0_input	Input σ_c and T_0 for rock specimen	**UD** for uniform distribution, **ND** for normal distribution **WD** for Weibull distribution
other_input	Input other parameters for rock, platen and interfaces, and calculate zone area	**r_input** for rock specimen, **p_input** for platen, **if_input** for interface and **zone_area** for computing zone area
con_stress	Apply confining stress and solve for equilibrium	
loading	Apply external loading	
dmanalysis	Perform model analysis in each timestep	**degradation** for degradation operation
degradation	Operate degradation and the associated calculations	**MC_degradation** for Mohr-Coulomb criterion, **HB_degradation** for Hoek-Brown criterion, **G_degradation** for Griffith criterion, and **energy_diss** for strain energy dissipation calculation
dmoutput	Output model results	**stress** for axial stress, **astrain** for axial strain and **ed_rate** for energy dissipation rate
dmsolve	Operate step loops	**dmstep** for step monitoring

to the associated equations or the prefix '`xy_`' for their names, where '`xy`' is an abbreviation of the procedure name, *e.g.* procedure '**`stress`**' has local variables of the form '`st_...`'.

B.3 Operation procedure for the FLAC code

In performing a numerical test on rock specimens, all the individual modules listed in Table B.1 have to be defined prior to their execution. Then, after the setting of associated parameters, the modules may be called as required. However, the modules that are responsible for the setup of a problem model (the modules listed before **`dmanalysis`** in Table B.1) may be called together once all of the parameters have been set. Thus, these modules are called from the module **`dmrs`** (representing degradation model for rock samples-see Section B.4). In addition, the module **`dmanalysis`** allows automatic execution of **`degradation`** in each step via the Fish statement `while_stepping` (see section B.4; and also see Itasca, 1995a), so that the module **`degradation`** is not called explicitly during the performance of model analysis. Hence, we may organise a concise procedure for operating the FLAC code in a numerical test, and this is given in Figure B.1.

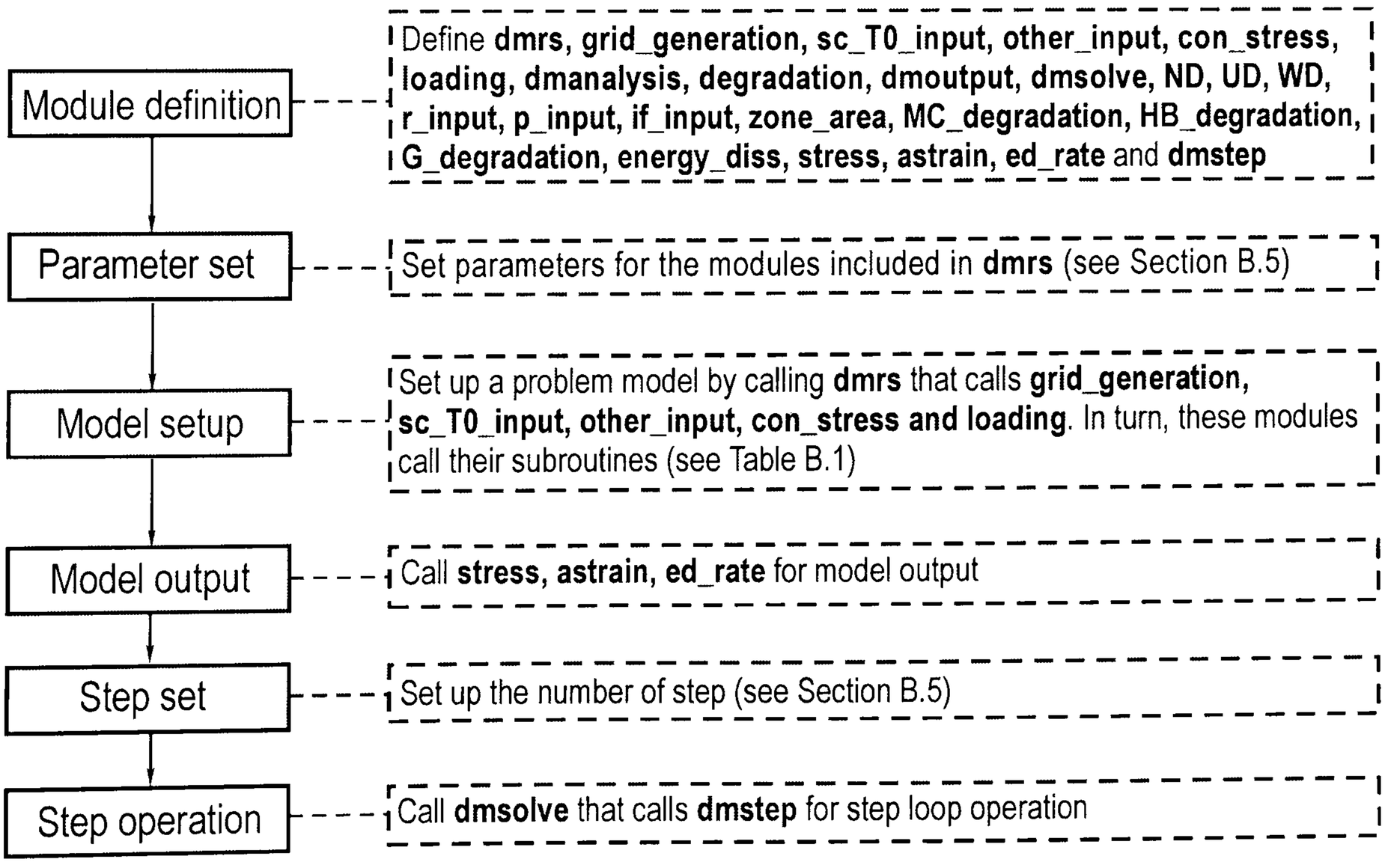


Figure B.1. Operation procedures for FLAC degradation model code for rock specimens

B.4 Code listing

```
; ************************************************************************

; Code for the local degradation model for rock specimens.

; In this code, global variables have the prefix 'dm_', and local variables within
; procedures have either similar form to the associated equations, or the prefix ;
; 'xy_', where 'xy' is an abbreviation of the procedure, eg. procedure 'stress' has
; local variables 'st_...'.

; criterion=1 for MC, 2 for HB and 3 for Griffith criterion

; distribution=1 for UD, 2 for ND and 3 for WD

; dm=1 for degradation and zero for non-degradation operation


; The structure of this file is:

;  1) memory configuration

;  2) procedure and command definitions

;  3) model operation


; ************************************************************************

;-----------------------------------------------------------------------

; Memory Configuration

;-----------------------------------------------------------------------


config extra 15                    ; configure extra memory for a grid


;-----------------------------------------------------------------------

; Procedure and Command Definitions

;-----------------------------------------------------------------------


def dmrs                           ; main function for model analysis

  grid_generation                  ;

  sc_T0_input                      ;

  other_input                      ;

  con_stress                       ;

  loading

end
```

```
def grid_generation
  ; required parameters: dm_width, dm_rl, dm_ph, dm_iz, dm_jz and dm_zp
  ; dm_width: rock specimen width in m
  ; dm_rl: rock specimen length in m
  ; dm_ph: platen height in m
  ; dm_iz: total zone number in i direction
  ; dm_jz: total zone number in j direction
  ; dm_zp: zone layer number for platens
  ; ------------------------------------------

  ; grid geometry calculation
  gg_x=dm_width                    ; maximum x layout
  gg_y1=dm_ph                      ; height to top of bottom platen
  gg_y2=dm_ph+dm_rl                ; height to top of specimen
  gg_y3=gg_y2+dm_ph                ; height to top of upper platen

  ; i & j limits for rock specimen
  dm_irz=dm_iz                     ; total zone number in i direction for specimen
  dm_jrz=dm_jrtz-dm_jrbz+1         ; total zone number in j direction for specimen
  dm_irlz=1                        ; i-zone for rock left
  dm_irrz=dm_iz                    ; i-zone for rock right
  dm_irlgp=1                       ; i-gp for rock left
  dm_irrgp=dm_iz+1                 ; i-gp for rock right
  dm_jrbz=dm_zp+2                  ; j-zone for rock bottom, less 1 for interfaces
  dm_jrbgp=dm_jrbz                 ; j-gp for rock bottom
  dm_jrtz=dm_jz-dm_zp-1            ; j-zone for rock top
  dm_jrtgp=dm_jrtz+1               ; j-gp for rock top

  ; i & j limits for platens
  dm_jpboz=1                       ; outer j-zone for bottom platen
  dm_jpbogp=dm_jpboz               ; outer j-gp for bottom platen
  dm_jpbiz=dm_zp                   ; inner j-zone for bottom platen
  dm_jpbigp=dm_jpbiz+1             ; inner j-gp for bottom platen
  dm_jptoz=dm_jz                   ; outer j-zone for top platen
  dm_jptogp=dm_jptoz+1             ; outer j-gp for top platen
```

```
dm_jptiz=dm_jz-dm_zp+1              ; inner j-zone for top platen
dm_jptigp=dm_jptiz                  ; inner j-gp for top platen
dm_iplgp=1                          ; i_gp for platen left
dm_iprgp=dm_irrgp                   ; i_gp for platen right

; grid and geometry generation
command
  ; grid generation
   grid dm_iz dm_jz
   m e j dm_jpboz  dm_jpbiz       ; Fish elastic model for bottom platen
   m e j dm_jptiz  dm_jptoz       ; Fish elastic model for top platen
   m m j dm_jrbz   dm_jrtz        ; Fish Mohr-Coulomb model for rock specimens
   ; geometry generation
   gen 0,0 0,gg_y1 gg_x,gg_y1 gg_x,0 i=1,dm_irrgp j=1,dm_jpbigp
   gen 0,gg_y1 0,gg_y2 gg_x,gg_y2 gg_x,gg_y1 i=1,dm_irrgp j=dm_jrbgp,dm_jrtgp
   gen 0,gg_y2 0,gg_y3 gg_x,gg_y3 gg_x,gg_y2 i=1,dm_irrgp j=dm_jptigp,dm_jptogp
  end_command
end

def sc_T0_input
  ;
  ; input sc and T0
  ;
  if distribution=1 then                ; check for UD
    UD
  else
  if distribution=2 then                ; check for ND
    ND
  else
    if distribution=3 then              ; check for WD
      WD
    end_if
  end_if
```

```
  end_if
end




def UD
  ;
; uniform distribution
;
; parameters required: ud_sc_a, ud_sc_b, ud_st_a and ud_st_b
; ud_sc_a and ud_sc_b: lower and upper bounds for sc
; ud_st_a and ud_st_b: lower and upper bounds for sc/T0
loop i (1,izones)
  loop j (dm_jrbz,dm_jrtz)
    u_rand1=urand                          ; random uniform number between 0 and 1
    u_rand2=urand                          ; obtain another random number
    ud_ts_a=1.0/ud_st_a                    ; convert sc/T0 to T0/sc
    ud_ts_b=1.0/ud_st_b                    ; convert sc/T0 to T0/sc
    ex_5(i,j)=ud_sc_a * (1.0-u_rand1) + ud_sc_b * u_rand1      ; initial sc
    ud_ts=ud_ts_a * (1.0-u_rand2) + ud_ts_b * u_rand2          ; T0/sc
    tension(i,j)=ex_5(i,j)*ud_ts                               ; T0
  end_loop
 end_loop
end




def ND
;
; normal distribution
;
; parameters required are: nd_sc nd_st nd_sdev and nd_stdev
;nd_sc: mean for u/x comp. strength
;nd_st: mean for tensile strength
;nd_sdev: deviation for u/x comp. strength
```

```
;nd_stdev: deviation for sc/T0
command                                          ; assign sc and sc/T0 ratio
  prop cohesion nd_sc rdev nd_sdev i dm_irlz dm_irrz j dm_jrbz dm_jrtz      ;sc
  prop tension nd_st rdev nd_stdev i  dm_irlz dm_irrz j dm_jrbz dm_jrtz     ;sc/T0
end_command
; replace variable for sc and calculate T0
loop i (1,izones)
  loop j (dm_jrbz,dm_jrtz)
    nd_ts=1.0/tension(i,j)                       ; convert sc/T0 to T0/sc
      ex_5(i,j)=cohesion(i,j)                    ; replacing variables for sc
      tension(i,j)=ex_5(i,j)*nd_ts               ; T0
    end_loop
  end_loop
end
```

```
def WD
;
; weibull distribution
;
; parameters required: wd_sc_0, wd_sc_u, wd_st_0, wd_st_u and wd_m
; wd_sc_0 and wd_sc_u: scale and location parameters for sc
; wd_st_0 and wd_st_u: scale and location parameters for sc/T0
; wd_m: shape parameter
wd_ts_0=1.0/wd_st_0                              ; convert sc/T0 to T0/sc
wd_ts_u=1.0/wd_st_u                              ; convert sc/T0 to T0/sc
; distribute sc and T0
  loop i (1,izones)
    loop j (dm_jrbz,dm_jrtz)
      ex_5(i,j)=wd_sc_0*(-ln(1.0-urand))^(1/wd_m)+wd_sc_u                    ; sc
      tension(i,j)=ex_5(i,j)*(wd_ts_0*(-ln(1-urand))^(1/wd_m)+wd_ts_u)      ; T0
    end_loop
  end_loop
end
```

```
def other_input
  ;
  ; input other parameters of the model
  ;
  r_input
  p_input
  if_input
  zone_area
end



def r_input
  ;
  ; assign variables to zones for rock specimens
  ;
  ; parameters required:  dm_rei, dm_rpr, dm_rdila, dm_ratio and dm_rdens
  ; dm_rei: initial rock Young's modulus
  ; dm_rpr: Poisson's ratio for rock
  ; dm_rdila: dilation angle for rock
  ; dm_ratio: degradation ratio
  ; dm_rdens: rock density

dm_grad=1.0/degrad                          ; rad to deg conversion

loop i (1,izones)
  loop j (dm_jrbz,dm_jrtz)
  s_c=ex_5(i,j)                             ; restore sc
  s_i=1.0                                   ; intact H-B parameter s
  m_i=s_c/tension(i,j) - tension(i,j)/s_c   ; intact H-B parameter m_i
  k_i=1.0+0.5*m_i/s_i^(0.5)                 ; slope of s1--s3 line
  dm_rshear=0.5*dm_rei/(1.0+dm_rpr)         ; rock shear modulus
  dm_rbulk=dm_rei/(3*(1.0-2.0*dm_rpr))      ; rock bulk-modulus
  shear_mod(i,j)=dm_rshear                  ; input shear modulus
```

```
bulk_mod(i,j)=dm_rbulk                          ; input bulk modulus
temp1=sqrt(k_i)
friction(i,j)=2*atan(temp1)*dm_grad-90          ; friction angle
cohesion(i,j)=0.5*s_c/temp1                     ; cohesion
density(i,j)=dm_rdens                           ; density
dilation(i,j)=dm_rdila                          ; rock dilation angle
ex_1(i,j)=0.0                                   ; degradation index
ex_2(i,j)=dm_rei                                ; initial Young's mod.
ex_3(i,j)=dm_rei*dm_ratio                       ; u/x comp. degraded secant mod.
ex_4(i,j)=dm_rei                                ; degraded secant mod. (as initial
                                                ; value if no degradation)

ex_6(i,j)=cohesion(i,j)                         ; initial cohesion
ex_7(i,j)=tension(i,j)                          ; initial tensile strength
ex_8(i,j)=cohesion(i,j)*dm_ratio                ; degraded cohesion in u/x comp.
ex_9(i,j)=m_i                                   ; H-B m_i for intact elements
ex_10(i,j)=m_i                                  ; H-B m_i for degraded elements
ex_11(i,j)=s_i                                  ; H-B s for degraded elements (as
                                                ; initial value if no degradation)
      ex_12(i,j)=tension(i,j)                   ; Griffith tensile strength for
                                                ; degraded  elements (as initial
                                                ; value if no degradation)

    end_loop
  end_loop
end



def p_input
;
; assign variables to zones for platens
;
; parameters required:  dm_pei, dm_ppr, dm_pdens
; dm_pei: platen Young's modulus
; dm_ppr: Poisson's ratio for platen
; dm_pdens: platen density
```

```
;calculate platen shear and bulk moduli
dm_pshear=0.5*dm_pei/(1.0+dm_ppr)                    ; platen shear modulus
dm_pbulk=dm_pei/(3*(1.0-2.0*dm_ppr))                 ; platen bulk modulus
; assign density and moduli for platens
command
  prop dens=dm_pdens  j dm_jpboz  dm_jpbiz                  ; bottom platen
  prop dens=dm_pdens  j dm_jptiz  dm_jptoz                  ; top platen
  prop bulk=dm_pbulk shear=dm_pshear j=dm_jpboz,dm_jpbiz    ; bottom platen
  prop bulk=dm_pbulk shear=dm_pshear j=dm_jptiz,dm_jptoz    ; top platen
end_command

end



def if_input
  ;
  ; set interfaces (between the platens and sample ends) and properties
  ;
  ; parameters required: if_ratio, if_fri
  ;if_ratio: interface/surrounding stiffness ratio
  ;if_fri: interface friction angle
  ifi1=1                ; left i
  ifi2=dm_irrgp         ; right i
  ifj1=dm_jpbigp        ; bottom i for interface 1
  ifj2=dm_jrbgp         ; top i for interface 1
  ifj3=dm_jrtgp         ; bottom i for interface 2
  ifj4=dm_jptigp        ; top i for interface 2
  ; determine shear and bulk moduli for calculation of interface stiffness
  if dm_pei > dm_rei then
    if_shear=dm_pshear
    if_bulk=dm_pbulk
  else
    if_shear=dm_rshear
    if_bulk=dm_rbulk
```

```
end_if
; determine interface stiffness
if_s=if_ratio*(if_bulk + 4.0 * if_shear/3.0)/dm_ph
; set interfaces and properties
command
  ; interface 1
  int 1 Aside from ifi1,ifj1 to ifi2,ifj1 Bside from ifi1,ifj2 to ifi2,ifj2
    ; interface 2
    int 2 Aside from ifi1,ifj3 to ifi2,ifj3 Bside from ifi1,ifj4 to ifi2,ifj4
    int 1 ks=if_s kn=if_s fric=if_fri     ; properties for interface 1
    int 2 ks=if_s kn=if_s fric=if_fri     ; properties for interface 2
  end_command
end



def zone_area
  ;
  ; compute rock zone area
  ;
  delt_x=dm_width/dm_irz                  ; rock zone length in x-direction
  delt_y=dm_rl/dm_jrz                     ; rock zone length in y-direction
  delt_A=deltx*delt_y                     ; rock zone area
end



def con_stress
;
; apply confining pressure
;
; parameter required: st_con and cp_step
; st_con: confining stress
; cp_step: steps for equilibrium
command
```

```
app pres st_con i dm_irlgp j dm_jrbgp dm_jrtgp     ; rock left
app pres st_con i dm_irrgp j dm_jrbgp dm_jrtgp     ; rock right
app pres st_con i dm_iplgp j dm_jpbogp dm_jpbigp   ; bottom platen left
app pres st_con i dm_iprgp j dm_jpbogp dm_jpbigp   ; bottom platen right
app pres st_con i dm_iplgp j dm_jptigp dm_jptogp   ; top platen left
app pres st_con i dm_iprgp j dm_jptigp dm_jptogp   ; top platen right
app pres st_con j dm_jpbogp                        ; top of top platen
app pres st_con j dm_jptogp                        ; bottom of bottom platen
step cp_step                                       ; step for equilibrium
end_command
end



def loading
;
; apply loading
;
; parameters required: yv_up and yv_down
;yv_up: bottom platen velocity
;yv_down: top platen velocity
command
fix  y j=dm_jpbogp
fix  y j=dm_jptogp
initial yv yv_up  j=dm_jpbogp      ; bottom platen
initial yv yv_down  j=dm_jptogp    ; top platen
end_command
end

def dmanalysis
;
; model analysis
;
```

```
  if dm=1 then                                    ; degradation operation?
     ; perform degradation procedure once a cycle
    while_stepping
    degradation
  end_if
end
```

```
def degradation
  ;
  ; degradation operation
  ;
  ; additional parameters required: n_d
  ; n_d: degradation parameter
  loop i (1,izones)
    loop j (dm_jrbz,dm_jrtz)
      ; convert stress sign convention
      dmsxx=-sxx(i,j)
      dmsyy=-syy(i,j)
      dmsxy=-sxy(i,j)
      dmszz=-szz(i,j)
      ; calculate minor principal stress (Eq. 5-28)
      temp1=0.5*(dmsxx+dmsyy) ;
      temp2=sqrt(dmsxy^2+0.25*(dmsxx-dmsyy)^2)
      s3=min(temp1-temp2,dmszz)
      s_c=ex_5(i,j)                    ; restore initial u/x compressive strength
      if state(i,j) = 1 then           ; check shear failure
        ex_14(i,j)=1.0                 ; shear failure indicator
        r_d=exp(-s3*1e-6*n_d)          ; degradation index
        if r_d > ex_1(i,j) then        ; check degradation
          ; compute stiffness degradation
          d_E=r_d*ex_3(i,j)            ; Eq. 4-37
          E_d=ex_2(i,j)-d_E            ; Eq. 4-38
          ; compute moduli degradation
```

```
shear_mod(i,j)=0.5*E_d/(1+dm_rpr)       ; degraded Shear modulus
bulk_mod(i,j)=E_d/(3.0*(1-2*dm_rpr))    ; degraded Bulk modulus
; compute degraded uniaxial compressive strength
d_sc=r_d*ex_8(i,j)                      ; Eq. 4-37
s_cd=s_c-d_sc                           ; Eq. 4-38
; degradation operation
if criterion=1 then
  MC_degradation                        ; degradation with MC criterion
else
  if criterion=2 then
    HB_degradation                      ; degradation with HB criterion
  else
    if criterion=3
      G_degradation                     ; degradation with G criterion
    end_if
  end_if
end_if
    energy_diss                         ; elemental strain energy dissipation
    ex_1(i,j)=r_d
    ex_4(i,j)=E_d                       ; update stiffness degradation
  end_if
end_if
if state(i,j) = 3 then                  ; check tensile failure
  ex_15(i,j)=1.0                        ; tensile failure indicator
  r_d=exp(-s3*1e-6*n_d)                 ; degradation index
  if r_d > ex_1(i,j) then               ; check degradation
    ; compute stiffness degradation
    d_E=r_d*ex_3(i,j)                   ; Eq. 4-37
    E_d=ex_2(i,j)-d_E                   ; Eq. 4-38
    ; compute moduli degradation
    shear_mod(i,j)=0.5*E_d/(1+dm_rpr)       ; degraded shear modulus
    bulk_mod(i,j)=E_d/(3.0*(1-2*dm_rpr))    ; degraded bulk modulus
    ; compute degraded uniaxial compressive strength
    d_sc=r_d*ex_8(i,j)                  ; Eq. 4-37
    s_cd=s_c-d_sc                       ; Eq. 4-38
```

```
; degradation operation
if criterion=1 then
  MC_degradation                ; degradation with MC criterion
else
  if criterion=2 then
    HB_degradation              ; degradation with HB criterion
  else
      if criterion=3
        G_degradation           ; degradation with G criterion
      end_if
    end_if
  end_if
  energy_diss                   ; elemental strain energy dissipation
  ex_1(i,j)=r_d                 ; update stiffness degradation
  ex_4(i,j)=E_d
 end_if
end_if
  end_loop
 end_loop
end
```

```
def MC_degradation
  ;
  ; degradation with Mohr-Coulomb criterion
  ;
  cohesion(i,j)=ex_6(i,j)*s_cd/s_c          ; Eq. 5-32
  if tension(i,j) # 0.0 then                ; check tensile strength
    tension(i,j)=ex_7(i,j)*s_cd/s_c         ; equiv. tensile strength degradation
  end_if
end
```

```
def HB_degradation
  ;
  ; degradation with Hoek_Brown criterion
  ;
  m_i=ex_9(i,j)                                    ; restore intact H-B parameter m
  s_d=(s_cd/s_c)^2.0                               ; Eq. 4-57
  m_d=m_i*exp((9*ln(s_d))/28.0)                    ; Eq. 4-58
  temp1=1.0/(m_d*s3/s_c+s_d)^(0.5)
  k_hd=1.0+0.5*m_d*temp1                           ; Eq. 5-17
  s_chd=(0.5*m_d*s3+s_d*s_c)*temp1                 ; Eq. 5-18
  temp2=sqrt(k_hd)
  cohesion(i,j)=0.5*s_chd/temp2                    ; Eq. 5-19
  friction(i,j)=2*atan(temp2)*dm_grad-90           ; Eq. 5-20
  if tension(i,j) # 0.0 then                       ; check tensile strength
    tension(i,j)=0.5*s_c*(sqrt(m_d^2+4*s_d)-m_d)   ; tensile strength
  end_if
  ex_10(i,j)=m_d
  ex_11(i,j)=s_d
end
```

```
def G_degradation
  ;
  ; degradation with Griffith criterion
  ;
  T_0d=s_cd*0.125                                  ; Eq. 4-59
  temp1=sqrt(T_0d/(s3+T_0d))
  k_gd=1.0+2.0*temp1                               ; Eq. 5-21
  s_cgd=4.0*T_0d+(2.0*s3+4.0*T_0d)*temp1           ; Eq. 5-22
  temp2=sqrt(k_gd)
  cohesion(i,j)=0.5*s_cgd/temp2                    ; Eq. 5-24
  friction(i,j)=2*atan(temp2)*dm_grad-90           ; Eq. 5-25
  if tension(i,j) # 0.0 then                       ; check tensile strength
    tension(i,j)=T_0d                              ; equiv. tensile strength degradation
```

```
  end_if
  ex_12(i,j)=T_0d                                    ; update T_0d
end

def energy_diss
  ;
  ; calculation of elemental strain energy dissipation
  ;
  E_0=ex_4(i,j)                                      ; restore Young's modulus
  temp1=dm_rpr*E_0/((1.0+dm_rpr)*(1.0-2.0*dm_rpr))   ; Eq. 4-80
  temp2=0.5*E_0/(1.0+dm_rpr)                         ; Eq. 4-81
  temp3=(1.0+dm_rpr)/E_0
  temp4=dm_rpr*(dmsxx+dmsyy)
  temp5=temp3*(dmsxx-temp4)                          ; Eq. 5-33
  temp6=temp3*(dmsyy-temp4)                          ; Eq. 5-34
  temp7=temp3*dmsxy                                  ; Eq. 5-35
  temp8=temp5+temp6                                  ; sum of strain components
  u_e0=0.5*temp1*temp8^2+temp2*(temp5^2+temp6^2+temp7^2) ; Eq. 4-82
  d_ued=(1.0-E_d/E_0)*u_e0*delt_A                    ; Eq. 4-83
  ex_13(i,j)=ex_13(i,j)+d_ued
end

def stress
  ;
  ; compute axial stress
  ;
  ; st_sum: summation of axial stresses
  ; st_ave: average axial stress
  ; st_dif: axial differential stress
  ; st_con: confining stress
  st_sum=0.0
```

```
loop i (1,izones)                          ; summation function
  loop j (dm_jrbz,dm_jrtz)
    dmsyy=-syy(i,j)                        ; change to tension positive
    st_sum=st_sum+dmsyy                    ; summation over all zones
  end_loop
end_loop
st_ave=st_sum/(dm_irz*dm_jrz)              ; average axial stress
  st_dif=st_ave-st_con                     ; axial differential stress
  stress=st_dif
end




def astrain
  ;
  ; compute axial strain
  ;
  ; ast_sum: summation of axial strains
  ; ast_ave: average axial strains
  ast_sum = 0.0
  loop i (1,izones)                        ; summation function
    ast_sum=ast_sum+(ydisp(i,dm_jrbgp)-ydisp(i,dm_jrtgp))/dm_rl
  end_loop
  ast_ave=ast_sum/dm_irz                   ; average axial strain
  astrain=ast_ave
end


def ed_rate
  ;
  ; calculate strain energy dissipation rate over entire body
  ;
  ; ed_temp: temporary variable for strain energy dissipation
  ed_temp=0.0                              ; reset to zero
```

```
loop i (1,izones)
  loop j (dm_jrbz,dm_jrtz)
    if ex_13(i,j) # 0.0 then          ; degradation determination
      ed_temp=ed_temp + ex_13(i,j)    ; summation
    end_if
    ex_13(i,j)=0.0                    ; reset to zero
  end_loop
  ed_rate=ed_temp
end
```

```
def dmoutput
  ;
  ; model output
  ;
  command
    hist nstep 50                     ; recording interval
    hist stress                       ; history 1 (axial stress)
    hist astrain                      ; history 2 (axial strain)
    hist ed_rate                      ; history 3 (energy dissipation rate)
  end_command
end
```

```
def dmstep
  ;
  ; step monitor
  ;
  if dmns=0.0 then
    dmns=10                           ; minimum no. of steps
  end_if
  command
```

```
    step dmns
    print ns
  end_command
end

def dmsolve
  ;
  ; step loop operation
  ;
  loop dmls (dmls1,dmls2)
    loop ns (1,dmnsup)
      dmstep                                ; step monitor
    end_loop
  end_loop
end

;-----------------------------------------------------------------------
; Model Operation
;-----------------------------------------------------------------------

; set variables for grid_generation
set dm_iz 30
set dm_jz 76
set dm_zp= 1
set dm_ph 0.025
set dm_rl 0.12
set dm_width 0.05
; set variables for sc and T0 distribution
; (UD, distribution=1)
set ud_sc_a 70e6
set ud_sc_b 270e6
set ud_st_a 30
set ud_st_b 3
```

```
; (ND, distribution=2)
set nd_sc 1e8
set nd_st 15
set nd_sdev 1e6
set nd_stdev 3
; (WD, distribution=3)
set wd_sc_0=100e6
set wd_sc_u=30e6
set wd_st_0=10
set wd_st_u=30
set wd_m=2.5
; set variables for deformation properties
set dm_rei=30e9
set dm_pei=30e10
set dm_rdila=4.0
set dm_rdens=2300
set dm_pdens=2300
set dm_rpr=0.25
set dm_ppr=0.25
; set variables for interfaces
set if_ratio 10
set if_fri 10
; set variables for confinement and equilibrium
set st_con 2e7
set cp_step=2000
; set loading condition
set yv_up 1e-8
set yv_down -1e-8
;set variables for degradation properties
set dm_ratio=0.1
set n_d=0.05              ; set degradation parameter n_d

set distribution=3        ; choice of distribution
set criterion=2           ; choice of strength criterion
```

```
dmrs                        ; call main analysis function

dmoutput                    ; call function for model output


; set variables for model analysis

set dmls1=1 dmls2=5

set dmns=50 dmnsup=60

set dm=1                    ; degradation operation

dmsolve                     ; perform analysis

ret                         ; return to command mode
```